Corrosion Behaviour of Proprietary Micro-alloyed Steels

Lawrence Ibe Onyeji

School of Chemical and Process Engineering (SCAPE)

University of Leeds

Submitted in accordance with the requirements for the degree of
Doctor of Philosophy

November 2018

Declaration of Originality

The candidate confirms that the work submitted is his own, except where work that has formed part of jointly authored publications has been included. The contribution of the candidate and the other authors to this work has been explicitly indicated below. The candidate also confirms that appropriated credit has been given within the thesis where reference has been made to the work of others.

This copy has been supplied on the understanding that it is copyright material and that no quotation from the thesis may be published without proper acknowledgement.

Publication Statements

In all the papers listed below, the primary author completed all the experimental studies, evaluation of data and preparation of publications. In the third paper, the second author conducted the profilometry analysis while the third author proof read all the papers prior to publication.

Papers contributing to this thesis:

1. Onyeji, L., G. M. Kale and B. M. Kermani, "Comparative Studies of the effect of Microstructures on the Corrosion Behaviour of Micro Alloyed Steels in Unbuffered 3,5 wt% NaCl Saturated with CO_2", World Academy of Science, Engineering and Technology (WASET), International Journal of Chemical, Molecular, Nuclear, Materials and Metallurgical Engineering, 2017, 11(2): p. 131-138.
2. Onyeji, L. and G. Kale, "Preliminary Investigation of the Corrosion Behaviour of Proprietary Micro-alloyed Steels in Aerated and Deaerated Brine Solutions", Journal of Materials Engineering and Performance, 2017 Vol 26(1): p. 1-12.
3. Onyeji, L., S. Mohammed and G. Kale, "Electrochemical response of micro-alloyed Steels under potentiostatic polarization in CO_2 saturated brine", Corrosion Science, 138(2018): p. 145-153.
4. Lawrence I. Onyeji and Girish M. Kale, "Corrosion Performance of High Strength-Low Alloyed Steels in Aerated and CO_2 Saturated Lyman Fleming Solution" (Expanded Abstract), in Conference Proceedings of 2017 MS&T Conference held at David I. Lawrence Convention Centre, Pittsburgh, Pennslyvania for October 8-12, 2017.

© *2018 The University of Leeds and Lawrence Ibe Onyeji*

Acknowledgements

To God Almighty who began this research work with me, sustained and brought it to a successful and fulfilled end, be all the glory for ever and ever.

I sincerely appreciate the unrelenting support, encouragement, guidance and accommodating spirit of my supervisor, Dr Girish Kale that propelled this research through seemingly unsurmountable hurdles to this undeniable fruitful end. Dr Girish was everything, a friend, a brother, a mentor, a boss, a teacher and even a times a father which culminated to the success of this Thesis. His leadership quality linked members (both past and present) of his researched group with a family bond that evolved into a synergistic academic force and focus. I therefore say thank you to Steve, Mohammed, Philip, Sri and Suneela who like a team supported me throughout the course of this research.

My gratitude goes to Petroleum Technology Development Fund (PTDF), Nigeria for sponsoring and funding this research.

Late Professor Mathew Obichukwu Edoga, unfortunately you did not live to witness this great feat you initiated and facilitated because the cold hand of death snatched you from us on the 27th of July 2018. Nevertheless, I acknowledge the labour of love you showed to me and my family from the time I began this programme until your death. May God grant your soul eternal rest.

I thank Dr. James Young, Deputy Head, School of Chemical and Process Engineering (SCAPE) for his wise counsels in time of trials. With great pleasure I wish to recognise the assistance of all the Technical staff and Post-Docs of SCAPE. I am also grateful to my fellow PGRs particularly Steven Parirenyatwa, Maje Haruna and Kwabena Offeh Gyimah for their encouragement and motivation.

I am indebted to the entire members of IFS research institute, School of Mechanical Engineering under the leadership of Professor Anne Neville OBE. Sikiru Mohammed, Richard Barkar and Frederick Oritseweneye Pessu were undeniably helpful.

I wish to express my profound appreciation to my mother Mrs Anne Onyeji for her sleepless night in prayer, inspirational words and care. I cannot forget to say thank you to

members of my family Engr M. I. Ezedinma, Professor C. O. Onyeji, Messer M. Didigwu, S. O. Ezike, S. Akubue, B. O. Onyeji, Ify Onyeji and their families. I appreciate the prayers of all the members of Onyejekwe family. May God continue to bind us together in His love and unity.

Mr James Ugada and family, you made UK a home out of home for me and my family. May God bless and reward you all. Lastly to my wife, Mrs Dorcas Bose Onyeji, you have been a dependable pillar of support, may the glory of God continue to shine in and through you. Finally to my sweet children Joshua, Mary, Martha, Love and Ruth may you continue to be sources of pleasure and gladness. I love you all.

Abstract

Oil and gas industry is a strategic industry being of central importance for global economy as a vital source of energy for all other sectors of engineering industry. This vital role is being challenged as the important reserves of oil and gas which are left to be discovered and produced are mainly concentrated in difficult locations which are under severe operational conditions of high pressure, high temperature and aggressive environments. Therefore the materials and the technology required for exploration, production and transportation must possess appropriate properties considering the excessive cost of replacements or failures in these difficult-to-access locations.

Carbon steel because of its tremendous and inherent properties such as low cost; easy to shaping, forming and machining; good weldability; wide availability; its properties have been studied in depth and are well understood; good mechanical properties etc is preferred over all other conventional engineering materials and has found extensive use in the oil and gas industry. However, carbon steels are susceptible to corrosion attack particularly in harsh oilfield environments thus affecting the capital expenditure (CAPEX), operational expenditure (OPEX) and health, safety and environment (HSE). Regardless of these disadvantages, carbon steel still remains the material of choice because no alternative materials have adequately exhibited better properties for oil and gas applications. Therefore efforts are being continuously made to improve the properties of carbon steel through diverse physical, chemical and thermo-mechanical processes with the aim of developing new materials which are stronger, lighter, and more resistant to corrosion.

The quest to mitigate the corrosion susceptibility of carbon and low alloy steels for effective use as structural materials in oil and gas industry particularly in challenging locations and under severe conditions has led to the development of micro-alloyed steels. For the past six decades when micro-alloying was generally accepted, micro-alloy steels have become an indispensable class of structural materials providing desirable combinations of properties such as strength, toughness, formability, weldability, and corrosion resistance at affordable cost. This excellent combination of properties can be attributed to the presence of fine grain structures occasioned by the addition of small quantity of alloying elements, controlled processing technologies and appropriate heat treatments. Most of the elements located at the left of iron in the periodic table are

considered as strong carbide-formers. These elements have found extensive application in micro-alloying of steels. Among these elements, Zr and Hf have not received comparative application like the other neighbouring elements such as Ti, V, Nb, and Cr.

A comparative and systematic assessment of the corrosion behaviour of three proprietary micro-alloy steels designated as (i) ASTM A694-F65 forged steel bar (F65) (ii) improved collapsed grade P110 IC pipe (P110) and (iii) high collapsed sour service grade TN95 HS pipe (TN95) were conducted in different media/electrolytes using different environmental parameters, electrochemical techniques (Linear polarization resistance (LPR), Tafel polarization (TP), Electrochemical impedance spectroscopy (EIS) and potentiostatic polarization (PP)), weight loss measurements and surface analyses. API 5L X65 steel grade (X65) was used as reference sample. The results of the preliminary investigations showed that the corrosion rates of these micro-alloy steels using different electrochemical techniques and in all the environments corroborated each other and revealed a ranking order of F65 < X65 < P110 < TN95. The main reasons for this behaviour were microstructure and chemical composition of the respective microalloy samples.

The two worst corrosion rate steels (P110 IC and TN95 HS) were selected for alloying with different quantities (0.1, 0.2 and 0.4 wt%) of Zr and Hf with a view to improving their corrosion resistance. The analysis of the alloyed specimens showed microstructural modification exhibiting grain refinement with increase in alloying elements (Zr and Hf). This was attributed to the formation of Zr- and/or Hf-base intermetallic precipitates. These precipitates have the ability to pin down grain boundaries thus limiting grain growth which resulted in improved mechanical properties such as increased hardness and tensile strength without any negative impact on toughness of the alloyed samples. The alloyed steels were subjected to corrosion tests in simulated produced water (SPW) saturated with 99.98% CO_2 at 25^0C and pH 6.5. The results showed that the specimens alloyed with Zr and Hf exhibited superior corrosion resistance than the unalloyed and the reference samples with the corrosion rate of the alloyed steel decreasing with increase in the quantity of alloying elements. This signified that Zr and Hf has suppressive effect on electrochemical reactions thus leading to passivation with the resultant improvement in corrosion resistance ranging from 3% - 35% for Hf addition and 27% - 44% for Zr addition in TN95. This can be attributed to higher dissolution with the corresponding formation of more intermetallic precipitate of Zr in Fe than Hf.

Table of Contents

Declaration of Originality i
Acknowledgements ii
Abstract iv
List of Figures x
List of Tables xxiii
Symbols and Abbreviations xxvi
Chapter 1: Introduction 1
1.1 Background 1
1.1.1 Corrosion defined 2
1.1.2 Cost of corrosion 4
1.1.3 Micro-alloyed Steels 8
1.1.4 Zirconium (Zr) and Hafnium (Hf) 13
1.2 Aim and scope of study 14
1.3 Objectives 15
1.4 Hypothesis 17
1.5 Novelty 18
1.6 Thesis layout 19
Chapter 2: Theory of micro-alloying and corrosion mechanism 21
2.1 Metallurgy and the development of micro-alloy steel 21
2.1.1 Definitions and types of micro-alloy steels 23
2.1.2 Design concepts of micro-alloyed steels 25
2.1.3 Solubility of micro-alloy precipitates 29
2.1.4 Zirconium (Zr) and Hafnium (Hf) as alloying elements 32
2.2 Theory of electrochemical corrosion 37
2.2.1 Mixed potential theory 39
2.2.2 The Thermodynamics of Corrosion 41
2.2.3 Kinetics of electrochemical corrosion 42
2.3 Types of electrochemical corrosion 43
2.4 Corrosion and measurement techniques 44
2.4.1 Weight loss measurement 44
2.4.2 Electrochemical corrosion and measurement techniques 45
2.4.3 Resistance polarization (IR-drop) effects 51
2.4.4 Electrochemical impedance spectroscopy (EIS) 52

Chapter 3: Literature Review **56**

3.1 Application of Micro-alloying Technology in Enhancing Corrosion Resistance 56

3.2 Carbon Dioxide (Sweet) Corrosion 61

3.2.1 Electrochemistry and mechanism of carbon dioxide (CO_2) corrosion 62

3.2.2 Electrochemistry of CO_2 corrosion, ... 62

3.2.3 Key factors affecting CO_2 corrosion 65

Chapter 4: Materials and Experimentations **86**

4.1 Materials Preparation, Characterization, Examinations and Analysis 86

4.1.1 Materials 86

4.1.2 Materials (Samples) Preparations 87

4.1.3 Materials Characterization. 90

4.2 Corrosion Tests 95

4.2.1 Weight Loss 95

4.2.2 Electrochemical Corrosion Techniques 96

4.2.3 Experimental Set up for this study 99

4.2.4 Electrochemical corrosion tests 101

4.3 Investigations in 99.98% (pure) CO_2 108

4.3.1 Assessing the propensity of the Micro-alloyed Steels to form $FeCO_3$ in 3.5 wt% NaCl solution saturated with 99.98% CO_2. ... 108

4.4 Alloying of micro-alloyed steels with Zr and Hf. 109

4.4.1 Weight of added alloying elements (Zr and Hf) 109

4.4.2 Alloying of samples 111

4.4.3 Microstructural, chemical and mechanical properties of the alloyed samples 113

4.4.4 Electrochemical Behaviour of the alloyed samples 114

Chapter 5: Results **115**

5.1 Preliminary investigations of the effects of environmental and materials parameters on the corrosion behaviour of micro-alloy steels. 115

5.1.1 Characterization and identification of the as-supplied samples ... 115

5.1.2 Weight Loss in naturally aerated 3.5 wt% NaCl 118

5.1.3 Effect of NaCl concentrations on the corrosion behaviour of micro alloy steels in aerated and de-aerated environment 119

5.1.4 Effect of temperature on the corrosion behaviour of the steels in 3.5 wt% NaCl solution saturated with 0.5% CO_2 131

5.1.5 Effect of pH on the corrosion behaviour of the steels in 0.5 % CO_2 environments 142

5.1.6 Assessing the corrosion behaviour of the micro-alloyed steels in simulated seawater (Lyman and Fleming solutions). 150

5.1.7 Assessing the corrosion behaviour of the micro-alloyed steels in 3.5 wt% NaCl using potentiostatic polarization and electrochemical impedance spectroscopy (EIS). 157

5.1.8 Further investigation in 3.5 wt% NaCl saturated with 99.98% CO_2 174

5.2 Alloying of steels P110 and TN95 with Zr and Hf and investigating the corrosion behaviour of these alloyed specimens in simulated produce water (SPW) 198

5.2.1 Characterization of alloyed specimens 198

5.2.2 Corrosion behaviour of steels P110 and TN95 alloyed with Zr and Hf in simulated produce water (SPW) 205

Chapter 6: Discussions 218

6.0 Influence of environmental and materials parameters on the corrosion of micro-alloyed steels. 218

6.1 Microstructures of the as-received micro-alloyed steels 219

6.2 Weight Loss 222

6.3 Effect of NaCl concentrations in aerated and de-aerated environment 223

6.3.1 Tafel extrapolation results on the effect of NaCl concentrations in aerated and de-aerated environment 227

6.4 Effect of temperature on the corrosion behaviour of the steels in 0.5 % CO_2 environments 228

6.5 Effect of pH on the corrosion behaviour of the steels in 0.5 % CO_2 environments 231

6.6 Assessing the corrosion behaviour of the micro-alloyed steels in simulated produced seawater (Lyman and Fleming solutions) 233

6.7 The corrosion behaviour of the micro-alloyed steels in 3.5 wt% NaCl using potentiostatic polarization and electrochemical impedance spectroscopy (EIS). 237

6.7.1 EIS investigation of the stability of the corrosion product formed on the steels by applying different anodic potentials at constant time. 239

6.7.2 EIS investigation of the stability of the corrosion product formed on the steels by applying constant anodic potentials for different time interval. 242

6.8 Further investigation in 3.5 wt% NaCl saturated with 99.98% CO_2 243

6.8.1 Effect of temperature variations on the corrosion behaviour of the specimens in 3.5 wt% NaCl saturated with 99.98% CO_2 environments 243

6.8.2 Corrosion behaviour of the micro-alloyed steels in simulated seawater saturated with 99.98% CO_2. 246

6.8.3 The corrosion behaviour of the steels by weight loss in 3.5 wt% NaCl solution saturated with 99.98% CO_2 at 25^0C and pH 6.5 ... 249

6.8.4 The tendency of the micro-alloyed steels to form protective $FeCO_3$ film in 3.5 wt% NaCl solution saturated with 99.98% CO_2 at 25^0C and pH 6.5 ... 249

6.9 Alloying of steels P110 and TN95 with Zr and Hf and investigation of the Corrosion behaviour of alloyed specimens in simulated produce water (SPW). ... 253

6.9.1 Characterization of the alloyed steels ... 253

6.9.2 Corrosion behaviour of steels P110 and TN95 alloyed with Zr and Hf in simulated produce water (SPW) ... 255

6.10 Summary ... 262

6.10.1 Preliminary investigation and assessments of the corrosion behaviours of the three micro-alloyed steels in brine and simulated oilfield environments. ... 263

6.10.2 Alloying the micro-alloyed steels with non-conventional carbide forming elements. ... 264

6.10.3 Corrosion behaviour of the alloyed specimens in simulated produced water saturate with 99.98% CO_2 ... 265

Chapter 7 Conclusions, Industrial Relevance and Future Study ... 269

7.1 Conclusions ... 269

7.1.1 Preliminary investigation and assessments of the corrosion behaviours of the proprietary micro-alloyed steels in brine and simulated oilfield environments. ... 269

7.1.2 Characterization and corrosion performance of the alloy. ... 271

7.2 Relevance of the study to the industry ... 273

7.3 Recommended future research ... 273

Reference ... 275

Appendices ... 291

Appendix A: Average grain size of $FeCO_3$ crystals formed on the surface of the steels ... 291

Appendix B1: EDS spectra of alloyed steels P110 and TN95 ... 292

Appendix B2: EDS mapping of alloyed steels P110 and TN95 ... 298

Appendix C1: EDS spectra of corroded alloyed P110 and TN95 ... 304

Appendix D: ASTM grain size No and grain size ... 310

List of Figures

Figure 1- 1: The tendency of materials to return to their native, low energy oxide state. 2
Figure 1- 2: Common Forms of Corrosion [21]. 4
Figure 1- 3: Cost of corrosion Per Analyzed Economic Sector (data from [19]) 7
Figure 1- 4: Causes of Corrosion Related Failure in Petroleum Industry (data from [23]) 8
Figure 1- 5: Schematic representation of the scope of this work 16
Figure 1- 6: The periodic table showing the positions of strong carbide-forming elements[15] 17
Figure 2- 1: Evolution of microstructure and mechanical properties of steels (TM – Thermomechanical treatment, ACC – Accelerated Cooling) [27, 72] 25
Figure 2- 2: Enthalpies of formation of carbides, nitrides and borides [15, 74] 27
Figure 2- 3: Correlation between the micro-alloying content (M%) and the solubility temperatures for the precipitates in the steel [29] 30
Figure 2- 4: Schematic of the relationship between precipitate type, solubility, composition and temperature where it is expected that the indicated precipitates would be effective in modifying product properties [31] 31
Figure 2- 5: Phase diagram of the Fe-Zr system [82] 33
Figure 2- 6: Gibbs free energy of formation of one mole of carbides [49, 86] 35
Figure 2- 7: Hf-Zr system [45] 36
Figure 2- 8: The Fe-Hf Phase diagram [89] 37
Figure 2- 9: A corroding metal at steady state of electrical double layer (modified from [94]). 38
Figure 2- 10: Evans diagram for iron in acid solution ([96] www.npl.co.uk/upload/pdf/the_electrochemistry_of_corrosion_with_figures.pdf, 27/11/2018). 40
Figure 2- 11: Summaries of DC Corrosion Measurement Methods [94] 45
Figure 2- 12: Polarization curve for R_p measurement about E_{corr} (modified from [94]). 46
Figure 2- 13: Tafel Plot showing extrapolated lines and Tafel parameters (modified from [94]). 49
Figure 2- 14: Comparison of Pourbaix Diagram and Polarization Curve for Iron. [104] 50
Figure 2- 15: Cyclic Scanning showing positive Hysteresis (modified from [94]). 51

Figure 2- 16: AC voltage - current phase angle showing one polarization cycle and a negative amplitude [94]. 53
Figure 2- 17: (A) Nyquist Plot and (B) Bode Plot (modifiesd from [109, 113]) 54
Figure 2- 18: The Randles Cell Equivalent Circuit 55
Figure 3- 1: Effect of elements on corrosion losses based on the models developed by [48] (more negative indicates less corrosion). 58
Figure 3- 2: Schematic presentation of relative effect of additional micro alloying elements on corrosion rate [13]. 59
Figure 3- 3: Temperature dependence of the change in the standard Gibbs free energy ΔG^0, kJ/mol, for carbide-formation reactions [60] 61
Figure 3- 4: The SEM micrographs of the specimens exposed at 85^0C at pH (a) 5.5, (b) 6 and (c) 6.5 for 72h [147]. 67
Figure 3- 5: pH effect in CO_2 solution, water + 3% NaCl, P_{CO2} = 1 bar, T = 20°C, 1,000 rpm, and St52 steel [140]. 68
Figure 3- 6: Schematic representation of the effects of increase in temperature on the corrosion of carbon steel in CO_2 saturated aqueous solution showing the nature of the corrosion products and their protective properties (modified from [23, 157, 158]) 70
Figure 3- 7; The dependency of $FeCO_3$ solubility on C_{Fe2+} and pH [160] 74
Figure 3- 8: Corrosion rates and potentials vs NaCl concentration of API-X100 steel at 20^0C [170]. 75
Figure 3- 9: The corrosion rates of X65 steel exposed in water saturated with CO_2 under low partial pressure and supercritical condition at 80^0C for various immersion time [129]. 82
Figure 4- 1: As received proprietary grades of steel 87
Figure 4- 2: Specimen dimensions (a) F65 and X65, (b) P110 IC and (c) TN95 HS 89
Figure 4- 3: Optical Microscope (OM) 91
Figure 4- 4: The Carl Zeiss EVO MA15 Scanning Electron Microscopy and Energy-Dispersed X-ray (SEM/EDAX) 92
Figure 4- 5: Philips X'pert X-ray diffractometer was used in this study for XRD analysis 93
Figure 4- 6: NPFLEX 3D interferometer 94
Figure 4- 7: Model K0235 Flat Cell 100
Figure 4- 8: Bubble (Glass) setup 101
Figure 4- 9: A schematic diagram of the corrosion experimental set up 101
Figure 4- 10: Buhler arc melter (AM with avrio 800) and power supply 111

Figure 4- 11: Inside the vacuum chamber showing the copper crucible base plate with mould cavities, tungsten electrode and mechanical manipulator. 112
Figure 5- 1: Optical Micrographs of as-received samples (a) F65, (b) P110, (c) TN95 and (d) X65 116
Figure 5- 2: SEM micrographs of as-received samples with backscattering image overlaid (a) F65, (b) P110, (c) TN95 and (d) X65 117
Figure 5- 3: EDS spectra of as-received steel P110 with elemental compositions at points 'a' and 'b' insert 118
Figure 5- 4: XRD pattern of as-received steel P110 revealing only Fe peaks 118
Figure 5- 5: Corrosion rate by weight loss of specimens in 3.5 wt% NaCl at ambient temperature 119
Figure 5- 6: Average LPR corrosion rates of the steels in aerated brine solutions at ambient temperature and for 6 hours: (a) 1 wt% aerated, (b) 3.5 wt% aerated, (c) 10 wt% aerated. 121
Figure 5- 7: Average LPR corrosion rates of the steels in de-aerated brine solutions at ambient temperature and for 6 hours: (a) 1 wt% de-aerated, (b) 3.5 wt% de-aerated, (c) 10 wt% de-aerated 121
Figure 5- 8: Average corrosion rates of the steels in different concentration of naturally aerated NaCl solutions at ambient temperature and for 6 hours 122
Figure 5- 9: Average corrosion rates of the steels in different concentration of deaerated NaCl solutions at ambient temperature and for 6 hours 122
Figure 5- 10: Comparison of corrosion rates of steels in aerated and de-aerated NaCl solutions at ambient temperature and for 6 hours 123
Figure 5- 11: Tafel Plots of specimens in different concentrations of naturally aerated NaCl solution at ambient temperature and for 6 hours (a) 1% Aerated, (b) 3.5% Aerated and (c) 10% Aerated 124
Figure 5- 12: Tafel Plots of specimens in different concentrations of de-aerated NaCl solution at ambient temperature and for 6 hours (a) 1% Deaerated, (b) 3.5% Deaerated and (c) 10% Deaerated 125
Figure 5- 13: Comparison of the Tafel plot of the steels in aerated and de-aerated 1 wt% NaCl solution at ambient temperature (a) F65, (b) P110, (c) TN95 and (d) X65 125
Figure 5- 14: Comparison of the Tafel plot of the steels in aerated and de-aerated 3.5 wt% NaCl solution at ambient temperature (a) F65, (b) P110, (c) TN95 and (d) X65 126
Figure 5- 15: Comparison of the Tafel plot of the steels in aerated and de-aerated 10 wt% NaCl solution at ambient temperature (a) F65, (b) P110, (c) TN95 and (d) X65 127

Figure 5- 16: SEM micrographs of the specimens corroded in naturally aerated 1 wt% NaCl solution at ambient temperature for 6 hours (a) F65, (b) P110, (c) TN95 and (d) X65 128
Figure 5- 17: SEM micrographs of the specimens corroded in deaerated 1 wt% NaCl solution of at ambient temperature for 6 hours (a) F65, (b) P110, (c) TN95 and (d) X65 129
Figure 5- 18: SEM micrographs of the specimens corroded in naturally aerated 3.5 wt% NaCl solution at ambient temperature for 6 hours (a) F65, (b) P110, (c) TN95 and (d) X65 129
Figure 5- 19: SEM Micrographs of the samples corroded in de-aerated 3.5 wt% NaCl solutions at ambient temperature and for 6 hours (a) F65, (b) P110, (c) TN95 and (d) X65 130
Figure 5- 20: SEM Micrographs of the samples corroded in naturally aerated 10 wt% NaCl solutions at ambient temperature and for 6 hours (a) F65, (b) P110, (c) TN95 and (d) X65 130
Figure 5- 21: SEM Micrographs of the samples corroded in de-aerated 10 wt% NaCl solutions at ambient temperature and for 6 hours (a) F65, (b) P110, (c) TN95 and (d) X65 131
Figure 5- 22: Comparison of the corrosion rate of specimens in the 3.5 wt% NaCl solution saturated with 0.5% CO_2 at (a) 25^0C; (b) 45^0C and (c) 60^0C.....132
Figure 5- 23: Effect of temperature on the corrosion rate of specimens in the 3.5 wt% NaCl solution saturated with 0.5% CO2 (a) F65; (b) P110, (c) TN95 and (d) X65 133
Figure 5- 24: Tafel plots of the specimens in the 3.5 wt% NaCl solution saturated with 0.5% CO_2 at different temperatures (a) F65; (b) P110, (c) TN95 and (d) X65.....134
Figure 5- 25: Plots of the Specimens corroded in 3.5 wt% NaCl Solution saturated with 0.5% CO_2 at 25^0C (a) Nyquist and (b) Bode.....135
Figure 5- 26: Equivalent electrical circuit (EEC) used to fit EIS data of the Steels corroded in 3.5 wt% NaCl Solutions containing CO_2 at different temperatures.....136
Figure 5- 27: The fitted EIS plots of steel F65 corroded in 3.5 wt% NaCl saturated with 0.5% CO_2 at 60^0C: (a) Nyquist Plots and (b) Bode plots 137
Figure 5- 28: SEM Micrographs of the specimens corroded in 3.5 wt% NaCl solution Saturated with 0.5% CO_2 at 25^0C; (a) F65, (b) P110, (c) TN95 and (d) X65.....138
Figure 5- 29: SEM Micrographs of the specimens corroded in 3.5 wt% NaCl solution Saturated with 0.5% CO_2 at 45^0C: (a) F65, (b) P110, (c) TN95 and (d) X65.....139

Figure 5- 30: SEM Micrographs of the specimens corroded in 3.5 wt% NaCl solution Saturated with 0.5% CO_2 at 60^0C: (a) F65, (b) P110, (c) TN95 and (d) X65 140
Figure 5- 31: XRD pattern of the steels in unbuffered 3.5 wt% NaCl Solution Saturated with 0.5% CO_2 at (a) 25^0C, (b) 54^0C and (c) 60^0C 141
Figure 5- 32: Bi-logarithmic plots of the 24 hours LPR date of the steels corroded in 3.5 wt% NaCl solutions containing 0.5% CO_2 at different temperatures (a) F65, (b) P110, (c) TN95 and (d) X65 142
Figure 5- 33: Evolution of corrosion rate with time of the steels in 3.5 wt% NaCl saturated with CO_2 at 60^0C (a) pH 3.5 (b) pH 5 and (c) pH 6.5 143
Figure 5- 34: Evolution of corrosion rate with time of the steels in 3.5 wt% NaCl saturated with CO_2 at 60^0C and different pH; (a) F65, (b) P110, (c) TN95 and (d) X65 144
Figure 5- 35: Tafel plots of the steels in 3.5 wt% NaCl saturated with 0.5% CO_2 at 60^0C and different pH; (a) F65, (b) P110, (c) TN95 and (d) X65 145
Figure 5- 36: Tafel plot of F65 in 3.5 wt% NaCl solution saturated with 0.5% CO_2 at 60^0C and pH 5 displaying Tafel extrapolation parameters. 146
Figure 5- 37: SEM micrographs of the specimens corroded in 3.5 wt% NaCl solution saturated with 0.5% CO_2 at 60^0C and pH 3.5; (a) F65, (b) P110, (c) TN95 and (d) X65 147
Figure 5- 38: SEM micrographs of the specimens corroded in 3.5 wt% NaCl solution saturated with 0.5% CO_2 at 60^0C and pH 5; (a) F65, (b) P110, (c) TN95 and (d) X65 148
Figure 5- 39: SEM micrographs of the specimens corroded in 3.5 wt% NaCl solution saturated with 0.5% CO_2 at 60^0C and pH 6.5; (a) F65, (b) P110, (c) TN95 and (d) X65 148
Figure 5- 40: XRD spectra of the steels corroded in 3.5 wt% NaCl solution saturated with 0.5% CO_2 at 60^0C and different pH (a) F65, (b) P110 (c) TN95 and (d) X65 149
Figure 5- 41: Evolution of corrosion rate with time for the micro-alloyed steels in simulated seawater at 25^0C, pH 6.5 and for 24 hours (a) naturally aerated and (b) 0.5% CO_2 saturated 151
Figure 5- 42: Comparison of the corrosion rate of the micro-alloyed steels in naturally aerated and 0.5% CO_2 saturated simulated seawater at 25^0C, pH 6.5 and for 24 hours (a) F65, (b) P110, (c) TN95 and (d) X65 152
Figure 5- 43: Tafel plots of the micro-alloyed steels corroded in simulated seawater at 25^0C and pH 6.5 (a) naturally aerated and (b) 0.5% CO_2 saturated 153

Figure 5- 44: Comparing Tafel plots of the micro-alloyed steels corroded in naturally aerated and 0.5% CO_2 saturated simulated seawater at 25^0C and pH 6.5 (a) F65, (b) P110, (c) TN95 and (d) X65 153
Figure 5- 45: SEM Micrographs of the samples corroded in aerated simulated water for 24 hrs at 25^0C and pH 6.5: (a) F65, (b) P110, (c) TN95 and (d) X65 155
Figure 5- 46: SEM Micrographs of the samples corroded in CO_2 saturated simulated water for 24 hrs at 25^0C: (a) F65, (b) P110, (c) TN95 and (d) X65 156
Figure 5- 47: XRD pattern of the samples corroded in simulated seawater for 24 hrs at 25^0C: (a) aerated (b) 0.5% CO_2 Saturated 156
Figure 5- 48: Evolution of current density with time of the specimens for 24 hours potentiostatic polarization at different anodic potentials in 3.5 wt% NaCl solution containing 0.5% CO_2 at 60^0C and pH 6.5. 158
Figure 5- 49: Nyquist plots of the specimens after potentiostatic polarization at different anodic potentials in 3.5 wt% NaCl solution containing 0.5% CO_2 at 60^0C and pH 6.5. 158
Figure 5- 50: Bode plots of the specimens after potentiostatic polarization at different anodic potentials in 3.5 wt% NaCl solution containing CO_2 at 60^0C and pH 6.5. 159
Figure 5- 51: Relative residual error resulting from the equivalent circuits of the specimens after 24 h potentiostaic polarization in 3.5 wt% NaCl solution containing CO_2 at 60^0C and pH 6.5 for P110 (a) 100 $mV_{(Ag/AgCl)}$, (b) 150 $mV_{(Ag/AgCl)}$ and (c) 200$mV_{(Ag/AgCl)}$; for X65 (d) 100 $mV_{(Ag/AgCl)}$, (e) 150 $mV_{(Ag/AgCl)}$ and (f) 200 $mV_{(Ag/AgCl)}$ 161
Figure 5- 52: SEM surface morphology of the specimens after 24 hours potentiostatic polarization in 3.5 wt% NaCl solution containing CO_2 at 60^0C and pH 6.5 for P110X (a) 100 $mV_{(Ag/AgCl)}$, (b) 150 $mV_{(Ag/AgCl)}$ and (c) 200 $mV_{(Ag/AgCl)}$ for X65 (d) 100 $mV_{(Ag/AgCl)}$, (e) 150 $mV_{(Ag/AgCl)}$ and (f) 200 $mV_{(Ag/AgCl)}$ 162
Figure 5- 53: SEM micrographs showing the primary layer and the partially detached secondary layer of steel P110X after 24 hours potentiostatic polarization in 3.5 wt% NaCl solution containing CO_2 at 60^0C and pH 6.5: (a) 100 $mV_{(Ag/AgCl)}$, (b) 150 $mV_{(Ag/AgCl)}$ and (c) 200 $mV_{(Ag/AgCl)}$. 163
Figure 5- 54: XRD Spectra of the steels after 24 hours potentiostatic polarization at different anodic potentials in 3.5 wt% NaCl solution containing CO_2 at 60^0C and pH 6.5: (a) P110X and (b) X65 163

Figure 5- 55: SEM cross section of corrosion products on anodically polarized P110X in 3.5 wt% NaCl solution containing CO_2 at 60^0C and pH 6.5: (a) 100 $mV_{(Ag/AgCl)}$, (b) 150 $mV_{(Ag/AgCl)}$ and (c) 200 $mV_{(Ag/AgCl)}$ 164
Figure 5- 56: SEM micrographs of the evolution of pits after 24 hours potentiostatic polarization in 3.5 wt% NaCl solution containing CO_2 at 60^0C and pH 6.5 for P110X (a) 100 $mV_{(Ag/AgCl)}$ (b) 150 $mV_{(Ag/AgCl)}$ and (c) 200 $mV_{(Ag/AgCl)}$ for X65 (d) $mV_{(Ag/AgCl)}$ (e) 150 $mV_{(Ag/AgCl)}$ and (f) 200 $mV_{(Ag/AgCl)}$ 165
Figure 5- 57: 3D White light profilometry images of deepest pit formed on the specimens after 24 h potentiostaic polarization in 3.5 wt% NaCl solution containing CO_2 at 60^0C and pH 6.5 for P110X (a) 100 $mV_{(Ag/AgCl)}$, (b) 150 $mV_{(Ag/AgCl)}$ and (c) 200 $mV_{(Ag/AgCl)}$; for X65 (d) 100 $mV_{(Ag/AgCl)}$, (e) 150 $mV_{(Ag/AgCl)}$ and (f) 200 $mV_{(Ag/AgCl)}$ 166
Figure 5- 58: Nyquist plots of the steels passivated in naturally aerated 3.5 wt% NaCl solution at ambient temperature and different time (a) P110 and (b) TN95. 167
Figure 5- 59: Bode plots of the steels passivated in naturally aerated 3.5 wt% NaCl solution at ambient temperature and different time (a and b) P110 and (c and d) TN95. 168
Figure 5- 60: Open circuit potential after corrosion product has been formed at a constant potential of 150 $mV_{Ag/AgCl}$ on the steels in naturally aerated 3.5 wt% NaCl solution at ambient temperature and different time (0, 1, 2, 4, 8, 12 and 24 h) 168
Figure 5- 61: Polarization resistance (Rp) from the fitted parameters of the steels passivated in naturally aerated 3.5 wt% NaCl solution at ambient temperature and different time (0, 1, 2, 4, 8, 12 and 24 h) 170
Figure 5- 62: Evolution of SEM surface morphology of P110 in naturally aerated 3.5 wt% NaCl solution at ambient temperature and at (a) 1h, (b) 2h, (c) 4h, (d) 8h, (e) 12h and (f) 24h 172
Figure 5- 63: Evolution of SEM surface morphology of TN95 in naturally aerated 3.5 wt% NaCl solution at ambient temperature and at (a) 1h, (b) 2h, (c) 4h, (d) 8h, (e) 12h and (f) 24h 173
Figure 5- 64: XRD pattern of the samples in naturally aerated 3.5 wt% NaCl solution at ambient temperature and different time interval (a) P110, (b) TN95 174
Figure 5- 65: Evolution of corrosion rate with time of samples in 3.5 wt% NaCl solution saturated with 99.98% CO_2 at different temperatures: (a) 25^0C, (b) 45^0C and (c) 60^0C 176

Figure 5- 66: Comparison of corrosion rate of specimens in 3.5 wt% NaCl solution saturated with 99.98% CO_2 at different temperatures: (a) P110, (b) TN95 and (c) X65 176
Figure 5- 67: Comparison of the average corrosion rate of specimens in 3.5 wt% NaCl solutions saturated with 0.5 % CO_2 and 99.98% CO_2 at different temperatures 177
Figure 5- 68: Tafel plot of samples in 3.5 wt% NaCl solution saturated with pure CO_2 at different temperatures: (a) P110, (b) TN95 and (c) X65 178
Figure 5- 69: Comparison of Tafel plots of P110 in 3.5 wt% NaCl solutions saturated with 0.5 % CO_2 and 99.98% CO_2 at different temperatures: (a) 25^0C; (b) 45^0C and (c) 60^0C. 178
Figure 5- 70: Comparison of Tafel plots of TN95 in 3.5 wt% NaCl solutions saturated with 0.5 % CO_2 and 99.98% CO_2 at different temperatures: (a) 25^0C; (b) 45^0C and (c) 60^0C.....179
Figure 5- 71: Comparison of Tafel plots of X65 in 3.5 wt% NaCl solutions saturated with 0.5 % CO_2 and 99.98% CO_2 at different temperatures: (a) 25^0C; (b) 45^0C and (c) 60^0C 179
Figure 5- 72: SEM surface micrographs of P110 steel corroded in 3.5 wt% NaCl Solution saturated with 99.98% CO_2 at different temperatures for 24 hours: (a) 25^0C; (b) 45^0C and (c) 60^0C 181
Figure 5- 73: SEM surface micrographs of TN95 steel corroded in 3.5 wt% NaCl Solution saturated with 99.98% CO_2 at different temperatures for 24 hours; (a) 25^0C; (b) 45^0C and (c) 60^0C 181
Figure 5- 74: SEM surface micrographs of X65 steel corroded in 3.5 wt% NaCl Solution saturated with 99.98% CO_2 at different temperatures for 24 hours; (a) 25^0C; (b) 45^0C and (c) 60^0C 182
Figure 5- 75: XRD pattern of the samples corroded in 3.5 wt% NaCl Solution saturated with CO_2 at different temperatures for 24 hours (a) P110, (b) TN95 and (c) X65. 183
Figure 5- 76: Evolution of corrosion rate and potentials with time for the steels corroded in simulated seawater (SSW) saturated with 99.98% CO_2 at 25^0C and pH 6.5 (a) P110, (b) TN95 and (c) X65 184
Figure 5- 77: Variation of corrosion rate with time of steels corroded in simulated seawater (SSW) saturated with 99.98% CO_2 at 25^0C and pH 6.5.....185
Figure 5- 78: Potential vs current density of samples corroded in simulated seawater (SSW) saturated with 99.98% CO_2 at 25^0C and pH 6.5.....186

Figure 5- 79: EIS Plots of samples corroded simulated seawater (SSW) saturated with 99.98% CO_2 at 25^0C and pH 6.5 (a) Niquist and (b) Bode plots. 187
Figure 5- 80: Equivalent electrical circuit for EIS data fittings of the specimens corroded simulated seawater (SSW) saturated with 99.98% CO_2 at 25^0C and pH 6.5 187
Figure 5- 81: SEM micrographs of samples corroded simulated seawater (SSW) saturated with 99.98% CO_2 at 25^0C and pH 6.5 (a) P110, (b) TN95 and (c) X65 188
Figure 5- 82: XRD spectra of samples corroded simulated seawater (SSW) saturated with 99.98% CO_2 at 25^0C and pH 6.5 189
Figure 5- 83: Comparison of the evolution of corrosion vs time plots of specimens corroded in three different simulated seawater environments at 25^0C and pH 6.5 (a) P110, (b) TN95 and (c) X65. 189
Figure 5- 84: Transition of corrosion rate by weight loss of P110 and TN95 in 3.5 wt% NaCl Saturated with 99.98% CO_2 at ambient temperature for 5 different days 190
Figure 5- 85: SEM micrographs of the surface morphology of P110 after immersion in 3.5 wt% NaCl saturated with pure CO_2 at ambient temperature for 5 different days. ..191
Figure 5- 86: SEM micrographs of the surface morphology of TN95 after immersion in 3.5 wt% NaCl saturated with pure CO_2 at ambient temperature for 5 different days ...192
Figure 5- 87: XRD analysis of (a) P110 and (b) TN95 after immersion in 3.5 wt% NaCl saturated with 99.98% CO_2 at ambient temperature for 5 different days. 193
Figure 5- 88: Evolution of corrosion rate and OCP with time for Specimens in 3.5 wt% NaCl Saturated with 99.98% CO_2 at 60^0C, pH6.5 for 4 days (a) P110, (b) TH95 and (c) X65 194
Figure 5- 89: Transitions of SEM surface morphology of P110 corroded in 3.5 wt% NaCl saturated with 99.98% CO_2 at 60^0C, pH6.5 for 4 days (a) Day 1, (b) Day 2 and (c) Day 4 194
Figure 5- 90: Transitions of SEM surface morphology of TN95 corroded in 3.5 wt% NaCl saturated with 99.98% CO_2 at 60^0C, pH6.5 for 4 days (a) Day 1, (b) Day 2 and (c) Day 4 195
Figure 5- 91: Transitions of SEM surface morphology of X65 corroded in 3.5 wt% NaCl saturated with 99.98% CO_2 at 60^0C, pH6.5 for 4 days (a) Day 1, (b) Day 2 and (c) Day 4 196
Figure 5- 92: XRD pattern of the specimens corroded in 3.5 wt% NaCl Saturated with 99.98% CO2 at 60^0C, pH6.5 for 4 days (a) P110, (b) TN95and (c) X65 197
Figure 5- 93: SEM micrographs of P110 alloyed with (a) 0.1 wt% Zr, (c) 0.2 wt% Zr, (e) 0.4 wt% Zr, (b) 0.1 wt% Hf, (d) 0.2 wt% Hf and (f) 0.4 wt% Hf 198

Figure 5- 94: SEM micrographs of TN95 alloyed with (a) 0.1 wt% Zr, (c) 0.2 wt% Zr, (e) 0.4 wt% Zr, (b) 0.1 wt% Hf, (d) 0.2 wt% Hf and (f) 0.4 wt% Hf 199
Figure 5- 95: EDS analyses of P_1-Zr_1 (a) microstructure of as cast P_1-Zr_1, (b) EDS at point A in (a), (c) EDS at point B in (a) and (d) EDS of small particle at point C in (a).....200
Figure 5- 96: EDS analyses of T_1-Zr_1 (a) microstructure of as cast T_1-Zr_1, (b) EDS at point A in (a), (c) EDS at point B in (a) and (d) EDS of small particle at point C in (a).....201
Figure 5- 97: EDS elemental mapping of P_1-Zr_1 showing the uniform distribution of the elements within the matrix of the steel.....202
Figure 5- 98: EDS elemental mapping of T_1-Zr_1 showing the uniform distribution of the elements within the matrix of the steel.....202
Figure 5- 99: Variation in ASTM grain size number (GSN) and grain size of the specimens with increase in addition of alloying elements 203
Figure 5- 100: XRD analysis of the specimens alloyed with different wt% Zr and Hf (a) P110-Zr, (b) P110-Hf, (c) TN95-Zr and (d) TN95-Hf.....203
Figure 5- 101: Evolution of corrosion rate with time of the unalloyed and alloyed specimens in CO_2 saturated simulated produced water at 25^0C and pH 6.5 (a) P110-Zr, (b) P110-Hf, (c) TN95-Zr and (d) TN95-Hf. 206
Figure 5- 102: Evolution of OCP with time of the unalloyed and alloyed specimens in CO_2 saturated simulated produced water at 25^0C and pH 6.5 (a) P110-Zr, (b) P110-Hf, (c) TN95-Zr and (d) TN95-Hf.....207
Figure 5- 103: Tafel plots of corroded alloyed specimens in CO_2 simulated sea water at 25^0C, pH6.5 and after 24 hours LPR (a) P110-Zr, (b) P110-Hf, (c) TN95-Zr and (d) TN95-Hf.....208
Figure 5- 104: Nyquist plots of corroded alloyed specimens in CO_2 simulated sea water at 25^0C, pH6.5 and after 24 hours LPR (a) P110-Zr, (b) P110-Hf, (c) TN95-Zr and (d) TN95-Hf.....210
Figure 5- 105: Bode plots of corroded alloyed specimens in CO_2 simulated sea water at 25^0C, pH6.5 and after 24 hours LPR (a) P110-Zr, (b) P110-Hf, (c) TN95-Zr and (d) TN95-Hf.....211
Figure 5- 106: SEM micrographs of corroded P110 alloyed with (a) 0.1 wt% Zr, (c) 0.2 wt% Zr, (e) 0.4 wt% Zr, (b) 0.1 wt% Hf, (d) 0.2 wt% Hf and (f) 0.4 wt% Hf 213
Figure 5- 107: SEM micrographs and EDS elemental analysis of three different locations on alloy P_2-Zr_2 corroded in simulated sea water at 25^0C, pH6.5 and for 24 hours. 214
Figure 5- 108: SEM micrographs of corroded TN95 alloyed with (a) 0.1 wt% Zr, (c) 0.2 wt% Zr, (e) 0.4 wt% Zr, (b) 0.1 wt% Hf, (d) 0.2 wt% Hf and (f) 4 wt% Hf. 215

Figure 5- 109: SEM micrographs and EDS elemental analysis of three locations on alloy T_3-Zr_3 (0.4 wt% Zr) corroded in simulated sea water at 25^0C, pH6.5 and for 24 hours 216
Figure 5- 110: XRD patterns of the alloyed specimens corroded in CO_2 simulated sea water at 25^0C, pH6.5 and after 24 hours LPR (a) P110-Zr, (b) P110-Hf, (c) TN95-Zr and (d) TN95-Hf 217
Figure A- 1: Average grain size of $FeCO_3$ crystals formed on the surface of the specimens corroded in 3.5 wt% NaCl solution saturated with 99.98% CO_2 at 60^0C, pH 6.5 for 96 hours. 291
Figure B1- 1: EDS analyses of P_1-Zr_1 (a) microstructure of as cast P_1-Zr_1, (b) EDS of point A in (a), (c) EDS at point B in (a) and (d) EDS of small particle at point C in (a) 292
Figure B1- 2: EDS analyses of P_2-Zr_2 (a) microstructure of as cast P_2-Zr_2, (b) EDS of point A in (a), (c) EDS at point B in (a) and (d) EDS of small particle at point C in (a) 292
Figure B1- 3: EDS analyses of P_3-Zr_3 (a) microstructure of as cast P_3-Zr_3, (b) EDS of point A in (a), (c) EDS at point B in (a) and (d) EDS of small particle at point C in (a) 293
Figure B1- 4: EDS analyses of P_1-Hf_1 (a) microstructure of as cast P_1-Hf_1, (b) EDS of point A in (a), (c) EDS at point B in (a) and (d) EDS of small particle at point C in (a) 293
Figure B1- 5: EDS analyses of P_2-Hf_2 (a) microstructure of as cast P_2-Hf_2, (b) EDS of point A in (a), (c) EDS at point B in (a) and (d) EDS of small particle at point C in (a) 294
Figure B1- 6: EDS analyses of P_3-Hf_3 (a) microstructure of as cast P_3-Hf_3, (b) EDS of point A in (a), (c) EDS at point B in (a) and (d) EDS of small particle at point C in (a) 294
Figure B1- 7: EDS analyses of T_1-Zr_1 (a) microstructure of as cast T_1-Zr_1, (b) EDS of point A in (a), (c) EDS at point B in (a) and (d) EDS of small particle at point C in (a) 295
Figure B1- 8: EDS analyses of T_2-Zr_2 (a) microstructure of as cast T_2-Zr_2, (b) EDS of point A in (a), (c) EDS at point B in (a) and (d) EDS of small particle at point C in (a) 295

Figure B1- 9: EDS analyses of T_3-Zr_3 (a) microstructure of as cast T_3-Zr_3, (b) EDS of point A in (a), (c) EDS at point B in (a) and (d) EDS of small particle at point C in (a) 296
Figure B1- 10: EDS analyses of T_1-Hf_1 (a) microstructure of as cast T_1-Hf_1, (b) EDS of point A in (a), (c) EDS at point B in (a) and (d) EDS of small particle at point C in (a) 296
Figure B1- 11: EDS analyses of T_2-Hf_2 (a) microstructure of as cast T_2-Hf_2, (b) EDS of point A in (a), (c) EDS at point B in (a) and (d) EDS of small particle at point C in (a) 297
Figure B1- 12: EDS analyses of T_3-Hf_3 (a) microstructure of as cast T_3-Hf_3, (b) EDS of point A in (a), (c) EDS at point B in (a) and (d) EDS of small particle at point C in (a) 297
Figure B2- 1: EDS elemental mapping of P_1-Zr_1 298
Figure B2- 2: EDS elemental mapping of P_2-Zr_2 298
Figure B2- 3: EDS elemental mapping of P_3-Zr_3 299
Figure B2- 4: EDS elemental mapping of P_1-Hf_1 299
Figure B2- 5: EDS elemental mapping of P_2-Hf_2 300
Figure B2- 6: EDS elemental mapping of P_3-Hf_3 300
Figure B2- 7: EDS Elemental mapping of T_1-Zr_1 301
Figure B2- 8: EDS Elemental mapping of T_2-Zr_2 301
Figure B2- 9: EDS Elemental mapping of T_3-Zr_3 302
Figure B2- 10: EDS Elemental mapping of T_1-Hf_1 302
Figure B2- 11: EDS Elemental mapping of T_2-Hf_2 303
Figure B2- 12: EDS Elemental mapping of T_3-Hf_3 303
Figure C1- 1: EDS elemental analysis of alloyed specimen P_1-Zr_1 corroded in simulated sea water at 25^0C, pH6.5 and for 24 hours 304
Figure C1- 2: EDS elemental analysis of alloyed specimen P_2-Zr_2 corroded in simulated sea water at 25^0C, pH6.5 and for 24 hours 304
Figure C1- 3: EDS elemental analysis of alloyed specimen P_3-Zr_3 corroded in simulated sea water at 25^0C, pH6.5 and for 24 hours 305
Figure C1- 4: EDS elemental analysis of alloyed specimen P_1-Hf_1 corroded in simulated sea water at 25^0C, pH6.5 and for 24 hours 305
Figure C1- 5: EDS elemental analysis of alloyed specimen P_2-Hf_2 corroded in simulated sea water at 25^0C, pH6.5 and for 24 hours 306

Figure C1- 6: EDS elemental analysis of alloyed specimen P_3-Hf_3 corroded in simulated sea water at 25^0C, pH6.5 and for 24 hours.....306
Figure C1- 7: EDS elemental analysis of alloyed specimen T_1-Zr_1 corroded in simulated sea water at 25^0C, pH6.5 and for 24 hours.....307
Figure C1- 8: EDS elemental analysis of alloyed specimen T_2-Zr_2 corroded in simulated sea water at 25^0C, pH6.5 and for 24 hours.....307
Figure C1- 9: EDS elemental analysis of alloyed specimen T_3-Zr_3 corroded in simulated sea water at 25^0C, pH6.5 and for 24 hours.....308
Figure C1- 10: EDS elemental analysis of alloyed specimen T_1-Hf_1 corroded in simulated sea water at 25^0C, pH6.5 and for 24 hours.....308
Figure C1- 11: EDS elemental analysis of alloyed specimen T_2-Hf_2 corroded in simulated sea water at 25^0C, pH6.5 and for 24 hours.....309
Figure C1- 12: EDS elemental analysis of alloyed specimen T_3-Hf_3 corroded in simulated sea water at 25^0C, pH6.5 and for 24 hours.....309

List of Tables

Table 1- 1: Summarized Corrosion Mode 5
Table 1- 1: Summarized Corrosion Mode (Continues) 6
Table 1- 2: Alloying elements and their influence in micro-alloyed steels [28] 9
Table 1- 3: Categories and Characteristics of Micro-alloyed steels (6) 12
Table 1- 4: Uses of Micro alloyed steels in offshores [36] 12
Table 2- 1: Definitions of alloy steel, low alloy steel and micro-alloy steel [14]. 23
Table 2- 2: Comparison of Classes of Micro-alloyed steels [51] 24
Table 2- 3: Historical evolution of the controlled rolling and accelerated cooling processes, as well as the strengthening mechanisms and technical standards associated to them. [73] 26
Table 2- 4: The value of constant (K) for calculating corrosion rate in various units [100]: 44
Table 2- 5: The value of constant (K) for calculating metal loss in various units: ...**Error! Bookmark not defined.**
Table 3- 1: The functions of various micro-alloying elements [14]. 57
Table 3- 2: Mechanisms of Anodic dissolution of iron in CO_2 saturated Media [23]. ...64
Table 4- 1: Mechanical properties of the samples 87
Table 4- 2: Samples and their characteristics 88
Table 4- 3: Elemental Specifications of the samples 88
Table 4- 4: Experimental setups and corrosion conditions 102
Table 4- 5: Test Matrix of experiments conducted at different temperature and unbuffered pH 104
Table 4- 6: Test Matrix of experiments conducted at varying pH and constant temperature 104
Table 4- 7: Lyman and Fleming Composition of Seawater (SW) 107
Table 4- 8: Test Matrix of experiments conducted with Lyman Fleming solutions 107
Table 4- 9: The test matrix of the experiments aimed at assessing the propensity of the steels to form $FeCO_3$ 109
Table 4- 10: Alloying specifications 110
Table 5- 1: ASTM Grain Size number and Ferrite/Pearlite Ratio (%) for the samples 116
Table 5- 2: Diffractometer data of steel P110 for the diffraction peaks of α-iron metallic (BCC) 117

Table 5- 3: Tafel extrapolation parameters of the specimens in aerated and de-aerated solutions of three NaCl concentrations. 128
Table 5- 4: Graphically determined Corrosion parameters of the samples using Tafel Extrapolation Technique 134
Table 5- 5: Electrochemical Impedance Parameters of the Specimens corroded in 3.5 wt% NaCl Solution Saturated with 0.5% CO_2 at different temperatures after 24 hours LPR. 137
Table 5- 6: EDX Elemental Analysis at two sites on the SEM micrographs of the samples in unbuffered 3.5 wt% NaCl solution saturated with 0.5% CO_2 at 60^0C as shown in Figure 5-30..... 140
Table 5- 7: Tafel extrapolated parameters of the steels in 3.5 wt% NaCl saturated with CO_2 at 60^0C and different pH..... 146
Table 5- 8: EDS elemental analysis at two sites on the SEM micrographs of the specimens corroded in 3.5 wt% NaCl solution saturated with 0.5% CO_2 at 60^0C and pH 3.5 as in Figure 5-37 149
Table 5- 9: Tafel extrapolation parameters of the steels corroded in naturally aerated simulated seawater at 25^0C and pH 6.5 154
Table 5- 10: Tafel extrapolation parameters of the steels corroded in 0.5% CO_2 saturated simulated seawater at 25^0C and pH 6.5 154
Table 5- 11: Fitted EIS data for the specimens after 24 hours potentiostatic polarization at different potentials in 3.5 wt% NaCl solution saturated with 0.5% CO_2 at 60^0C and pH6.5. 160
Table 5- 12: EEC Fitted parameters of P110 in naturally aerated 3.5 wt% NaCl solution at ambient temperature and different time 169
Table 5- 13: EEC Fitted parameters of TN95 in naturally aerated 3.5 wt% NaCl solution at ambient temperature and different time 170
Table 5- 14: Tafel extrapolation parameters of the specimens corroded in 3.5 wt% NaCl solutions saturated with 99.98% CO_2 (a) 25^0C, (b) 45^0C and (c) 60^0C. 180
Table 5- 15 Tafel extrapolation parameters of the steels corroded in simulated seawater (SSW) saturated with 99.98% CO_2 at 25^0C and pH 6.5 186
Table 5- 16: Fitted EIS parameters of samples corroded simulated seawater (SSW) saturated with 99.98% CO_2 at 25^0C and pH 6.5..... 188
Table 5- 17: XRD identification of elements and compounds of the unalloyed and alloyed specimens 204

Table 5- 18: Vickers Hardness number (VHN) of the specimens alloyed with different amount of Zr and Hf. 205
Table 5- 19: Tafel extrapolation parameters of the alloyed specimens corroded in simulated produced water (SPW) saturated with pure CO_2 at 25^0C and pH 6.5..... 209
Table 5- 20: Fitted EIS parameters of the alloyed specimens corroded in simulated produced water (SPW) saturated with pure CO_2 at 25^0C and pH 6.5 212
Table 6- 1: The different electrolytes, electrochemical techniques, environmental parameters used for assessments and corrosion current densities obtained using Tafel extrapolation methods 266
Table 6- 1: The different electrolytes, electrochemical techniques, environmental parameters used for assessments and corrosion current densities obtained using Tafel extrapolation methods 267
Table 6- 1: The different electrolytes, electrochemical techniques, environmental parameters used for assessments and corrosion current densities obtained using Tafel extrapolation methods 268
Table D- 1: ASTM grain size number and grain size of the specimens alloyed with different amount of Zr and Hf 310

Symbols and Abbreviations

Abbrevation, Symbols and Names		Units
LPR	- Linear Polarization Resistance	
PDP	- Potentiodynamic Polarization	
TP	- Tafel Plot	
EIS	- Electrochemical Impedance Spectroscopy	
ECN	- Electrochemical Noise	
pH	- 'Potential of Hydrogen' (A measure of acidity or alkalinity of a solution)	
PPP	- Primary Passivation Potential	Volts
i_c	- Critical Current Density	Ampere/cm^2
i	- Electrode Current	
i_{corr}	- Corrosion Current Density	Ampere/cm^2
I_{MEANS}	- Measured cell Current	Ampere
I_L	- Limiting Current	Ampere
E_{corr}	- Corrosion Potential	Volts
E_{APP}	- Applied Potential	Volts
E_p	- Actual potential (Voltage)	Volts
η	- $E_{APP} - E_{corr} = \Delta E$ - Overpotential	Volts
Rp	- Polarization Resistance	Ohms.meter (Ω.m)
IR	- Eu - Potential or Voltage drop	Volts
Ru	- Rs - Ohmic resistance or Solution resistance	Ohms.meter (Ω.m)
TLC	- The Luggin Cappilary	
B_a	- Anodic Tafel Constant	Volts/decade
B_c	-Ccathodic Tafel Constant	Volts/decade
Q	- Charge	Coulumbs
n	- Number of Electrons involved in an electrochemical reaction	
wt	- Weight of electro-active species	Grams (g)
M	- Molecular weight	Grams (g)
E.W	- Equivalent Weight	Grams (g)
t	- Time	Hours
F	- Faradays Constant	Coulumbs/mole
T	- Temperature	Degree celsius (^{0}C)

C.R	- Corrosion Rate	mm/Y
A	- Cross sectional area	cm^2
ρ	- Density of active species	
d	- Distance	Meter (m)
K	- Specific Conductivity	Siemens/meter (S/m)
Z	- Impedance	Ohms (Ω)
R_{ct}	- Charge Transfer resistance	Ohms (Ω)
ω	- Angular frequency	Radian/second
π	- Theta	
θ	- Phase angle	
C_o	- Y_o - Coating capacitance	farad (F)
α	- Constant between 0 - 1	
ε_0	- Permittivity of free space (Electric constant)	farad/meter (F/m)
ε_r	- Dielectric constant (relative electric constant)	
CPE	- Constant Phase Element	
Q&T	- Quenched and Tempered	
TMCP	– Thermo-mechanical control process	
C_{dl}	- Double layer capacitance	ohms (Ω)
R_{pore}	- Pore resistance	ohms (Ω)
W	- Warburg (Diffusion) Impedance	
WE	- Working Electrode	
CE	- Counter Electrode	
RE	- Reference electrode	
OM	- Optical Microscopy	
SEM	- Scanning Electrons Microscopy	
EDS	- Electron Dispersive Spectroscopy	
XRD	- X-ray diffraction	
XRF	- X-ray fluorescence	
CAPEX	- Capital expenditure	
OPEX	- Operational expenditure	
HSE	- Health and safety environment	
GDP	- Gross Domestic Product	

GSN - ASTM Grain Size Number

GS - Grain Size

YS_{obs} - Observed yield strength

ΔYS_{lf} - Lattice friction (Peierls Nabarro)

ΔYS_{ss} - Solid solution strengthening

ΔYS_{dis} - Dislocation strengthening

ΔYS_{ppt} - Precipitation hardening

K_y - Strengthening coefficient (a constant specific to each material)

RDS - Rate determining step

A - Aerated

DA - Deaerated

SPW - Simulated Produced Water

SSW - Simulated Seawater

P_1-Zr_1 – Steel P110 alloyed with 0.1 wt% Zr

P_2-Zr_2 - Steel P110 alloyed with 0.3 wt% Zr

P_3-Zr_3 - Steel P110 alloyed with 0.3 wt% Zr

P_1-Hf_1 – Steel P110 alloyed with 0.1 wt% Hf

P_2-Hf_2 - Steel P110 alloyed with 0.3 wt% Hf

P_3-Hf_3 - Steel P110 alloyed with 0.3 wt% Hf

T_1-Zr_1 – Steel TN95 alloyed with 0.1 wt% Zr

T_2-Zr_2 - Steel TN95 alloyed with 0.3 wt% Zr

T_3-Zr_3 - Steel TN95 alloyed with 0.3 wt% Zr

T_1-Hf_1 – Steel TN95 alloyed with 0.1 wt% Hf

T_2-Hf_2 - Steel TN95 alloyed with 0.3 wt% Hf

T_3-Hf_3 - Steel TN95 alloyed with 0.3 wt% Hf

Chapter 1: Introduction

1.1 Background

Oil and gas industry is a strategic industry being of central importance for global economy as a vital source of energy required for all other engineering sectors [1]. This vital role is being challenged as the important reserves of oil and gas which are left to be discovered and mined are concentrated in difficult locations such as deep water offshore, remote arctic locations and not easily managed reserves. These locations are also under severe operational conditions of high pressure, high temperature and aggressive environments. This means that materials and the technology required in such high demanding conditions and locations must possess appropriate properties considering the excessive cost of replacements or failures in these difficult-to-access locations [2].

Carbon steel because of its inherent properties such as low cost; easy to shaping, forming and machining; good weldability; availability; its properties have been studied in depth and are well understood; good mechanical properties etc [3, 4] is preferred over all other conventional engineering materials for the production and transportation of crude oil (and its products) from where they are produced (oil well) to where they are processed (refineries) and the refined products further transmitted to where they are consumed [5]. However, carbon steel is susceptible to corrosion attack particularly in the harsh environments of the oil and gas industry thus affecting the capital expenditure (CAPEX), operational expenditure (OPEX) and health and safety environment (HSE) [6, 7]. Regardless of these drawbacks, carbon steel still remains the material of choice in the oil and gas industry since no alternative materials have adequately exhibited better properties for oil and gas applications. Thus researchers [8-11] have for decades engaged in enhancing the properties of carbon steel through diverse physical, chemical and thermo-mechanical processes. Alloying with strong carbide forming elements to produce micro-alloy steels has been one of the major techniques employed to improve the corrosion performance of carbon steels [11, 12]

Micro-alloy steels are steel grades that contain small amounts of strong carbide forming elements such as Tantalum (Ta), vanadium (V), Niobium (Nb) and Titanium (Ti). These elements are called strong carbide formers because they preferentially combine with carbon in carbon steels thus leaving chromium (Cr) in solution in the ferrite structure of the steel [13]. This un-combined chromium provides enhanced corrosion resistance which

is not possible if allowed to form carbide. The carbides of the micro-alloying elements provide precipitation strengthening as well as high yield strength regardless of the low carbon content of the steel. The individual percentage of these alloying elements is generally less than 0.1 wt% while their overall percent in any micro-alloyed steel is often less than 1.5 wt% [13, 14]. Most of the elements that are located at the left of iron in the periodic table are considered as strong carbide-formers [15]. These elements have found extensive application in micro-alloying of steels. However, Hafnium (Hf) and Zirconium (Zr) have not receive comparative application as the other neighbouring elements (Ti, V, Nb, Cr etc) [16]. Therefore in this work, the effects of Hf and Zr (as strong carbide formers) on the corrosion performance of three proprietary micro-alloyed steels were investigated.

1.1.1 Corrosion defined

Corrosion is an inevitable, thermodynamically feasible and naturally occurring process occasioned by the interaction of materials, particularly metals with the environments that culminates in the deterioration of the material's properties. Corrosion is inevitable because it can never be prevented but can be managed or controlled. It is also thermodynamically feasible because most pure or refined materials are in unstable states due to the energy acquired during manufacturing processes. The processed materials therefore have strong driving force to return to their stable, native and original low energy oxide state (ore). This is illustrated in Figure 1.1.

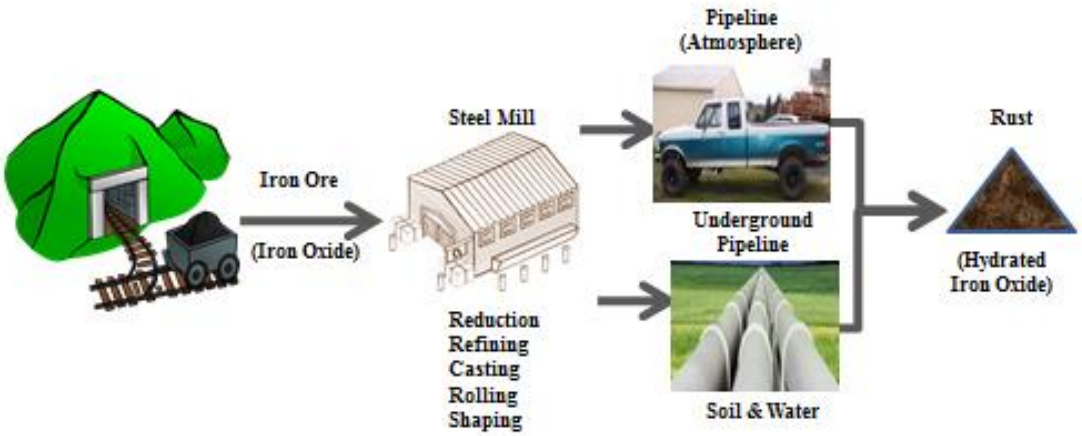

Figure 1- 1: The tendency of materials to return to their native, low energy oxide state.

Corrosion can equally be considered as a natural process because the major corrosive species which are oxygen (air) and water (moistures) are present in most natural environment. Therefore corrosion can occur everywhere without inducement and its

impacts which can cause dangerous and expensive damages affect virtually all facets of world's infrastructures ranging from domestic, highway, bridges and buildings to oil and gas, chemical processing and water and wastewater, etc [5, 17-21].

It then means that a combination of interaction between environment and material must be involved before corrosion can be fully discussed. This is because, the corrosion behaviour of a material depends on the environment in which it is subjected and the corrosivity of an environment depends on the material exposed to that environment. This combination can be natural (desirable) if the interaction between the material and the environment does not result in detrimental or costly corrosion problem. On the other hand, undesirable combination occurs when the interaction between a material and its environment results in severe corrosion damage [21].

Although the fundamental mechanism of corrosion involves the creation or existence of corrosion cells which generally consist of an anode where corrosion (oxidation) occurs and at least one cathode where reduction takes place, yet the various forms in which corrosion manifest itself are myriad [22]. Researchers [21, 22] attributed this to the complexity of corrosion phenomenon occasioned by several factors involved. However, literatures [21, 22] classified these factors into three major groups namely: nature of corrosive medium which may be wet or dry; mechanism of corrosion which may be electrochemical or chemical and the appearance of the corroded metal which may be uniform or localized. The morphology of the corrosion attack which can be identified by visual observation either with naked eye or by magnification is the basis for classification by appearance. The most common forms of corrosion are illustrated in Figure 1-2 while a summary of the mode of corrosion are listed in Table 1-1

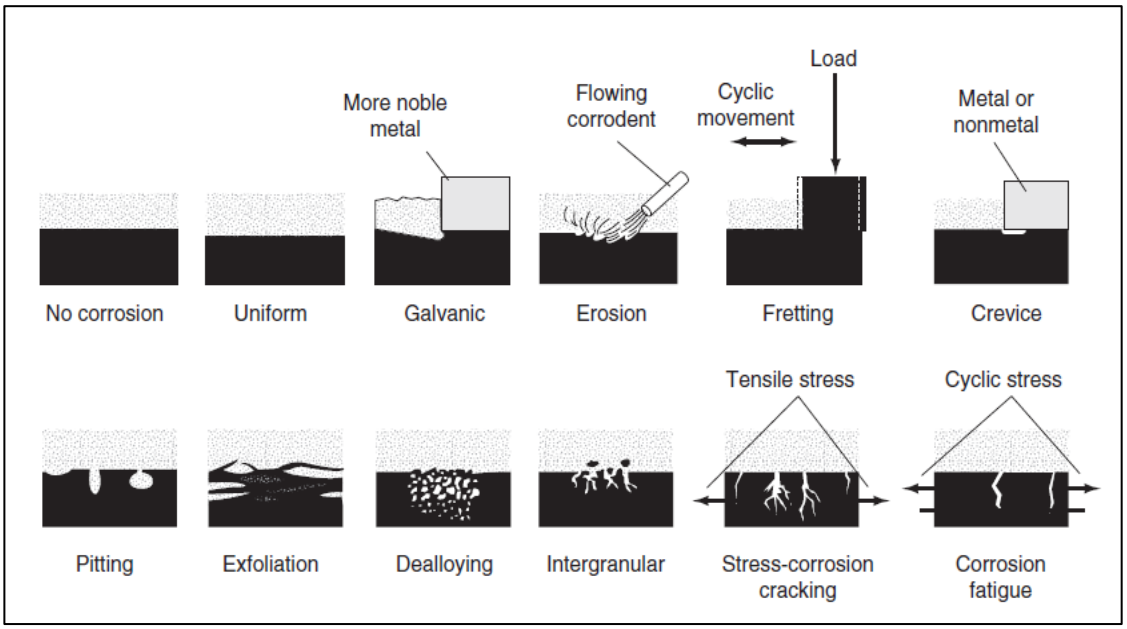

Figure 1- 2: Common Forms of Corrosion [21].

1.1.2 Cost of corrosion

Corrosion affects the society on the daily basis, causing dangerous and expensive damages to everything from pipelines, bridges, and public buildings to vehicles, water and wastewater systems, and even home appliances. The cost of corrosion control and the associated damages are enormous [18, 19, 21]. A two years (1999 - 2001) study titled 'Corrosion Cost and Preventive Strategies in US', conducted by Gerhardus, et al [19] with support from U.S Federal Highway Administration (FHWA) and NACE International revealed that the total annual estimated direct cost of corrosion in the US economy is $276 billion. This is approximately 3.1 % of the nation's Gross Domestic Product (GDP) [18]. Due to inflation, this amount increased to about $1 trillion in 2013 and rose to $ 1,1 trillion in 2016 representing about 6.1 % of US GDP. This figure does not include the indirect cost which is estimated to be equal to the direct cost [18, 19]. The total estimated annual cost of corrosion for some selected economic sector in US is shown in Figure 1-3. Researchers [18, 19, 21], estimated the global annual direct cost of corrosion to about 3 - 4 % of the industrialized nations GDP which amounts to over $1.8 trillion. Total direct annual cost includes costs incurred by owners and operators of structures, manufacturers of products and suppliers of services. On the other hand, indirect cost are factors such as loss of production, environmental impact, transportation disruptions, injuries and fatalities [18, 19].

Table 1- 1: Summarized Corrosion Mode

Type of Corrosion	**Material System**	**Driving Force**	**Control Point**	**Remark**
Uniform/General Corrosion	All metals in Atmospheric Environment	- Atmosphere -Temperature	- Painting - Hot Dip galvanizing	- This forms about 50% of the total corrosion cost -Seldom lead to failure
Intergranular Corrosion	All Alloys	-Third phase Precipitate - Temperature	-Heat Treatment in Manufacturing -Welding during Fabrication	- Loss of strength and ductility - Severe attack can lead to failure
Galvanic Corrosion	Galvanic Coupling Materials e.g. Fe with Cu, Carbon Steel with Stainless Steel	Different metals in electrolytic solution	- Proper Design -Riveting/Joining Materials	Moderate effect but can be detrimental for a longer period
Crevice Corrosion	Metal to Metal/Non Metal in electrolyte Metal in two electrolytes	-Small Gap in electrolyte (<3.18mm) - Stagnant fluid	- proper Design - Casketing Materials - Proper Drainage Practice	Moderate effect but can be detrimental for a longer period
Pitting	Stainless Steel and Aluminium in Chloride or bromide environment (water/soils)	- Surface Irregularity - Presence of Cl^- or Br^- ion - Chemical composition - Temperature	- Surface Quality Control - Proper welding Practice - Proper Material Handling - PREN (Material Selection) - CPT (critical Pitting Temperature)	Severe attack can lead to failure (Second biggest corrosion failure)

Table 1- 2: Summarized Corrosion Mode (Continues)

Type of Corrosion	**Material System**	**Driving Force**	**Control Point**	**Remark**
Erosion corrosion Tribo- Corrosion	Carbon steel, stainless steel in Flowing fluid containing abrasives	Synergy effect of passive film breakdown by abrasives and localized corrosion	Corrodent turbulence Corrodent impingement in elbow and tees	Severe attack can lead to failure
Stress Corrosion Cracking SCC/HE-SCC	Stainless steel, carbon Steel in High pH (pH>9.3) - temperature Sensitive near neutral pH (5.5 - 7.5) - Free potential - non Temperature Sensitive	- Moisture - temperature Region - Existence of Residual Stress - Suitable pH -Presence ofH_2S, Chloride ion	-Moisture control -H_2S content - Operation temperature	- Biggest cause of corrosion failure - SCC found in gas and liquid pipelines
Biological Corrosion/Microbial Induced corrosion	All metals in environments with - Sulfate reducing Bacteria (SRB) - Sulphur/sulfate oxidizing bacteria -Fe/Mn Oxidizing Bacteria - Organic Acid Producing bacteria	Gravitational and pellicle water - pH 6 - 8 - Potential -42 - 820 mV - Temperature 20 - 45 ^{0}C	Application of organic coating Cleaning Practice Use of Biocide	In US $1.2 billion Spent annually on biocidal chemicals to fight MIC.

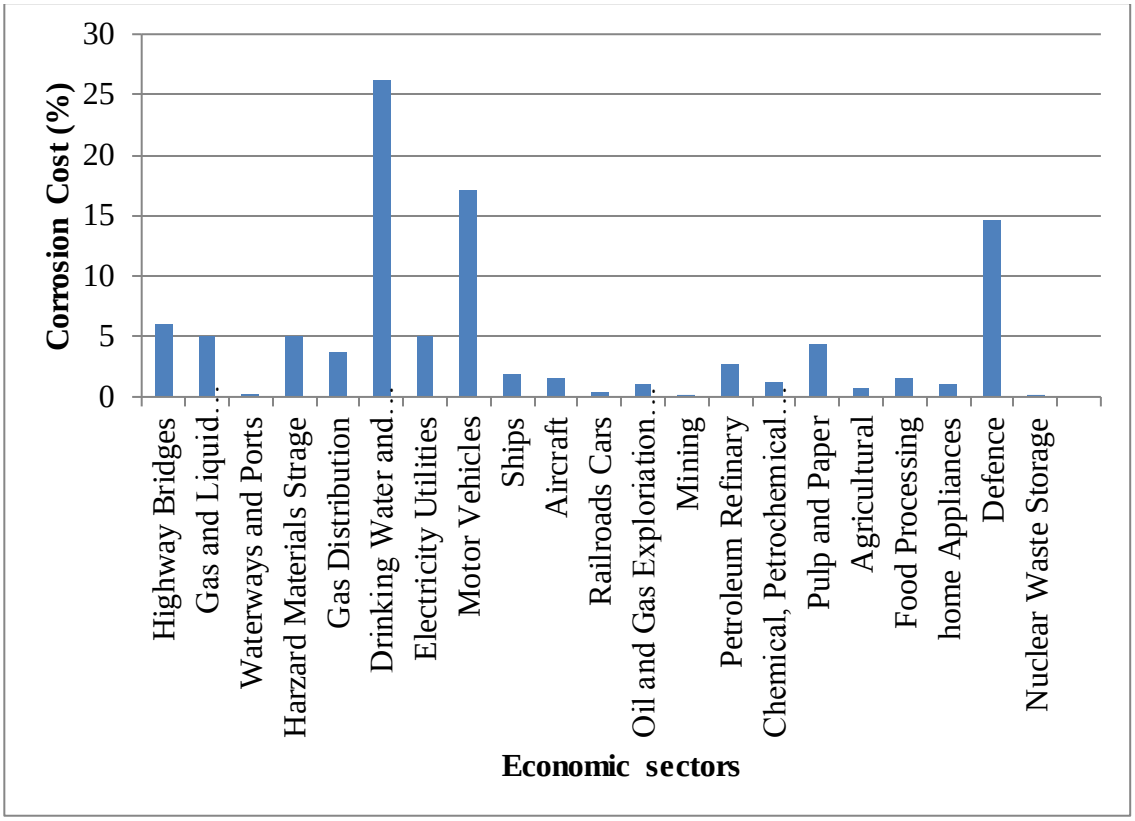

Figure 1- 3: Cost of corrosion Per Analyzed Economic Sector (data from [19])

Although corrosion is so prevalent and takes so many forms, its occurrence and associated costs can never be completely eliminated. However, studies [17-19] estimated that about 25 to 30% of annual corrosion costs could be saved if optimum corrosion management practices are employed. The most commonly used corrosion prevention methods include organic and metallic protective coatings; corrosion resistant alloys, plastics, and polymers; corrosion inhibitors; and cathodic protection. Cathodic protection is a technique used for protecting pipelines, underground storage tanks, and offshore structures by creating electrochemical cell in which the surface to be protected is the cathode and corrosion reactions are mitigated. [19, 20]. These methods are either uneconomical and/or too cumbersome to practive and sustain.

The impact of corrosion on the integrity of facilities is witnessed in every stage of operations in the petroleum industry ranging from drilling, production, transportation, refinery and distribution. This impact can be considered in terms of its effects on the capital expenditures (CAPEX), operational expenditures (OPEX), and health, safety and environment (HSE) [6, 17-19]. Kermani and Harr [6] reported that corrosion related failures constitutes about 25% of the failures experienced in oil and gas industry. Half of

these failures are linked to sweet (CO_2) and sour (H_2S) producing fluids while the balance are linked to other contributing factors as shown in Figure 1-4.

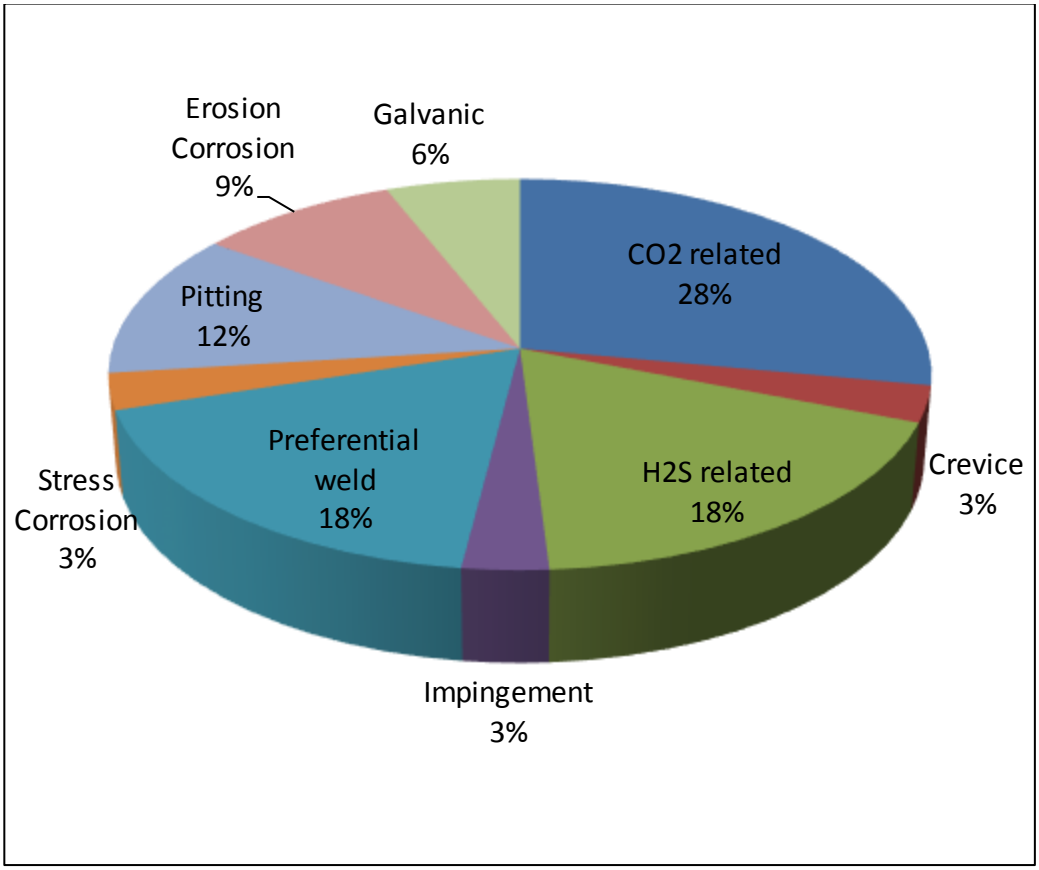

Figure 1- 4: Causes of Corrosion Related Failure in Petroleum Industry (data from [23])

Kermani and Harr [6] enumerated four major ways in which cost can be incurred due to corrosion. These include:

a) Design expenditure (CAPEX); these are extra costs incurred as a result of additional capital outlay on preventing, minimizing and controlling corrosion at the project stage.

b) Operating expenditures (OPEX): these are daily expenses associated with planned and unplanned maintenance, repair of corrosion damaged facilities and other corrosion control activities.

c) Replacement expenditure. These are capital expenditure incurred during operations due to replacing or repairing major components of corroded facilities.

d) Lost revenue are cost associated with lost production, spoilage, contamination of products and delay in production due to corrosion related problem.

1.1.3 Micro-alloyed Steels

Iron and steel development which started at about 1850 [24, 25] has evolved through many technological and industrial evolutions aimed at producing better and newer grades

of steels suitable for broad and diverse range of applications. These evolutions which were anchored on different manufacturing processes accounted for the production of variety of grade of steels with specific combination of desirable properties such as strength, toughness, weldability, corrosion resistance, favourable strength-to-weight ratio and formability [14, 26-28]. The evolution can be chronicled from Bessemer process, Open hearth process, Basic oxygen steelmaking (BOS), to Electric arc furnaces (EAF) [24, 25]. One of these variety of steels is the various grades of micro-alloy steel. Micro-alloy steels typically contain 0.07 - 0.12 wt% C, up to 2 wt% Mn and small additions of alloying elements such as niobium, vanadium, titanium, include molybdenum, zirconium, boron, aluminium, nitrogen and rare earth metals (all usually max. 0.1%) in various combinations [26, 28-30]. Alloying elements are usually present in micro-alloy steels and their functions as reported by Baker [28] are shown in Table 1-2.

Table 1- 3: Alloying elements and their influence in micro-alloyed steels [28]

Element	wt%	Influence
C	< 0.25	- Strengthener
Mn	0.5 - 2.0	- Delays austenite decomposition during accelerated cooling.
		-Decreases ductile to brittle transition temperature
Si	0.1 - 0.5	-Deoxidiser in molten steel;
		-Solid solution strengthener.
Al	< 0.2	-Deoxidiser. -Limits grain growth as AlN
Nb	0.02 - 0.06	-Very strong ferrite strengthener as Nb(C,N)
		-Delays $\gamma \rightarrow \alpha$ transformation
Ti	0 - 0.06	-γ grain size control be TiN
		-Strong ferrite strengthener
V	O - 0.10	-Strong ferrite strengthener by V(C,N)
Zr	0.002 -	-γ grain size control by Zr(C,N)
	0.05	-Strong sulphide former
N	< 0.012	-Forms nitride and carbo-nitrides
Mo	0 - 0.3	-Promotes bainite formation
Ni	0 - 0.5	-Increases fracture toughness
Cu	0 - 0.55	-Improves corrosion resistance, -Ferrite strengthener
Cr	0 - 1.25	-Increases atmospheric corrosion resistance
B	0.0005	-Promotes bainite formation

Davis [26] and Matlock and Speer [31] reported that low carbon content of micro-alloy steels is responsible for adequate formability and weldability. On the other hand, the alloying elements contribute to improved strength by forming carbides, nitrides and/or carbo-nitrides which induce grain refinements, precipitation hardening and solid solution strengthening [29, 31]. The formation and presence of these fine grains, which is achieved through micro additions, controlled rolling and appropriate heat treatment is the most essential requirements for meeting the desired mechanical properties in micro-alloy steels [14, 27].

DeArdo, et al [27] reported that the role of micro-alloying elements in improving the strength of micro-alloy steels can be achieved through a combined effects of grain refinement, solid solution strengthening, dislocation strengthening and precipitation hardening. This relationship is summarized using expanded Hall-Petch Equation as shown in Equation 1.1.

$$YS_{obs} = \Delta YS_{lf} + \Delta YS_{ss} + \Delta YS_{dis} + \Delta YS_{ppt} + K_y d^{-\frac{1}{2}} \qquad 1.1$$

Where

YS_{obs} = Observed yield strength

ΔYS_{lf} = Lattice friction (Peierls Nabarro)

ΔYS_{ss} = Solid solution strengthening

ΔYS_{dis} = Dislocation strengthening

ΔYS_{ppt} = Precipitation hardening

K_y = Strengthening coefficient (a constant specific to each material)

d = Grain size diameter

There are contradictory reports on the effects of grain size on the corrosion resistance of metals. While some authors claimed decrease in corrosion rate with decrease in grain size, others postulated the opposite [32]. This was attributed to the inability to decouple the effects of processing and processing route from grain size effect on corrosion resistance. Grain boundaries and triple junctions have been reported to have unique electrochemical properties, which will cause preferential dissolution in specific electrochemical circumstances, while being unaffected in other circumstances. It was then observed that grain refinement may act to aggravate the behaviour observed from coarser grain structures in any specific environment. For example, if an electrolyte simulates active behaviour on a coarse-grained sample, then grain refinement will likely make the surface

"more" active and tend to enhance corrosion. On the other hand, if a coarse-grained microstructure is passive in a given electrolyte, then grain refinement will likely result in the formation of more stable passive film. This means that the electrolyte play significant role on the effects of grain refinement on the corrosion behaviour of alloys [32, 33].

The estimated world production of all grade of steels in 2014 was about 1.65 billion tonnes of which 200 million tonnes accounting for about 12% was micro-alloy steels [14, 28]. According to Davis [26], Matlock and Speer [31] and Fernandez, et al [29], micro-alloyed steels are designed to provide specific desirable combination of mechanical properties (strength, toughness, weldability) and better corrosion resistance than the conventional carbon steels. Thus micro-alloyed steels are classified not on the basis of chemical composition but on the specific mechanical properties they are designed to meet. Davis [26] identified six (6) categories of micro-alloyed steels. These categories and their functions are shown in Table 1-3.

Micro-alloyed steel because of its unique combination of mechanical properties has found applications in virtually all facet of engineering sectors such as oil and gas pipelines, heavy-duty highway and off-road vehicles, construction and farm machinery, industrial equipment, storage tanks, mine and railroad cars, bridges, offshore structures, power transmission towers, light poles, and building beams etc [24, 26, 34, 35]. This increase in interest in the use of micro-alloy steel, particularly in the oil and gas industry is in recognition of some of its advantages over other structural engineering materials [14, 31, 36]. These advantages include:

i) Savings in materials used due to improved strength to weight ratio.

ii) Reduced manufacturing cost due to savings in handling, transportation and welding costs.

iii) Savings in operational cost since less energy will be required

iv) The development of new steels that can be tailored to specific applications

Many studies [13, 36-38] on the use of micro-alloyed steels in oil and gas industry have been published. For instance Billinghan, et al [36] reviewed the use of various grades of micro-alloyed steel and presented their results according to area of applications as shown in Table 1-4.

Table 1- 4: Categories and Characteristics of Micro-alloyed steels (6)

S/No	Class	Major Additions	Characteristics/Applications
1	Dual Phases Steels	V,	-Ferrite-Martensite structure -High tensile strength and ductility. (Automobile Industries)
2	Weathering Steels	Cr, Cu, Ni, P	- Bainite Structures - Atmospheric corrosion resistance - Solid solution strengthening (Bridges, Utility towers, Light Poles, High way guiderails).
3	Micro-alloyed ferrite-Pearlite Steels	Nb, V, Ti, etc	- Precipitation Strengthening - Grain refinements, (Transmission temperature control).
4	As-rolled Pearlite Steels	V	Strength, toughness, formability, Weatherbility
5	Aciculate Ferrite (Low-carbon Bainite) Steels	V, Nb	High yield strength, Weldability, formability and good toughness.
6	Inclusion-Shape Controlled Steels	Ca, Zr, Ti or Rare earth elements	- Improved ductility and - Through-thickness toughness.

Table 1- 5: Uses of Micro alloyed steels in offshores [36]

Strength MPa (grade)	Process Route	Application Area
350 (X52)	-Normalised -TMCP	-Structures - Structures and Pipelines
450 (X65)	- Q & T - TMCP	- Structures - Pipelines
550 (X80)	- Q & T - TMCP	- Structures & Moorings - Pipelines
650	- Q & T	- Jack-ups & Moorings
750	- Q & T	- Jack-ups & Moorings
850	- Q & T	- Jack-ups & Moorings

Edmond and Cochrane [37] investigated the influence of a wide range of alloying elements such as Nb, Ti, V, Cr, Mn, Si, Cu, Mo and Ni and different processing conditions such as controlled rolling and quenching and tempering on the CO_2 corrosion resistance of micro-alloyed steels. These authors produced steels with improved CO_2 corrosion resistance suitable for oilfield applications. Kermani, et al [13] designed, developed and produced Cr-Mo steels with 3 - 10 times improvement in CO_2 corrosion resistance and less than 1.5 times increase in manufacturing cost than the conventional carbon steel grades. The use of Zr and Hf as alloying elements has not received comparative attention as other traisition metal. Therefore, this study focused on the effects of Zr and Hf (as alloying elements) on the corrosion resistance of micro-alloy steels

1.1.4 Zirconium (Zr) and Hafnium (Hf)

1.1.4.1 Zirconium (Zr)

Zirconium (Zr) is one of the transition metals with atomic number 40 and atomic weight 91.22. It resides in group IVA of the periodic table with titanium and hafnium. It is not one of the abundant elements but is widely distributed in nature ranking 11th in the earth crust. The estimated content of Zr in the earth's crust is about 0.028% which is more than those of common metals like Ni (0.02 %), Cu (0.01 %), Zn (0.004 %) and Pb (0.001 %). About 10% of Zr produced is used as alloying elements in steel while 90% is used in nuclear reactors [39-42].

Zirconium is always found in combination with Hafnium (Hf) which has almost identical chemical properties [39-41]. According to Holmes [40] the chemical similarity between zirconium and hafnium is more pronounced than any other two elements in the periodic table thus making their separation extremely difficult. Golden [43] classified zirconium based on hafnium content as 'ordinary purity Zr' containing 2 to 2.5 % Hf and 'high purity Zr' containing less than 0.1 % Hf. In most cases, zirconium is often considered for the same applications as Hafnium, because of their very similar physical and chemical characteristics [40, 42].

1.1.4.2 Hafnium (Hf)

Hafnium is a heavy sliver-grey metal with atomic number 72 and atomic weight 178.49. Hafnium resides in the reactive metal group IVA with zirconium (Zr) and titanium (Ti). It is naturally found in association with Zr and these two elements have similar chemical and physical characteristics which makes their separation very difficult. Hafnium is a

moderately common element in the Earth's crust. Its abundance is estimated to be about 5 parts per million making it as abundant as bromine, uranium, or tin. Naturally the ratio of Hf to Zr is approximately 1:50 from where Hf can be exclusively produced as a co-product of nuclear-grade Zr [40, 44, 45]. Nielsen [46] reported that because of the similar chemical properties between Hf and Zr, a review of the chemical behaviour of Zr can be a useful indicator of the chemical behaviour of Hf . Also Aerospace Technology Institute (ATI) in their technical data sheet [45] and Holmes [40] reported that the corrosion behaviour of Hf is very similar to that of Zr and in the absence of data can be considered to be roughly equivalent.

1.2 Aim and scope of study

This research is aimed at improving the corrosion performance of three proprietary micro-alloy steels by alloying them with non-conventional carbide forming elements. To achieve this aim, this work was grouped into three (3) major steps namely:

1) Preliminary investigation of the corrosion behaviours of three proprietary micro-alloyed steels in brine solutions and simulated oilfield environment.
2) Alloying of the micro-alloy steels with non-conventional carbide forming elements (Zr and Hf).
3) Investigating the corrosion improvements and/or otherwise of the alloyed steels in comparison with the results obtained in selected media of step (1) above. API 5L X65 grade steel, which many authors [29, 47, 48] have reported is the most widely accepted and used steel for production and transportation of oil and gas was used as reference sample.

Pipelines, being the major means of transporting crude oil and its products, are laid all over the world criss-crossing continents and countries. Also oil wells are located at different places with varying environmental conditions and the constituents of the crude oil that flow through these pipes differ depending on oil well locations. This means that both the internal and external surfaces of the pipelines are in contact with extensively varied corrosive environments. Studies [4, 11, 23] have shown that the major constituent of oilfield environments include carbon dioxide (sweet), hydrogen sulfide (sour) in the produced fluids and oxygen in injected water. Among these major corrosive constituents, CO_2 (sweet) corrosion is far more prevalent accounting for about 60% of oilfield failure [11, 13]. The aggressiveness of CO_2 corrosion in oil and gas industries is affected by

environmental and metallurgical factors some of which include temperature, CO_2 partial pressure, pH, solution chemistry, surface film, steel composition and microstructure/heat treatment [12]. Thus this work intend to alloy commercially supplied micro-alloyed steels with Zr and Hf. The corrosion behaviour of the unalloyed and alloyed steels in different simulated oilfield environment will be compared so as to determine the the improvement and/or otherwise in corrosion resistance of the alloyed steels. The scope of this study is schematically presented in Figure 1-5. These shall involve varying the environmental factors and investigating their effects on the corrosion propensity of the micro-alloy steels and their specimens alloyed with Zr and Hf.

1.3 Objectives

The aim of this work will be pursued under the following objectives:

i) **To investigate the corrosion propensity of three micro-alloy (as-received) steels**: This is aimed at assessing the corrosion behaviour of the steels by subjecting them to simulated oilfield environments and investigating the influence of major environmental factors such as temperatures, solution pH, solution chemistry and chemical compositions. The role played by the various alloying elements in determining the corrosion behaviour of the steels will be investigated.

ii) **To determine the effect of Zr and Hf on the CO_2 corrosion of the steels in simulated produced water (SPW)**.

V, Ti and Nb have found wide application as alloying elements in micro-alloy steels [14, 26, 28, 29] but Zr and Hf which are their neighbours in the periodic table have not received comparative attention [16]. These elements which are called strong carbide formers are located at the left of iron in the periodic table as shown in Figure 1-6. These elements improve the strength of micro-alloy steels through grain refinements, controlled rolling and appropriate heat treatment [14, 15, 27].

From thermodynamic data [49], Zr and Hf have lower Gibbs free energy of carbide formation than the conventional alloying elements (Ti, V and Nb). Therefore, Zr and Hf can precipitate more carbides and strengthen the steel more than these elements. Thus, this work investigated the effect of Hf and Zr on the mechanical and corrosion properties of the proprietary micro-alloyed steels.

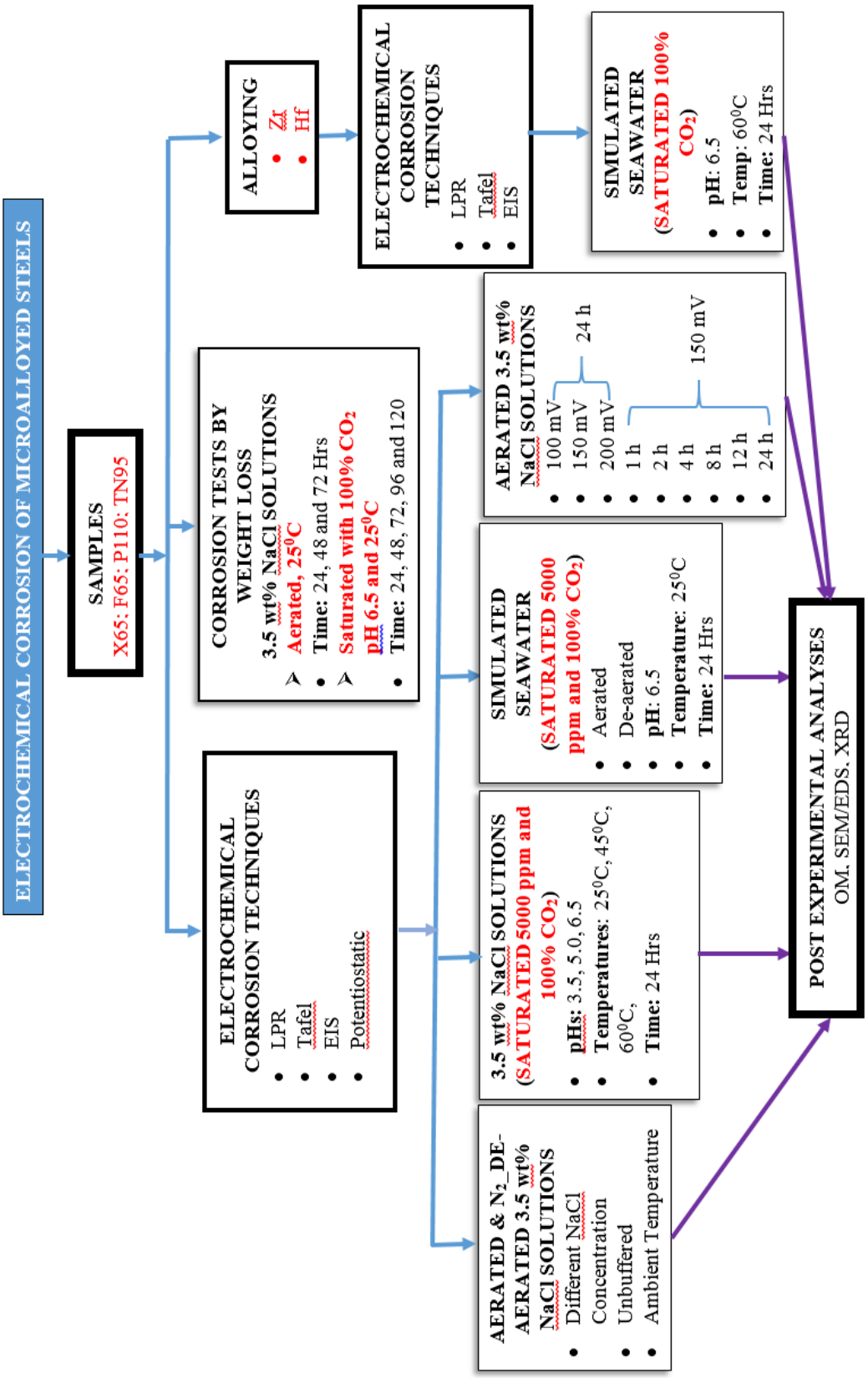

Figure 1- 5: Schematic representation of the scope of this work

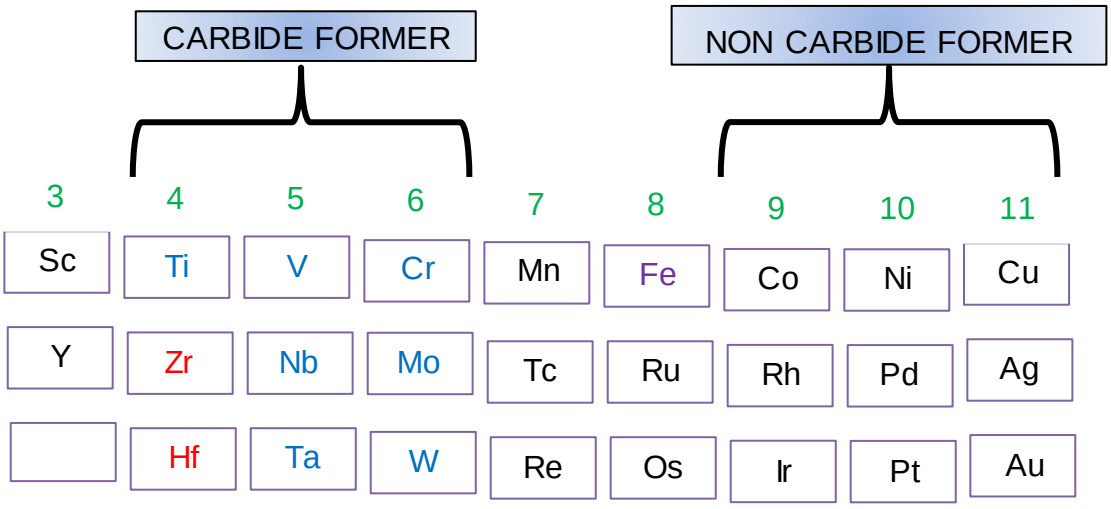

Figure 1- 6: The periodic table showing the positions of strong carbide-forming elements[15]

iii) **To compare the changes in the corrosion behaviour occasioned by alloying the steels with Zr and Hf.** This involved a systematic and empirical assessment of the improvement of the corrosion behaviour of the steel samples as a result of alloying them with Zr and Hf. Since very few works [50] have been conducted on alloying carbon steel with Zr and Hf, these will be one of the major relevance of this work.

1.4 Hypothesis

This work is aimed at investigating the corrosion behaviour of commercially supplied micro-alloyed steels and their alloys with Zr and Hf in various simulated corrosive media. API 5L X65 steel grade was used as reference sample. The principles and motivations of this work were based on the following four fundamental assumptions.

i) Low carbon content (0.12 – 0.25 wt%) of the samples [51]**.**

Experimental evidence [52, 53] revealed that decrease in carbon content in steel decreases corrosion rate. This is because high carbon content favours the formation of pearlite (ferrite + Fe_3C) which has been adjudged to have detrimental effect on the corrosion behaviour of carbon steel because it enhances and acts as cathodic site [53]. The proprietary commercial micro-alloy steels for this work are low carbon steels and so exhibit the capabilities for possible improvement in corrosion resistance.

ii) Strong alloying influence of Zr and Hf:

When carbon steel is alloyed with Zr and Hf, alloyed solid solution is formed as these elements dissolved in **α**-ferrite phase. In an electrochemical system, these alloyed solid

solutions favour micro anodic effect more than the cathodic effect [50] providing more anodic sites than cathodic sites thus enhancing the corrosion resistance.

iii) Strong affinity of Zr and Hf for oxygen, nitrogen, sulfur and carbon:

Deeley, et al [35] and Baker [39] reported that Zr and/or Hf has strong chemical affinity for oxygen, nitrogen, sulfur and carbon. Thus Zr/Hf react with oxygen to form chemically inert, tenaciously adherent oxide film. These oxide films are formed when there are free un-dissolved Zr and Hf above the solubility limit. Kovalenko and Zats [50] reported that increase of Zr beyond the solubility limit does not reduce the corrosion rate but only results to constant corrosion due to the passivation effect of the oxide.

iv) High negative energy (ΔG) of carbide formation of Zr and Hf.

Literatures [53-56] have reported an increase in corrosion rate with decrease in grain size. However there are also opposite view [57, 58]. It is also an established facts among many authors [14, 29, 31, 59] that one of the basic functions of alloying elements in carbon steel is grain refinements occasioned by the formation of carbide with the attendant improved mechanical properties. From thermodynamic point of view, Zr and Hf have more negative Gibbs free energy for carbide formation than most of the conventionally used micro alloying elements [49, 60]. Therefore the presence of Zr and Hf in micro-alloy steel will yield better properties than the conventional alloying elements. This is one of the strong motivations for this work.

1.5 Novelty

Zr and Hf as micro alloying elements in steels have not witnessed an increased application like other conventional micro alloying elements such as Ti, V, Nb, etc [15] probably due to their reactive nature and limited availability [35]. However, thermodynamic records [60] showed that Zr and Hf form more stable carbides than the widely used strong carbide formers in carbon steel. The addition of Zr and Hf to carbon steel, depending on the quantity, can form either solid solution or carbide precipitates. If in micro quantity (<0.15), it will dissolve in α-Fe phase thus influencing micro anodic effect and so decreases corrosion rate [50]. On the other hand, if the added Zr and Hf exceeds solubility limit, the free Zr and Hf help to scavenge impurities (oxygen, nitrogen, sulfur,) [35]. These precipitates increase the micro cathodic sites which in turn increases the anodic passivation of the rest of the substrate by strengthening and anchoring the corrosion products on the surface. This facilitates the formation of stable passive state [50]. Thus

alloying the samples with Zr and Hf whether in micro (< 0.15) or macro (> 0.15) quantity will substantially improve the corrosion resistance of the samples. Therefore the development of Zr and Hf base micro-alloyed steels with improved corrosion behaviour more than the widely used micro-alloyed steel is one of the novelties of this work.

The three steels, ASTM A694-F65, P110 IC and TN95 HS that were investigated are proprietary steel grades. Very few works [61, 62] with regards to the corrosion behaviour of P110 IC have been published. On the other hands, no work on the corrosion behaviour of ASTM A694-F65 (F65) and TN95HS have been published. This work also investigated the corrosion performance of these steels in different simulated oilfield environments and correlated the results with equivalent standard steel grades (API 5L X65).

1.6 Thesis layout

This work is focused on the comparative assessment of the corrosion performance of as-received and alloyed proprietary micro-alloyed steels and is presented here in 7 chapters

Chapter 2 presents a brief overview of the evolution of steel making technology which resulted in the production of different grades of steel with desired properties for specific applications. The design concept of micro-alloyed steels was discussed highlighting the theory of alloying process and the functions of the alloying elements. The theory of electrochemistry with emphasis on the thermodynamic, kinetic and types of electrochemical corrosion techniques employed in assessing the corrosion propensity of the steels are also discussed in this chapter.

Chapter 3 reviews some of the literatures devoted to micro-alloyed steel as a potential material for mitigating corrosion menace in oil and gas industry. The specific functions of various alloying elements as presented by certain authors were reviewed. The mechanism of CO_2 corrosion which is considered the dominant form of corrosion in oil and gas industry and the influence of various environmental and metallurgical factors on the corrosion behaviour of oilfield equipment are reviewed also.

Chapter 4 describes the characteristics of the materials used, sample preparation, experimental set-up, test conditions, electrochemical techniques employed, alloying methods and equipment operation procedure. Post experimental surface analysis techniques deployed to validate the corrosion results are also highlighted in this chapter.

Chapter 5 presents all the experimental results of the unalloyed and alloyed specimens, the effects of environmental and metallurgical factors on the corrosion behaviour of the as-received and alloyed samples. The confirmation of the experimental results using appropriate surface analysis techniques are also shown in this chapter.

Chapter 6 discusses all the experimental results of the un-alloyed and alloyed specimens and the influence of environmental and metallurgical factors namely steel microstructures, chemical composition, dissolved oxygen, solution pH, temperature and solution chemistry using different electrochemical polarization and surface analysis techniques with a view to assessing the corrosion propensity of the proprietary micro-alloyed steels and their alloys.

Chapter 7 summarises the overall research findings and compared the corrosion performance of the as-received micro-alloyed steels with the alloyed micro-alloy steels highlighting the contribution of Zr and Hf to the final results. The contribution of this work to scientific knowledge and its practical applicability to the industrial use is drawn as conclusion.

Chapter 2: Theory of micro-alloying and corrosion mechanism

This chapter presents a brief overview of the evolution of steel making technology which culminated in different grades of steel with desired properties for specific applications. One of such grades of steel is micro alloyed steel which is the material of interest in this work. The grade and design concept of micro-alloyed steels were discussed highlighting the types, solubility and functions of alloying elements. This chapter also examined the theory of alloying with the aim of enhancing the corrosion resistance of steels through micro addition of elements. This is followed by discussion on the theory and techniques of corrosion mechanism which could be either by weight loss or electrochemical corrosion. The thermodynamic, kinetic and types of electrochemical corrosion techniques employed in assessing the corrosion propensity of steels were emphasized.

2.1 Metallurgy and the development of micro-alloy steel

The development of iron and steels as structural materials began at about 1850 [24, 25] and it has gone through several evolutions in a bid to achieving specific properties suitable for desired applications. These evolutions can be attributed to different manufacturing processes aimed at improving the properties of steels in order to meet the preferred properties and for specific structural applications. These desired properties include but not limited to strength, toughness, formability, weldability and corrosion resistance [63]. The evolution in the steel manufacturing processes can be chronicled as Bessemer Process, Open Hearth Process, Basic Oxygen Steelmaking (BOS), Electric arc Furnace (EAF), etc [24, 25].

The products of these early steel manufacturing processes did not meet the stringent excellent combination of mechanical properties required for some specific structural materials used in the oil and gas industry [25, 27, 64]. This was occasioned by high carbon content with coarse ferrite-pearlite microstructures leading to low yield strength of about 300 MPa with the attendant poor ductility, toughness and weldability. These poor mechanical properties can be attributed to large grain size which according to Hall-Petch formula in Equation 2-1 is detrimental to yield strength.

$$\sigma_y = \sigma_0 + \frac{K_y}{\sqrt{d}} \qquad 2\text{-}1$$

Where

σ_y = yield stress,

σ_0 = a materials constant for the starting stress for dislocation movement

K_y = the strengthening coefficient (a constant specific to each material), and

d = the average grain diameter.

Equation 2-1 shows that fine grain size significantly improves the mechanical properties and crack resistance of carbon steels. Other properties that make carbon steel suitable for structural applications include ability to obtain preferred and different properties via appropriate thermo-mechanical treatments, low cost, availability, and easy to shaping, forming and machining. These properties of carbon steel have been studied in depth and are found to exhibit good weldability and good mechanical properties (strength, toughness, formability) [3, 4, 65]. However, the use of carbon steel in the oil and gas industries is hampered because of its susceptibility to corrosive environments of oilfield. Efforts to reduce the susceptibility of carbon steels (in corrosive environments) through the use of inhibitors such as benzimidazole [12], 2,5-disubstituted-1,3,4-oxadiazoles [66] and rhodanine azosulpha in conjunction with constant monitoring have been adjudged very expensive and difficult to sustain [67, 68]. Also literatures [13, 23, 37, 68] on mitigating the effects of corrosion by using high corrosion resistant alloys (CRA) such as Cr-steels, other stainless and high alloyed steels were reported uneconomical due to increase in capital expenditure (CAPEX) and operation expenditure (OPEX) [23, 37].

Since carbon steel cannot be replace economically as structural materials for oil and gas facilities [68, 69], there has been an increased research to alter the microstructures, composition and/or modify its surface morphology. This is aimed at producing steels with appropriate strength, toughness, formability, weldability and corrosion resistance [63] that can withstand the aggressive sweet (CO_2) and sour (H_2S) corrosive environments and at relative low cost. According to Dugstad [69], carbon steel is so attractive and is widely used in oil and gas industry because its surface are covered by a protective layer of corrosion products. These protective corrosion product layer acts as physical barrier which

retards the mass transfer of corrosive species and prevent further metal dissolution of the blocked steel surface [23, 70]. Stressing on the must use of Carbon steel in oil and gas industries, Edmond and Cochrane [37] reported that about 95% of the construction materials used in oil and gas industries is, and will be for the foreseeable future, carbon steel. Therefore the challenge of reducing the corrosion propensity of carbon steel requires the knowledge of the performance of these protective layers, the means of predicting the breakdown of these layers and the techniques to ensure that robust layers are formed on the surface. This has led to the development of micro-alloy (high strength-low alloy) steels whereby the addition of small amounts of alloying elements will promote the production of low-cost steels with improved mechanical and corrosion properties [23, 71].

2.1.1 Definitions and types of micro-alloy steels

Micro-alloy (high strength low alloy) steels have been categorized as steels with an alloy level of 0.1% for a single alloying elements (such as niobium, vanadium, titanium, molybdenum, zirconium, boron, chromium, copper, nickel, nitrogen and rare-earth metals) and 0.15% for a combination of micro additions [14, 64]. Morrison [14] defined alloy steel, low-alloy steel and micro-alloy Steel using the criteria shown in Table 2-1.

Table 2- 1: Definitions of alloy steel, low alloy steel and micro-alloy steel [14].

Alloy steel	Steel containing significant quantities of alloying elements (other than carbon and the commonly accepted amounts of manganese, silicon etc.) to effect changes in the mechanical or physical properties.
Low alloy steel	Steel containing less than 3.5% of alloying elements e.g. 2.25% Cr 1% Mo.
Aicro-alloy steel	Steel containing small amounts of vanadium, niobium and/or titanium. Individual elements generally less than 0.1% and total micro-alloying elements generally less than 0.15%. Also known as HSLA steels.

Micro-alloy steels constitute about 12% of total world steel products [14] and their development has been instrumental to the expansion of most engineering infrastructures where they find wide applications[14, 31, 48].

Table 2- 2: Comparison of Classes of Micro-alloyed steels [51]

S/No	Class	Major Additions	Functions/properties/application
1	Dual Phases Steels	V, Nb, Ni	-Ferrite-Martensite structure -High tensile strength and ductility. -Automobile Industries
2	Weathering Steels	Cr, Cu, Ni, P	- Bainite Structures - Atmospheric corrosion resistance - Solid solution strengthening Bridges, Utility towers, Light poles, High way guiderails.
3	Micro-alloyed ferrite-Pearlite Steels	Nb, V, Ti, etc	- Precipitation strengthening - Grain refinements, Transmission temperature control.
4	As-rolled Pearlite Steels	V, Ti	Strength, toughness, formability, weatherbility
5	Aciculate Ferrite (Low-carbon bainite) Steels	V, Nb	High yield strength, Weldability, formability and good toughness.
6	Inclusion-shape controlled Steels	Ca, Zr, Ti or Rare earth elements	- Improved ductility and - Through-thickness toughness.

Carbon steels are classified based on chemical compositions but micro-alloy steels are designed to meet specific and excellent combination of mechanical properties such as strength, toughness, formability, good weldability and corrosion resistance. These improved mechanical properties are obtained by adding alloying elements in micro quantities [14, 31]. Depending on the micro additions, microstructures and area of applications, six (6) classes of micro-alloy steels have been identified [31, 47, 48, 51]. A comparison of these classes is shown in Table 2.2.

2.1.2 Design concepts of micro-alloyed steels

Micro-alloyed steels are designed to provide special combination of excellent mechanical properties such as strength, toughness, formability, weldability and corrosion resistance than conventional carbon steel [63].

A combination of improved steelmaking processes, micro-alloying technology and appropriate rolling and cooling practices are necessary for the development of micro-alloyed steels. These consist of mixtures of ferrite, bainite and martensite microstructures in various proportions with yield strengths above 900 MPa and with acceptable levels of ductility, toughness and weldability. These advances in alloy design and processes with the attendant microstructural and property changes within the past five decades are shown in Figure 2-1. This figure shows a progressive reduction in the carbon content of steel and simultaneously increased mechanical strength leading to reduction in pipe thickness, pipe weight, ease of transportation, ease of installation and the accruing low cost [27, 72].

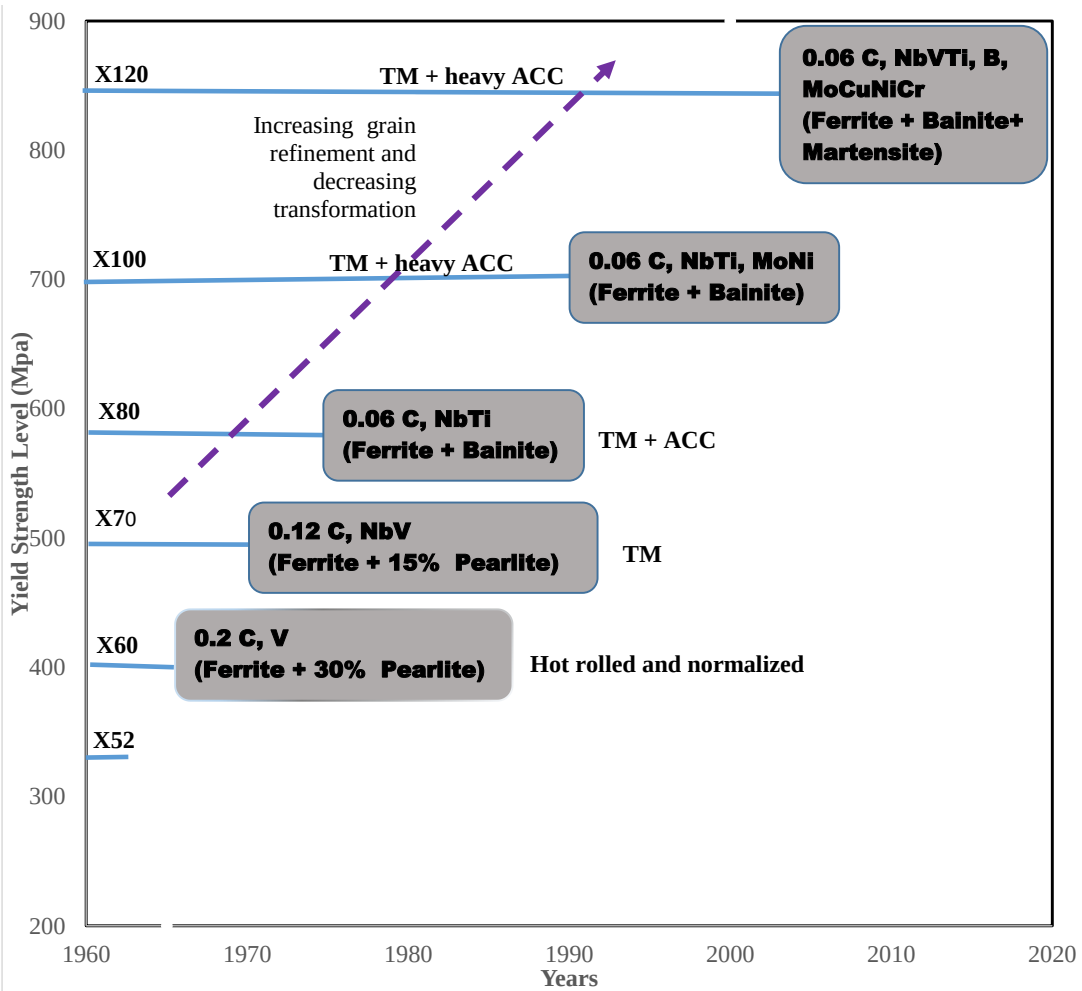

Figure 2- 1: Evolution of microstructure and mechanical properties of steels (TM – Thermomechanical treatment, ACC – Accelerated Cooling) [27, 72]

These amazing properties were achieved in lower carbon content steel through two process routes which impact very high strength irrespective of the composition of the steel. These process routes are interrupted accelerated cooling (IAC) and accelerated direct quenching (ADQ) [27, 72]. The basic objective of accelerated cooling process (thermomechanical controlled processing-TMCP) is to produce steels with higher strength, good toughness and good weldability by grain refinement occasioned by the addition of micro-alloying elements, precipitation hardening and solid solution strengthening [25, 27, 31]. The historical evolution of this process and the associated metallurgical mechanisms as presented by Ouchi [73] is shown in Table 2-3

Table 2- 3: Historical evolution of the controlled rolling and accelerated cooling processes, as well as the strengthening mechanisms and technical standards associated to them. [73]

Year →	1960 1965	1970 1975	1980	1985	1990	1995 2000
Thermomechanical processes	Controlled rolling	Two-phase region rolling				R & D for ultra-fine grain steel
	Low temperature rolling	SHT process				
			Accelerated cooling			
		Low reheating temperature rolling				
					Direct quenching	
					Modeling studies for hot rolling processes	
Strengthening mechanisms	Grain refinement	Deformation strengthening		Strengthening due to Martensite or Bainite		Ultra-fine grain refinement
		Transformation strengthening				
Technical standards				ASTM A841 (TMCP Steel)		
						JIS-SN (Building use)

SHT=Sumitomo High Toughness; TMCP=Thermomechanical Controlled Process with Accelerated Cooling

A comprehensive understanding of the effects of alloying elements in micro-alloying technology is very crucial since it is required for a successful alloy design and for the adoption of appropriate thermo-mechanical treatments in order to produce steel with the desired properties [29, 31]. Alloying elements added in steel making processes may appear in diverse form such as (i) remaining in the steel in the free state, (ii) forming intermetallic compound with iron and/or other elements or with each other, (iii) forming oxides, sulphide or other non-metallic inclusions, (iv) dissolving in iron to form solid solutions or (v) precipitate as carbide. These carbides play significant role in determining the behaviour of the steel and therefore form the focal point for characterising alloying elements as follows:

1) Elements that do not form carbide in steel such as Ni, Si, Co, Al, Cu and Ni
2) Elements that for stable carbides in steel such as Cr, Mn, Mo, W, V, Ti, Zr and Nb.

Addition and/or the presence of non-carbide forming elements in steel does not basically alter the microstructures of the steel. On the other hand, the addition of carbide forming elements will radically alter the microstructures by preferentially forming carbide even at relatively alloying concentration less than 0.1 wt% [15, 25, 27, 31]. These carbides contribute significantly to the strength of the alloy by restricting the movements of dislocations through precipitation strengthening and grain refinements [31].

Enthalpy of formation at 298.15K ΔH_f/KJ mol^{-1}

ΔH_f/KJ mol^{-1}	Carbides	Nitrides
0	Co_3C Fe_3C Mn_3C	
	MoC WC $CR_{23}C_6$ Cr_3C_2 Cr_7C_3 W_2C Mo_2C	Fe_2N Fe_4N Mo_2N
-100	Mo_3C_2	
		Cr_2N CrN VN
-200	VC NbC TaC TiC Nb_2C **ZrC** Ta2C Al_3C **HfC**	NbN AlN TaN Nb_2N Ta_2N
-300		T1N ZrN HfN
-400		

Figure 2- 2: Enthalpies of formation of carbides, nitrides and borides [15, 74]

The fineness of these grains which depends on the activation energy barrier (G*) for nucleation and the volume fraction precipitated determine the strengthening capability of the carbides. The activation energy barrier (G*) for nucleation is a function of the free energy of formation of the carbide, the interfacial energy and the misfit [15]. For these carbide to effectively replace cementite, their free energy of formation must be lower than that of cementite. Therefore, using cementite as the reference ($\Delta H_{f\text{-cementite}} = 0$) and the enthalpies of formation of these carbides, the stability of these carbides and nitrides in steel is shown in Figure 2-2. The carbides at the lower part of this plot such as HfC, ZrC, NbC, VC etc precipitate the finest grains [15, 74]

These precipitates do not match well with the ferrite lattice but are located on crystalline defects thus affecting the strength of the alloy through strain strengthening/hardening. Therefore the effects of micro-alloying elements in strengthening of steel can be attributed to grain refinements, solid solution strengthening, dislocation strengthening and precipitation hardening [27]. This is summarised in an expanded Hall-Petch formula as expressed in Equation 2-2

$$YS_{obs} = \Delta YS_{l_f} + \Delta YS_{ss} + \Delta YS_{dist} + \Delta YS_{pptn} + \frac{K_y}{\sqrt{d}} \qquad 2\text{-}2$$

Where

YS_{obs} = the observed yield strength,

ΔYS_{l_f} = the stress increments caused by lattice friction (Peierls-Nabarro),

ΔYS_{ss} = the stress increments caused by solid solution

ΔYS_{dist} = the stress increments caused by dislocations and

ΔYS_{pptn} = the stress increments caused by precipitation

$\frac{K_y}{\sqrt{d}}$ = the contribution by the ferrite grain size and

K_y = the strengthening coefficient (a constant specific to each material),

The added micro alloying elements (Nb, V, Ti), form dispersive particles MX interstitial phases (where M = Nb, Ti, V and X = N and C). These particles limit recrystallized

austenite grain coarsening during thermo-mechanical treatments which in turn improves the strength of the alloy through grain refinement [25].

2.1.3 Solubility of micro-alloy precipitates

The understanding of the MX interstitial phases is crucial in knowing the effects of micro additions in forming fine grain structures [25, 75]. Adamczyk [25], explained that micro-additions M when dissolved in austenite are bonded at certain temperature T (which is dependent of solubility), with the metalloid X to form interstitial phases MX as expressed in Equation 2-3

$$(C_{Ma}) + (C_{Xa}) = MX \qquad 2\text{-}3$$

The solubility of MX in the solid solution of austenite (allowing for activation energy of nucleation which is dependent on temperature) can be explained by Arrhenius relationship as shown in Equation 2-4

$$\text{Log}\,(C_{Ma})(C_{Xa}) = \frac{A^{/}}{2.303} - \frac{Q}{2.303RT} \qquad 2\text{-}4$$

Equation 2-4 can be simplified to Equation 2-5

$$\text{Log}\,(C_{Ma})(C_{Xa}) = A - \frac{B}{T} \qquad 2\text{-}5$$

Where

(C_{Ma}) = micro addition M in weight percent (Nb, V, Ti, Zr, B, etc)

(C_{Xa})= metalloid X in weight percent (C or N)

Q = activation energy of MX phases (J/mol)

R = gas constant (J/mol-K)

T = Temperature, K

$A^{/}$ = Constant depending on phase type

$A = \frac{A^{/}}{2.303}$ and $B = \frac{Q}{2.303R}$ are tabulated constants for selected phases/Precipitates [75].

Equation 2-5 can be used to evaluate the initial and final temperatures of MX phase precipitation at certain concentration of micro-additions of M introduced into the steel [29].

Fernandez, et al [29] studied the effects of micro-alloying elements on the austenite grain growth in HSLA steel. Carbide and nitride prediction models expressed in Equations 2-6 and 2-7 were used to determine the solubility products and the solubility temperatures for each of the precipitates in the austenite matrix.

$$K_{MX} = C * 10^{B-4} - \frac{(Fe)^2}{10^2 * (M) * (X)} - (C_{Ma}) * (C_{Xa}) \qquad 2\text{-}6$$

$$T = \frac{A}{-\mathrm{Log}\frac{M\%(Fe)}{100(M)} - \mathrm{Log}\frac{X\%(Fe)}{100(X)} + \mathrm{Log}\frac{(Fe)^2}{10^2 * (M) * (X)} + B} \qquad 2\text{-}7$$

Where

A and B are tabulated constants for selected phases (Precipitates) in literatures [29, 75].

X% = carbon or nitrogen content and M% = micro-alloying element contents

Using Equations 2-6 and 2-7, Fernandez et al [29] plotted micro-alloyed content versus solubility temperature curves as shown in Figure 2-3. From this figure, the different solubility of each precipitate can be evaluated and the solubility temperature computed using the composition of the various elements in the steel.

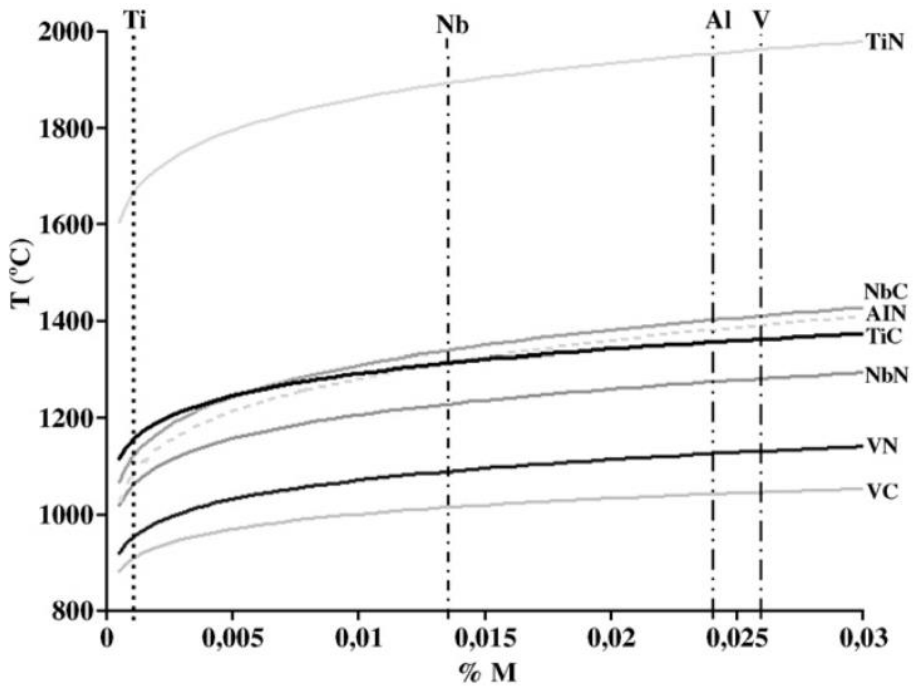

Figure 2- 3: Correlation between the micro-alloying content (M%) and the solubility temperatures for the precipitates in the steel [29]

Figure 2-3 corroborated very well with the results of the investigation by Matlock and Speer [31] on the relationship between precipitate type, solubility, composition and temperature as presented in Figure 2-4

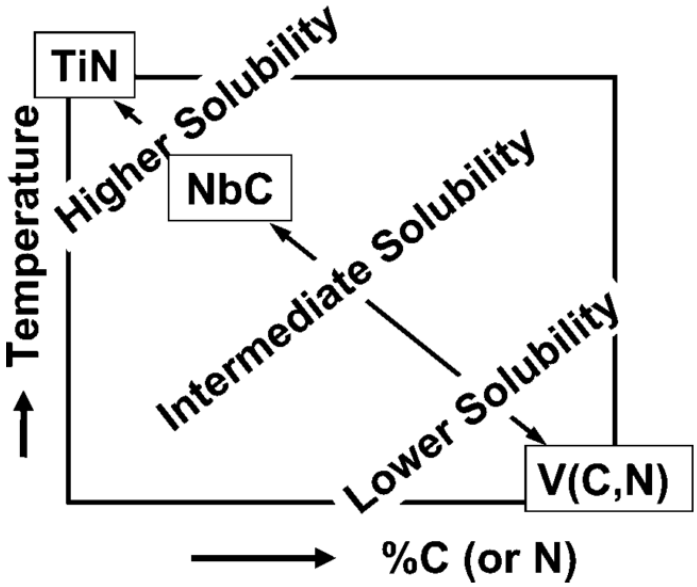

Figure 2- 4: Schematic of the relationship between precipitate type, solubility, composition and temperature where it is expected that the indicated precipitates would be effective in modifying product properties [31]

A comparison of Figures 2-3 and 2-4 shows that TiN is very stable and usually precipitates at high temperatures in the austenite regime and resists subsequent coarsening. Vanadium carbon-nitride, V(C,N) is much less stable and in general dissolved easily during austenitization and precipitates at lower temperature. Niobium has intermediate solubility and may be employed as either a solute or precipitate in austenite (to influence the austenite thermo-mechanical processing response), or as a fine grain strengthening precipitate in ferrite [29, 31].

Demiroren and Aksoy [76] worked on the electrochemical synthesis of ferritic stainless steel alloyed with 1 wt% Ti, V and Nb in sulphuric acid solution and proposed that the effectiveness of the micro additions in forming stable passive film and their re-passivation kinetics increased in order of V < Nb < Ti. This is in agreement with literature reports [29, 31] and the Gift free energy of formation of carbides [60] and nitrides [77] of these elements.

2.1.4 Zirconium (Zr) and Hafnium (Hf) as alloying elements

2.1.4.1 Zirconium (Zr) as an alloying element

Zirconium (Zr) is one of the transition metals with atomic number 40 and atomic weight 91.22. It resides in group IVA of the periodic table with titanium and hafnium. It is not one of the abundant elements but is widely distributed in nature ranking 11th in the earth crust. The estimated content of Zr in the earth's crust is about 0.028% which is more than the content of certain common metals like Ni (0.02 %), Cu (0.01 %), Zn (0.004 %) and Pb (0.001 %). About 10% of Zr is used as alloying elements while the balance is used in nuclear reactors [39-42]

Most literatures [39-41] state that zirconium is always found in combination with Hafnium (Hf) which has almost identical chemical properties. According to Holmes [40] the chemical similarity between hafnium and zirconium is more pronounced than any other two elements in the periodic table thus making their separation extremely difficult. Zirconium is classified based on hafnium content as 'ordinary purity Zr' containing 2 to 2.5 % Hf and 'high purity Zr' containing less than 0.1 % Hf. [43]. In most cases, zirconium and hafnium are considered for the same applications because of their similarities in physical and chemical characteristics [40, 42]

Zr is widely used in variety of industrial and chemical processing applications due to its excellent resistance to many chemical solutions at elevated temperatures and pressures. It is very resistance to corrosion attack in most organic and mineral acid, strong alkalis and some molten salts thus making it suitable for most chemical processes. For example, the corrosion resistance of Zr in concentrated HCl acid is less than 5 mpy making it superior to any other engineering metal [78]. Zr alloys exhibit excellent oxidation-resistant properties up to 400^0C in air, steam, carbon dioxide, oxygen and nitrogen. The excellent corrosion resistance of Zr can be attributed to the natural formation of dense, stable oxide film on the metal surface. This adherent oxide film is self-healing and protects the base metal from chemical and mechanical attack. Zr alloys have high resistance to localized corrosion such as pitting, crevices etc, thus making it suitable for use in a wide variety of corrosive environments [78].

There are uncertainties over the Fe-Zr binary system as evidenced by different phase diagrams presented by various authors. The main controversy has been the existence and crystal structure of $Fe_{23}Zr_6$ (also known as Fe_3Zr) [79]. However, in 1995, Servant et al [80] reported $Fe_{23}Zr_6$ as a line compound containing 20.7 at% Zr in the Fe-Zr phase diagram as shown in Figure 2-5. Liu, et al [81] confirm this observation but indicated that $Fe_{23}Zr_6$ contains 23-25 at% Zr. The Fe-Zr system shown in Figure 2-5 also revealed four intermetallic phases namely Zr_3Fe, Zr_2Fe, ZrFe and $ZrFe_3$. The maximum solubility of Zr in Fe which occurs at 13670C is about 4.5 at% (7 wt%)

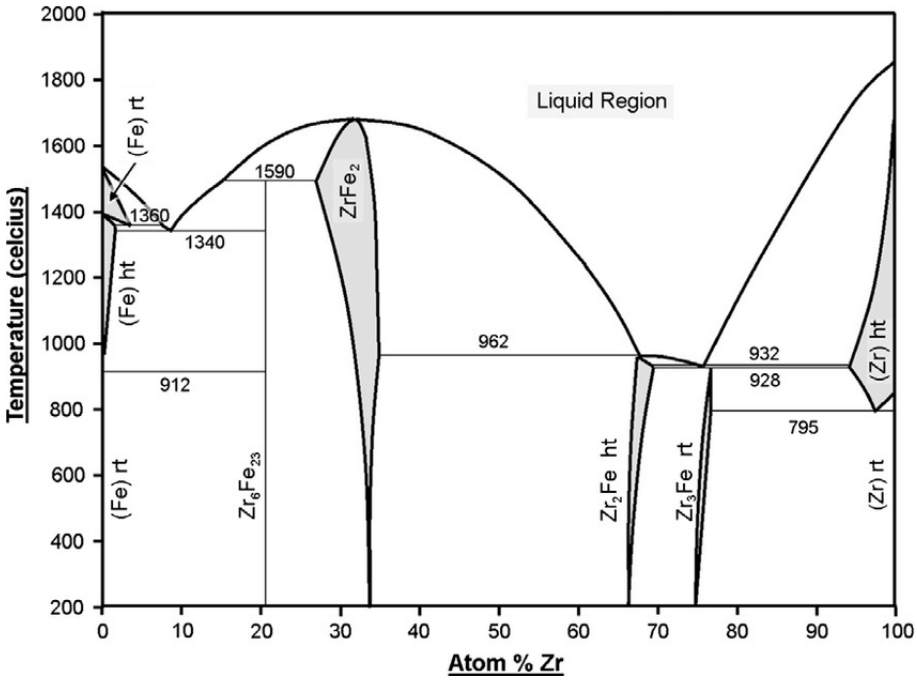

Figure 2- 5: Phase diagram of the Fe-Zr system [82]

Zirconium (Zr) has been used as micro-alloying elements in steels for over 10 decades but has never been universally employed like other carbide forming elements such as Niobium (Nb), Titanium (Ti), or vanadium (V) [39, 83]. Zr is a very reactive metal and is used in steelmaking due to its chemical affinity (in decreasing order) for oxygen, nitrogen, sulphur and carbon [39, 83-85]. The addition of Zr to steel is not to remain in solution but to scavenge impurities such as oxygen, sulphur and nitrogen or to modify inclusions through the formation of sulphides and oxy-sulphides [35]. Similarly Baker [39] and Satyendra [83] reported that Zr can preferentially combine with sulphur thus preventing the formation of MnS which has deleterious influence on the impact toughness of steels. The advantages and functions of Zr as alloying element in steels are summed up by researchers [39, 42, 83-85] as:

i) It controls the level of Oxygen, Nitrogen and Sulphur

ii) Overcome the red hotness effect of high sulphur

iii) Improving the mechanical properties of the steel by removing N as Zr_3N_2 and S as ZrS.

iv) Protects other alloying elements that would otherwise combine with O and N.

Nb, Ti and V both as individual and/or in combination with one another have found extensive used as alloying elements in micro-alloyed steel. Zr which is neighbour to Ti and Nb in the periodic table can be considered as a potential candidate for alloying element but has not received comparable attention [16]. Thermodynamically, Zr is a strong carbide and nitride former demonstrating a lower Gibbs free energy of formation for one mole of carbon than most conventional carbide forming elements (Ti, V and Nb). This is clearly expressed in Gibbs free energy of formation (ΔG^0) versus temperature (^0C) curves show in Figure 2-6 [49, 86].

Therefore, by replacement or in combination with other transition elements such as V, Nb and Ti, Zr precipitates as carbides, nitrides or carbo-nitrides which increases the yield strength of steels through grain refinement and dispersion strengthening. Aliakbarzadeh, et al [85, 87] reported that the addition of 0.005 wt% Zr to low carbon steel leads to the formation of precipitates which increases the hardness without any negative impact on toughness of the steel. This effect can be attributed to the decrease in the ferrite mean grain size attesting to the grain refining capability of Zr. Bairi, et al [88] reported that an optimum Zr content of 8 – 12 wt% resulted in the formation of best passive film stability and highest corrosion resistance.

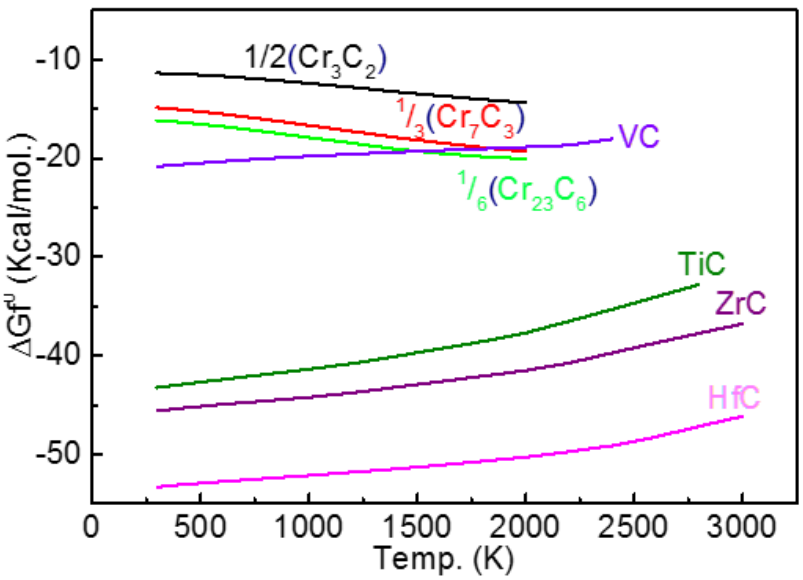

Figure 2- 6: Gibbs free energy of formation of one mole of carbides [49, 86]

2.1.4.2 Hafnium (Hf) as an alloying element

Hafnium is a heavy sliver-grey metal with atomic number 72 and atomic weight 178.49. Hafnium resides in the reactive metal group IVA with zirconium (Zr) and titanium (Ti). It is naturally found in association with Zr and these two elements have similar chemical and physical characteristics which make their separation very difficult. Hafnium is a moderately common element in the Earth's crust. Its abundance is estimated to be about 5 parts per million (ppm) making it as abundant as bromine, uranium, or tin. Naturally, the ratio of Hf to Zr is approximately 1:50 from where Hf can be exclusively produced as a co-product of nuclear-grade Zr [40, 44, 45]. Nielsen [46] reported that because of the similar chemical properties between Hf and Zr, a review of the chemical behaviour of Zr can be a useful indicator of the chemical behaviour of Hf . Also ATI Technical Data Sheet [45] and Holmes [40] stated that the corrosion behaviour of Hf is very similar to that of Zr and in the absence of data can be considered to be roughly equivalent. Hf-Zr system has almost ideal thermochemical properties forming continuous solid-solution alloys for all ratio of components as shown in Figure 2-7 [40, 45].

Like Zirconium, Hafnium has an extremely high affinity for oxygen, nitrogen and carbon. This makes Hf a strong carbide and nitride former that can be deployed for solid-solution strengthening via dispersion strengthening thus improving grain-boundary ductility [40, 44, 45].

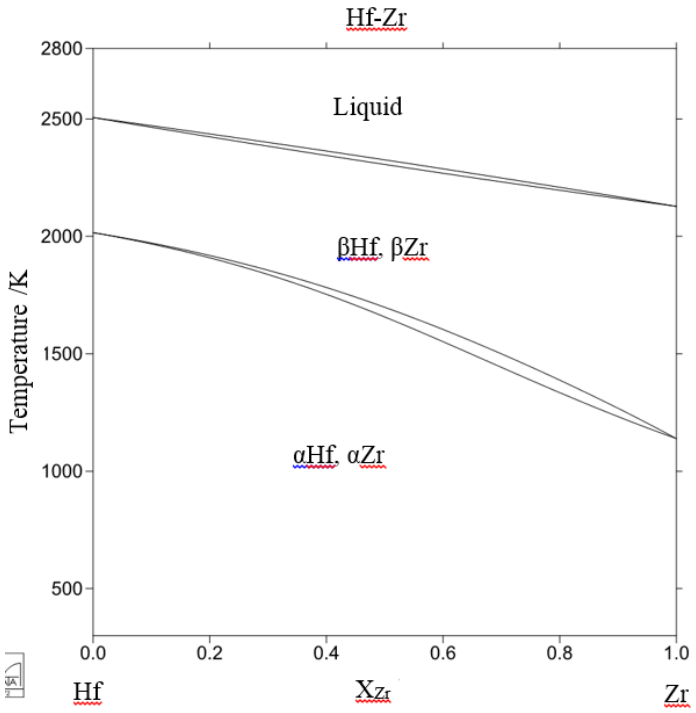

Figure 2- 7: Hf-Zr system [45]

According to Geanta, et al [44] the affinity of Hf for oxygen is capable of stabilising metallic structures and thus improve the oxide adherence to the substrate. This was evidenced from the work in which FeCrAl was micro-alloyed with different quantities of Hf (0.5 %, 1% and 1.5%). As a very reactive metal, Hf has a standard reduction potential of -1.72 V versus normal hydrogen electrode at 24^0C making it more reactive than Ti (-1.63 V) and Zr (-1.53V) (Figure 2-6). This makes Hf a very noble (cathode) metal in galvanic couples.

Hafnium has a good absorption cross section for thermal neutrons, excellent mechanical properties and is extremely corrosion resistant. It is used in a variety of applications where few substitutes are available. Hafnium, due to its ability to absorb ("soak up") neutrons very easily is used as control rods in nuclear reactors. This property is one of the few ways in which hafnium differs from zirconium. The absorption capacity of hafnium for neutrons is almost six times that of zirconium. Other areas where Hf has found applications are alloy additives, scavenger for oxygen and nitrogen in gas-filled and incandescent lamps, electrode in plasma cutting, gas-filled and incandescent lamps, aerospace, medical implant and devices [89, 90]. The properties of Hf are considerably influenced by the presence of Zr impurities. Depending on Zr content which is usually less than 4.5 at%, Hf is graded as rod/wire, powder, crystal bar and sponge.

The Fe-Hf equilibrium phase diagram has been severally evaluated and revised by many researchers. The more recent version constructed by Okamoto, H [89, 91] is shown in Figure 2-8. This figure revealed 4 sets of equllibrium phases which include 1) the liquid, L; (2) three polytypes Laves phases Fe_2Hf, Fe_2Hf and $FeHf_2$, (3) one λ sub-stoichiometric (around 0.30 at%. Hf, named (Fe_7Hf_3)), and (4) the five substitutional solid solutions (αFe), (γFe) (δFe), (βHf) and (αHf) [89]. The structural energies of the three different Laves polytypes are small due to the close relation between their crystal structures. Therefore, their phase relations are still very uncertain and the identification of the three phases is only tentative [92].

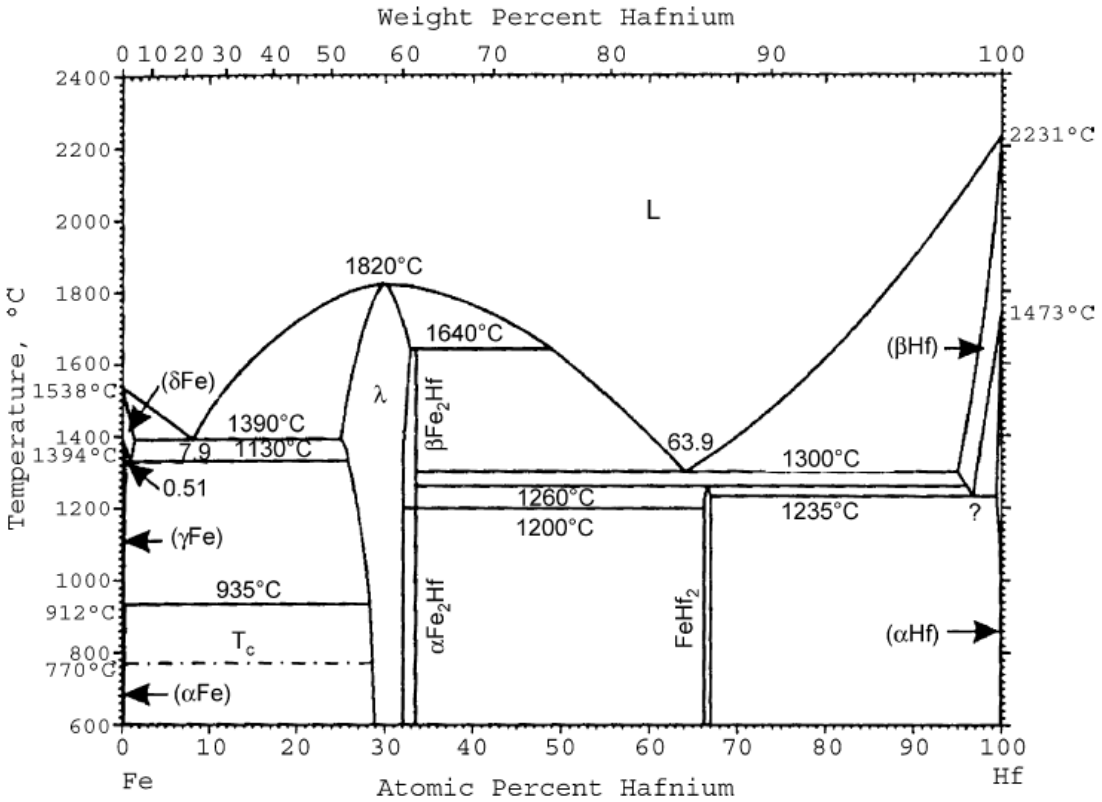

Figure 2- 8: The Fe-Hf Phase diagram [89]

2.2 Theory of electrochemical corrosion

Corrosion of materials is thermodynamically possible in most environments. This is because most (synthetic) materials are thermodynamically unstable having gained energy during production processes and thus are at high activation energy states. The tendency of these materials to return to their original thermodynamic stable energy state is referred

to as corrosion. Corrosion attack of metallic materials occurs through electrochemical reactions at the interface between the metal surface and the environment (electrolyte) [93-95].

When a metal is immersed in an electrolyte, oxidation reactions cause the metal ions (M^+) to leave the metal lattice and are surrounded by water molecules. However, the metal surface which is left with excess electrons (negative charge) attract some of the positive ions (such as H^+) causing them to remain at or near the metal surface but cannot be reduced because of the surrounding water molecules. This creates a region near the metal surface with distinct chemical composition from the bulk electrolyte. This region containing the negatively charged surface of the metal and the adjacent electrolyte is called electrical double Layer (EDL). EDL is in a state of equilibrium because the metal atoms that were oxidised and left the metal surface (as ions) are equal to the metallic ions that are reduced and re-entered the lattice (as atom) metal. However, corrosion is not an equilibrium process but a continuous process caused by electrochemically active species from the bulk electrolyte that diffuse to the metal surface where more metal atoms are oxidized in an effort to maintain equilibrium EDL[94]. Figure 2-9 is a simplified sketch of a corroding metal showing the electrochemically active species and the electrical double layer.

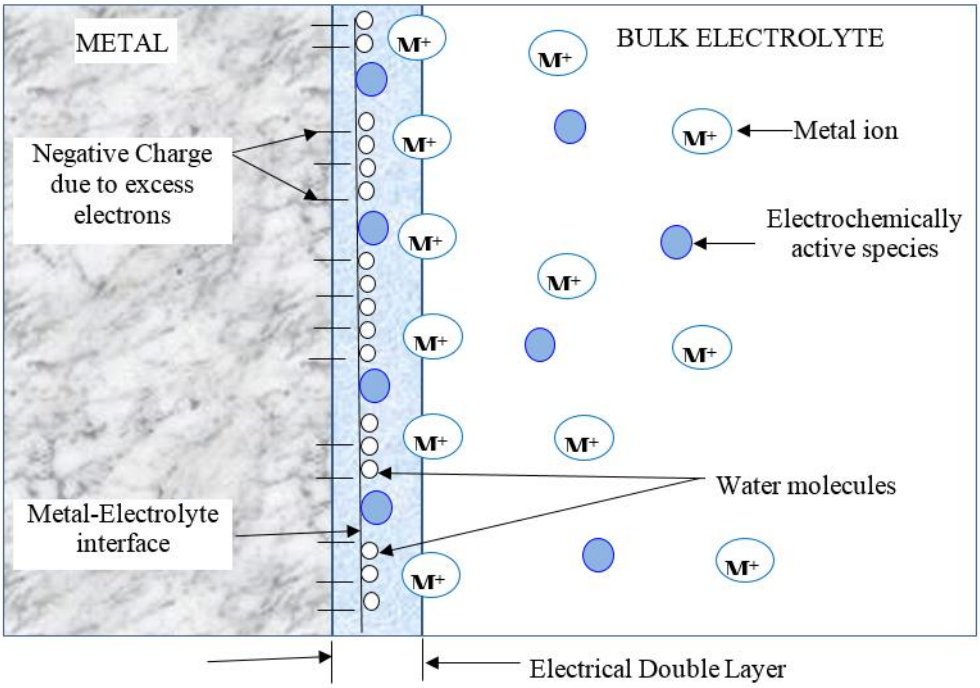

Figure 2- 9: A corroding metal at steady state of electrical double layer (modified from [94]).

In line with the theory of EDL, metallic corrosion can be referred to as an electrochemical reaction involving the generation and transfer of electrons from the metal atoms (M) to the electrochemical active species (Z^+) in the electrolyte as shown in Equations 2-8 and 2-9

$$M \rightarrow M^{2+} + e^- \qquad 2\text{-}8$$

$$Z^{2+} + e^- \rightarrow Z \qquad 2\text{-}9$$

Equation 2-8 is a generic half reaction for metal oxidation which occurs at the metal surface while Equation 2-9 is the half reaction for the reduction of electrochemical active species in the electrolyte which is needed to maintain electrical neutrality. Equation 2-9 occurs at another portion of the metal called the cathode. Depending on the distance between the anodic and cathodic sites, general (uniform) or localized corrosion may occur. The two half reactions must be present to initiate and sustain metallic corrosion. The summation of Equations 2-8 and 2-9 gives the overall corrosion reactions as indicated in Equation 2-10.

$$M + Z^{2+} \rightarrow M^{2+} + Z \qquad 2\text{-}10$$

A metal (eg Fe) in contact with an electrolyte (eg water, CO_2, etc) is electrically neutral since there are equal number of anodic and cathodic sites in the absence of an external voltage

2.2.1 Mixed potential theory

Mixed potential theory occurs when two electrochemical half reactions combine to form a corrosion reaction whose potential and corrosion rate are different from the two individual half reactions. This theory stipulates that the anodic current in an electrochemical cell must be equal to the cathodic current. This means that the electrons generated at the anode by all the oxidation reactions must be consumed by all the reduction reactions at the cathode. This is to maintain electrical neutrality. Mixed potential theory deals with anodic and cathodic reactions independently and can be coupled under the activation control polarization by the law of charge conservation.

This theory is aimed at resolving the problems of many electrochemical reactions proceeding simultaneously at the same metal-solution interface. For example, when iron is immersed in acidic solution, two basic participating (half) reactions take place as expressed in Equations 2-11 and 2-12.

Anodic dissolution (oxidation) of iron,

$$Fe \rightarrow Fe^{2+} + 2e^{-} \qquad 2\text{-}11$$

Hydrogen gas evolution (reduction reaction)

$$2H^{+} + 2e^{-} \rightarrow H_2 \qquad 2\text{-}12$$

The rest potential is the difference in the reversible or equilibrium potentials of each of these reactions occurring at the metal surface and it is the potential of the summation of Equations 2-11 and 2-12. This is expressed in Equation 2.13

$$\mathbf{Fe + 2H^{+} \rightarrow Fe^{2+} + H_2} \qquad 2\text{-}13$$

The potential of Equation 2.13 lies between the equilibrium potentials of the two half reactions (Equations 2-11 and 2-12). Theoretically, four reactions are possible in this system but two thermodynamically feasible reactions are shown as the Evans diagram in Figure 2-10

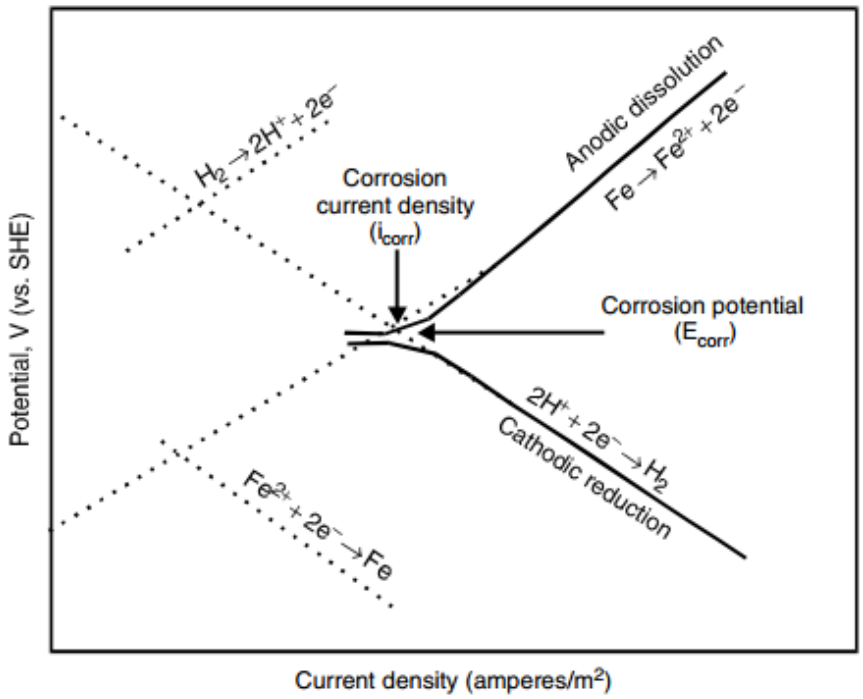

Figure 2- 10: Evans diagram for iron in acid solution ([96] www.npl.co.uk/upload/pdf/the_electrochemistry_of_corrosion_with_figures.pdf, 27/11/2018).

An extrapolation of the two solid lines intersect at the corrosion potential (E_{Corr}) with a corresponding corrosion current density (i_{Corr}) for the given system. Corrosion potential is a mixed potential indicating that its value depends on the rate of anodic and cathodic reactions. This intersection point is between the potentials of the two half reactions and the current density at intersect is higher than that of the individual half reactions. This

means that the corrosion of iron proceeds at a higher rate in the presence of hydrogen ions [94, 96-98].

2.2.2 The Thermodynamics of Corrosion

Nernst equation which relates the potential of a system to the activity (or concentration) of the products and reactants of the cell is the controlling thermodynamics equation for electrochemical process and it can generally be expressed as in Equation 2-14

$$K_{eq} = \frac{\text{Product of the activities (a) of the Products raised to stoichiomaticncoefficent}}{\text{Product of the activities (a) of the Reactants raised to stoichiomaticncoefficent}} \qquad 2\text{-}14$$

Where K_{eq} is the equilibrium constant (K)

Thus the Nernst equation for the overall electrochemical reaction in Equation 2-10 can be written as Equation 2-15

$$K_{eq} = \frac{a(M^{2+}) * a(Z)}{a(M) * a(Z^{2+})} \qquad 2\text{-}15$$

The activity (which can be approximated as concentration) of pure substance in its standard state is equal to 1. Therefore Equation 2-15 can be re-written as Equation 2-16

$$K_{eq} = \frac{C_{M^{2+}}}{C_{Z^{2+}}} \qquad 2\text{-}16$$

Where a(x) is the activity of species 'x' and $C_{(x)}$ is the concentration of species 'x'

The methods of corrosion monitoring rely on electrochemical corrosion theory and the measurement of the electrochemical potentials or currents. The electrochemical potential is fundamentally related to the thermodynamics of corrosion reactions. This is based on the basic concept of thermodynamic that for any spontaneous reaction, energy is lost (negative). Similarly, in electrochemistry, the feasibility of metal to corrode can be expressed in terms of the electrode potential. Thus the relationship between free energy (ΔG) and electrode potential (E) can be expressed as in Equation 2-17.

$$\Delta G = -RTIn\left(K_{eq}\right) = -nFE \qquad 2\text{-}17$$

Where n is the number of electrons (chemical equivalent) taking part in the reaction and F is the Faraday constant (96500 C/eq), E is the electrode potential for the reaction in volts, R is the gas constant (8.314 $Jmol^{-1}K^{-1}$), T is temperature (K) and $Ln(K_{eq})$ is the natural log of equilibrium constant for the reaction. Therefore it can be deduced from Equation 2-17 that:

If E > 0, then $\Delta G_{reaction} < 0$ leading to loss of ions and so corrosion becomes spontaneous. On the other hand, if $E < 0$, then $\Delta G_{reaction} > 0$ with gain of electron and corrosion becomes non-spontaneous [94, 99].

Also from Equation 2-17, the electrode potential can be expressed via Nernst equation as in Equation 2-18

$$E = -\frac{RT}{nF}\text{In}\left(K_{eq}\right) = \frac{RT}{nF}\text{In}\frac{a(M^{2+}) * a(Z)}{a(M) * (Z^{2+})} \qquad 2\text{-}18$$

Thus for a redox reaction, the corrosion of iron in water as shown in Equation 2-13 ($Fe + 2H^+ = Fe^{2+} + H_2$) and Nernst equation for this system in equilibrium can be written as Equation 2-19

$$E = E^0 - \frac{RT}{nF}\text{In}\frac{C_{Fe^{2+}} * P_{H_2}}{C_{Fe} * C_{(H^+)^2}} \qquad 2\text{-}19$$

Where R is gas constant (8.314 Joules/mol K), T is temperature (K), $C_{Fe^{2+}}$, C_{H^+}, and C_{Fe} are the concentration of the individual species while P_{H_2} is the partial pressure of hydrogen.

2.2.3 Kinetics of electrochemical corrosion

Thermodynamic principles can only be used to predict the conditions under which a metal is stable or unstable and corrosion cannot or can occur respectively. It does not predict how fast corrosion reaction can occur. The rate of corrosion reaction (reaction kinetic) can be expressed as current or the number of electrons generated per unit time. For a reaction which is limited by activation reaction, the relationship between the rate of reaction and the driving force for the reaction (potential) can be expressed by Butler Volmer equation. Butler Volmer equation for a single kinetically control electrochemical reaction at equilibrium relates electrical current to changes in metal potentials caused by an external power source as shown in Equation 2-20.

$$i = i_o(\exp\left(\alpha\frac{nF}{RT}\eta\right) - \exp((1-\alpha)\frac{nF}{RT}\eta)) \qquad 2\text{-}20$$

Where i_o is the exchange current density (Amp/cm^2), η is the overpotential ($E - E_{OCP}$) in Volts and α is a dimensionless charge transfer coefficient whose value is usually close to 0.5 but must be between 0 to 1. At high anodic potentials, the first term in Equation 2-20 dominates the second term. Thus Butler Volmer equation can be expressed as in Equation 2-21

$$i_a = i_o \exp\left(\alpha \frac{nF}{RT} \eta_a\right) \qquad 2\text{-}21$$

Equation 2-21 can further be simplified as in Equation 222

$$\eta_a = \beta_a \mathrm{Log}\frac{i_a}{i_o} \qquad 2\text{-}22$$

Also for cathodic activation polarization, a similar equation can be written as in Equation 2-23

$$\eta_c = -\beta_c \mathrm{Log}\frac{i_c}{i_o} \qquad 2\text{-}23$$

Where $\beta_a = 2.303\frac{RT}{n\alpha F}$ is the anodic Tafel slope and

$\beta_c = 2.303\frac{RT}{n(1-\alpha)F}$ is the cathodic Tafel slope.

2.3 Types of electrochemical corrosion

Although the fundamental mechanism of corrosion involves creation and/or the existence of corrosion cell with distinct anodic and cathodic sites where oxidation and reduction reactions occur respectively, corrosion manifests itself in myriad forms. However, most corrosion attack can generally be grouped into uniform (general) and localized corrosions. General corrosion occurs uniformly over the entire metal surface while localised corrosion occurs at small (about 1 to 10 micron to several centimetres) discrete locations on a metal surface. Localized corrosion is characterized by rapid penetration through the metal and it can be several orders of magnitude faster than general corrosion [94]. The most common forms of corrosion are illustrated in Figure 1-2.

2.4 Corrosion and measurement techniques

2.4.1 Weight loss measurement

This is a quantitative method of monitoring and measuring the external or internal corrosion caused by chemical attack in industrial plant and equipment. It involves recording the difference in weigh or changes in the mechanical, structural and or physical-chemical properties of the materials over specific time intervals [93]. It is the simplest corrosion monitoring method since it only deals with time and weight, which are easy indices to measure. Weight loss analysis is also the longest-established method of estimating corrosion losses in metallic structures. It is used to establish the type of corrosion in a certain environment and the suitability of different materials in design. A weighed sample (coupon) of the metal or alloy under consideration is introduced into the process, and later removed after a reasonable time interval. The coupon is then cleaned of all corrosion product and reweighed. The weight loss is converted to corrosion rate (CR) using Equations 2-24.

$$CR = \frac{\Delta W * K}{\rho * A * t} \qquad 2\text{-}24$$

Where CR = corrosion rate (the unit depends on the value of K as listed in Table 2-4)

Table 2- 4: The value of constant (K) for calculating corrosion rate in various units [100]:

Desired Corrosion Rate Unit (CR)	Area Unit (A)	K-Factor
mils/year (mpy)	in^2	5.34×10^5
mils/year (mpy)	cm^2	3.45×10^6
millimetres/year (mm/y)	cm^2	8.76×10^4

K = Constant that determine the unit of corrosion rate.

ρ = Alloy density (g/cm^2)

A = Exposed surface area of the specimen (depends on the value of K used)

t = Exposure time (hr)

Weight loss determination has a number of attractive features that account for its sustained popularity:

- Simple - No sophisticated instrumentation is required to obtain results.
- Direct - A direct measurement is obtained, with no theoretical assumptions or approximations.
- Versatile - It is applicable to all corrosive environments, and gives information on all forms of corrosion.
- Easy - Can easily be done in the laboratory and on a service equipment and
- Sample Size - It permits the use of different measurable sizes and shapes of samples

However, it has some disadvantages which include long time of exposure and applicable to only uniform /general corrosion

2.4.2 Electrochemical corrosion and measurement techniques

The relationship between potential and current is the fundamental principle used to develop various techniques for corrosion rate measurement and monitoring [93, 94]. Corrosion rate measurement and monitoring may be achieved either by direct current (DC) or alternating current (AC) methods. DC electrochemical corrosion techniques include but not limited to potentiodynamic polarization, linear polarization resistance (LPR), Tafel method (TP) and cyclic polarization. These techniques are shown schematically in Figure 2-11. On the other hand, electrochemical impedance spectroscopy (EIS) technique uses alternating current (AC) to monitor corrosion rate [94].

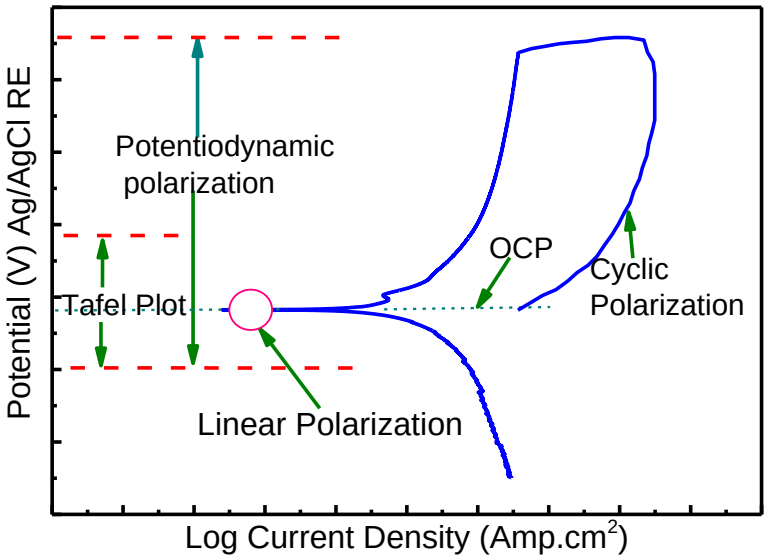

Figure 2- 11: Summaries of DC Corrosion Measurement Methods [94]

2.4.2.1 Linear Polarization Resistance Technique (LPR)

Of all the DC methods of corrosion measurement, linear polarization resistance technique uses the smallest potential spectrum which approximately spans within the potential range of ± 20 mV from the rest (equilibrium) potential ($E_{corr.}$). This small potential spectrum makes this technique fast, sensitive, non-destructive and reproducible. Being non-destructive, LPR technique can be repeatedly measured on the same sample thus allowing for long term corrosion monitoring and the determination of the steady state corrosion rate of a sample. The long term corrosion monitoring is programmed to alternate the electrode potential measurement with polarization within the specified potential range which is very close to E_{corr}. Near $E_{corr.}$, the current versus voltage curve approximates a straight line. The slope of the straight line expressed in Equation 2-25 when determined about the corrosion potential, $E_{corr.}$ as shown in the Figure 2-12 gives the polarization resistance Rp [94, 101].

$$\text{Slope} = R_P = \frac{\Delta E}{\Delta i} \qquad 2\text{-}25$$

Where $\Delta E = \eta$ = change in potential (volts) and

Δi = the corresponding change in current density (Amps/cm^2). Corrosion current can be converted into corrosion rate using Stern and Geary equation shown in Equation 2-26.

$$R_P = \frac{\eta}{I_{MEAS}} = \frac{\beta_A * \beta_C}{2.303 * i_{Corr}(\beta_A + \beta_C)} \qquad 2\text{-}26$$

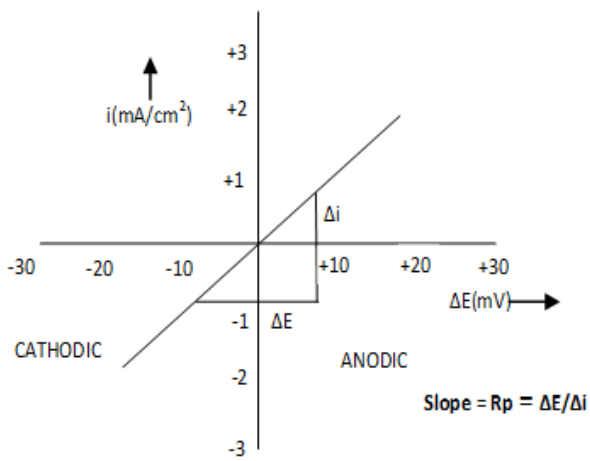

Figure 2- 12: Polarization curve for R_p measurement about E_{corr} (modified from [94]).

Rearranging Equation 2-26

$$i_{Corr} = \frac{\beta_A * \beta_C}{2.303\,(\beta_A + \beta_C)} * \frac{1}{R_P} = \frac{B}{R_P} \qquad 2\text{-}27$$

$$B = \frac{\beta_A * \beta_C}{2.303 * (\beta_A + \beta_C)} \qquad 2\text{-}28$$

Where

i_{Corr} = Corrosion Current (Amp)

E_{Corr} = the corrosion potential (Volts)

R_P = Polarization Resistance (ohms)

β_A = the anodic Tafel constant (Volts/decade)

β_c = the cathodic Tafel constant (Volts/decade)

I_{MEAS} = Measured cell current (Amp)

$\eta = E_{APP} - E_{Corr} = \Delta E$ = Over-potential (Volts)

E_{APP} = Applied Potential (Volts)

2.4.2.2 Tafel plot measurement technique

The Tafel plot spectra (eg $\pm$250 mV) spans more than the potential range used for linear polarization resistance ($\pm$ 20mV) with the data plotted as potential versus the log of current density. Tafel plot has anodic and cathodic curves corresponding to the anodic (oxidation) and cathodic (reduction) corrosion half reactions for the metal. These curves can be generated from the same sample by scanning from the most negative potential (-250 mV) to the most positive potential (250mV) of the selected scan range. Alternatively, the branches can be obtained by scanning the sample separately in the same electrolyte starting with the cathode, then allowing some time for potential stabilization before anodic polarization [94, 95, 101].

Tafel plot may be activation (kinetic) or diffusion (concentration) controlled. It is activation controlled when the rate of corrosion is determined by the transfer of electrons (charges) from the working electrode (metal) to the electrolyte. This is characterized by increase in current density as potential increases on both anodic and cathodic branches and represents the linear portion of the Tafel plot. Usually, this linearity begins approximately from $\pm$50mV about OCP as shown in Figure 2-13. The slopes of these linear portions are the anodic (β_A) and cathodic (β_c) Tafel constants. Unlike LPR technique, Tafel plot provides values of Tafel constants (β_A and β_C) which can be used

with Stern and Geary Equation in conjunction with Rp from LPR (Equation 2-25) to compute corrosion current density (i_{Corr}) which in turn is required to calculate corrosion rate using Equation 2-29. Also i_{Corr} can be obtained by extrapolating the linear portions of both Tafel branches to intersect at corrosion potential (E_{Corr}). The point of intersection gives i_{Corr}. The i_{Corr} thus obtained can be used to calculate corrosion rate from Equation 2-29

$$C_R\ (mm/Y) = \frac{3.27 * 10^{-3} * i_{Corr} * (E.W)}{\rho} \qquad 2\text{-}29$$

Where C_R = is the corrosion rate (mm/Y), i_{Corr} is corrosion current density ($\mu Amps/cm^2$) E.W is the equivalent weight and ρ is density of the corroding species (g/cm^2).

As stated earlier, Tafel Plot may be diffusion controlled. This occurs when the corrosion rate is determined by the rate of diffusion of the electrochemical active species (EAS). This represents a condition when the reaction rate is so high that the electrochemical-active species cannot reach or be removed from the electrode surface at a sufficiently rapid rate. In this case, the reaction rate becomes diffusion control which is the mass transfer of products (metal ions) from the electrode surface [101]. In order to maintain the reaction rate, diffusion becomes the kinetic limitation, and the reaction becomes diffusion controlled at the limiting current density, (I_L)[102]. Diffusion (concentration) controlled polarization is primarily for cathodic reduction process and theoretically causes the cathodic current density to become constant at I_L. Diffusion (concentration) controlled polarization for anodic oxidation during corrosion are usually ignored because unlimited supply of metal atom is available at the surface [103]. Diffusion polarization can be minimized by solution stirring which reduces its value or by using a rotating electrode where mass transport can be detected by its dependence on rotation speed.

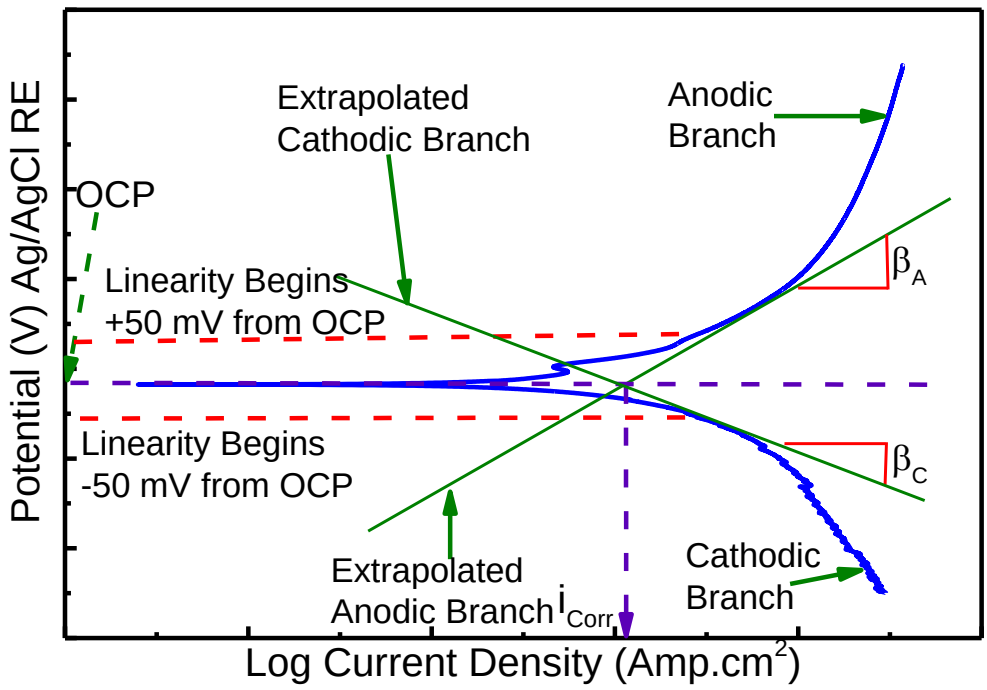

Figure 2- 13: Tafel Plot showing extrapolated lines and Tafel parameters (modified from [94]).

2.4.2.3 Potentiodynamic polarization

The potentiodynamic potential spectra spans more than the potential range of Tafel plot ($\pm$ 250mV) with the data plotted as potential versus the log of current density. Traditionally, the anodic branch is scanned more above OCP (eg $\geq$ 1000 mV) than the cathodic branch (eg - 250mV) from OCP. The anodic branch is non-linear and in many cases assumed an S-shape as shown in Figure 2-14. This figure shows the comparison of Pourbaix Diagram and potentiodynamic plot for metal in water at pH = 6. It revealed how some critical potential values relate to boundaries in the Pourbaix diagram. Region F, is the immunity region where corrosion does not occur. Region A is the active region, in which the specimen corrodes along I-II as the applied potential is increased in the positive direction. At B, for further increase in potential, the rate of corrosion (as measured by the current) ceases to increase indicating the onset of passivation. Point B is characterized by the primary passive potential (E_{pp}) and the critical current density (i_{Crit}). The loss of chemical reactivity under certain environmental conditions, probably due to the formation of resistive film on the surface of the metal is referred to as specimen passivation. It relates to the process of oxidation leading to a solid corrosion product that forms in such a way as to provide a significantly protective film. This corrosion product is thermodynamically or at least kinetically, stable, continuous, without substantive defects, relatively insoluble

and generally resistant to further oxidation or reduction. In region C, the current decreases rapidly within line II - III as the passivating film forms on the substrate. This region according to Jones [103] is termed 'negative resistance' portion of the anodic curve. It is the active-to-passive transition region artfact. Region D is a region of low passive current density where there is little change in current as the potential is increased. This region is under diffusion control because the electrochemical active special cannot easily access the electrode-electrolyte interface. The current remains relatively constant from point III until point IV where the current suddenly begins to increase again with increase in potential in region E. The region of constant current (III - IV) is also called passive region. The point (IV) where the current began to increase again after passivation is called the breakdown potential since it is where the passivating film begins to break down. This occurs at very high potentials, allowing high currents to pass again. This region E is called the trans-passive region. Trans-passive current may be associated with oxygen evolution or dissolution as indicated in the Pourbaix diagram in Figure 2-14

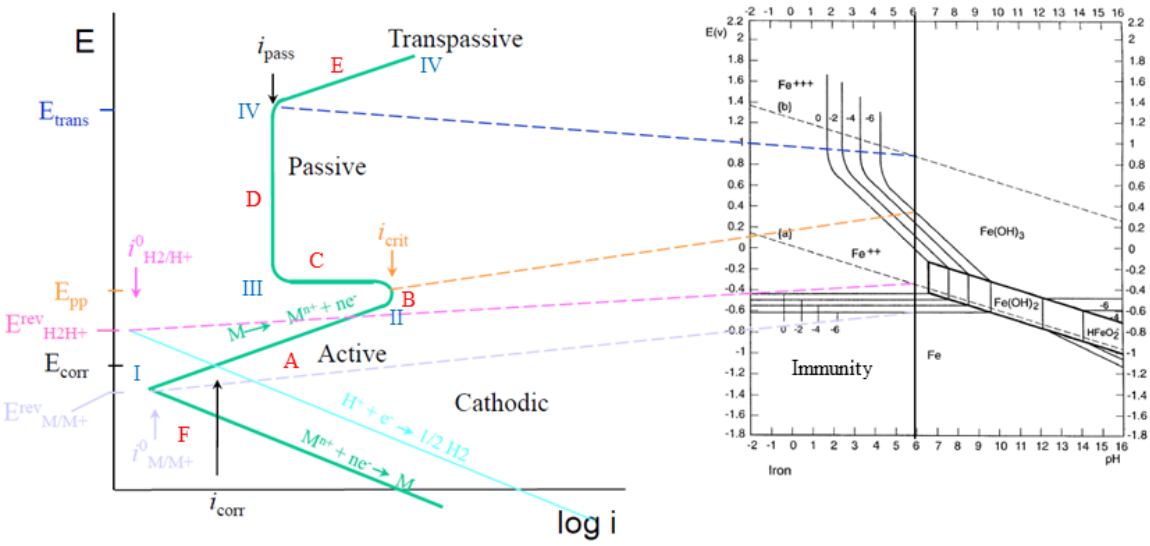

Figure 2- 14: Comparison of Pourbaix Diagram and Polarization Curve for Iron. [104]

2.4.2.4 Cyclic polarization (Cp) plot

Cyclic polarization plot can be viewed as an extension of potentiondynamic polarization because at the end of the potentiodynamic scanning, the voltage is reversed (applied in the negative direction) towards OCP. Cyclic potentiondynamic polarization may display negative hysteresis or positive hysteresis. Negative hysteresis occurs when the reverse scan current density is less than the forward scan or positive when the reverse scan current density is greater than the forward scan. Figure 2-15 shows a positive hysteresis. Where

E_b is the breakdown potential, E_{rp} is the re-passivation potential and E_{pp} is the primary passivation potentials.

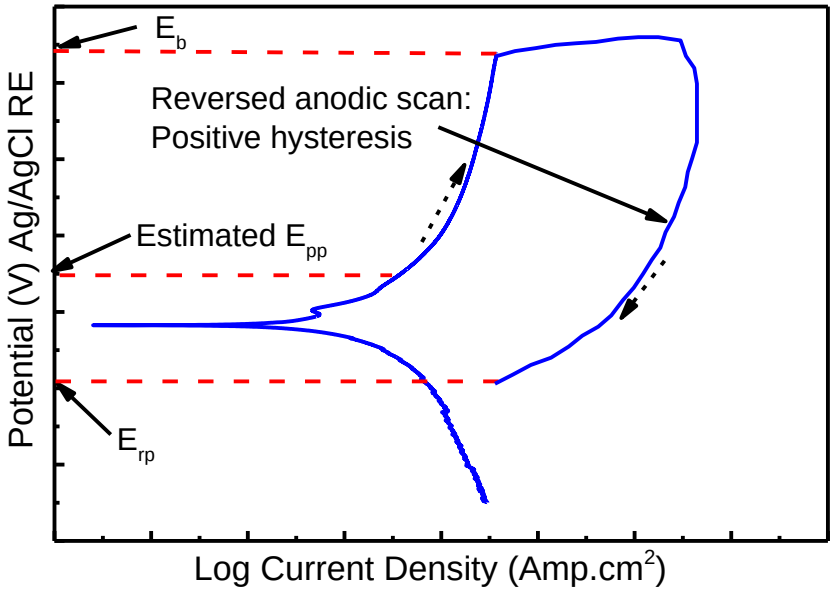

Figure 2- 15: Cyclic Scanning showing positive Hysteresis (modified from [94]).

2.4.2.5 Potentiostatic polarization

Potentiostatic polarization is a technique that allows for the controlled polarization of metal surfaces in electrolytes, in order to observe cathodic and anodic behaviours. This technique applies a constant potential to the metal-solution interface and measures its electrochemical behaviour as a function of time. It monitors the corrosion reactions on a surface of the desired metal. A number of characteristics of the metal/environment pairing can be determined using this technique.

2.4.3 Resistance polarization (IR-drop) effects

IR-drop is the voltage error introduced between the corroding electrode and the tip of the Luggin-probe in a corrosion system. It is caused by the resistance of the electrolyte between the surface of the working electrode and the tip of the Luggin capillary, (TLC) [95, 102]. If current (I) is applied from the working electrode through the cell to the counter electrode, a potential drop (E_U) = IR_U arises across R_U which reduces the actual polarization voltage of the working electrode (Ep) in relation to the applied voltage (E_{APP}) to Equation 2-30:

$$E_P = E_{APP} - IR_U \qquad 2\text{-}30$$

The Ohmic resistance (R_U) can considerably adulterate the results of electrochemical corrosion investigations and so the electrochemical polarization measurements.

Oelssner et al [105], worried that regardless of so much effort and work on IR drop (R_u), most published articles corrosion measurements are incorrect due to underestimation or neglect of the effect of IR drop (R_u). They stated that R_u depends on the specific conductivity of the test solution and the design and arrangement of the electrodes in the measuring cell. They then derived an expression for computing Ru based on these two parameters as in Equation 2-31:

$$R_u = \frac{d}{2KA} \qquad 2\text{-}31$$

Where A = Area of the working electrode exposed to the electrolyte

K = the specific conductivity of the electrolyte (K) and

d = the distance between the tip of the luggin capillary and the chemically active surface region of the working electrode [67, 106].

It follows that increasing the gap between the tip of the Luggin capillary and the chemically active surface region of the working electrode (d) will increase the ohmic resistance (R_u) and vices versa while increasing the specific conductivity of the electrolyte (K) will reduce the effect of ohmic resistance (R_u).

2.4.4 Electrochemical impedance spectroscopy (EIS)

Electrochemical Impedance Spectroscopy (EIS) is an AC method of monitoring and measuring the corrosion behaviour of materials/systems. Unlike DC voltage that has constant magnitude for both positive and negative polarity, AC voltage oscillates from positive (anodic peak) amplitude to negative (cathodic peak) amplitude with different magnitude for both polarities in one polarization cycle. EIS is a sensitive, essentially non-destructive technique that is ideally suited for detecting and monitoring of corrosion of metal and coatings on metallic substrates [107]. According to Scully [102], the electrochemical impedance is a frequency-dependent proportionality factor that acts as a transfer function by establishing a relationship between the excitation voltage signal and the current response of the system.

2.4.4.1 Theory of electrochemical impedance spectroscopy (EIS)

The definition of resistance by Ohm's Law as "the ability of a system to resist the flow of current" ($R = \frac{E}{I}$) is limited to resistor as the only circuit elements. In a real system however, there are other circuit elements such as capacitor, inductor and admittance which contributes significantly in determining the ease of flow of current. These circuit elements make the behaviour of the current flowing through a system very complex. To account for this complexity, the theory of resistance (R) was replaced by impedance (Z) [103, 108]. Impedance, like resistance, is a measure of the tendency of a circuit to resist (impede) the flow of current but unlike resistance, it does not obey Ohm's Law at all current and voltage.

When a small sinusoidal signal, in an extensive frequency range, is applied to a system at corrosion potential (E_{Corr}), the response at every frequency is another sinusoidal signal with different amplitude and phase angle shift relative to the input signal. Small excitation signal is used so as to obtain a pseudo-linear response. The phase angle shift in the response signal is as a result of time lag necessitated by various processes at the material substrate that absorbed electrical energy at different frequencies [103, 109-111]. Figure 2-16 shows the current response to a sinusoidal potential signal across a system and the current lag behind the potential.

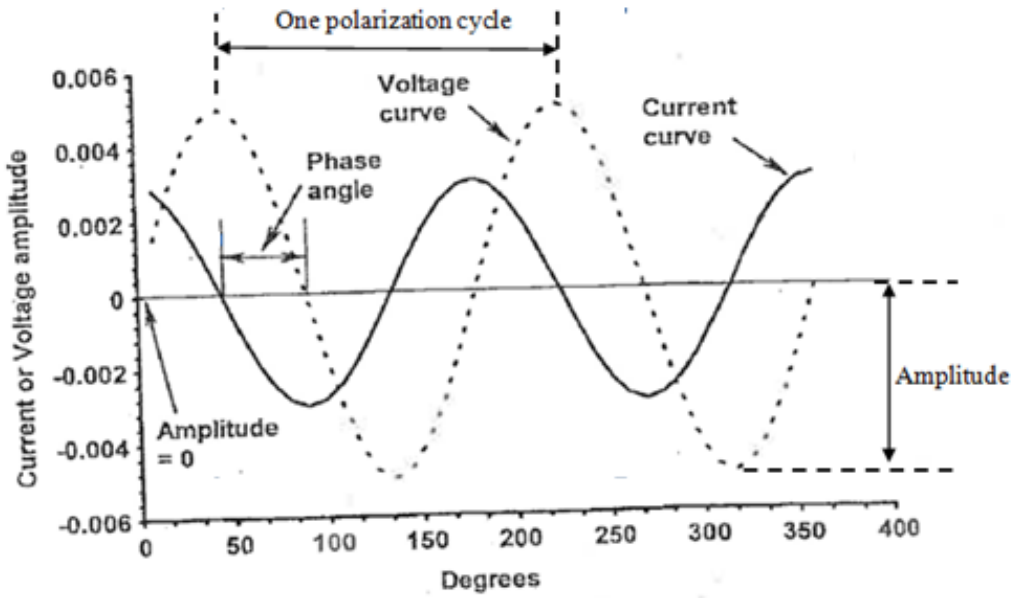

Figure 2- 16: AC voltage - current phase angle showing one polarization cycle and a negative amplitude [94].

The excitation signal can be expressed as a function of time as shown in Equation 2.32

$$E_t = E_0 \mathrm{Sin}(\omega t) \qquad 2\text{-}32$$

Where E_t = the potential at time t, E_0 is the amplitude of the signal, and ω is the radial frequency. The relationship between radial frequency ω (radians/second) and frequency f (hertz) is given in Equation 2-33:

$$\omega = 2\pi f \qquad 2\text{-}33$$

Also the relationship between the response signal, I_t that is shifted by phase angle (∅) and the corresponding amplitude I_0 can be expressed as in Equation 2-34

$$I_t = I_0 \sin(t\ \omega t + \emptyset) \qquad 2\text{-}34$$

Using the principles of Ohms Law, and combining Equations 2-32 and 2.34, an expression for calculating impedance of a system can be written as in Equation 2-35

$$Z = \frac{E_t}{I_t} = \frac{E_0 \sin(\omega t)}{I_0 \sin(\omega t + \emptyset)} = Z_0 \frac{\sin(\omega t)}{\sin(\omega t + \emptyset)} \qquad 2\text{-}35$$

Applying Euler's relationship, impedance can then be represented by a complex number as shown in Equation 2-36 [112].

$$Z(\omega) = \frac{E}{I} = Z_o \exp(j\emptyset) = Z_0(\cos\emptyset + j\sin\emptyset) \qquad 2\text{-}36$$

2.4.4.2 Impedance Data Presentation

There are two major ways of Presenting EIS data. These are Nyquist and Bode Plots which are presented schematically in Figure 2.17. Both formats complement each other. The subtle features that are difficult to identify in the Nyquist plot may be ready apparent in the Bode plot and vice versa.

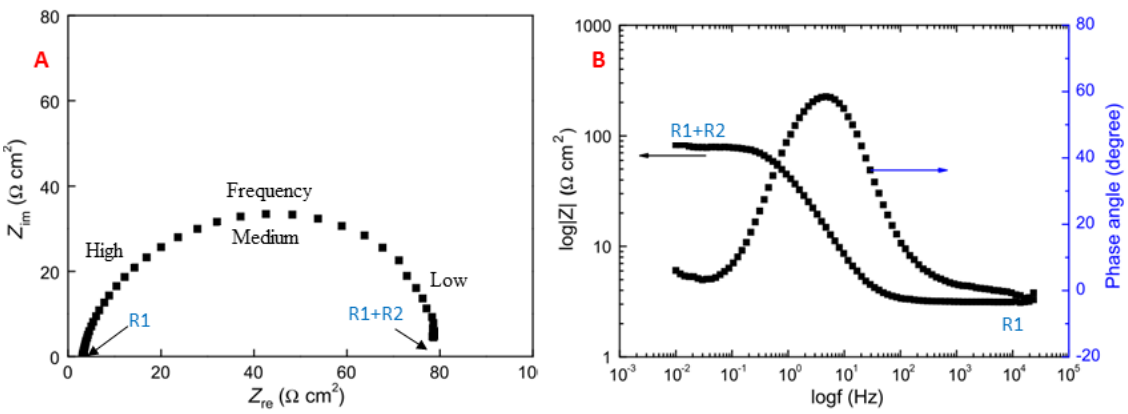

Figure 2- 17: (A) Nyquist Plot and (B) Bode Plot (modifiesd from [109, 113])

2.4.4.3 Electrical Equivalent Circuits

In EIS, the response of an electrode to alternating potential signal of varying frequency is interpreted on the basis of electrical models of the electrode-electrolyte interface. The simplest circuit model is called Randle Cell and is used to stimulate electrical behaviour of corroding metal and coated surfaces. This simple circuit is an adequate representation of a simple corroding surface under activation control reactions [110]. The circuits consist of elements each of which models a specific function of the corroding sample. A simple Randles Cell representing the circuit elements is shown in Figure 2-18.

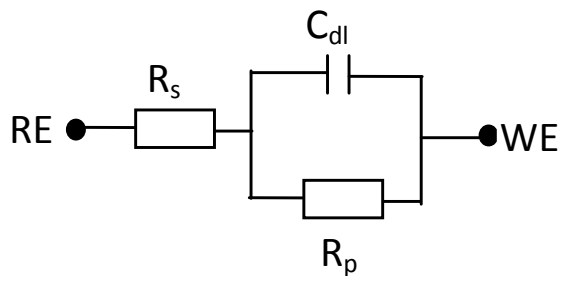

Figure 2- 18: The Randles Cell Equivalent Circuit

Where

i) Rs is the solution resistance, which is the resistance of the solution between the working and the reference electrodes. It is the point of intercept on the real axis at high frequency end of the Nyquist plot.

ii) Rp is the charge transfer resistance which corresponds to the corrosion resistance at the metal/electrolyte interface and it represents the difficulty of electrochemical reactions.

iii) CPE is the constant phase elements; this is used to represent the double layer capacitance (C_{dl}) in order to account for deviation from the ideal capacitive behaviour due to surface inhomogeneity, roughness and adsorption effect. The impedance of CPE can be expressed as shown in Equation 2- 27

$$Z_{CPE} = \frac{1}{Y_o} (j\omega)^{-n} \qquad 2\text{-}37$$

Where Yo is the magnitude of CPE, $\omega = 2\pi f$ is the angular frequency, j is the imaginary number and n is the dispersion coefficient related to surface inhomogeneity. CPE may be resistance, capacitance or inductance depending on the value of n. When CPE is pure resistor (ie if n = 0 then Z_0 = R), pure capacitor (meaning that n = 1 when Z_0 = C) or inductor (ie when n = 0.5 and Z_0 = W) [54, 113]

Chapter 3: Literature Review

This chapter highlights some of the literatures devoted to micro-alloying technology and its applications in oilfield for alleviating the effect of corrosion. The specific functions of various alloying elements as presented by certain authors were highlighted. This was followed by the mechanism of CO_2 corrosion which is considered as the dominant form of corrosion in oil and gas industries. The influence of various environmental and material/metallurgical factors that affect the corrosion behaviour of oilfield equipment in CO_2-containing environments as presented in literature were reviewed in this chapter. Some of these factors include temperature, solution pH, microstructures, solution chemistry, flow condition, CO_2 partial pressure and material composition.

3.1 Application of Micro-alloying Technology in Enhancing Corrosion Resistance

About 12 % of the 1650 MT of steels produced worldwide in 2014 are micro-alloy steels and these have been instrumental to the expansion of most engineering infrastructures where they found wide applications particularly in line-pipes [14, 28, 31, 48]. Micro-alloyed steel gained this privilege because of its amazing properties which include improved mechanical strength, light weight, ease of transportation, ease of installation and the accruing low cost [27]. These excellent properties can be attributed to the functions of micro-alloying elements (V, Ti and Nb) which form precipitates after appropriate thermo-mechanical treatments. Morrison [14] tabulated some of these elements and their functions in micro-alloyed steels as shown in Table 3-1.

The influence of alloying elements on the corrosion resistance of steels is dependent on various corrosive environments [114]. Cr, Cu and P in weathering steels have proved to be effective additions for increased corrosion resistance to electrochemical dissolution [115]. Small amounts of Cr, Cu, Ni and Ca in low-alloy steels have shown to improve corrosion resistance in electrolytic solutions [116].

Table 3- 1: The functions of various micro-alloying elements [14].

Functions / Micro elements	V	Nb	Ti
Precipitation strengthening after hot rolling	VN, VC	NbCN	TiC
Precipitation strengthening after normalizing	V	-	-
Influences Recrystallization during hot rolling	-	Nb, NbCN	-
Refines grain size on normalising	VN	NbCN	TiC
Refines grain size during High temperature austenitising	-	-	TiN
Influences transformation characteristic after hot rolling	-	Nb	-

Shifler [117] reported that Cr, Al and Mo added to low-alloy steels demonstrated enhanced corrosion resistance in marine environments while Si- and Al-bearing steels with ultra-fine grains exhibited excellent corrosion resistance when compared with Si–Mn–C steel [118]. Matlock, et al [59] also reported that micro-alloying elements affect the microstructures which in turn affect the properties of the steels. The addition of Mo, Mn and Cr promote the formation of bainitic structures while Ti, V, and Nb were used for grain size control and precipitation strengthening. On the other hand, Ti (TiN) was used for grain refinement while V (VC) enhanced precipitation strengthening. Other authors [29, 31] have also reported similar results concerning the functions of some of these alloying elements in micro-alloyed steels.

Experimental evidence have shown that the addition of small amounts of alloying elements can promote the production of low-cost steels with improved corrosion resistance [71]. These elements improve corrosion potential of steel which inhibits anodic and cathodic reactions and thus enhancing corrosion resistance. It has also been shown that some alloying elements promote the formation of a protective rust layer which slows down the corrosion rate of steel substrate [71, 119, 120]. Park, et al [71] reported that the addition of small quantity of W, Mo and Ti promote the development of low cost steel with improved corrosion resistance. This study showed that W can improve abrasion and corrosion resistance by ameliorating passivity while Mo improves re-passivation and

deactivation of growing pits by reducing the size and number of pit nucleation. This suppressed the probability of generating stable pits. On the other hand, Ti impacts mechanical properties by influencing grain refinements as observed by other researchers [25, 29, 31].

Townsend [48] produced steels with various alloying additions using induction furnace. These steels were exposed to three different industrial sites. Using mass-loss method, the corrosion performance of the steels was found to fit properly to an exponential function shown in Equation 3-1

$$C = At^{B} \qquad 3\text{-}1$$

Where A and B are constant, C is corrosion loss and t is time of exposure.

Developing models for the constants (A and B), the effect of the individual elements on the weight loss of the steels were computed and presented in Figure 3-1. It is apparent from this figure that P has the largest beneficial effect on corrosion resistance but due to its harmful effect on the toughness and weldability of structural steels, its addition is limited to 0.04%. On the other hand, S demonstrated a huge detrimental effect attesting to the low addition of S due to its harmful effect to the mechanical properties of steels. Other elements and the level of their beneficial effects are also shown in Figure 3-1.

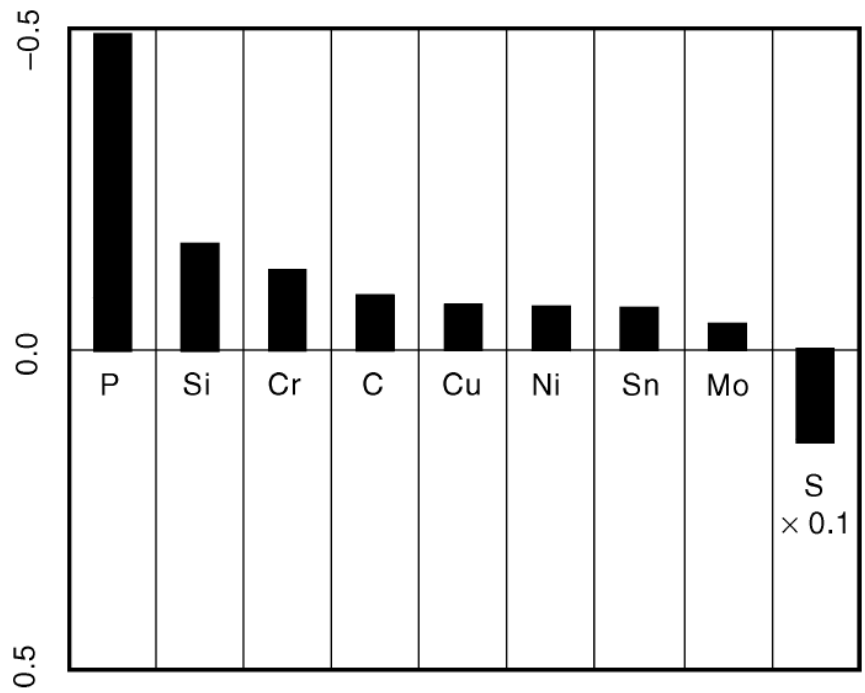

Figure 3- 1: Effect of elements on corrosion losses based on the models developed by [48] (more negative indicates less corrosion).

Kermani, et al [13, 65] in an extensive studies highlighted two principles that influence the improvement of the corrosion resistance of alloy steels by alloying elements. These principles are:

(i) lowering the carbon content and adding carbide-forming alloying elements to maximize the effect of chromium and molybdenum by ensuring that they remain in solid solution and

(ii) Achieving the desired properties by micro alloying additions mechanical and heat treatments.

Figure 3-2 summarised qualitatively the results of these studies in terms of individual alloying elements. This figure shows a progressive reduction in corrosion rate with increasing Cr content. V has a major beneficial effect in reducing corrosion rate. Other alloying elements such as Ti, Si, Cu and Mo etc are also shown to exhibit some level of positive influence on corrosion resistance of steel depending on other parameters like microstructure, heat treatment and their interaction and corrosion conditions.

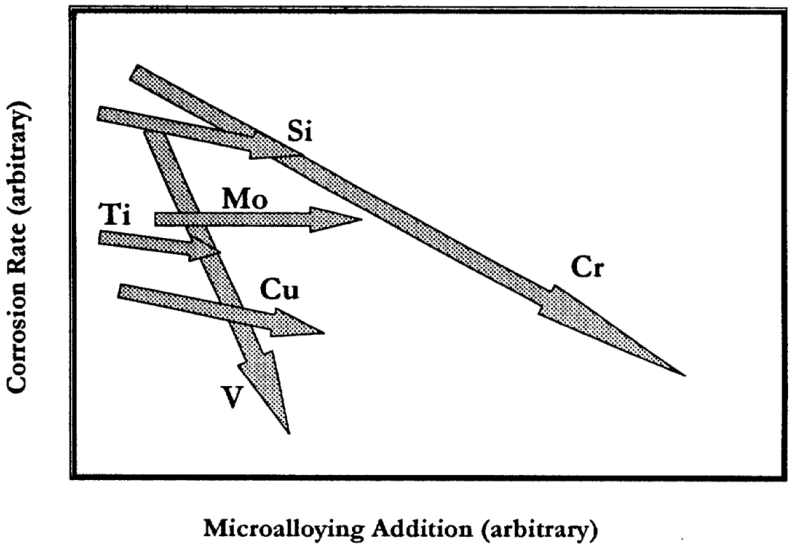

Figure 3- 2: Schematic presentation of relative effect of additional micro alloying elements on corrosion rate [13].

Recently, Qiufa, et al [119] investigated the effects of Cr and Cu on the corrosion behaviour of carbon and low-alloy steels in simulated groundwater solution. Alloy steel containing Cr or Cu alone exhibited better general corrosion resistance than the alloy containing both elements. This was mainly because Cr or Cu can individually enrich the surface matrix of the steel to form protective corrosion product film thus improving the uniform corrosion resistance of the steel. On the other hand, the addition of Cr and Cu

demonstrated a synergistic effects on the acceleration of crevice corrosion because Cu promotes the enrichment of Cr along the grain boundaries of the steel [121].

API 5L X65 grade steel is increasingly being used as material for oil and gas facilities. Many authors [61, 122, 123] have reported that API 5L X65 carbon steel is the most widely used material for production and transportation of hydrocarbon. This was attributed to strict thermo-mechanical treatments and addition of micro alloying elements which impact the desired properties to the steel. Depending on the applied conditions, experimental evidence has shown that the corrosion rate of API 5l X65 steel grade in simulated oilfield environments ranges from 0.048 to 2.493 mm/y [67, 122, 124]

In this work, the corrosion behaviour of three proprietary micro-alloyed steels were compared with that of API 5L X65. Two of these micro-alloyed steels were subsequently alloyed with non-conventional carbide forming elements aimed at improving their corrosion resistance to surpass that of API 5L X65. One of the functions of micro-alloying elements is to precipitate as carbides or nitrides. The carbides of hafnium (Hf) and zirconium (Zr) have more negative Gibbs free energy of formation than most conventional carbide forming elements [125]. This can be deduced from Figure 3-3. Therefore it is expected that hafnium and zircornium will form more stable carbides than the conventional alloying elements. Thus two of the proprietary steels were alloyed with Zr and Hf and the corrosion propensity of the Hf- and Zr- alloyed steels compared with the unalloyed specimen and X65 steel grade.

Zirconium has found several uses in modern industries because of its unique combination of physical, chemical and nuclear properties [42]. Some of these industries include electronics, surgery, chemical equipment and nuclear power. One of the outstanding properties of zirconium employed for these applications is its excellent corrosion resistance in most aqueous media [41, 42]. Owing to its corrosion resistance, Golden [43] reported that there is little hope of producing an alloy with a better corrosion resistance than pure Zr since adding alloying elements to Zr decreases the corrosion resistance of the alloy. Yau [126] prepared Zr-Fe alloys with varying amount of iron and reported that the corrosion resistance of Zr decreased with addition of iron. On the other hand, the corrosion resistance of other metals is greatly increased by addition of Zr [50, 83].

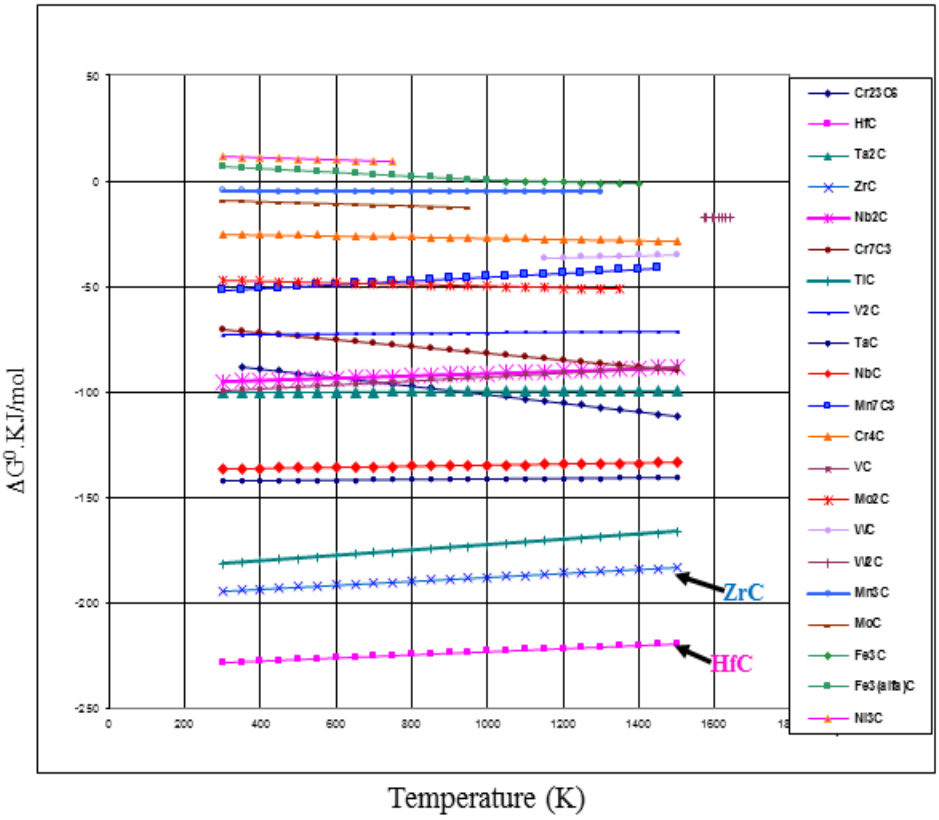

Figure 3- 3: Temperature dependence of the change in the standard Gibbs free energy ΔG^0, kJ/mol, for carbide-formation reactions [60]

There are many published works [41, 84, 85, 127] on the effects of zirconium on the mechanical properties of steels but very few systematic studies [50, 126] have been devoted to the effect of zirconium (Zr) on the corrosion resistance of steels. Kovalenko and Zats [50] observed three characteristics trend of corrosion rates with increase in zirconium content. Similarly, Bairi, et al [88] reported that an optimum Zr content of 8 – 12 wt% resulted in the formation of best passive film stability and highest corrosion resistance in de-mineralized water. On the other hand, no published studies have been reported (to the best of my knowledge) regarding the effect of Hf on the corrosion resistance of steels. This is one of the significants of this studies.

3.2 Carbon Dioxide (Sweet) Corrosion

CO_2 (sweet) corrosion is the most prevalent types of corrosion in oil and gas industry [7, 11, 23, 128]. About 60% of oilfield facility failures are caused by CO_2 corrosion [11]. This is attributed to inadequate knowledge and predictive capacity couple with poor resistance of carbon and low alloy steels to CO_2 corrosion. Popoola, et al [128] and

Kermani and Morsheed [23] reported that dry CO_2 gas is not corrosive at the temperatures encountered within the oil and gas production lines. However, when dissolved in an aqueous phase, CO_2 can promote electrochemical reactions which can lead to failures of oil and gas pipelines and facilities [7, 11, 12, 23, 69, 128-130]. Literature reports [131-133] showed that CO_2 are introduced into oil and gas production systems through (a) the use of enhanced oil recovery (EOR) technology which involves the injection of CO_2 gas into the reservoirs and (b) the presence of CO_2 gas in deeper oil and gas wells.

3.2.1 Electrochemistry and mechanism of carbon dioxide (CO_2) corrosion

The mechanism of CO_2 corrosion in oil and gas industry has been studied in depth and different predictive models developed and published [23, 69, 134-141]. These variety of models are attributed to the complexity of the processes involved in CO_2 corrosion [142] which is turn are occasioned by the myriad of environmental and material factors that influence it (CO_2 corrosion) [135, 143]. Confirming this complexity, Dugstad, et al [69] stated that CO_2 corrosion does not depend on one mechanism but on some chemical, electrochemical and physical processes that occur simultaneously. Thus for adequate understanding and explanation of CO_2 corrosion mechanism, these processes must be taken into consideration. Although there are diverse CO_2 corrosion models, there is a general consensus on the dissolution of iron at the anode and the evolution of hydrogen gas from the reduction of either H^+, H_2CO_3 or H_2O at the cathode [23, 69, 135, 136] depending on pH of the solution. Equation 3-2 shows the overall chemical reaction of CO_2 corrosion [23] of steel.

$$Fe_{(s)} + CO_{2(g)} + H_2O_{(l)} \rightarrow FeCO_{3(s)} + H_{2(g)} \qquad 3\text{-}2$$

$FeCO_3$ is the main product of CO_2 corrosion of carbon steels and depending on the experimental conditions, it ($FeCO_3$) can act as either protective or non-protective scales on the surface of the substrate. However, the main point of controversy is on the multi-steps involved in the anodic and cathodic processes and which of these reactions is the rate determining step (RDS).

3.2.2 Electrochemistry of CO_2 corrosion,

Several mechanisms have been proposed for CO_2 corrosion of carbon and low alloy steels in aqueous CO_2 solution. In general, all the mechanisms consist of three cathodic reactions involving the evolution of hydrogen gas and one anodic reaction which is the

dissolution of iron. The first significant and most widely used model for predicting CO_2 corrosion was proposed by de Waard and Williams in 1975 [134, 136, 138, 144]. This initial model identified the combined effects of CO_2 partial pressure (P_{CO2}) and temperature on the corrosion rate as the key parameters in CO_2 corrosion. This model has been revised many times to incorporate other parameters such as pH, solution chemistry, flow condition, etc [134, 144].

3.2.2.1 Anodic reaction

The overall anodic reaction for the dissolution of iron in carbon and low alloy steels is shown in Equation 3-3.

$$\mathrm{Fe}_{(s)} \rightarrow \mathrm{Fe}^{2+}_{(aq)} + 2\mathrm{e}^- \qquad 3\text{-}3$$

This reaction is pH dependent. The extensive studies by Nesic et al [136] revealed that this reaction involves multiple steps and this led to the revision of the well-known de Waard and Williams Model [134] on the dissolution of iron in CO_2 saturated solutions. This was because de Waard and Williams assumed and subsequently extrapolated the original proposal of Bockris et al [145] which was based on pH < 4. Recent experimental results showed that the pH dependency of iron dissolution in CO_2 environment decreases rapidly with increasing pH (the reaction order with respect to OH^- being 2 at pH < 4 but decreased to 1 and 0 at pH > 4). Therefore extrapolation of the work of Bockris et al [145] to pH > 4 by de Waard and Williams was considered inaccurate. Nesic et al [136] then reported three distinct pH regimes with three different anodic mechanisms. These regimes are pH < 4 and pH > 5 with an intermediate regime 4 < pH < 5 where transition from one mechanism to another occurs. At pH < 4, the mechanisms suggested by Bockris et al [145], for strong acid as given in Equations 3-4 to 3-6 remain valid.

$$\mathrm{Fe}_{(s)} + \mathrm{H_2O}_{(l)} \leftrightarrow \mathrm{FeOH}_{(ad)} + \mathrm{H}^+_{(aq)} + \mathrm{e}^- \qquad 3\text{-}4$$

$$\mathrm{FeOH}_{(ad)} \rightarrow \mathrm{FeOH}^+_{(aq)} + \mathrm{e}^- \qquad 3\text{-}5$$

$$FeOH^+_{(aq)} + \mathrm{H}^+ \rightarrow Fe^{2+}_{(aq)} + \mathrm{H_2O}_{(l)} \qquad 3\text{-}6$$

On the other hand, the mechanisms to explain experimental results for pH > 5 as expressed in Equations 3-7 to 3-12 were proposed by Nesic , et al [136]

$$Fe + CO_2 \leftrightarrow Fe_L \quad 3\text{-}7$$

$$Fe_L + H_2O \leftrightarrow Fe_LOH_{(ad)} + H^+ + e^- \quad 3\text{-}8$$

$$Fe_LOH_{(ad)} \rightarrow Fe_LOH^+_{(ad)} + e^- \quad 3\text{-}9$$

$$Fe_LOH^+_{(ad)} + H_2O \leftrightarrow Fe_L(OH)_{2(ad)} + H^+ \quad 3\text{-}10$$

$$Fe_L(OH)_{2(ad)} \leftrightarrow Fe_L(OH)_{2(sol)} \quad 3\text{-}11$$

$$Fe_L(OH)_{2(sol)} + 2H^+ \leftrightarrow Fe^{2+} + CO_2 + 2H_2O \quad 3\text{-}12$$

Where Fe_L = the complex Fe-CO_2

The experimental results and the proposal of Nesic et al [136] on the dissolution of iron in CO_2 solution were confirmed by Crotel et al [146] and summed up by Kermani and Morshed [23] as shown in Table 3-2

Table 3- 2: Mechanisms of Anodic dissolution of iron in CO_2 saturated Media [23].

Reaction No	Reaction or Equilibrium	pH<4	4<pH<5	pH>5
1a	$HCO_3^- \leftrightarrow (HCO_3^-)_{ads}$	1a	1a	1b
1b	$CO_2 + (OH^-)_{ads} \leftrightarrow (HCO_3^-)_{ads}$			
2	$(HCO_3^-)_{ads} \rightarrow (HCO_3)_{ads} + e^-$	↔	↔	RDS →
3	$(HCO_3)_{ads} \rightarrow (HCO_3^+)_{ads} + e^-$	↔	RDS$^{(A)}$ →	→
4	$(HCO_3^+)_{ads} + OH^- \rightarrow (CO_3)_{ads} + H_2O$	RDS →	→	→
5	Fe + $(CO_3)_{ads} + H_2O \rightarrow Fe^{2+} + HCO_3^- + OH^-$	→	→	→
1 → 5	Tafel Slope (mV/log)	$\frac{60}{2} = 30$	$\frac{60}{1.5} = 40$	$\frac{60}{0.5} = 120$
1 → 5	H^+ reaction order	-2	-1	0
1 → 5	CO_2 reaction order	1	1	1

RDS = rate determining step

3.2.2.2 Cathodic reactions

The cathodic reactions in a CO_2-water system can generally be represented by three main reactions as shown in Equations 3-13 to 3-15 [23, 137, 141]

H^+ reduction: $$2H^+_{(aq)} + 2e^- \leftrightarrow H_{2(g)} \quad 3\text{-}13$$

H_2CO_3 reduction: $$2H_2CO_{3(aq)} + 2e^- \rightarrow H_{2(g)} + 2HCO^-_{3(aq)} \quad 3\text{-}14$$

HCO_3^- reduction: $$2HCO^-_{3\,(aq)} + 2e^- \leftrightarrow H_{2(g)} + 2CO^{2-}_{3\,(aq)} \quad 3\text{-}15$$

The end product of these three reactions is hydrogen gas evolution which increases the rate of dissolution of iron in the presence of CO_2. The contributions of each of these species (ions) in CO_2-corrosion of steel as reported by some authors [69, 136, 147, 148] depend on various parameters such as temperature, pH and concentration of ions in the medium.

Nazari, et al [147] and Moiseeva and Rashevskaya [148] reported that the predominant cathodic reaction at pH < 4 is the reduction of hydrogen ion as shown In Equation 3-13. At 4 < pH < 6 the most important cathodic reaction is carbonic acid reduction of Equation 3-14 while at pH > 6 the reduction of bicarbonate ion represented by Equation 3-15 dominates. Furthermore at pH ≥ 7, reduction of water occurs as shown in Equation 3-16.

$$2H_2O_{(l)} + 2e^- \rightarrow H_{2(g)} + 2OH^-_{(aq)} \quad 3\text{-}16$$

Two opinions exist among researchers on the mechanism of H_2CO_3 reduction. Some proposed a direct reduction ($H_2CO_{3(aq)} + 2e^- \rightarrow H_{2(aq)} + CO^-_{3(aq)}$) [134] while others proposed two steps dissociation of H_2CO_3 ($2H_2CO_{3(aq)} + 2e^- \rightarrow H_{2(g)} + 2HCO^-_{3(aq)}$ $\rightarrow H_{2(g)} + CO^-_{3(aq)}$) [142]. For instance, Tran et al [149] described the mechanism in which adsorbed carbonic acid directly reduced on the surface of the steel. This means that both H^+ reduction and direct reduction of carbonic acid contribute to the corrosion process leading to a higher corrosion attack than mineral acid at the same pH.

3.2.3 Key factors affecting CO_2 corrosion

Different authors [23, 69, 142, 150] have reported that the mechanism of CO_2 corrosion of steels is very complex. This was ascribed to a number of inter-functionally related key factors which can be grouped into environmental and metallurgical (material) factors. The

environmental factors include temperature, CO_2 partial pressure, pH, solution chemistry, surface film, flow velocity etc. On the other hand, the metallurgical factors are steel composition and microstructures/heat treatments. [12, 23, 69, 128, 129, 134, 135, 139]. The effects of some of these factors are heighted in this section.

3.2.3.1 Effects of pH

The effect of pH on CO_2 corrosion has been widely studied and reported to involve different mechanisms depending on the environmental conditions. However, both field and experimental experience has shown that increase in pH reduces the rate of cathodic reduction of H^+ which significantly decreases the rate of anodic dissolution of iron [151]. This in turn reduces $FeCO_3$ solubility resulting in less Fe^{2+} ions required to exceed the solubility limit thereby enhancing the formation of protective $FeCO_3$ films and eventual reduction in corrosion rate [152, 153]. This technique has been used to mitigate the corrosion rate of pipelines through the addition of alkaline chemicals (e.g. NaOH or $NaHCO_3$) in a process known as pH-stabilisation [151].

Nesic et al [136], reported three distinct pH regimes (pH<4, 4<pH<5 and pH>5) with different mechanisms for anodic dissolution. The influence of pH in each of these regimes was briefly discussed in Section 3.2.2. Nesic [137] also noted that the effect of pH on general CO_2 corrosion of steel can be direct and indirect. It is direct at pH ≤ 4 where H^+ ions are directly reduced due to complete dissociation of strong (mineral) acid as shown in Equation 3.12. On the other hand, the indirect effect occurs at high pH and is related to how pH changes the conditions for the formation of $FeCO_3$ films. These indirect effects of pH can be ascribed to the decrease in solubility of $FeCO_3$ leading to increased precipitation rate and scaling tendency [135, 137, 139, 140, 154]. Scaling tendency (ST) is a dimensionless parameter which can be quantified by Equation 3.17 [147, 155].

$$\mathrm{ST} = \frac{\mathrm{R}_{\mathrm{FeCO_3}}}{\mathrm{CR}} \qquad 3\text{-}17$$

Where R_{FeCO_3} = the rate of precipitation of $FeCO_3$ and CR is the corrosion rate. If $ST \leq 1$, then a porous and non- protective film forms which can cause local corrosion. On the other hand if $ST \geq 1$ then a compact and protective layer of iron carbonate can form which decreases the corrosion rate. It has been reported that the growth of iron carbonate film depends on two simultaneous phenomena which complement each other. These phenomena are (1) the corrosion of steel and (2) the precipitation of iron carbonate.

Increasing the temperature accelerates diffusion of species involved in the electrochemical reactions, thus increases the corrosion rate. However, iron carbonate solubility limit is a thermodynamic factor and decreases with increasing temperature [23, 147]. Therefore, raising the temperature improves the precipitation rate of $FeCO_3$.

Nazari et al [147], investigated the effects of temperature (55 to 85^0C) and pH (5.5 to 6.5) on the composition and morphology of corrosion product layers in CO_2 corrosion of X70 steel for 72 h. pH was found to have little or no role on $FeCO_3$ formation if the temperature is not sufficiently high (> 60^0C) signifying that the role of temperature on the precipitation of $FeCO_3$ is more pronounced than that pH. This demonstrated an increase in $FeCO_3$ grain size at pH 5.5 which remain the same with further increase of pH to 6 beyond which the grain size increased again at pH 6.5. This progressive change in the morphology of $FeCO_3$ layer on X70 steel at 85^0C for 72 hours with change in pH as observed by Nazari, et al [147] is shown in Figure 3-4. Similar results have been reported by Nesic, et al [155].

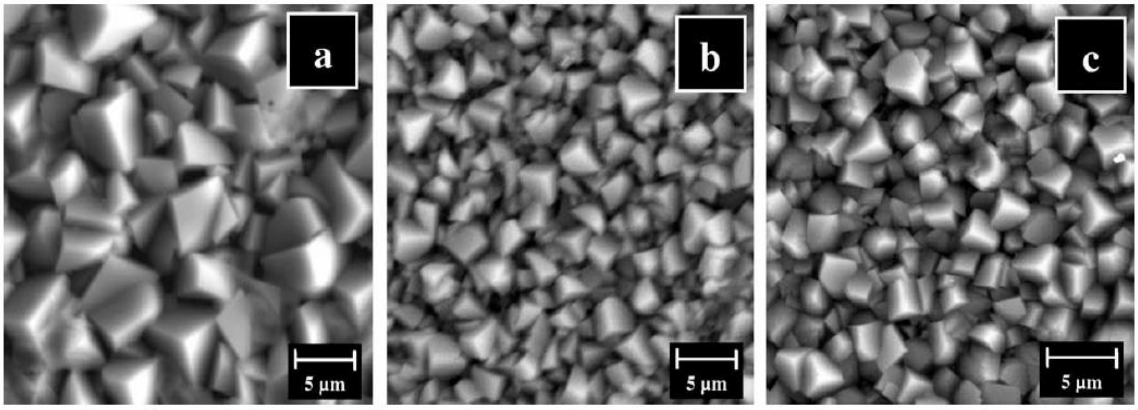

Figure 3- 4: The SEM micrographs of the specimens exposed at 85^0C at pH (a) 5.5, (b) 6 and (c) 6.5 for 72h [147].

In the experiments conducted using St52 steel in CO_2 saturated 3 wt% NaCl, Nesic, et al [140] observed a threefold decrease in limiting diffusion current (i_{lim}) with increase in pH from 4 to 5 as shown in Figure 3-5. This was considered much less than the tenfold decrease in H^+ ion concentration if the cathodic reaction was composed of H^+ ion reduction alone. This low limiting diffusion current was attributed to complex cathodic reactions involving other electrochemical species in CO_2 corrosion environments [23, 137, 141]. These species are considered as chemical reaction-limiting component of the

system [140]. Figure 3-5 also showed that pH has insignificant effect on the anodic dissolution of iron. This agrees with the report of Nazari, et al [147].

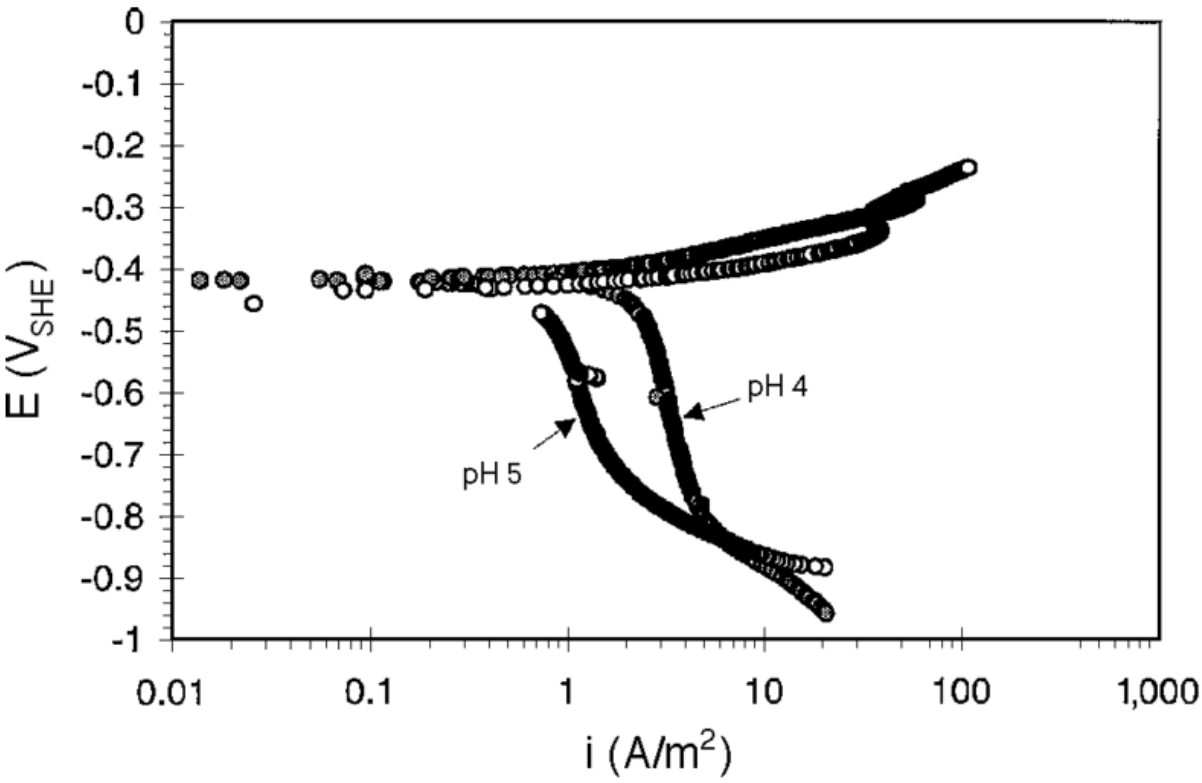

Figure 3- 5: pH effect in CO_2 solution, water + 3% NaCl, P_{CO2} = 1 bar, T = 20°C, 1,000 rpm, and St52 steel [140].

Li, et al [154] investigated the stability of protective $FeCO_3$ layer on API 5L X65 at 80^{0}C over a wide pH range of 5.6 to 7.8 and reported a pseudo-passive behaviour. This resulted in about 200 mV shift in potential toward the positive direction with a corresponding significant low corrosion rate of about 0.01mm/y at pH 7. This is in agreement with other reports [38] indicating that at pH 7.0 a stable, protective, pseudo-passive layer formed. The stable and protective corrosion layer was also observed between pH 6.0 to 6.6 for experiments conducted for 3 days. However, the results showed lower positive shift in potential (100 mV) and a corresponding lower corrosion rate (0.1 mm/y). These effects were not achieved at pH 5.6 even after 22 days until ferrous chloride ($FeCl_2$) was added to the system.

Tanaporn et al [62] used linear polarization resistance (LPR) and electrochemical impendence spectroscopy (EIS) to investigate the effect of pH on CO_2 corrosion of API 5L X65 steel at elevated temperatures (80 ^{0}C - 200 ^{0}C). The results showed that at pH 4

and 80 ^{0}C, $FeCO_3$ (corrosion product) did not form and the corrosion rate was higher than at pH 6 over all the temperature range tested. This is in agreement with Zhao, et al [38] who reported that at low temperatures ($\leq 80^0$C) $FeCO_3$ forms only at high pH (≥ 6) and that at high temperature ($\geq 80^0$C), $FeCO_3$ forms readily.

3.2.3.2 Effect of temperatures

Temperature is one of the key environmental factors influencing CO_2 corrosion of steels in oil and gas industry. Yap, et al [156] summarised the effect of temperature on the corrosion rate of steels in CO_2 environments as follows.

- Corrosion process increases with increase in temperature below 60^{0}C.
- Formation of a protective scale in aqueous CO_2 environments at elevated temperatures.
- Increasing temperature increases the aggressiveness of chloride ions in aqueous solutions by thermal activation.
- Increasing temperature decreases solubility of dissolved gases such as CO_2, which increases the pH of the environment.
- Equilibrium constants change with temperature change which causes pH change.
- Water phase behaviour change with temperature change.

The major effect of temperature on the corrosion rate of steels in CO_2 environment can be attributed to its influence on the formation of protective $FeCO_3$ as enumerated in literatures [23, 157, 158]:

1) Increase in solubility of $FeCO_3$ at temperature below 60^{0}C results in the formation of non-compact, loose, soft, and non-adhesive corrosion product scale and thus increasing corrosion rate.
2) A transitional range between 60°C and 80°C during which corrosion product scale with certain protective property formed on the steel substrate thereby reducing corrosion rate slightly.
3) Decrease in solubility of $FeCO_3$ at temperatures between 80^{0}C and 150^{0}C results the formation of more compact, dense, and adhesive corrosion product scale which significantly decreased corrosion rate.
4) Above 150°C, fine, dense and adhesive grains consisting of $FeCO_3$ and magnetite (Fe_3O_4), and the corrosion rate is relatively lower.

The influences of temperature on the protective properties of $FeCO_3$ is schematically shown in Figure 3-6

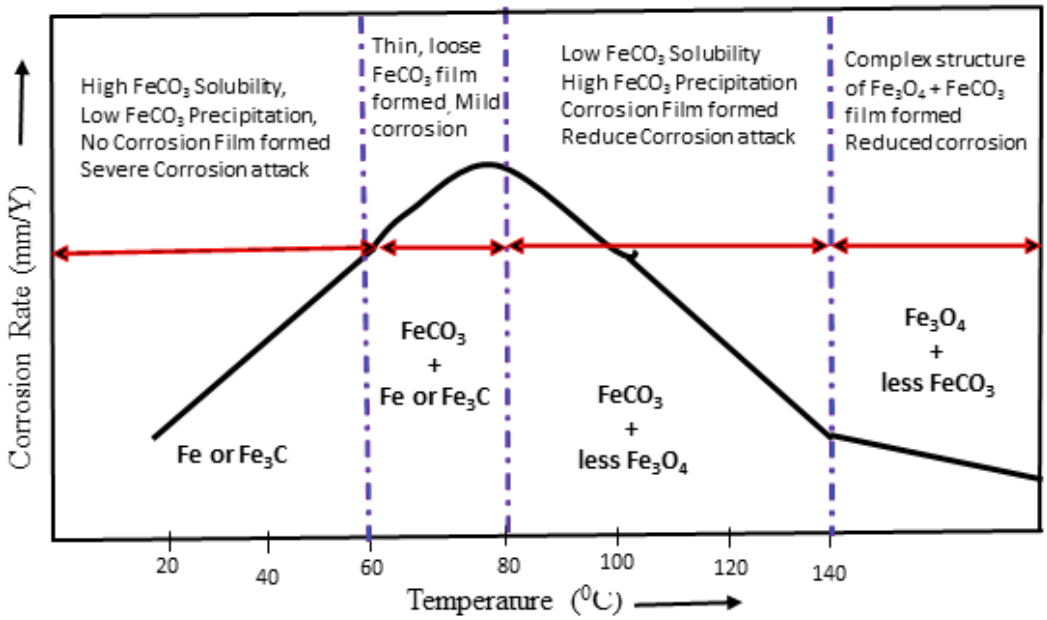

Figure 3- 6: Schematic representation of the effects of increase in temperature on the corrosion of carbon steel in CO_2 saturated aqueous solution showing the nature of the corrosion products and their protective properties (modified from [23, 157, 158])

The mechanism of reducing corrosion rate of steel in CO_2 environment by $FeCO_3$ is achieved through (a) the provision of a "diffusion barrier" which extend the diffusion length between the metal substrate and the corrosive medium; (b) the formation of a low-porosity protective layer thereby lowering the exposed surfaces compared with the steel surface and hence less areas to be corroded and (c) the creation of concentration gradients of the principal chemical species (Fe^{2+} and HCO_3^-) [23].

The driving force for precipitation of $FeCO_3$ is supersaturation which in principle involves nucleation and particle growth [69]. The nucleation step increases exponentially with relative supersaturation (RS), whereas the growth rate has an approximately linear relationship with this parameter. The relative supersaturation (RS) is defined as in Equation 3-18

$$\mathrm{RS} = \frac{\mathrm{Q} - \mathrm{Q_{eq}}}{\mathrm{Q_{eq}}} = (\mathrm{S} - 1) \qquad 3\text{-}18$$

Where Q is the concentration of the solute at any instant, Q_{eq} the equilibrium solubility and S is supersaturation defined as in Equation 3-19

$$S = \frac{C_{Fe^{2+}} * C_{CO_3^{2-}}}{K_{sp}} \quad 3\text{-}19$$

Where K_{sp} is the solubility product for $FeCO_3$ [69, 155, 157].

On the other hand, the mechanism and kinetics of crystalline film growth has a quadratic dependence on supersaturation as expressed in Equation 3-20

$$R_{gr} = K_{gr}(S-1)^2 \quad 3\text{-}20$$

Where R_{gr} is the growth rate, K_{gr} is the growth rate constant.

For protective corrosion scale to be formed, the growth rate of iron carbonate has to be equal or higher than the corrosion rate. If the growth rate is less than the corrosion rate, the gap develop between the iron carbonate filled part of the film and the steel surface will never be filled with dense iron carbonate, and the corrosion film thus formed will be porous or non-adherent [70]. The corrosion rate is dependent on the growth rate through a dimensionless parameter termed "scaling tendency" as shown in Equation 3-17. The influence of scaling tendency on the morphology and characteristics of corrosion product films was briefly discussed in Section 3.2.3.1.

It has been reported that temperature accelerates most chemical and electrochemical processes [140]. However, in CO_2 corrosion of carbon and low alloy steels this is only feasible at low temperature (< 60^0C) when the precipitation of corrosion product ($FeCO_3$) and its subsequent protection of the substrate has not occur. This results in increase in corrosion rate. On the other hand, at higher temperature (> 80^0C), when the solubility of $FeCO_3$ is exceeded, increase in temperatures rapidly accelerates the kinetic of precipitation and the formation of protective film which then decreases corrosion rate [137, 139]. Many authors [23, 159] have reported that the kinetics of $FeCO_3$ precipitation seems to be a controlling factor for the protectiveness of the corrosion product layer.

El Sayed, et al, [124] studied the corrosion behaviour of API 5L X65 steel in oilfield seawater under the influence of temperature, CO_2 and acetic acid. The authors reported that the corrosion rate increased with increase in temperature from 20 to 90^0C above which it decreased due to the formation of protective corrosion product ($FeCO_3$). Kermani and Morshed [23] and Schmitt and Michaela [135] specified that at low temperatures (<

60^0C), the corrosion rate increases with temperature up to intermediate range (60^0C - 80^0C) which was ascribed to high solubility of $FeCO_3$ at low temperature. This slows down precipitation rate and so protection films cannot form. However, above 80^0C the protectiveness of $FeCO_3$ layer increases with temperature due to the decrease in $FeCO_3$ solubility and thus the corrosion rate is reduced. Vuppu and Jepson [160] also reported similar temperature versus corrosion rate profile in multiphase pipeline of seawater and oil saturated with CO_2. The effect of temperature on the morphology and composition of the corrosion products for the corrosion of P110 oil tube steel in CO_2 saturated solution was reported by Zhao et al [38]. The results showed that below 60^0C, only Fe matrix was detected suggesting that the corrosion product could not adhere to the steel surface because it has loose structure resulting in severe corrosion attack. At 80^0C, both Fe and $FeCO_3$ were detected. However, $FeCO_3$ could not provide effective corrosion protection but showed a peak in corrosion rate. Between 80^0C and 140^0C, compact, tight and adherent corrosion product consisting of mainly $FeCO_3$ which significantly reduced the corrosion rate was observed. The work of Tanaporn et al [62] on API 5L X65 centred at elevated temperatures (80^0C - 200^0C). Like other researchers, the authors observed decreased corrosion rate at temperatures between 80^0C and 150^0C above which magnetite (Fe_3O_4) was observed along with $FeCO_3$ resulting in further increase in the corrosion resistance. This was attributed to the direct reaction between steel and water according to Schikorr reaction in Equation 3-21 [135]

$$3Fe(OH)_2 \rightarrow Fe_3O_4 + 2H_2O + H_2 \qquad 3\text{-}21$$

3.2.3.3 Effect of solution chemistry

One of the most important and influential parameters affecting CO_2 corrosion of carbon and low alloy steels in oilfield is solution chemistry. This is attributed to the presence of dissolved gasses such as CO_2, O_2 and H_2S [135, 137, 154]. Dissolved CO_2 hydrates to form carbonic acid (H_2CO_3) which dissociate partially in two steps to form HCO_3^-, H^+ and CO_3^- [137, 154] as shown in Equations 3-14 and 3-15.

$$H_2CO_{3(aq)} \overset{K_{ca}}{\leftrightarrow} HCO^-_{3(aq)} + H^+_{(aq)} \qquad 3\text{-}14$$

$$HCO^-_{3(aq)} \overset{K_{bi}}{\leftrightarrow} CO^{2-}_{3(aq)} + H^+_{(aq)} \qquad 3\text{-}15$$

From the equilibria of Equations 3-14 and 3-15, the concentration of carbonic ion (CO_3^{2-}) can be expressed as a function of C_{H^+} and $C_{H_2CO_3}$ as in Equation 3-22

$$C_{CO_3^{2-}} = \frac{K_{ca} K_{bi} C_{H_2CO_3}}{(C_{H^+})^2} \qquad 3\text{-}22$$

Where K_{Ca} and K_{bi} are the solubility constants of carbonic and bicarbonate ions. But for an open system, $C_{H_2CO_3}$ is constant thus a simple relationship exists between $C_{CO_3^{2-}}$ and C_{H^+} as expressed in Equation 3-23.

$$K_{sp} = C_{CO_3^{2-}} * C_{(H^+)^2} \qquad 3\text{-}23$$

Where $K_{sp} = K_{ca}K_{bi}$ = solubility product

Iron carbonate ($FeCO_3$) is the main product of CO_2 corrosion in oil and gas pipelines [61, 154] and ferrous ion (Fe^{2+}) is the main product of dissolution of steels in corrosive environments [61]. Thus in CO_2 corrosion system, as long as the concentration of Fe^{2+} and CO_3^{2-} are sufficiently high (ie exceeding saturation with respect to $FeCO_3$), precipitation and crystal growth will occur according to Equation 3-24

$$Fe^{2+}_{(aq)} + CO^{2-}_{3(aq)} \rightarrow FeCO_{3(s)} \qquad 3\text{-}24$$

The saturation value of $FeCO_3$ can be expressed as in Equation 3-19.

$$S_{FeCO_3} = \frac{C_{Fe^{2+}} * C_{CO_3^{2-}}}{K_{sp}} \qquad 3\text{-}19$$

Substituting CO_3^{2-} from Equation 3-23 into Equation 3-19 a dependency of S_{FeCO_3} on $C_{Fe^{2+}}$ and pH was obtained as presented schematically in Figure 3-7 [161].

Two main regions divided by S_{FeCO_3} = 1 are clearly seen in Figure 3-7. These include $FeCO_3$ supersaturation region (S_{FeCO_3} > 1) where the concentration of Fe^{2+} and CO_3^{2-} ions are in excess leading to the precipitation of $FeCO_3$ and subsequent formation of $FeCO_3$ layer on the steel surface. The second region is the $FeCO_3$ under saturation region (S_{FeCO_3} < 1) where the rate of $FeCO_3$ dissolution is faster than its precipitation and so $FeCO_3$ layer cannot formed. A transition region (0.5 < S_{FeCO_3} < 2) exist where neither

precipitation nor dissolution of $FeCO_3$ dominates thus leading to the surface of the metal being partially covered by $FeCO_3$ layer and a possibility of localised corrosion.

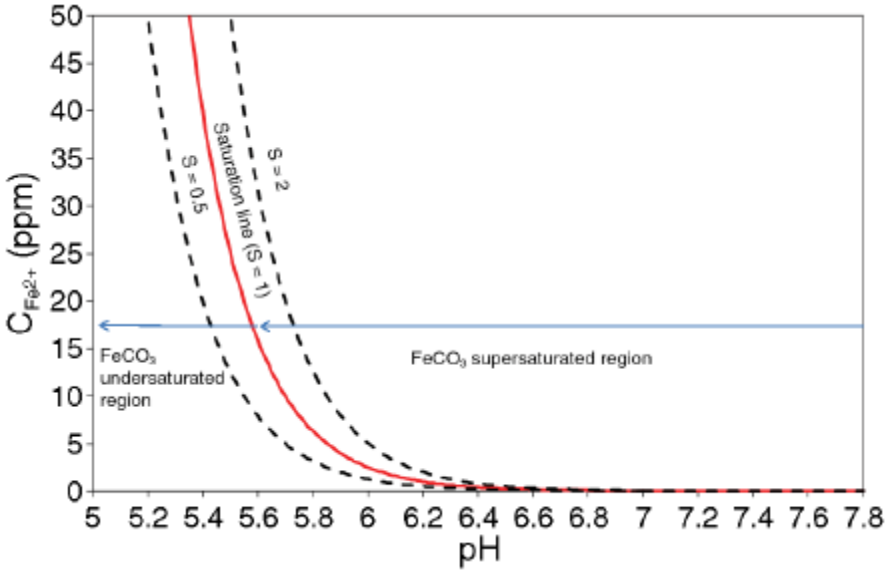

Figure 3- 7; The dependency of $FeCO_3$ solubility on C_{Fe2+} and pH [161]

As natural contaminants and constituents in oil field environments, chloride ions play significant role in the corrosion process of oil and gas facilities [162, 163]. The effect of chloride ion concentration on corrosion mechanism of carbon steel depend on the type, morphology, structure and protective capabilities of the oxide phases formed on the surface of the substrate in different environments. Such environments which include atmospheric environment [163-166], natural and seawater environment [4, 167-169], sodium chloride (brine) solutions [54, 56, 67, 170] have been extensively studied. In O_2-free environment, increase in chloride concentration above certain threshold (>1000 ppm) has been reported to decrease the solubility of CO_2 resulting to "salting out" or surface inhibition with the attendant reduction in corrosion rate [139]. This was demonstrated in the works of Eliyan, et al [171] on the electrochemical corrosion behaviour of API-X100 steel in different concentration (5 to 80 g/L) of saline CO_2-saturated solutions at 20^0C and 90^0C. The results at 20^0C showed that the corrosion rate increased with chloride ions concentration and i_{corr} reaching a maximum of 185 µA/cm^2 in 15 g/L chloride solution, decreasing rapidly with chloride concentration up to 40 g/L and then became almost insensitive at about 120 µA/cm^2 in the more concentrated solutions. This is presented schematically in Figure 3-8. This agrees with the report of Fang, et al [138] on the general carbon dioxide (CO_2) corrosion rates of C1018 (UNS G10180) carbon steel in different sodium chloride (NaCl) concentrations (3 wt% to 25 wt%) at 20°C.

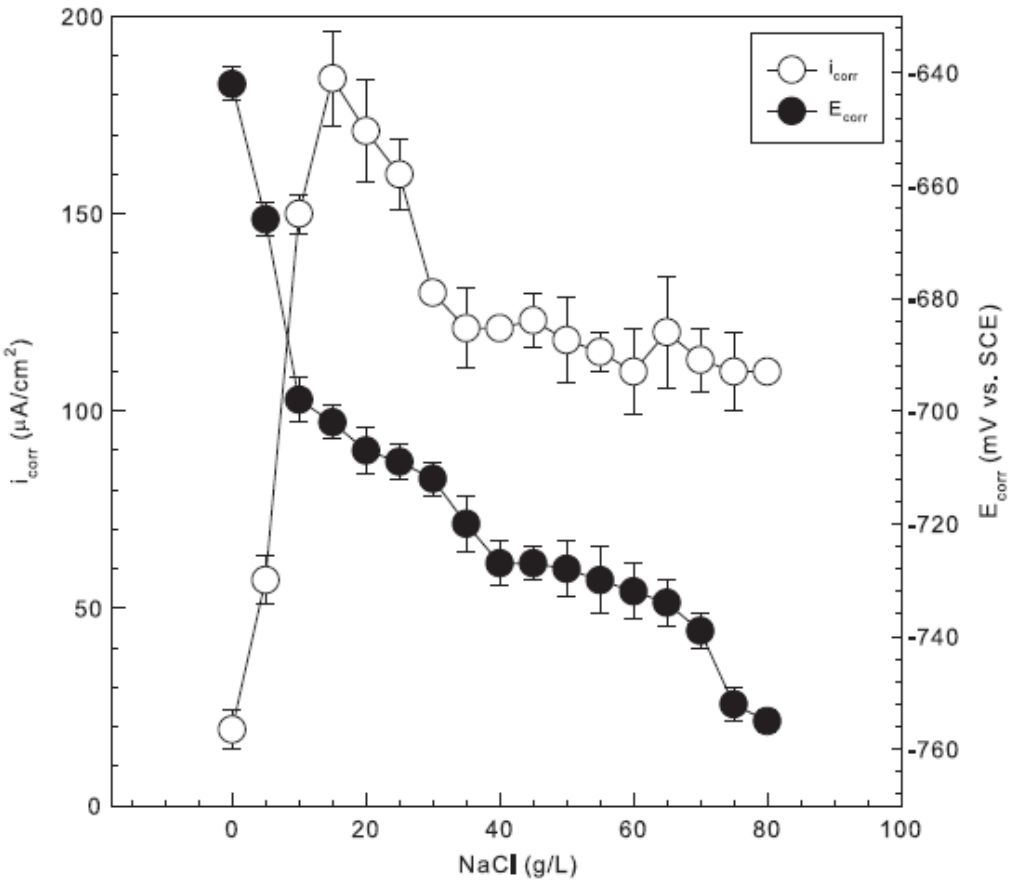

Figure 3- 8: Corrosion rates and potentials vs NaCl concentration of API-X100 steel at 20^0C [171].

Similarly, Zeng, et al [172] reported that corrosion rate of steels decreased with increasing salt concentration, and the highest corrosion rate was found at the lowest salt concentration. This result was attributed to the competitive adsorption of hydroxyl and chloride ions during anodic dissolution of iron in NaCl containing acidic solution. It has been generally accepted that the overall anodic dissolution of iron expressed in Equation 3-3 involves many steps as proposed by Bockris, et al [145] and recently reviewed by Nesic, et al [136] (Equations 3-4 to 3-12). Thus at low or in the absence of NaCl concentration, Equation 3-5

$$FeOH_{(ads)} \rightarrow FeOH^{+} + e^{-} \qquad 3\text{-}5$$

is the rate determining step leading to dissolution of iron and so the adsorption of hydroxyl ions prevails over chloride ions resulting in higher Tafel Slope. However, at higher salt

concentration and based on Equations 3-25 and 3-26, chloride adsorption tends to prevail with Equation 3-26 being the rate determining step resulting in lower Tafel slope [172].

$$Fe.H_2O_{(ads)} + Cl^- \rightarrow FeCl^-_{(ads)} + H_2O \qquad 3\text{-}25$$

$$FeCl^-_{(ads)} + OH^- \rightarrow FeOH^+ + Cl^- + 2e^- \qquad 3\text{-}26$$

Recently, Han et al [173], noted that NaCl concentrations play three major roles in corrosion kinetics of carbon steels. These include (i) accelerating the corrosion process by forming intermediate corrosion species, (ii) decreasing the solution pH which also accelerates the corrosion process and (iii) reducing the solubility of dissolved oxygen (DO) which decreased the corrosion rate. However, the net effect of increase in NaCl concentration above a certain quantity as reported in literatures [138, 139, 172] was reduction in corrosion rate. This means that the effect of reducing the solubility of DO (salting out) dominates the other two competing effects. In agreement with this Yari [174] observed that in a basic or neutral solution, oxygen reduction reaction is the predominant cathodic reaction in competition with the hydrogen evolution reaction. Similarly, Caceres et al [175] stated that the major reaction governing corrosion in most practical oilfield application is the reduction reaction of oxygen present in solution.

The presence of dissolved oxygen (DO) in CO_2 environment is yet another factor that influences the corrosion of crude oil component. Liu et al [167], Ismail and Adan [176] and Jung et al [177] reported that the effect of dissolved oxygen on corrosion of steels is more prevalent than all other impurities present in crude oil. Jung et al [177] after an extensive laboratory experiments specifically reported that the corrosion rates of carbon steel pipe (CSP) decreased by 75% when DO concentration was reduced from 9±0.5 to 2±0.5 mg/L. The study of Martin [178] also revealed that corrosion rate of steels is accelerated by 0.5 mm/y per ppm of oxygen in CO_2 environment contaminated with O_2 at medium velocity and ambient temperature.

However, the effect of NaCl on the corrosion rate of carbon steel in CO_2-saturated solutions has not been clearly understood as some other authors presented divergence

results. The contrary view summarized the mechanism of chloride attack by series of step wise electrochemical reactions as shown in Equations 3-27 to 3-34 [4, 124, 179]

At the anode;

$$Fe \rightarrow Fe^{2+} + 2e^{-} \qquad 3\text{-}3$$

At the cathode (basic or neutral):

$$\frac{1}{2}O_2 + H_2O + 2e^{-} \rightarrow 2OH^{-} \qquad 3\text{-}27$$

Adding Equations 3-3 and 3-27:

$$Fe + \frac{1}{2}O_2 + H_2O \rightarrow Fe(OH)_2 \qquad 3\text{-}28$$

In the presence of chloride, the ferrous ion in Equation 3-3 reacts with chloride ion to form iron-chloride complex as indicated in Equation 3-29

$$Fe^{2+} + 2Cl^{-} \rightarrow (FeCl_{complex})^{+} \qquad 3\text{-}29$$

$$(FeCl_{complex})^{+} + 2OH^{-} \rightarrow Fe(OH)_2 + Cl^{-} \qquad 3\text{-}30$$

$$Fe(OH)_2 + (FeCl_{complex})^{+} \rightarrow Fe + FeOH^{+} + Cl^{-} + 2e^{-} \qquad 3\text{-}31$$

Also the passive film $(Fe(OH)_2)$ in Equation 3-28 can directly react with chloride ion as follows

$$2Fe(OH)_2 + 2Cl^{-} \rightarrow 2FeOCl + 2OH^{-} + H_2 \qquad 3\text{-}32$$

$$FeOCl + H_2O \rightarrow Fe^{2+} + Cl^{-} + 2OH^{-} \qquad 3\text{-}33$$

Equations 3-30, 3-31 and 3-33 show that the chloride ions are not consumed but remain available to continue corrosion process. Chloride ions are considered as aggressive corrosive agents. This is attributed to the small size, high diffusivity, strong anionic nature and high solubility of chloride salts [162, 179]. Therefore most chloride attack on steels, particularly passive steels usually results in pitting corrosion [54, 170, 179].

In the presence of oxygen, the ferrous hydroxide in Equation 3-28 also transforms to magnetite film (Equation 3-34) which partially protects the substrate from further dissolution.

$$3Fe(OH)_2 + \frac{1}{2}O_2 \rightarrow Fe_3O_4 + 3H_2O \qquad 3\text{-}34$$

The nature, protectiveness, stability, adherence, coverage and the chemistry of these oxide films depend on the kinetics of the corrosion reactions and the formation of corrosion products. This in turn is related to the composition of carbon steel and microstructures of the protective oxide film [162]. Alizadeh and Bordbar observed that the structures of the corrosion product play essential role on the corrosion resistance of carbon steel by preventing the corrosive species from reaching the steel substrate.

The chemical composition and the thermo-mechanical treatment applied during manufacturing process of carbon steel determine its microstructure. Microstructure on the other hand plays important role in the corrosion behaviour of carbon steel in different environments [11, 62]. It has been demonstrated that the films of corrosion product can develop and cover the surface of the substrates protecting them from corroding in aqueous solutions [4, 162, 179, 180]. Some of these corrosion product films are mainly oxides of iron which are generally porous with poor adherence and are prone to cracking [162, 165, 179]. Research has shown that about nine different types of iron oxide phases which provide different levels of protection can form on the surface of carbon steels [67, 124, 175, 181]. Each of these oxide phase is uniquely characterized by different hyperfine parameters [181] and most of them do not give adequate protection to the steel surface [165]. On the other hand, few of these oxides that may offer protection are broken down in the presence of aggressive corrosion agents such as chloride ions [162, 167, 179]. It then follows that chloride ions can easily penetrate and migrate through the passive film and upon reaching the rust (oxide)-steel interface form intermediates containing chloride which breakdown the passive films [165, 179]. El-Desouky and Aboeldahab [182] studied the effect of different concentration of NaCl (0.1–2 M) on maraging steel and reported a continuous increase in corrosion rate with increase in NaCl concentration. Similarly, Liu et al [167] categorized the effect of chloride ion on corrosion of carbon steels as smooth invariant stage, slow rise stage and the rapid rise stage.

Corrosion rate of steels can also be significantly influence by the ionic composition of the solution. Nesic, et al [183] reported that an increase in Fe^{2+} concentration, which is the product of anodic dissolution of iron in CO_2 corrosion, results in higher supersaturation leading to the precipitation of protective corrosion passive. Mishra, et al [139] and Popoola, et al [128] also observed that laboratory tests conducted with pure salt solutions exhibited higher corrosion rate than that with actual formation waters in CO_2

environment. This is because of the presence of calcium ions (Ca^{2+}), HCO_3^-, magnesium ions (Mg^{2+}), etc in the formation water. These cations react with carbonic acid and deposit other carbonates which in conjunction with iron carbonates (main CO_2 corrosion product) enhances the scale formation and hence reduces the corrosion rates.

3.2.3.4 Effect of surface film

The main product of CO_2 corrosion of carbon and low alloy steel is $FeCO_3$ which is formed when the concentration of Fe^{2+} and CO_3^{2-} ions in the solution exceeds super-saturation [23, 62, 69, 129, 134, 135, 137, 139, 184]. The formation, nature, growth and function of $FeCO_3$ on the corrosion behaviour of carbon steel depend largely on temperature, pH, flow condition, material characteristics, etc [135, 139]. At low temperature ($\leq 60^0$C), the solubility of $FeCO_3$ is high which decreases precipitation rate and so protective film cannot form leading to increase in corrosion rate with increase in temperature. At higher temperatures ($\geq 60^0$C), the solubility of $FeCO_3$ decreases leading to high super-saturation, high precipitation rate and subsequent formation of protective film with eventual decreases in corrosion rate. The works of Yucheng et al [62, 129] on X65 carbon steel within 50^0C - 130^0C, Tanaporn et al on X65 at 80^0C - 200^0C and Palacious and Shadley [133] on API N-80 and C-1018 steels are in agreement regarding the effect of temperature on the formation of protective $FeCO_3$ in CO_2 corrosion environments.

The protectiveness of surface film also depends on the characteristic of the materials (chemical composition and microstructures) [62, 133, 135]. Experimental results [54, 133] have shown that when a steel with ferrite-pearlite microstructures is immersed in a brine solution, selective dissolution of the ferrite phase takes place leaving the pearlite (Fe + Fe_3C) which is more difficult to dissolve on the metal surface. Fe_3C being an electronic conductor enhanced the corrosion rate by causing a galvanic effect and acting as relatively high surface cathodic site (area) for hydrogen evolution reaction (HER). The adherence and protective properties of the corrosion product films are related to the presence of these cementite (Fe_3C) platelets which strengthen and anchor the films to the metal substrate. Fe_3C is not a corrosion product but merely existed in the scale as a result of its presence in the steel and acts as cathode while the ferrite acts as the anode in ferrite-pearlite microstructure [52, 62, 137]. The preferential dissolution of ferrite results in high

ferrous ion (Fe^{2+}) concentration between the lamellar Fe_3C where it also facilitates cathodic reactions through internal acidification of the solution imprisoned within the layer due to local depletion in HCO^{3-} ions [143, 185]. These tripartite functions (acting as cathodic site, formation of galvanic effect and internal acidification form by accumulated F^{2+}) of Fe_3C promote the formation of iron carbonate on carbon steel with normalized (ferritic-pearlitic) microstructure resulting in better adherent to the metal surface than on quenched-and-tempered steels (martensitic-bainitic microstructure) [135]

There are reports of the presence of magnetite (Fe_3O_4) in CO_2 corrosion product at temperatures above 130^0C depending on other parameters [62, 135, 148]. This has been ascribed to direct reaction between steel and water through Schikorr reaction. The global reaction proposed by Schikorr which is the decomposition of $Fe(OH)_2$ is shown in Equation 3-21

$$3Fe(OH)_2 \rightarrow Fe_3O_4 + 2H_2O + H_2 \qquad 3\text{-}21$$

$Fe(OH)_2$ is the product of the overall anodic electrochemical reaction for ferrous metals as expressed in Equation 3-35. This is in accordance with the pH dependent anodic reaction steps proposed by Bockris [145]

$$Fe + 2H_2O \rightarrow Fe(OH)_{2(s)} + 2H^+ + 2e^- \qquad 3\text{-}35$$

Fe_3O_4 is a thin, dense, and adherent corrosion product layer formed on the steel surface, (beneath a thick, porous, and loose layer), and is usually associated with lower corrosion rate.

Another corrosion product in CO_2 corrosion of carbon steel is iron hydroxycarbonate ($Fe_2(OH)_2CO_3$) [52]. $Fe_2(OH)_2CO_3$ scale is mostly formed at temperatures above 60^0C and may be considered as a mixed transition phase, (if written as $FeCO_3 \cdot Fe(OH)_2$), between non-protective $FeCO_3$ (which may form below 60^0C) and ferrous hydroxide ($FeOH_2$). $Fe_2(OH)_2CO_3$ has shown to be more adherent, protective, and therefore, more effective in reducing corrosion rate than $FeCO_3$ [52]. $FeCO_3 \cdot Fe(OH)_2$ could also be called basic ferro carbonate.

In general, CO_2 corrosion products most often reduce the corrosion rate of steels by physically forming a diffusion barrier on the steel surface thereby hindering further corrosion [23, 135, 137]. Dugstad et al [184], stated that the requirements for satisfactory protection of carbon steel from CO_2 corrosion are (i) high super-saturation of $FeCO_3$

without which protective $FeCO_3$ cannot form, (ii) proper adherence of the protective film which is facilitated by the presence of carbide that strengthens and anchors it on the substrate and (iii) complete coverage of the substrate by corrosion product which eliminate the tendency for localise corrosion to occur.

3.2.3.5 Effect of carbon dioxide partial pressure (P_{CO_2})

Carbon dioxide partial pressure (P_{CO_2}) is one of the environmental factors affecting the CO_2 corrosion of carbon steel in oil and gas industry. Due to the enormous problems caused by CO_2 corrosion in this industry, extensive studies to mitigate these problems resulted in a number of prediction models. The mechanism, predictability and functionality of these models have been described, compared and discussed in literature [186, 187]. However, none of these models, collectively or individually presented adequate understanding of the mechanism nor mitigation techniques of CO_2 corrosion. This is due to the complexities arising from the myriad of factors affecting CO_2 corrosion process [7, 69, 128]

The first and most widely used model for predicting CO_2 corrosion of carbon steels in wells and pipelines was proposed by de Waard and Milliams in 1975 [134]. This model depended on the effects of P_{CO_2} and temperature only and is expressed in Equation 3-36 [129, 134]

$$\text{Log } C_R = 5.8 - \frac{1710}{T} + 0.67 \text{Log} P_{CO_2} \qquad 3\text{-}36$$

Where

C_R = the corrosion rate in mm/yr.

T = the temperature in K and

P_{CO2} = the CO_2 partial pressure in Pa.

This simple model has been revised serveral times by the same and/or other authors to incorporate more influencing environmental parameters such as pH, water chemistry, scaling tendency, total pressure, hydraulic diameter, fluid flow velocity, oil wetting, glycol concentration and steel composition [129]. The models of de Waard–Milliams [134] correlated very well between experimental and field data for very low carbon dioxide partial pressure up to 1 MPa predicting an increase in corrosion rate of carbon steel with increase of CO_2 partial pressure.

Other models have generally predicted the same correlation particularly in scale-free CO_2 corrosion. This is because under scale-free condition, increase in P_{CO_2} increases the concentration of H_2CO_3 which reduces the pH of the system. This in turn accelerates the cathodic reactions generating more CO_3^{2-} ions in the solution and ultimately enhances the corrosion rate. On the other hand, in film-formed condition and at high pH, increased P_{CO2} leads to increase in bicarbonate and carbonate ion concentration and higher super-saturation which then accelerate precipitation and scale formation [129, 135, 137, 188].

Zhang, et al [129] compared the corrosion behaviour of X65 carbon steel pipeline in low CO_2 partial pressure (1 MPa) and supercritical CO_2 condition (9 MPa) at different time interval. The results which is shown in Figure 3-9 revealed that the corrosion rates under supercritical CO_2 conditions were much higher (about 3–4 times) compared with low CO_2 partial pressure. This variation in corrosion rate was attributed to the transition of CO_2 from gaseous to liquid or supercritical condition with increasing pressure resulting in different interaction with water which is non-ideal and so does not obey Henry's law [188].

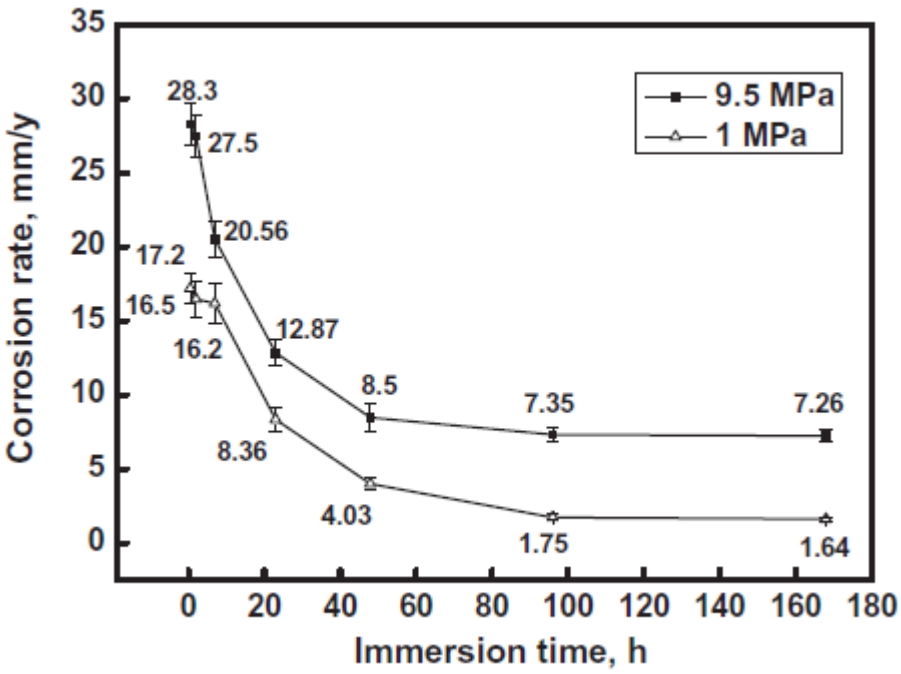

Figure 3- 9: The corrosion rates of X65 steel exposed in water saturated with CO_2 under low partial pressure and supercritical condition at 80^0C for various immersion time [129].

It is well known that an increase in CO_2 partial pressure increases the solubility of CO_2 in water phase. This enhances the concentrations of carbonic species (H_2CO_3, HCO^{3-} and CO_3^{2-}) in the solution and consequently increases corrosion rate. The results of the variation of temperature showed similar trend with regards to characteristics of CO_2 corrosion products and variation of corrosion rate with time and temperature. However the intensity and magnitude of the effects of these parameters were much higher under super critical condition than at low partial pressure. This confirmed the reports of many authors [11, 23, 135, 137] that increase in P_{CO2} leads to increase in corrosion rate.

Nesic, et al [189] used electrochemical techniques to investigate the corrosion behaviour of mild steel under different CO_2 partial pressures (3 – 10 bar), and different water flow velocities (0 – 2 m/s) in 1 wt% NaCl at 60^0C and pH 5. The results of the Nyquist impedance plots showed that the radius of the capacitive semicircle decreased with increase in velocity but the shape of the impedance plots were insensitive to increase in CO_2 partial pressure. This implies that with an increase in CO_2 partial pressure, the corrosion rates of the mild steel increased while the corrosion mechanism of the corrosion process was not affected.

3.2.3.6 Effect of Microstructure

The microstructure of carbon and low alloy steel is determined by its chemical composition and the thermomechanical treatments used during the production processes [54]. These variables are not independent as the same microstructure can be obtained with different chemical compositions and/or heat treatments [185]. Experimental evidence [11, 54, 185] has shown that different microstructures can be obtained from carbon steels with the same chemical composition and vice versa depending on heat treatment route. This can be attributed to the presence, quantity and type of alloying elements and thermo-mechanical processes (heat treatment routes) which consequently determine the precipitation, volumetric fraction, uniformity, size and distribution of microstructural constituents in the steels [52].

The effect of microstructure and chemical composition on the CO_2 corrosion of steels has been extensively investigated and found to be of great important [52, 135, 139, 159, 184]. The dependent of corrosion rate on the chemical composition and microstructures of the steel is not systematic as the protective and adherence properties of the film can vary

greatly even for similar carbon steels. Therefore, it is not possible to draw a general behaviour pattern. Consequently, some authors [133, 185] have reported that normalized plain steel with a ferrite-pearlitic microstructure exhibit better corrosion resistance than the hardened and tempered alloy steel with martensitic-bainitic microstructure under the same conditions. However, other authors [11, 52] have reported opposite results. This discrepancy has been ascribed to the complexities arising from the myriad of other factors affecting CO_2 corrosion process [7, 11, 69, 128].

Al-Hassan et al [52] reported that annealed specimens exhibit lower corrosion rate than as-received materials (Thermo-mechanical control process – TMCP) while the quenched and tempered specimens showed corrosion rates between these two extremes. This is understandable since in the ferrite-pearlite (α-Fe + Fe_3C) microstructures, Fe_3C being an electronic conductor and having lower over-potential for hydrogen evolution is more cathodic than ferrite leading to the formation of micro-galvanic cells with the attendant selective dissolution of ferrite. This leaves the Fe_3C exposed to the electrolyte as large cathodic sites and ultimately increases corrosion rate [62, 137, 159]. From heat treatment point of view, the microstructures of annealed steel has more refined pro-eutectoid ferrite than the normalized specimen. Conversely, the normalised steel has more segregation along the ferrite/Fe_3C interfaces and less pro-eutectoid ferrite and consequently increased pearlite (Fe_3C) phase [52, 190]. It then means that the normalised steel has more cathodic site than the annealed steel resulting in higher corrosion rate for the normalized specimen than the annealed sample. Similarly, Ochoa, et al [185] used heat treatment to impact different microstructures on API 5L X42 and observed that the corrosion rate of carbon steel decreased in the following order: banded (B- as-received) > normalised (N) > quenched and tempered (Q&T) > annealed (A). This was ascribed to the formation of $FeCO_3$ between the non-oxidised Fe_3C platelets which anchored and strengthened it ($FeCO_3$) on the steel surface of the annealed steel. Palacious and Shadley [133] also shared this line of thought suggesting that the structural characteristics of $FeCO_3$ depend on microstructure of the matrix and thus reported that for the quenched and tempered steel with martensitic microstructure, $FeCO_3$ is less tenacious and less crystalline than the large and dense crystals that formed on annealed steel with ferritic-pearlite microstructure resulting to the former demonstrating more corrosion susceptibility.

On the contrary, Lopez, et al [12] and Dugstad et al [184] opined that quenched and tempered microstructures have better corrosion resistance than the annealed ones. In this case, the un-dissolved Fe_3C platelet of the quenched and tempered steel was assumed to be completely detached and removed from the steel surface leaving a new area of exposed cementite equivalent to the initial one thus reducing the corrosion rate by eliminating the galvanic effect. This is the point of disagreement since Al-Hassan, et al [52], Ochoa, et al [185] and Palacious and Shadley [133] postulated that the undissolved laminar platelet of Fe_3C in quenched and tempered (Q&T) microstructure are not removed but enhanced the formation of internal acidification and subsequent saturation and precipitation of $FeCO_3$.

The presence of alloying elements in steel have tremendous effect on the type of microstructure formed as a result of heat treatment of the steel. These alloying elements increase the time required for austenite to decompose to ferrite and/or ferrite-Fe_3C mixture, and, therefore, made it possible for the martensite or bainite to form at lower cooling rates [191]. In the quenched and tempered samples, alloying elements (such as Cr, Mo, etc) delay and retard the decomposition of martensite to ferrite and carbides upon tempering. This is due to the sluggish diffusion process of the atoms of these elements in forming carbides. Thus the normalized specimen, in which most Fe_3C could not precipitate due to the presence of the alloying elements, corrode at a rate lower than the annealed steel which provided ample time for Fe_3C to precipitate [52]. This is contrary to the observation for the steel with little or no alloying elements.

It is evidenced from this review that the corrosion rate of micro-alloy steels has been widely investigated in different environmental parameters such as temperature, pH, and partial pressure using different electrochemical measurement techniques. The results showed that corrosion resistance increased with increase in pH, increase in partial pressure but decreased with increase with temperatures lower than $< 60^0C$. However, at higher temperatures ($> 60^0C$) the corrosion resistance increased due to the formation of $FeCO_3$ which physically block to corrosive species from accessing the steel substrates in CO_2 saturated environments. This review also presented divergent reports from different authors on the effects of steel microstructures on corrosion rate. This research is aimed at improving the corrosion resistance of three proprietary micro-alloy steels by alloying them with non-conventional carbide forming elements. A systematic procedure for achieving this aim is presented in the following chapters.

Chapter 4: Materials and Experimentations

In this chapter the characteristics of the materials used, the method of sample preparation and the electrochemical techniques employed to assess the corrosion behaviour of three proprietary micro-alloyed steels and API 5L X65 steel grade were highlighted. This was followed by experimental set-up, test conditions and preliminary investigations of the corrosion behaviour of the steels in different simulated corrosion media. Alloying methods, heat treatment schedule and equipment operation procedure utilized to alloy and investigate the mechanical, physical and chemical characteristics of the alloyed samples were also presented. This chapter also enumerates the procedure deployed to investigate the corrosion behaviour of the alloyed steels using the test set up and test conditions in simulated produced water. This chapter explained the procedure of validating the results obtained using some post experiment surface analysis techniques such as optical microscope (OM), Fiji ImageJ analysis, Scanning Electron Microscopy/Energy Dispersed X-ray (SEM/EDS), X-ray Diffraction (XRD) and white light interferometry.

4.1 Materials Preparation, Characterization, Examinations and Analysis

4.1.1 Materials

Three proprietary micro alloyed steels supplied by commercial steel industries and whose electrochemical behaviour has not been fully investigated were used in this work. These steels are designated as ASTM A694-F65 forged steel bar (F65) of 52 mm diameter and 3000 mm long; improved collapsed steel grade P110 IC pipe (P110) of 114.3 mm diameter and 8.56 mm thickness and high collapsed sour service steel grade TN95 HS pipe (TN95) of 244.475 mm diameter and 13.843 mm thickness. Figure 3-1 shows the image of the as-supplied P110 IC and TH95 HS proprietary steel grades. A fourth sample, API 5L X65 steel grade with a proven integrity for oil and gas application, [12, 13, 122] was chosen as reference specimen. Tables 4-1, 4-2 and 4-3 present the mechanical properties, the physical characteristics and the chemical specifications of these steel samples respectively. It can be seen from Table 4-1 that the mechanical properties of the micro-alloyed steel samples satisfies the minimum standard specifications for oil and gas pipeline [36]

Figure 4- 1: As received proprietary grades of steel

Table 4- 1: Mechanical properties of the samples

Grade	Min. Yield Strength (ksi)	Max. Yield Strength (ksi)	Min. Tensile Strength (ksi)	Max. Hardness (VH)
P110 IC	110	140	125	129
TN95 HS	95	110	105	248
ASTM A694-F65	65	87	77	180

Pipe Body Performance Properties Catalogue, Tenaris [192]

4.1.2 Materials (Samples) Preparations

Metallography is the study of the microstructure of metals and alloys. It uses microscopy to provide important information about the structure and properties of metal and alloy samples. Before metallographic analysis/examination, the specimens were prepared using successively fine abrasive paper to remove material from the surface until the desired surface quality is achieved. The sample preparation for this work was conducted according to ASTM E 3-01 "Standard Guide for Preparation of Metallographic Specimens" [193]. Five steps namely cutting, mounting, grinding, polishing and etching as briefly explained in this section were used.

Table 4- 2: Samples and their characteristics

S/No	Proprietary grade	API equivalent grade	Application	As-received Geometry	Specimen size
1	ASTM A694-F65 (F65)	ISO 11960/**API 5LX65** PSL1	Line Pipe	25mmØ * 300mm Long	25mmØ * 5mm Thick
2	P110 IC (P110)	ISO 11960/API 5CT P110 PSL1	Casing & Tubing	114.3mmØ * 8.56mm Thick	18mm * 16mm * 5mm
3	TN95HS (TN95)	ISO 11960/API 5CT TH95 PSL1	Casing & Tubing	244.5mmØ * 13.84mm Thick	18mm * 16mm * 8mm
4	API 5L X65	API 5L X65	Line Pipe	25mmØ * 300mm Long	25mmØx 50 mm Thick

Table 4- 3: Elemental Specifications of the samples

Samples	**C**	**Mn**	**S**	**P**	**Si**	**Ni**	**Cr**	**Mo**	**V**	**Cu**	**Sn**	**As**	**Al**	**Ca**	**Nb**	**Ti**	**B**
F65	0.12	1.27	0.002	0.008	0.18	0.07	0.11	0.17	0.057	0.12	0.008		0.022		0.054	0.001	5E-04
P11OIC	0.22	1.4	0.001	0.012	0.32	0.019	0.25	0.07	0.005	0.03	0.003	0.002	0.025	0.001	0.002	0.023	0.002
TN95HS	0.25	0.54	0.001	0.01	0.26	0.04	0.99	0.46	0.005	0.098	0.006	0.004	0.02	0.001	0.022	0.008	9E-04
X65	0.12	1.27	0.002	0.008	0.18	0.07	0.11	0.17	0.057	0.12	0.008		0.022		0.054	0.001	5E-04
	Cu+8Sn	**N**	**O**	**Alsol**	**Pb**	**Sb**	**BI**	**Mg**	**B_{Sol}**	**Co**	**Cd**	**W**	**Zr**	**H**	**Ce**	**Pcm**	
P11OIC	0.054	0.004		0.024	0.002	0.001	0.002	3E-04	0.002	7E-04		0.002	0.002		0.052	0.33	
TN95HS	0.146	0.005		0.02	0.001	0.001	0.002	3E-04	9E-04	0.007		0.002	0.002		0.64	0.376	

4.1.2.1 Cutting

The as-supplied ASTM A694-F65 F65 and API 5L X65 steels were machined to 25 mm diameter and 5 mm thickness (4.91 cm^2 surface area) at the Mechanical Engineering Department Workshop, University of Leeds. On the other hand, samples P110 IC and TN95 HS with dimensions 18 mm x 16 mm x 5 mm (2.88 cm^2 surface area) and 18 mm x 16 mm x 8 mm (2.88 cm^2 surface area) respectively were supplied with the steel pipes by the commercial steel industry (Tenaris). The dimensions of the specimens are shown in Figure 4-2. More samples of cuboid and cylindrical shapes of 1 cm^2 base surface area were later machined from the supplied pipes of Steels P110 and TH95.

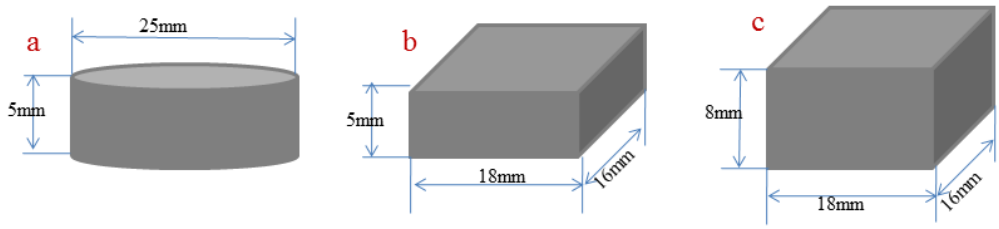

Figure 4- 2: Specimen dimensions (a) F65 and X65, (b) P110 IC and (c) TN95 HS

4.1.2.2 Mounting

For ease of handling and to protect the edges of the specimens during grinding and polishing, the specimens were enclosed in phenolic resin to about 38.1 mm diameter and 40 mm height using SimpliMet 1000 automatic mounting press. The press was set at a pressure of 290 bars with a heating temperature of 250^0C. Heating was done for 2 minutes and then cooled for 3 minutes. Thus it took about 5 minutes to complete a mounting cycle/process.

4.1.2.3 Grinding

Grinding was done using a Metserv 250 twin grinding-polisher with Silicon Carbide (SiC) grit paper. Five sizes P120, P320, P600, P800 and P1200 of SiC grit papers with increasing successive abrasive fineness were used. Grinding ensured that the scratches on the surface of the samples are uniform and oarallel to each other at any of the grainging stage. This was achieved by turning the samples 900 after each grinding stage. At the completion of each grinding stage, the specimens were washed using de-ionised water and dried in warm air before proceeding to the next stage. These procedures were repeated for all the four grinding stages and for all the specimens.

4.1.2.4 Polishing.

Polishing is similar in operation to grinding but has no restrictions with regards to the polishing angle. Polishing was done on a Buehler Metaserv 250 twin grinder-polisher using diamond slurry. Polishing was performed using 6 µm and 3 µm abrasive diamond slurry. The specimens after each stage of polishing were rinsed in de-ionised water, degreased with ethanol and dried in warm air. The final polished surface gave a mirror-like finish with minimal or no defect (scratches/marks).

4.1.2.5 Etching

No matter how mirror-like a polished surface is, some surface layers of disturbed metal resulting from the final polishing stage are always present and need to be removed. This was achieved by the process of etching. Etching was also used to reveal the grain boundaries. The etchant used in this work was Nital. This is a mixture of 5 mL Nitric acid in alcohol. Each of the specimens were respectively dipped in Nital solution ensuring that the polished surface was fully covered by the solution and held for 20 to 30 seconds with shaking until the mirror-like surface became dull. The specimens were removed from the nital and quickly washed in de-ionised water, rinsed with alcohol and dried in warm air. The specimens were then examined, characterised and analysed using various metallographic analysis techniques.

4.1.3 Materials Characterization.

The etched specimens were characterised to determine the microstructure, elemental composition, structural properties and spatial distribution of the constituents or phases, grain and grain size distribution and mechanical property (hardness). These investigations were carried out using various combination of surface analyses techniques such as optical microscope (OM), Fiji ImageJ, Scanning Electron Microscopy/Energy Dispersed X-ray (SEM/EDX), X-ray Diffraction (XRD) and white light interferometry. A brief description of the operating principles of these analysis techniques are provided in the next subsections

4.1.3.1 Optical Microscope

The optical microscope (light microscope) uses visible light and a system of lenses to magnify images of small subjects. The optical microscope used in this work was Zeiss AxioCam MRc 5 optical microscopy (OM) with the set-up shown in Figure 4-3. It was used to examine, capture the image and identify the type of microstructure of the as

received micro-alloyed steels, the alloyed steel samples and the surfaces of the corroded specimens.

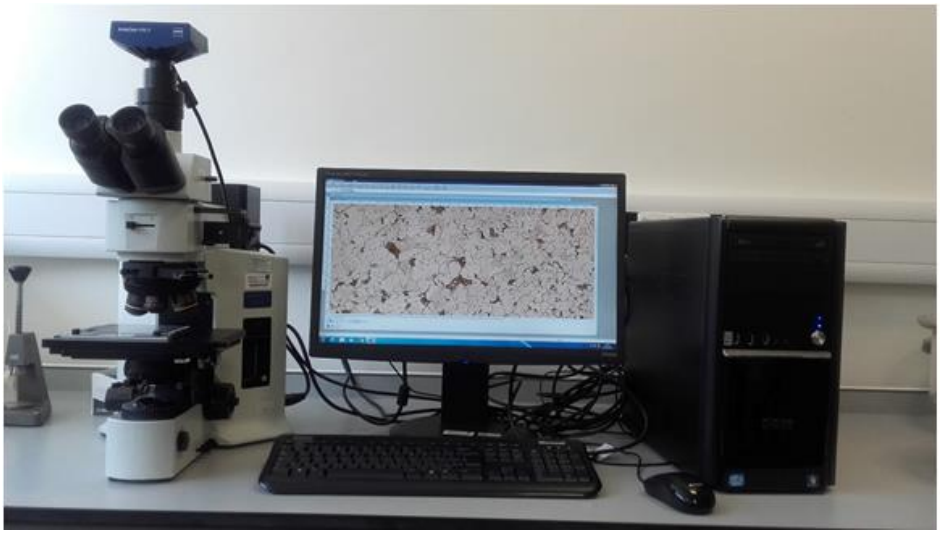

Figure 4- 3: Optical Microscope (OM)

4.1.3.2 Grain Size Analysis

This techniques was used to measure the quantity, the ratio and the grain size of microstructural components of the as-received and alloyed specimens. The grain size number of the as-received and alloyed specimens were calculated according to ASTM E112-12 Standard [194]. The grain size of metallic materials according to this standard can be measure using three different procedures which include comparison procedure, planimetric (Jeffries) procedure and intercept procedures. In this work, the planimetric (Jeffries) procedure was used to estimate the grain size of both the as-received and alloyed specimens. The planimetric method involves an actual count of the number of grains within a known area using Fiji ImageJ software. The number of grains per unit area (N_A), was then calculated using Equation 4-1.

$$N_A = \frac{M^2}{A}(N_{Inside} + 0.5N_{Intercepted} + 1) \qquad 4\text{-}1$$

Where

M is the magnification, A is the test area in mm^2, N_A is the number of grains per square millimetre, $N_{(Inside)}$ is the number of grains completely inside the test area and $N_{(Intercepted)}$ is the number of grains intercepted by the edges (perimeter) of the area. The ASTM grain size number (G) was computed using Equation 4-2 [194].

$$G = 3.322 \log N_A - 2.954 \qquad 4\text{-}2$$

4.1.3.3 Scanning Electron Microscopy (SEM)

Carl Zeiss EVO MA15 Scanning electron microscopy/Energy-Dispersed X-ray (SEM/EDS) was used to characterize the as-received samples, as well as the alloyed specimens and the corroded surfaces of specimens so as to identify their morphology and elemental composition. SEM is an essential scientific instrument employed for the observation and characterization of surface morphology of solid materials. It uses a focused beam of high energy electron to generate a variety of signal such as backscattered electrons, secondary electrons, absorbed electrons, characteristic and continuum x-rays at the surface of solid materials. These signals are derived from electron-sample interactions and reveal information about the sample such as external morphology (texture), chemical composition, crystalline structure and orientation of materials within the sample. These signals are collected by the detector, amplified and displayed on the computer revealing specific information of the samples.

At the end of every experiments, the corroded samples were removed from the cell, rinsed with deionised water, dried with warm air and kept in a desiccator prior to post experimental surface analysis. SEM analysis was performed using secondary electron mode with an operating voltage of 15 kV. The Carl Zeiss EVO MA15 Scanning Electron Microscopy/Energy-Dispersed X-ray (SEM/EDS) used during this study is shown in Figure 4-4.

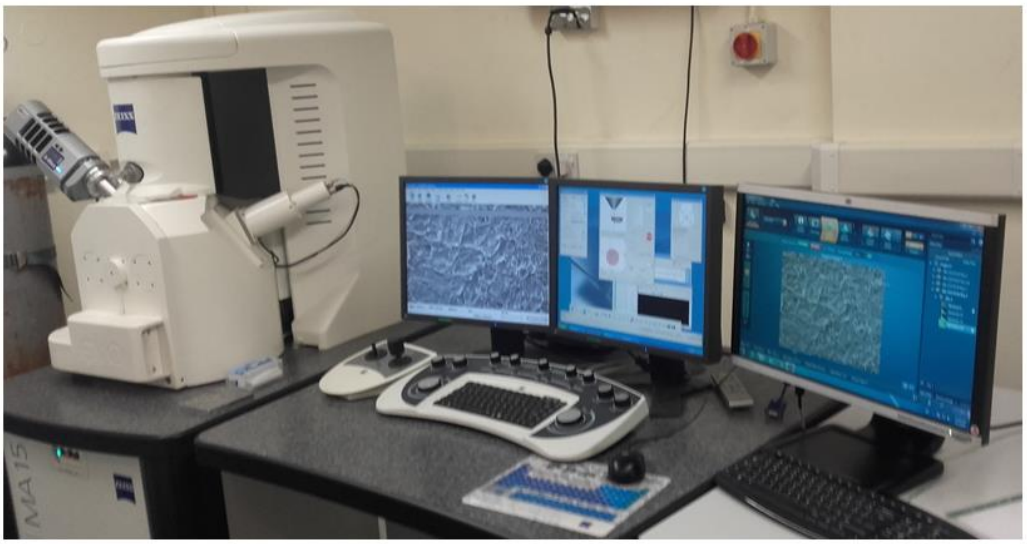

Figure 4- 4: The Carl Zeiss EVO MA15 Scanning Electron Microscopy and Energy-Dispersed X-ray (SEM/EDS)

4.1.3.4 X-ray Diffraction (XRD) analysis

X-ray diffraction (XRD) analysis is a unique technique for determining the crystallinity of a compound. It is based on the principles of constructive interference of monochromatic X-rays and a crystalline sample. In XRD analysis, a focused X-Ray beam is shot at the sample at a specific angle of incidence. The X-Rays deflect or "diffract" in various directions depending on the crystal structure (inter-atomic distances) of the sample. The locations (angles) and intensities of the diffracted X-rays are then measured. If the interaction between the incident X-rays and the sample satisfy Bragg's law ($n\lambda=2d \sin \theta$), then constructive interference is produced. Where, λ is the wavelength of the X-ray, θ is the scattering angle, d is the interatomic (lattice) spacing and n is an integer representing the order of the diffraction peak. This occurs when the angle of incidence equals the angle of scattering and the path length difference is equal to an integer number of wavelengths. The XRD analysis of the micro-alloyed steels was conducted using the Philip X'pert. Data were recorded for the 2θ range of 20 to 80 degrees with a step size of 0.05 degree, resulting to a scan time of 26 minutes. The picture of the Philips X'pert X-ray diffractometer used in this study is shown in Figure 4-5.

Figure 4- 5: Philips X'pert X-ray diffractometer was used in this study for XRD analysis

4.1.3.5 White Light Interferometry

Interferometer is an optical device that divides a beam of monochromatic light exiting a single source (like a laser or LED) into two beams and then recombines them to create an interference pattern. The combined pattern can be analyzed to determine the difference in paths the two beams travelled [195]. This makes white light interferometry an extremely powerful tool for optical measurements. It combines the old white light interferometry techniques with modern electronics, computers, and software to produced extremely powerful measurement tools. White light interferometry is a non-contact optical technique that is insensitive to material type and is designed to measure surface height on 3-D structures with surface profiles of varying sizes and shapes without damaging the sample.

NPFLEX 3D interferometer was used in this work to assess the extent of pitting on the specimens after 24 hours of potentiostatic polarization. NPFLEX 3D interferometer is an optical metrology system built to handle nano- to macro-features effortlessly on samples of widely varying shapes and sizes. It uses non-contact techniques, open-access sample loading, and intuitive analysis software to characterize surface texture, finish, roughness, curvature, slope, and numerous other features with sub-micron resolution. The identified pits on surface of the specimens that were potentiostatic polarized for 24 hours were characterized on top-ten average (for deepest pits) pits using multiple region analysis tool of the white light interferometer. Figure 4-6 shows the NPFLEX 3D interferometer used in this work.

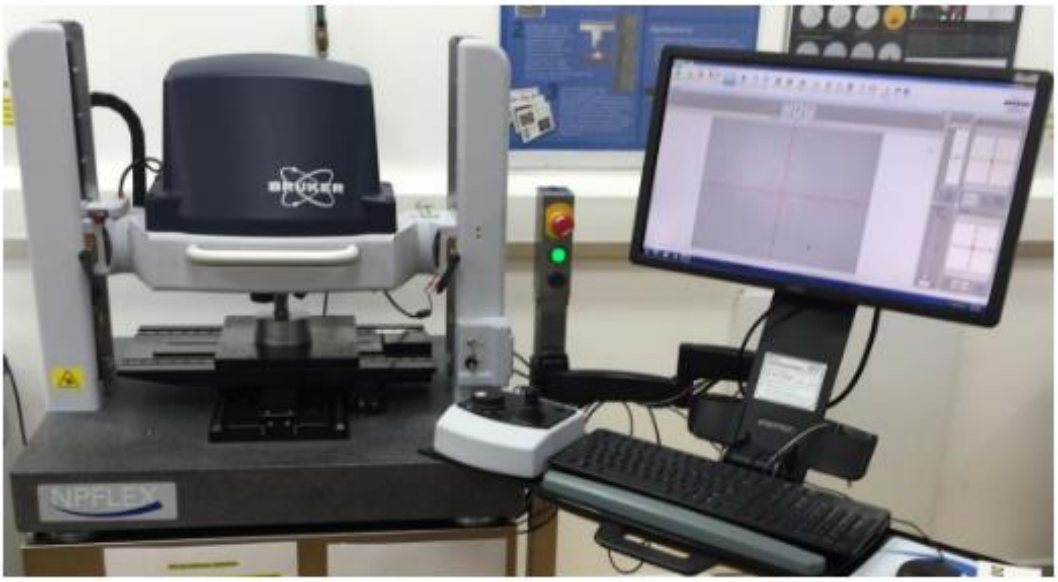

Figure 4- 6: NPFLEX 3D interferometer

The NPFLEX 3D interferometer is an excellent spectroscopy instrument with an outstanding measurement capabilities such as;

i. Extremely precise and accurate non-contact 3D surface measurements of extra-large samples with challenging angles
ii. Ability to accommodate samples of different sizes and shapes due to its open bridge design and robust stage.
iii. Measurement capability can be extended to large areas by automatically switching overlapping scans using software.
iv. Fast, repeatable and easy measurements
v. Yield accuracy in the nanometer range for rough and stepped surfaces but sub-nanometer resolution for super-smooth polished surfaces.

4.2 Corrosion Tests

Corrosion experiments were conducted in this work to assess and compare the corrosion properties of micro-alloy steels. Weight loss measurements were first conducted for initial assessment of the corrosion behaviour of the micro-alloy steel in aerated 3.5 wt% NaCl solution at ambient temperature and atmospheric pressure. Four different electrochemical techniques were performed using the conventional three electrode experimental set-ups. These experiments were conducted using two types of corrosion cells namely the EG&G Princeton applied research model K0235 flat cell and 1 litre beaker cell. The mechanism and operating principles of these corrosion cells are highlighted in Section 4.2.3.1. Corrosion experiments were performed in three different simulated oilfield conditions (media) which include aerated/deaerated solutions, CO_2 saturated brine and aerated/CO_2 saturated simulated formation water. All experiments were conducted 2 – 3 times to ensure repeatability and reproducibility. The experimental procedures for all these techniques and environmental conditions are briefly explained in this sections.

4.2.1 Weight Loss

The corrosion rates of the steels were assessed by weight loss technique. The tests were performed according to ASTM G31 - 72 standard [196]. This standard recommends a minimum ratio of test solution volume to test specimen surface area of 0.20 ml/mm^2 in order to avoid any appreciable change in the corrosiveness of the test solutions. The specimens were wet grinded up to 1200 silicon carbide grit paper, washed with distilled

water, ultrasonically cleaned in acetone for 4 minutes and dried in warm air. This was followed by careful measurements of the surface dimensions with which the surface area of the specimens were computed. The specimens were weighed using Adam PW124 analytical precision weighing balance with 4 digits decimal places and the weight recorded as W_1. Three of each of the specimens were prepared. The specimens were hung inside a beaker containing 3.5 wt% NaCl at ambient temperature. One of the specimens was removed from the beaker after 24, 48 and 72 hours respectively. The corrosion products formed on the surface of the specimens were chemically cleaned in specific solution (500 mL of HCl + 450 mL of deionized water + 5 g of hexamethylenetetramine) with vigorous stirring for 10 minutes, rinsed with distilled water, dried in warm air and reweighed (W_2). The weight loss of the samples due to immersion for the respective time was then calculated as ($W_1 - W_2$) while the corrosion rate was computed using Equation 4-3. The tests were repeated 2 – 3 times to ensure reproducibility.

$$\mathrm{CR} = \frac{8.76 * 10^4 * (W_1 - W_2)}{\rho \mathrm{At}} \qquad 4\text{-}3$$

Where: CR = Corrosion rate (mm/Y)

ρ = density (g/cm^3),

A = Surface are of the sample (cm^2) and

t = immersion time (hours).

4.2.2 Electrochemical Corrosion Techniques

Four different electrochemical corrosion measurement techniques whose principles and operation procedures were briefly explained in section 2.4.2 were used during the course of this work. These techniques include linear polarization resistance (LPR), Tafel plots, electrochemical impedance spectroscopy (EIS) and potentiostatic polarization techniques. Before the electrochemical measurements were conducted, Stern-Geary constant was calculated for each of the specimen using Tafel polarization techniques. This was achieved by immersing the specimen in 3.5 wt% NaCl for 3 hours for the open circuit potential (OCP) to stabilized and polarised at the rate of 0.5 mV/sec within the scan range of ±250 mV versus OCP. The choice of 3 hours immersion time was to ensure that polarization was conducted when the surface of the specimen is within the active state. This was to avoid changes in the electrochemical corrosion process at the sample-electrolyte interface which may occur due to the evolution of corrosion product with

longer immersion time. Tafel constants (β_a and β_c) were estimated using Tafel extrapolation method as explained in Section 4.2.2.1. The Stern-Geary constant was calculated for each sample using Equation 2.29 and it varied between 16 - 21 mV/decade depending on the specimen. However, since this work was based on comparative assessments and to ensure uniformity of the experimental parameters, 26 mV/decade was adopted as Stern-Geary constant for all the experiments.

Each of the electrochemical corrosion measurement was preceded with sample preparation during which one face of the specimens was soldered with insulated copper wires before enclosing with non-conductive resin. The resin covered all the surfaces of the specimen leaving only the working surface as the electrodes exposed to the elctrolyte. The non-conductive resin also helped in handling the specimen during grinding and polishing. Grinding conducted as specified in Section 4.1.2.3 was achieved using silicon carbide (SiC) grit paper. After grinding, the specimens were rinsed with distilled water, degreased with methanol, dried in warm air and immediately immersed in the electrolyte for electrochemical experiments.

4.2.2.1 Tafel measurement

Tafel results were obtained by polarizing the steels at the rate of 0.5 mV/cm^2 within a scan range of ±250 mV about OCP after sufficient time (3 hours) was allowed for stabilization of OCP. The anodic and cathodic branches were performed separately starting with the cathodic scan, followed by 15 minutes monitoring to stabilize the OCP before the anodic sweep. This was to avoid surface alteration and electrolyte contamination as a result of dissolution of iron during anodic sweep [137, 140]. The anodic (positive polarization) and cathodic (negative polarization) branches of Tafel plots were presented in a Potential versus Log current density plot. The linear portions of the anodic and cathodic Tafel branch were extrapolated to intersect at a potential and current density corresponding to corrosion potential (E_{corr}) and corrosion current density (i_{corr}) respectively. The corrosion current density (i_{corr}) was used to calculate the corrosion rate of the specimens using Equation 2-30. The slope of the straight line portion of Tafel branches were estimated using ASTM G 102 – 89 (reapproved 1999) Standard [95] and the methods outlined by Tait [94]. These slopes on the anodic and cathodic curve represent the anodic (β_a) and cathodic (β_c) Tafel constants respectively. Tafel polarization technique provided very useful corrosion parameters such as anodic constant

(β_a), cathodic constants (β_c), corrosion current density (i_{Corr}) and corrosion potential (E_{Corr}). The Tafel constants and the corrosion current density were used with Stern-Geary equation (Equations 2-28 and 2-29) to calculate the polarization resistance (R_p). On the other hand, the corrosion current density (i_{Corr}) in conjunction with Faraday's Law as shown in Equation 2-30 were used to estimate the corrosion rates.

$$i_{Corr} = \frac{\beta_A * \beta_C}{2.303\,(\beta_A + \beta_C)} * \frac{1}{R_P} = \frac{B}{R_P} \qquad 2\text{-}28$$

$$B = \frac{\beta_A * \beta_C}{2.303 * (\beta_A + \beta_C)} \qquad 2\text{-}29$$

$$C_R\ (mm/Y) = \frac{3.27 * 10^{-3} * i_{Corr} * (E.W)}{\rho} \qquad 2\text{-}30$$

The descriptions and units of the symbols are given in Sections 2.2.4.1 and 2.2.4.2

4.2.2.2 Linear Polarization Resistance (LPR)

This is a non-destructive DC measurement technique and was conducted repeatedly on the test samples to monitor long term corrosion performance. LPR measurement was programmed to alternate the working electrode potential with polarization by scanning the samples at the rate of 0.25mV/sec and within a sweep range of ±15 mV vs OCP after monitoring the corrosion potential for 13 minutes.

4.2.2.3 Potentiostatic polarization measurement

Potentiostatic polarization measurement was used to form corrosion product films on the surface of the specimens. The stability of the films was subsequently investigated using AC impedance measurements. The corrosion films were formed using two procedures:

(a) Constant time (24 hours) at different formation potentials (100 $mV_{Ag/AgCl}$, 150 $mV_{Ag/AgCl}$ and 200 $mV_{Ag/AgCl}$). This was aimed at investigating the effect of applied potentials on the stability of corrosion product layer.

(b) Constant formation potential (150 $mV_{Ag/AgCl}$) applied at different times (1, 2, 4, 8, 12, 24 hours respectively). This was aimed at investigating the effect of time on the stability of corrosion product layer.

4.2.2.4 Electrochemical impedance spectroscopy (EIS) measurement

EIS measurement was used in conjunction with linear polarization resistance and potentiostatic polarization to mainly assess the electrochemical behaviour of the corrosion

product layer formed on the surface of the specimens. All the EIS tests were conducted with potential perturbation of 5 $mV_{Ag/AgCl}$ and at a frequency range of 100 KHz to 0.1 Hz.

All the DC polarization measurements were performed using Solartron analytical Model SI 1287 electrochemical interface analyser equipped with CorrWare for data acquisition and CorrView for data interpretation. On the other hand, Solartron analytical Model SI 1260 impedance/gain-phase analyser equipped with ZPlot for data acquisition and ZView for data analysis based on equivalent circuit methods was used for all the AC impedance experiments.

4.2.3 Experimental Set up for this study

All the experimental set ups were based on the conventional three-electrode system consisting of the working electrode (specimen), platinum mesh/wire as counter electrode and the reference electrode comprising of Ag/AgCl saturated with KCl. The simulated oilfield environments (electrolytes) were made from analytical chemical reagents bubbled with three different gases to deaerate and or saturate the environment in two different types of corrosion cells.

4.2.3.1 Electrochemical corrosion cells.

Two types of corrosion cells were used. These include:

i) **EG&G princeton applied research model K0235 flat cell**. This was used for short time (6 hours) initial preliminary investigation of the corrosion susceptibility of the micro-alloyed steels in aerated and deaerated 3.5 wt% NaCl solutions. The cell consists of a Pyrex glass cylinder clamped horizontally between two polypropylene end plates. One end of the plate housed the working electrode, and the other end housed the platinum wire mesh counter electrode of 2.54 cm x 2.54 cm. This provided a high surface area of 6.45 cm^2. The silver-silver chloride (Ag/AgCl) reference electrode was housed in a Luggin well with a fixed polytetrafluoroethylene (PTFE) Teflon Luggin capillary (TLC) protruding from the bottom of the well. A PTFE gasket exposed a 1-cm^2 area of working electrode to the electrolyte in the cell. The cell has a volume of 250 mL. The Model K0235 flat cell used in this work is shown in Figure 4-7.

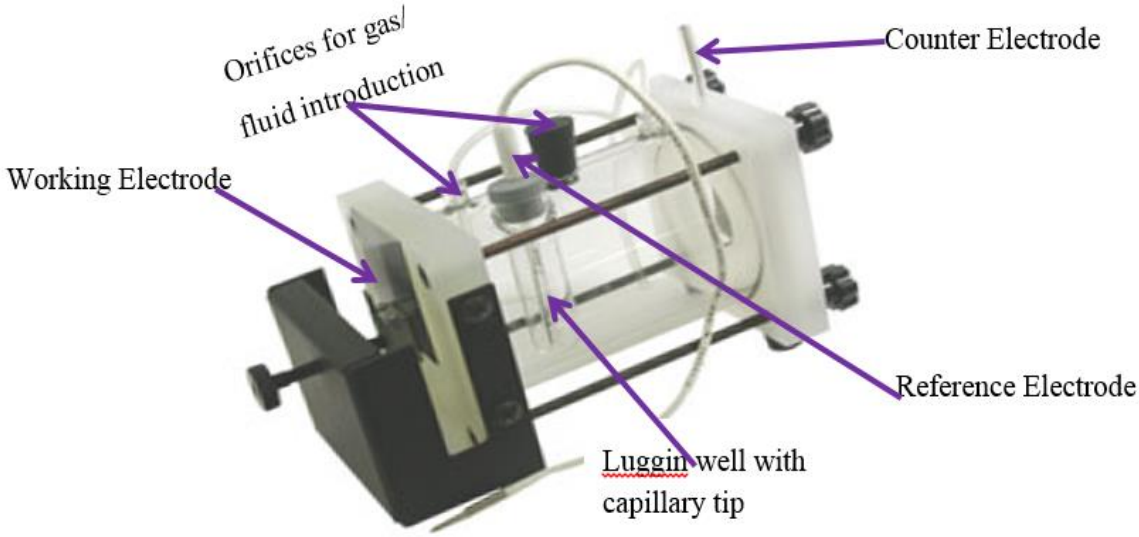

Figure 4- 7: Model K0235 Flat Cell

ii) **1 litre beaker cell**. This was used for long time (minimum of 24 and 96 hours) investigation of the corrosion behaviour of the steels in different simulated oilfield environments. This cell is a 1000 mL glass beaker with a polytetrafluoroethylene (PTFE) cover (lid). Slots were provided on the lid for inserting some of the components of the cell such as working electrode (specimen), temperature probe, bubbling of gases (CO_2 and/or N_2), counter and reference electrodes. Figure 4-8 shows the image of a glass beaker cell mounted on a hotplate. A feedback from thermocouple enabled temperature control of the hotplate during the experiments. With the help of a magnetic stirrer, the hotplate was also used for stirring for stirring the electrolyte so as to ensure concentration homogeneity within the bulk electrolyte in the cell.

4.2.3.2 Gases

Three types of gasses namely 100% Nitrogen gas (N_2), 0.5% CO_2 (5000 ppm in N_2) and 99.98% CO_2 were used in this work. These gases were used to de-oxygenate and/or saturate the electrolyte with CO_2 depending on the specific aim of the experiment. In CO_2 saturated corrosion system, only very small fraction (0.2% to 1%) of dissolved CO_2 hydrates to form carbonic acid which is the precursor for CO_2 corrosion attack [69]. Therefore, the use of 0.5% CO_2 (5000 ppm in N_2) was to investigate the effect of lower concentration of CO_2 gas during CO_2 corrosion. The gases were first dried with silica crystal contained in a dreschel bottle and bubbled into the corrosion cell through a flowmeter which was used to regulate the flowrate (at 250 cm^3/mins) of the gases into the cell during experiments. Figure 4-9 shows a sketch of experimental set-up.

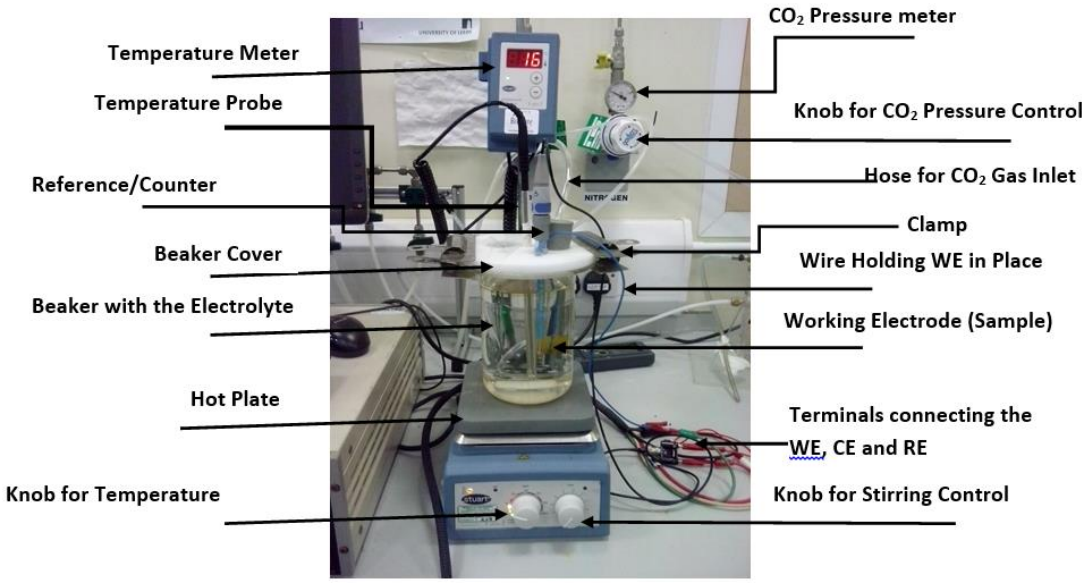

Figure 4- 8: Bubble (Glass) setup

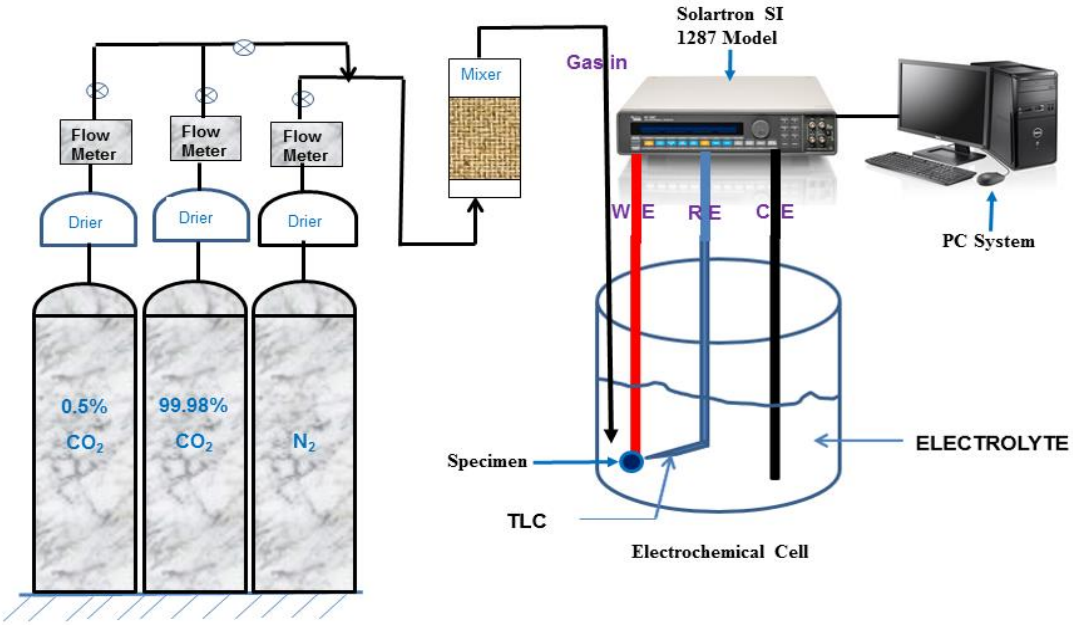

Figure 4- 9: A schematic diagram of the corrosion experimental set up

4.2.4 Electrochemical corrosion tests

Depending on the experimental conditions/electrolytes and the corrosion cell used, three different procedures were employed to investigate the corrosion performance of the proprietary micro-alloy steels. These procedures are explained in the next three sub-sections:

4.2.4.1 Different concentration of aerated and de-aerated 3.5 wt% NaCl solutions

Preliminary short time corrosion experiments were aimed at initial comparison of the corrosion propensity of the micro-alloy steels in different concentration of aerated and/or deaerated 3.5 wt% NaCl solution.

Table 4- 4: Experimental setups and corrosion conditions

Description of Items	Parameters
Electrode (Working) Materials	F65, X65, P110 IC and TN95 HS
Counter Electrode	Platinum Wire Mesh
Reference Electrode	Silver/Silver Chloride (Ag/AgCl)
Working Electrode Surface Area (cm^2)	1
Electrolytes NaCl (wt%)	1, 3.5, and 10
Corrosion Cell	EG&G Princeton applied research model K0235 flat cell
Electrolyte Volume per test (mL)	250
Electrolyte Environmental Conditions	Aerated and De-aerated
Test Pressure (bar)	1
Temperature (^{0}C)	Ambient
Solution pH	Unbuffered
Test Period for LPR (hours)	6
Potentiostat	Solartron Analytical SI 1287 Electrochemical Interface
Analytical Softwares	CoreWare and CoreView
Electrochemical Measurements	**Potentiodynamic Polarization (LPR, Tafel Plot)**
LPR Sweep Range vs OCP (mV)	± 15
LPR Sweep Rate (mV/s)	0.25
Tafel Plot Scan Range (mV)	± 250
Tafel Plot Scan Rate (mV/s)	0.5

The aerated experiments were performed by equilibrating the electrolyte with oxygen in open air (with all the orifices of the flat cell opened) without gas bubbling. On the other hand, N_2 gas was bubbled for 1 hour to de-oxygenate the solution before inserting the specimens for measurements in de-aerated electrolyte. Purging of nitrogen gas was maintained throughout the 6 hours duration of the test.

Linear Polarization Resistance (LPR) and Tafel polarization were used to assess the corrosion behaviour of the steels in these media. LPR was performed for 6 hours by polarizing the steel at a scan rate of 0.25 mV/s and a scan range of ± 15 $mV_{Ag/AgCl}$. A duration of 13 minutes was allowed to stabilize the potential before each LPR scan at the open circuit potential (OCP). Tafel polarization experiments were conducted at a scan rate of 0.5 mV/s and a sweep range of ± 250 $mV_{Ag/AgCl}$. Table 4-4 shows the parameters and conditions used for the aerated and de-aerated corrosion tests.

4.2.4.2 Experiments in 3.5 wt% NaCl Solution Saturated with 0.5% CO_2.

The conventional three-electrode, (1 litre glass beaker cell) was used for all the experiments under these conditions. The ground surface of the specimens were the working electrodes; Ag/AgCl electrode (sat. KCl) was used as the reference electrode while platinum wire served as the counter electrode. The electrolyte containing 3.5 wt% NaCl was prepared from analytical grade reagent. The electrolyte was bubbled with 0.5% CO_2 for 3 hours before inserting the specimens and the purging maintained throughout the corrosion tests. Efforts were made to ensure that the working electrodes were kept as close as possible to the reference electrode and with the high conductivity of aqueous NaCl (50 mS/cm); the solution resistance was maintained at a very negligible value.

Three electrochemical techniques namely linear polarization resistance (LPR), Tafel polarization and electrochemical impedance spectroscopy (EIS) were used to compare the corrosion performance of the micro-alloy steels. The procedures and measurement parameters for these techniques were outlined in Section 4.2.2.

Two sets of experiments were performed under these conditions. These include

(i) Temperature variations (25^0C, 45^0C and 60^0C) in unbuffered solution and at atmospheric pressure

(ii) pH variations (3.5, 5 and 6.5) at 60^0C and atmospheric pressure

In temperature variation experiments, 0.5% CO_2 gas was bubbled into the electrolytes for 3 hours before polarization and purging of CO_2 continued throughout the tests. The desired temperature was maintained using a hotplate with a control thermocouple immersed into the solution. The hotplate was also set at a rotating speed of 200 rpm and with a magnetic stirrer, a homogeneous condition was maintained within the bulk electrolyte.

The pH variation experiments were conducted at constant temperature (60^0C) and atmospheric pressure (1bar) but at different pH values of 3.5, 5 and 6.5. Tables 4.5 and 4.6 show the test matrices of the experiments conducted at varying temperature (unbuffered pH) and different pH values (60^0C) respectively. Figure 4.8 and 4.9 show the setup of a 1 litre bubble (glass) cell.

Table 4- 5: Test Matrix of experiments conducted at different temperature and unbuffered pH

Conditions	Specifications
Solution pH	Unbuffered
Electrolyte (wt% NaCl)	3.5
Temperature (^{0}C)	25, 45 and 60
Solution Pressure (bar)	1
LPR Duration (hrs)	24

Table 4- 6: Test Matrix of experiments conducted at varying pH and constant temperature

Conditions	Specifications
Solution Temperature	60^0C
Electrolyte (wt% NaCl)	3.5
Solution pH	3.5, 5.0 and 6.5
Solution Pressure (bar)	1
LPR Duration (hrs)	24

4.2.4.3 Potentiostatic polarization experiments in 3.5 wt% NaCl

Potentiostatic polarization measurement was aimed at forming corrosion products on the surface of the specimen under controlled conditions. The protectiveness and/or otherwise of the corrosion films formed on the specimen were investigated using AC impedance measurements. The micro-alloy steels were prepared as detailed in Section 4.1.2 and immersed in 3.5 wt% NaCl solution. Before conducting potentiostatic polarization, the samples were cathodically polarized for 30 minutes at -800 $mV_{Ag/AgCl}$ to reduce the pristine oxide formed in air and during the immersion of samples in the test solution. The corrosion films were formed using two procedures:

(i) Variation of applied anodic potential at constant time;

Potentiostatic polarization was conducted in 3.5 wt% NaCl solution saturated with 0.5% CO_2 for 24 hours at different formation potentials of 100 mV, 150 mV and 200 mV versus OCP respectively. This was aimed at investigating the effect of applied potentials on the stability of the corrosion product layer. Three specimens of each of the steels were immersed in solution in each experiments. At the end of 24 hours anodic polarization, two of the samples were removed from the solution, rinsed with distilled water and dried in warm air. One of the sample was used for SEM analysis of the corrosion products on the surface. After the SEM surface investigation, the layers of the corrosion film were chemically removed using a specific chemical solution consisting of 500 mL of HCl, 450mL of deionized water and 5 g of urotropine (hexamethylenetetramine) prepared in accordance with American Standard of Test and Measurements (ASTM) practice standard G1-90 (reapproved 1999) [197]. The specimens were vigorously stirred in the solution for 10 minutes, cleaned in deionized water and surface dried using warm air. The surface of the cleaned specimens was examined in SEM and pits were identified. The identified pits were characterized using the white light coherence scanning interferometer. Top ten average pit depth were recorded for each test condition and repeated to obtain an average value. Pit identification was in accordance with standard procedures as stipulated in ASTM G46-94 for pitting corrosion examination and evaluation [198]. Multiple region analysis was used to obtain relevant statistics such as location and threshold of the formed pit. The scanned areas were stitched by adding a series of small data sets using the inbuilt stitching function of the interferometer.

The second specimen was used to investigate the thickness of the corrosion products on the surface of the steels with respect to the applied anodic potential. This specimen was

placed vertically, enclosed with non-conductive resin and carefully cut horizontally so as to expose the thickness of the corrosion layer. The cut surface was wet ground with silicon carbide paper down to P1200 grit and then examined with SEM. The third specimen which was left in the corrosion cell was used to assess the stability of the corrosion films using EIS. EIS was conducted immediately after potentiostatic polarization at OCP using the procedure out lined in Section 4.2.2.4 with a sinusoidal potential excitation of 5mV amplitude in the frequency range from 100 kHz to 0.1 Hz. The impedance data were fitted with Zview software using equivalent electrical circuit (EEC) model. Specimens P110 and X65 were used for the potentiostatic polarization investigation of the effect of applied potential on the stability of corrosion product films on the samples.

(ii) Variation of time with constant applied potential:

This was the second technique used to grow corrosion products on the surface of the samples and it was aimed at investigating the effect of time on the stability of the corrosion product layer formed at constant applied potential. A formation potential of 150 $mV_{Ag/AgCl}$ was applied to the micro-alloyed steels in naturally aerated 3.5 wt% NaCl solutions for 1, 2, 4, 8, 12, 24 hours respectively. Samples P110 and TN95 were used for this investatgation.

After each potentiostatic polarization, EIS was conducted immediately at OCP using the procedure out lined in Section 4.2.2.4 with a sinusoidal potential excitation of 5mV amplitude in the frequency range from 100 kHz to 0.1 Hz. The impedance data were fitted with Zview software using equivalent electrical circuit (EEC) model.

4.2.4.4 Lyman Fleming solution saturated with 0.5% CO_2.

Lyman and Fleming formula (solution) is the most frequently and widely used recipe for simulating seawater in laboratories. The composition of this formula is shown in Table 4.7 and is similar to the constituents of ASTM D1141-98 (updated 2003) [199] which is the standard practice for the preparation of substitute ocean water. Lyman and Fleming solution was prepared from analytical grade chemicals using the ratio detailed in Table 4.7. DC electrochemical measurements (LPR and Tafel polarization) using the same parameters as in Section 4.2.2 were conducted under naturally aerated and 0.5 % (5000 ppm) CO_2 saturated Lyman and Flaming solutions at pH 6.5, ambient temperature and atmospheric pressure. For the naturally aerated conditions, experiments were conducted

in 1 litre beaker cell with all the orifices (slots) uncovered. This permits the ingress of air (oxygen) into the corrosion cell. For the CO_2 saturated conditions, 0.5% CO_2 gas was bubbled into the electrolytes for 3 hours before polarization and purging of CO_2 was maintained throughout the tests. The test matrix of the experiments conducted in Lyman Fleming solutions is shown in Table 4-8.

Table 4- 7: Lyman and Fleming Composition of Seawater (SW)

S/No	Salt	Molecular weight	Concentration (g/kg)
1	Sodium Chloride (NaCl)	58.44	23.926
2	Sodium Sulphate (Na_2SO_4)	142.04	4.008
3	Sodium Bicarbonate ($NaHCO_3$)	84.00	0.196
4	Potassium Chloride (KCl)	74.56	0.677
5	Boric Acid (H_3BO_3)	61.83	0.026
6	Potassium Bromide (KBr)	119.01	0.098
7	Sodium Fluoride (NaF)	41.99	0.003
8	Calcium Chloride ($CaCl_2.2H_2O$)	147.03	1.16
9	Magnesium Chloride ($MgCl_2.6H_2O$)	203.33	5.20
10	Strontium Cloride ($SrCl_2.6H_2O$)	266.64	0.025

ASTM D1141 D 98 (2003) – From Lyman & Fleming Formula (1940) [199]

Table 4- 8: Test Matrix of experiments conducted with Lyman Fleming solutions

Conditions	Specifications
Solution Temperature	Ambient
Electrolyte conditions	Aerated and 0.5 % CO_2 saturated Lyman and Fleming solutions
Solution pH	6.5
Solution Pressure (bar)	1
LPR Duration (hrs)	24

4.3 Investigations in 99.98% (pure) CO_2

From the results of the preliminary investigations, it was established that the corrosion rate of the micro-alloyed steels can be ranked as ASTM F65 < API 5L X65 < P110 IC < TN95 SH. The corrosion rates of the specimens in the various environments were also found to be lower when compared with literature results of the same specifications. This could be linked to the low concentration (0.114 mol/l, 0.5% (5000 ppm in N_2)) of CO_2 used. Thus, the following experiments conducted in 0.5% CO_2 were repeated using higher concentration of CO_2 (99.98% CO_2):

i) Temperature variations (25^0C, 45^0C and 60^0C) in unbuffered solution and atmospheric pressure. These involved repeating the experiments explained in Section 4.2.4.2 using the matrix outlined in Table 4-5.

ii) Saturating Lyman and Flaming solution with 99.98% CO_2 at pH 6.5, ambient temperature and atmospheric pressure. The experiments conducted in Section 4.2.4.4 were repeated using the matrix outlined in Table 4-8

iii) The weight loss experiments conducted in Section 4.2.1 was also repeated. In this case however, five of each of the two worst corrosive specimens (P110 and TN95) were prepared. The electrolyte (3.5 wt% NaCl) was purged with 99.98% CO_2 for three hours before immersing the specimens and purging continued throughout the duration of the experiments. One specimen was removed at a time from the corrosion cell after 24, 48, 72, 96 and 120 hours respectively. The changes in pH of the electrolytes were also measured each day after removing of the specimen. The corrosion products formed on each specimen, after removal were chemically cleaned, reweighed and the corrosion rate calculated using Equation 4-3.

4.3.1 Assessing the propensity of the Micro-alloyed Steels to form $FeCO_3$ in 3.5 wt% NaCl solution saturated with 99.98% CO_2.

Experimental evidence [69] has shown that at temperatures above 60^0C, the precipitation of $FeCO_3$, which is the main corrosion product of CO_2 corrosion of carbon steel, is fast and the supersaturation is low resulting in the formation of dense and adherent crystalline films which often give good protection to the substrate. Therefore, the two worst case steels (P110 and TN95) were subjected to conditions that would initiate the formation of $FeCO_3$. This was to assess how easy these steels can form protective $FeCO_3$ which could in turn reduce corrosion rate. To achieve this, LPR experiment was conducted for 96

hours in 3.5 wt% NaCl solution saturated with 99.98% CO_2 at 60^0C and pH 6.5. The test matrix of the experiments aimed at assessing the propensity of the steels to form $FeCO_3$ is shown in Table 4.9

Table 4- 9: The test matrix of the experiments aimed at assessing the propensity of the steels to form $FeCO_3$

Conditions	Specifications
Solution Temperature	60^0C
Electrolyte conditions	3.5 wt% NaCl solutions saturated with 99.98% CO_2
Solution pH	6.5
Solution Pressure (bar)	1
LPR Duration (hrs)	96

4.4 Alloying of micro-alloyed steels with Zr and Hf.

The results of the preliminary investigations showed that the micro-alloyed steels exhibited a ranking corrosion rate of ASTM F65 < API 5L X65 < P110 IC < TN95 SH. This means that P110 IC and TN95 SH recorded the extreme corrosion rates. These two steels were then alloyed with Zr and Hf with a view to improving their corrosion resistance.

4.4.1 Weight of added alloying elements (Zr and Hf)

Three of each steel (P110 IC and TN95 SH) were weighed using Adam PW124 analytical precision weighing balance with 4 digits decimal places and the weight recorded in Table 4-10. Each of the three P110 and TN95 were alloyed with (0.1 wt%, 0.2 wt% and 0.4 wt%) Zr and Hf of the samples respectively. The exact weight (g) of the elements corresponding to these wt% were calculated using charge calculation formula expressed in Equation 4-4

$$\text{Amount to be Added (g)} = \frac{(\text{Required Amount} - \text{Amount Present}) * \text{Total Weigth}}{\text{Purity of Alloying Element}} \qquad 4\text{-}4$$

Where:

Required amount is the wt% of element (Zr or Hf) to be added.

Amount present is the wt% of the element already existing in the steel samples as listed in Table 4-3

Total weight is the weight (in grams) of the steel sample as listed in Table 4-10.

Purity of the alloying elements: Zr = 99.2% and Hf = 97.0%

Using Equation 4-4, the required parameters of alloy steel P110 IC with 0.1 wt% Zr were calculated as follows:

wt% of Zr required = 0.1

wt% of Zr present in Steel P110 IC = 0.002

Weight (g) of P110 IC (P_1) = 11.811

Purity (%) of Zr = 99.2.

Substituting these parameters into Equation 4-4

$$\text{Amount of Zr to be added} = \frac{(0.1 - 0.002) * 11.811}{99.2} = 0.0116$$

This method was used to calculate the quantity of Zr and/or Hf (see column 3 of Table 4-10) that were added to produce each alloy.

Table 4- 10: Alloying specifications

Sample	Sample Weight (g)	Element Added (g)	Element Added (%)	Total weight (g)	After Arc Melting (g)	After AFTech (g)
T_1-Hf_1	21.456	0.038	0.13	21.494	21.472	21.471
T_2-Hf_2	23.814	0.085	0.23	23.899	23.848	23.843
T_3-Hf_3	22.8	0.168	0.43	22.968	22.945	22.936
P_1-Hf_1	11.55	0.021	0.12	11.571	11.527	11.527
P_2-Hf_2	11.624	0.043	0.23	11.667	11.616	11.610
P_3-Hf_3	12.027	0.088	0.43	12.115	12.090	12.078
T_1-Zr_1	22.267	0.024	0.11	22.291	22.271	22.233
T_2-Zr_2	22.538	0.043	0.21	22.581	22.558	22.555
T_3-Zr_3	22.8	0.083	0.36	22.883	22.859	22.853
P_1-Zr_1	11.811	0.0113	0.11	11.822	11.807	11.067
P_2-Zr_2	11.504	0.0214	0.19	11.525	11.507	11.501
P_3-Zr_3	11.275	0.04	0.41	11.315	11.297	11.287

4.4.2 Alloying of samples

The samples were alloyed at the Process Laboratory of Materials Science and Metallurgy Department, Cambridge University, UK. Buhler Arc Melter (AM with Vario 800) shown in Figure 4-10 was used for melting of the specimens. A stable and reliable arc ignition was achieved with the help of an arc melting power supply also shown in Figure 4-10.

Figure 4- 10: Buhler arc melter (AM with avrio 800) and power supply

The melter is equipped with water-cooled high vacuum chamber with a double walled, water cooled stainless steel container consisting of the following:

- Tungsten electrode with tilting and adjustable facilities for multiple cavity melting.
- Water cooled pure copper crucible base plate with multiple cavities of different geometry.
- A built in mechanical manipulator for tilting and rotating the specimens when re-melting is needed without breaking the vacuum
- A tinted observation window for monitoring the melting process during arcing.

Figure 4-11 shows the copper crucible base plate with mould cavities, tungsten electrode and mechanical manipulator.

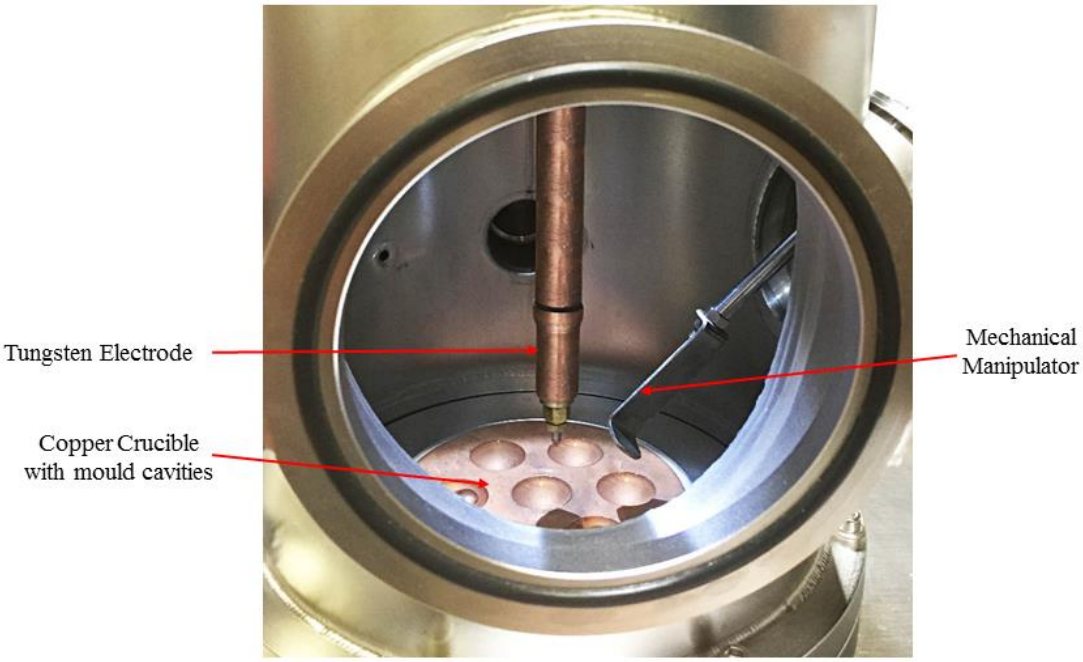

Figure 4- 11: Inside the vacuum chamber showing the copper crucible base plate with mould cavities, tungsten electrode and mechanical manipulator.

The procedures used to melt and alloy the samples with Zr and Hf are summaries below:

1. The water was turned on for 5 minutes to ensure complete circulation.
2. Open the chamber and place the samples in a suitable cavity on the copper hearth plate.
3. The Zr wire was placed on the copper plate while the steel sample was placed on top of the Zr wire. This was to prevent the Zr wire from being dispersed or blown off during arcing.
4. The furnace chamber was closed and the argon cylinder regulator set to 50 psi.
5. The chamber vacuum valve was opened to evacuate the chamber until the gauge indicates 2^{-3} mbar.
6. The Chamber was backfilled with argon by pressing the backfill valve until the vacuum gauge indicated 20 inches Hg
7. The Arc-Melter safety control box interlock system was switched on and checked to ensure that all indicators (temperatures, pressures, water flow etc) showed green light.
8. The current control knob was set at 100 Amps.

9. The electrode height control was used to position the electrode 2 mm above the hearth plate but away from the sample with the manipulation arm fully retracted.
10. The electrode was moved over the charge material maintaining a steady arc of approximately 20 – 25 mm in length using the arc control handle.
11. When the melt was completed, the viewing window was opened and the ingot/melted sample turned over using the manipulator arm. Figure 4-11 is the melter chamber showing the copper crucible, the tungsten electrode and mechanical manipulator.
12. Steps 5 to 11 were repeated 3 – 4 times 'stirring' the molten metal with the electrode in order to achieve ingot homogeneity (ie the Zr wire was properly distributed within the matrix of the steel sample).
13. The melter was turned off and allowed to cool by maintaining flow of cooling water.
14. The alloyed samples were then removed for analysis.

To further ensure that Zr and Hf were uniformly distributed within the samples thereby avoiding segregation of the alloying elements along the grain boundaries, the alloyed specimens were heat treated (homogenised) at the Process Laboratory of the Department of Materials Science and Metallurgy, Cambridge University, UK using AFTech graphite vacuum furnace. This (vacuum) furnace ensured the absence of air or other gasses thus preventing oxidation from other contamination sources and also guarantee that heat is not lost through convention. However, during the homogenization of the samples, the furnace was backfilled with argon gas thus creating an inert atmosphere that is free of oxidation and contamination. Homogenization was conducted by heating the samples to 950^0C, held at this temperature for 2 hours and then allowed to cool. This allowed appreciable time for diffusion of atoms of the alloying elements (Zr and Hf) within the matrix of the steel samples to attain equilibrium distribution.

4.4.3 Microstructural, chemical and mechanical properties of the alloyed samples

Before assessing the corrosion propensity, the alloyed samples were characterized using the same parameters and procedures outlined in Section 4.1.3. The microstructural images of the alloyed samples were captured by Zeiss AxioCam MRc 5 Optical Microscopy (OM), the imaging and identification of the elemental compositions were performed using Carl Zeiss EVO MA15 scanning electron microscopy/energy-dispersed X-ray

(SEM/EDS), the structural components and phases were verified by the XRD Philips X'Pert diffractometer while the hardness of the alloyed steels were measured using Wilson Vickers Hardness Tester 452 SVD and the grain size analysis was calculated using ImageJ software and Jeffries Planimetric methods.

4.4.4 Electrochemical Behaviour of the alloyed samples

The corrosion propensity of steels P110 IC and TH95 HS alloyed with different weight percent of Zr and Hf respectively were investigated in simulated produced water (using Lyman Fleming formula) saturated with 99.98% CO_2 at pH 6.5, 25^0C and for 24 hours. The choice of simulated produced water was to simulate natural sea/marine environment. The test matrix shown in Table 4-8 and the procedures outlined in Section 4.2.4.4 were used. This was aimed at assessing the effects of Zr and Hf on the corrosion behaviour of the alloyed specimens and unalloyed specimens in the same conditions (simulated produced water).

Chapter 5: Results

5.1 Preliminary investigations of the effects of environmental and materials parameters on the corrosion behaviour of micro-alloy steels.

Carbon steel because of its inherent properties such as low cost, easy to shaping, forming and machining, good weldability, availability, its properties have been studied in depth and are well understood; good mechanical properties and ability to form protective corrosion products that cover the surface of steel, has found significant used as materials for exploration, production and transportation in the oil and gas industry [3, 4]. However, the susceptibility of carbon steel to the corrosive oilfield environments is a great drawback in terms of alleviating the cost of corrosion of oilfield facilities. Yet carbon steel remains and shall in the next predictable future the most economical materials for oilfield structures [37]. Therefore, extensive research on how to improve the corrosion resistance of carbon steel has been ongoing for over 6 decays. Micro-alloy steel is an improved carbon steels produced by adding micro quantity of alloying elements to impact excellent combination of properties to carbon steel [26]. Thus in this work, different corrosion assessment techniques such as weight loss (WL), linear polarization resistance (LPR), Tafel polarization, potentiostatic polarization, electrochemical impedance spectroscopy (EIS) and surface analysis techniques such as scanning electron microscopy/energy dispersion X-ray spectroscopy (SEM/EDXS), X-ray diffraction (XRD) and interfilometry techniques were used to evaluate the corrosion propensity of commercially supplied proprietary micro-alloyed steels in different oilfield simulated environments. The results of these assessments are presented in this chapter.

5.1.1 Characterization and identification of the as-supplied samples

Three commercially supplied micro-alloy steels and X65 carbon steel were characterized using different surface analysis techniques in order to identify their chemical composition, structures and properties. The representative of the Optical and SEM micrographs of the as-supplied samples are presented in Figures 5-1 and 5-2 respectively. These figures show that the samples have different microstructures which can be attributed to the chemical composition and thermo-mechanical treatment applied during manufacturing processes [12, 52, 185]. However, a closer observation of Figure 5-2 revealed that steels X65, F65 and P110 have light and dark zones which are colonies of pearlite in ferrite matrix [185]. These Ferrite and pearlite phases consist of grains whose

sizes, shapes and distributions are relatively uniform within each specimen but differ among specimens. This can vividly be observed from the backscattering images inserted in Figure 5-2.

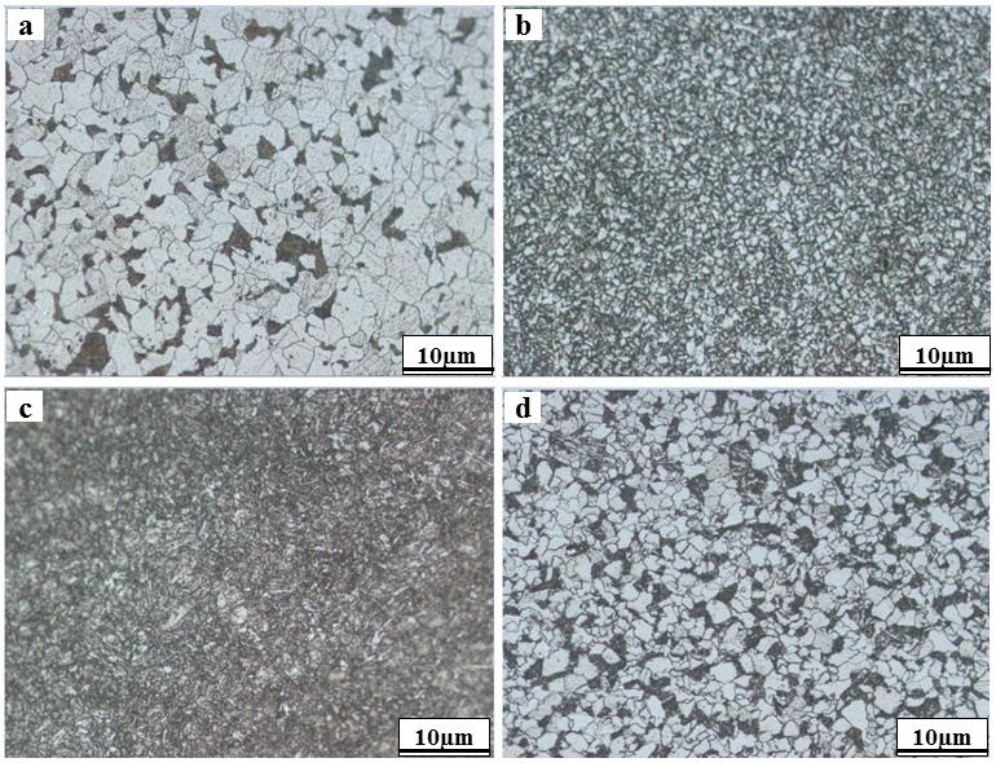

Figure 5- 1: Optical Micrographs of as-received samples (a) F65, (b) P110, (c) TN95 and (d) X65

The grain size numbers of the samples calculated according to ASTM E112-12 Standard test methods for determining average grain size [194] are shown in Table 5.1. This table shows that the grain sizes of the three samples with ferrite-pearlite microstructure can be ranked as P110 < X65 < F65. This ranking format also sufficed for ferrite (dark)-pearlite (light) volume ratio. Increase in ASTM grain size number signifies a decrease in (actual) grain size [54, 194].

Table 5- 1: ASTM Grain Size number and Ferrite/Pearlite Ratio (%) for the samples

Samples	F56	X65	P110	TN95
ASTM Grain Size No	3.89	4.5	5.57	5.77
Ferrite/Pearlite (%)	63.61	57.48	48.23	
Average Grain Size (µm)	68.54	63.5	53.4	44.9

The optical and SEM micrographs of TN95 shown in Figures 5-1 (c) and 5-2 (c) respectively revealed bainitic structure with some acicular ferrites evenly distributed within the structure [122]. TN95 as shown in Table 4-2 contains 0.99 wt% Cr and 0.46

wt% Mo. This elements because of their sluggish diffusion process retard the decomposition of martensite and/or austenite into ferrites and carbides [13, 23]. This must have necessitated the formation of bainitic structure.

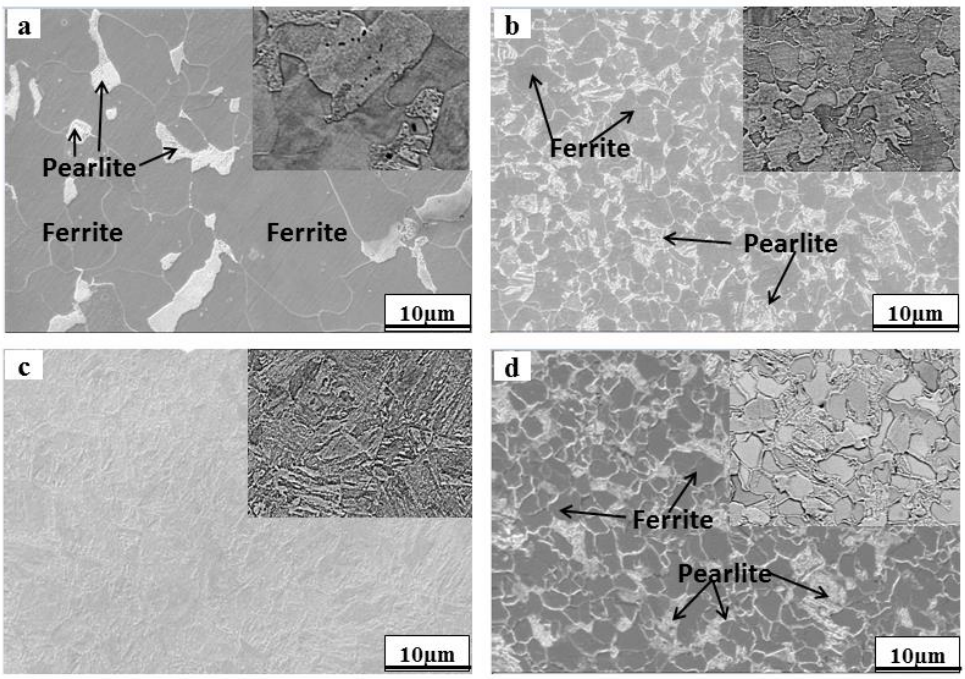

Figure 5- 2: SEM micrographs of as-received samples with backscattering image overlaid (a) F65, (b) P110, (c) TN95 and (d) X65

The EDS analysis of all the as-received micro-alloy steels showed Fe and C as the major elements with traces of other elements such as Mn, Cr, Si, V, etc as displayed in Figure 5-3 for steel P110. This was corroborated by XRD analyses patterns which also revealed only iron peaks at 2θ values of 44.59, 64.98, and 82.30 degrees corresponding to (110), (200), and (211) planes of iron. The XRD spectrum for steel P110 is shown in Figure 5-4 as an example while the entire diffractometer data for steel P110 are tabulated in Table 5-2.

Table 5- 2: Diffractometer data of steel P110 for the diffraction peaks of α-iron metallic

2θ intense peak (^{0})	Intensity (CPS)	d-spacing (Å)	Miller Indices (h k l)
44.5859	904.58	2.0323	110
64.9805	106.01	1.43522	200
82.2971	225.91	1.17161	211

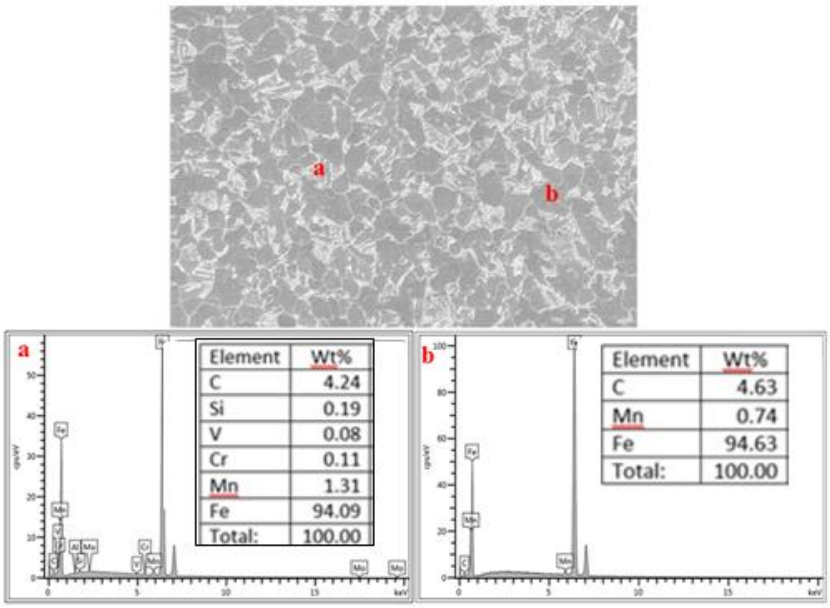

Figure 5- 3: EDS spectra of as-received steel P110 with elemental compositions at points 'a' and 'b' insert

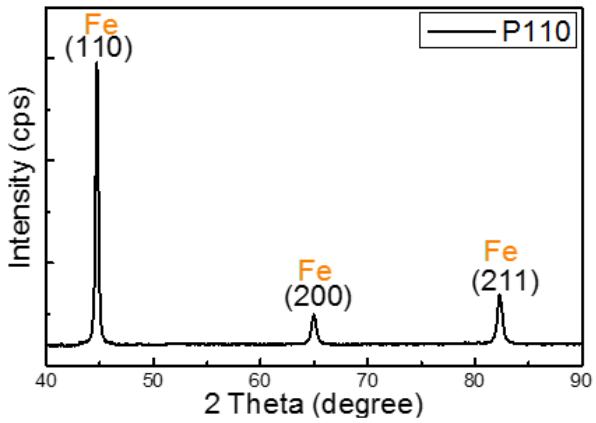

Figure 5- 4: XRD pattern of as-received steel P110 revealing only Fe peaks

5.1.2 Weight Loss in naturally aerated 3.5 wt% NaCl

Weight loss was used for initial assessment of the corrosion behaviour of the specimens in naturally aerated 3.5 wt% NaCl solution at ambient temperature and atmospheric pressure. The results of the experiments are shown in Figure 5-5. This figure revealed that there was an initial high corrosion attack (0.075 – 0.085 mm/Y depending on the specimen) during the first 24 hours of immersion. This was followed by a sharp decrease in corrosion rate within the first 48 hours of immersion but exhibited a mild or almost stable decrease in corrosion attack between the second day (48 hours) and the third day (72 hours). This figure also shows that the weight loss (WL) of the steels can be ranked as $WL_{F65} < WL_{X65} < WL_{P110} < WL_{TN95}$. This difference in weight loss can be attributed to difference in microstructure and chemical composition of the micro-alloy steels. The

weight loss results showed that the corrosion rate of the steels with ferrite-pearlite microstructures is lower than the steel with bainitic structure [185, 200].

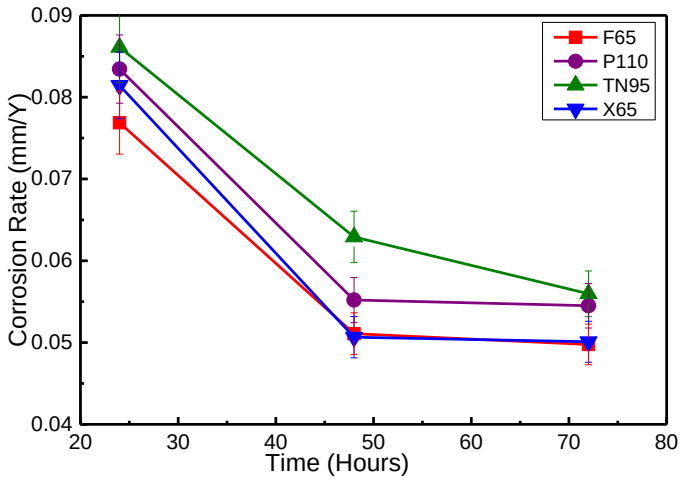

Figure 5- 5: Corrosion rate by weight loss of specimens in 3.5 wt% NaCl at ambient temperature

5.1.3 Effect of NaCl concentrations on the corrosion behaviour of micro alloy steels in aerated and de-aerated environment

Electrochemical corrosion behaviour of the specimens was investigated using linear polarization resistance (LPR) and Tafel extrapolation techniques. LPR was performed for 6 hours at a scan rate of 0.25 mV/sec and a sweep range of ±15 mV versus OCP. The anodic and cathodic Tafel branches were obtained separately at a sweep rate of 0.5 mV/sec and an effective scan range of ±250mV versus OCP. EG&G princeton applied research model K0235 flat cell and Solartron analytical SI 1287 electrochemical interface were used for all the experiments in this section. The electrolytes consist of three (1.0, 3.5 and 10.0 wt%) different concentrations of NaCl solutions. A complete experimental parameters and conditions for these investigations are listed in Table 4-4. The ohmic drop of the experimental setup was calculated and found to be very small and so was neglected in all the experiments conducted in this work. The value of ohmic drop was computed using Equation 5-1 [105]

$$R_u = \frac{Z}{2KA} \qquad 5\text{-}1$$

Z = the gap between the working electrode and the reference electrode (mm) = 1 mm,
K = the electrical conductivity of 3.5 wt% NaCl solution (mS/cm) [201] = 50 mS/cm
A = the area of the working electrode (mm^2) = 1 cm^2 = 100 mm^2

Substituting these values into Equation 5- 1

$$R_u = \frac{1\ \text{mm}}{2 * 50\frac{\text{mS}}{\text{cm}} * 1\text{cm}^2} = \frac{1\ \text{mm}}{2 * 50\frac{\text{mS}}{10\ \text{mm}} * 100\ \text{mm}^2} = 0.0001\ \Omega = 0.1\ \mu\Omega \qquad 5\text{-}2$$

The calculated ohmic drop was about 0.1μΩ as shown in Equation 5-2. This was considered negligible and hence was neglected. The results of the corrosion behaviour of the micro-alloy specimens in different concentration of aerated and de-aerated NaCl solutions using the conditions outlined in Table 4-4 are presented in this section.

5.1.3.1 LPR results on effect of NaCl concentrations in aerated and de-aerated environment.

The average LPR curves for the four specimens in three different concentrations (1.0 wt%, 3.5 wt% and 10.0 wt%) of aerated and de-aerated NaCl solutions at ambient temperature and for 6 hours are show in Figures 5-6 and 5-7 respectively. Figures 5-6 (a) and (b) showed that the corrosion rate of all the four specimens in aerated 1.0 wt% NaCl and 3.5 wt% NaCl solution increased continuously with time signifying that the air-formed oxide and the corrosion product films on the surface of the specimens were porous and therefore could not protect the steels from corrosion attack [21, 94]. However, Figure 5-6 (c) in aerated 10 wt% NaCl and Figures 5-7 (a, b and c) in the three deaerated brine exhibited decrease in corrosion rate with time. This means that the air formed oxide-film [94, 136] and the corrosion products on the surface of the specimens possessed certain protective properties which reduced the corrosion rate of the steels [122, 182].

Figures 5-8 aerated and 5- 9 de-aerated compared the corrosion rate of the respective steels in 1.0 wt%, 3.5 wt% and 10.0 wt% NaCl solutions at ambient temperature and for 6 hours. These figures showed that the corrosion attack for all the four specimens was more severe in 3.5 wt% NaCl solution for both aerated and de-aerated solutions than in the other two concentrations (1.0 wt% and 10.0 wt%).

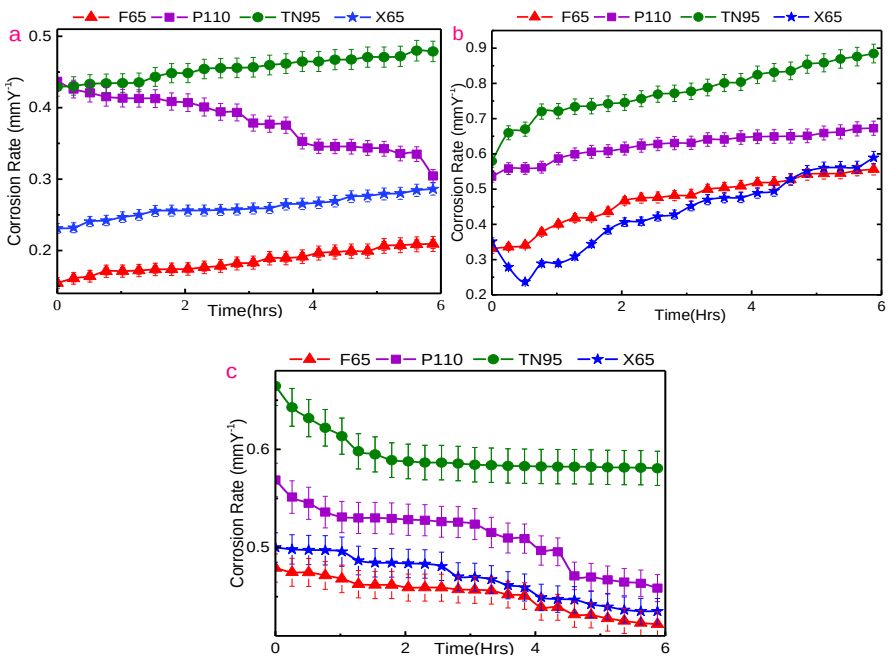

Figure 5- 6: Average LPR corrosion rates of the steels in aerated brine solutions at ambient temperature and for 6 hours: (a) 1 wt% aerated, (b) 3.5 wt% aerated, (c) 10 wt% aerated.

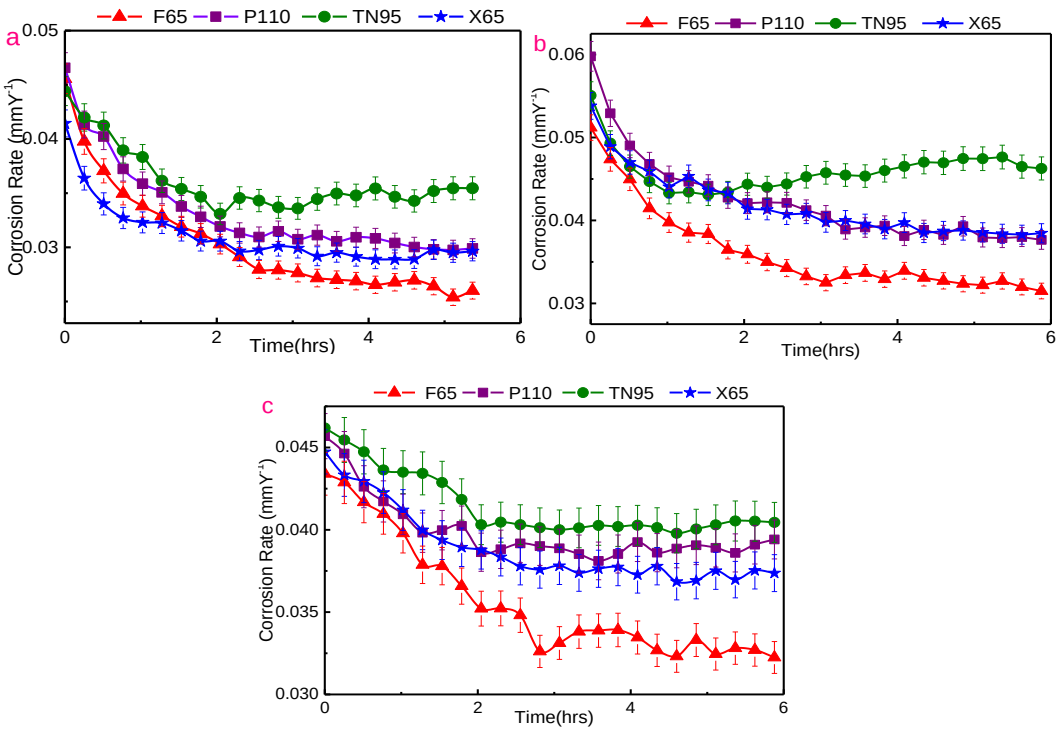

Figure 5- 7: Average LPR corrosion rates of the steels in de-aerated brine solutions at ambient temperature and for 6 hours: (a) 1 wt% de-aerated, (b) 3.5 wt% de-aerated, (c) 10 wt% de-aerated

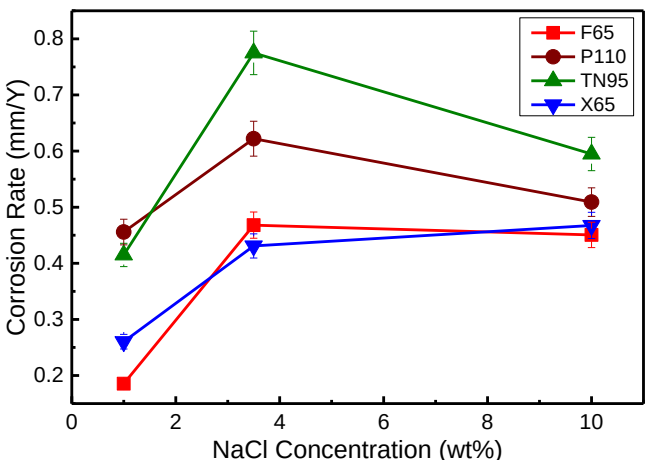

Figure 5- 8: Average corrosion rates of the steels in different concentration of naturally aerated NaCl solutions at ambient temperature and for 6 hours

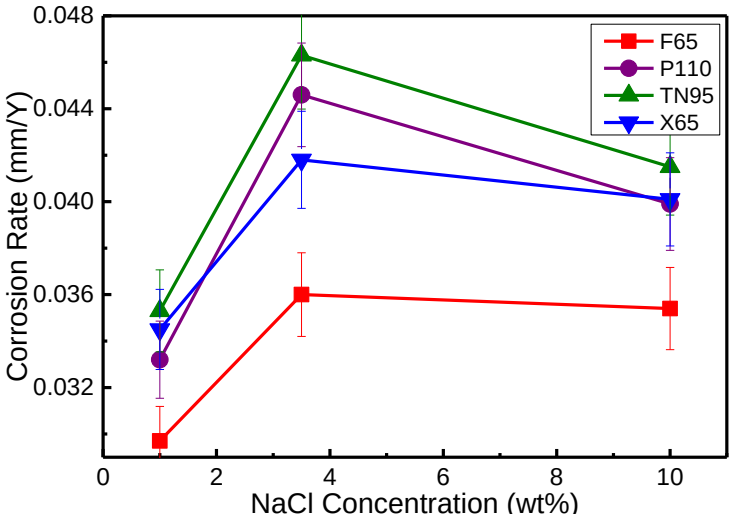

Figure 5- 9: Average corrosion rates of the steels in different concentration of deaerated NaCl solutions at ambient temperature and for 6 hours

Figure 5- 10 compared the corrosion rates of samples in aerated and de-aerated NaCl solutions at ambient temperature and for 6 hours. This figure shows that all the specimens exhibited higher susceptibility to corrosion attack in aerated solutions than in de-aerated solutions demonstrating a decrease of about 89% in 1.0 wt% NaCl, 93% in 3.5 wt% NaCl and 92% in 10.0 wt% NaCl of deaerated solutions when compared with the respective aerated solutions. Similar observations were reported by other researchers [167, 173, 202, 203]. Jung, et al [177] specifically reported a decrease of 91% when the concentration of dissolved oxygen was decreased from 9 mg/L to 2 mg/L

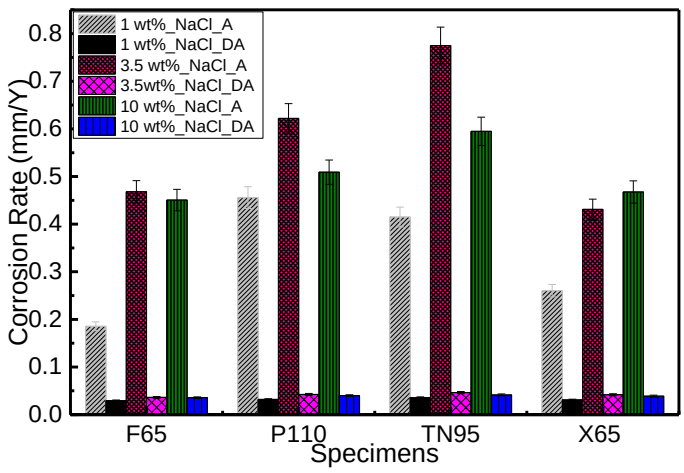

Figure 5- 10: Comparison of corrosion rates of steels in aerated and de-aerated NaCl solutions at ambient temperature and for 6 hours

5.1.3.2 Tafel polarization results of the effect of NaCl concentrations on the corrosion behaviour of micro-alloy steels in aerated and de-aerated environment

Tafel polarization tests were conducted in both aerated and de-aerated 1.0 wt% NaCl, 3.5 wt% NaCl and 10.0 wt% NaCl at ambient temperature within a sweep range of ±250 $mV_{(Ag/AgCl)}$ and scan rate of 0.5 mV/sec. Figures 5-11 and 5-12 show the Tafel plots of the four micro-alloyed steels corroded in the three different concentrations of NaCl solutions. A closer look at these figures showed that the anodic polarization curves of all the specimens in both aerated and de-aerated solutions increased continuously with increase in potential. This signified active corrosion behaviour with the attendant anodic dissolution. This also indicated that the anodic reactions exhibit the same corrosion mechanism displaying a well-defined Tafelian regions within the low over-potentials in both aerated and deaerated conditions.

On the other hand, the cathodic branch demonstrated a mixed activation- and mass transfer control behaviour revealing a well-defined current plateau which can be ascribed to the mass transport limitation of the proton reduction reaction in all the aerated solutions [204]. This is not so with the deaerated solutions where a well-defined Tafellian characteristics can be observed signifying that the cathodic kinetic of the deaerated condition is under activation control.

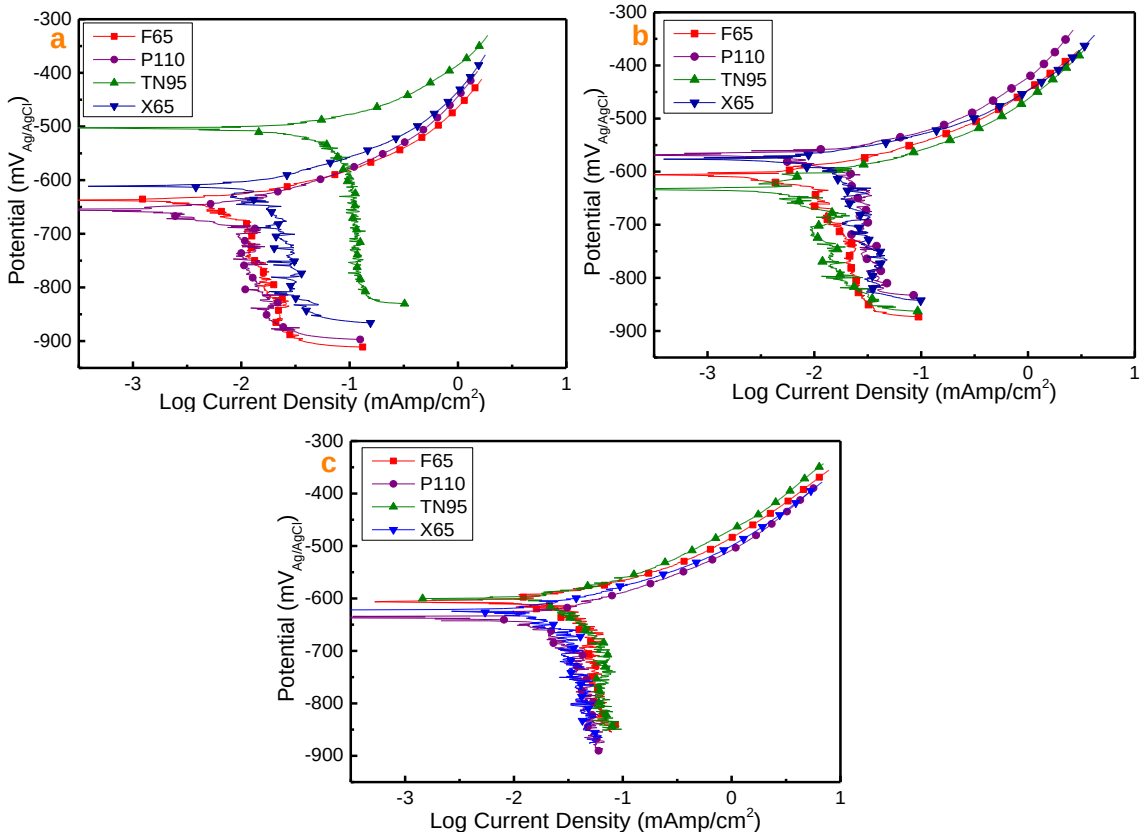

Figure 5- 11: Tafel Plots of specimens in different concentrations of naturally aerated NaCl solution at ambient temperature and for 6 hours (a) 1% Aerated, (b) 3.5% Aerated and (c) 10% Aerated

These figures also showed significant variation in the corrosion potentials of the specimens particularly in the aerated solutions. This variation decreased with increase in NaCl concentration spanning about 180 mV$_{(Ag/AgCl)}$, 100 mV$_{(Ag/AgCl)}$, and 40 mV$_{(Ag/AgCl)}$, in 1 wt%, 3.5 wt% and 10 wt% NaCl respectively. On the other hand, the corrosion potential of the specimens corroded in deaerated condition did not exhibit such wide potential variation with increase in NaCl concentrations. Figures 5-13 to 5-15 compare the Tafel plots of the micro-alloy steels in the different concentrations of aerated and deaerated NaCl solutions while the Tafel extrapolated parameters are listed in Table 5-3. This table showed that the Tafel cathodic constants (βc) are larger than the corresponding Tafel anodic constants indicating that the corrosion processes are mainly under the control of cathodic reaction.

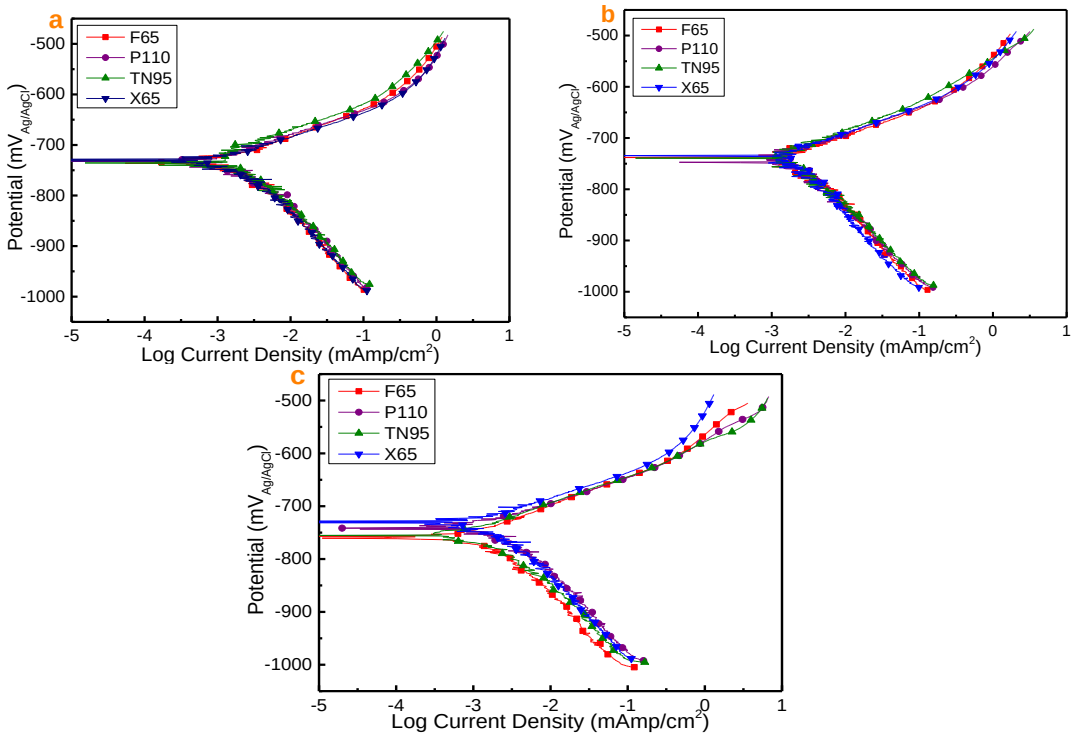

Figure 5- 12: Tafel Plots of specimens in different concentrations of de-aerated NaCl solution at ambient temperature and for 6 hours (a) 1% Deaerated, (b) 3.5% Deaerated and (c) 10% Deaerated

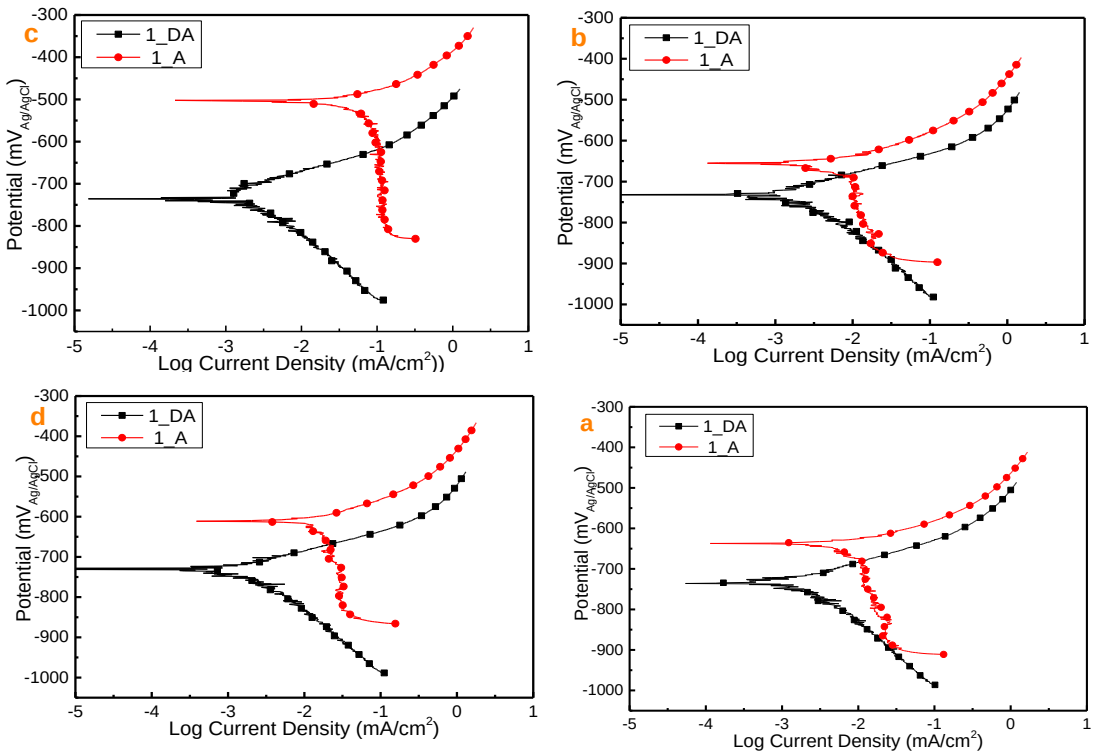

Figure 5- 13: Comparison of the Tafel plot of the steels in aerated and de-aerated 1 wt% NaCl solution at ambient temperature (a) F65, (b) P110, (c) TN95 and (d) X65

It can clearly be seen from the polarization curves (anodic and cathodic curves) that the cathodic current density for the aerated solutions were higher than that in the deaerated solutions as shown in Figures 5-13 to 5-15. This gave for instance a corresponding decrease in corrosion current density from 17 µA.cm^{-2} in the aerated 10 wt% NaCl solution to 0.9 µA.cm^{-2} in the de-aerated 10 wt% NaCl solution of steel F65. Similar observation has been reported in literature [205].

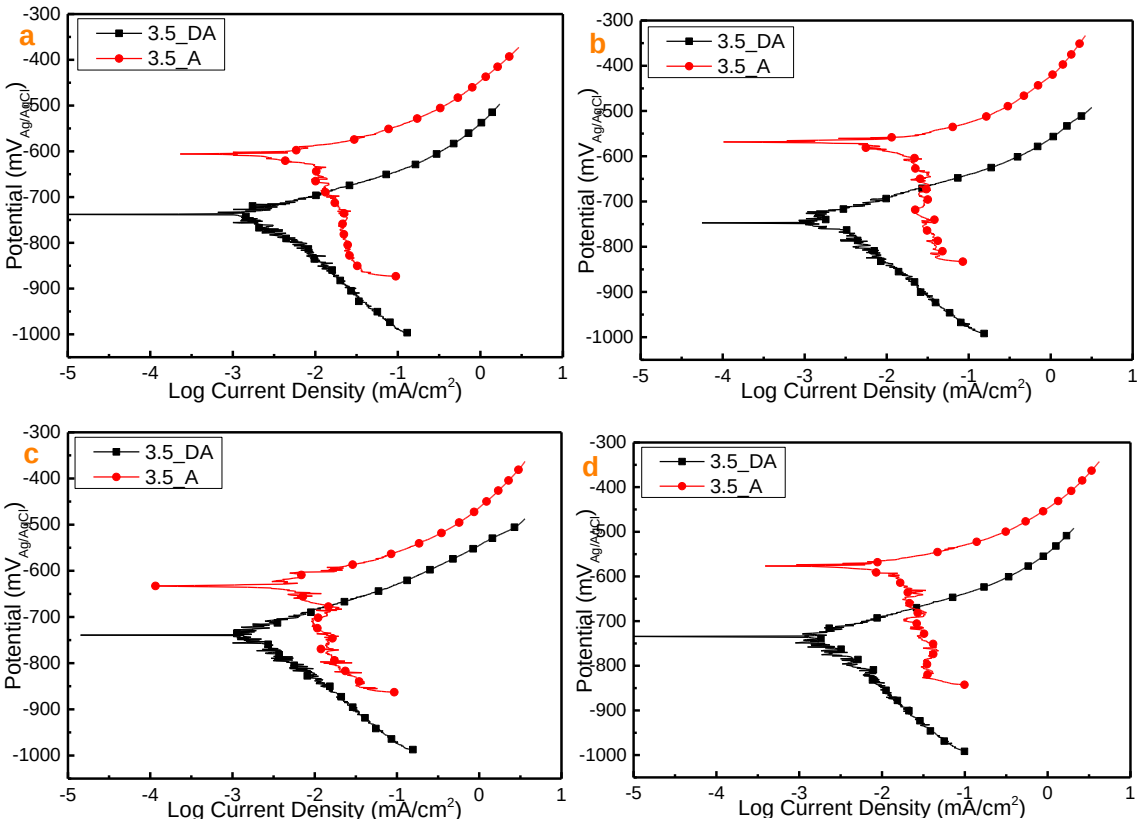

Figure 5- 14: Comparison of the Tafel plot of the steels in aerated and de-aerated 3.5 wt% NaCl solution at ambient temperature (a) F65, (b) P110, (c) TN95 and (d) X65

These values are comparable with the report of other authors [4, 67, 124] suggesting that the samples with lower corrosion current density exhibited higher corrosion resistance in the chloride solution. Since corrosion current density i_{Corr} is proportionally related to corrosion rate (CR) [47, 205] and from the values of i_{Corr} in Table 5-3, the corrosion rates of the steels in both aerated and de-aerated solutions can be ranked as $CR_{F65} < CR_{X65} < CR_{P110} < CR_{TN95}$. This trend of corrosion rate corroborated the linear polarization resistance results and can be attributed to the chemical compositions and microstructures of the samples.

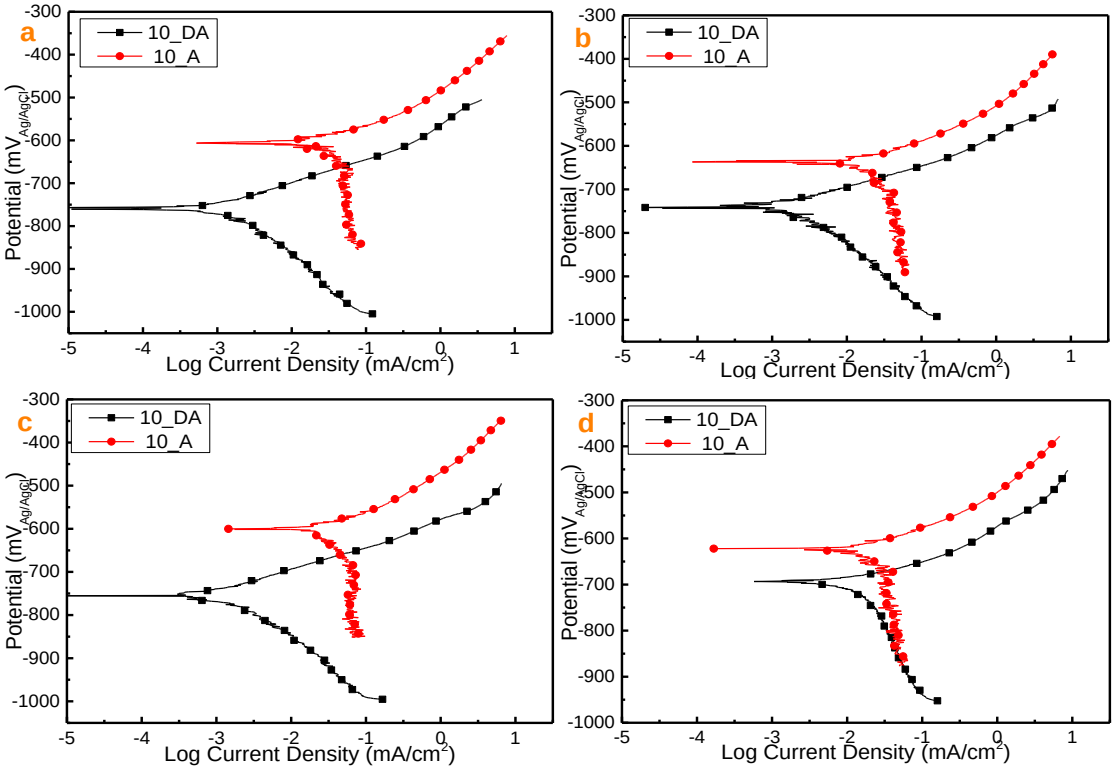

Figure 5- 15: Comparison of the Tafel plot of the steels in aerated and de-aerated 10 wt% NaCl solution at ambient temperature (a) F65, (b) P110, (c) TN95 and (d) X65

5.1.3.3 Analyses of surface morphology of specimens corroded in aerated and deaerated media

Figures 5- 16 to 5- 21 show the SEM micrographs of the specimens corroded in different concentration of aerated and de-aerated NaCl solutions. It is evidence from these figures that the steels exhibited more severe corrosion attack in aerated condition than in de-aerated solution. Also a closer look at the surface morphologies of these figures showed more aggressive attack displaying greater protrusion of Fe_3C for the steels corroded in 3.5 wt% NaCl solutions than in the other two conditions. This is an indication that more ferrites were selectively dissolved in 3.5 wt% NaCl solutions. This corroborated with the results of LPR and Tafel experiments and the reports in literature [138, 174]. The micrographs of the specimens corroded in deaerated 1 wt% and 10 wt% NaCl solution shown in Figures 5-17 and 5-21 respectively indicated very mild corrosion attack when compared with Figure 5-19 for the deaerated 3.5 wt% NaCl. Localized corrosion in the form of shallow pits can be seen with steels F65 and X65 corroded in naturally aerated solution particularly in aerated 1 wt% NaCl solution

Table 5- 3: Tafel extrapolation parameters of the specimens in aerated and de-aerated solutions of three NaCl concentrations.

NaCl (wt%)	Sample	E_{Corr} (mV)	i_{Corr} (µAmp/cm²)	β_a (mV/dec)	β_c (mV/dec)
1.0 Aerated	F65	-637	6.00	38	145
	P110	-656	7.50	60	175
	TN95	-502	11.00	38	120
	X65	-611	6.50	65	120
1.0 De-aerated	F65	-733	1.19	54	94
	P110	-732	1.25	53	96
	TN95	-726	1.37	57	122
	X65	-730	1.22	49	105
3.5 Aerated	F65	-590	21.00	65	449
	P110	-591	24.00	69	411
	TN95	-581	28.00	55	530
	X65	-580	21.50	64	450
3.5 De-aerated	F65	-742	1.40	53	99
	P110	-740	1.50	55	117
	TN95	-738	1.60	55	108
	X65	-738	1.40	53	111
10.0 Aerated	F65	-607	17.00	40	80
	P110	-634	20.00	65	265
	TN95	-600	23.00	55	155
	X65	-621	18.00	50	120
10.0 De-aerated	F65	-758	0.90	54	86
	P110	-741	1.35	51	90
	TN95	-742	1.4	56	101
	X65	-731	1.16	40	64

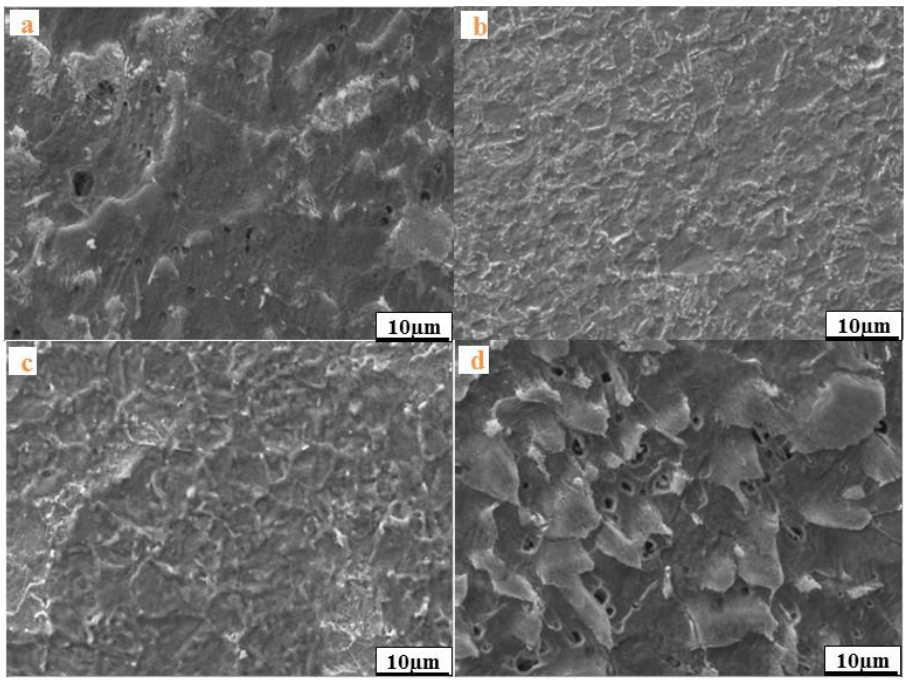

Figure 5- 16: SEM micrographs of the specimens corroded in naturally aerated 1 wt% NaCl solution at ambient temperature for 6 hours (a) F65, (b) P110, (c) TN95 and (d) X65

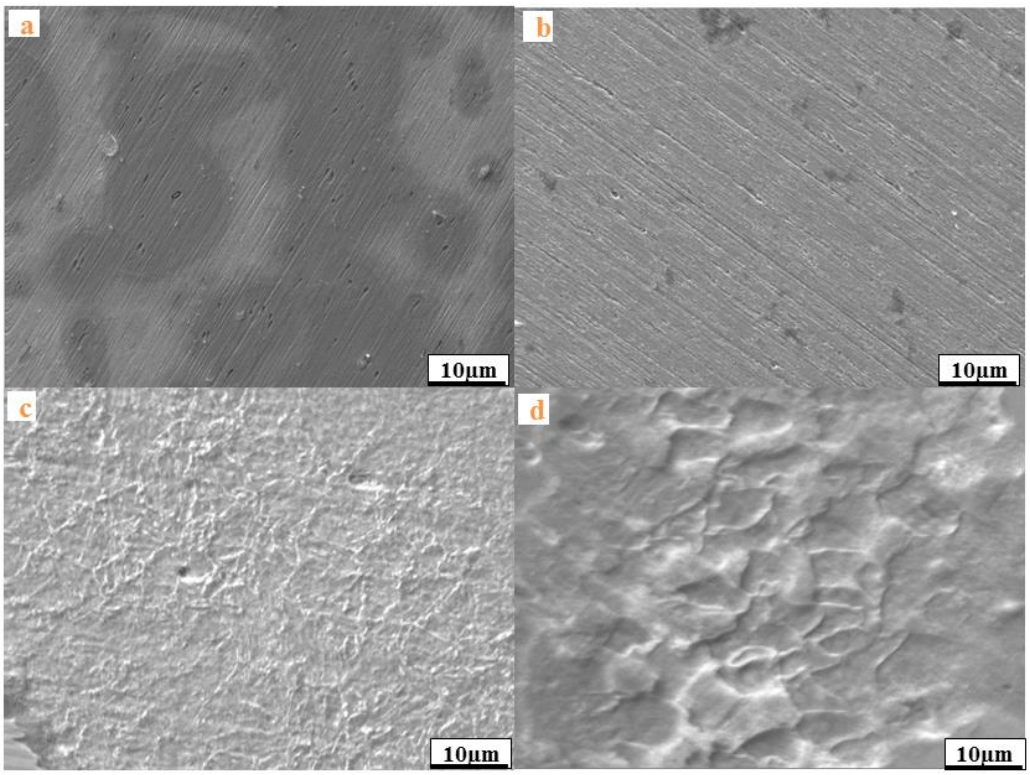

Figure 5- 17: SEM micrographs of the specimens corroded in deaerated 1 wt% NaCl solution of at ambient temperature for 6 hours (a) F65, (b) P110, (c) TN95 and (d) X65

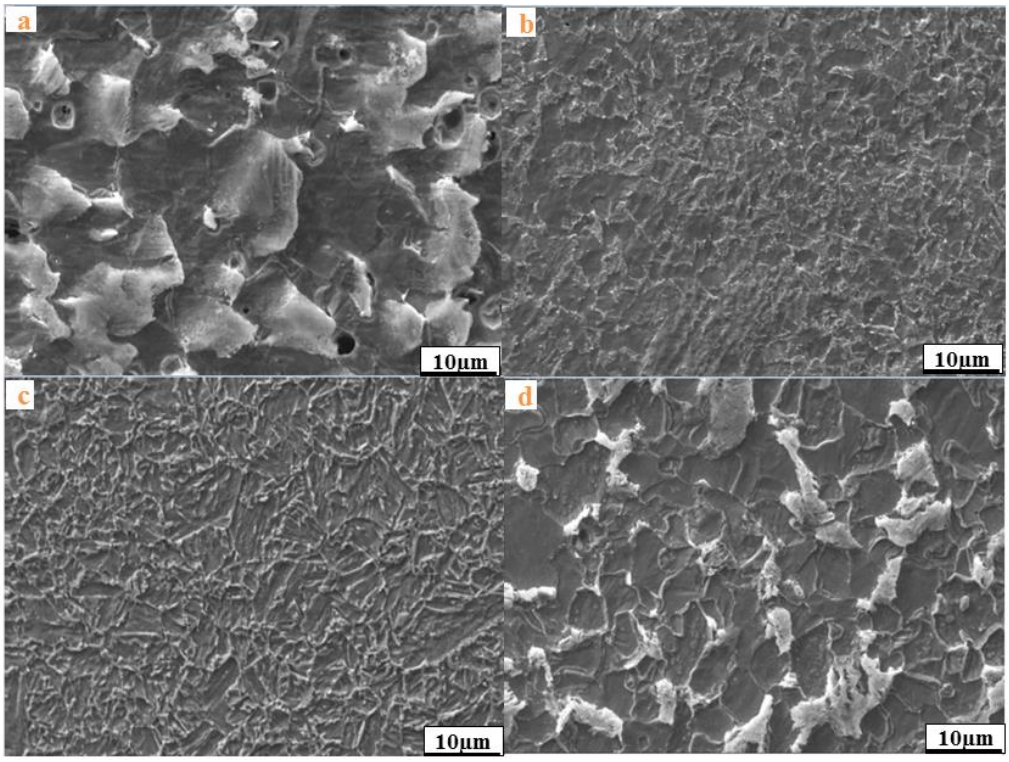

Figure 5- 18: SEM micrographs of the specimens corroded in naturally aerated 3.5 wt% NaCl solution at ambient temperature for 6 hours (a) F65, (b) P110, (c) TN95 and (d) X65

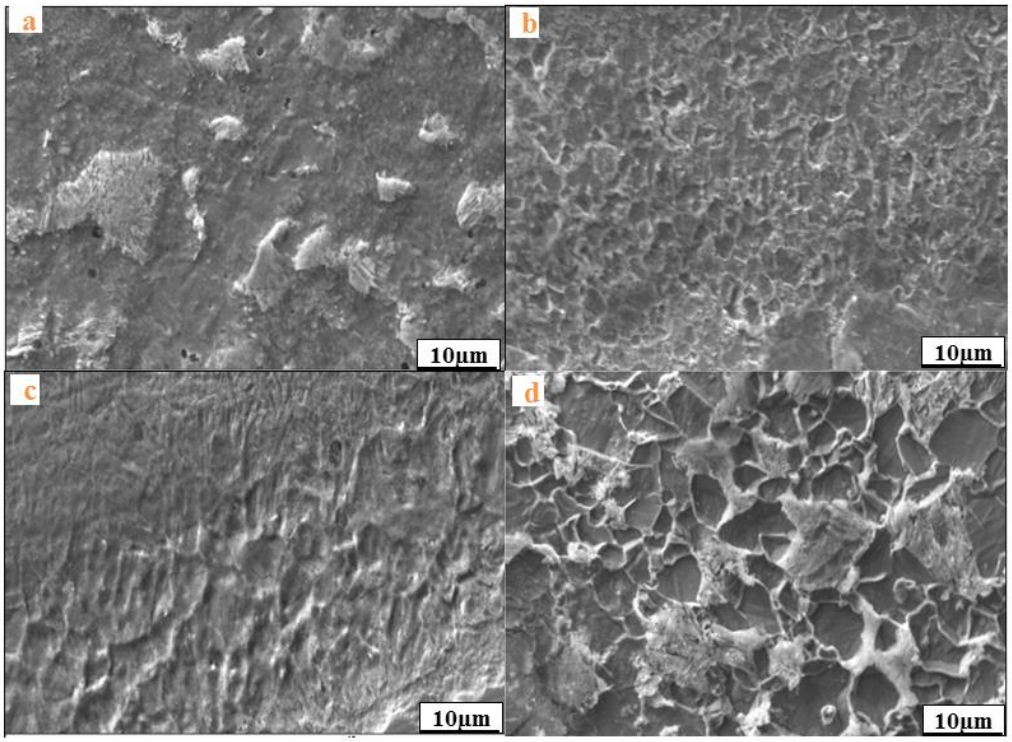

Figure 5- 19: SEM Micrographs of the samples corroded in de-aerated 3.5 wt% NaCl solutions at ambient temperature and for 6 hours (a) F65, (b) P110, (c) TN95 and (d) X65

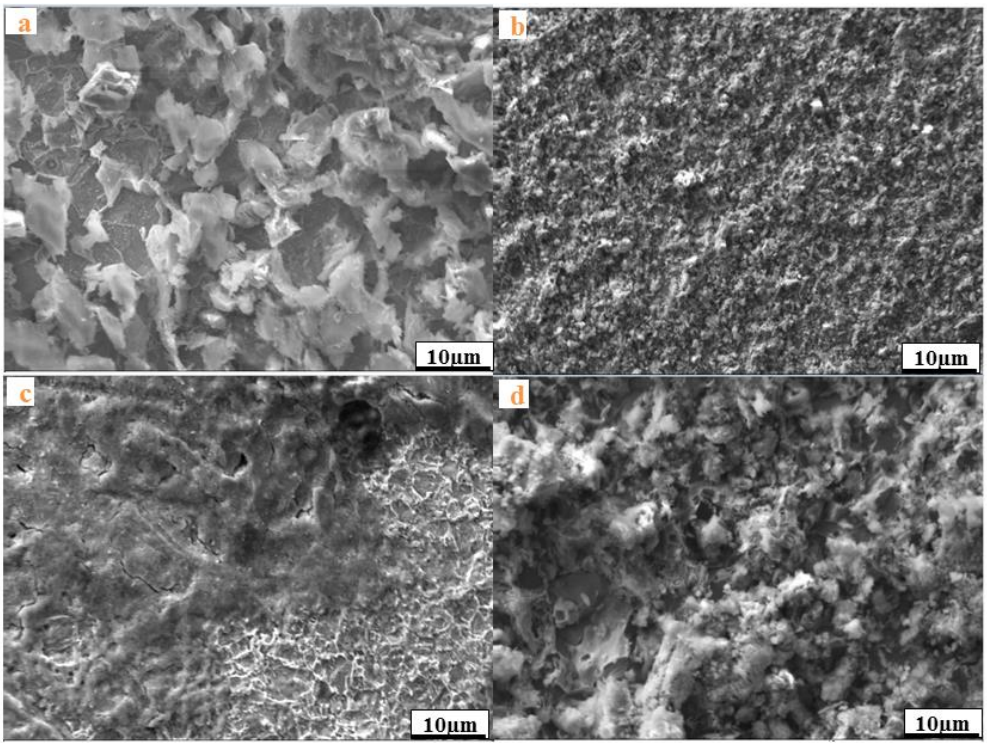

Figure 5- 20: SEM Micrographs of the samples corroded in naturally aerated 10 wt% NaCl solutions at ambient temperature and for 6 hours (a) F65, (b) P110, (c) TN95 and (d) X65

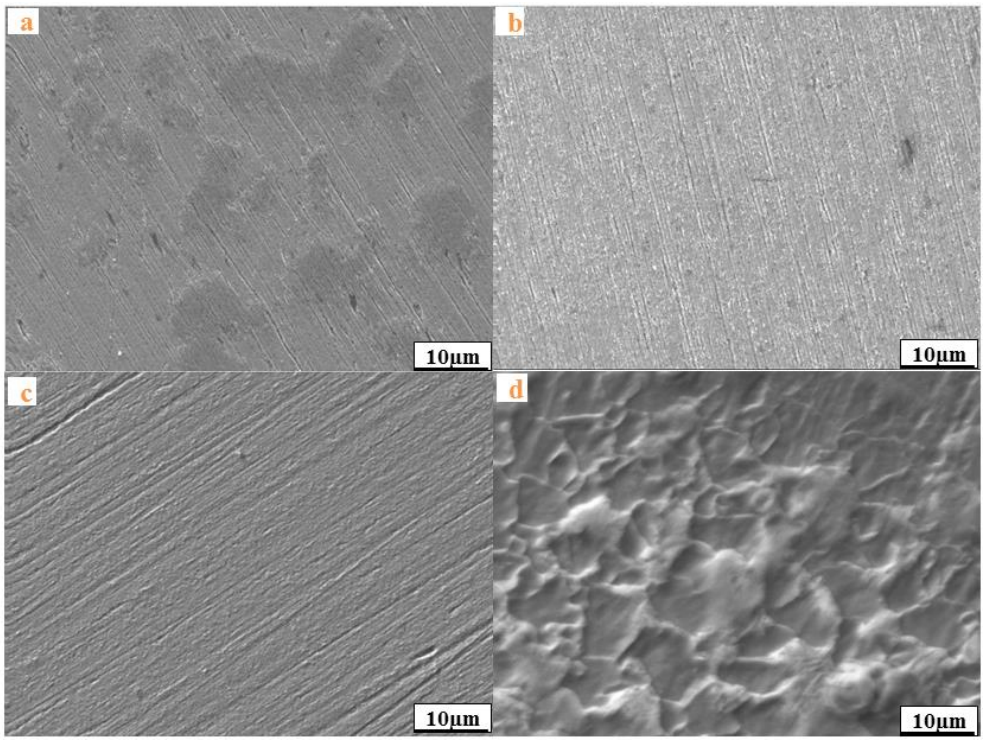

Figure 5- 21: SEM Micrographs of the samples corroded in de-aerated 10 wt% NaCl solutions at ambient temperature and for 6 hours (a) F65, (b) P110, (c) TN95 and (d) X65

5.1.4 Effect of temperature on the corrosion behaviour of the steels in 3.5 wt% NaCl solution saturated with 0.5% CO_2

The corrosion behaviour of the three proprietary micro-alloyed steels and X65 steel grade as reference specimen were investigated in 3.5 wt% NaCl solution saturated with 0.5% CO_2 at temperatures below 60^0C using electrochemical polarization (linear polarization resistance-LPR, potentiodynamic polarization, electrochemical impedance spectroscopy-EIS) and surface analysis (SEM/EDS and XRD) techniques. The results of these investigations are presented in this section.

5.1.4.1 Linear Polarization Resistance (LPR) of the steels in 3.5 wt% NaCl saturated with 0.5% CO_2 at different temperatures

The evolution of corrosion rate with time for the specimens corroded in unbuffered 3.5 wt% NaCl solutions bubbled with 0.5% CO_2 gas at three different temperatures are shown in Figure 5-22. This figure showed that the corrosion rate for all the specimens deceased within the first 3 hours and remained relatively stable at various corrosion rates which are dependent on temperatures and the specimen. This decrease in corrosion rate can be attributed to the formation of corrosion products on the surface of the specimens. The

formed corrosion products slowed down corrosion attack by presenting a physical diffusion barrier thereby preventing the electrochemical species involved in the corrosion process from accessing the steel substrates [62, 159].

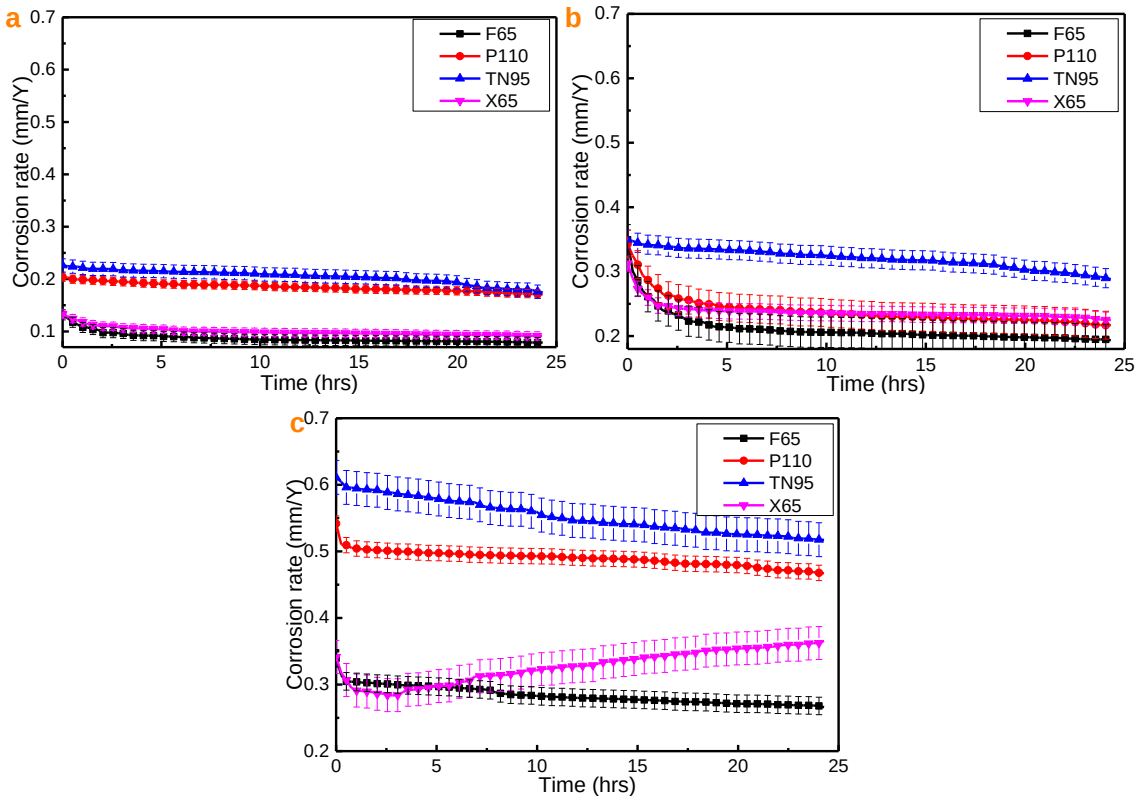

Figure 5- 22: Comparison of the corrosion rate of specimens in the 3.5 wt% NaCl solution saturated with 0.5% CO_2 at (a) 25^0C; (b) 45^0C and (c) 60^0C

Another notable feature of Figure 5-22 is the corrosion rate (CR) of the micro-alloyed steels which can be ranked as $CR_{F65} < CR_{X65} < CR_{P110} < CR_{TN95}$ in the three temperature values. It is also obvious from Figure 5- 22 that the value of the corrosion rate at which the specimens became stable increased with temperature. For instance the corrosion rate at which steel F65 stabilized increased from 0.1 mm/y at 25^0C to 0.2mm/y at 45^0C and further increased to 0.25mm/y at 60^0C. This variation is made clearer in Figure 5-23 which showed that the corrosion rate of the specimens increased with increase in temperature.

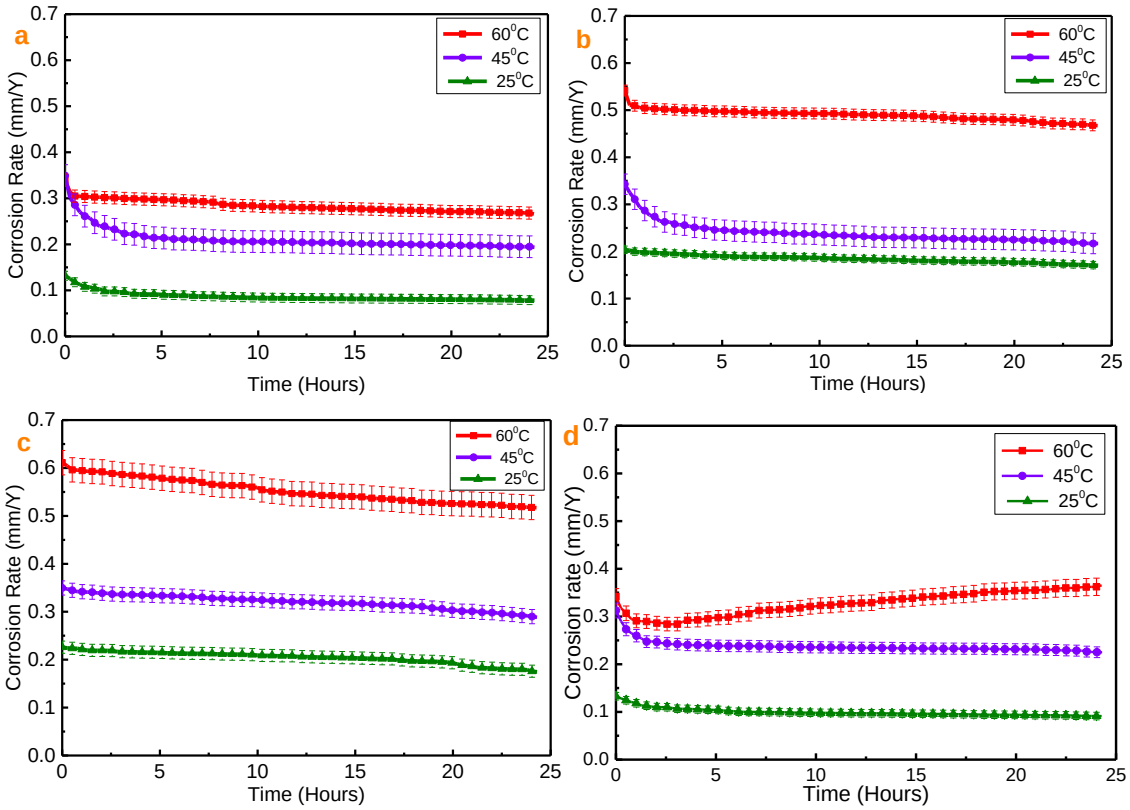

Figure 5- 23: Effect of temperature on the corrosion rate of specimens in the 3.5 wt% NaCl solution saturated with 0.5% CO2 (a) F65; (b) P110, (c) TN95 and (d) X65

5.1.4.2 Tafel polarization of the steels in 3.5 wt% NaCl solution saturated with 0.5 % CO_2 at different temperatures

The corrosion behaviour of the steels was also assessed by potentiodynamic polarization using a scan rate of 0.5mV/sec and a sweep range of ±250 $mV_{(Ag/AgCl)}$. The Tafel plots are shown is Figure 5-24 for temperature variation while the Tafel parameters obtained using extrapolation techniques are shown in Tables 5-4. Tafel extrapolation parameters obtained in this work was based on ASTM G 102-89 standard as explained in section 4.2.2.1 and demonstrated later in Section 5.1.5.2 (see Figure 5-36).

Figure 5- 24 shows that the curves of the log current density versus potential ($mV_{(Ag/AgCl)}$) for all the micro-alloyed steels are similar for the three temperatures suggesting that the corrosion mechanism is the same [142, 206]. The anodic current densities increased with increase in potential particularly within the low overvoltage depicting a well-defined Tafel slopes. This signified an active dissolution of the specimens and that no corrosion product was formed. However at about – 600 $mV_{(Ag/AgCl)}$ (Sat. KCl), the current densities slightly decreased with increase in potential suggesting the occurrence of pseudo-passivation displaying current plateaus. These signatures became more pronounced as

temperature increases. This behaviour was also reported by Ochoa, et al [185] and Henriquez et al [204]. The witnessed anodic current plateau also indicated the formation of poorly protective anodic corrosion film [207]

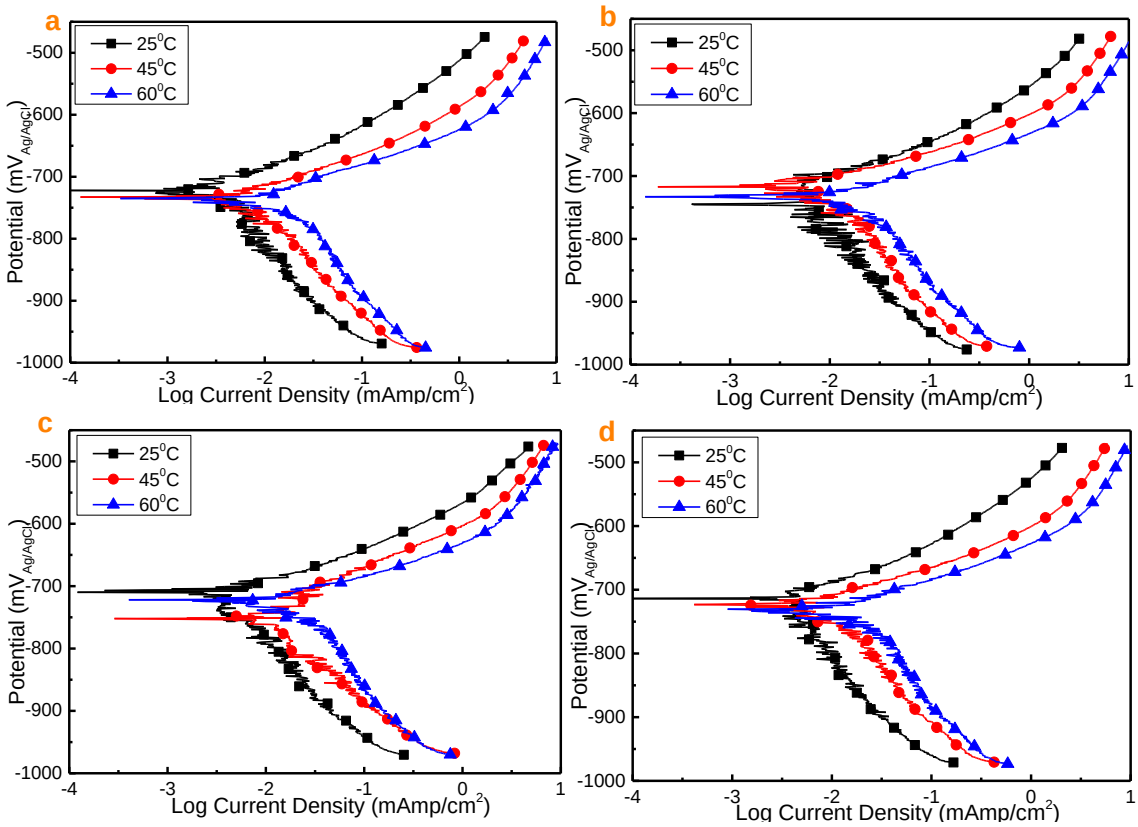

Figure 5- 24: Tafel plots of the specimens in the 3.5 wt% NaCl solution saturated with 0.5% CO2 at different temperatures (a) F65; (b) P110, (c) TN95 and (d) X65

Table 5- 4: Graphically determined Corrosion parameters of the samples using Tafel Extrapolation Technique

Tafel Parameters	25^0C				45^0C				60^0C			
	F65	P110	TN95	X65	F65	P110	TN95	X65	F65	P110	TN95	X65
E_{corr} (mV)	-723	-720	-710	-713	-735	-720	-760	-724	-735	-733	-722	-732
β_a (mV/dec)	50	52	56	52	54	53.5	75	53	58	55	48	54
β_c (mV/dec)	149	154	170	146	111	149	105	125	120	125	135	120
I_{corr} (μAmp/cm^2)	2.4	3.6	4.1	2.6	5.0	8.1	9.0	7.0	12.0	15.0	17.0	14

5.1.4.3 Electrochemical impedance spectroscopy (EIS) of the steels in 3.5 wt% NaCl solutions saturated with 0.5% CO_2 at different temperatures

Electrochemical impedance spectroscopy (EIS) measurements were conducted at OCP in 3.5 wt% NaCl solutions saturated with 0.5% CO_2 at 25^0C with 5 mV perturbation and a frequency range of 100 KHz – 0.1 Hz for the three proprietary steels. Figure 5-25 shows a representative EIS spectra using steel F65 at different temperatures. This figure reveals that the Nyquist plots for steel F65 displayed similar features of one semi-capacitive loops. According to literature [54, 208], this can be ascribed to non-homogeneity of the surface of the specimens, frequency dispersion and mass transport resistant. This figure also shows that the radius of the capacitive loop of steel F65 decreased with increase in temperature. The same trend of behaviour was also observed with steels P110 and TN95.

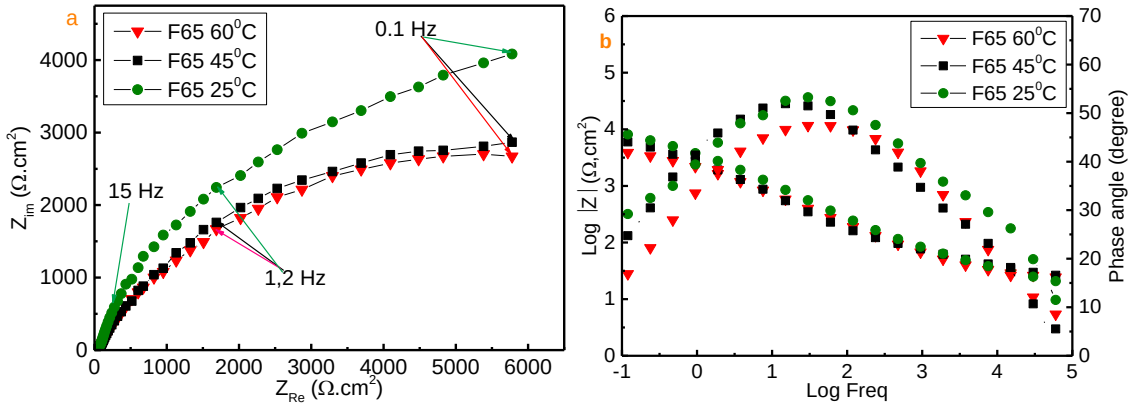

Figure 5- 25: Plots of the Specimens corroded in 3.5 wt% NaCl Solution saturated with 0.5% CO_2 at 25^0C (a) Nyquist and (b) Bode

The Bode plots for the micro-alloy steel F65 are shown in Figure 5-25 (b) for different temperature. This figure shows that the high frequency impedance magnitude (|Z|), which represents the solution resistance (R_s), is about 25 $\Omega.cm^2$ and 5 $\Omega.cm^2$ for steel A at temperature and pH conditions respectively for steel F65. At low frequency, the impedance magnitude (|Z|), which signifies the charge transfer resistance (R_{ct}). On the other hand, the phase angle value of steel F65 at high frequency is 0^0. This suggests that the impedance value at high frequency is solely dependent on the resistance of the electrolyte. The maximum phase angle values appeared within the intermediate frequencies demonstrating a highest phase angle of 55^0 at 25^0C. At low frequency, the phase angle values of steel F65 lie between 15^0-30^0. The other two proprietary micro alloy steels used in this work exhibited the same behavioural trend. This is in agreement with the report of Luo, et al [208] and chen Bian, et al [61].

To quantify the effects of temperature on the EIS results of the specimens corroded in 3.5 wt% NaCl solution saturated with 0.5% CO_2, the simple Randle cell (equivalent electrical circuit, EEC) model shown in Figure 5-26 was adopted.

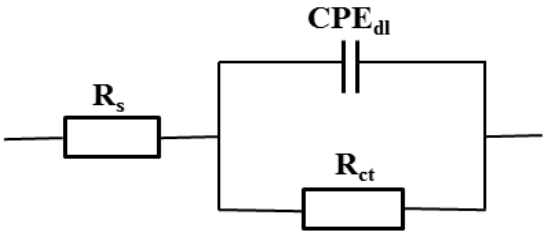

Figure 5- 26: Equivalent electrical circuit (EEC) used to fit EIS data of the Steels corroded in 3.5 wt% NaCl Solutions containing CO_2 at different temperatures

This model consists of three main elements which include the electrolyte resistance (Rs), the double layer capacitance (C_{dl}) and the charge transfer resistance (R_{ct}). The electrolyte resistance (Rs) depicts the resistance of the solution between the working and reference electrodes. On the other hand, the double layer capacitance (C_{dl}) and the charge transfer resistance (R_{ct}) which are in parallel represent the corrosion reactions at the metal/electrolyte interface. The constant phase element (CPE) was introduced in the equivalent electrical circuit (EEC) in place of pure double layer capacitance [61, 204]. CPE is widely used in EEC because of the effect of different physical phenomenon such as surface heterogeneity resulting from surface roughness, impurities, dislocations, grain boundaries, distribution of the active sites, adsorption of inhibitors and formation of porous layers [209]. CPE has been defined as in Equation 5-3.

$$Z_{CPE} = \frac{1}{Y_o} (j\omega)^{-n} \qquad 5\text{-}3$$

Where Y_o is the magnitude of CPE, $\omega = 2\pi f$ is the angular frequency, f is the ordinary frequency (measured in Hertz), j is the imaginary number and n is the dispersion coefficient related to surface non-homogeneity. Depending on the value of n, CPE may be pure resistor (ie if n = 0 then Z_0 = R), pure capacitor (meaning that n = 1 when Z_0 = C) or inductor (ie when n = 0.5 and Z_0 = W) [61, 113, 204].

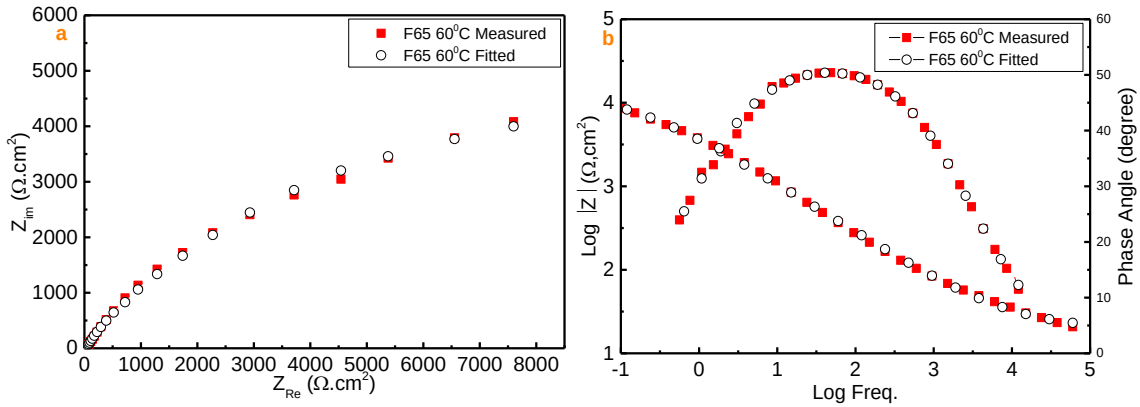

Figure 5- 27: The fitted EIS plots of steel F65 corroded in 3.5 wt% NaCl saturated with 0.5% CO_2 at 60^0C: (a) Nyquist Plots and (b) Bode plots

Figure 5-27 shows a representative of the fitted results of the impedance spectra for steel F65 corroded in 3.5 wt% NaCl saturated with 0.5% CO_2 at 60^0C. It can be observed from this figure that the measured results matched relatively well with the fitted results in both Nyquist and Bode plots. This is made more vivid by the low % error of the fitted electrochemical parameters listed in Tables 5-5.

Table 5- 5: Electrochemical Impedance Parameters of the Specimens corroded in 3.5 wt% NaCl Solution Saturated with 0.5% CO_2 at different temperatures after 24 hours LPR.

Temp (^{0}C)	Specimens	Rs		CPE_{dl}		n		R_{ct}	
		Value (Ω.cm²)	% Error	Value (μF⁻¹cm⁻²)	% Error	Value	% Error	Value (kΩ.cm²)	% Error
25	F65	29.22	3.45	$7.27 * 10^{-4}$	3.25	0.5	1.0	5.57	4.27
	P110	25.90	0.84	$5.90 * 10^{-4}$	1.10	0.6	0.3	5.41	1.37
	TN95	21.47	1.49	$7.1 * 10^{-4}$	1.73	0.6	0.41	5.24	2.03
45	F65	26.53	1.51	$6.66 * 10^{-4}$	1.60	0.6	0.46	11.50	3.14
	P110	31.17	2.80	$5.10 * 10^{-4}$	3.17	0.6	1.0	10.62	6.56
	TN95	26.23	1.23	$4.35 * 10^{-4}$	1.65	0.6	0.45	5.77	1.85
60	F65	19.02	2.24	$4.6 * 10^{-4}$	1.8	0.6	0.59	14.12	3.55
	P110	28.7	3.25	$3.21 * 10^{-4}$	3.46	0.6	1.10	12.01	8.60
	TN95	17.40	1.73	$1.1 * 10^{-4}$	1.56	0.6	0.44	10.84	3.29

This Table shows that as temperature increases, the charge transfer resistance (R_{ct}) decreases while the double layer capacitance (CPE_{dl}) increases. Decrease in charge

transfer resistance (R_{ct}) indicates faster rate of reactions at the corrosion product/electrolyte interface. This corroborate with the results of the LPR and Tafel polarization as presented in Sections 5.1.4.1 and 5.1.4.2 suggesting that the corrosion rate of the steels increased with increase in temperature in agreement with reports in literatures [172]. Steels P110 and TN95 demonstrated the same trend.

5.1.4.4 Surface morphology and analysis of the steels corroded in 3.5 wt% NaCl solutions saturated with 0.5% CO_2 at different temperatures

The SEM micrographs of the surface of the corroded micro-alloyed steels at 25^0C, 45^0C and 60^0C are shown in Figures 5-28, 5-29 and 5-30 respectively. These figures revealed that no significant corrosion product was formed on the surface of the steels with ferrite-pearlite microstructures (F65, P110 and X65) but showed some embossed patterns and the ground scratches at all the three test temperatures. These embossed patterns became more obvious while the ground scratches reduced with increase in temperature. The embossed (protrusions) patterns are the non-dissolved lamellar cementite which were left behind after the ferrites were preferentially dissolved.

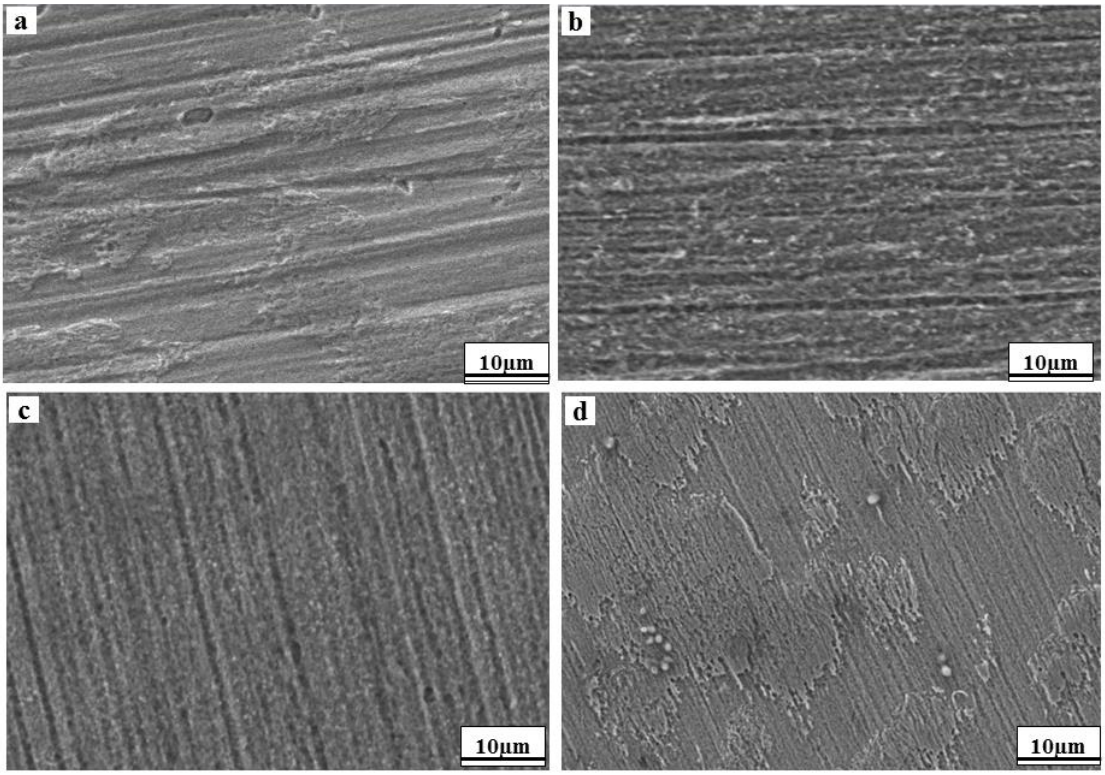

Figure 5- 28: SEM Micrographs of the specimens corroded in 3.5 wt% NaCl solution Saturated with 0.5% CO_2 at 25^0C; (a) F65, (b) P110, (c) TN95 and (d) X65

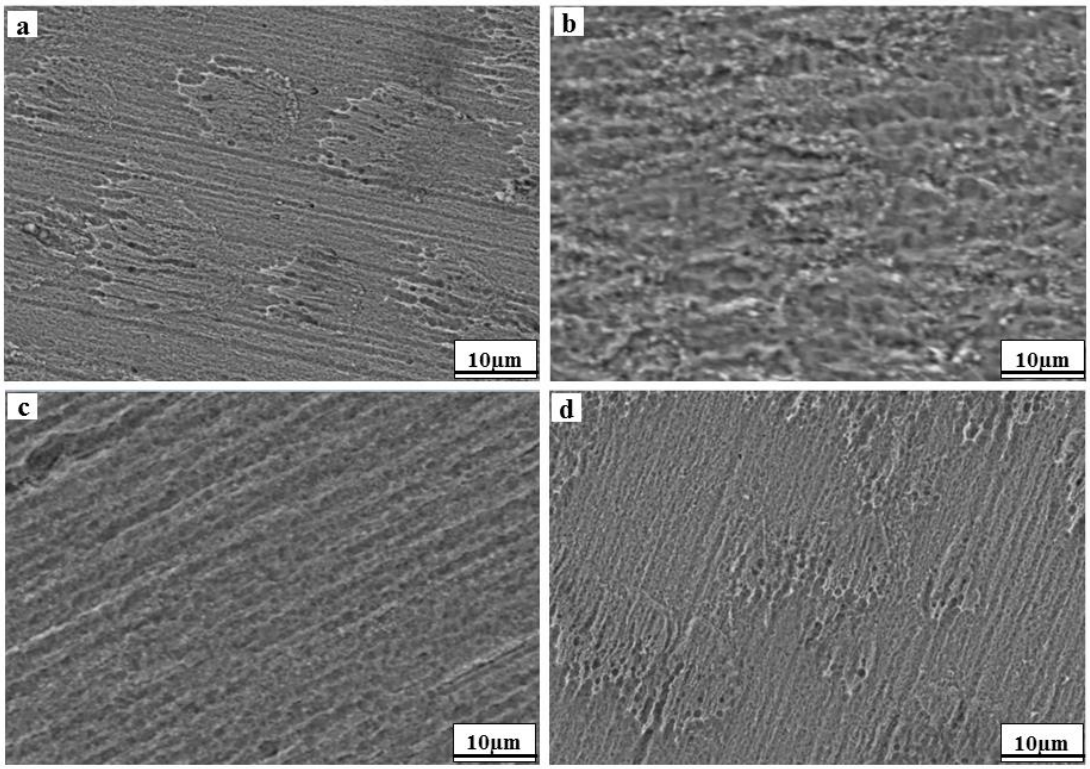

Figure 5- 29: SEM Micrographs of the specimens corroded in 3.5 wt% NaCl solution Saturated with 0.5% CO_2 at 45^0C: (a) F65, (b) P110, (c) TN95 and (d) X65

The micro-alloy steel with bainitic structure had no embossed pattern but displayed a flaky, cracked and loosely held corrosion product as shown in Figure 5-30 (c) for TN95 corroded at temperature 60^0C but showed smooth surfaces as presented in Figures 5-28 (c) and 5-29 (c) for the same steel corroded in 25^0C and 45^0C. The cracks on the micrographs of steel TN95 corroded at 60^0C permitted the ingress of active corrosion species which when in contact with the steel surface continued the corrosion process. This can be linked to the witnessed high corrosion rate of TN95.

The EDS analyses of all the specimens at all the temperatures revealed that the main elemental composition of the corrosion products are Fe, C and O with traces of Mn, Cr, Cu and Si as shown in Table 5-6. These elements were obtained from the sites marked 'a' to 'h' on the SEM surface morphology of the specimens corroded in unbuffered 3.5 wt% NaCl solution saturated with 0.5% CO_2 at 60^0C as shown in Figure 5-30. This uniform distribution of the corrosion product and the effects of grain size could have necessitated the trend of corrosion rate exhibited by the steels in all the test temperatures. This is in agreement with the report of Asiful [54].

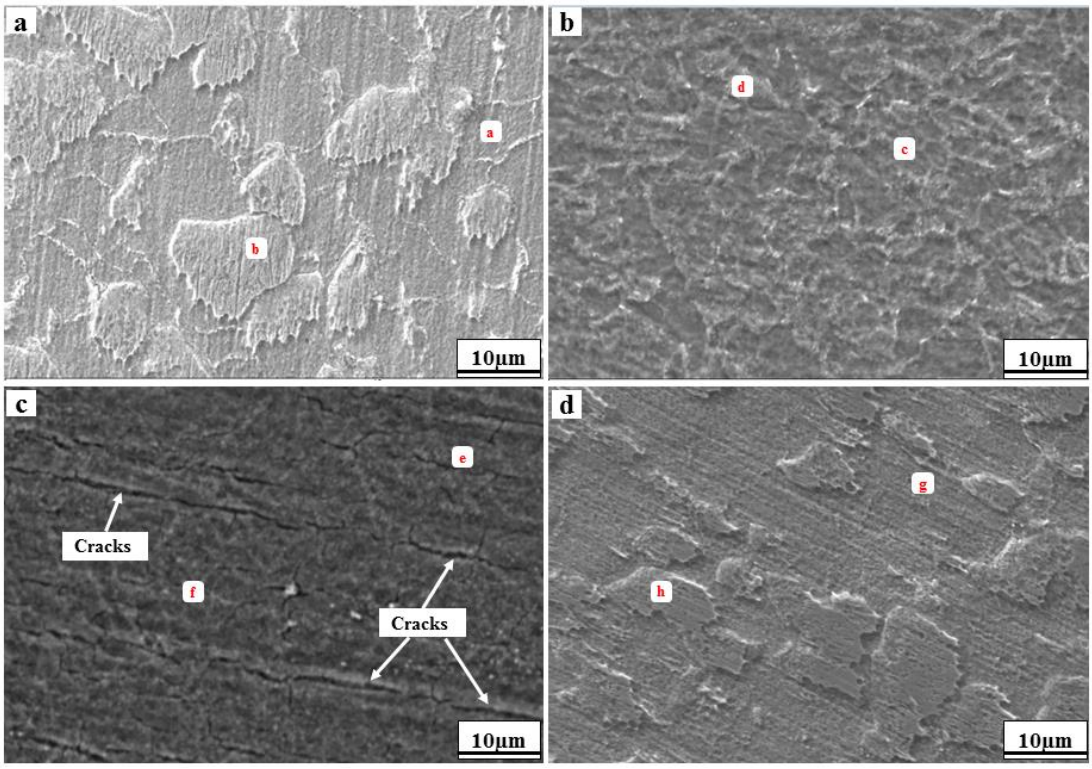

Figure 5- 30: SEM Micrographs of the specimens corroded in 3.5 wt% NaCl solution Saturated with 0.5% CO_2 at 60^0C: (a) F65, (b) P110, (c) TN95 and (d) X65

From Table 5-6, it may be assumed, as is the inherent attribute of CO_2 corrosion of carbon steel, that the corrosion product was $FeCO_3$. However, $FeCO_3$ was not detected by the XRD analyses of the surface of the corroded specimens as shown in Figure 5-31.

Table 5- 6: EDX Elemental Analysis at two sites on the SEM micrographs of the samples in unbuffered 3.5 wt% NaCl solution saturated with 0.5% CO_2 at 60^0C as shown in Figure 5-30

Samples	Site	C	O	Cu	Mn	Cr	Si	Fe
F65	a	7	2	0.8	0.6	0.3	0.2	89.1
	b	6	2.5	1	1.2	0.1	0.2	87
P110	c	9	4	1	1	0.3	0.1	84.6
	d	4	2	1.5	1	0.3	0.1	91.1
TN95	e	11	7	1	1	2	0.3	77.7
	f	13	7	1	1	3	0.2	74.8
X65	g	9	4	1.5	0.6	0.4	0.2	84.3
	h	10	2	0.4	0.7	0.2	0.1	86.6

The XRD pattern showed Fe_3C as the main phase on all the steel substrates. Fe_3C was part of the steel microstructure left behind after the anodic dissolution of Ferrite [210]. It means that the concentrations of the dissolved Fe^{2+} ions and the CO_3^{2-} ions from carbonic acid were not high enough to precipitate $FeCO_3$ [143, 210].

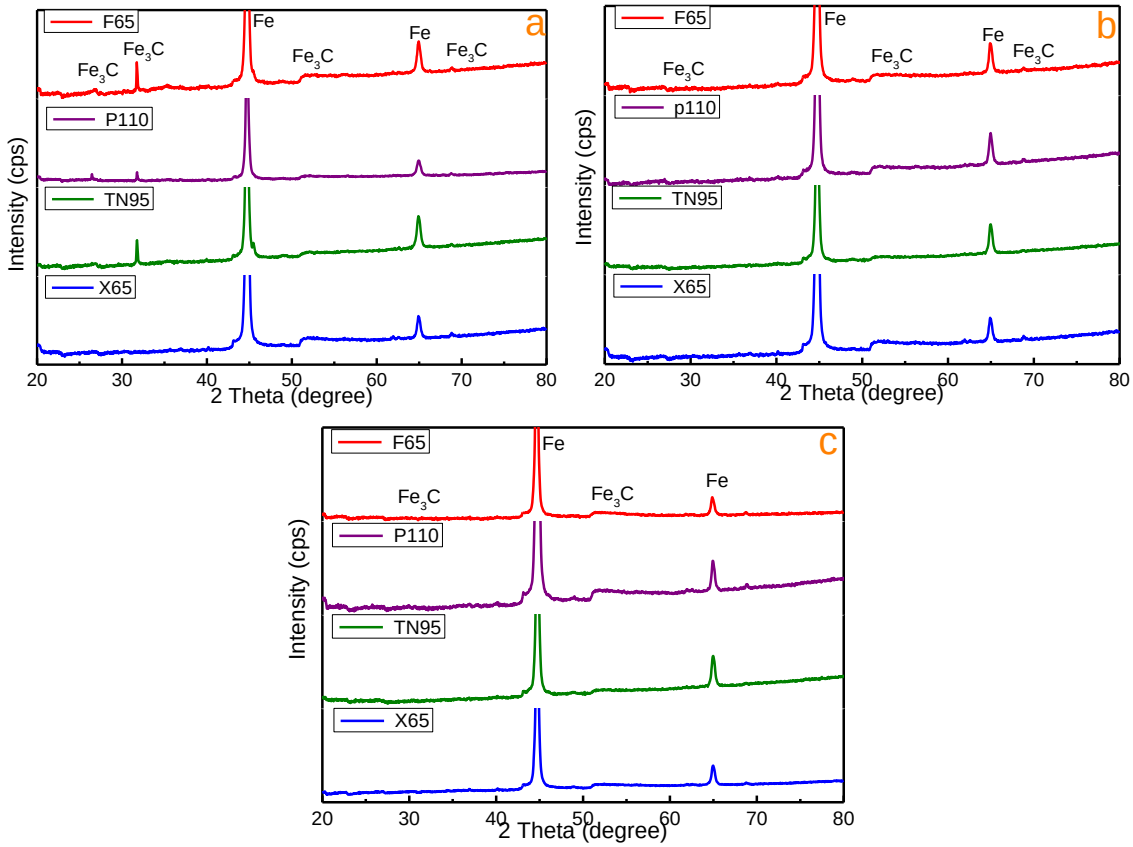

Figure 5- 31: XRD pattern of the steels in unbuffered 3.5 wt% NaCl Solution Saturated with 0.5% CO_2 at (a) 25^0C, (b) 54^0C and (c) 60^0C

Figure 5-32 shows the bi-logarithmic plots of weight loss (W) against time (t) for the 24 hours LPR data points for the specimens corroded in 3.5 wt% NaCl solutions containing 0.5% CO_2 at 25^0C, 45^0C and 60^0C. These plots obeyed the long term prediction models given by the expression in Equation 5-4 which can be represented by a log-log equation shown in Equation 5-5.

$$W = At^B \qquad 5\text{-}4$$

$$\text{Log } W = \text{Log } A + B\text{Log } t \qquad 5\text{-}5$$

Where W is weight loss (mg), t is time (hrs) while A is a constant representing the intercept on the weight loss axis and can be considered as the initial corrosion resistance (ie W = A when t = 1). B is also a constant depicting the slope of the plot. The values of these constants and the correlation coefficient (R^2) are shown in Figure 5-32.

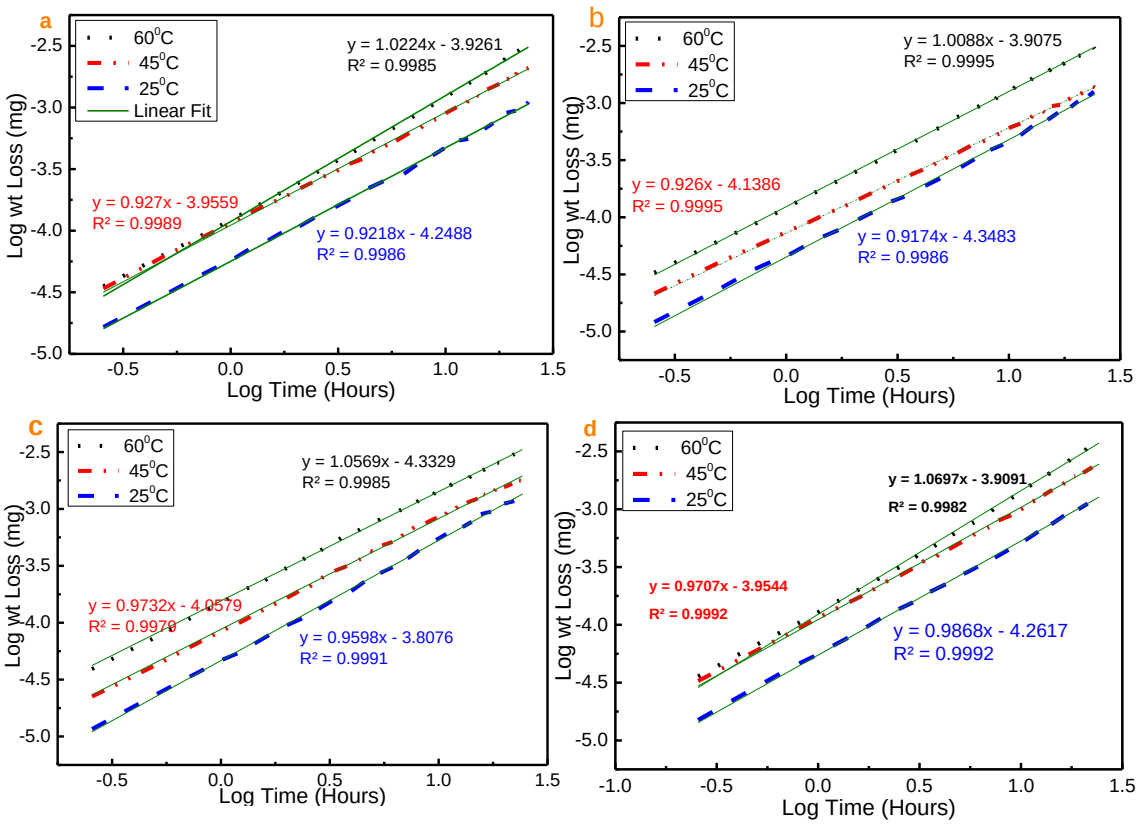

Figure 5- 32: Bi-logarithmic plots of the 24 hours LPR date of the steels corroded in 3.5 wt% NaCl solutions containing 0.5% CO_2 at different temperatures (a) F65, (b) P110, (c) TN95 and (d) X65

The values of B signified the corrosion kinetic of the corroding steels. B < 1 indicates corrosion deceleration process, B > 1 means an acceleration process while B = 1 suggests that the corrosion rate is constant [163, 164, 211]. The value of B for all the specimens increased with temperature signifying increase in corrosion kinetic with temperature. This corroborates with the LPR results of this work. R^2 values are almost equal to 1 for all the specimens indicating that the fitted model explained all the variables of the response data around its mean [211].

5.1.5 Effect of pH on the corrosion behaviour of the steels in 0.5 % CO_2 environments

The corrosion susceptibility of the three proprietary micro-alloyed steels and API 5L X65 as the reference specimen were studied in 3.5 wt% NaCl solution saturated with 0.5% CO_2 at 60^0C and different pH (3.5, 5 and 6.5). Linear polarization resistance (LPR) technique, Tafel polarization and surface analysis (SEM/EDAX and XRD) technique were used in these investigations. The results of these studies are presented in this section.

5.1.5.1 Linear Polarization Resistance (LPR)

The LPR curves for the specimens corroded in 3.5 wt% NaCl solutions saturated with 0.5% CO_2 at 60^0C and different pH values are shown in Figure 5-33.

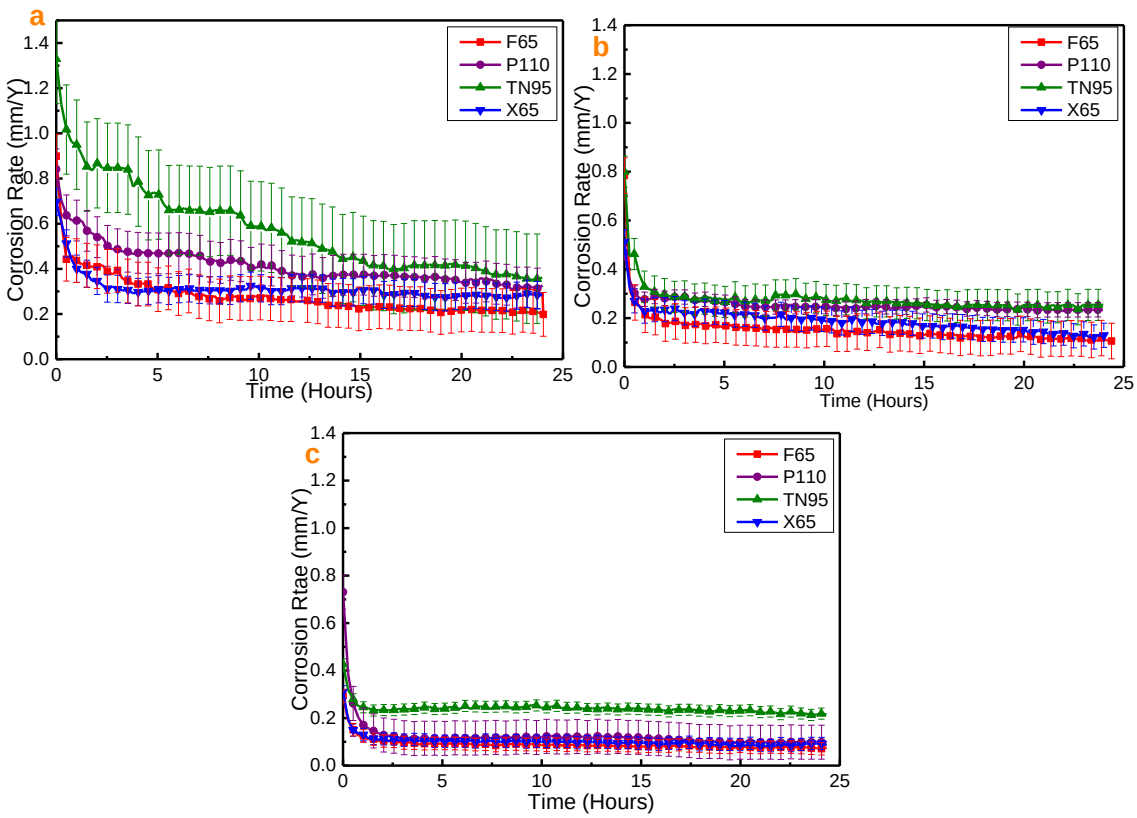

Figure 5- 33: Evolution of corrosion rate with time of the steels in 3.5 wt% NaCl saturated with CO_2 at 60^0C (a) pH 3.5 (b) pH 5 and (c) pH 6.5

It can be observed from this figure that there was a sharp decrease in corrosion rate for all the steels in the three pH values within the first 3 hours after which a relatively stable corrosion rate was maintained throughout the 24 hours experiment. The values at which the corrosion rate stabilized decreased with increase in pH. For instance, steel P110 became stable at the corrosion rate of about 0.45 mm/y in pH 3.5. However, this stability occurred at 0.38 mm/y in pH 5.0 and deceased further to about 0.12 mm/y in pH 6.5. Similarly the period during which the corrosion rate became relatively stable decreased with increase in pH. For instance, the corrosion rate of steel F65 became relatively stable within 7 hours in pH 3.5 solution but decreased to about 2 hours in pH 5 solution with further decrease to about 1 hour in pH 6.5 NaCl solution. This signified that the rate of deposition of corrosion products increased with increase in pH. This is made more clearer in Figure 5-34 which compared the corrosion rates of individual steels in the three pH values and revealed that the stability of the corrosion at pH 3.5 for the specimens was not

as pronounced as at higher pH values. All other specimens exhibited similar trend. It is also evidence from Figures 5-33 and 5-34 that the corrosion rate (CR) of the steels decreased with increase in pH and vice versa. Similar results have been reported by other authors [212, 213]. Both figures also show that the corrosion rate of all the specimens can be ranked as $CR_{F65}<CR_{X65}<CR_{P110}<CR_{TN95}$.

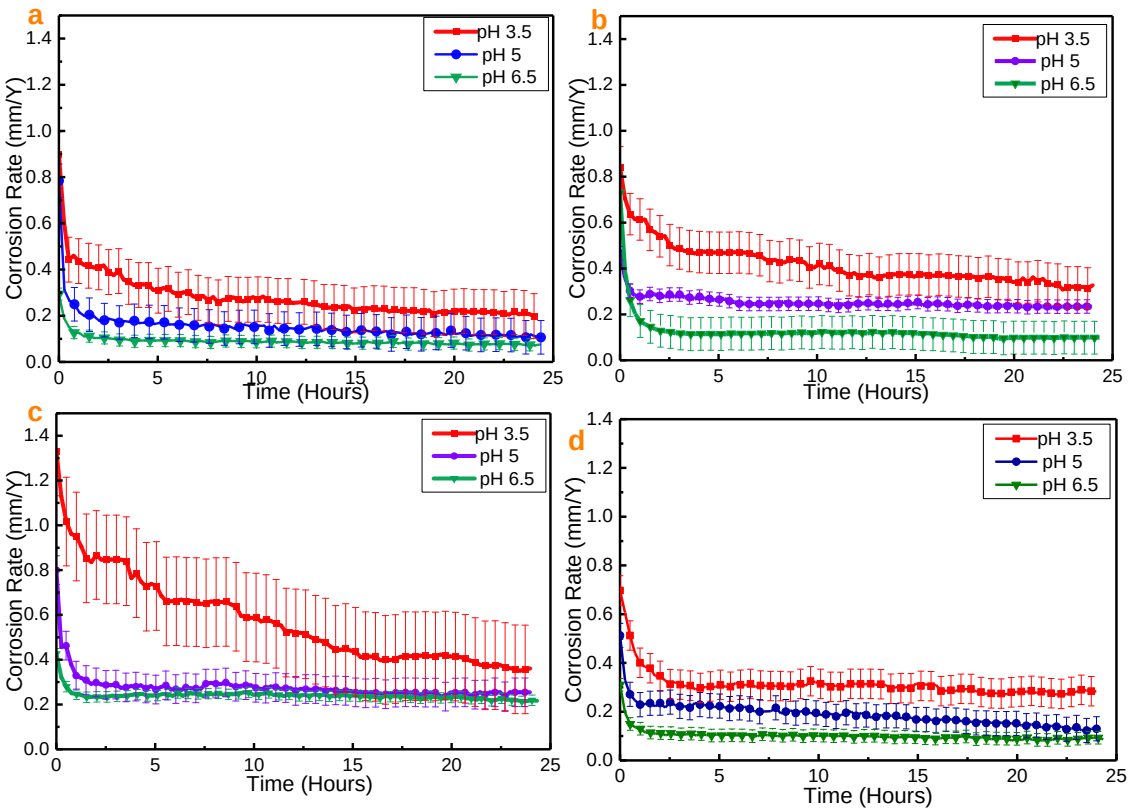

Figure 5- 34: Evolution of corrosion rate with time of the steels in 3.5 wt% NaCl saturated with CO_2 at 60^0C and different pH; (a) F65, (b) P110, (c) TN95 and (d) X65

5.1.5.2 Tafel extrapolation measurements

Tafel extrapolation measurements were conducted to access the corrosion resistance of the micro-alloyed steels in different pH values. These measurements were performed at a scan rate of 0.5 mV/sec. The Tafel branches were scanned separately with an effective sweep range of ±250 $mV_{(OCP)}$. Figure 5-35 shows the Tafel plots of the steels corroded in 3.5 wt% NaCl saturated with 0.5% CO_2 at 60^0C and different pH values. This figure revealed that both the anodic and cathodic branches exhibited Tafelian behaviour with the anodic current density increasing continuously with increase in potential within the lower over potential which can be attributed to activation control reactions.

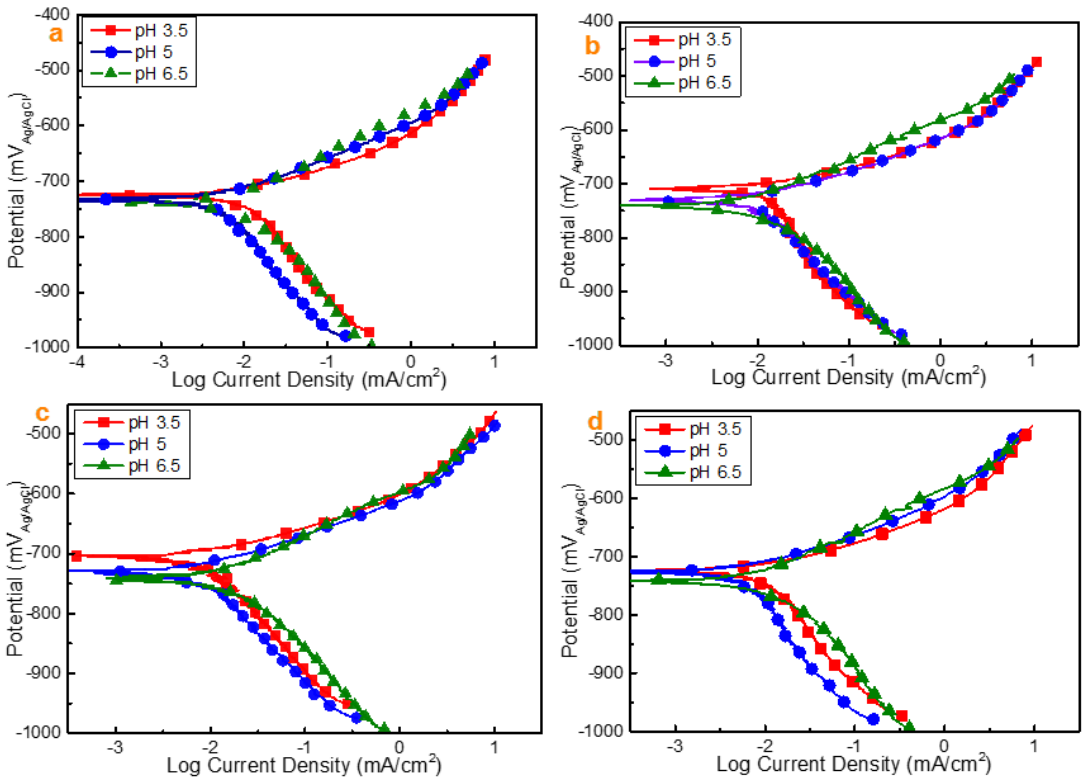

Figure 5- 35: Tafel plots of the steels in 3.5 wt% NaCl saturated with 0.5% CO_2 at 60^0C and different pH; (a) F65, (b) P110, (c) TN95 and (d) X65

The Tafel parameters recorded in Table 5-7 were obtained by extrapolating the anodic and cathodic Tafel curves to intersect at the corrosion potential (E_{Corr}) in accordance with ASTM G102-89 standard. The slopes of the anodic and cathodic branches gave the anodic (β_a) and cathodic (β_c) Tafel constants while the value of the current density at the intersect of the Tafel branches gave the corrosion current density (i_{Corr}). Figure 5-36 used the Tafel plot of steel F65 in 3.5 wt% NaCl solution saturated with 0.5% CO_2 at 60^0C and pH 5 to illustrate how Tafel extrapolation parameters were obtained. It can be observed from Table 5-7 that there was a cathodic shift (move towards the negative direction) in corrosion potentials with increase in pH. This is contrary to the conventional definition that the more negative the E_{corr}, the less noble the material. According to C op't et al [33] this revealed that the understanding of (physical) structure-corrosion relationships is somewhat non-intuitive. However, the corresponding corrosion current density decrease with increase in pH indicating lower anodic dissolution with increase in pH.

Table 5- 7: Tafel extrapolated parameters of the steels in 3.5 wt% NaCl saturated with CO_2 at 60^0C and different pH

Tafel Parameters	pH 3.5				pH 5.0				pH 6.5			
	F65	P110	TN95	X65	F65	P110	TN95	X65	F65	P110	TN95	X65
Ecorr (mV)	-726	-710	-705	-724	-733	-731	730	-726	-740	-741	-742	-741
β_a (mV/decade)	42	33	43	41	58	46	55	53	63	73	54	47
B_c (mV/decade)	110	112	171	141	202	134	167	251	89	96	72	58
i_{Corr} (µAmp/cm^2)	6.7	8.1	8.3	7.3	5.3	7.6	7.8	6.6	5.1	6.7	7.4	4.9

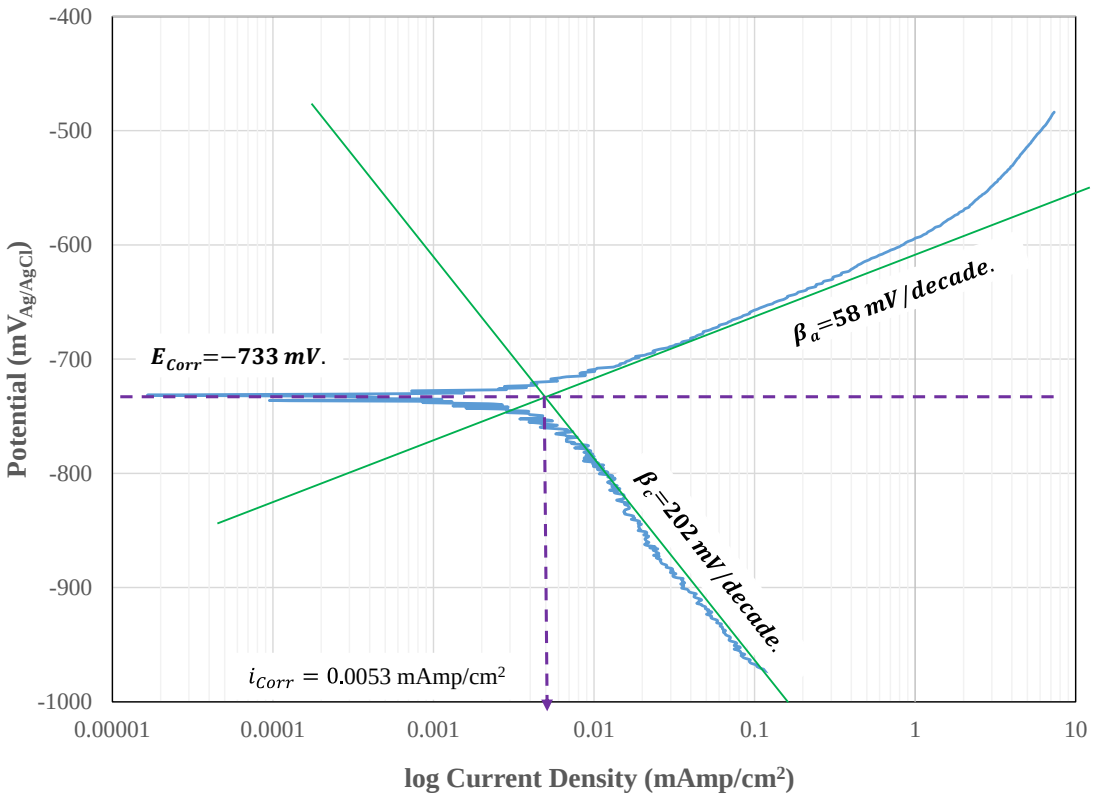

Figure 5- 36: Tafel plot of F65 in 3.5 wt% NaCl solution saturated with 0.5% CO_2 at 60^0C and pH 5 displaying Tafel extrapolation parameters.

5.1.5.3 Surface analyses

The SEM surface morphology of the specimens corroded in different pH values are shown in Figures 5-37, 5-38 and 5-39. These figures showed that the aggressiveness of the corrosion attack decreased with increase in pH exhibiting a more pronounced embossed pattern with lower pH for the steels that have ferrite-pearlite microstructures. Like the morphology of the steels in temperature variation experiments, there were no evident of

significant formation of corrosion products. The absence of corrosion products was corroborated by the EDS analysis which revealed the major elemental composition of the surface morphology as Fe, C and O with Mn, Cr, Si, and Cu in traces. The EDS elemental analysis at two locations on the SEM micrographs of the specimens corroded in 3.5 wt% NaCl solution saturated with 0.5% CO_2 at 60^0C and pH 3.5 (Figure 5-37) is shown in Table 5-8

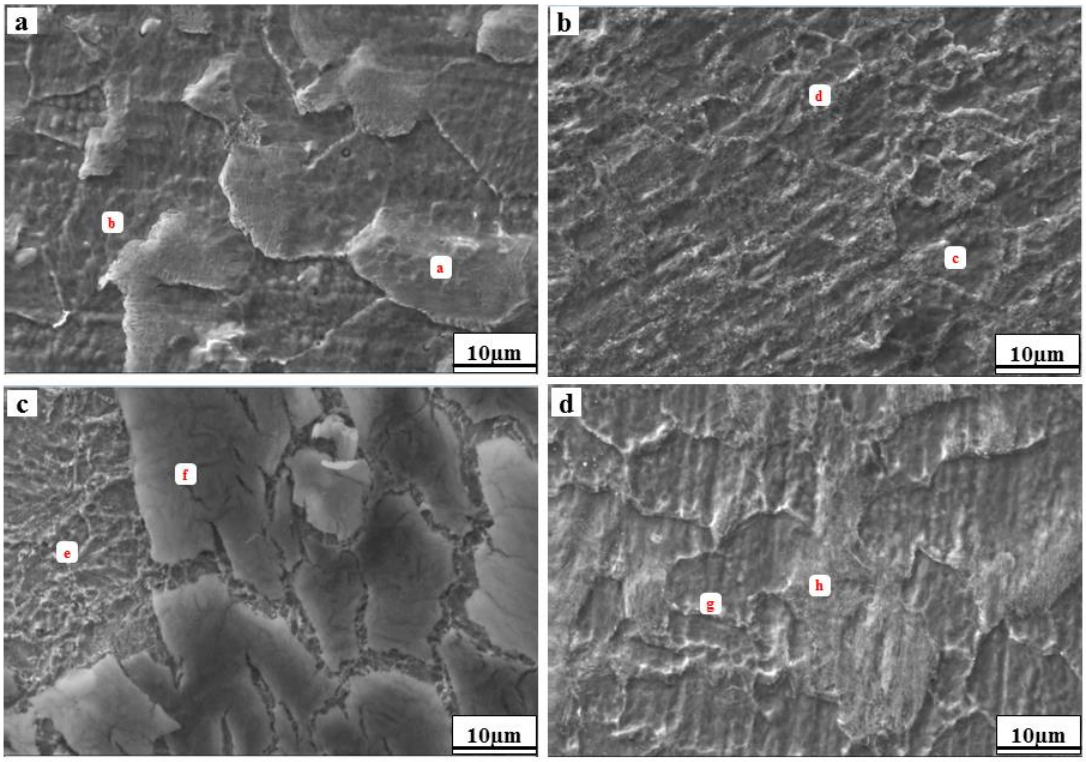

Figure 5- 37: SEM micrographs of the specimens corroded in 3.5 wt% NaCl solution saturated with 0.5% CO_2 at 60^0C and pH 3.5; (a) F65, (b) P110, (c) TN95 and (d) X65

A closer look at Figure 5-37 (C) revealed that the surface morphology of TN95 corroded in pH 3.5 did not exhibit the characteristic embossed pattern of ferrite-pearlite microstructure but displayed a loosely held and partly detached corrosion product. This indicated the formation of double corrosion layers which has been reported in literature [133, 202, 214] as primary (inner) and secondary (outer) layers respectively. The SEM micrographs of the same steel (TN95) corroded in environments at higher pH (Figure 5-38 (C) and Figure 5-39 (C)) did not show such double layer but displayed a loosely held, flaky and cracked corrosion products signifying less corrosion attack.

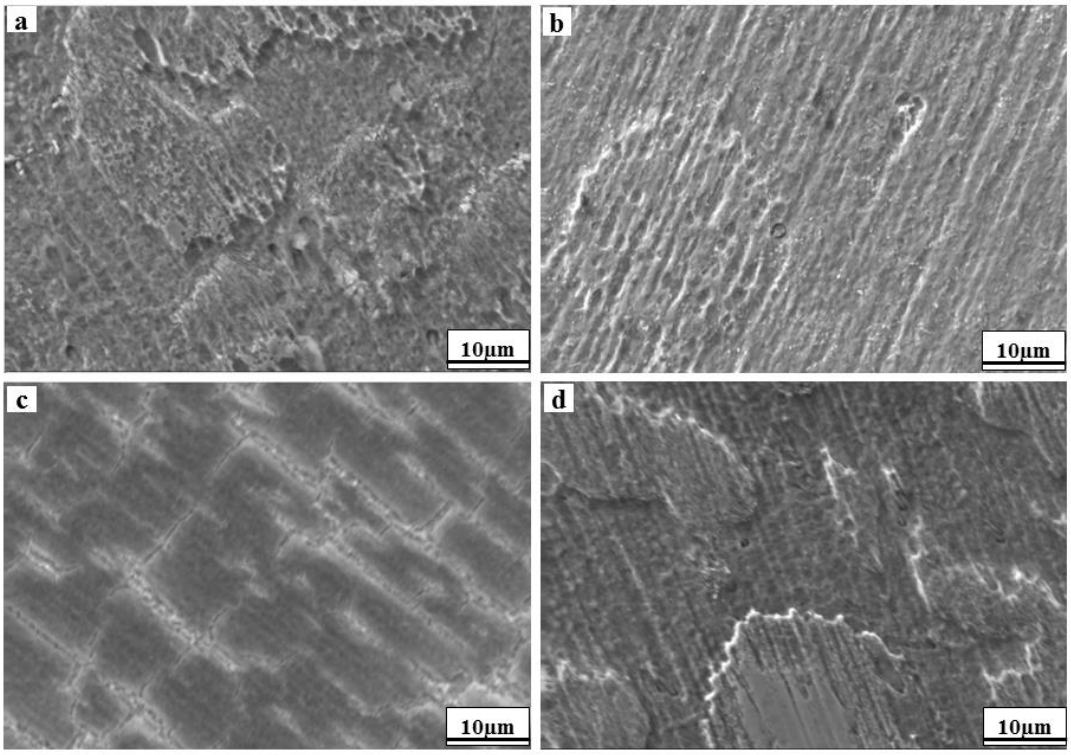

Figure 5- 38: SEM micrographs of the specimens corroded in 3.5 wt% NaCl solution saturated with 0.5% CO_2 at 60^0C and pH 5; (a) F65, (b) P110, (c) TN95 and (d) X65

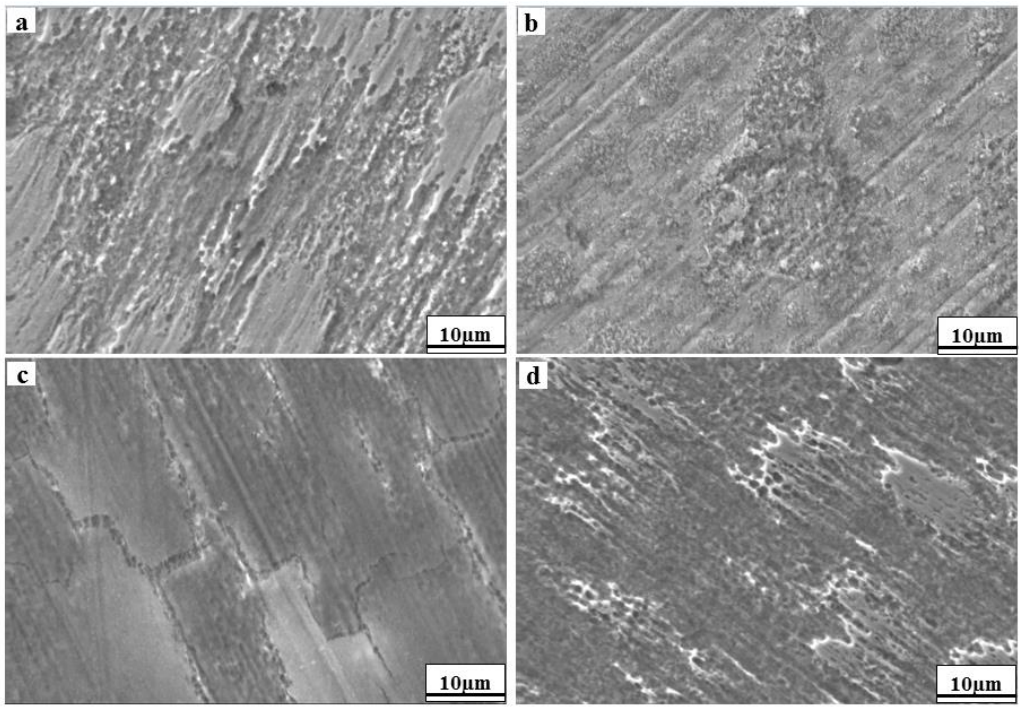

Figure 5- 39: SEM micrographs of the specimens corroded in 3.5 wt% NaCl solution saturated with 0.5% CO_2 at 60^0C and pH 6.5; (a) F65, (b) P110, (c) TN95 and (d) X65

Table 5- 8: EDS elemental analysis at two sites on the SEM micrographs of the specimens corroded in 3.5 wt% NaCl solution saturated with 0.5% CO_2 at 60^0C and pH 3.5 as in Figure 5-37

Samples	Site	C	O	Cu	Mn	Cr	Si	Fe
F65	a	6.24	-	0.74	0.94	0.16	0.26	91.65
	b	8.55	3.43	0.89	0.71	0.26	0.21	85.76
P110	c	7.34	4.57	7.66	1.00	-	0.18	79.25
	d	8.28	6.89	11.53	0.94	0.18	0.15	72.03
TN95	e	2.76	-	-	0.59	1.05	0.17	95.44
	f	6.96	4.65	-	0.60	1.49	-	85.39
X65	g	6.61	4.03	0.52	1.38	0.22	0.24	86.69
	h	9.56	3.39	0.41	1.30	-	0.19	85.15

From the results in Table 5-8, it may be assumed, as is the inherent attribute of CO_2 corrosion of carbon steel, that the corrosion product is $FeCO_3$. However, $FeCO_3$ was not detected by the XRD analyses of the surface of the corroded specimens shown in Figure 5-40. The XRD pattern showed Fe_3C as the main phase on all the steel substrates.

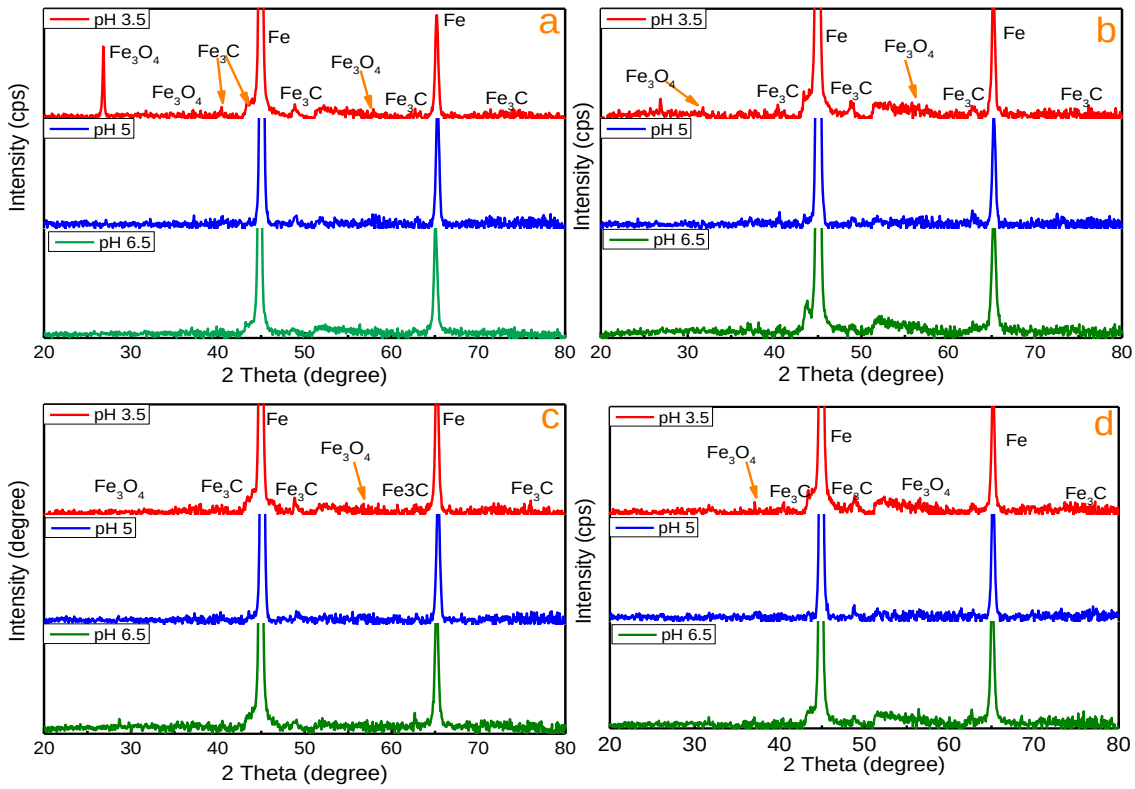

Figure 5- 40: XRD spectra of the steels corroded in 3.5 wt% NaCl solution saturated with 0.5% CO_2 at 60^0C and different pH (a) F65, (b) P110 (c) TN95 and (d) X65

5.1.6 Assessing the corrosion behaviour of the micro-alloyed steels in simulated seawater (Lyman and Fleming solutions).

The proprietary micro-alloyed steels were subjected to electrochemical corrosion tests in naturally aerated and 0.5% CO_2 saturated Lyman and Fleming solution so as to investigate the corrosion performance of the steels and to validate the corrosiveness of the two corrosive environments. The composition of Lyman and Fleming formula is listed in Table 4-7 and is equivalent to the constituents of ASTM D1141-98 (updated 2013) which is the standard practice for the preparation of substitute ocean water. Electrochemical polarization techniques such as linear polarization resistance and Tafel extrapolation coupled with surface analysis techniques such as SEM/EDS and XRD were used for this investigation and the results are presented in this section.

5.1.6.1 Linear polarization resistance (LPR) measurements of the steels in simulated seawater (Lyman and Fleming solutions).

Linear polarization resistance measurements were performed using a scan range of 15 $mV_{(Ag/AgCl)}$ and a scan rate of 0.25 mV/sec in naturally aerated and 0.5% CO_2 saturated Lyman and Fleming solutions at 25^0C, pH 6.5 and for 24 hours. Figure 5-41 shows the evolution of corrosion rate with time for the micro-alloyed steels corroded in naturally aerated and 0.5% CO_2 saturated simulated seawater at 25^0C, pH 6.5 and for 24 hours.

Figure 5-41 (a) shows the corrosion rate with time of the steels immersed in naturally aerated Lyman and Fleming solutions. This figure revealed that there was an initial increase in corrosion rate forming a threshold within the period of 0.5 to 2.5 hours of immersion. This increase peaked at about 1.2 mm/y for steel P110 within the first 2 hours, rapidly decreased to about 0.53 mm/y in the 11th hour and then remains relatively stable throughout the remaining duration for the test. All the other specimens displayed similar corrosion trend with steel F65 appearing stable at 0.3 mm/y, steel TN95 at 0.64 mm/y and X65 at 0.48 mm/y. On the other hand, it can be deduced from Figure 5-41 (b) that all the steels upon immersion in 0.5% CO_2 saturated Lyman and Fleming solution began to corrode at a relatively high corrosion rate (0.2 – 0.52 mm/Y) but decreased rapidly to a seemingly steady rate within the first 3 to 4 hours depending on the specimen. For instance, steel TN95 decreased from an initial corrosion rate of 0.52 mm/y to 0.20 mm/y in the first 2.5 hours of immersion. This is about 62% decrease in corrosion rate.

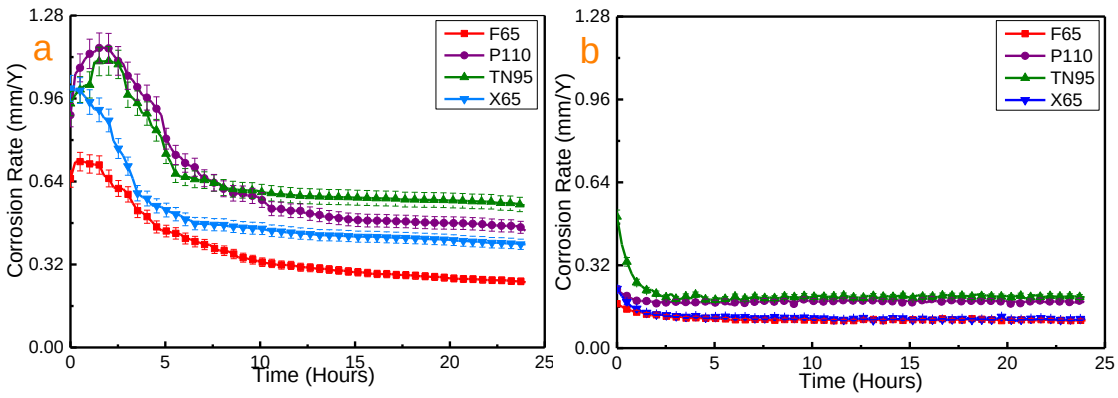

Figure 5- 41: Evolution of corrosion rate with time for the micro-alloyed steels in simulated seawater at 25^0C, pH 6.5 and for 24 hours (a) naturally aerated and (b) 0.5% CO_2 saturated

This rapid decrease in corrosion rate can be ascribed to the dissolution of the air-formed oxide film on the surface of the specimens which partially hinders the corrosive species from accessing the surface of the specimens resulting in reduced corrosion rate [21, 94] After this initial decrease, all the specimens exhibited a relatively stable corrosion rate of 0.11 mm/y for steel F65, 0.12 mm/y for steel X65, 0.18 for steel P110 and 0.20 for steel TN95. In general, Figure 5-41 vividly shows that the corrosion rate for all the specimens in both naturally aerated and 0.5% CO_2 saturated Lyman and Fleming solutions can be ranked in ascending order as $CR_{F65} < CR_{X65} < CR_{P110} < CR_{TN95}$.

Figure 5-42 compares the corrosion rate of the individual specimen in naturally aerated and 0.5% CO_2 saturated Lyman and Fleming solutions. It is evidenced from this figure that the corrosion rate for all the specimens was higher in naturally aerated than in 0.5% CO_2 saturated Lyman and Fleming solutions. This difference in corrosion rate ranged from about 50% for steel F65 to about 70% for steel P110.

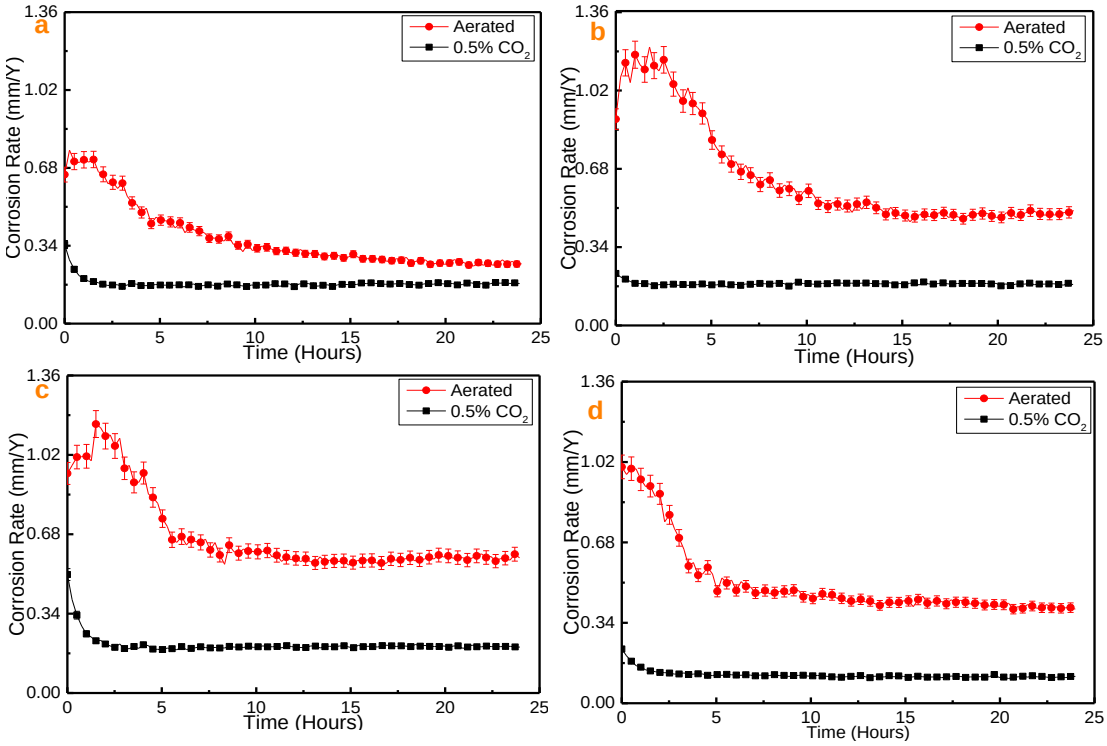

Figure 5- 42: Comparison of the corrosion rate of the micro-alloyed steels in naturally aerated and 0.5% CO_2 saturated simulated seawater at 25^{0}C, pH 6.5 and for 24 hours (a) F65, (b) P110, (c) TN95 and (d) X65

5.1.6.2 Tafel extrapolation measurements of the steels corroded in aerated and 0.5% CO_2 saturated simulated seawater at 25^{0}C, pH 6.5 and for 24 hours.

The corrosion characteristics of the steels were also assessed in naturally aerated and 0.5% CO_2 saturated simulated seawater at a 25^{0}C, pH 6.5 and for 24 hours using Tafel polarization. The Tafel plots were obtained using a scan rate of 0.5 mV/sec and a sweep range of ±250 $mV_{(Ag/AgCl)}$. Figure 5- 43 shows the Tafel plots for all the specimens in both naturally aerated and 0.5% CO_2 saturated simulated seawater solutions.

It can be observed from Figure 5-43, that all the specimens exhibited the similar corrosion behaviour in both solutions suggesting similar corrosion mechanism and that no passive film was formed [67, 206, 215]. This is evidenced by the continuous increase in anodic current density with increase in potentials thus displaying a well-defined anodic Tafel region. Alternatively, the cathodic polarization curves for all the steels exhibited a mixed activation- and diffusion- controlled characteristics for all the steels. However this is more pronounced in the aerated environment where limiting diffusion current density was observed. Henriquez, et al [204] ascribed this behaviour to the mass-transport limitation (seemingly current plateau) of hydrogen evolution reduction.

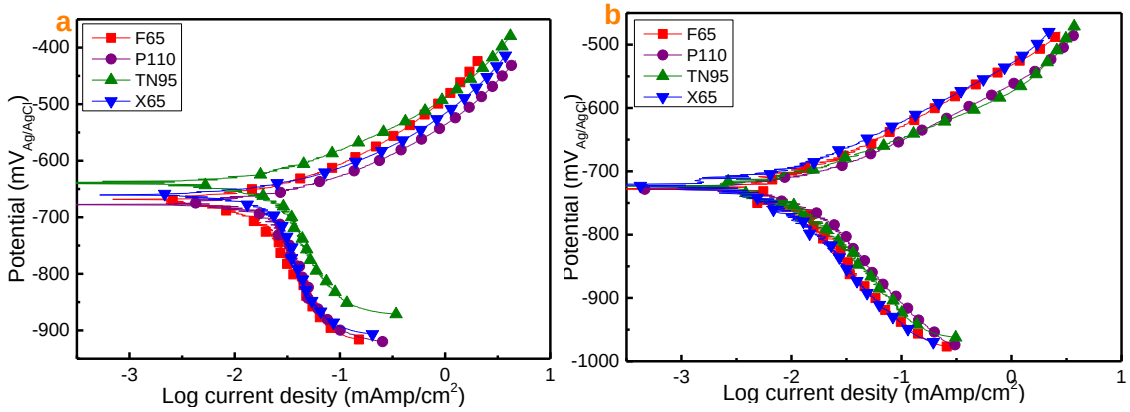

Figure 5- 43: Tafel plots of the micro-alloyed steels corroded in simulated seawater at 25^0C and pH 6.5 (a) naturally aerated and (b) 0.5% CO_2 saturated

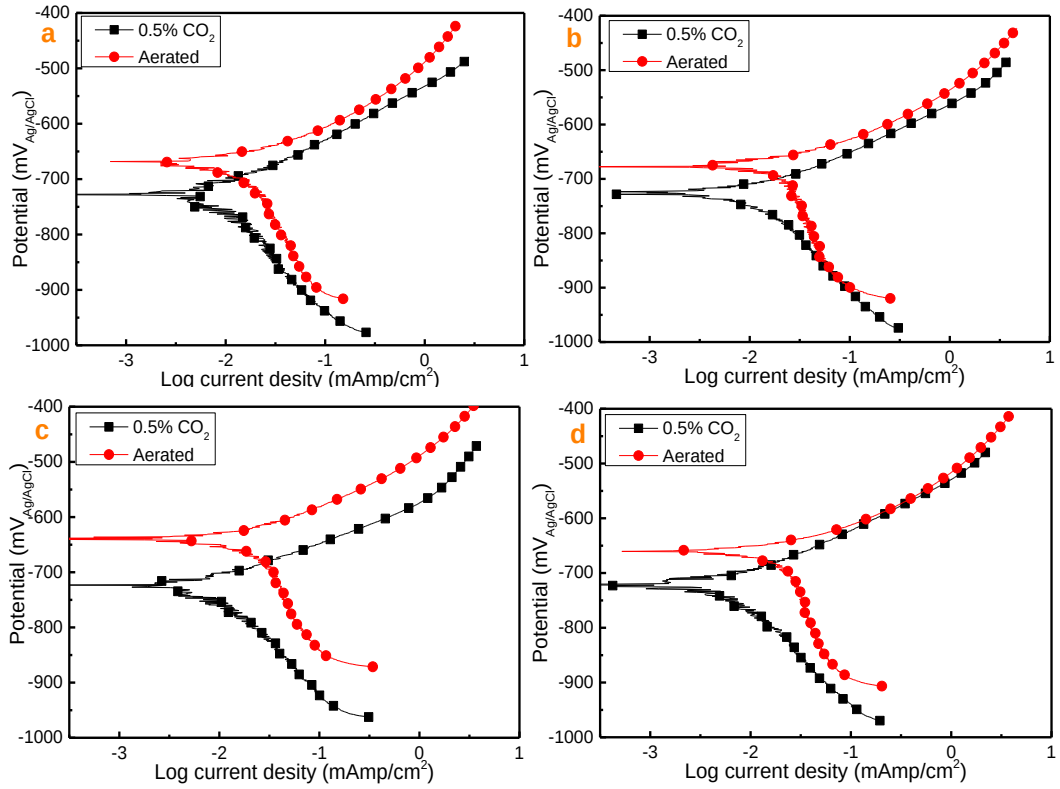

Figure 5- 44: Comparing Tafel plots of the micro-alloyed steels corroded in naturally aerated and 0.5% CO_2 saturated simulated seawater at 25^0C and pH 6.5 (a) F65, (b) P110, (c) TN95 and (d) X65

Figure 5-43 also showed significant variation in the corrosion behaviour of the steels in aerated environment revealing a variation in current density i_{Corr} from 0.95 $\mu Amp/cm^2$ for steel F65 to a maximum of 1.55 $\mu Amp/cm^2$ for steel TN95. The corrosion potential of the steels also showed a variation that spanned within 40 $mV_{(Ag/AgCl)}$ in aerated environment whereas in 0.5% CO_2 saturated electrolyte the corrosion potential varied

within 10 $mV_{(Ag/AgCl)}$. This variation in corrosion behaviour is made more vivid in Figure 5-44 and Tables 5-9 and 5-10 which compared the Tafel plots and the values of Tafel extrapolation parameters for the steels in naturally aerated and 0.5% CO_2 saturated simulated seawater solutions at 25^0C and pH 6.5 respectively.

Table 5- 9: Tafel extrapolation parameters of the steels corroded in naturally aerated simulated seawater at 25^0C and pH 6.5

Samples	E_{corr} (mV)	I_{corr} (mAmp/cm^2)	β_a (mV/decade)	β_c (mV/decade)	Rp(Ω)	CR (mm/Y)
F65	-668	0.0095	57	165	1936.37	0.110
X65	-661	0.0097	45	100	1389.25	0.113
P110	-676	0.0104	48	102	1362.77	0.121
TN95	-639	0.0155	72	181	1443.00	0.180

Figure 5-44 revealed that the corrosion potentials are more negative in 0.5% CO_2 saturated solutions than in aerated solution varying from -49 mV vs OCP for steel P110 to a maximum of -84 mV vs OCP for steel TN95. The cathodic polarization curves displayed more limiting diffusion current density which can be attributed to the presence of dissolved oxygen (DO) in the aerated solution thus facilitating corrosion rate.

Table 5- 10: Tafel extrapolation parameters of the steels corroded in 0.5% CO_2 saturated simulated seawater at 25^0C and pH 6.5

Samples	E_{corr} (mV)	I_{corr} (mAmp/cm^2)	β_a (mV/decade)	β_c (mV/decade)	Rp(Ω)	CR (mm/Y)
F65	-728	0.0062	76	150	3532.73	0.072
X65	-722	0.0064	75	155	3429.19	0.074
P110	-725	0.0068	57	115	2433.56	0.079
TN95	-723	0.0085	75	175	2681.92	0.099

The values of cathodic Tafel constants (β_c) as shown in Tables 5-9 and 5-10 for all the specimens are more than the corresponding anodic Tafel constants (β_a). This behaviour according to Yin, et al [205] shows that the overall corrosion processes were mainly under the control of cathodic reactions. This is elucidated by higher cathodic current curves in the naturally aerated solutions than in 0.5% CO_2 saturated solutions as presented in Figure 5-44.

5.1.6.3 Surface morphology examinations of the steels corroded in naturally aerated and 0.5% CO_2 saturated simulated seawater at 25^0C, pH 6.5 and for 24 hours.

The surface of the micro-alloyed steels after corrosion in naturally aerated and 0.5% CO_2 saturated simulated seawater at 25^0C, pH 6.5 and for 24 hours was examined and analysed using SEM/EDS and XRD techniques. Figure 5-45 compares the surface morphology of the four micro-alloyed steels corroded in aerated Lyman and Fleming solution at 25^0C, pH 6.5 and for 24 hours. These micrographs revealed corroded surfaces with corrosion products that were not uniformly deposited but had peeled off from the steel substrates indicating the formation of double layer corrosion products.

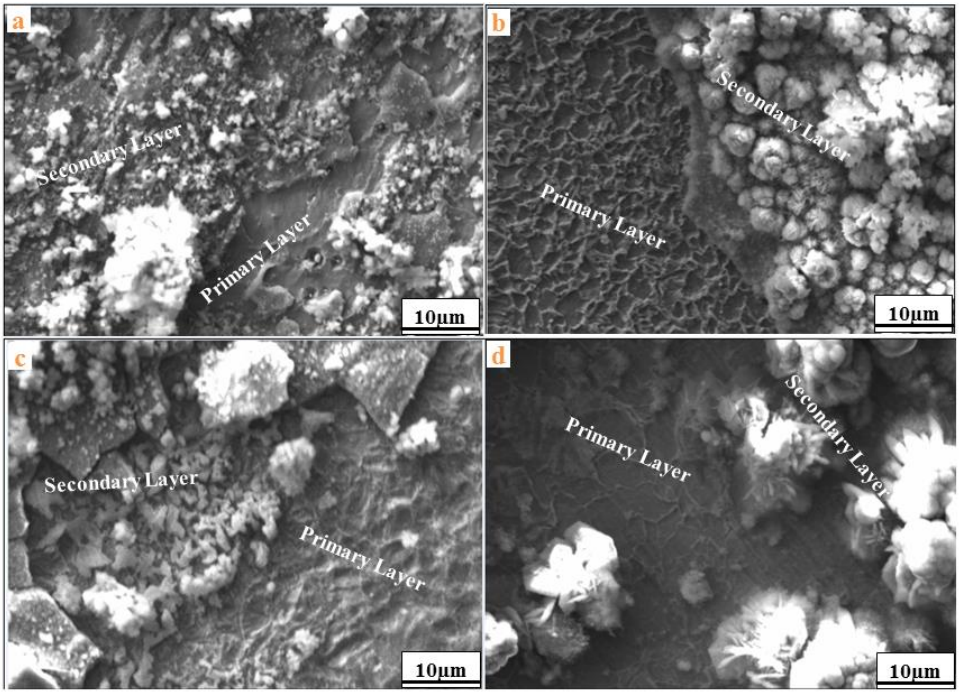

Figure 5- 45: SEM Micrographs of the samples corroded in aerated simulated water for 24 hrs at 25^0C and pH 6.5: (a) F65, (b) P110, (c) TN95 and (d) X65

The EDS analysis of the surface indicated Fe, O and C as the major elements while Ca, Si, Mn, Cr etc were in traces. Mg was not detected on any of the corroded steel substrates regardless of high Mg content in Lyman and Fleming solution as listed in Table 4-7. This was attributed to high solubility of $MgCO_3$ when compared to $CaCO_3$ [216]. Thus $MgCO_3$ was not detected by the XRD analysis as presented in Figure 5-47(a)

The micrographs of the specimens corroded in 0.5% CO_2 saturated Lyman Fleming solution shown in Figure 5-46 revealed corrosion product free surfaces. However, the

characteristics embossed pattern of the corroded surface of ferrite-pearlite microstructures and the ground scratches can clearly be seen in the micrographs of steels F65, P110 and X65. The absence of corrosion products on the surfaces of these steels was corroborated by the XRD analysis which displayed only Fe and Fe_3C peaks as shown in Figure 5- 47(b).

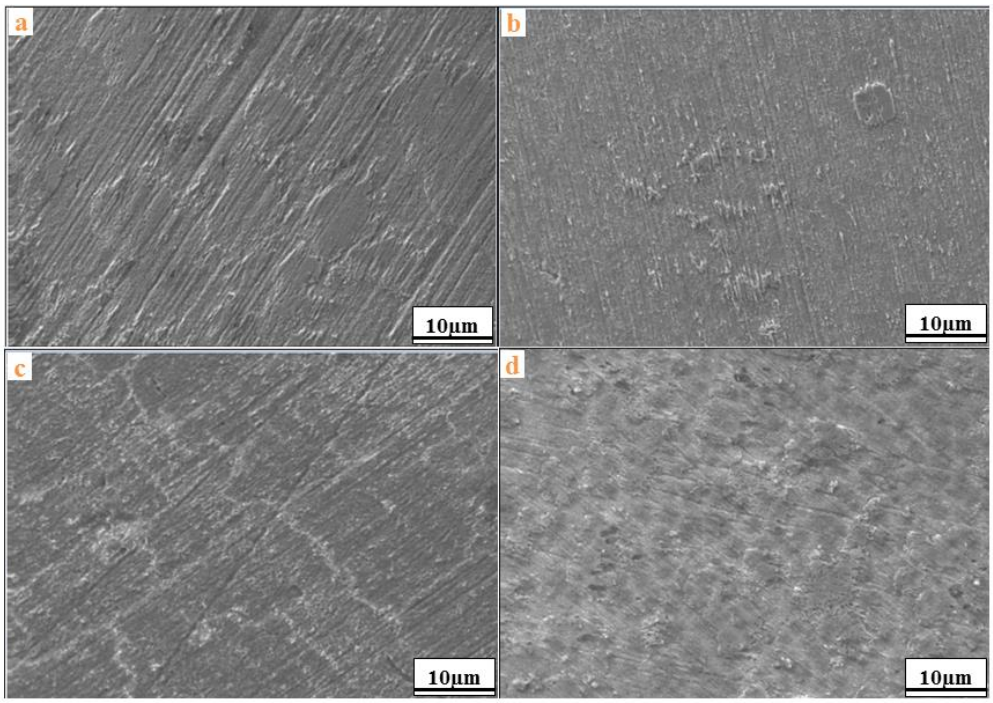

Figure 5- 46: SEM Micrographs of the samples corroded in CO_2 saturated simulated water for 24 hrs at 25^0C: (a) F65, (b) P110, (c) TN95 and (d) X65

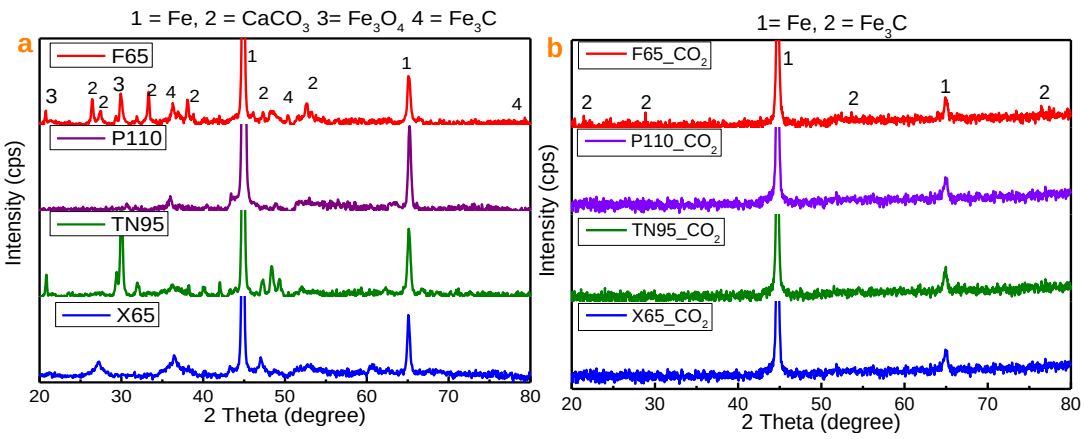

Figure 5- 47: XRD pattern of the samples corroded in simulated seawater for 24 hrs at 25^0C: (a) aerated (b) 0.5% CO_2 Saturated

5.1.7 Assessing the corrosion behaviour of the micro-alloyed steels in 3.5 wt% NaCl using potentiostatic polarization and electrochemical impedance spectroscopy (EIS).

The preliminary investigation performed so far revealed that steels P110 and TN95 have lower corrosion resistance than steels F65 and X65 (the reference specimen). Thus P110 and TN95 were chosen (individually and/or collectively) for further investigations and alloying with Zr and Hf so as to improve their corrosion resistance. Potentiostatic polarization was used to form corrosion products on the specimens while electrochemical impedance spectroscopy (EIS) was used to investigate the ability of the corrosion product scale to protect the surface of the steel from corroding. Prior to each potentiostatic polarization, the specimens were cathodically reduced at - 800 $mV_{(Ag/AgCl)}$ for 30 min to remove air-formed oxides. Two procedures were used in forming the corrosion products. These include:

(i) Applying different anodic potentials (100 $mV_{(Ag/AgCl)}$, 150 $mV_{(Ag/AgCl)}$ and 200 $mV_{(Ag/AgCl)}$) at constant time (24 hours).

(ii) Applying constant anodic potentials (150 $mV_{(Ag/AgCl)}$) for different time interval (1, 2, 4, 8 12 and 24 hours).

For each of these routes, surface analysis techniques such as SEM/EDS, XRD and/or white light profilemetry were used to characterise the structure, thickness, composition of the film and pitting tendency. In the present Section, the results of the investigation of the stability of the corrosion products formed on the micro-alloyed steels using these two routes are presented.

5.1.7.1 EIS investigation of the stability of the corrosion product formed on the steels by applying different anodic potentials at constant time.

For this investigation, only steels P110 and X65 were used. Corrosion products were formed on the surface of steels P110 and X65 using anodic potentials of 100 $mV_{(Ag/AgCl)}$, 150 $mV_{(Ag/AgCl)}$ and 200 $mV_{(Ag/AgCl)}$. Figure 5-48 shows the evolution of current density versus time for specimens P110 and API 5L X65 for the three anodically applied potentials for 24 hours in 3.5 wt% NaCl solution saturated with 0.5 %CO_2 at 60^0C and pH 6.5. This figure shows that the current density increased as the applied potential increased. This agrees with literature reports [4, 206, 217] which indicated that current density increased with potential within the active region due to activation control reaction. It is also very clear from Figure. 5-48 that the measured current density for X65 steel is

lower than that of steel P110. This was attributed to the variation in chemical composition and microstructures of the specimens.

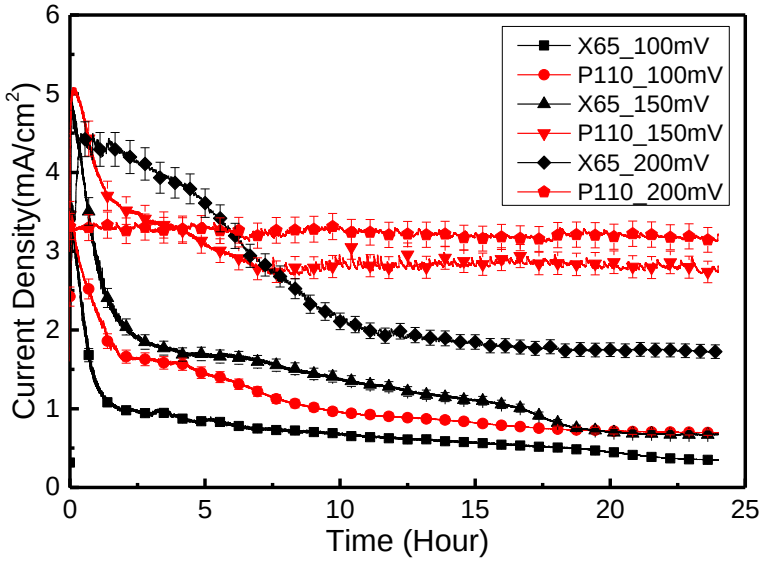

Figure 5- 48: Evolution of current density with time of the specimens for 24 hours potentiostatic polarization at different anodic potentials in 3.5 wt% NaCl solution containing 0.5% CO_2 at 60^{0}C and pH 6.5.

Electrochemical Impedance Spectroscopy Measurements

Figure 5-49 shows the Nyquist plots of specimens P110 and X65 in 0.5% CO_2 containing 3.5 wt% NaCl at 60^{0}C and pH 6.5 after corrosion product was grown at different anodic potentials for 24 hours. The specimens are actively corroding steels and the applied potentials were within the active regions. It can be seen from Figure 5-49 that the Nyquist plots for the two steels in the three applied potentials displayed similar features of one semi-capacitive-arcs at high frequency which is as a result of the non-homogeneity of the surface, frequency dispersion and mass transport resistant [54, 208].

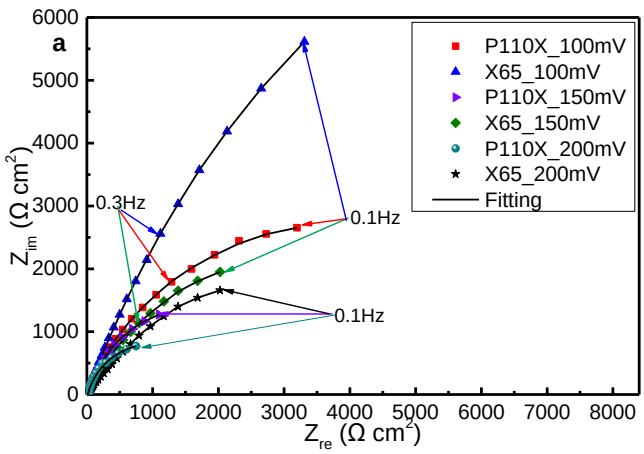

Figure 5- 49: Nyquist plots of the specimens after potentiostatic polarization at different anodic potentials in 3.5 wt% NaCl solution containing 0.5% CO_2 at 60^{0}C and pH 6.5.

It can be seen from the Nyquist plots (Figure 5-49) that increase in applied anodic potential decreased the radius of the capacitive arc demonstrating the effects of high applied potential on actively corroding steels. Experimental evidence have shown that increase in capacitive arc indicates an increase in the film stability (ie ability to resist corrosion) and vice versa [209]. Thus it is obvious from Figure 5-49 that the impedance response for the film formed at 100 $mV_{(Ag/AgCl)}$ (particularly for X65) was higher when compared with that of 150 $mV_{(Ag/AgCl)}$ and 200 $mV_{(Ag/AgCl)}$ indicating better corrosion resistance for film formed at 100 $mV_{(Ag/AgCl)}$. This shows that increasing the applied anodic potential decreases the radius of the semi-arcs. This is the characteristics of actively corroding steels that increase in potential increases the anodic current density [206]. This behaviour can be attributed to the ferrite-pearlite microstructure of the specimens as presented schematically by Sun, et al [113].

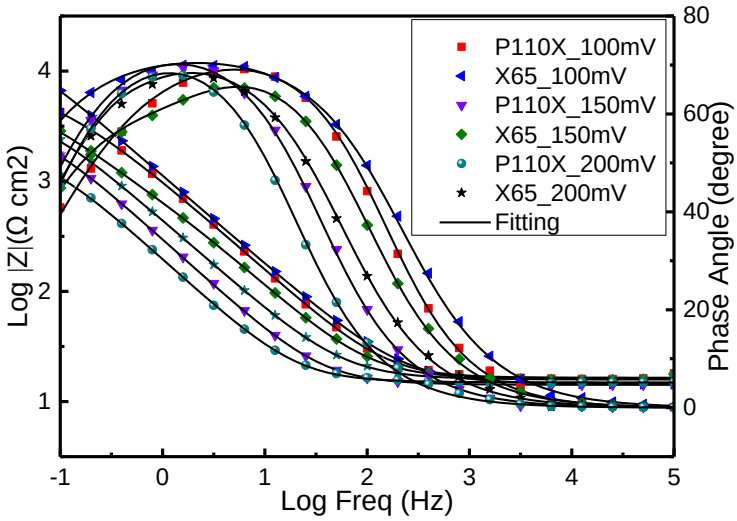

Figure 5- 50: Bode plots of the specimens after potentiostatic polarization at different anodic potentials in 3.5 wt% NaCl solution containing CO_2 at 60^0C and pH 6.5.

The Bode plots of specimens P110 and X65 in 0.5% CO_2 containing 3.5 wt% NaCl at 60^0C and pH 6.5 after corrosion product was grown at different anodic potentials for 24 hours are shown in Figure 5-50. This figure shows that the high frequency impedance magnitude (|Z|), which represents the solution resistance (R_s), is about 16 Ωcm^2 while the phase angle is 0^0 for both specimens and for all the applied potentials. This means that at high frequency, the impedance value was determined by the resistance of the electrolyte only. Alternatively, the charge transfer resistance (R_{ct}), which is the low frequency value of impedance lie between 2.0 – 26.0 $K\Omega cm^2$ as shown in Table 5-11. The maximum phase angle values for all the specimens appeared within the intermediate frequencies with the specimen polarized at 100 $mV_{(Ag/AgCl)}$ exhibiting the highest phase angle of 70^0. This

shows that the phase angle values for the two steels decreased with increased anodic (applied) potentials. Similar trend was observed at the low frequency phase angles demonstrating medium values between 40^0 - 60^0 [208, 209]

To elucidate how applied anodic potentials affect the EIS results on the specimens in 0.5% CO_2 containing 3.5 wt% NaCl solution at 60^0C and pH6.5, the simple Randle cell (equivalent electrical circuit, EEC) model consisting of a parallel combination of a double layer capacitance (C_{dl}) and a charge transfer resistance (R_{ct}) corresponding to the corrosion reactions at the metal/electrolyte interface and the electrolyte resistance (Rs) between the working and reference electrodes as shown in Figure 5-26 was used. The constant phase element (CPE) was introduced in the equivalent circuit (EC) instead of pure double layer capacitance. This is to reduce the effect of surface irregularities and compositional inhomogeneity of the steels [54, 208]. The impedance of CPE is defined in Equation 5-3.

Table 5- 11: Fitted EIS data for the specimens after 24 hours potentiostatic polarization at different potentials in 3.5 wt% NaCl solution saturated with 0.5% CO_2 at 60^0C and pH6.5.

Potential (mV)	Specimens	Rs		CPE_{dl}		n		R_{ct}	
		Value ($\Omega.cm^2$)	% Error	Value ($\mu F^{-1}cm^{-2}$)	% Error	Value	% Error	Value ($k\Omega.cm^2$)	% Error
100	P110X	16.19	1.31	$2.2 * 10^{-4}$	2.38	0.983	0.68	6.514	5.48
	X65	14.39	1.6	$2.0 * 10^{-4}$	2.5	0.91	0.72	25.501	7.59
150	P110X	14.18	1.2	$6.70 * 10^{-4}$	2.4	0.87	0.92	3.526	8.75
	X65	15.78	1.4	$3.51 * 10^{-4}$	2.68	0.88	0.84	5.052	7.32
200	P110X	14,93	1.04	$7.04 * 10^{-4}$	2.25	0.82	0.84	1.993	7.08
	X65	15.4	1.18	$4.86 * 10^{-4}$	2.26	0.83	0.75	4.665	7.82

To validate the proposed EEC, the simulated parameters and the % error of the impedance data obtained for the anodically polarised specimens are presented in Table 5-11. The virtually perfect fits of the Nyquist curves (Figure. 5-49) and the simulated data attest to the reliability of the proposed equivalent electrical circuit (EEC) revealing acceptable relative % errors for the corresponding fitted values as indicated in Table 5-11. This table showed that as the applied potential increased, the CPE_{dl} representing the surface

heterogeneity increased reflecting the porosity of the corrosion product film. Alternately, the charge transfer resistance, R_{ct}, decreased as the anodic potential increased indicating faster rate of reactions at the corrosion product/electrolyte interface. This signified that when the applied potential increased, the corrosion rate also increased. This effect was attributed to micro-galvanic effect. The EIS results are in agreement with the trend of the corrosion film formed at different potentials demonstrating a decline in impedance as the applied potential is increased [206, 218].

To further buttress the reliability and effectiveness of the fitted data for the proposed EEC, the relative residual errors for the real (η_{re}) and imaginary (η_{im}) components of the impendence were calculated using Equations 5-8 and 5-9 respectively [206].

$$\eta_{re} = \left(\frac{Z_{re.exp} - Z_{re.fit}}{Z_{re.exp}}\right) * 100\% \qquad 5\text{-}8$$

$$\eta_{im} = \left(\frac{Z_{im.exp} - Z_{im.fit}}{Z_{im.exp}}\right) * 100\% \qquad 5\text{-}9$$

Where $Z_{re.exp}$ and $Z_{re.fit}$ are the real impedance obtained from EIS experimental results and EEC fitting respectively. Similarly $Z_{im.exp}$ and $Z_{re.fit}$ are the imaginary impendences measured from EIS experimental results and EEC fitting respectively. The residual errors can be used to elucidate the quality of the fitting obtained from the chosen EEC.

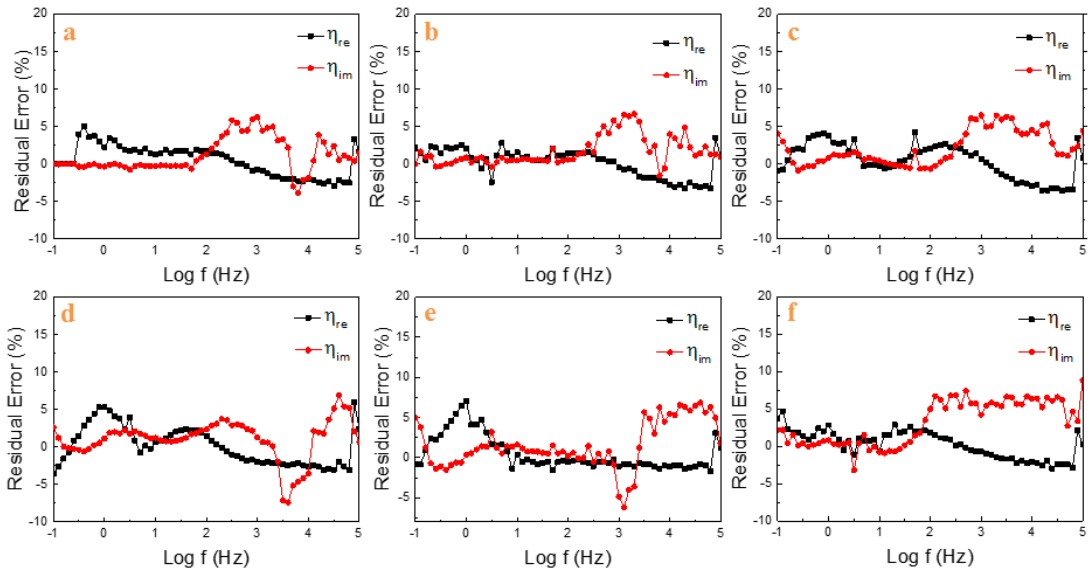

Figure 5- 51: Relative residual error resulting from the equivalent circuits of the specimens after 24 h potentiostaic polarization in 3.5 wt% NaCl solution containing 0.5% CO_2 at 60^0C and pH 6.5 for P110 (a) 100 $mV_{(Ag/AgCl)}$, (b) 150 $mV_{(Ag/AgCl)}$ and (c) 200$mV_{(Ag/AgCl)}$; for X65 (d) 100 $mV_{(Ag/AgCl)}$, (e) 150 $mV_{(Ag/AgCl)}$ and (f) 200 $mV_{(Ag/AgCl)}$

Figure 5-51 shows the relative residual error curves from the equivalent circuits of the specimens after 24 hours potentiostaic polarization in 3.5 wt% NaCl solution containing 0.5% CO_2 at 60^0C and pH 6.5. The two steels exhibited similar curves in all the applied potentials demonstrating relative error values within the range of 6% to 8%. This is almost the same with the values of the relative % errors obtained with ZView interpretation of the EEC. This indicates that the quality of the fit is within acceptable error and attested to a good choice of EEC.

Surface analysis of corrosion product formed on the surface of the specimens using different anodic potentials in 3.5 wt% NaCl solution containing 0.5% CO_2 at 60^0C, pH 6.5 and for 24 hours

Figure 5-52 shows SEM micrograph of the steels illustrating the evolution of surface morphology after 24 hours potentiostatic polarization at 100, 150 and 200 $mV_{(Ag/AgCl)}$ in 3.5 wt% NaCl solution saturated with 0.5% CO_2 at 60^0C and pH6.5.

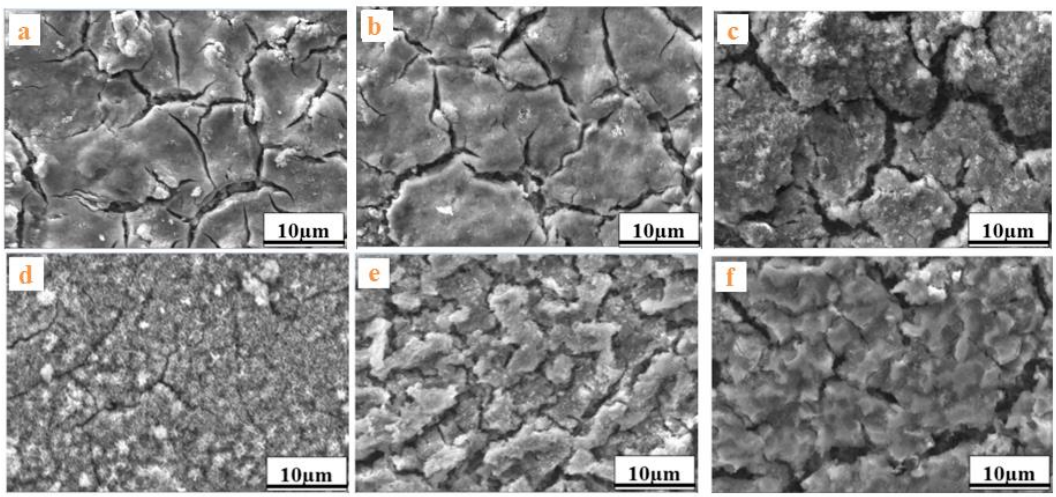

Figure 5- 52: SEM surface morphology of the specimens after 24 hours potentiostatic polarization in 3.5 wt% NaCl solution containing CO_2 at 60^0C and pH 6.5 for P110X (a) 100 $mV_{(Ag/AgCl)}$, (b) 150 $mV_{(Ag/AgCl)}$ and (c) 200 $mV_{(Ag/AgCl)}$ for X65 (d) 100 $mV_{(Ag/AgCl)}$, (e) 150 $mV_{(Ag/AgCl)}$ and (f) 200 $mV_{(Ag/AgCl)}$

The micrographs showed the deposition of porous corrosion layers on the surface of the steels which progressively increased in thickness but decreased in density as the applied potentials increased. This was revealed by the Fiji ImageJ analysis of the film which showed an increase in percent porosity with increase in applied potentials. The micrographs also showed propagation of cracks on the corrosion layers. These cracks became wider and the corrosion layer less adhesive (flaky) with increase in applied

potential indicating the formation of double corrosion layers as presented in Figure 5-53 for steel P110.

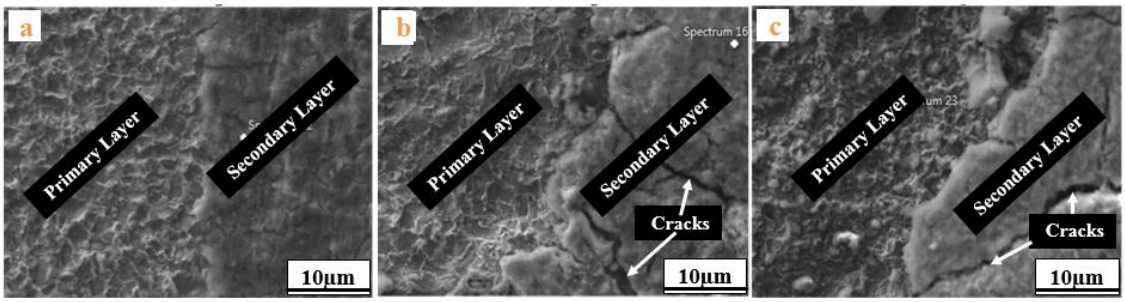

Figure 5- 53: SEM micrographs showing the primary layer and the partially detached secondary layer of steel P110X after 24 hours potentiostatic polarization in 3.5 wt% NaCl solution containing CO_2 at 60^0C and pH 6.5: (a) 100 $mV_{(Ag/AgCl)}$, (b) 150 $mV_{(Ag/AgCl)}$ and (c) 200 $mV_{(Ag/AgCl)}$.

EDS examination showed that the main elemental composition of the corrosion products are Fe, C, and O with traces of some alloying elements. The analysis of the corrosion double layer revealed that the primary layer consists of about (average taken from 4 different points on each layer of steel P110 passivated at 150 mV) 87 %Fe, 2 %O_2 and 6 %C while the secondary layer showed about 69 %Fe, 13 %O_2 and 7 %C. This revealed that there were more Fe in the primary layer and more O_2 in the secondary layer. The presence of higher oxygen content in the secondary layer is in agreement with the oxide of iron identified by XRD pattern shown in Figure 5-54 as Fe_3O_4 while the primary layer was identified as mainly Fe/Fe_3C. Similar observation was reported by Moiseeva and Rashevskaya [148]

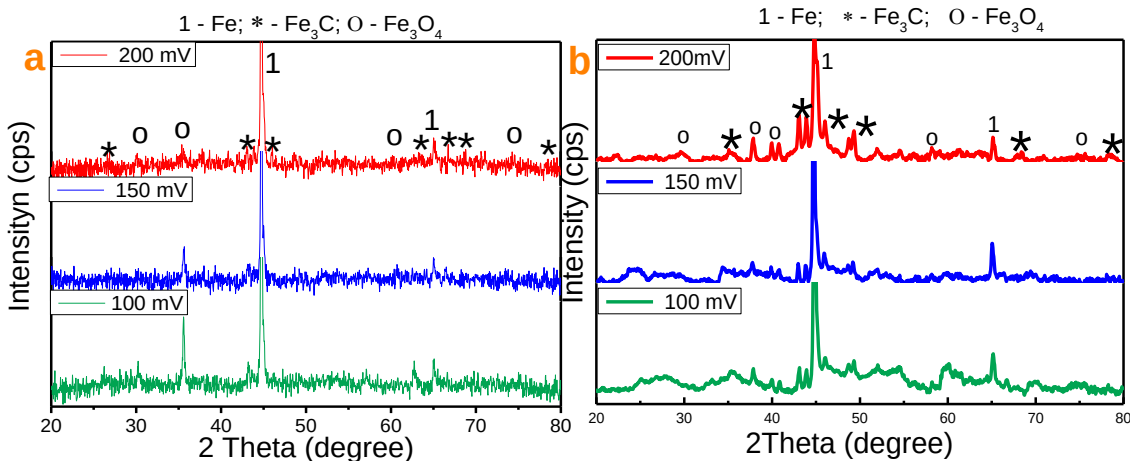

Figure 5- 54: XRD Spectra of the steels after 24 hours potentiostatic polarization at different anodic potentials in 3.5 wt% NaCl solution containing CO_2 at 60^0C and pH 6.5: (a) P110X and (b) X65

The increase in thickness of the corrosion layer with increase in the polarization potential is illustrated in the SEM micrographs of the cross-section of the corroded steels shown in Figure 5-55. It can be seen from this figure that the layers are thick and porous with some cracks. Also there are separations between the steels and the scale demonstrating a small gap where electrochemical active species can penetrate and have contact with the steels. This gap is more pronounced at higher formation potentials and the contact of the solution under the scale with the steel surface enabled continuous corrosion since the scale appeared to have covered the surface of the steels which is porous.

To assess the extent of pitting, the corrosion product was cleaned before conducting scan and profilometry tests. Pits were recorded beneath the corrosion products due to the porosity, non-compact and non-adherent characteristics of the corrosion scales. The SEM micrographs showing the evolution of pits after 24 hours anodic polarization at 100 $mV_{(Ag/AgCl)}$ 150 $mV_{(Ag/AgCl)}$ and 200 $mV_{(Ag/AgCl)}$ in 3.5 wt% NaCl solution containing 0.5% CO_2 at 60^0C and pH 6.5 for the two specimens are shown in Figure 5-56.

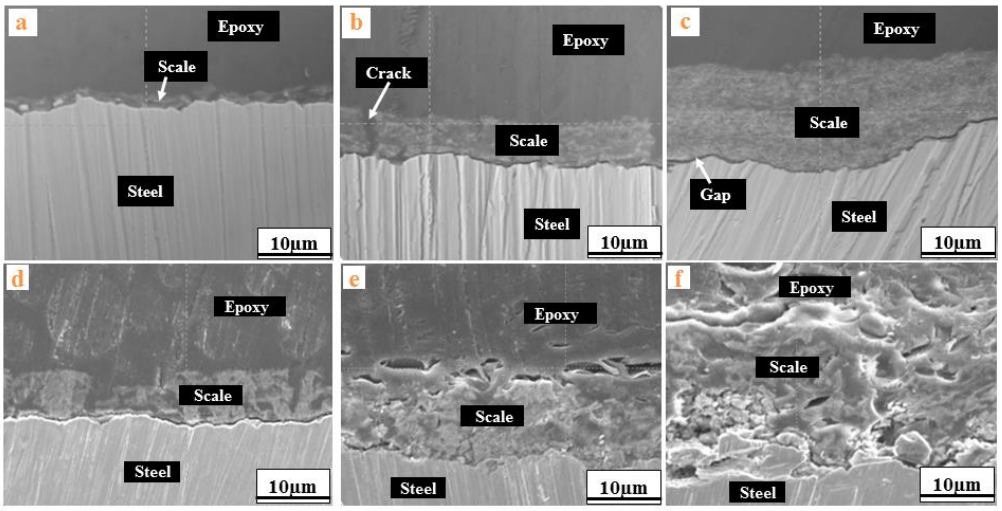

Figure 5- 55: SEM cross section of corrosion products on anodically polarized P110X in 3.5 wt% NaCl solution containing CO_2 at 60^0C and pH 6.5: (a) 100 $mV_{(Ag/AgCl)}$, (b) 150 $mV_{(Ag/AgCl)}$ and (c) 200$mV_{(Ag/AgCl)}$

It is evident from this figure that pits became wider and deeper with increase in applied potentials in agreement with the potentiostatic polarization (increase in current density with increase in anodic potential) and EIS (decrease in capacitive semi-arc with increase in anodic potential) results of this work. A closer observation of Figure 5-56 showed that steel P110 recorded wider but shallow pits than X65 which exhibited deeper but narrow pits.

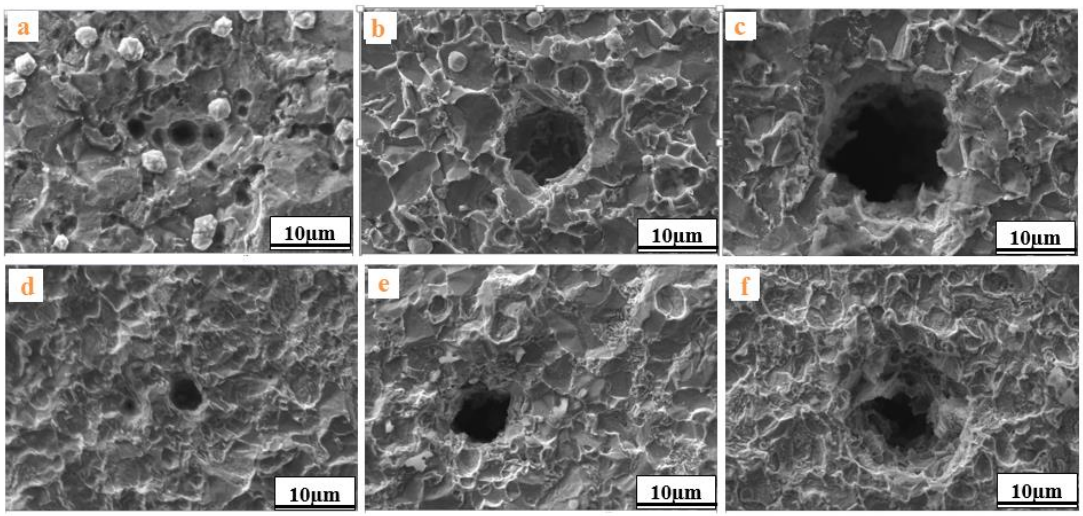

Figure 5- 56: SEM micrographs of the evolution of pits after 24 hours potentiostatic polarization in 3.5 wt% NaCl solution containing CO_2 at 60^0C and pH 6.5 for P110X (a) 100 $mV_{(Ag/AgCl)}$ (b) 150 $mV_{(Ag/AgCl)}$ and (c) 200 $mV_{(Ag/AgCl)}$ for X65 (d) $mV_{(Ag/AgCl)}$ (e) 150 $mV_{(Ag/AgCl)}$ and (f) 200 $mV_{(Ag/AgCl)}$

The identified pits were characterized using multiple region analysis tool of the white light profilometer. The 3D white light profilometry images showing samples of pits with top-ten average (for deepest pits) pits after 24 hours of 100 $mV_{(Ag/AgCl)}$, 150 $mV_{(Ag/AgCl)}$ and 200 $mV_{(Ag/AgCl)}$ potentiostatic polarizations in 3.5 wt% NaCl solution containing 0.5% CO_2 at 60^0C and pH 6.5 are shown in Figure 5- 57 for steels P110X and X65. These figures demonstrated an increase in pit depth of 22 µm, 40 µm and 73 µm with increase in anodic polarization potentials of 100 $mV_{(Ag/AgCl)}$, 150 $mV_{(Ag/AgCl)}$ and 200 $mV_{(Ag/AgCl)}$ respectively for steel P110X. Also, the same behavioural trend was observed for API 5L X65 steel which recorded pit depths of 45 µm, 69µm and 81µm for 100 $mV_{(Ag/AgCl)}$, 150 $mV_{(Ag/AgCl)}$ and 200 $mV_{(Ag/AgCl)}$ potentials respectively. Similar trend was reported recently for API 5L X65 steel by Mohammed , et al [217]

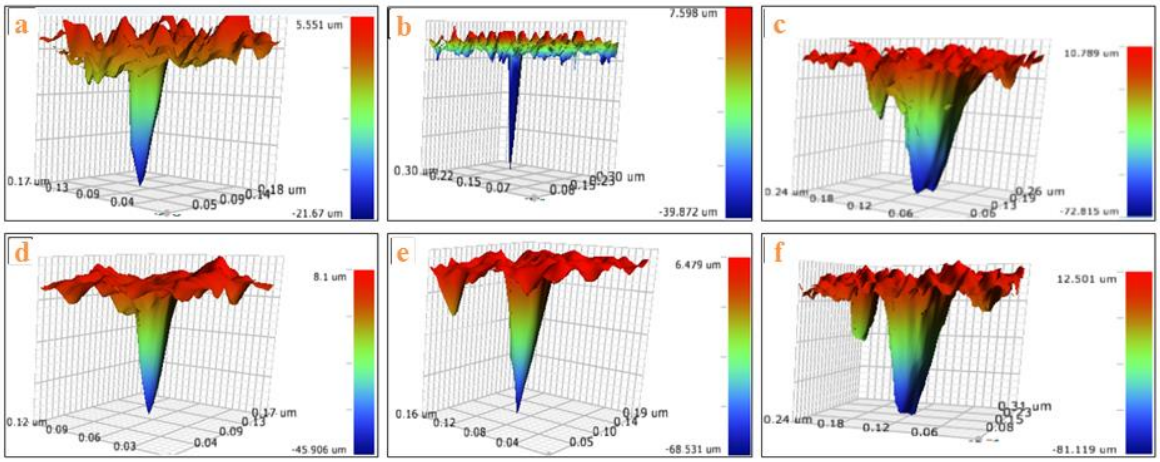

Figure 5- 57: 3D White light profilometry images of deepest pit formed on the specimens after 24 h potentiostaic polarization in 3.5 wt% NaCl solution containing CO_2 at 60^0C and pH 6.5 for P110X (a) 100 $mV_{(Ag/AgCl)}$, (b) 150 $mV_{(Ag/AgCl)}$ and (c) 200 $mV_{(Ag/AgCl)}$; for X65 (d) 100 $mV_{(Ag/AgCl)}$, (e) 150 $mV_{(Ag/AgCl)}$ and (f) 200 $mV_{(Ag/AgCl)}$

5.1.7.2 EIS investigation of the stability of the corrosion product formed on the steels by applying constant anodic potentials for different time interval.

Two of the micro-alloyed steels namely P110 and TN95 were used for this studies. The electrochemical behaviour of potentiostatically formed corrosion product films was investigated using EIS and OCP while the surface morphology of the film was observed with SEM/EDS and XRD. The corrosion films were grown at varying times between 1 to 24 hours using constant anodic potential of 150 $mV_{(Ag/AgCl)}$ in naturally aerated 3.5 wt% NaCl solution at ambient temperature. This was aimed at observing the relationship between the applied potential time and the stability of the corrosion film formed. Unlike in the preceding section where the steels were passivated using varying applied anodic potentials at constant time, the plot of current density versus time did not exhibit any obvious differences suggesting that time has no significant effect on the corrosion kinetic of the process.

Figure 5- 58 shows the Nyquist plots of the steels passivated in naturally aerated 3.5 wt% NaCl solution at ambient temperature and different time. It is apparent from this figure that the two steels exhibited similar feature of Nyquist plots presenting an incomplete capacitive arc that did not meet at the low frequency axis. The radius of the capacitive arc which is correlated to the corrosion resistance [209], decreased as the applied anodic potential time increased. This indicates the degradation of the passive film with the attendant decrease in its protective capability signifying that the corrosion rate of the

steels increased with anodic polarization time. Although this behaviour is contrary to the result when stainless steel was used as the electrode [208, 209] similar behaviour using low carbon alloy steel has been reported [113]. This difference in electrochemical behaviour of the passive film form on stainless and micro-alloyed steels can be attributed to difference in the electrochemical reactions occurring at the passive region (passive steel) and active region (active steel) in a corroding system.

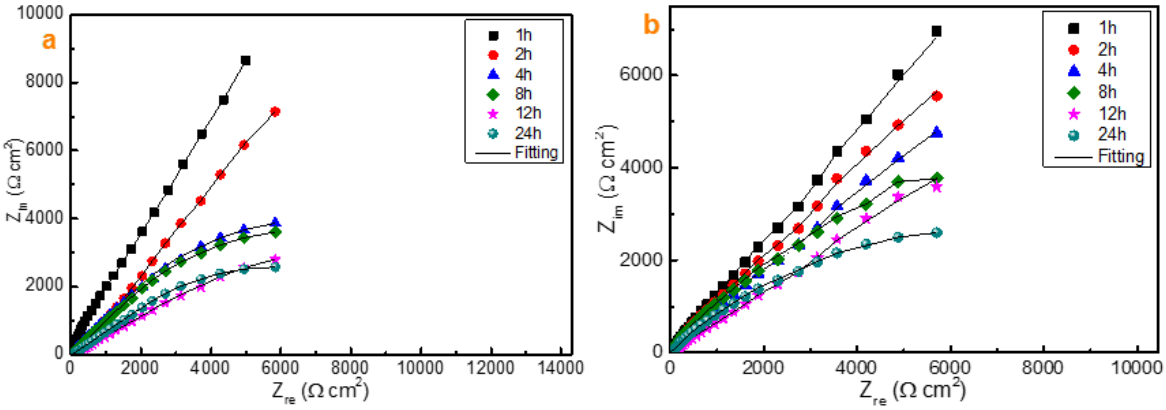

Figure 5- 58: Nyquist plots of the steels passivated in naturally aerated 3.5 wt% NaCl solution at ambient temperature and different time (a) P110 and (b) TN95.

Figure 5-59 shows the corresponding Bode plots for the steels in naturally aerated 3.5% NaCl solution at ambient temperature for different polarization time. This figure displayed maximum phased angle of about 60^0 at the medium frequencies with a shift towards the lower frequency as polarization time increases. The phase angle at the high frequency gave a value of 0^0 while the high frequency impedance magnitude /Z/ value of about 32 µm is observed. This shows that the high frequency impedance for both steels is under the effect of the solution resistance only.

A closer look at Figure 5- 58 revealed that for both steels, a rapid decrease in impedance was observed during the first 4 hours of applied potential time but then slightly decreased with longer polarization time. This is more pronounced for steel P110. This showed that the rate of decrease in impedance of the corrosion film is reduced with longer polarization time suggesting that the rate of loss of protective property of the film is reduced. This is made more vivid in the plot of transition of OCP values conducted at the end of application of each 150 $mV_{(Ag/Ag/Cl)}$ anodic potential in naturally aerated 3.5 wt% NaCl solution at ambient temperature and for different time as shown is Figure 5- 60.

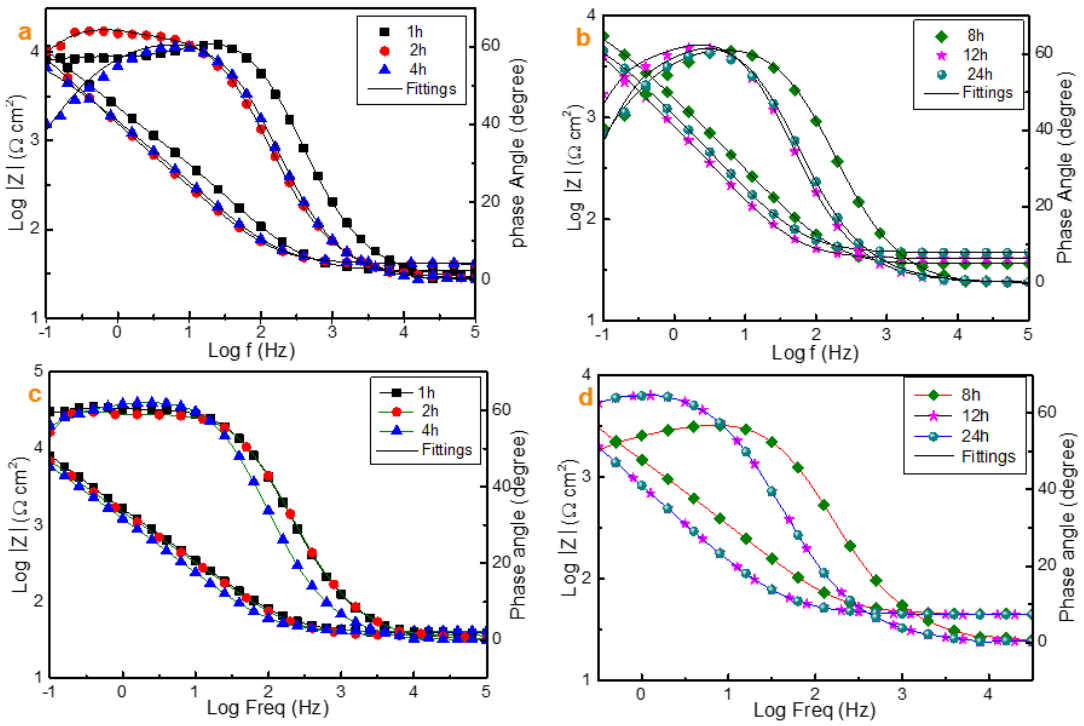

Figure 5- 59: Bode plots of the steels passivated in naturally aerated 3.5 wt% NaCl solution at ambient temperature and different time (a and b) P110 and (c and d) TN95.

This figure shows that the OCP values decreased with increase in applied anodic potential time changing from -541 $mV_{(Ag/Ag/Cl)}$ at 0 hour applied potential to -658 $mV_{(Ag/Ag/Cl)}$ at 24 hours applied anodic potential for steel P110. Similar features were observed for steel TN95.

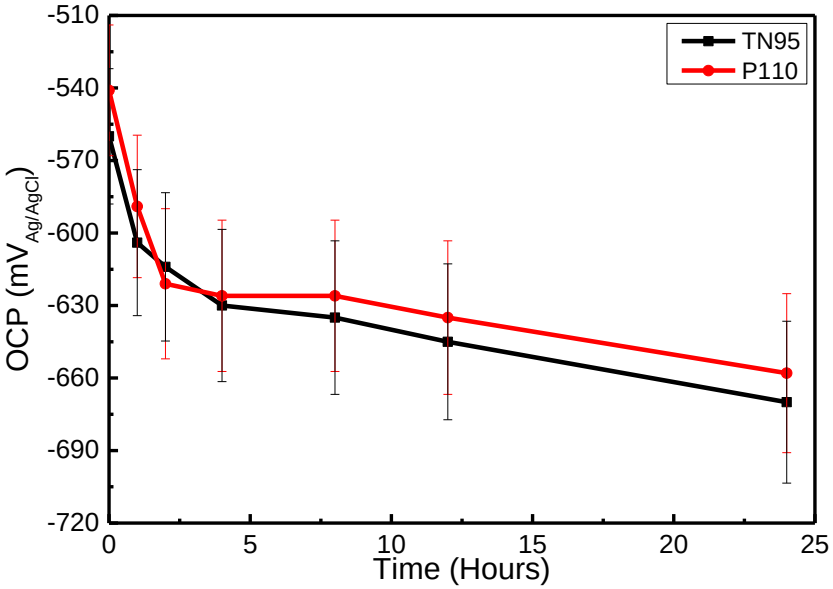

Figure 5- 60: Open circuit potential after corrosion product has been formed at a constant potential of 150 $mV_{Ag/AgCl}$ on the steels in naturally aerated 3.5 wt% NaCl solution at ambient temperature and different time (0, 1, 2, 4, 8, 12 and 24 h)

This shows that the OCP shift to the negative direction as the applied potential time increased validating the observation that the stability of the corrosion film decreased with applied polarization time as indicated in the Nyquist plots (Figure 5- 58). Figure 5- 60 also showed that the OCP for steel P110 is more positive than that of steel TN95 indicating that steel TN95 passivated at 150 mV in naturally aerated 3.5 wt% NaCl solution at ambient temperature is more prone to corrosion attack that than steel P110.

To interpret the impedance spectra, a simple equivalent electrical circuit (EEC) shown in Figure 5-26 of Section 5.1.4.3 was adopted. All the circuit elements were defined and explained in Section 5.1.4.3. The fitted impedance parameters for the two steels are listed in Tables 5-12 and 5-13 respectively. These table show that the charge transfer resistance (R_1) of the steels decreased with increase in polarization time. This is in good agreement with the actual impedance measurements as presented by the Nyquist plot (Figure 5-58). Also the small percentage error (2 – 13%) of the fitted parameters in Tables 5-12 and 5-13 confirmed the reliability of the chosen equivalent electrical circuit (EEC).

Table 5- 12: EEC Fitted parameters of P110 in naturally aerated 3.5 wt% NaCl solution at ambient temperature and different time

Time (hrs)	Rs ($\Omega.cm^2$)		CPE1 ($\mu F^{-1}cm^{-2}$)		n		R_1 ($\Omega.cm^2$)	
	Value	% Error	Value	% Error	Value	% Error	Value	% Error
1	40.31	0.65	$1.57*10^{-4}$	1.1	0.75	0.37	46764	11.69
2	32.13	1.45	$1.07*10^{-4}$	2.30	0.72	0.69	36736	13.00
4	40.52	0.81	$1.40*10^{-4}$	1.57	0.75	0.49	18585	3.68
8	35.12	0.93	$1.51*10^{-4}$	1.46	0.76	0.49	10997	3.90
12	40.38	0.56	$2.86*10^{-4}$	1.16	0.78	0.42	8539	4.16
24	46.28	0.52	$2.18*10^{-4}$	1.11	0.78	0.38	7254	2.72

Table 5- 13: EEC Fitted parameters of TN95 in naturally aerated 3.5 wt% NaCl solution at ambient temperature and different time

Time (hrs)	Rs ($\Omega.cm^2$)		CPE1 ($\mu F^{-1}cm^{-2}$)		n		R_1 ($\Omega.cm^2$)	
	Value	% Error	Value	% Error	Value	% Error	Value	% Error
1	34.77	1.00	$1.77*10^{-4}$	1.66	0.72	0.54	31016	12.89
2	40.04	0.72	$2.02*10^{-4}$	1.36	0.76	0.47	19890	7.80
4	44.16	0.44	$2.83*10^{-4}$	0.88	0.80	0.33	16273	5.76
8	35.94	1.45	$1.42*10^{-4}$	2.76	0.70	0.84	10366	6.26
12	39.99	0.65	$2.08*10^{-4}$	1.36	0.75	0.45	7143	3.62
24	35.82	1.47	$1.55*10^{-4}$	3.10	0.69	0.93	5534	4.50

Polarization resistance, Rp is correlated to charge transfer resistance R_1 ($Rp = R_1 - R_s$) obtained from the fitted parameters listed in Tables 5- 12 and 5- 13 and can be considered as the resistance of the metal to corrosion attack [209]. The transition of Polarization resistance, (Rp) with potential time is shown in Figure 5-61. This figure shows a rapid decrease in polarization resistance with time in the first 4 hours of polarization and then slightly decrease with further increase in applied potential time depicting lost in protective properties of the film and thus decreases the corrosion resistance.

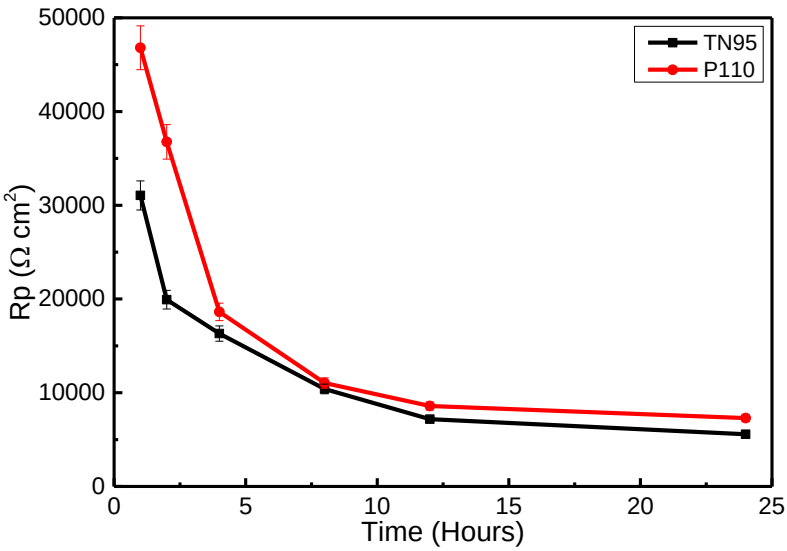

Figure 5- 61: Polarization resistance (Rp) from the fitted parameters of the steels passivated in naturally aerated 3.5 wt% NaCl solution at ambient temperature and different time (0, 1, 2, 4, 8, 12 and 24 h)

This figure also shows very close resemblance with the plot of OCP versus time (Figure 5-60) validating the results that protective capability of the passive film formed on micro-alloyed steel at constant applied anodic potential decreases with polarization time. The protective property of the film formed on steel P110 is better than that formed on steel TN95 which is in agreements with OCP plot and the EEC fitted parameters.

Figure 5-62 shows the SEM surface morphology of steel P110 in naturally aerated 3.5 wt% NaCl solution at ambient temperature after different time of applied anodic potential. Figure 5- 62 (a) shows that no obvious corrosion attack took place after the first 1 hour of applying 150 $mV_{Ag/AgCl}$ since the ground scratches on the surface of the electrode can still be observed. XRD pattern of this surface shown in Figure 5-64 (a) displayed only Fe and Fe_3C peaks. The SEM micrograph of steel P110 after 2 hours of polarization shown in Figure 5-62 (b) revealed a sludge-like morphology covering the entire substrate. As in the case for 1 hour, only Fe and Fe_3C peaks were observed in the XRD pattern suggesting that the sludge-like layer has little or no significate protective property. The surface morphology of steel P110 after 4 hours showed a thick layer that is loosely attached to the substrate with cracks on the surface. It could be assumed that the sludge-like layer formed after 2 hours polarization grew in thickness with prolongation of polarization. The presence of the cracks must have also allowed the ingress of active corrosive species to the steel surface which continued the corrosion attack resulting in the reduction in charge transfer resistance of about 18 $K\Omega.cm^2$ from the result of the 2 hours polarization (Table 5-12). The SEM surface morphologies of steel P110 after 8, 12 and 24h polarization presented similar features of exposed crater-like layers. This suggests that the loosely held slugde-like layer observed for the SEM micrograph of 4 hours must have detached from the substrate thus exposing the characteristic structure of actively corroede ferrite-pearlite microstructures in which the ferrite phase has preferentially dissolved leaving a protruded laminar cementite phase.

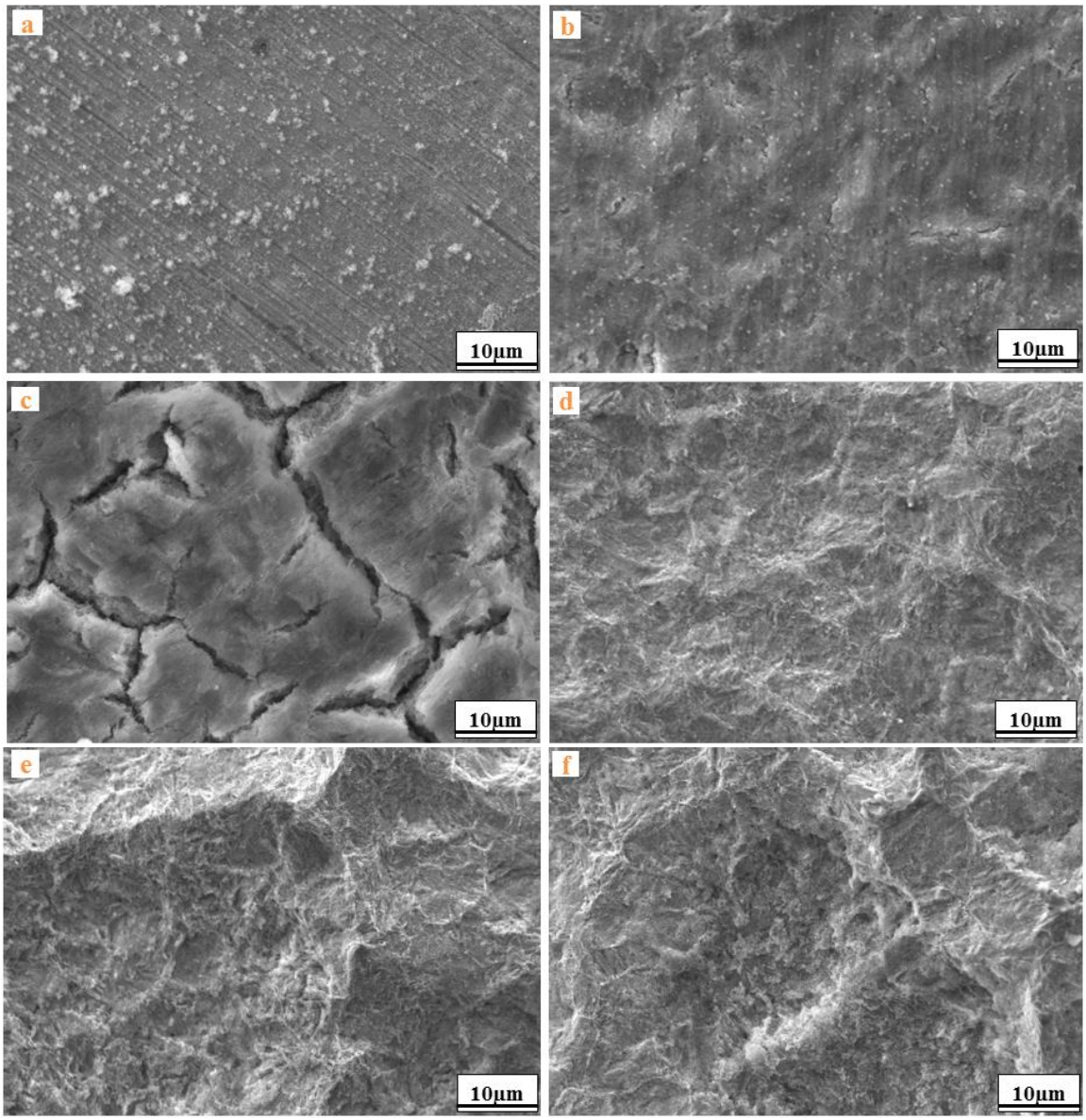

Figure 5- 62: Evolution of SEM surface morphology of P110 in naturally aerated 3.5 wt% NaCl solution at ambient temperature and at (a) 1h, (b) 2h, (c) 4h, (d) 8h, (e) 12h and (f) 24h

It can also be seen as depicted in Figures 5- 62 (d, e and f) that the intensity of the corrosion attack (revealed seemingly by high ferrite dissolution) increased with increase in the applied anodic polarization time. The XRD pattern shown in Figure 5- 64(a) displayed Fe, Fe_3C, Fe_3O_4 and NaCl. The intensities of these peaks increased with time of polarization.

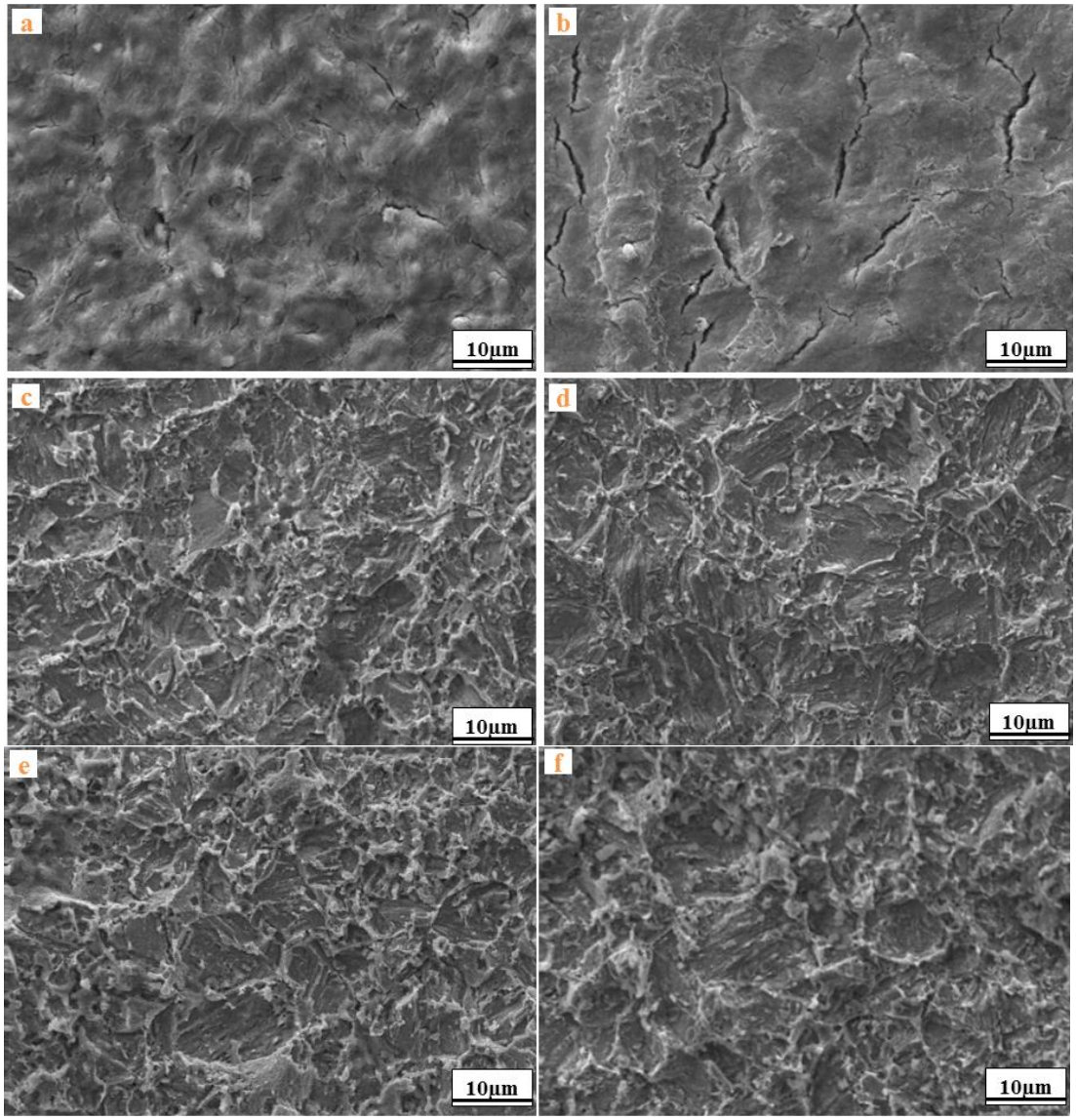

Figure 5- 63: Evolution of SEM surface morphology of TN95 in naturally aerated 3.5 wt% NaCl solution at ambient temperature and at (a) 1h, (b) 2h, (c) 4h, (d) 8h, (e) 12h and (f) 24h

The SEM surface morphology of steel TN95 passivated in naturally aerated 3.5 wt% NaCl solution at ambient temperature after different time of applied anodic potential is shown in Figure 5- 63. The surface micrograph of steel TN95 after the first 1 hour of applying anodic potential shown in Figure 5- 63 (a) did not show the ground scratches as displayed in steel P110 instead a resemblance of the sludge-like morphology noticed in the 2 hour of steel P110 was observed. Some cracks can also be noticed on the surface of this micrograph. These cracks expanded and the sludge-like morphology grew in thickness presenting a poorly adherence layer as revealed in Figure 5-63 (b) for 2 hours polarization. Figures 5-63 (c, d, e and f) showed that the thick and poorly held sludge-like morphology

observed in Figure 5-63 (b) have been detached revealing the corroded surface of the steel.

The XRD pattern for the two steel shown in Figure 5- 64 indicates that Fe, Fe_3C, Fe_3O_4 and NaCl as the main components of the corrosion products. The intensities of this compounds increased with prolongation of formation potential signifying that more of these compounds were formed with time. The presence of NaCl in the XRD pattern could be from the electrolyte used for the corrosion experiments.

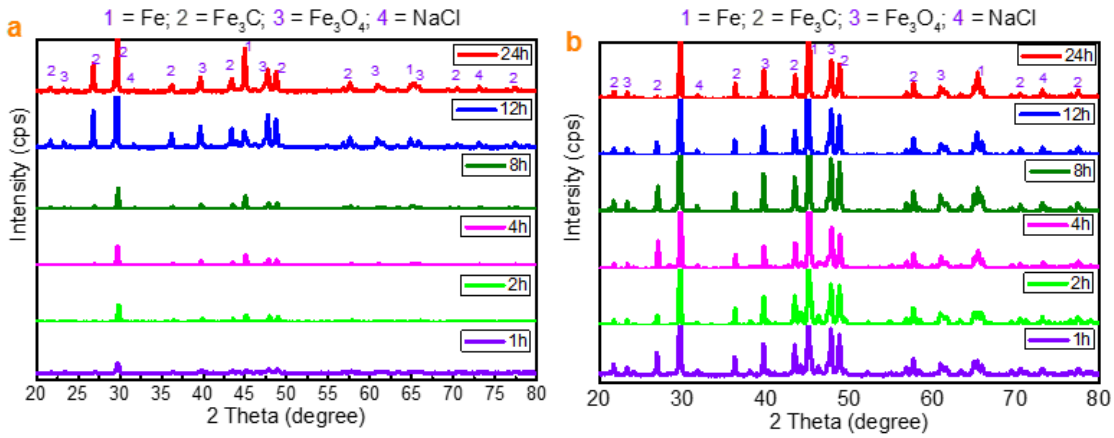

Figure 5- 64: XRD pattern of the samples in naturally aerated 3.5 wt% NaCl solution at ambient temperature and different time interval (a) P110, (b) TN95

5.1.8 Further investigation in 3.5 wt% NaCl saturated with 99.98% CO_2

From the results of the preliminary investigations, the corrosion rate of the micro-alloyed steels can be ranked as follows ASTM F65 < API 5L X65 < P110 IC < TN95 SH. The values of the corrosion rate of the specimens obtained in this work were less than the values reported in literature for carbon and micro-alloyed steels in similar conditions. For instance, corrosion current density of 84.7 µA/cm^2 was obtained by potentiodynamic polarization of X65 steel in simulated produced water saturated with CO_2 at 20^{0}C [219]. This is about 97% more than the corrosion current density obtained from potentiodynamic measurement of X65 steel in simulated produced water saturated with 0.5% CO_2 of this work (Table 5-10). This was ascribed to low CO_2 concentration (5000 ppm CO_2 in N_2 i.e. 0.5% CO_2) used in this work which is about 0.114 mol/l. Therefore, further investigations were conducted on the two worst case specimens namely P110 IC and TN94 SH in 3.5 wt% NaCl solutions saturated with 99.98% CO_2 for

(i) Temperature variations as specified in the test matrix of Table 4-5,

(ii) Lyman and Flaming solutions as specified in the test matrix of Table 4-8 and

(iii) Weight loss experiments as conducted in Section 4.2.1.

5.1.8.1 Effect of temperature on the corrosion behaviour of steels P110 and TN95 in 99.98% CO_2 environments

The corrosion behaviour of the two worst corrosion specimens (P110 and TN95) and X65 as reference specimen were further investigated in 3.5 wt% NaCl solution saturated with 99.98% CO_2 at temperatures (25^0C, 45^0C and 60^0C). The text matrix in Table 4-5 was used. SEM/EDAX and XRD surface analysis techniques were used to characterise the surface morphology of the corroded specimens. The results of these investigations are presented in this section.

Figure 5- 65 shows the evolution of corrosion rate with time for steels P110, TN95 and X65 in 3.5 wt% NaCl solution saturated with 99.98% CO_2 at 25^0C, 45^0C and 60^0C respectively. This figure displayed seemingly a linear increase in corrosion rate with time. The specimens exhibited similar ranking order but demonstrated about 9 order of magnitude higher in corrosion rate than in 3.5 wt% NaCl solution saturated with 0.5% (5000 ppm in N_2) CO_2. It was also evident, like in the 0.5% CO_2 environment that the corrosion rate increased with increase in temperature as revealed in Figure 5-66 that compares the effect of temperature on individual specimen.

Figure 5-67 compares the average LPR corrosion rate of the specimens in 3.5 wt% NaCl solution saturated with 0.5% CO_2 and 99.98% CO_2. All the specimens exhibited about 90% increase in corrosion rate in 99.98% when compared with 0.5% CO_2. This corroborates the difference in mol/l of CO_2 in the solutions which is about 0.89 mol/l.

The potentiodynamic polarization experiments of the steels corroded in 3.5 wt% NaCl solutions saturated with 99.98% CO_2 at 25^0C is shown in Figure 5-68. This figure exhibited similar potential vs log current density curves for the specimens corroded in 3.5 wt% NaCl solutions saturated with 0.5% CO_2 at 25^0C as shown in Figure 5- 24. This demonstrated that the corrosion mechanisms in both environments (0.5% and 99.98% CO_2) are similar. However, a closer examination of the two figures revealed some variations in certain critical corrosion parameters.

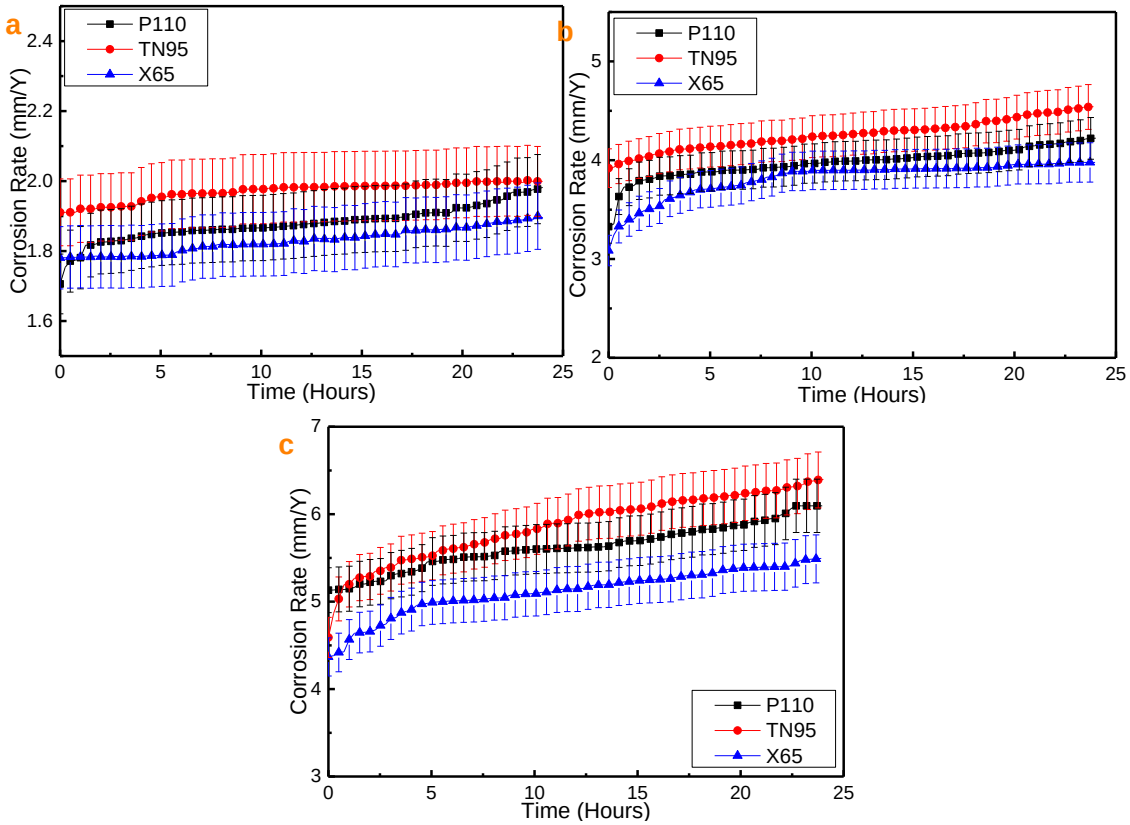

Figure 5- 65: Evolution of corrosion rate with time of samples in 3.5 wt% NaCl solution saturated with 99.98% CO_2 at different temperatures: (a) 25^{0}C, (b) 45^{0}C and (c) 60^{0}C

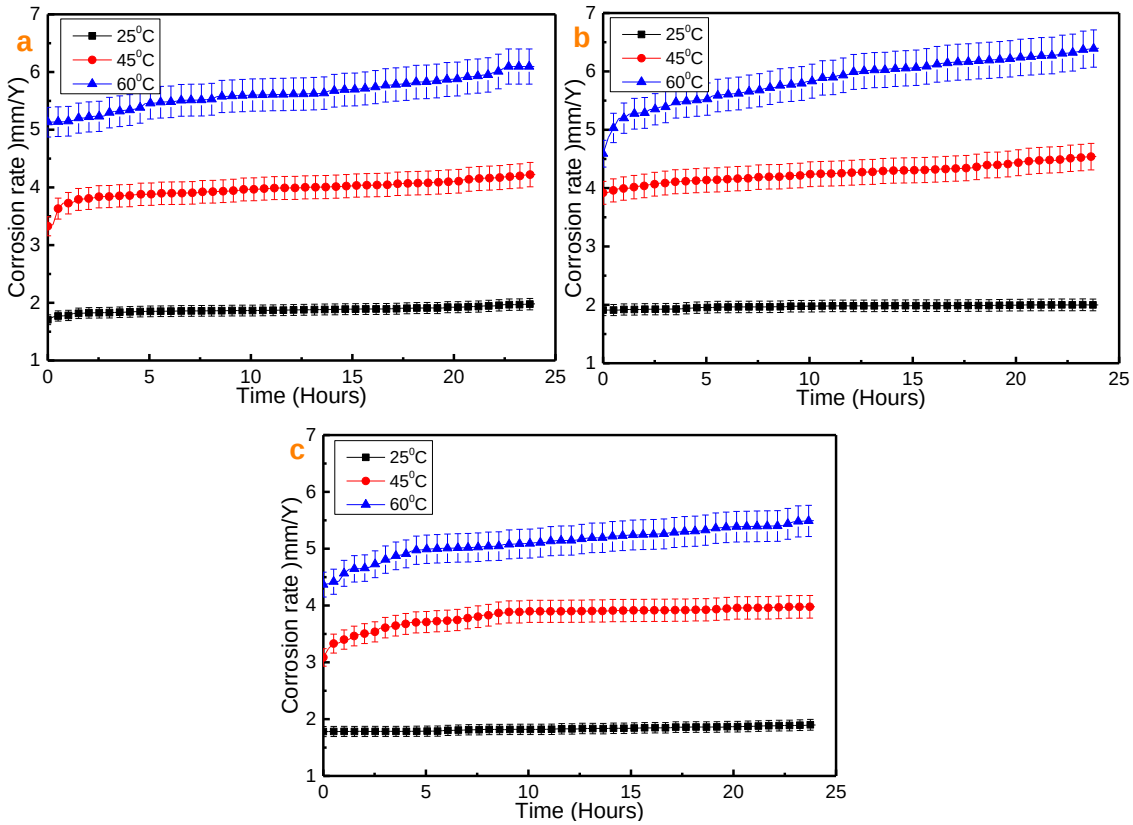

Figure 5- 66: Comparison of corrosion rate of specimens in 3.5 wt% NaCl solution saturated with 99.98% CO_2 at different temperatures: (a) P110, (b) TN95 and (c) X65

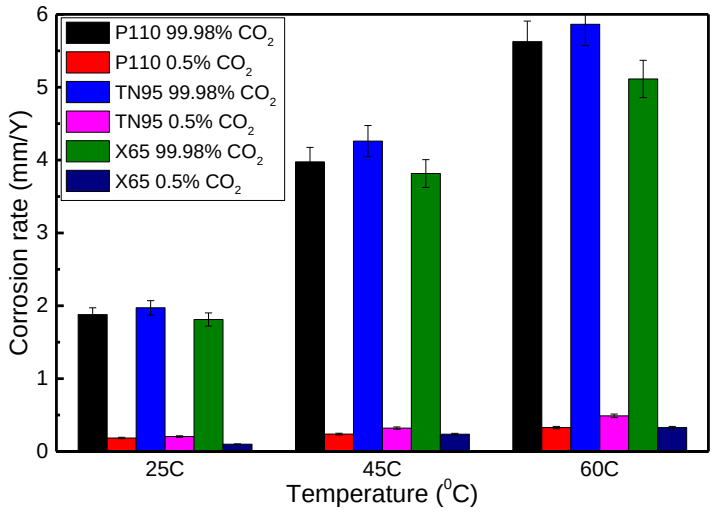

Figure 5- 67: Comparison of the average corrosion rate of specimens in 3.5 wt% NaCl solutions saturated with 0.5 % CO_2 and 99.98% CO_2 at different temperatures

Figures 5- 69 to 5- 71 compare these two Tafel plots for all the specimens in the two CO_2 environments. It can be deduced from these Figures that the anodic current density for all the steel samples corroded in both CO_2 environments increased continuously with increase in potentials exhibiting a well-defined Tafelian slope within the lower potential (ie near corrosion potential) suggesting that protective corrosion product layer was not formed. This was also evidenced by the higher current densities for the steels corroded in 99.98% CO_2 which also corresponds to higher corrosion rate indicating an unhindered anodic dissolution of iron [154]. Another characteristics of all the anodic Tafel branches is a slight decrease in current density with increase in potential above -600 mV (ie towards the positive direction) which has been reported as pseudo-passivation [154]. This signified the formation of poorly protective corrosion products that slightly blocked the steel substrates thereby reducing the active surface area for iron dissolution [204]

On the other hand, the cathodic slope of all the specimens in 0.5% CO_2 as can be deduced from Figures 5- 69 to 5- 71 showed a mixed charge- and mass- transfer control reaction depicting Tafelian behaviour. This is contrary to the cathodic curves of the steels corroded in 99.98% CO_2 which exhibited well-defined cathodic current plateau revealing limiting diffusion current density occasioned by hydrogen evolution reaction (HER) [185, 204]. The corrosion parameters obtained using Tafel extrapolation techniques are listed in Table 5- 14. The high values of Tafel cathodic constants signified that the overall corrosion process is under the control of cathodic reactions.

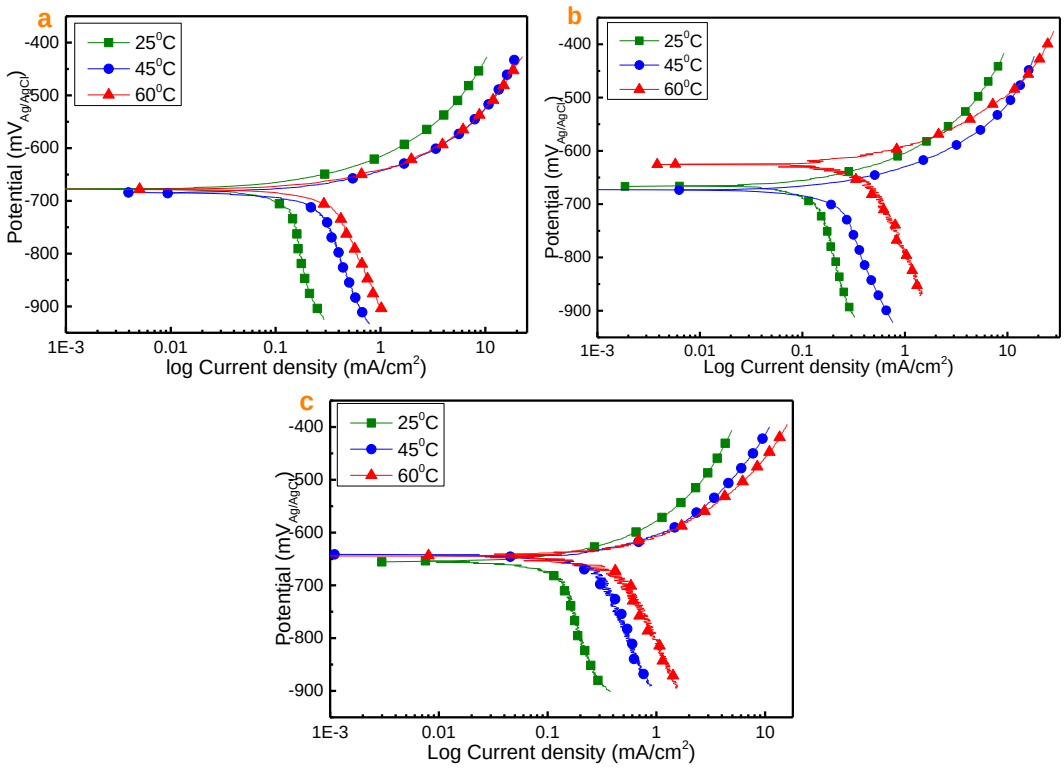

Figure 5- 68: Tafel plot of samples in 3.5 wt% NaCl solution saturated with pure CO_2 at different temperatures: (a) P110, (b) TN95 and (c) X65

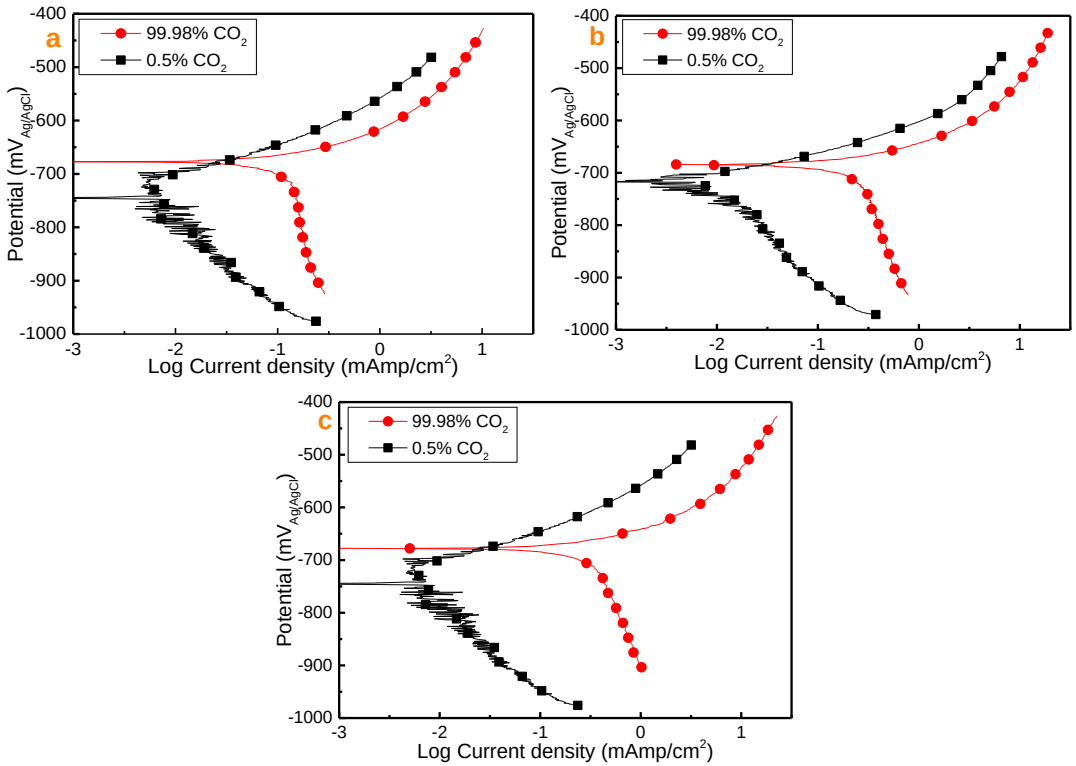

Figure 5- 69: Comparison of Tafel plots of P110 in 3.5 wt% NaCl solutions saturated with 0.5 % CO_2 and 99.98% CO_2 at different temperatures: (a) 25^0C; (b) 45^0C and (c) 60^0C.

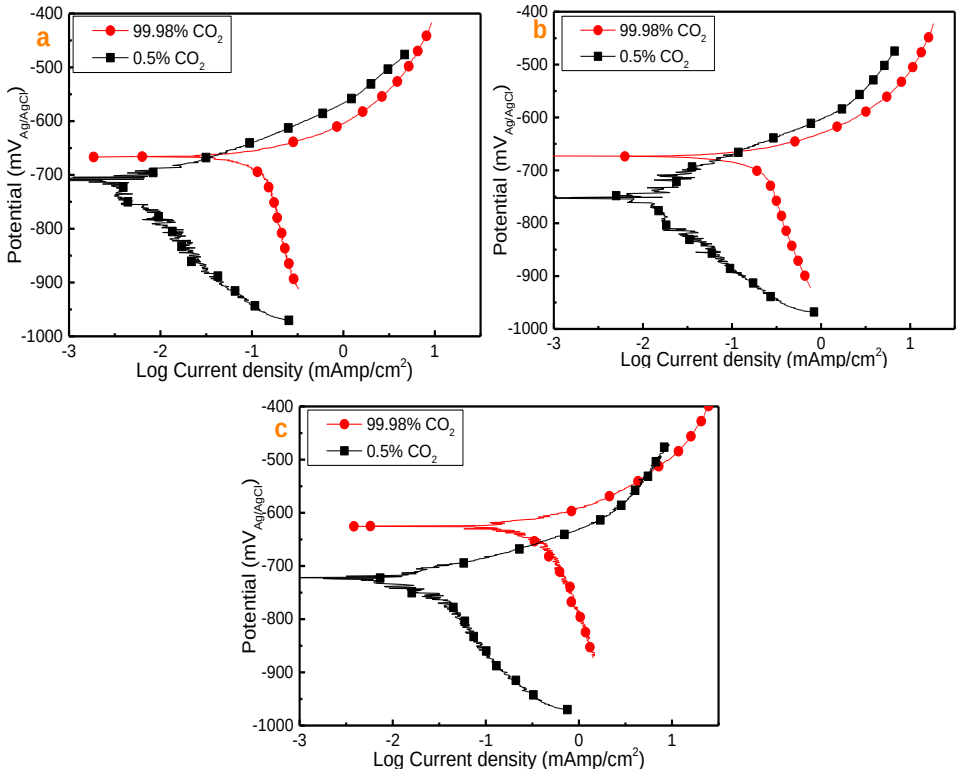

Figure 5- 70: Comparison of Tafel plots of TN95 in 3.5 wt% NaCl solutions saturated with 0.5 % CO_2 and 99.98% CO_2 at different temperatures: (a) 25^{0}C; (b) 45^{0}C and (c) 60^{0}C

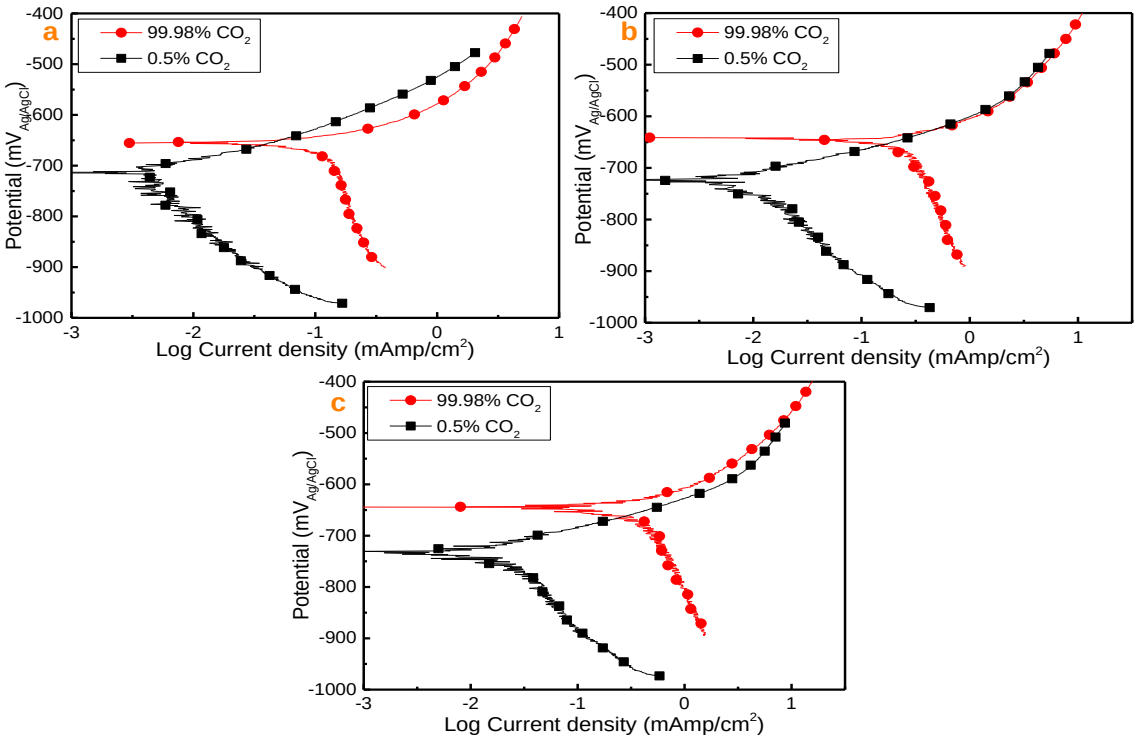

Figure 5- 71: Comparison of Tafel plots of X65 in 3.5 wt% NaCl solutions saturated with 0.5 % CO_2 and 99.98% CO_2 at different temperatures: (a) 25^{0}C; (b) 45^{0}C and (c) 60^{0}C

Table 5- 14: Tafel extrapolation parameters of the specimens corroded in 3.5 wt% NaCl solutions saturated with 99.98% CO_2 (a) 25^0C, (b) 45^0C and (c) 60^0C.

Temperature	Samples	E_{corr} (mV)	i_{corr} ($\mu A/cm^2$)	β_a (mV/decade)	β_c (mV/decade)	Rp ($\Omega.cm^2$)	CR (mm/Y)
	P110	-678	112	65	520	224	1.30
25^0C	TN95	-665	114	60	500	204	1.32
	X65	-654	110	70	480	241	1.28
	P110	-685	123	65	450	201	1.43
45^0C	TN95	-672	125	60	440	183	1.45
	X65	-642	122	70	480	217	1.42
	P110	-677	133	70	440	197	1.54
60^0C	TN95	-624	140	70	420	186	1.63
	X65	-645	130	80	410	224	1.51

Figures 5-72, 5-73 and 5-74 illustrate the SEM evolution of microscopic surface morphology of steels P110, TN95 and X65 respectively corroded in 3,5 wt% NaCl solution saturated with 99.98% CO_2 at different temperatures. It is clear from these figures that the aggressiveness of the attack, judging by the increasing roughness of the surface morphology, increased with temperature. This roughness is caused by the selective dissolution of ferrite leading to valleys in surface morphology while lamellar cementite phase is unaffected resulting in protrusion on the surface. This phenomenon is more pronounced in Figures 5-72 and 5-74 which composed of ferrite-pearlite microstructures (Figure 5-2).

It can be seen from Figures 5-72 (a) and 5-74(a) for the steels corroded at 25^0C that the lamellae structure of the undissolved cementite are clearly visible revealing that no corrosion product was formed. This is contrary to the images of the steels corroded at 45^0C and 60^0C shown in Figures 5-72 (b and c) and 5-74 (b and c) where amorphous-like corrosion products covered the undissolved cementite. Figure 5-75 is the XRD pattern revealing the component of the amorphous-like corrosion products as Fe and Fe_3C peaks. Both Fe and Fe_3C are part of the steel's microstructures. The amorphous-like corrosion products could not protect the steel substrate leading to the continuous increase in current densities with increase in potential as exhibited by all the steels as shown in Figure 5-68

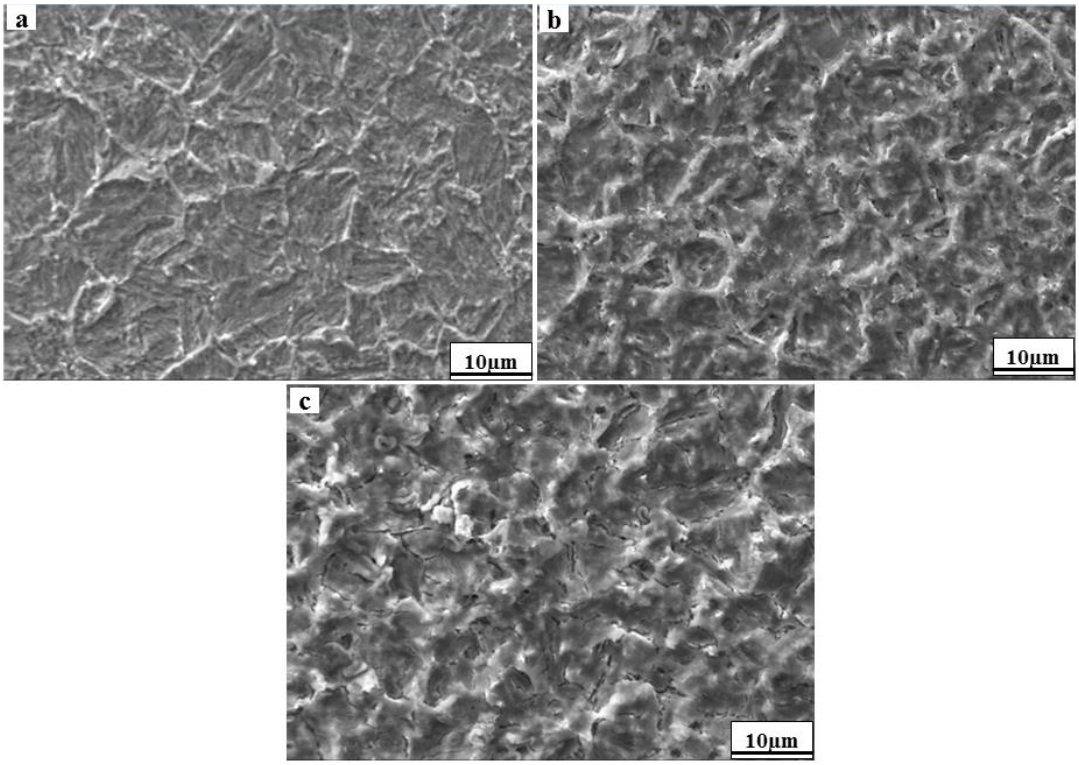

Figure 5- 72: SEM surface micrographs of P110 steel corroded in 3.5 wt% NaCl Solution saturated with 99.98% CO_2 at different temperatures for 24 hours: (a) 25^0C; (b) 45^0C and (c) 60^0C

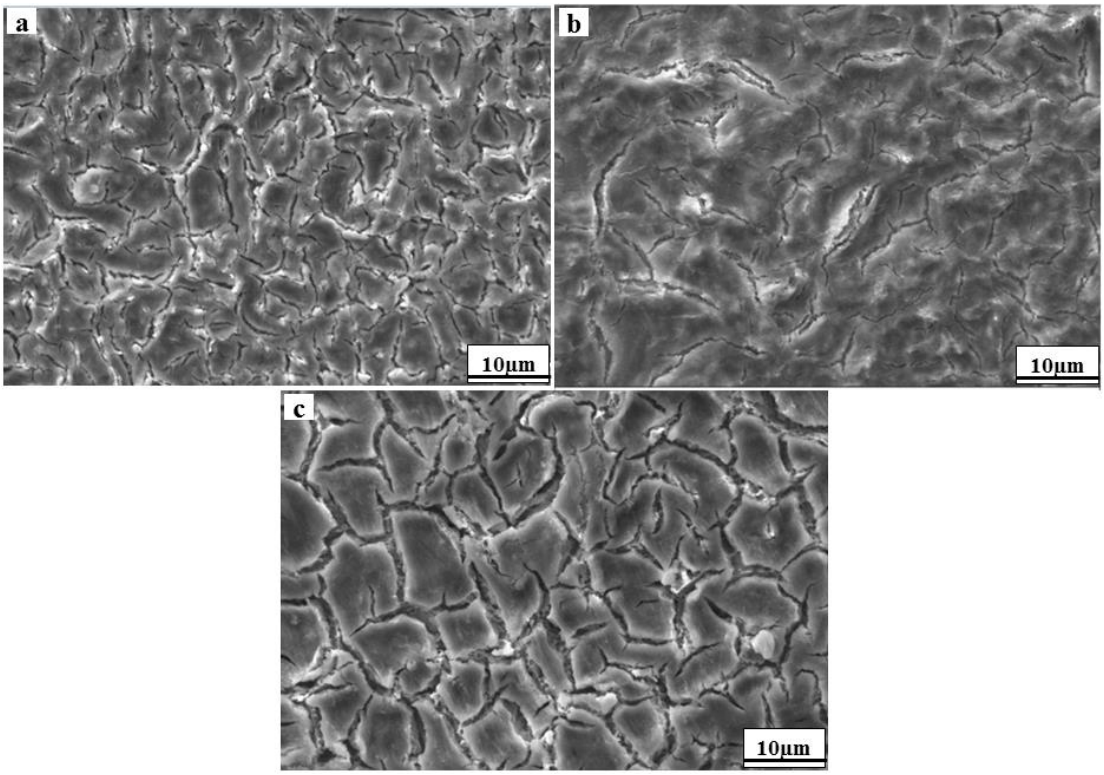

Figure 5- 73: SEM surface micrographs of TN95 steel corroded in 3.5 wt% NaCl Solution saturated with 99.98% CO_2 at different temperatures for 24 hours; (a) 25^0C; (b) 45^0C and (c) 60^0C

Valleys and protrusions were not observed in Figure 5-73 for steel TN95 whose surface morphology composed of cracks. These cracks became longer and wider with increase in temperature and allow diffusion of corrosive ions to the steel surface resulting in higher corrosion rate observed. Similar observation has been reported in literature [220],

It is clear from the surface morphology in Figures 5-72 to 5-74 for the specimens corroded in 99.98% CO_2 environments is different from that in Figures 5-27 to 5-29 for the specimens corroded in 0.5% CO_2 environments at the same temperatures. The surface morphologies of the steels corroded in 0.5% CO_2 did not exhibit the characteristic rough surface morphology of ferrite-pearlite microstructures leading to less surface area and therefore lower corrosion rate than the steels corroded in 99.98% CO_2.

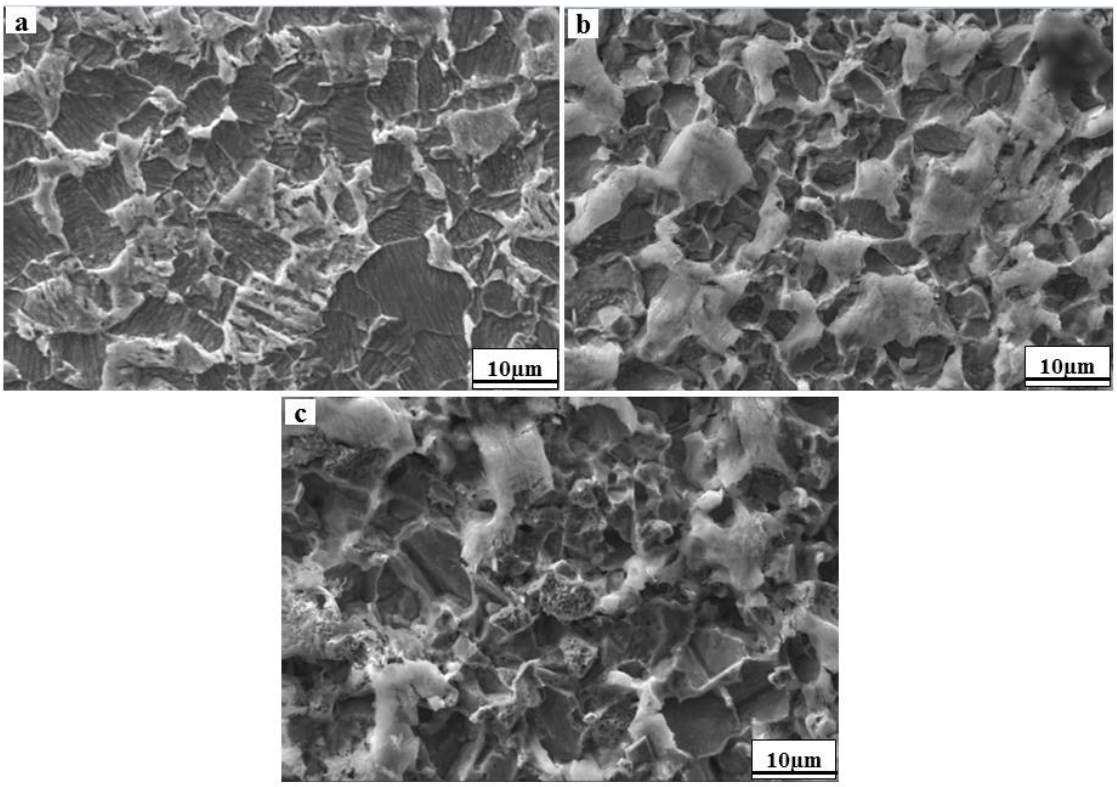

Figure 5- 74: SEM surface micrographs of X65 steel corroded in 3.5 wt% NaCl Solution saturated with 99.98% CO_2 at different temperatures for 24 hours; (a) 25^0C; (b) 45^0C and (c) 60^0C

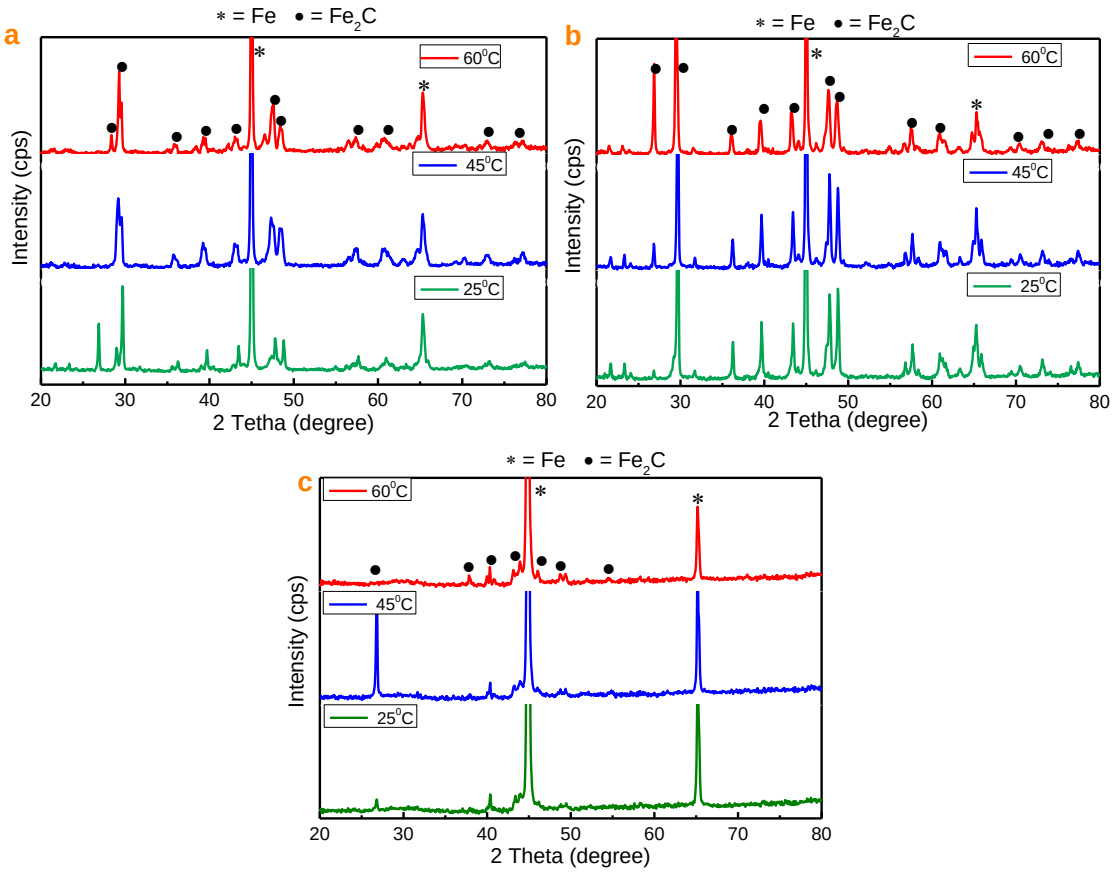

Figure 5- 75: XRD pattern of the samples corroded in 3.5 wt% NaCl Solution saturated with CO_2 at different temperatures for 24 hours (a) P110, (b) TN95 and (c) X65.

5.1.8.2 Corrosion behaviour of the steels corroded in simulated seawater (SSW) saturated with 99.98% CO_2 at 25^{0}C and pH 6.5

The corrosion behaviour of specimens P110, TN95 and X65 was studied in 99.98% CO_2 saturated environments using the test matrix in Table 4-8. This was aimed at comparing the effect of low (0.5%) and high (99.98%) CO_2 concentration on the corrosion susceptibility of the steels in simulated seawater (Lyman and Flaming solution). The results of these experiments and the surface morphology analysis of the corroded surfaces using SEM/EDX and XRD are presented in this section.

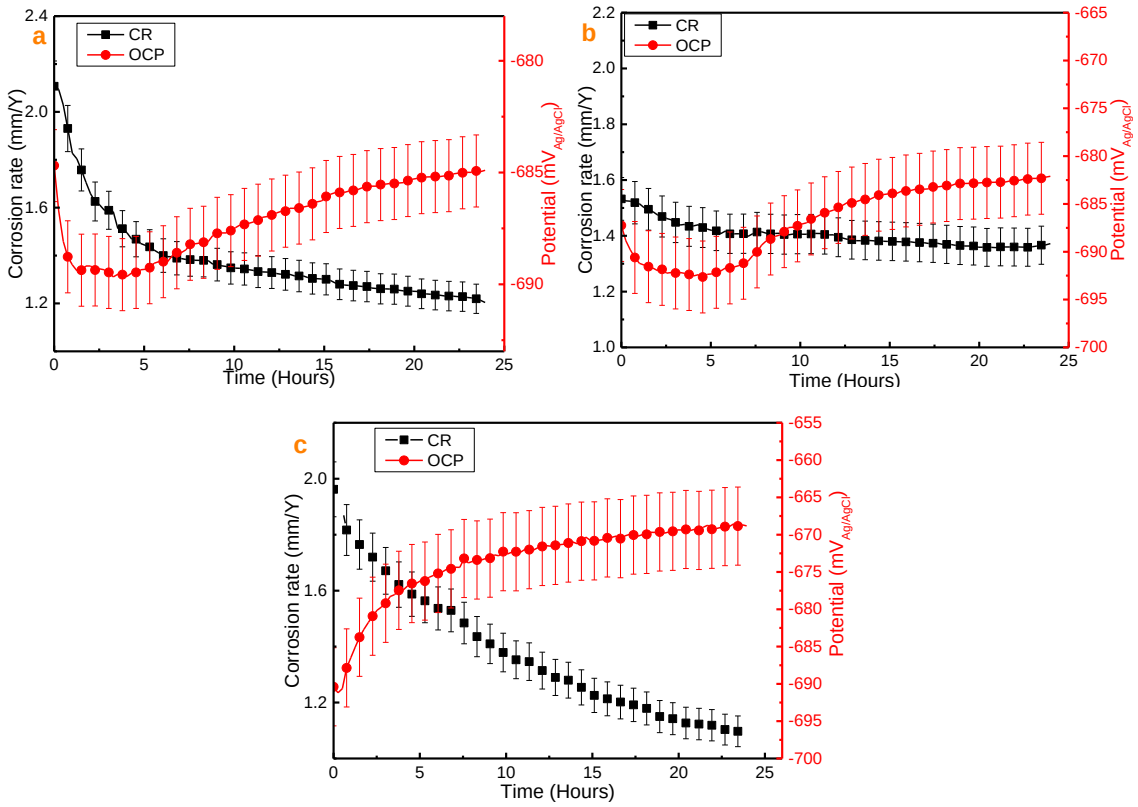

Figure 5- 76: Evolution of corrosion rate and potentials with time for the steels corroded in simulated seawater (SSW) saturated with 99.98% CO_2 at 25^0C and pH 6.5 (a) P110, (b) TN95 and (c) X65

Figure 5-76 shows the variation in corrosion rate and corrosion potential for the specimens as a function of time in simulated seawater saturated with 99.98% CO_2 at 25^0C and pH 6.5. This figure shows that the corrosion potentials of all the tested steels initially started at high potentials but decreased rapidly with time signifying the dissolution of the specimens. However, threshold potential was observed at -690 $mV_{Ag/AgCl}$, -693 $mV_{Ag/AgCl}$ and -689 $mV_{Ag/AgCl}$ within 4 hours, 4.6 hours and 1 hours of experiments for steels P110, TN95 and X65 respectively. This was followed by a sharp increase in corrosion potential within 15 to 18 hours of the tests portraying the formation of corrosion products which frustrated further dissolution of the steels. The potential curves then exhibited gradual increase with time for the remaining duration of the tests depicting that the corrosion products were porous, non-protective and so simply slowed down the rate of corrosion [168, 206]. This corroborated with the plots of evolution of corrosion rate with time for the steels as shown in Figures 5-76 and 5-77. A closer look at these figures show initial rapid decrease in corrosion rate but showed slow variation with time demonstrating the ability of the corrosion products to reduce the corrosion rate of the specimens [216].

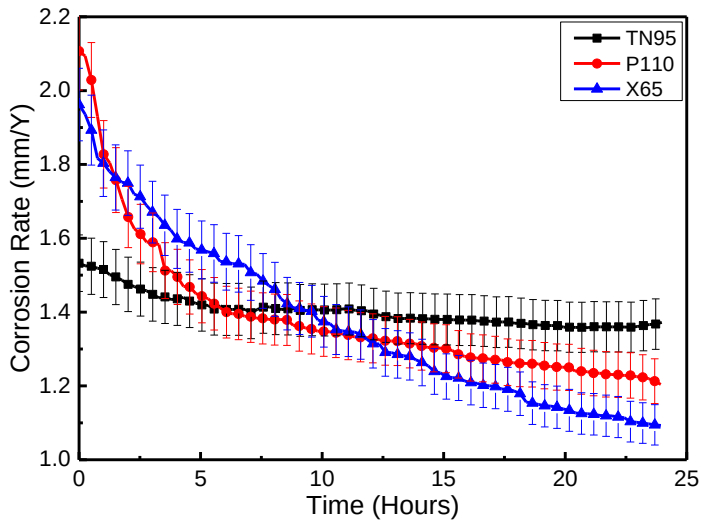

Figure 5- 77: Variation of corrosion rate with time of steels corroded in simulated seawater (SSW) saturated with 99.98% CO_2 at 25^0C and pH 6.5

Potentiodynamic polarization was performed using a scan rate of 0.5 mV/cm^2 and an effective scan range of ±250 $mV_{Ag/AgCl}$ in simulated seawater saturated with 99.98% CO_2 at 25^0C and pH 6.5. Figure 5-78 show the plots of potential vs log current density for the steels. The anodic curves of the three specimens exhibited initial active dissolution zone ($Fe_{(s)} \rightarrow Fe^{2+}_{(aq)} + 2e^-$) near the corrosion potential. Steel X65 depicted a well-defined Tafellian slope.

The specimens displayed a slight decrease in potential at about -600 $mV_{Ag/AgCl}$ with the attendant decrease in current density displaying pseudo-passivation plateau occasioned by the formation of porous corrosion product [132, 185]. Judging by the current densities of the specimens at a potential of -550 $mV_{Ag/AgCl}$ which is about 17µA/cm^2, 120 µA/cm^2 and 160 µA/cm^2 for steels X65, P110 and TN95 respectively, it can be deduced that the corrosion resistance of the steels can be ranked as X65 > P110 > TN95. This is confirmed by the electrochemical corrosion parameters extracted by Tafel extrapolation techniques as listed in Table 5-15.

The values of the Tafel cathodic constants are more than the anodic constants suggesting that the corrosion process is under the control of cathodic reaction [221]. The cathodic curves showed a mixed activation- and mass transfer- reactions displaying limiting current densities for steels P110 and TN95. This can be ascribed to the mass transport limitation of hydrogen evolution reaction [204]

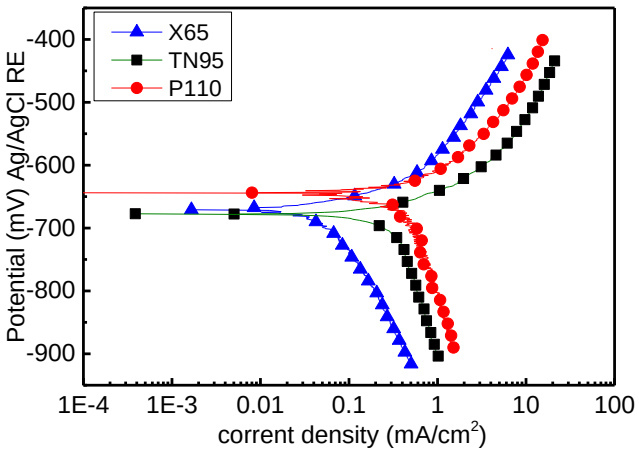

Figure 5- 78: Potential vs current density of samples corroded in simulated seawater (SSW) saturated with 99.98% CO_2 at 25^0C and pH 6.5

Table 5- 15 Tafel extrapolation parameters of the steels corroded in simulated seawater (SSW) saturated with 99.98% CO_2 at 25^0C and pH 6.5

Samples	E_{corr} (mV)	i_{Corr} (mAmp/cm^2)	β_a (mV/decade)	βc (mV/decade)	Rp (Ω.cm^2)	CR (mm/Y)
P110	-666	0.055	55	280	362.93	0.25
TN95	-680	0.062	70	280	392.20	0.29
X65	-671	0.045	55	190	411.57	0.21

The corrosion susceptibility of the steels was also assessed using EIS technique. The Nyquist and Bode plots of the steels are illustrated in Figure 5-79. The EIS diagrams of the specimens displayed two overlapped incomplete semicircle capacitive loops and the arc of the second capacitive loop for X65 is more prominent than the other two steels. Also the capacitive arc of steel P110 is more than that of steel TN95 signifying that steel P110 indicated better corrosion resistance than Steel TN95. This is in conformity with the LPR and the potentiodynamic polarization results presented in this section.

The EIS data were fitted using ZView software with equivalent electrical circuit (EEC) model shown in Figure 5-80, where Rs is solution resistance, CPE_1 is double layer capacitance between corrosion film and the solution, R_1 is charge transfer resistance, R_2 and CPE_2 are in parallel representing charge transfer resistance and the constant phase element which is the double charge layer capacitance between corrosion film and the

substrate. The fitted parameters are listed in Table 5- 16. The near perfect fitting as shown in Figure 5-79 confirmed the validity of the chosen equivalent electrical circuit (EEC).

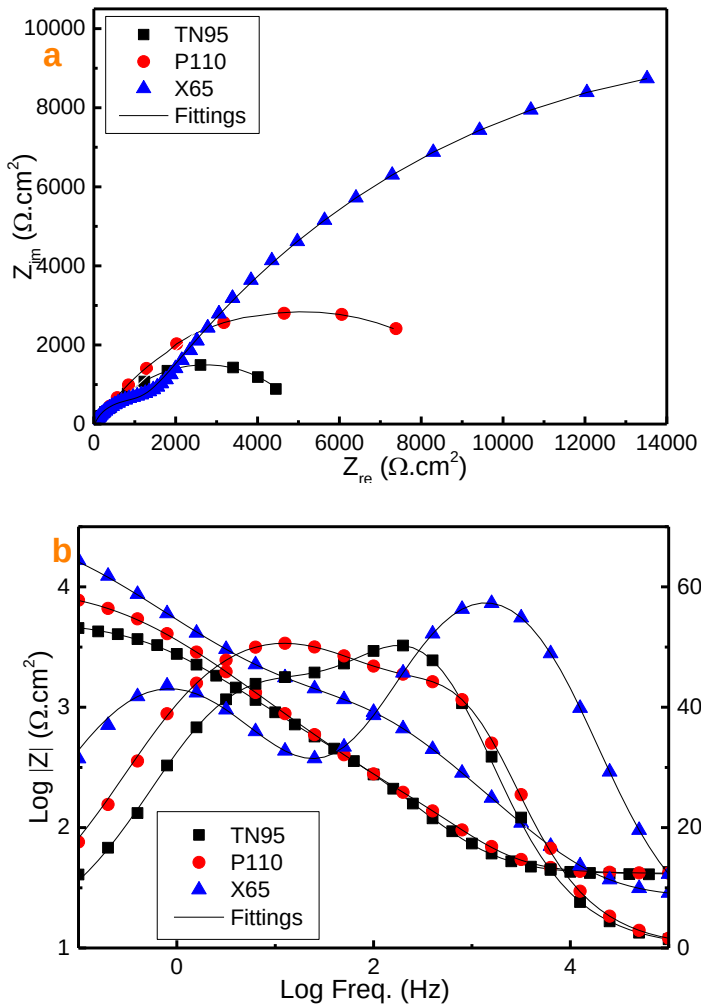

Figure 5- 79: EIS Plots of samples corroded simulated seawater (SSW) saturated with 99.98% CO_2 at 25^{0}C and pH 6.5 (a) Niquist and (b) Bode plots.

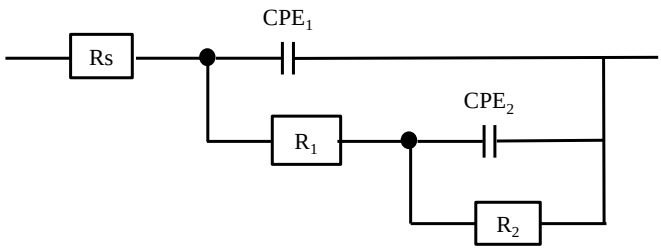

Figure 5- 80: Equivalent electrical circuit for EIS data fittings of the specimens corroded simulated seawater (SSW) saturated with 99.98% CO_2 at 25^{0}C and pH 6.5

Table 5- 16: Fitted EIS parameters of samples corroded simulated seawater (SSW) saturated with 99.98% CO_2 at 25^0C and pH 6.5

Sample	Rs ($\Omega.cm^2$)	CPE_1 ($\mu F^{-1}cm^{-2}$)	n_1	R_1 ($\Omega.cm^2$)	CPE_2 ($\mu F^{-1}cm^{-2}$)	n_2	R_2 ($K\Omega.cm^2$)
P110	41.53	$6.97*10^{-6}$	0.88	797.9	$6.15*10^{-5}$	0.63	9.992
TN95	40.99	$1.49*10^{-5}$	0.83	566	$6.83*10^{-5}$	0.65	4.626
X65	25.84	$3.96*10^{-5}$	0.79	1356	$5.71*10^{-5}$	0.65	31.735

To further understand the surface morphology of the corroded samples and how it affects the electrochemical performance, SEM/EDX and XRD analyses were conducted. Figure 5-81 showed the SEM micrographs of the three specimens which revealed mild general corrosion exposing the ground scratches with little corrosion product formed.

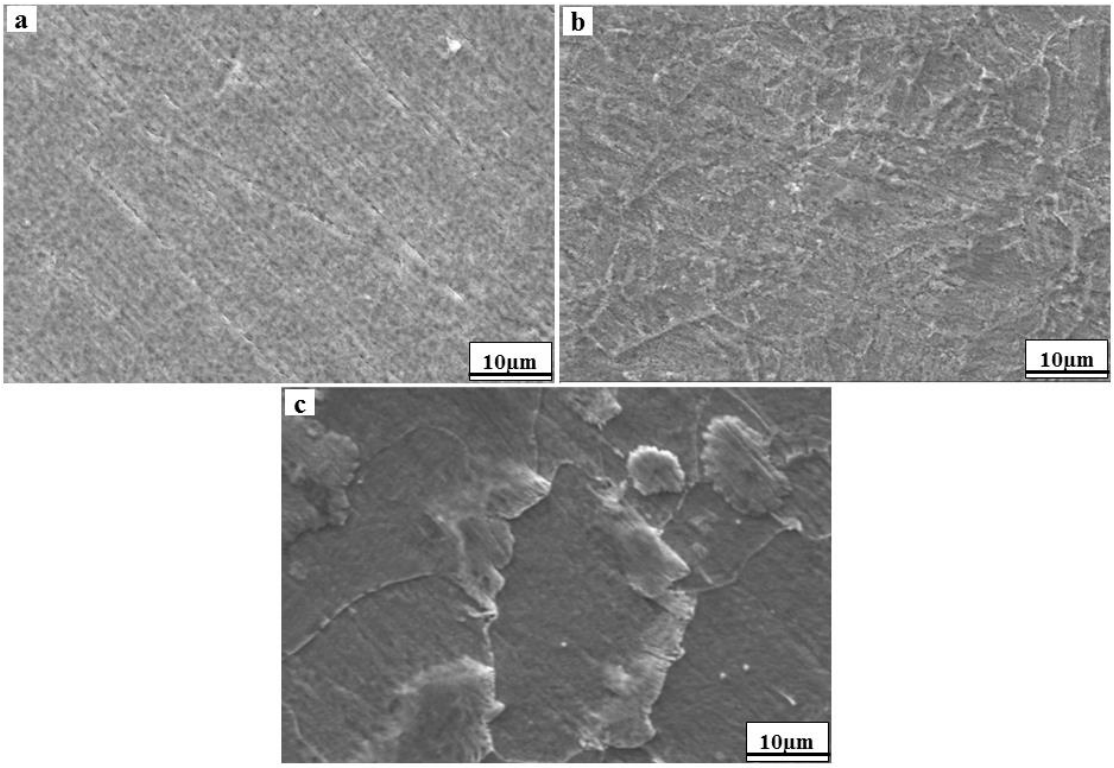

Figure 5- 81: SEM micrographs of samples corroded simulated seawater (SSW) saturated with 99.98% CO_2 at 25^0C and pH 6.5 (a) P110, (b) TN95 and (c) X65

The XRD pattern shown in Figure 5-82 indicated Fe, (Ca, Mg)CO_3 and $CaCO_3$ as the constituents of the corrosion products. The high intensity pick of Fe is a confirmation that the corrosion product did not cover the surface of the steels.

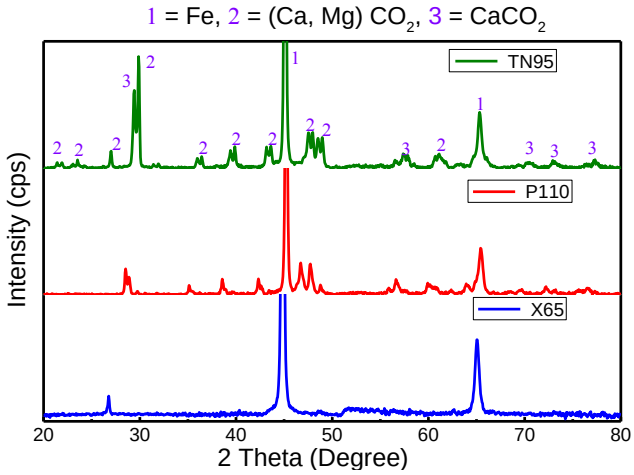

Figure 5- 82: XRD spectra of samples corroded simulated seawater (SSW) saturated with 99.98% CO_2 at 25^{0}C and pH 6.5

Figure 5-83 illustrates the evolution of corrosion rate with time for the three steels corroded in three different simulated seawater (SSW) environments. These conditions are naturally aerated SSW, SSW saturated with 0.5% CO_2 and SSW saturated with 99.98% CO_2. The results of the investigations of the effect of each of these SSW environments are shown in Figures 5- 41(a), 5- 41 (b) and 5-77 respectively.

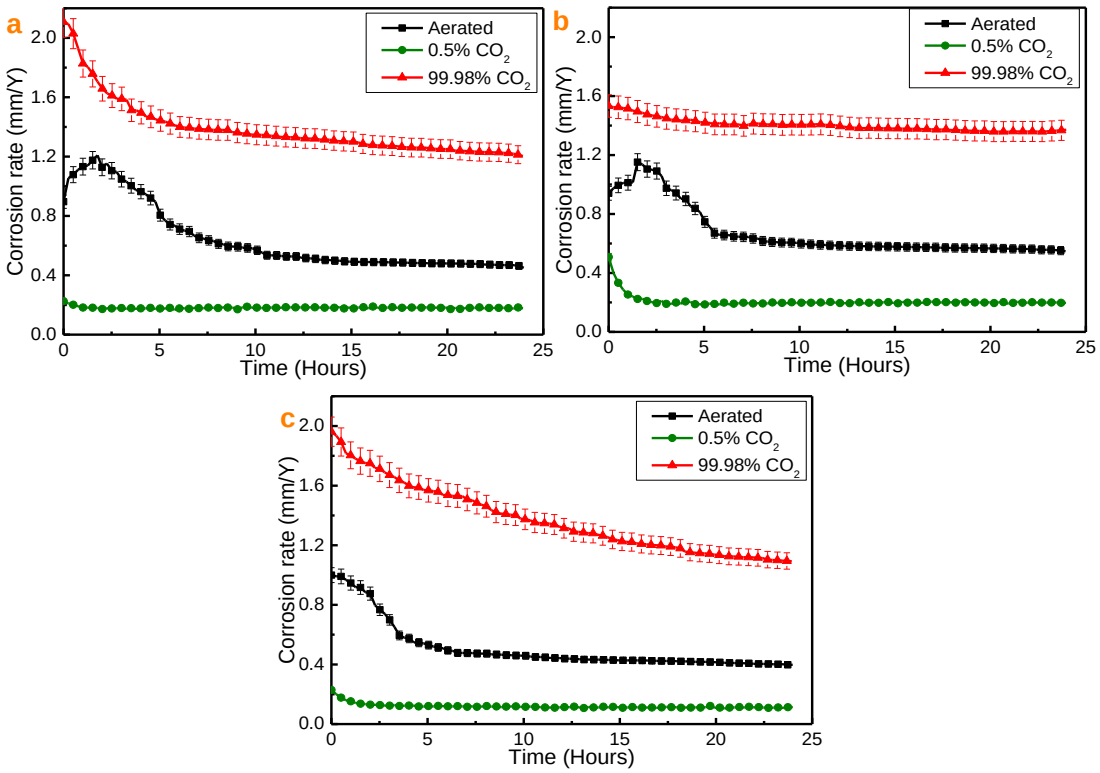

Figure 5- 83: Comparison of the evolution of corrosion vs time plots of specimens corroded in three different simulated seawater environments at 25^{0}C and pH 6.5 (a) P110, (b) TN95 and (c) X65.

5.1.8.3 The Corrosion behaviour of the steels by weight loss in 3.5 wt% NaCl solution saturated with 99.98% CO_2 at 25^0C and pH 6.5

The corrosion rate of steels P110 and TN95 was further investigated by weight loss in 3.5 wt% NaCl solution saturated with 99.98% CO_2 at 25^0C and pH 6.5. Five coupons of steels P110 and TN95 were prepared and immersed in the electrolyte for 24, 48, 72, 96 and 120 hours respectively. Figure 5-84 shows the transition of corrosion rate and pH with time for the specimens. From this figure, significant corrosion rate of about 0.11 mm/Y and 0.127 mm/Y for steels P110 and TN95 respectively can be observed after the first 24 hours. This was followed by a rapid decrease in corrosion rate which can be attributed to the formation of corrosion product films on the surface of the steels. This corrosion film formed barrier between the corrosive solution and the surface of the steels thus partially protecting the steel substrate from corroding. About 13% and 17% decrease in corrosion rate for steels P110 and TN95 respectively was observed as immersion time increased from 24 to 72 hours. With further increase in immersion time steel TN95 exhibited about 2% drop in corrosion rate. On the other hand, steel P110 showed higher drop of about 6% in corrosion rate as immersion time increased from 72 hours to 120 hour. This means that more stable and protective corrosion products formed on the surface of steel TN95 than on the surface of steel P110 within this time interval.

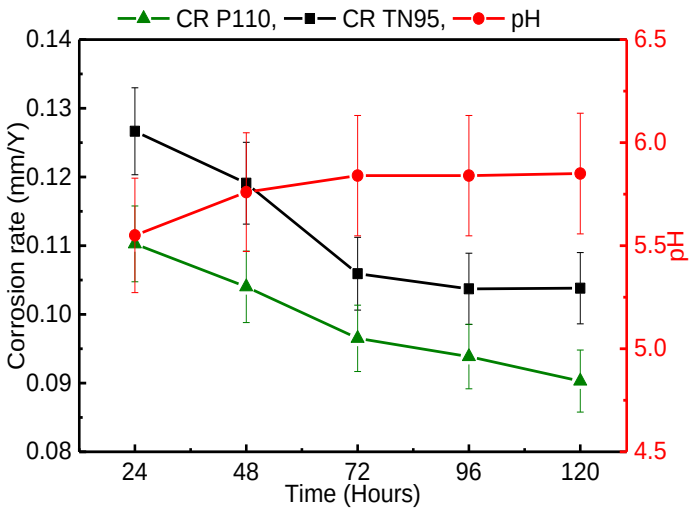

Figure 5- 84: Transition of corrosion rate by weight loss of P110 and TN95 in 3.5 wt% NaCl Saturated with 99.98% CO_2 at ambient temperature for 5 different days

The pH of the solution was monitored and the change in pH with time is also shown in Figure 5-84. The figure showed that the pH of the solution increased from 5.55 to 5.84 after 72 hours and remain virtually stable between 72 and 120 hours with only 0.29% increase in pH.

Figure 5-85 shows the SEM micrographs of the evolution of surface morphology of P110 corroded in 99.98% CO_2 saturated 3.5 wt% NaCl for different time interval. Steel P110 has ferrite-pearlite (Fe + Fe_3C) microstructures. The SEM micrograph of Day 1 (Figure 5-85) showed that few ferrites were dissolved. However, with the prolongation of immersion time, there was a gradual increase in ferrite dissolution with a corresponding decrease in surface area of the protruded Fe_3C. This is made more vivid in the SEM micrograph of Day 5 (Figure 5-85) which revealed wide selective dissolution of ferrite phase leaving the protruded cementite (Fe_3C) along the grain boundary.

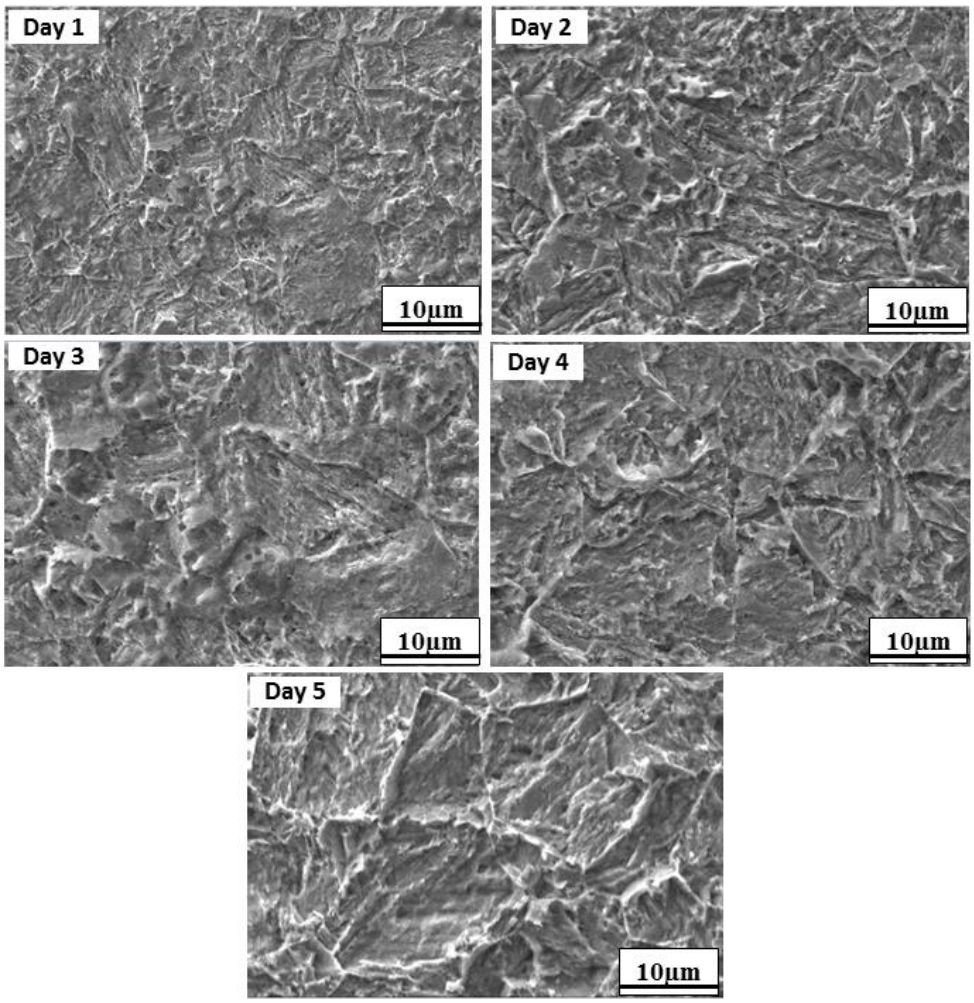

Figure 5- 85: SEM micrographs of the surface morphology of P110 after immersion in 3.5 wt% NaCl saturated with pure CO_2 at ambient temperature for 5 different days.

The SEM micrographs of the evolution of surface morphology of steel TN95 corroded in 3.5 wt% NaCl saturated with 99.98% CO_2 after 24, 48, 72, 96 and 120 hours are presented in Figure 5-86. It is evidenced from this figure that the corrosion products that formed on the surface of the steel substrate at the initial stage (Day 1) are sparse, scattered and thin. This could not form sufficient barrier against the penetration of chloride ions and other

corrosive ions to the steel substrate resulting to high corrosion rate. However, the quantity of corrosion products gradually increased, and became denser and thicker with the prolongation of immersion time thereby frustrating a direct contact of the corrosion medium with the surface of the specimen. The SEM surface morphology at Day 5 showed concentrated, denser and more compact corrosion products with the capacity to effectively inhibit corrosion reaction and consequently decreased and relatively stabilised the corrosion rate with immersion time as revealed in Figure 5-84.

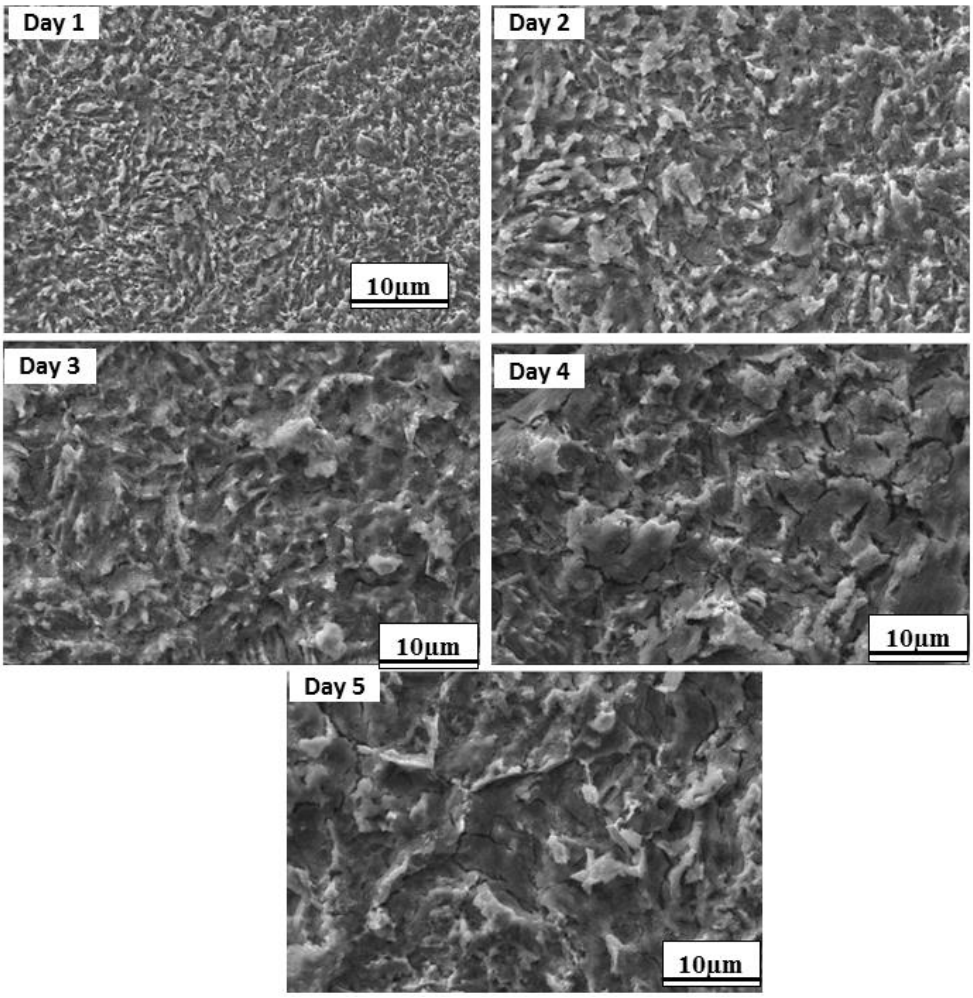

Figure 5- 86: SEM micrographs of the surface morphology of TN95 after immersion in 3.5 wt% NaCl saturated with pure CO_2 at ambient temperature for 5 different days

To identify the chemical composition and structure of the corrosion products on the surface of the specimens, XRD analyses were conducted. Figure 5.87 shows the XRD patterns of the steels corroded in 3.5 wt% NaCl saturated with 99.98% CO_2 after 24, 48, 72, 96 and 120 hours of immersion time. This figure indicated that the main corrosion products are Fe_3C and Fe_3O_4. The intensity of these compounds increased with immersion time attesting to the compactness and capability of the corrosion product to effectively protect the metal substrate from corroding as shown in the SEM micrographs (Figures 5-85 and 5-86). This resulted in the decrease in corrosion rate with immersion time (Figure 5-84).

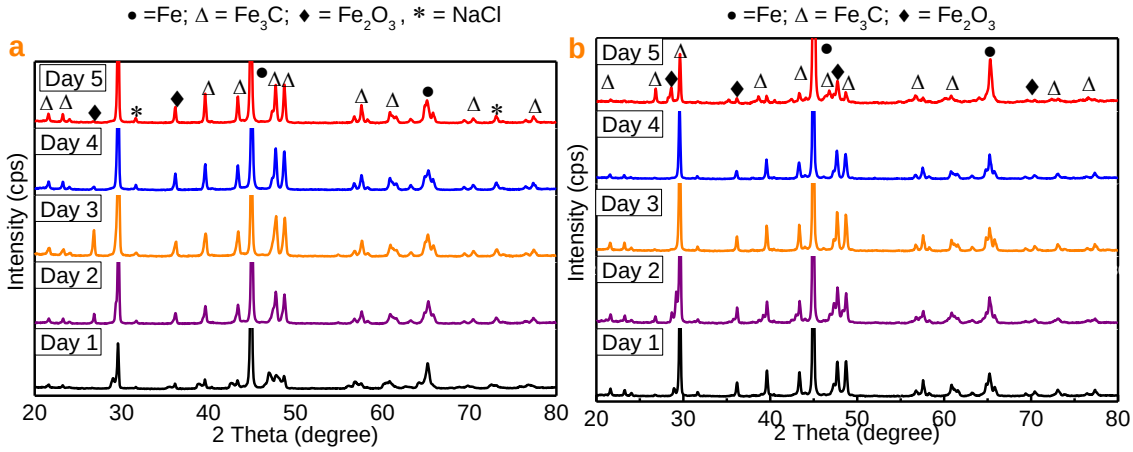

Figure 5- 87: XRD analysis of (a) P110 and (b) TN95 after immersion in 3.5 wt% NaCl saturated with 99.98% CO_2 at ambient temperature for 5 different days.

5.1.8.4 The tendency of the micro-alloyed steels to form protective $FeCO_3$ film in 3.5 wt% NaCl solution saturated with 99.98% CO_2 at 60^0C and pH 6.5

Figure 5- 88 shows the transition of corrosion rate and OCP with time for the micro-alloy steels corroded in 3.5 wt% NaCl solution saturated with 99.98% CO_2 at 60^0C, pH 6.5 and for 96 hours. At the beginning of the electrochemical corrosion tests, the three specimens exhibited sharp decrease in corrosion rate with a corresponding increase in OCP within the first 5 to 10 hours depending on the specimen. This can be attributed to a spontaneous corrosion process resulting in the formation of stable protective pseudo-passive layer on the surface of the substrate [154].

It can be seen from SEM surface morphologies of the specimens in Figures 5-89 (a), Figure 5-90 (a) and Figure 5-91 (a) that $FeCO_3$ crystals formed on the surface of the specimens. These $FeCO_3$ crystals are uniformly scattered on the surface of the specimens

and barely cover the surface of the specimen presenting an average grain size of 1.87 µm for steel P110, 1.58 µm for steel TN95 and about 3.00 µm for steel X65. This is the nucleation stage of $FeCO_3$ formation and so do not provide good corrosion protection.

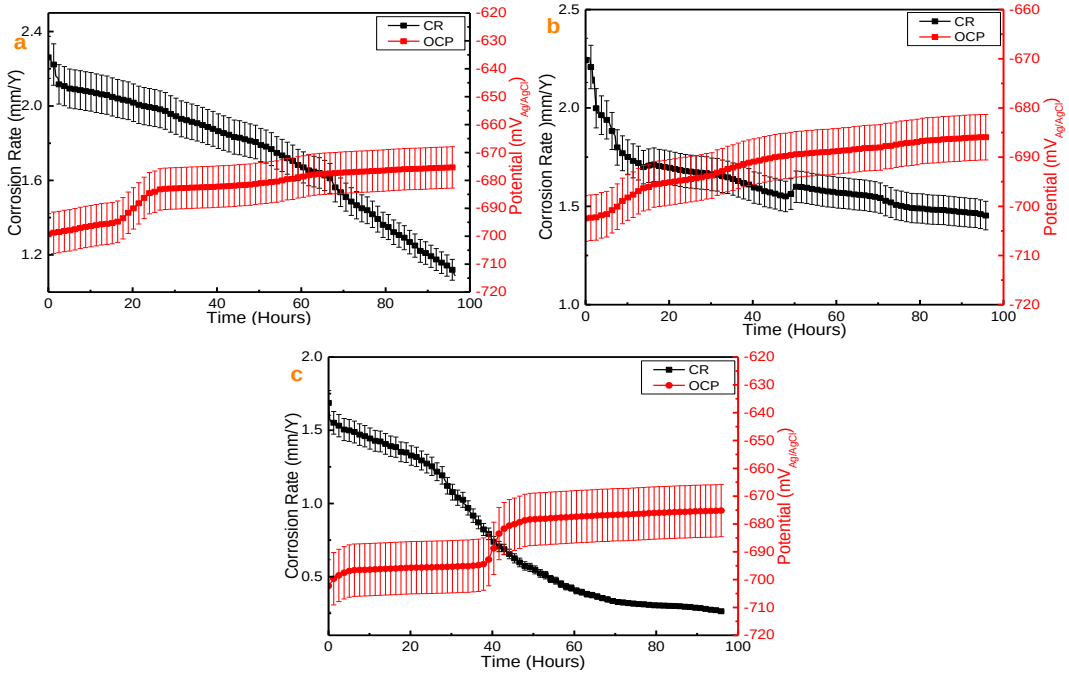

Figure 5- 88: Evolution of corrosion rate and OCP with time for Specimens in 3.5 wt% NaCl Saturated with 99.98% CO_2 at 60^0C, pH6.5 for 4 days (a) P110, (b) TH95 and (c) X65

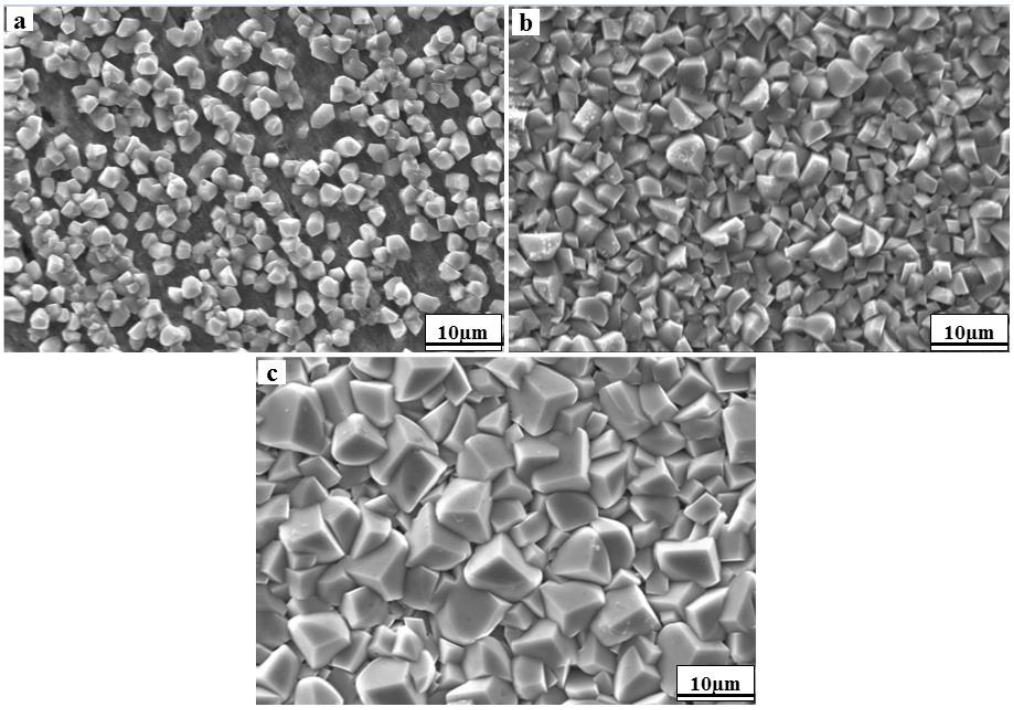

Figure 5- 89: Transitions of SEM surface morphology of P110 corroded in 3.5 wt% NaCl saturated with 99.98% CO_2 at 60^0C, pH6.5 for 4 days (a) Day 1, (b) Day 2 and (c) Day 4

The formation of $FeCO_3$ crystals appear to be a gradual process. At the initial stage, few $FeCO_3$ crystals nucleated. As the corrosion process continued, more crystals precipitated and deposited on the surface of the specimen. The thickness of the corrosion product layer ($FeCO_3$ crystals) increased gradually with time and the deposits continually fill the pores within the product layer. The gaps and pores between the crystals continue to reduce thereby increasing the density of the layer. This prevented the diffusion of corrosive species to the substrate of the steel and ultimately reduced the corrosion rate [132]. Between 24 hours and 48 hours for steel P110, 20 hours and 38 hours for steel TN95 and 8 hours and 38 hours for steel X65, the specimens demonstrated an increase (shift towards positive direction) in OCP with resultant decrease in the corrosion rate as revealed in Figure 5-88. It can also be noted from SEM surface morphologies shown in Figures 5-89 (b), 5-90 (b) and 5-91 (b) for day 2 that the size of the $FeCO_3$ crystals has increased to an average size of 2.94 µm for steel P110, 1.76 µm for steel TN95 and 3.91 µm for X65 suggesting a growth of the $FeCO_3$ crystals that formed on the first day. The growth in grain size with time was validated using Fiji imageJ analysis as shown in Appendix A. The decrease in corrosion rate and increase in OCP could be as a results of more compact and greater coverage of the specimen surface by these $FeCO_3$ crystals.

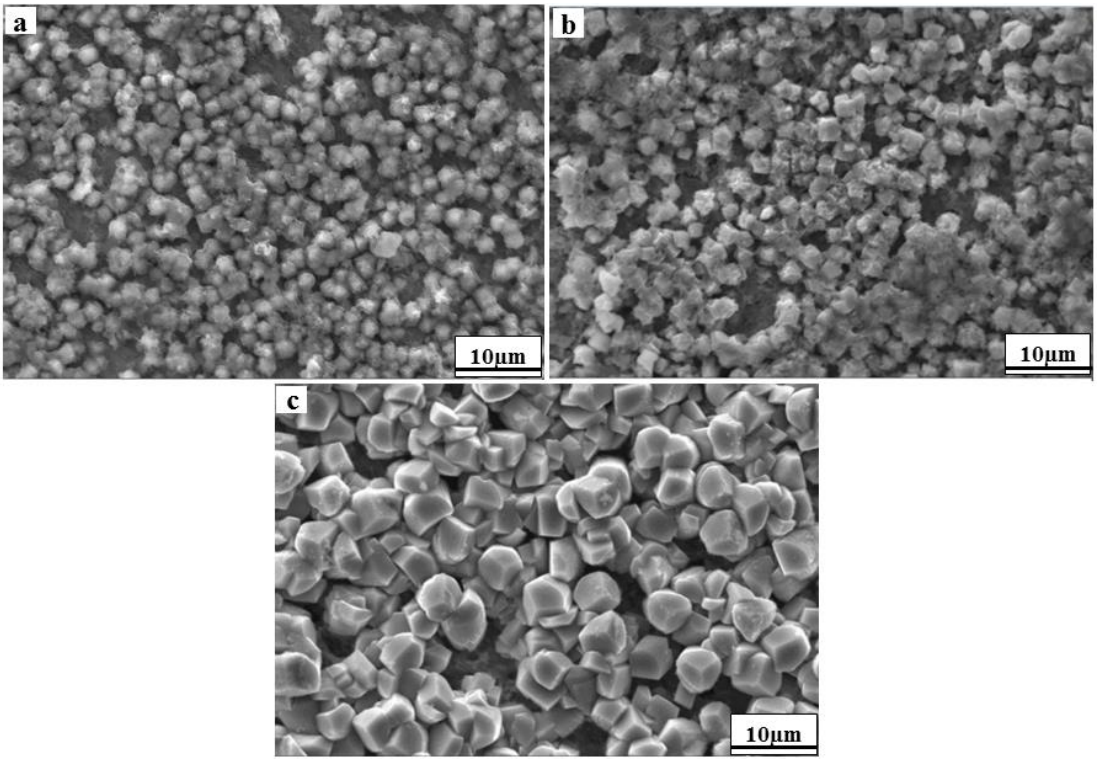

Figure 5- 90: Transitions of SEM surface morphology of TN95 corroded in 3.5 wt% NaCl saturated with 99.98% CO_2 at 60^0C, pH6.5 for 4 days (a) Day 1, (b) Day 2 and (c) Day 4

Figure 5-88 disclosed that the remaining duration of the linear polarization curves of the steels in 3.5 wt% NaCl solution saturated with 99.98% CO_2 at pH 6.5 exhibited virtually stable corrosion rate and OCP. This stability is more pronounced with steel X65 whose SEM surface morphology after 4 days of corrosion demonstrated a well-developed $FeCO_3$ crystal layer. This covered the entire steel surface thereby offering good corrosion protection as shown in Figure 5-91 (c). On the other hand, steel P110 (Figure 5- 89(c)) and Steel TN95 (Figure 5-90(c)) displayed less stable OCPs and corrosion rates. Although The SEM surface morphology of steel P110 seemingly displayed a well-covered and compacted prism shaped $FeCO_3$ after 4 days (Figure 5-89(c)), the plot of corrosion rate versus time showed almost a linear relationship suggesting continued corrosion attack. Figure 5-90(c) showed some defects on the SEM surface micrographs of steel TN95. This must have necessitated the witnessed continued declined in corrosion rate since some portions of the surface remain uncovered. In general, the continued increase in OCP with the corresponding steady decrease in corrosion rate can be linked to the suppression of anodic reaction relative to cathodic process. This can be attributed to slight blocking of active sites on the steel surface by the precipitation of $FeCO_3$ [132].

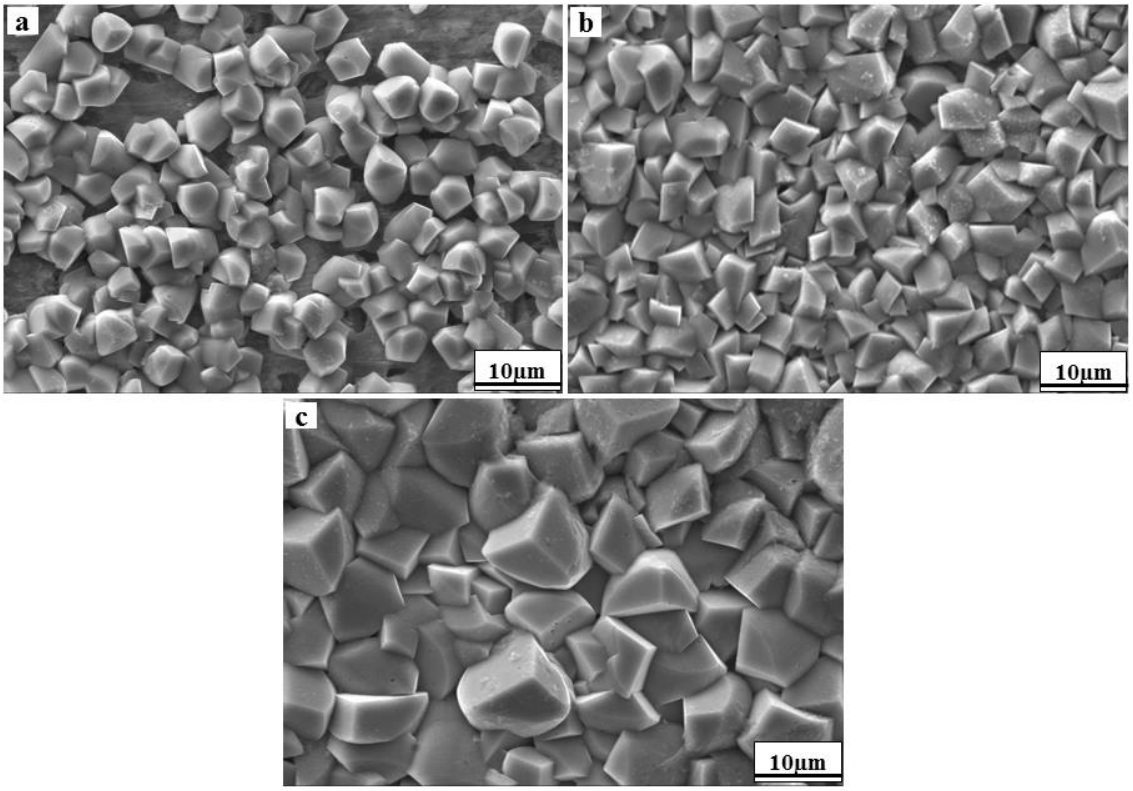

Figure 5- 91: Transitions of SEM surface morphology of X65 corroded in 3.5 wt% NaCl saturated with 99.98% CO_2 at 60^0C, pH6.5 for 4 days (a) Day 1, (b) Day 2 and (c) Day 4

Figure 5-92 shows the XRD pattern of the three steels corroded in 3.5 wt% NaCl solution saturated with 99.98% CO_2 at pH 6.5 for 4 days. The XRD pattern revealed that the main constituents of the corrosion product on the surface of the corroded specimens are Fe, Fe_3C and $FeCO_3$. Fe_3C is part the microstructure of the steel that were exposed after selective dissolution of ferrite while $FeCO_3$ is the inherent corrosion product of sweet corrosion. It can be observed from Figure 5-92 that the peaks of Fe and Fe_3C decreased while the peak of $FeCO_3$ increased with increase in polarization time suggesting that $FeCO_3$ nucleated, grew and covered the surface of the specimen. Figure 5-92 (c) for steel X65 shows that the XRD pattern did not detect Fe_3C peak. This is because the SEM surface morphology (Figure 5-91(c)) presented a well-covered and compacted prism-shaped $FeCO_3$ that provided adequate protection. The XRD pattern of steel P110 (Figure 5-92(a)) displayed few Fe_3C peaks and the Fe peaks which were almost consumed by the very high intensity $FeCO_3$ peak. Therefore as the amount of $FeCO_3$ crystals characteristic peak becomes larger with corrosion time, the intensities of Fe and Fe_3C characteristic peaks decreased depicting that the area of steel substrate, which corrosion products do not cover, also diminished gradually thereby reducing general corrosion.

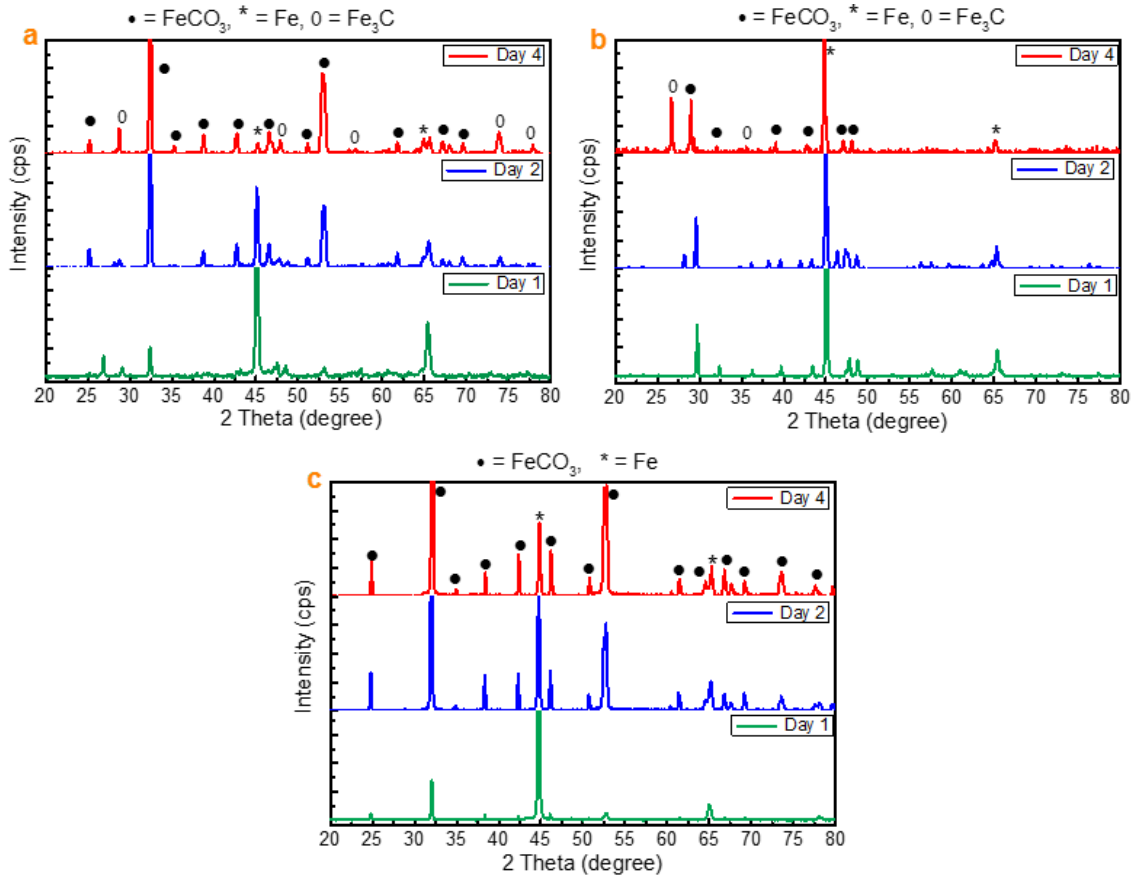

Figure 5- 92: XRD pattern of the specimens corroded in 3.5 wt% NaCl Saturated with 99.98% CO2 at 60^0C, pH6.5 for 4 days (a) P110, (b) TN95and (c) X65

5.2 Alloying of steels P110 and TN95 with Zr and Hf and investigating the corrosion behaviour of these alloyed specimens in simulated produce water (SPW)

The two worst corrosion proprietary micro alloy steels (P110 and TN95) were alloyed with Zr and Hf. This was aimed at improving the corrosion properties of the specimens. The corrosion performance of these alloys were investigated in simulated formation water and the results presented in this section.

5.2.1 Characterization of alloyed specimens

The alloyed samples were characterised using SEM/EDS, XRD, hardness test and grains size analysis. The SEM micrographs of samples P110 and TN95 alloyed with different quantities (0.1, 0.2 and 0.4 wt%) of Zr and Hf are shown in Figures 5-93 and 5-94 respectively.

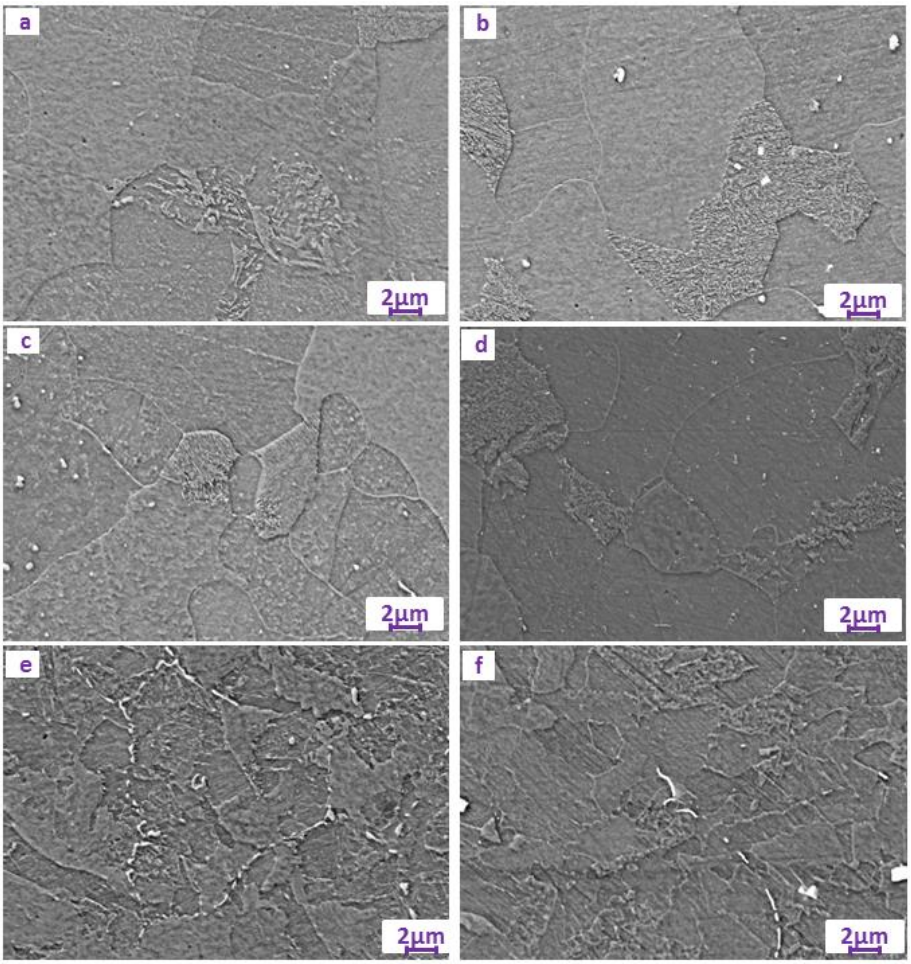

Figure 5- 93: SEM micrographs of P110 alloyed with (a) 0.1 wt% Zr, (c) 0.2 wt% Zr, (e) 0.4 wt% Zr, (b) 0.1 wt% Hf, (d) 0.2 wt% Hf and (f) 0.4 wt% Hf

These figures show that the grain size of the specimens decreased with increase in the amounts of alloying elements (Zr and Hf) added. White particles of sizes ranging from 2 µm to 5 µm and which are precipitates of Zr, Hf and/or their intermetallic compounds can be seen dispersed over the entire steel substrate for the alloys containing lower (0.1 and 0.2 wt%) Zr or Hf. These particles are more pronounced in the specimens alloyed with Hf. This was because very small percent (0.5 wt%) of Hf for solid solution as against 7 wt% of Zr in Fe. This means that more Hf precipitate as intermetallic compound. For alloyed specimens containing 0.4 wt% Zr or Hf, these particles are mainly located along the grain boundaries. The surface morphology of these micrographs (Figures 5-93 and 5-94) demonstrated two distinct regions which can be considered as solid solution matrix and the eutectic regions.

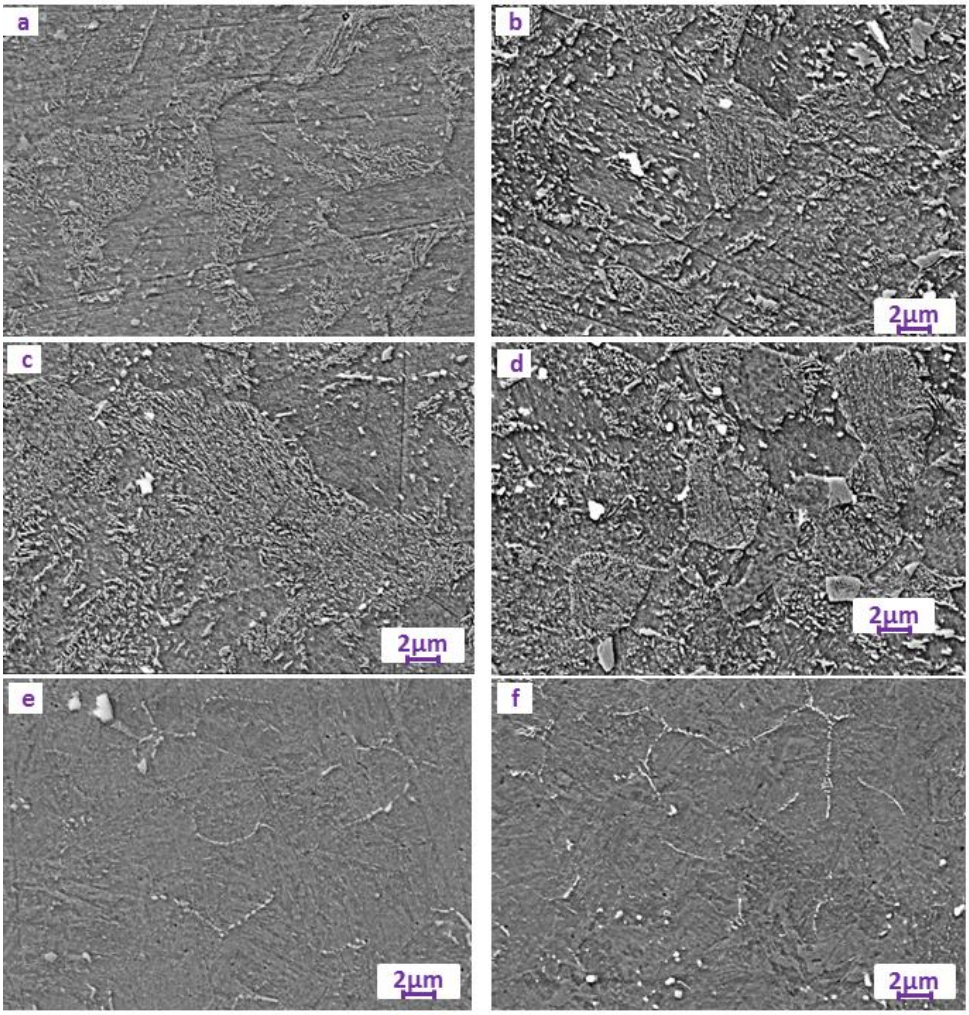

Figure 5- 94: SEM micrographs of TN95 alloyed with (a) 0.1 wt% Zr, (c) 0.2 wt% Zr, (e) 0.4 wt% Zr, (b) 0.1 wt% Hf, (d) 0.2 wt% Hf and (f) 0.4 wt% Hf

EDS elemental analysis presented in Figures 5-95 and 5-96 for specimens P_1-Zr_1 and T_1-Zr_1 showed that the matrix regions (B) consist of Fe and C as the main elements while Si, Cr, Mn and Mo are in traces. The matrix region marked "B" consists of Fe and C as the main elements while Si, Cr, Mn and Mo are presence in traces. The absent of detectable Zr or Hf (depending on the samples) within the matrix regions by the EDS analysis indicated that the precipitates segregated together and are separated from the matrix. Similar results have been reported [88]. On the other hand, the eutectic regions "C" also has Fe and C as the main elements but with other minor elements in higher concentrations than in region "B". It is interesting to note that point "A" is mostly located within the eutectic regions. The EDS elemental analyses for other alloyed samples are listed in Appendix B1.

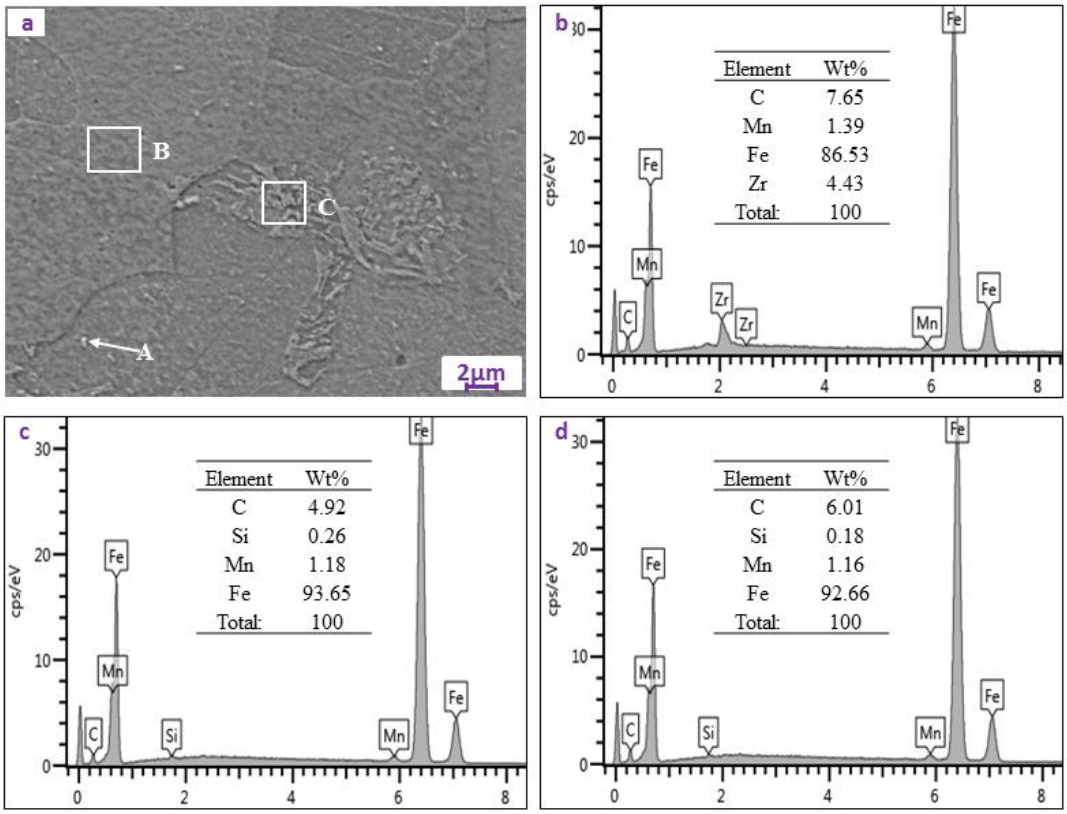

Figure 5- 95: EDS analyses of P_1-Zr_1 (a) microstructure of as cast P_1-Zr_1, (b) EDS at point A in (a), (c) EDS at point B in (a) and (d) EDS of small particle at point C in (a)

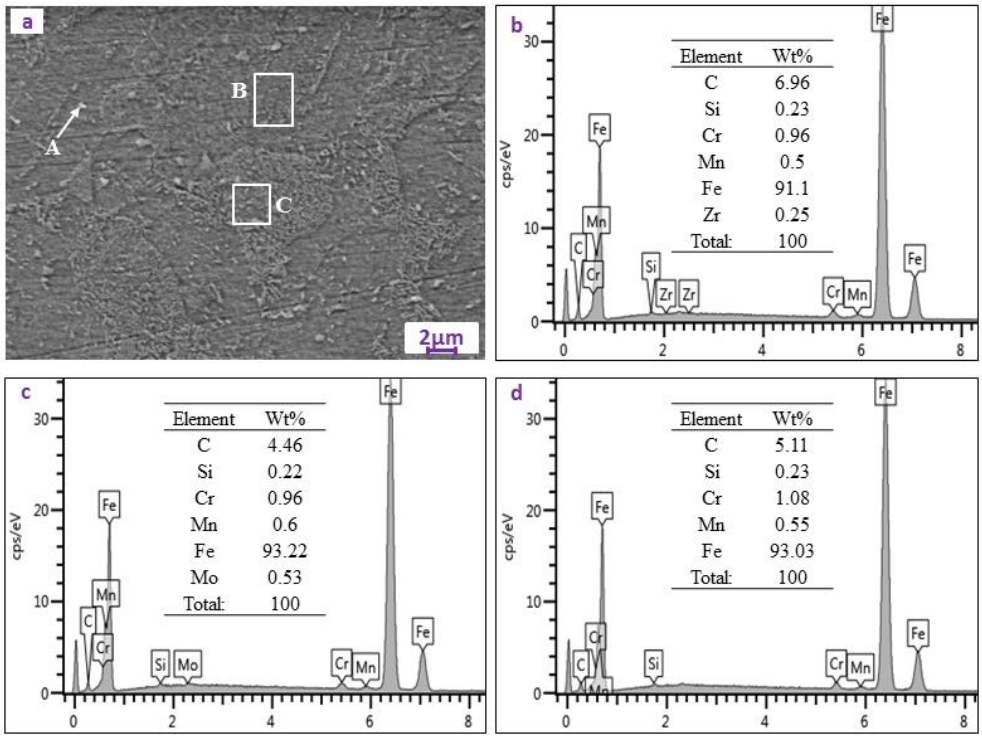

Figure 5- 96: EDS analyses of T_1-Zr_1 (a) microstructure of as cast T_1-Zr_1, (b) EDS at point A in (a), (c) EDS at point B in (a) and (d) EDS of small particle at point C in (a)

The EDS elemental mapping for alloyed specimens P_1-Zr_1 and T_1-Zr_1 are also shown in Figures 5-97 and 5-98 respectively. These figures revealed that both the major elements (Fe and C) and the minor elements (Si, Cr, Mo, Zr, Hf, etc) detected by EDS elemental analyses were nearly uniformly distributed within the entire steel substrate. However, there are few pockets of precipitates which were identified by XRD analyses (Figure 5-100) as Zr- and/or Hf-rich intermetallic phases. The EDS elemental mapping for other alloyed samples are listed in Appendix B2.

A closer look at the SEM micrographs of the alloyed specimens shown in Figures 5-93 and 5-94 revealed that the grain size decreased with increase in the quantity of alloying elements (Zr or Hf). Figure 5-99 shows the average grain size (GS) of the alloyed steels with the corresponding ASTM grain size number (GSN). These data (Appendix D) were calculated using imageJ software and the Jeffries planimetric method as specified in ASTM E-112 standard [194]. From this figure it can be observed that the ASTM grain size number for the alloyed specimens increased with increase in alloying elements addition. Alternatively, this figure indicated a decrease in average grain size with increase in alloying elements. It can then be adjudged that increase in Zr and/or Hf addition

increased the ASTM grain size number which invariable means a decrease in grain size [54, 194]. This decrease in grain size can be ascribed to the ability of Zr and Hf precipitates to pin austenite grain growth [84, 222].

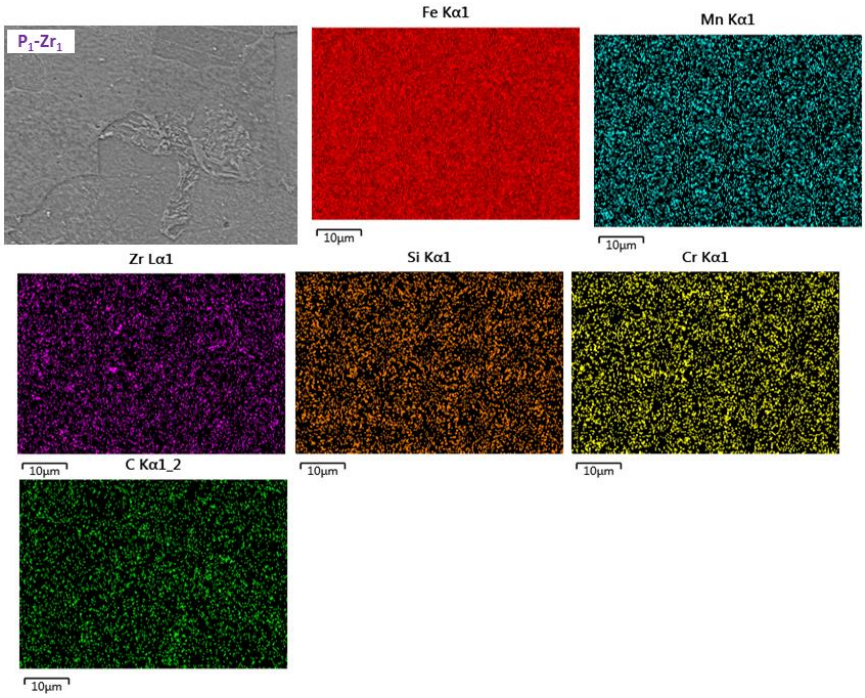

Figure 5- 97: EDS elemental mapping of P_1-Zr_1 showing the uniform distribution of the elements within the matrix of the steel

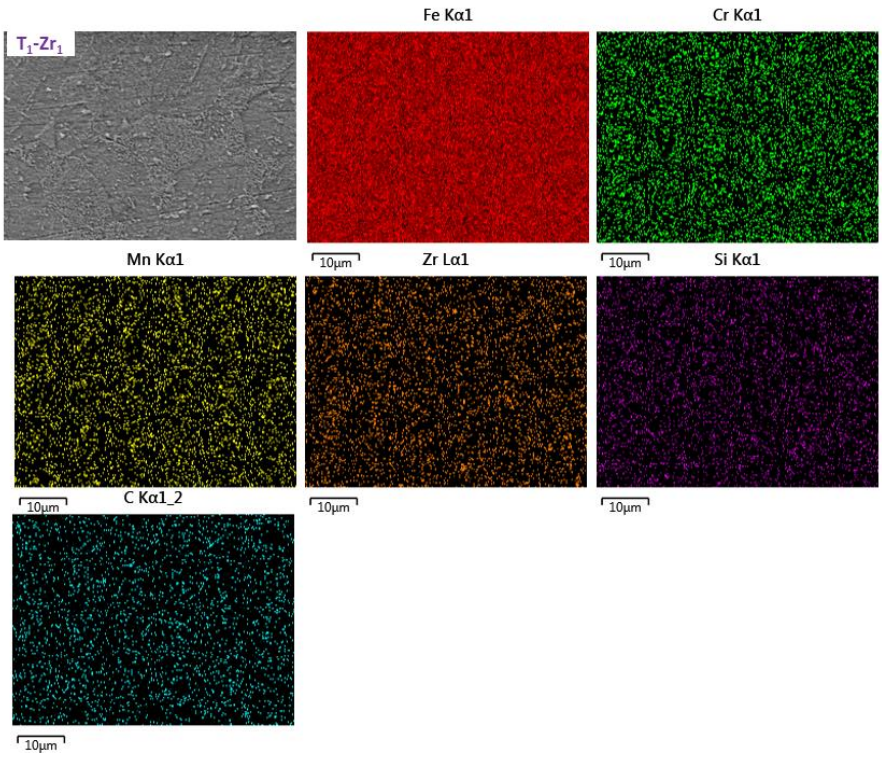

Figure 5- 98: EDS elemental mapping of T_1-Zr_1 showing the uniform distribution of the elements within the matrix of the steel

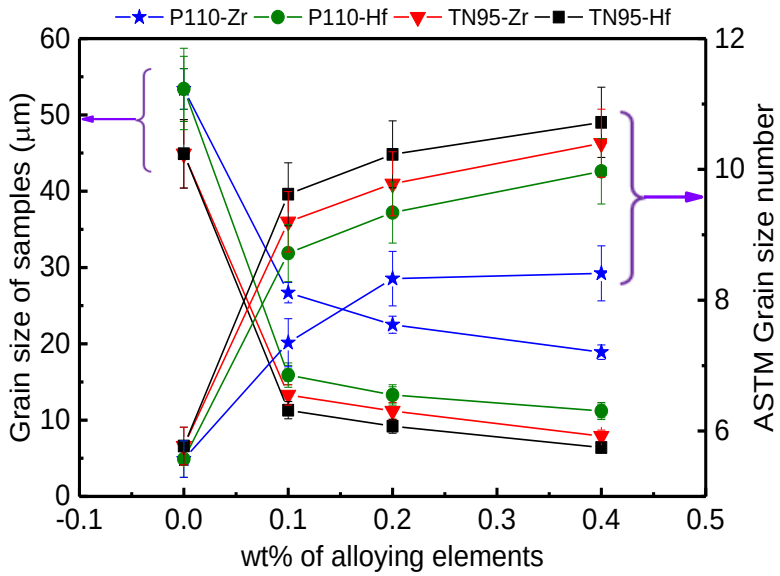

Figure 5- 99: Variation in ASTM grain size number (GSN) and grain size of the specimens with increase in addition of alloying elements

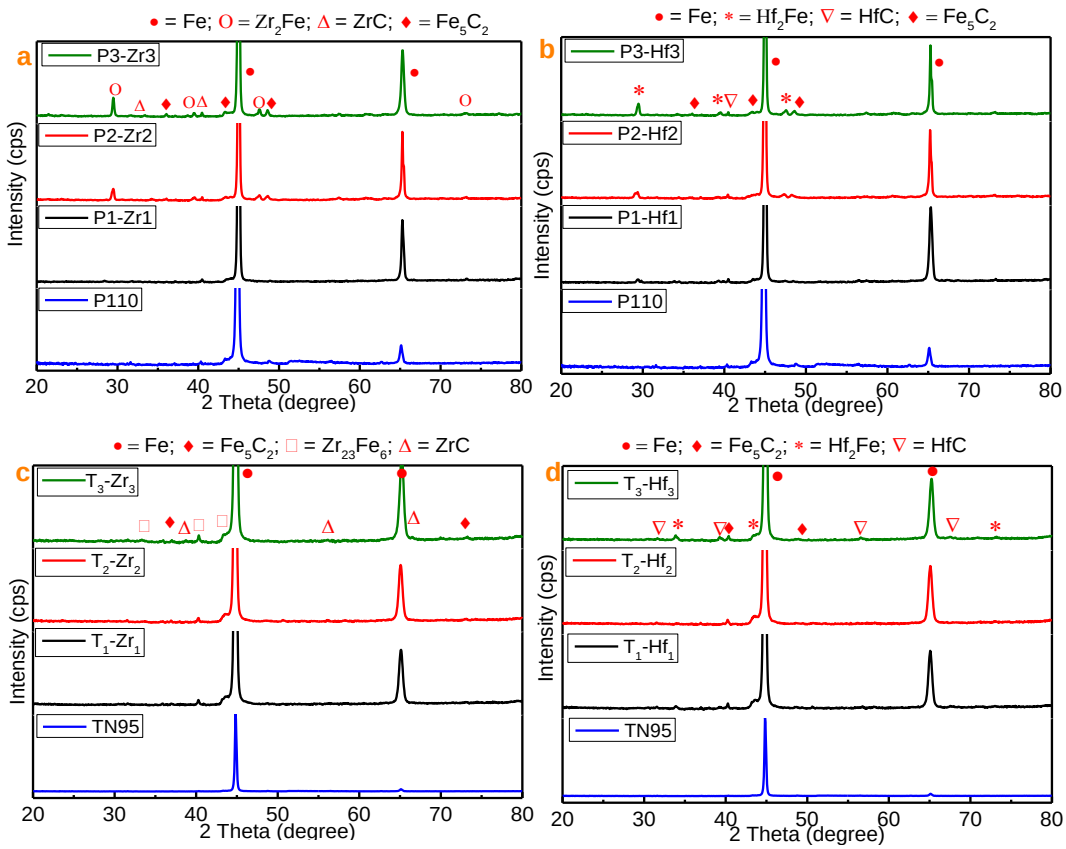

Figure 5- 100: XRD analysis of the specimens alloyed with different wt% Zr and Hf (a) P110-Zr, (b) P110-Hf, (c) TN95-Zr and (d) TN95-Hf

Figure 5-100 shows the XRD pattern of the unalloyed and alloyed micro-alloy steels P110 and TN95. Diffraction patterns were matched with reference patterns of pure substances from the powder diffraction database and the identified compounds with their matched 2θ values, diffraction planes and crystallographic structure are listed in Table 5-17. Pure Zr and Hf metal were not detected by the XRD analysis. However, intermediate compounds of these elements such as Fe_2Zr, $Fe_{23}Zr_6$ and ZrC for samples containing Zr and Fe_2Hf and HfC for samples alloyed with Hf were detected.

The results of the hardness tests and the corresponding tensile strength conducted on the unalloyed and alloyed specimens are presented in Table 5-18. This table shows that the hardness and the tensile strength of the alloyed steels increased with increase in Zr and/or Hf content. This is attributed to the formation of Zr- and/or Hf-rich intermetallic precipitates in the solid solution of the steels. These precipitates restrict grain growth during homogenization [79, 84, 87, 88] and frustrate dislocation movements during deformation.

Table 5- 17: XRD identification of elements and compounds of the unalloyed and alloyed specimens

Specimens	Identified elements	2Theta values	Diffraction planes	Crystal structures
P110/TN95	Fe	44.78, 65.19	(110), (200)	BCC
P_3-Zr_3	Fe	44.78, 65.19	(110), (200)	BCC
	Zr_2Fe	29.41, 36.22, 47.31, 74.5	(400), (422), (620), (931)	Tetragonal
	ZrC	33.35, 38,70	(111), (200)	Cubic
	Fe_5C_2	37.02, 42.74, 49.08	(3-11), (112), (-412)	Anorthic
P_3-Hf_3	Fe	44.78, 65.19	(110), (200)	BCC
	Hf_2Fe	29.69, 38.89	(400), (511)	Hexagonal
	HfC	38,97	(-200)	Cubic
	Fe_5C_2	37.02, 42.74, 49.08	(3-11), (112), (-412)	Anorthic
T_3-Zr_3	Fe	44.78, 65.19	(110), (200)	BCC
	$Zr_{23}Fe_6$	33.29, 40.00, 43.72	(331), (511), (440)	Cubic
	ZrC	38.70, 55.63, 66.35	(200), (220), (311)	Cubic
	Fe_5C_2	37.02, 42.74, 49.08	(3-11), (112), (-412)	Anorthic
T_3-Hf_3	Fe	44.78, 65.19	(110), (200)	BCC
	Hf_2Fe	38.89, 43.50, 74.89	(-511), (202), (218)	Hexagonal
	HfC	34.68, 38,9756.28, 70.56	(111), (-200), (220) (222)	Cubic
	Fe_5C_2	42.74, 49.08	(112), (-412)	Anorthic

Table 5- 18: Vickers Hardness number (VHN) of the specimens alloyed with different amount of Zr and Hf.

Specimens	Unalloyed		Alloyed with 0.1%		Alloyed with 0.2%		Alloyed with 0.4%	
	VHN	TS (MPa)	VHN	TS (MPa)	VHN	TS (MPa)	VHN	TS (MPa)
P110-Zr	129	410	132	420	139	440	212	680
P110-Hf	129	410	142	445	148	478	197	630
TN95-Zr	248	790	279	860	286	910	319	1020
TN95-Hf	248	790	288	920	297	945	299	960

5.2.2 Corrosion behaviour of steels P110 and TN95 alloyed with Zr and Hf in simulated produce water (SPW)

The alloyed specimens P110 and TN95 were subjected to electrochemical corrosion in order to investigate the impact of alloying elements (Zr and Hf) on their corrosion behaviour in comparison with the unalloyed specimens. All the experiments were conducted in simulated produced water saturated with 99.98% CO_2 at 25^0C, pH 6.5 and for 24 hours. This is to simulate the natural oil formation (water) environment. The composition of the simulated produce water is listed in Table 4-7.

5.2.2.1 Linear polarization resistance (LPR) of steels P110 and TN95 alloyed with Zr and Hf in simulated produce water (SPW)

The results of evolution of corrosion rate with time for specimens P110 and TN95 alloyed with different quantities (0.1, 0.2 and 0.4 wt%) of Zr and Hf in simulated produced water saturated with 99.98% CO_2 at 25^0C, pH 6.5 and for 24 hours are shown in Figure 5-101. The transient of corrosion rate with time for the unalloyed specimens (P110 and TN95) and the reference specimen (X65) are also incorporated in Figure 5-101. This figure shows that the unalloyed, alloyed and the reference specimens exhibited the same trend of corrosion demonstrating an initial high corrosion rate followed by a decrease in corrosion attack within the first 5 to 10 hours (depending on the specimen) of immersion time. This decrease in corrosion rate signifies that corrosion product film has begun to form on the surface of the samples thus presenting a barrier between the substrates and the electrolyte [166]. This manifested in a relatively nearly stable corrosion rate after about 10 hours of experiments for the unalloyed and alloyed specimens as shown in Figure 5-101. On the other hand, the reference specimen did not show stability but

presented a continuous slight decrease in corrosion rate. A closer look at this figure revealed that although the reference steel had an initial higher corrosion rate than both the unalloyed and the alloyed steels, it displayed a better corrosion performance after about 10 hours and 20 hours of experiments for the unalloyed and alloyed steels Zr_1 and Hf_1 respectively. On the other hand, both the unalloyed and the reference specimens indicated higher corrosion rate than all the alloyed specimens. This figure also shows that the alloyed steels demonstrated a decrease in corrosion rate with increase in alloying elements revealing very small variations (0.3 – 0.6 mm/Y) between the initial and final (24h) corrosion rate. This showed that the alloyed specimens presented better resistance to

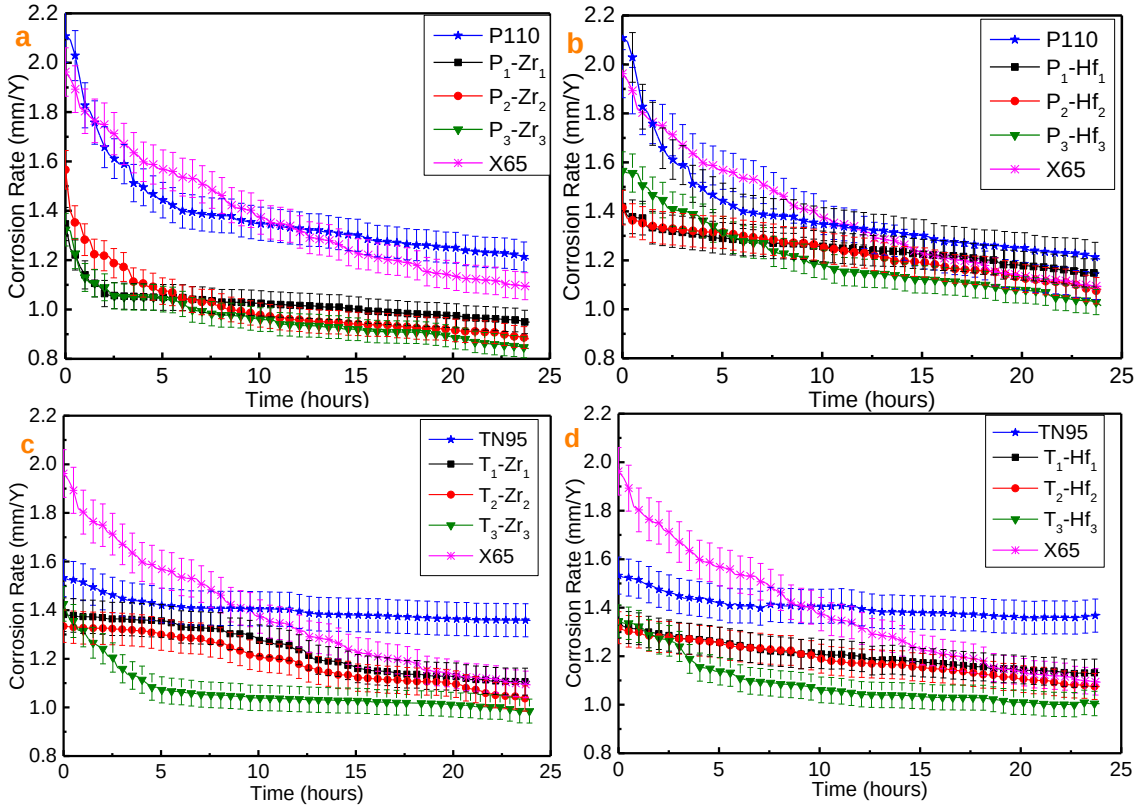

corrosion attack than the unalloyed specimens.

Figure 5- 101: Evolution of corrosion rate with time of the unalloyed and alloyed specimens in 99.98% CO_2 saturated simulated produced water at 25^0C and pH 6.5 (a) P110-Zr, (b) P110-Hf, (c) TN95-Zr and (d) TN95-Hf.

The open circuit potential (OCP) of the specimens was monitored during the 24 hours LPR and the results of the variation of OCP with time in simulated produced water saturated with 99.98% CO_2 at 25^0C and pH 6.5 are shown in Figure 5-102. This figure showed that the curves of the OPC versus time displayed a parabolic-image shape indicating an initial shift in the negative direction followed by a noble shift in potential within the last 14 hours of experiments. This figure also indicated that the curve of OPC

versus time demonstrated a shift in the positive direction with increase in the quantity of alloying elements added to the samples. This is in agreement with the results of the

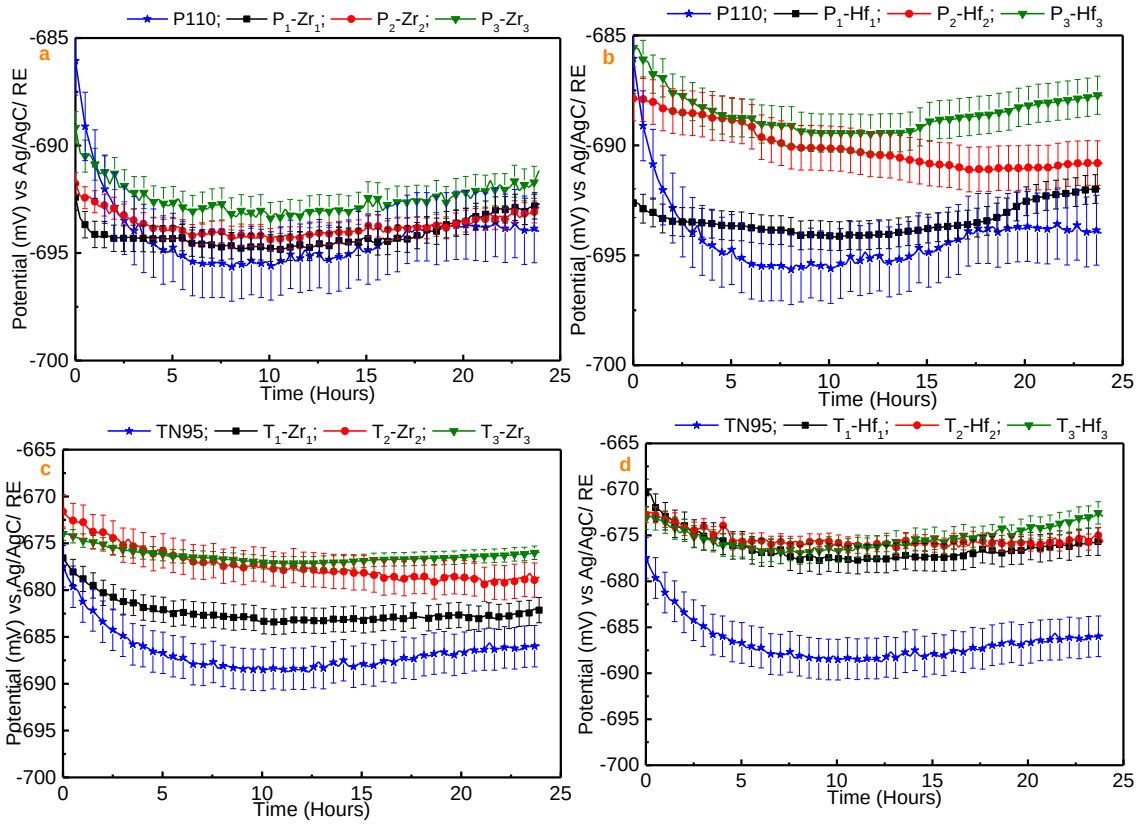

evolution of corrosion rate with time presented in Figure 5-101.

Figure 5- 102: Evolution of OCP with time of the unalloyed and alloyed specimens in CO_2 saturated simulated produced water at 25^0C and pH 6.5 (a) P110-Zr, (b) P110-Hf, (c) TN95-Zr and (d) TN95-Hf

5.2.2.2 Tafel polarization of steels P110 and TN95 alloyed with Zr and Hf in simulated produce water (SPW)

The corrosion behaviour of the alloyed specimens was also investigated using Tafel polarization method as detailed in Section 4.2.2.1. The Tafel plots for the unalloyed, alloyed (P110 and TN95) and reference steels (X65) are presented in Figure 5-103. It can be seen from this figure that the Tafel curves for all the specimens are similar. This indicates that the corrosion mechanism is the same. The anodic current density increased rapidly at potentials close to the corrosion potential but slightly reduced with further increase in potential signifying the formation of corrosion products. Both the anodic and cathodic branches demonstrated Tafel behaviour. Therefore, Tafel extrapolation method was used to extract Tafel parameters such as anodic Tafel constants (β_a), cathodic Tafel constants (β_c), corrosion potential (E_{corr}), and corrosion current density (I_{corr}) which are tabulated in Table 5-19.

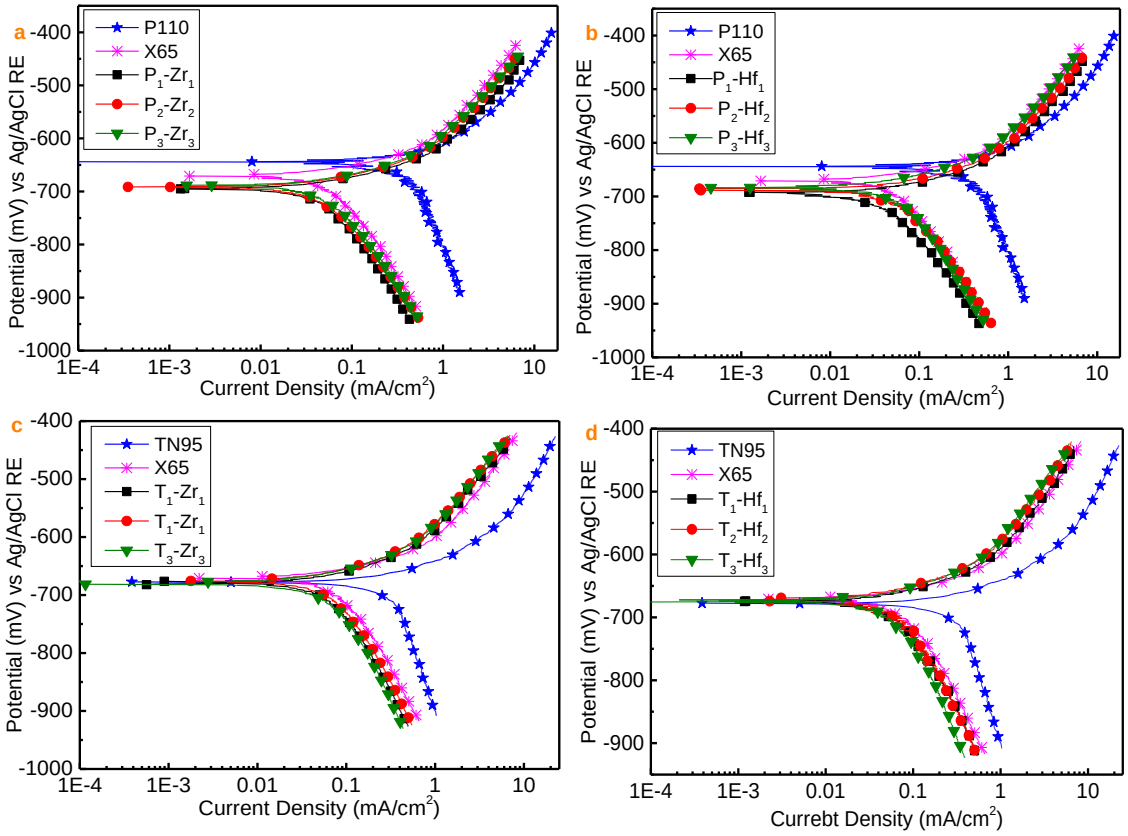

Figure 5- 103: Tafel plots of corroded alloyed specimens in CO_2 simulated sea water at 25^0C, pH6.5 and after 24 hours LPR (a) P110-Zr, (b) P110-Hf, (c) TN95-Zr and (d) TN95-Hf

It is obvious from Figure 5-103 that the anodic current densities of the unalloyed specimens are more than that of the reference sample which in turn is more than that of the alloyed specimens. Alternatively, the alloyed specimens showed a decrease in anodic current density as the quantity of alloying elements increased. This is in corroboration with the results of LPR suggesting that the corrosion resistance of the specimens increased with increase in alloying elements.

Table 5- 19: Tafel extrapolation parameters of the alloyed specimens corroded in simulated produced water (SPW) saturated with pure CO_2 at 25^0C and pH 6.5

Parameters	E_{corr} (mV)	i_{corr} (mA/cm^2)	β_a (mV/decade)	β_c (mV/decade)	Rp (Ω.cm^2)	CR (mm/Y)
X65	-671	0.045	55	190	411.57	0.21
P110	-666	0.055	55	280	362.93	0.25
P_1-Zr_1	-697	0.05	60	250	420.21	0.23
P_2-Zr_2	-691	0.045	50	170	372.81	0.21
P_3-Zr_3	-687	0.4	50	165	416.54	0.18
P_1-Hf_1	-692	0.045	60	230	459.17	0.21
P_2-Hf_2	-688	0.04	50	160	347.37	0.18
P_3-Hf_3	-684	0.035	45	140	422.48	0.16
TN95	-680	0.062	70	280	392.2	0.29
T_1-Zr_1	-677	0.045	45	160	338.9	0.21
T_2-Zr_2	-675	0.04	50	130	392	0.18
T_3-Zr_3	-681	0.035	40	120	372.19	0.16
T_1-Hf_1	-675	0.06	65	225	364.97	0.28
T_2-H_{f2}	-672	0.055	60	170	350.12	0.25
T_3-Hf_3	-671	0.04	60	160	473.69	0.18

5.2.2.3 Electrochemical impedance spectroscopy (EIS) of steels P110 and TN95 alloyed with Zr and Hf in simulated produce water (SPW)

In order to confirm the results of the linear polarization resistance and Tafel polarization tests and to investigate the effect of Zr and Hf on the stability of the corrosion product formed on the surface of the specimens, electrochemical impedance spectroscopy (EIS) was conducted at the end of 24 hours LPR. Figure 5-104 shows the Nyquist plots for the corroded alloyed specimens P110 and TN95 in simulated produced water saturated with 99.98% CO_2 at 25^0C and pH 6.5 after 24 hours polarization. It is apparent from Figure 5-104 that the Nyquist plots for all the alloyed samples exhibited depressed incomplete semicircle with centres below the real axis indicating that the charge-transfer process controls the electrochemical processes [58]. This figure also showed that the radius of the semicircle increased with increase in the quantity of Zr and Hf added. The charge transfer resistance (R_2) was obtained at the intercept of the semicircle on the real axis at low

frequency limits of the Nyquist spectra. From Figure 5-104, the intercepts (which is the diameter of the impedance spectra) for the specimens shifted toward (frequency reduction) the left side as the amount of Zr and Hf decreases signifying a decrease in charge-transfer resistance.

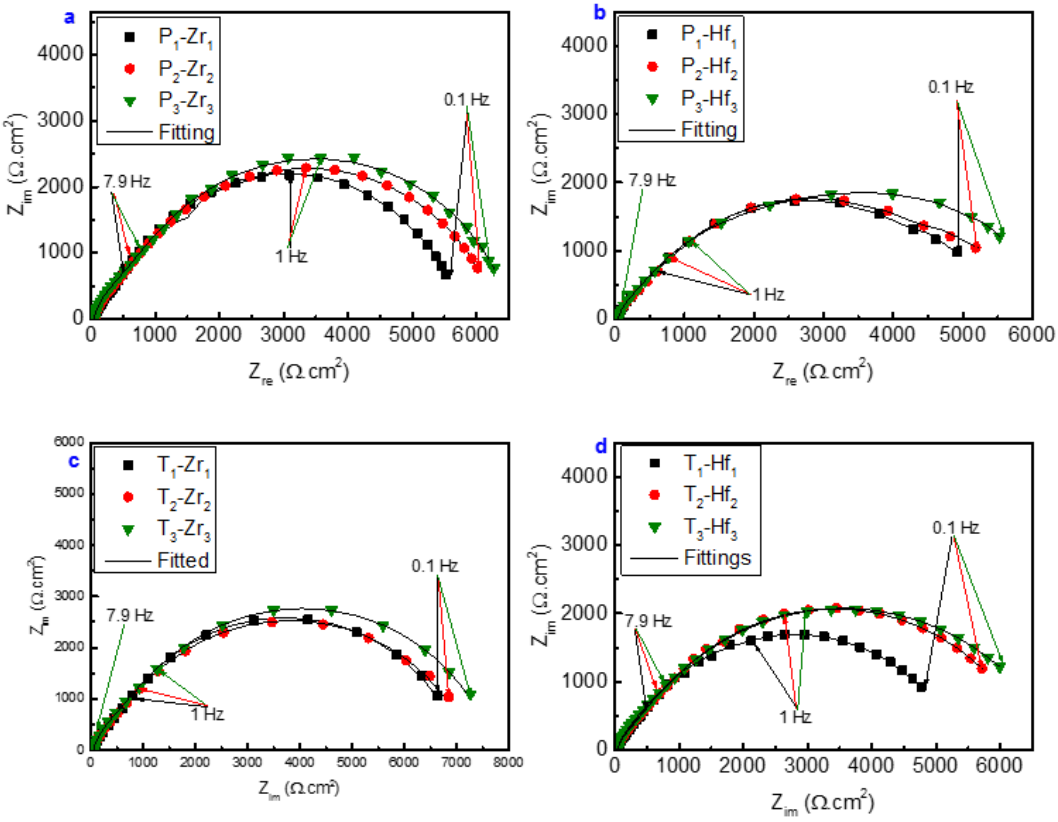

Figure 5- 104: Nyquist plots of corroded alloyed specimens in CO_2 simulated sea water at 25^0C, pH6.5 and after 24 hours LPR (a) P110-Zr, (b) P110-Hf, (c) TN95-Zr and (d) TN95-Hf

The Bode plots for the corroded alloyed specimens are presented in Figure 5-105. From this figure, the charge transfer resistance (R_2) corresponds to the intersection at modulus $|Z|$ axis at the low frequency while the solution resistance (Rs) corresponds to the intersection of the modulus $|Z|$ plot with the phase angle axis at the high frequency [109]. The Bode plots also revealed broad-phase angle spanning within the frequency range of 4 – 316 Hz with maximum phase angle at about 60^0 and corresponds to a frequency of about 160 Hz. The broad-phase angle of the Bode plots is an indication of a two time constants [206]. Thus equivalent circuit (EC) shown in Figure 5-80 was proposed for simulating the electrochemical behaviour of the corrosion products on the specimens after 24 hours of polarization. The variables of the circuit elements are

explained in Section 5.1.8.2 of this report. The fitted values of the elements of the equivalent circuit are listed in Table 5-20.

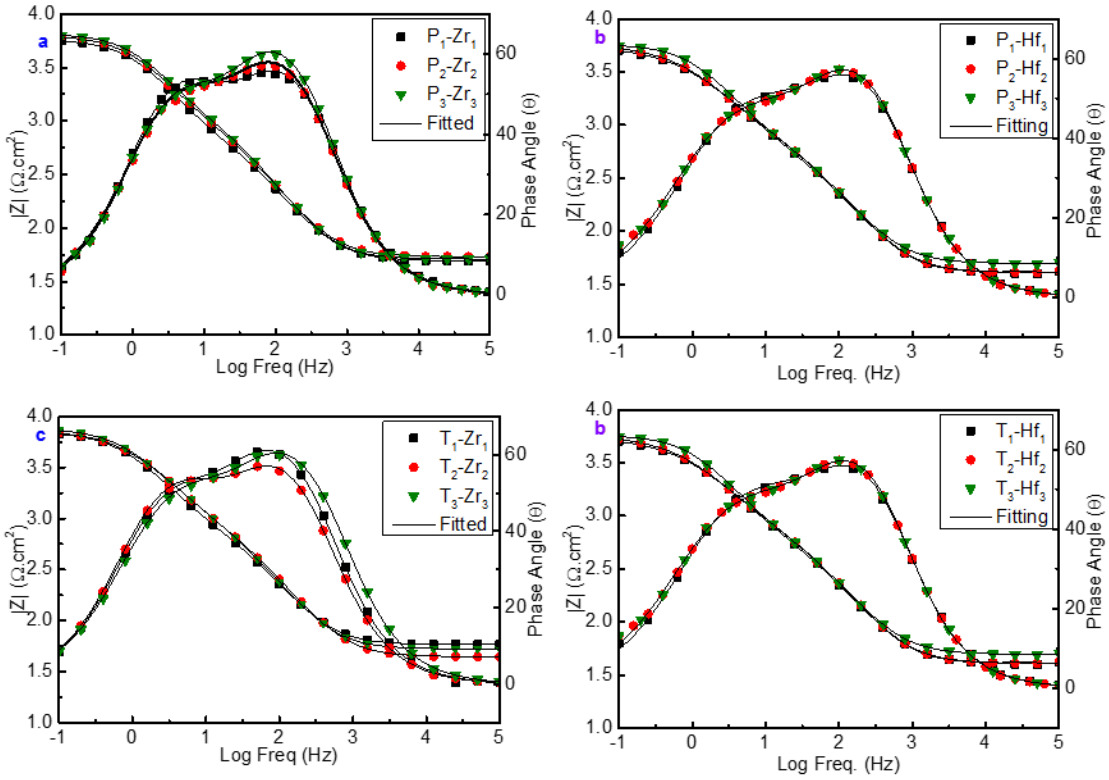

Figure 5- 105: Bode plots of corroded alloyed specimens in CO_2 simulated sea water at 25^0C, pH6.5 and after 24 hours LPR (a) P110-Zr, (b) P110-Hf, (c) TN95-Zr and (d) TN95-Hf

5.2.2.4 Analysis of the surface of alloyed steels P110 and TN95 corroded in simulated produce water (SPW)

The alloyed specimens of steels P110 and TN95 corroded in simulated produced water saturated with 99.98% CO_2 at 25^0C and pH 6.5 were subjected to surface analysis using SEM/EDS and XRD. The results of these analyses are presented in this section.

Scanning electron microscopy (SEM)/energy dispersive spectroscopy (EDS);

Figure 5-106 show the corroded SEM surface morphology of sample P110 alloyed with different quantities (0.1, 0.2 and 0.4 wt%) of Zr and Hf respectively. These alloyed samples were corroded for 24 hours in simulated produced water saturated with 99.98% CO_2 at 25^0C and pH 6.5.

Table 5- 20: Fitted EIS parameters of the alloyed specimens corroded in simulated produced water (SPW) saturated with pure CO_2 at 25^0C and pH 6.5

Parameters	Unit	P110	P_1-Zr_1	P_2-Zr_2	P_3-Zr_3	P_1-Hf_1	P_2-H_{f2}	P_3-Hf_3	TN95	T_1-Zr_1	T_2-Zr_2	T_3-Zr_3	T_1-Hf_1	T_2-H_{f2}	T_3-Hf_3
Rs	Value (Ω.cm2)	41.53	49.11	53.74	51.23	40.19	40.93	41.1	40.99	58.05	44.14	52.68	40.57	42.72	42.18
	% Error	1	0.63	0.63	0.57	0.74	0.74	0.74	0.97	0.51	0.67	0.55	0.79	0.71	0.74
CPE1	Value (μF^{-1} cm-2)	$6.97*10^{-5}$	$1.68*10^{-5}$	$1.47*10^{-5}$	$1.28*10^{-5}$	$1.43*10^{-5}$	$1.38*10^{-5}$	$1.32*10^{-5}$	$1.49*10^{-5}$	$1.52*10^{-5}$	$1.3*10^{-5}$	$1.39*10^{-5}$	$1.41*10^{-5}$	$1.46*10^{-5}$	$1.22*10^{-5}$
	% Error	22.61	7.2	6.89	5.65	10.11	8.26	9.2	12.34	6.22	7.1	5.7	12.4	8.65	9.79
n_1	Value	0.88	0.86	0.87	0.89	0.88	0.87	0.89	0.83	0.89	0.89	0.89	0.9	0.88	0.89
	% Error	2.65	1.06	1.01	0.83	1.38	1.16	1.26	1.7	0.91	1.01	0.84	1.65	1.21	1.31
R_1	Value (Ω.cm2)	198	1010	1254	1388	633	778	712	566	1078	1174	1473	497	802	773
	% Error	15.85	9	9.54	7.63	13.15	9.85	11.75	13.12	8.12	10.66	8.86	15.3	11.64	15.15
CPE2	Value (μF^{-1} cm-2)	$6.15*10^{-5}$	$2.48*10^{-5}$	$2.86*10^{-5}$	$2.62*10^{-5}$	$5.14*10^{-5}$	$5.23*10^{-5}$	$5.73*10^{-5}$	$6.83*10^{-5}$	$3.1*10^{-5}$	$3.21*10^{-5}$	$3.02*10^{-5}$	$5.93*10^{-5}$	$5.4*10^{-5}$	$5.21*10^{-5}$
	% Error	3.88	6.46	5.42	4.76	4.73	4.37	4.32	5.2	4.31	4.87	4.32	4.81	4.32	4.26
n_2	Value	0.63	0.86	0.81	0.83	0.69	0.71	0.68	0.65	0.8	0.76	0.79	0.68	0.69	0.64
	% Error	1.16	2.29	2.64	2.33	2.52	2.52	2.65	2.94	1.89	2.64	2.47	2.45	2.65	2.88
R_2	Value (Ω.cm2)	9992	4713	5025	5112	4815	5086	5232	4626	5948	6080	6177	4926	5756	6206
	% Error	2.72	2.59	3.29	2.89	3.29	3.14	3.43	3.8	2.32	3.29	3.14	3.33	3.45	3.85

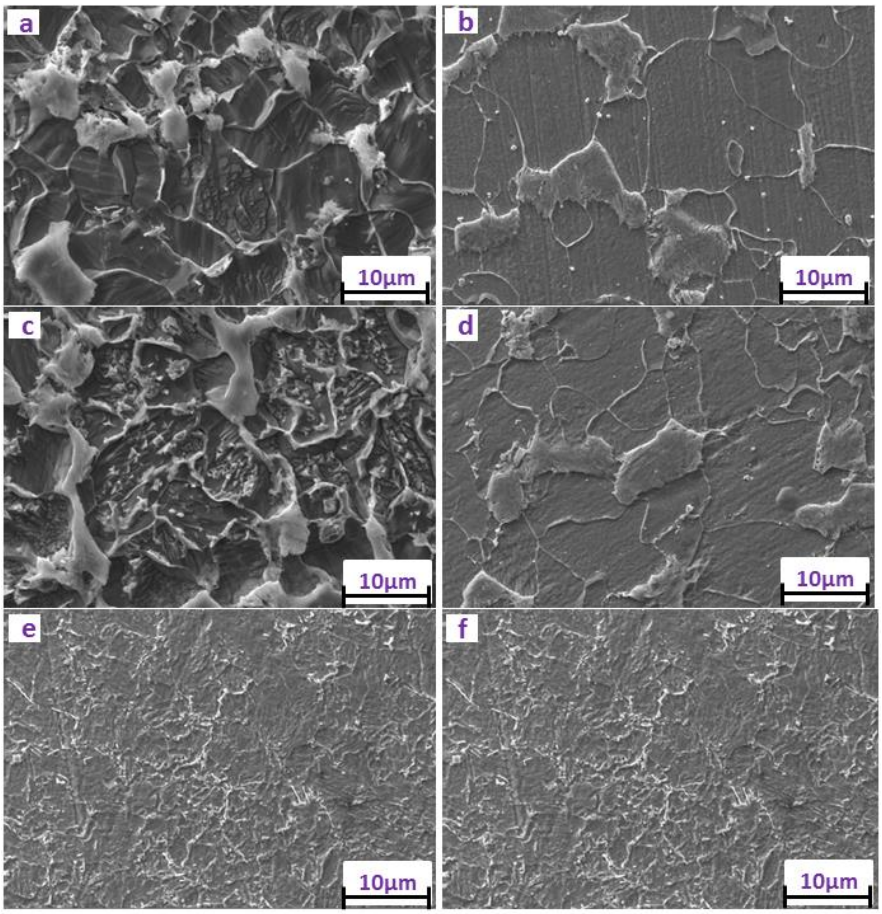

Figure 5- 106: SEM micrographs of corroded P110 alloyed with (a) 0.1 wt% Zr, (c) 0.2 wt% Zr, (e) 0.4 wt% Zr, (b) 0.1 wt% Hf, (d) 0.2 wt% Hf and (f) 0.4 wt% Hf

These SEM micrographs (Figure 5-106) displayed the evolution of surface morphology revealing slight decrease in corrosion attack (reduction in surface roughness) with increase in Zr and or Hf. Specimen P110 with ferrite-pearlite microstructures revealed a selective dissolution of the ferrite phase creating a valley-like matrix (structures) with a network of undissolved carbide on the surface of the micrographs. This network appeared continuous for the specimen alloyed with Zr while the carbide of the specimen alloyed with Hf are in discrete. The corrosion morphology of Figure 5-106 is similar with microstructure characteristics of the un-corroded alloyed sample P110 (Figure 5-93) with the valleys (ferrite dissolved region) tending to gather together while some regions are still plain (the undissolved cementite). Similar structure was reported in literatures as the characteristics behaviour of ferrite-pearlite phase in aqueous solution [143, 210].

Fine white particles can be seen scantly dispersed within the dissolved ferrite matrix. However, these tiny particles are segregated and separated along the grain boundaries and on the undissolved cementite phase. The EDS 'Point and ID' analysis at three different

locations on the surface micrograph of alloy P_2-Zr_2 are shown in Figure 5-107. It can be observed from Figure 5-107 (a) that the fine white particles consist of Zr, Fe, O and C as major elements while Cu, Mo, Mn, Ca etc were present in traces and are the constituents of the original steel. It is assumed that these particles are Zr- and Hf- rich intermetallic precipitates [88]. Zr was not detected within the matrix (Figure 5-107 (b)) but are segregated and separated towards the grain boundaries and undissolved cementite region as indicated in Figure 5-107 (c). The EDS 'Point and ID' spectra for other corroded alloys of steel P110 showed similar characteristics and are presented in Appendix C1.

Figure 5-108 showed the corroded SEM surface morphology of sample TN95 alloyed with different quantities (0.1, 0.2 and 0.4 wt%) of Zr and Hf respectively. This micrographs revealed a slight decrease in surface corrosion attack (reduction in surface roughness) with increase in Zr and or Hf content. Steel TN95 has bainitic structures which consists of cementite and dislocation-rich ferrite (acicular ferrites) [223]. These ferrites are evenly dispersed within the matrix (Figures 5-2 (c) and 5-94). Similar with ferrite-pearlite structure, the cementite in bainite could act as the cathodic site in which case ferrite dissolve preferentially with cementite un-attacked thus forming corrosion valleys on the surface of the specimen as observed in Figure 5-108

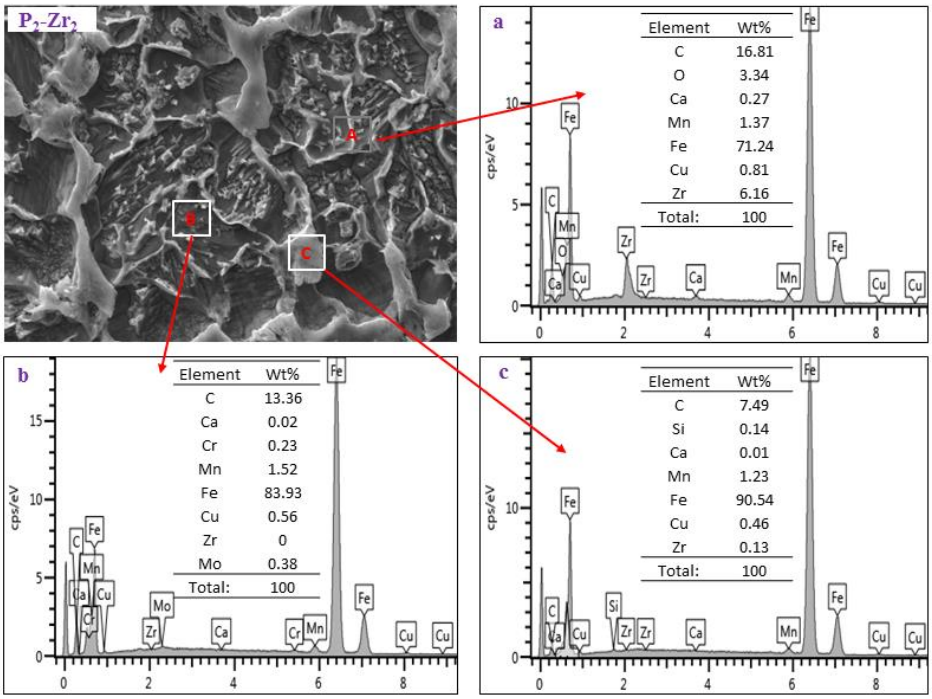

Figure 5- 107: SEM micrographs and EDS elemental analysis of three different locations on alloy P_2-Zr_2 corroded in simulated sea water at 25^0C, pH6.5 and for 24 hours.

The size of these valleys decreases with increase in Zr and or Hf content and ranges between 3 µm and 15 µm which is approximate to the size of ferrite in the steel substrate. The surface morphology of the corroded alloyed TN95 (Figure 5-108) has similar microstructure characteristics with the uncorroded alloyed (Figure 5-94).

Figure 5-109 shows the EDS analysis of three different locations on the surface micrograph of alloy T_3-Zr_3 corroded in simulated produced water saturated with CO_2 at 25^0C and pH 6.5. Some tiny particles can be observed scantly and uniformly dispersed along the grain boundaries on the SEM surface micrograph. The EDS spectrum presented in Figure 5-109 (a) revealed that these particles consist of Fe, Zr, C and O as major elements. Other elements such as Mn, Cr, Ca and Cu which were constituents of the as-received samples are also found in traces.

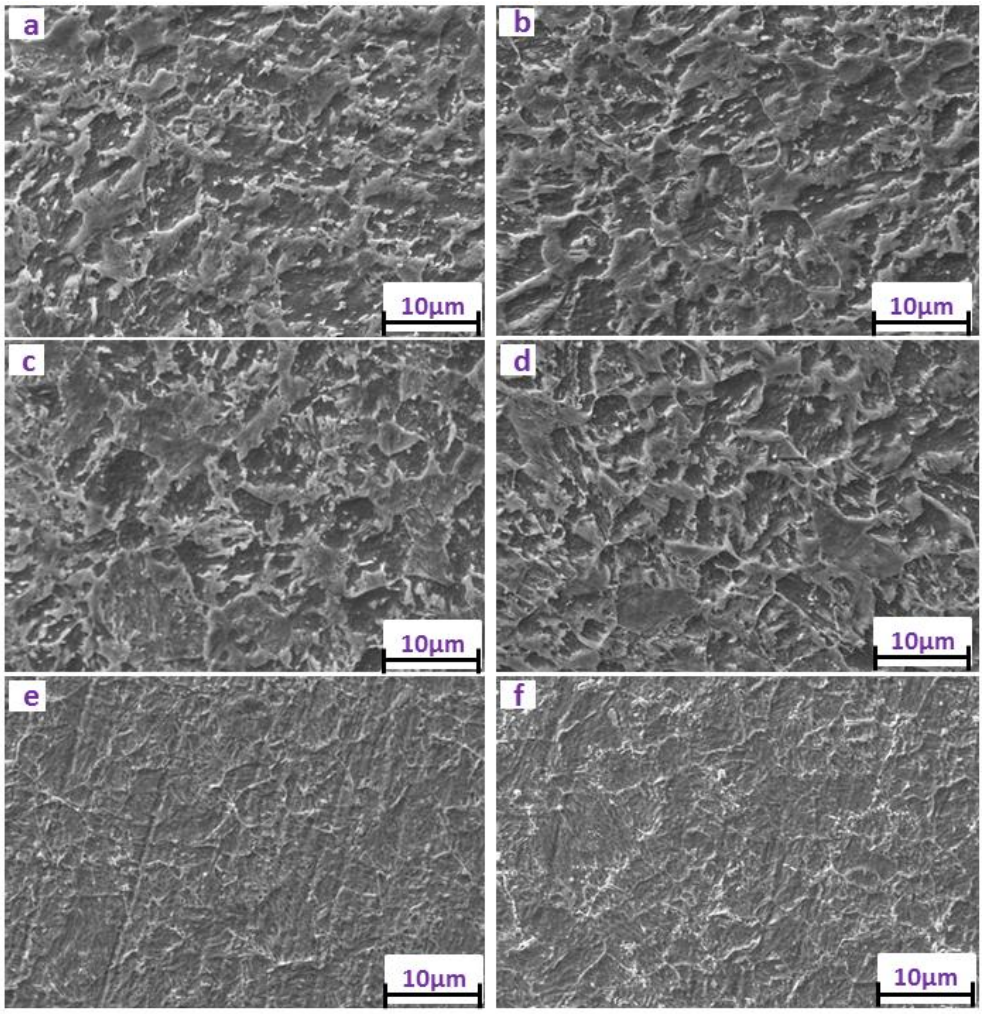

Figure 5- 108: SEM micrographs of corroded TN95 alloyed with (a) 0.1 wt% Zr, (c) 0.2 wt% Zr, (e) 0.4 wt% Zr, (b) 0.1 wt% Hf, (d) 0.2 wt% Hf and (f) 4 wt% Hf.

Similarly, the EDS analysis at the matrix of alloy T_3-Zr_3 shown in Figure 5-109 (b) showed major peaks for Fe, C and O plus very weak peaks of Zr, Mn, Cr, Si, Ca etc. This attested to the fact that the precipitates of Zr segregated together and were separated from the matrix and hence less Zr was detected at the matrix, These precipitates accumulate at the grain boundaries as Zr-rich intermetallic precipitates [88].

The undissolved cementite region shown in Figure 5-109 (c) indicated Fe, Zr, C and O as major elements with Mn, Cr, Si, Ca etc as minor elements. The EDS spectra for other alloys of steel TN95 showed similar characteristics and are presented in Appendix C2

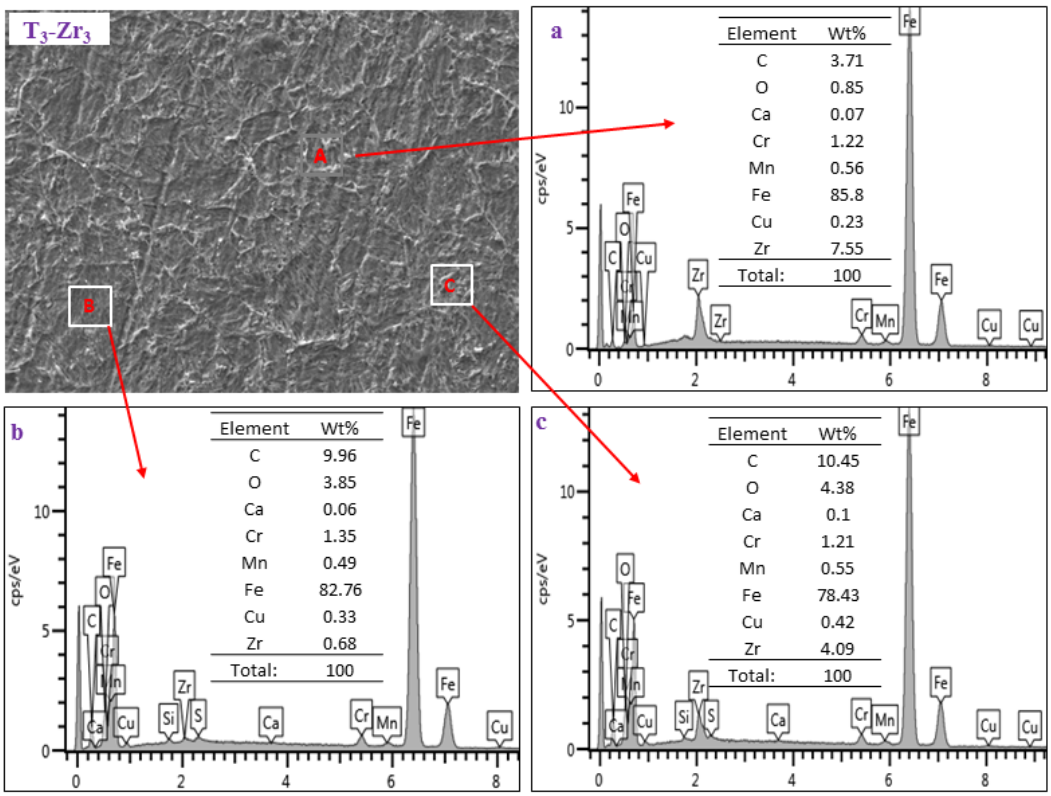

Figure 5- 109: SEM micrographs and EDS elemental analysis of three locations on alloy T_3-Zr_3 (0.4 wt% Zr) corroded in simulated sea water at 25^0C, pH6.5 and for 24 hours

X-Ray Diffraction of the corroded alloyed specimens

The structure of the corrosion products on the surfaces of the alloyed specimens were identified using Philip X'pert diffractometer. XRD spectra were obtained by employing Cu Kα radiation of 2θ range of 20 – 80^0 at a step size of 0.05% resulting in a total scan time of about 26 minutes. Figure 5-110 shows the XRD diffraction patterns of corroded alloys of P110 and TN95 (with different quantities of Zr and Hf) in simulated produced water saturated with 99.98% CO_2 at 25^0C and pH 6.5. It can be seen from this figure that all the alloys exhibited major peaks of pure α-Fe and Fe_5C_2 which are typical characteristics of the corrosion of steel in aqueous solution. Fe_5C_2 and pure α-Fe are not

corrosion products but are part of the original steel in the non-oxidised state that accumulates on the surface as corrosion of the iron proceeds [143]. The XRD analyses revealed that the main corrosion product were calcareous deposit ($CaCO_3$) as shown in Figure 5-110.

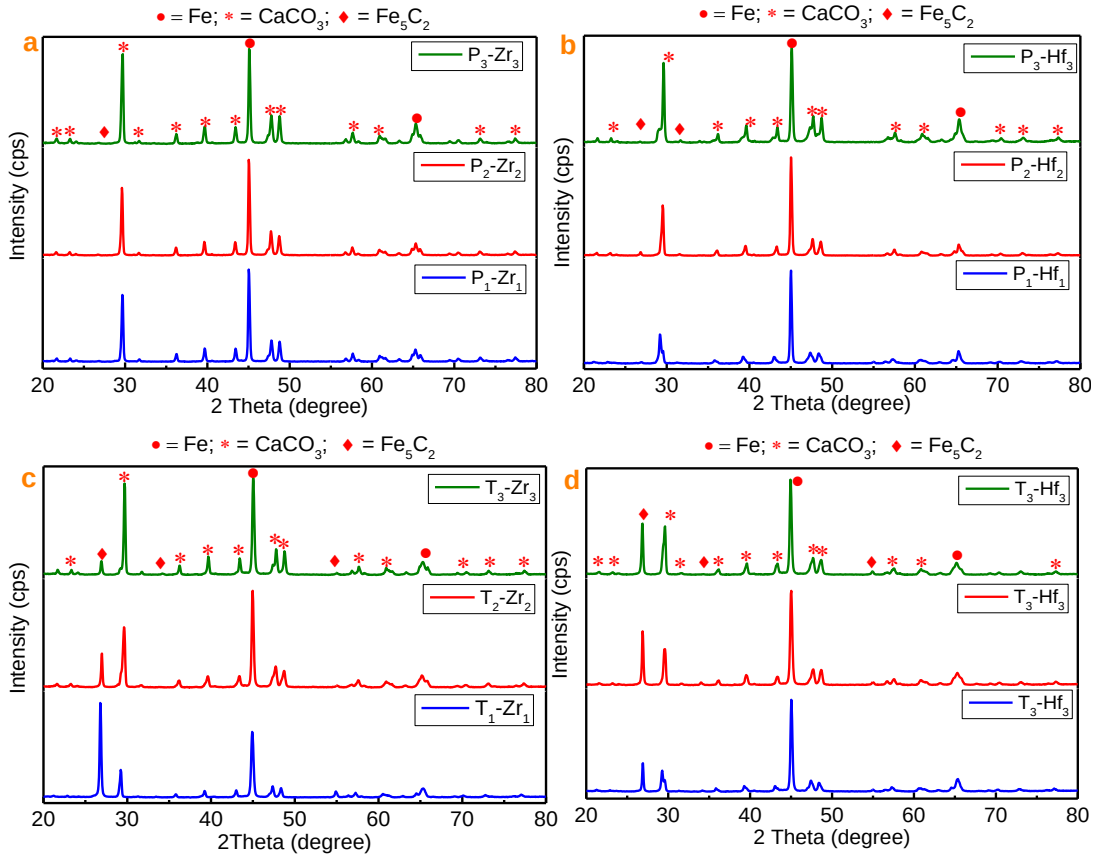

Figure 5- 110: XRD patterns of the alloyed specimens corroded in CO_2 simulated sea water at 25^0C, pH6.5 and after 24 hours LPR (a) P110-Zr, (b) P110-Hf, (c) TN95-Zr and (d) TN95-Hf

Chapter 6: Discussions

6.0 Influence of environmental and materials parameters on the corrosion of micro-alloyed steels.

The quest to mitigate the corrosion susceptibility of carbon and low alloy steels for effective deployment as materials for the exploration, production and transportation of hydrocarbon particularly in challenging locations and under severe conditions [2, 23, 69] has led to the development of micro-alloyed steels [13] with appropriate properties at minimal cost [14, 37]. Therefore, the past 6 decades have witnessed an increasing development and use of micro-alloy (high-strength low-alloy - HSLA) steels as structural materials [224] providing desirable combinations of properties such as strength, toughness, formability, weldability, and corrosion resistance [51]. This excellent combination of properties can be attributed to the presence of fine grain structures achieved by the addition of small quantity of alloying elements, controlled processing technologies and appropriate heat treatments [14, 51] with the attendant microstructures [37, 166].

Corrosion problems exist in every stage of oil and gas production [7]. These problems are the greatest challenges of the operators in the industry and have been identified as carbon dioxide (sweet) corrosion, hydrogen sulfide (sour) corrosion in the produced fluids and corrosion by oxygen in water injection [11, 23, 135]. The effects of corrosion problems if not controlled can affect production, cause economic loss and ecological problems with the resultant security risks to life and properties. Crude oil and its products are mixtures of hydrocarbon which by themselves are not corrosive. However, they become corrosive in the presence of impurities and other components such as water, chloride salts, carbon dioxide (CO2), hydrogen sulfide (H2S), elemental sulfur, dissolved oxygen, organic acids and sulfate-reducing bacteria (SRB) [4, 167, 168, 180]. These impurities facilitate the corrosion attack of oil and gas facilities in diverse and complex ways being enabled by a myriad of factors most of which are interrelated and have synergistic effect on the smooth operation in the industry [7, 128, 147].

Dissolved oxygen (DO) is one of the major corrosion enhancing components in crude oil. Field and experimental evidence have shown that dissolved oxygen (DO) being a depolarizer and electron acceptor in cathodic reaction can accelerates anodic dissolution

of metals [128, 167, 176, 177]. Sour (H_2S) corrosion is one of the major forms of corrosion found in oilfield and is caused by the presence of significant amounts of H_2S gas dissolved in produced fluid. Depending on environmental factors, the mechanism of H_2S corrosion culminate in the formation of different thermodynamically stable FeS (mackinawite, pyrrhotite, pyrite) as corrosion products [23, 169, 225, 226]. These FeS form amorphous crystal structure which could be either non-protective thus allowing local corrosion attack or protective with stable passive layer which protects the steel surface from further corrosion[226]. CO_2 (sweet) corrosion is yet another dominant problem in oil and gas industry. It has been adjudged as the most prevalent problem accounting for about 60% failures of pipelines and equipment. Therefore, the need to understand, minimize and control the effects of CO_2 corrosion on oilfield facilities is eminent for efficient and cost effective operation in oil and gas industry [11, 69, 113]. This had led to extensive studies resulting in a number of prediction models for CO_2 corrosion. These models both individually and/or collectively did not comprehensively present adequate understanding of the mechanism of CO_2 corrosion due to the complexities arising from the myriad of factors affecting the process [7, 11, 23, 69, 128]. These include environmental factors (pH, temperature, CO_2 partial pressure, solution chemistry and flow rate) and metallurgical factors (microstructures and material composition) [11, 128, 129, 147]. This chapter discusses the results of the influence of some of these factors using different electrochemical polarization and surface analysis techniques with a view to assessing the corrosion propensity of as supplied proprietary as well as the Zr and Hf modified micro-alloy steels.

6.1 Microstructures of the as-received micro-alloyed steels

The as-supplied microstructures of the three proprietary micro-alloy steel and API 5L X65 carbon steel reference alloy are shown in Figures 5-1 (optical) and 5-2 (SEM). These figures revealed that steels F65, P110 and X65 consist of ferrite-pearlite structures while steel TN95 exhibited bainitic structure with cementite and dislocation-rich ferrites that are evenly distributed within the matrix [52, 122]. Microstructures significantly depend on alloy's composition and thermo-mechanical treatment [159] and play major role on the corrosion resistance of micro-alloyed steels. This is because the different phases of microstructure provide sites for anodic and cathodic reactions [52]. However, the effects of microstructure on the corrosion rate of carbon steel is not systematic as the protective properties and the adherence of the film can vary greatly for apparently similar carbon

steels [52]. This influence of microstructure is more pronounced in ferrite-pearlite microstructure where Fe_3C (in pearlite) exhibit various functions. Fe_3C is difficult to dissolve and therefore is left behind after selective dissolution of ferrite where it forms non- protective porous layer. This layer accumulates with time to form a diffusion barrier for F^{2+} and CO_3^{2-} in CO_2 environment resulting in a high surface pH. If the solubility limit of $FeCO_3$ is exceeded, a protective $FeCO_3$ scale is formed within the porous layer regardless of the steel microstructure. Fe_3C is an electronic conductor, causing a galvanic effect by acting as cathodic site for the hydrogen evolution reaction (HER) and thus enhances the corrosion rate. Fe_3C is not a corrosion product but is presence in the steel as part of the microstructure. It strengthens and anchors $FeCO_3$ layer which protects the surface of micro-alloy steels from corrosion [210]

The grain size and the ferrite-pearlite ratio of the micro-alloy steels as listed in Table 5-1 shows a ranking order of P110 < X65 < F65. This difference in microstructures which is clearly observed in Figures 5-1 and 5-2 and demonstrated by ferrite-pearlite ratio can be attributed to chemical composition and thermo-mechanical treatment involved in manufacturing. Specimens X65 and F65 have the same chemical composition (Table 4-3) therefore it is obvious that the microstructural difference was caused by thermo-mechanical treatment. This is in agreement with the report of Ochoa, et al [185] who obtained different microstructures of API 5L X42 using three different heat treatment routes with each of the microstructures exhibiting different corrosion behaviour in CO_2 saturated 0.5 M NaCl solution. Seikh [54] used repeated quenching to impact different microstructures on E34 micro-alloy steel which showed different corrosion rate in 3.5 wt% NaCl solution. Thus Steel F65 manufactured by forging and steel X65 produced by rolling must have contributed to the different in microstructures and thus resulted in the difference in corrosion propensities of these steels as observed and discussed later in this section.

When a freshly polished micro-alloyed steel with ferrite–pearlite microstructures is immersed in an electrolyte, selective dissolution of the ferrite phase takes place leaving the pearlite unaffected. The undissolved pearlite forms cementite platelets protruding into the electrolytes. This protruding laminar cementite is clearly seen in all the SEM surface morphologies of the steels with ferrite-pearlite microstructures corroded in the different media and with different environmental parameters uysed in this work. The adherence and protective properties of the corrosion product are related to the presence of these

cementite platelets which strengthen and anchor the films to the metal substrate [11, 133]. Some authors [47, 52, 137] have also reported that cementite acts as cathode, while ferrite acts as the anode in ferrite–pearlite microstructures. It follows that the specimen with higher cathode–anode (pearlite–ferrite) ratio should be more susceptible to corrosion attack [128, 205, 227]. Pearlite phase has also been observed to increase with carbon content [37, 62]. Therefore, the specimen with higher carbon content has more pearlite phase and consequently greater cathode to anode ratio resulting in higher corrosion rate.

It was also observed that steel P110 has the lowest ferrite-pearlite ratio. This could be ascribed to higher carbon content (Table 4-3) in accordance with the observation that the precipitation, volumetric fraction, uniformity and distribution of pearlite in micro-alloyed steels depend significantly on carbon content and thermo-mechanical processes (heat treatment routes) [11, 54, 185]. The grain size of the specimens, as revealed by Fiji-ImageJ analysis and ASTM grain size number (Table 5-1) computed according to ASTM E112-12 standard [194], also demonstrated the same ranking format. The small grain size of the steels can be attributed to the presence of alloying elements such as Nb, Ti and V which have been reported are good grain refiners [13, 14, 122]. Seikh et al [54] noted that small grain microstructures have more surface area and so are more prone to corrosion attack. It can then be concluded that steel F65 with more ferrite-pearlite ratio and bigger grain size exhibited a better corrosion performance than X65. Similarly, steel X65 performed better than steel P110 based on the same criteria. These observations sufficed for the three alloys with ferrite–pearlite microstructures (Steels F65, P110 and X65) and is reproduced in all the media (electrolytes) and with all the environmental factors assessed in this work as presented in Chapter 5.

However, there are opposite reports claiming that decrease in grain size can variably increase corrosion resistance [228, 229].This was attributed to the inability to decouple the effects of processing and processing route from the effect grain size on corrosion resistance. Recent reports showed that grain size may act to aggravate the behaviour observed from coarser grain structures in any specific environment (electrolyte) and vice versa. This means that the electrolyte play significant role on the effects of grain refinement on the corrosion behaviour of alloys [32, 33]

The as-supplied steel TN95 is composed of bainite structure (Figure 5-2 (c)) and has different microstructure from the other three specimens and consequently exhibited

different corrosion behaviour. Bainite microstructure is a product of restricted and slow decomposition of austenite to ferrites and pearlites due to the presence of alloying elements [14, 31, 122]. This bainitic structure of steel TN95 can be linked to the relatively high content of Cr (0.99%) and Mo (0.46%) which are considered to delay and retard the decomposition of martensite and austenite into ferrites and carbides upon tempering. This is attributed to the sluggish diffusion process of the micro-additions to forming carbides [13, 23, 52]. Cr has been reported to enhance corrosion resistance of steel but this was not observed with steel TN95 in this work. Also noteworthy is the high carbon content of steel TN95 (Table 4-3) which has a negative effect on corrosion resistance of micro-alloyed steels [37, 62]. This high carbon content formed carbides with Cr [13, 159, 230, 231] leading to increased cathodic site and therefore decreased corrosion resistance [52, 122]. It then means that due to high carbon content the effect of Cr in enhancing corrosion performance was not effective. This explained why Steel TN95 exhibited the worst corrosion rate than all the other specimens used in this work.

6.2 Weight Loss

Measurement of corrosion rate by weight loss technique although takes longer time to obtain significant results when compared with electrochemical techniques, it is the simplest and gives the actual natural process. This technique was used in this work to simulate natural corrosion process and for initial assessment of the corrosion rate of the samples. The results of the corrosion rate by weight loss as presented in Figure 5-5 served as precursors for assessement in subsequent corrosion experiments. This figure shows that all the specimens exhibited high initial corrosion rate. This can be attributed to direct contact of the surface of the specimens with the corrosive medium and the presence of sufficient dissolved oxygen (DO) in the electrolyte. The electrochemical reaction is relatively active involving the high dissolution of iron to ferrous ion (Fe^{2+}) as expressed in Equation 6-1. With increase in immersion time, the dissolved oxygen is gradually consumed resulting in the slowing down of cathodic reaction of Equation 6-2 which, in turns, decreased the anodic dissolution rate of iron and the consequent formation of corrosion product as show in Equation 6-3. This is demonstrated by the rapid decrease in corrosion rate for all the steels with specimen F65 recording a decrease of about 35% after 48 hours of immersion. The product of Equation 6-3 ($Fe(OH)_2$) is unstable, loosely attached and is an intermediate corrosion product which was converted to a thermodynamically stable corrosion product (Fe_2O_3) [232] as shown in Equation 6-5.

More of these corrosion products (Fe_2O_3) are generated which hindered direct contact between the steel substrate and the corrosive solution (electrolyte) with prolongation of immersion time. This resulted in the reduction of the corrosion rate by only 1% between 48 and 72 hours for specimen F65. All other specimens exhibited similar corrosion mechanism demonstrating an increasing order of corrosion rate as F65 < X65 < P110 < TN95. This is in agreement with the mechanism advanced in Section 6.1 based on the effects of the microstructures of the specimens.

At the anode:

$$Fe_{(s)} \rightarrow 2Fe^{2+}_{(aq)} + 4e^- \qquad 6\text{-}1$$

At the cathode:

$$O_{2(g)} + H_2O_{(l)} + 4e^- \rightarrow 2OH^-_{(aq)} \qquad 6\text{-}2$$

Adding the two half-cell reactions:

$$2H_2O_{(l)} + O_{2(g)} + 2Fe^{2+} \rightarrow 2Fe(OH)_{2(s)} \qquad 6\text{-}3$$

$$4Fe(OH)_{2(s)} + O_{2(g)} + 2H_2O_{(l)} \rightarrow 4Fe(OH)_{3(s)} \qquad 6\text{-}4$$

$$2Fe(OH)_{3(s)} \rightarrow Fe_2O_3 + 3H_2O_{(s)} \qquad 6\text{-}5$$

6.3 Effect of NaCl concentrations in aerated and de-aerated environment

Oil pipelines are laid both on- and off- shore encountering different environmental conditions and terrains that are corrosive in nature. These terrains may be soil of different nature or seawater with all its complex constituents which most often act as corrosion catalyst affecting the integrity of the external surface of the pipelines. On the other hand, the internal wall of these pipes are subjected to corrosive attack of certain impurities in the produced water such as dissolved oxygen, hydrogen sulfide, chloride ions, carbon dioxide and sulphate reducing bacteria (SRB) [167]. In this section, the results of the effect of two of these impurities namely dissolved oxygen (DO) and chloride ions are discussed. Experimental evidence [167, 176, 177] shows that dissolved oxygen (DO) exhibits the most prevalent problem because it can accelerates anodic dissolution of metals by acting as depolarizer and electron acceptor in cathodic reaction [128, 202, 227]. Also in a basic or neutral solutions, oxygen reduction shown in Equation 6-2 dominates the cathodic reaction in competition with hydrogen evolution reaction (HER) of Equation 6-6 [174].

$$2H^{+}_{(aq)} + 2e^{-} \rightarrow H_{2(g)} \qquad 6\text{-}6$$

One of the significant component of crude oil stream that influences the effect of DO on the corrosion of oil and gas facilities is chloride salts. Chloride salt can influence the solubility of oxygen in produced water which increased with increase in Chloride concentration but decreased after peaking at certain chloride concentration [138, 139, 171, 174, 212]. This section is aimed at discussing the results, as presented in section 5-3, of the investigation on the effects of dissolved oxygen and chloride concentration on the corrosion behaviour of micro-alloy steels.

This investigation was conducted using the experimental parameters and conditions listed in Table 4-4 and the results of the linear polarization resistance are shown in Figures 5-6 and 5-7 for aerated and de-aerated conditions respectively. It is obvious from these figures that the corrosion attack for all the four specimens was more severe in 3.5 wt% NaCl solution for both naturally aerated and de-aerated solutions than in 1.0 wt% and 10.0 wt% NaCl solutions. This is attributed to the effect of sodium chloride concentration on the solubility of oxygen in aqueous solution, which is reported to be highest at 3.5 wt% NaCl [138, 174]. On the other hand, the witnessed decrease in corrosion rate with increase in NaCl concentration beyond 3.5 wt% as exhibited in both aerated and deaerated 10 wt% NaCl solutions was due to the decrease in the solubility of oxygen [171] and adsorption of chloride on the surface of the steels [138] with increase in NaCl concentration. There was a rapid increase in corrosion rate as the concentration increased from I.0 wt% NaCl to 3.5 wt% NaCl while a mild decrease was observed when NaCl concentration increased from 3.5 wt% NaCl to 10.0 wt% NaCl as presented in Figures 5-8 and 5-9 for aerated and de-aerated conditions respectively. This was attributed to the gradual salting out effect of chloride [173] which adsorbed on the surface of the steels thereby preventing further corrosion attack.

Recently Zeng, et al [172], reported similar decrease in corrosion rate of steels with increasing salt concentration in CO_2 saturated NaCl solutions with the lowest salt concentration exhibiting the highest corrosion rate. These were attributed to the competitive adsorption of hydroxyl and chloride ions during anodic dissolution of iron in NaCl containing acidic solution. It has generally been accepted that the overall anodic dissolution of iron expressed in Equation 6.1 involves many steps as proposed by Bockris,

et al [145] and recently reviewed by Nesic [136] (Equations 3-4 to 3-12). Thus in the absence or low NaCl concentration, Equation 3-5

$$FeOH_{(ads)} \rightarrow FeOH^{+} + e^{-} \qquad 3\text{-}5$$

is the rate determining step leading to dissolution of iron. Therefore the adsorption of hydroxyl ion prevails over chloride ion with the attendant higher Tafel Slope. However, at higher salt concentration and based on Equations 3-25 and 3-26, chloride adsorption tends to prevail with Equation 3-26 being the rate determining step resulting in lower Tafel slope [172].

$$Fe.H_2O_{(ads)} + Cl^{-} \rightarrow FeCl^{-}_{(ads)} + H_2O \qquad 3\text{-}25$$

$$FeCl^{-}_{(ads)} + OH^{-} \rightarrow FeOH^{+} + Cl^{-} + 2e^{-} \qquad 3\text{-}26$$

This is contrary to the reports of some authors, who observed a continuous increase in corrosion rate with increase in NaCl concentration [182]. Liu et al [167] recently categorized the effect of chloride ion on corrosion of carbon steels as smooth invariant stage, slow rise stage and the rapid rise stage.

It has been reported [173] that chloride salt affects the corrosion kinetics of carbon steels in three different ways; (i) It accelerate the corrosion process by forming intermediate corrosion species; (ii) It decreases the solution pH which also enhances the corrosion process and (iii) It reduces the solubility of the dissolved oxygen (DO) with the attendant decrease in corrosion rate. However, the net effect of increasing NaCl concentration above 3.5 wt% as revealed in this work was reduction of corrosion rate. It then follows that the reduction in the solubility of DO (salting out) dominates the other two competing effects. This is in agreement with the report of Yari [174] that in basic or neutral solutions, oxygen reduction reaction shown in Equation 3- 27 is the dominant cathodic reaction in competition with hydrogen evolution reaction of Equation 3- 13.

Neutral/basic solutions $$O_{2(g)} + 2H_2O_{(l)} + 4e^{-} \rightarrow 4OH^{-}_{(aq)} \qquad 3\text{-}27$$

In hydrogen revolution $$2H^{+}_{(aq)} + 2e^{-} \rightarrow H_{2(g)} \qquad 3\text{-}13$$

Caceres, et al [175] also reported that the major reaction governing corrosion in most practical oilfield application is the reduction reaction of oxygen in the oil fluid. Similarly,

Vera, et al [122] summarized the electrochemical and chemical reactions that occur during steel dissolution in aqueous solutions as shown in Equations 3-3, 3-27, 6-7 to 6-10.

Anodic reaction:	$Fe_{(s)} \rightarrow Fe^{2+}_{(aq)} + 2e^{-}$	3-3
Cathodic reaction	$O_{2(g)} + 2H_2O_{(l)} + 4e^{-} \rightarrow 4OH^{-}_{(aq)}$	3-27
Total reaction	$2Fe_{(s)} + O_{2(g)} + 2H_2O_{(l)} \rightarrow 2Fe^{2+}_{(aq)} + 4OH^{-}_{(aq)}$	6-7
	$Fe^{2+}_{(aq)} + 2OH^{-}_{(aq)} \rightarrow Fe(OH)_{2(s)}$	6-8
	$4Fe(OH)_{2(s)} + O_{2(g)} + 2H_2O_{(l)} \rightarrow 4Fe(OH)_{3(s)}$	6-9
	$2Fe(OH)_{3(s)} \rightarrow Fe_2O_3.H_2O_{(s)} + 2H_2O_{(l)}$	6-10

It was also obvious from the results of this investigation that all the specimens exhibited higher susceptibility to corrosion attack in naturally aerated 3.5 wt% NaCl solutions than in de-aerated 3.5 wt% NaCl solutions demonstrating the effect of dissolved oxygen. In redox reactions, dissolved oxygen (DO) is an electron acceptor and a depolarizer [128, 177, 202, 227] which accelerates the dissolution of metals in chloride environment [173, 176, 182].The decrease in corrosion rate of the specimens in deaerated solutions when compared with that of the aerated solutions was about 89% in 1.0 wt.% NaCl, 93% in 3.5 wt.% NaCl and 92% in 10.0 wt.% NaCl. This is in agreement with the report of Jung et al [177] who reported a decrease of 91% when the concentration of dissolved oxygen was decreased from 9 to 2 mg/L.

However, the effect of NaCl on the corrosion rate of carbon steel in O_2-free environment has not been clearly understood as some authors presented divergence results. The contrary view summarized the mechanism of chloride attack by a series of step wise electrochemical reactions expressed in Equations 3-27 to 3-34 [54, 162, 179]. Some of these equations show that the chloride ions are not consumed but remains available to continue corrosion process. Chloride ions are considered as aggressive corrosive agents. This is attributed to the small size, high diffusivity, strong anionic nature and high solubility of chloride salts [162, 179]. This is why most chloride attack on steels, particularly passive steels usually results to pitting corrosion [54, 170, 179].

6.3.1 Tafel extrapolation results on the effect of NaCl concentrations in aerated and de-aerated environment

Tafel law which according to literatures [233-235] has been empirically and theoretically proved, is one of the most frequently used laws in electrochemistry. This is because electrochemists and corrosion engineers always encounter Tafel constants (β) in literatures and instrumental manuals. According to Kear and Walsh [233], linear polarization resistance (LPR) technique, for instance, cannot be satisfactorily conducted without assuming values for Tafel constants (β) and or Stern-Geary constant. Tafel law states that the logarithm of the current density (*i*) in an electrochemical reaction varies linearly with the electrode potentials. When the plot of log (*i*) versus potential forms a straight lines on both side of open circuit (free) potential (OCP), it means that the process is kinetically controlled [235].

The corrosion propensities of the micro-alloyed steels were also investigated in different concentrations of aerated and de-aerated solutions of NaCl. The Tafel plots of these investigation are presented in Figure 5-11 and 5-12 while the Tafel extrapolated parameters are listed in Table 5-3. These Tafel plots showed that the anodic polarization curves of all the specimens in both aerated and de-aerated solutions increased continuously with increase in potential signifying active corrosion behaviour with the attendant metal dissolution. Also, the anodic branches showed sharp increase in slopes exhibiting well-defined Tafelian regions within the low over-potentials. Similar behaviour has been observed by researchers [67, 206, 215] suggesting that no corrosion film was formed on the surface of the steels and that the mechanism of corrosion attack is similar for all the steels in the three concentrations of both conditions. On the other hand, the cathodic curves for all the steels showed a mixed activation- and diffusion-controlled characteristics. This behaviour was more pronounced in the aerated environments where limiting diffusion current density was observed. This can be ascribed to the mass-transport limitations of oxygen reduction reactions since reduction of dissolved oxygen as shown in Equation 3-37 is the dominant reaction in aerated conditions [122, 174, 204]. On the other hand, under de-aerated condition, the cathodic reduction reaction shown in Equation 6-10 with a corresponding small rate of hydrogen evolution is the main reaction. This low hydrogen evolution resulted is the reason for the witnessed low corrosion rate in de-aerated condition.

$$O_{2(g)} + H_2O_{(l)} + 4e^- \rightarrow 4OH^-_{(aq)} \qquad 3.37$$

$$2H_2O_{(l)} + 2e^- \rightarrow H_{2(g)} + 2OH^-_{(aq)} \quad 6.10$$

Comparing the corrosion response of the individual steels in the different concentration of NaCl solution and in the two conditions vividly revealed that the specimens exhibited more corrosion attack in the aerated conditions than in the de-aerated conditions. Literature [33, 182, 206] have shown that the more negative the E_{corr}, the less noble the material. However, it can be observed from Figures 5-13 to 5-15 that the samples corroded in aerated solution with the higher corrosion rate also had the higher E_{corr}, whilst those corroded in the deaerated solution with the lower corrosion rate exhibited less noble E_{corr}. This cathodic shift in corrosion potential is an indication that the corrosion processes were under the control of cathodic reactions [205]. These figures also showed that the decrease in E_{corr} in the deaerated condition resulted in decreased anodic kinetics. This is unconventional and it revealed that the understanding of (physical) structure-corrosion relationships is somewhat non-intuitive [33]. All the same, these figures clearly demonstrated that the cathodic current density for the specimens in the aerated condition are higher than that in the deaerated conditions. This manifested in larger Tafel cathodic constants (βc) than the corresponding Tafel anodic constants as shown in Table 5-3 signifying that the overall corrosion processes are mainly under the control of cathodic reaction [205]. Table 5-3 showed that the corrosion current density (i_{corr}) of F65 was 17µA.cm^{-2} in the aerated solutions but 0.9µA.cm^{-2} in the de-aerated solutions demonstrating about 95% higher in naturally aerated 10 wt% NaCl solution than in de-aerated 10 wt% NaCl solution. These values are comparable with the report of other authors [4, 67, 124] suggesting that the samples with lower corrosion current density exhibited higher corrosion resistance in the chloride solution. Since corrosion current density i_{Corr} is proportionally related to corrosion rate (CR) [47, 205] and from the values of i_{Corr} in Table 5- 3, the corrosion rates of the steels in both aerated and de-aerated solutions can be ranked as $CR_{F65} < CR_{X65} < CR_{P110} < CR_{TN95}$. This trend of corrosion rate corroborated the linear polarization resistance results and can be attributed to the chemical compositions and microstructures of the samples.

6.4 Effect of temperature on the corrosion behaviour of the steels in 0.5 % CO_2 environments

Temperature generally accelerates most chemical and electrochemical processes [158, 204, 207]. Increase in temperature decreases the solubility of CO_2 thus reducing its concentration in solution which in turn decreases corrosion rate. However, most

experimental observations revealed that corrosion rate of steels generally increased at temperatures less than 60^0C. This is because, increase in reaction rate due to increase in thermal activation predominates the decrease caused by solubility of CO_2. One could have therefore expected the corrosion of steels in CO_2 environments to continuously increase with temperature but experimental evidence [23, 38, 52] indicated that CO_2 corrosion of steels exhibits an intrinsic change in kinetics at about 60^0C due to increase in kinetic of precipitation of $FeCO_3$ on the surface of the steels. This formed a diffusion barrier for the active corrosion species [62] to access the steel surface. There is no general agreement on the threshold temperature that will precipitate enough $FeCO_3$ to prevent the corrosion species from reaching the steel substrate. This could be linked to the myriad of factors such as pH, immersion time, corrosion potential and flow condition influencing CO_2 corrosion of steels [204]. Thus different authors have reported different threshold temperature ranging from 60^0C to 100^0C depending on other environmental factors [38, 124, 160].

Zhao et al, [38] observed that below 60^0C, the corrosion product could not adhere on the steel surface resulting in severe corrosion attack whereas at 80^0C, corrosion product ($FeCO_3$) was formed but could not provide effective corrosion protection due to poor surface adhesion. However, between 80^0C and 140^0C, a compact and adherent corrosion product consisting of mainly $FeCO_3$ was observed which drastically reduced the corrosion rate. Above 140^0C, complex corrosion products consisting of Fe_3O_4 and $FeCO_3$ which further increased the corrosion resistance was observed [23, 62, 135]. The effect of all other environmental factors affecting CO_2 corrosion of micro-alloyed steels are directly or indirectly influenced by this intrinsic change in CO_2 corrosion mechanism [207]. For instance, temperature has a strong and distinct effect on corrosion product formation affecting the phase identity and morphology and thus its protective properties [62, 158]. More recently, Schmitt and Horstemeier [135] reported that temperature has effect on the morphology and crystallinity of the protective carbonate scales. At temperatures above 90^0C, the scale is composed of well-defined, well packed and adherent crystals of $FeCO_3$ providing adequate protection but at lower temperatures porous, loose and flat grain-products with little or no protection was observed.

The results of the investigation on the effect of temperatures ($< 60^0$C) on the corrosion rate of the micro-alloyed steels in unbuffered 3.5 wt% NaCl solutions saturated with 0.5% CO_2 gas using different electrochemical techniques are presented in Section 5.1.4. It is

obvious from the results that the corrosion rate of all the specimens increased with increase in temperatures attesting to the reports in literatures [38, 124, 160]. This is linked to increase in mass transfer of the active species, reduction in the viscosity of the solution and increased in the diffusion coefficient of H^+ ions occasioned by increase in temperature [140]. Similar observations have been reported in literature [147, 160] The post experimental surface analysis showed that no significant protective corrosion product was formed. Thus the increase in corrosion rate was caused by thermal activation of the reacting species [158, 204], porous, loose and poor adherence corrosion product to the surface of the steels [38, 135] and limited Fe^{2+} and CO_3^{2-} ions which could not facilitate the precipitation of protective $FeCO_3$ [69, 143, 210] within the temperature range of these experiments.

The EDS analyses of all the specimens investigated at 25^0C, 45^0C and 60^0C as listed in Table 5-6 revealed that the main elements of the corrosion products were Fe, C and O with traces of Mn, Cr, Cu and Si. These elements were uniformly distributed within the corrosion product. This uniform distribution of the corrosion product and the large grain size could have necessitated the lower corrosion rate exhibited by steel F65. This is in agreement with the report of Asiful [54]. **T**he average ratio of Fe/O (wt%) computed from EDS analysis of at least three points on the surface of the corroded specimens decreased with increase temperature. For instance, the average ratio of Fe/O for steel F65 is 61.78, 49.30 and 41.17 at 25^0C, 45^0C and 60^0C respectively. This resulted in changes on the surface morphology of specimen due to the increasing dissolution of Fe as temperature increased. This is in agreement with the report of Yin et al [157] and corroborated with the LPR results of this work. Since Fe, C and O were the main elements of the corrosion product, it may be assumed, as is the inherent attribute of CO_2 corrosion of steel, that the corrosion product was $FeCO_3$. However, $FeCO_3$ was not detected by the XRD analyses of the corroded specimens as shown in Figure 5-31 for temperature variation. The XRD spectra showed Fe_3C as the main phase on the surface of all the steel substrates. Fe_3C was part of the steel microstructure left behind after the anodic dissolution of Ferrite [210]. It means that the concentrations of the dissolved Fe^{2+} ions and the CO_3^{2-} ions from the reduction of carbonic acid were not high enough to precipitate as $FeCO_3$ [143, 210]. All the results of the electrochemical polarization techniques and the surface analysis techniques corroborated each other that the corrosion rate of all the specimens increased with increase in temperature and attested to the ranking corrosion

rate of steels F65 < X65 < P110 < TN95. This is attributed to the microstructures of the steels as discussed in Section 6.1

6.5 Effect of pH on the corrosion behaviour of the steels in 0.5 % CO_2 environments

pH is one of the environmental factors that affects the rate and mechanism of CO_2 corrosion of micro-alloyed steels through acidification [135, 148]. Generally, decrease in pH (acidity increase) increases corrosion rate by providing hydrogen (H^+) ions which attack the surface of the steel through the processes of hydrogen evolution. On the other hand, increase in pH decreases corrosion rate due to the formation of protective corrosion product ($FeCO_3$ in CO_2 environment) [135, 147, 148, 236].When iron is immersed in CO_2-containing electrolyte, three major cathodic reactions involving the reduction of H^+, HCO_3^- and H_2CO_3 may occur as shown in Equations 6-11 to 6-13

$$2H^+_{(aq)} + 2e^- \leftrightarrow H_{2(g)} \qquad 6\text{-}11$$

$$2H_2CO3_{3(aq)} + 2e^- \leftrightarrow H_{2(g)} + 2HCO^-_{3(aq)} \qquad 6\text{-}12$$

$$2HCO^-_{3(aq)} + 2e^- \leftrightarrow H_{2(g)} + 2CO^{2-}_{3(aq)} \qquad 6\text{-}13$$

The contributions of each of these ions in CO_2 corrosion of micro-alloyed steel depend on various parameters such as temperature, pH, and concentration [69, 136, 147-149].

The predominant cathodic reaction at pH < 4 is the reduction of hydrogen ion (Equation 6-11) and at 4 < pH < 6 the most important cathodic reaction is carbonic acid reduction (Equation 6-13) while at pH > 6 the reduction of bicarbonate ion dominates (Equation 6-13) [147, 148]. At pH ≥ 7, reduction of water occurs as shown in Equation 6-14.

$$2H_2O_{(l)} + 2e^- \leftrightarrow H_{2(g)} + 2OH^-_{(aq)} \qquad 6\text{-}14$$

Similar cathodic reduction mechanism has been reported noting that the reduction of carbonic acid may act as additional source of hydrogen (H^+) ion leading to higher corrosion rate than hydrogen ion alone can offer [69, 149].

The overall anodic dissolution of iron shown in Equation 6-15

$$Fe_{(s)} \rightarrow Fe^{2+}_{(aq)} + 2e^{-} \qquad 6\text{-}15$$

is strongly pH dependent and various reaction steps have been suggested. Nesic, et al [136] argued that the anodic corrosion mechanism of iron dissolution proposed by de-Waard and Williams[134], which was predicated on the works of Bockris, et al [145] cannot be reliably applied to CO_2 corrosion at high pH. This was because the first order dependence for iron dissolution with respect to OH^- as observed by Bockris, et al [145] was applicable only for pH < 4. This cannot be directly extrapolated for higher pH [136]. Therefore, Nesic, et al [136] reported distinct and different anodic mechanisms at pH < 4 and pH > 5 with an intermediate region (4 < pH < 5) depicting a transition from one mechanism to another.

The pH of the solution plays important role in determining the rate and mechanism of CO_2 corrosion of micro-alloyed steels. It has been observed that the dominant cathodic reaction in CO_2 corrosion of steels is dependent on the pH of the solution [113]. pH affects corrosion rate of micro-alloyed steels through acidification of the medium whereby the corrosion rate increases with decrease in pH. This phenomenon was demonstrated by the results of the electrochemical corrosion tests conducted in 3.5 wt% NaCl solution saturated with 0.5% CO_2 at pH 3.5, 5 and 6.5 and 60^0C as presented in Section 5.1.5. The highest corrosion rate was recorded at the lowest pH (3.5) which can be ascribe to the cathodic reduction of H^+ ions with the corresponding anodic dissolution of the substrate through the process of hydrogen evolution as expressed in Equation 6-11. At pH 5, Nazari et al [147] reported the reduction of carbonic acid (H_2CO_3) shown in Equation 6-12 as the dominant cathodic reduction. Tran et al [149] described the mechanism in which adsorbed carbonic acid directly reduced on the surface of the steel revealing that both H^+ reduction and direct reduction of carbonic acid contribute to the corrosion process. This dual source of H^+ ions explained why there was higher corrosion rate at pH 5 than at pH 6.5 where the only cathodic reaction was due to hydrogen H^+ ions provided by the dissociation of bicarbonate ions (HCO_3^-) [147-149]. In other words, the reduction of additional H^+ ions is not favoured at pH 6.5 thus resulting in low corrosion rate [149]. This is in agreement with the results of the LPR corrosion rate shown in Figures 5-33 and the Tafel extrapolation parameters recorded in Table 5-7.

The EDS analysis of the surface of the corrosion product of the steels in 3.5 wt% NaCl solution in different pH shown in Table 5-8 consists of similar elemental composition as that of temperature variation. The XRD pattern did not also detect $FeCO_3$ but Fe_3O_4 in addition to Fe_3C. The trace of Fe_3O_4 in the XRD patterns can apparently be attributed to the preceding decomposition of $Fe(OH)_2$ by the reaction shown in Equation 6-16. The seemingly higher Fe_3O_4 peak at pH 3.5 as shown in Figure 5-40 is because Fe_3O_4 is thermodynamically more stable than $Fe(OH)_2$ at low pH which may be attributed to hydrogen evolution of Equation 6-16

$$3Fe(OH)_{2(s)} \rightarrow Fe_3O_{4(s)} + 2H_3O_{(l)} + H_{2(g)} \qquad 6\text{-}16$$

$Fe(OH)_2$ on the other hand is the product of the overall anodic electrochemical reaction for ferrous metals as expressed in Equation 6-17 [148] according to the pH dependent reaction mechanism proposed by Bockris [145]

$$Fe_{(s)} + 2H_2O_{(l)} \rightarrow Fe(OH)_{2(s)} + 2H^+_{(aq)} + 2e^- \qquad 6\text{-}17$$

6.6 Assessing the corrosion behaviour of the micro-alloyed steels in simulated produced seawater (Lyman and Fleming solutions)

Seawater, without the suspended solid materials of organic and inorganic origin may be considered as aqueous solution containing variety of dissolved solids and gasses. The chemical composition and concentration of these dissolved substances are difficult to determine due to their variation in quantities and similarities in chemical nature [237]. Thus seawater is a complex chemical system which is very difficult to exactly duplicate (simulate) and sustain in the laboratory due to the variabilities of the dissolved substances and the activities of living organisms [168, 237, 238]. This has led to the development and use of different formulae and compositions for simulating seawater in the laboratories by many researchers such as Dittmer (1884), McClendon et al (1917), Brujewicz (Subow, 1931) and Lyman and Fleming (1940) etc [237]. Lyman and Fleming formula is the most frequently and widely used recipe for simulated seawater in laboratories. The composition of this formula is shown in Table 4-7 and is equivalent to constituents of ASTM D1141-98 (updated 2013) which is the standard practice for the preparation of substitute ocean water. There are about 49 elements in seawater [237]. Lyman and Fleming recipe contains

only the major elements of sea water which constitutes about 99.7% of all dissolved substances [237].

Seawater is very difficult to prepare and sustain in the laboratory due to its complexity, activities of living organisms and the variations in the dissolved substances. Therefore 3.5 wt% NaCl solution is frequently used to simulate seawater for laboratory purposes [21, 103, 168, 237, 238]. However, reports have indicated that 3.5 wt% NaCl solution is more aggressive to steels than seawater. For instance, Moller et al [168] investigated the corrosion behaviour of low carbon steels in natural seawater, synthetic seawater and 3.5 wt% NaCl solution and reported that the steel corroded almost four times faster in 3.5 wt% NaCl solution than in natural seawater after an exposure period of 21 days. This lower corrosion rate of carbon steel in seawater was ascribed to the presence of Ca^{2+} and Mg^{2+} ions [168, 216, 238, 239]. In naturally aerated solution where dissolved oxygen (DO) is high, the principal cathodic reaction is the reduction of oxygen to hydroxyl ion as in Equation 6-18

$$O_{2(g)} + 2H_2O_{(l)} + 4e^- \rightarrow 4OH^-_{(aq)} \qquad 6\text{-}18$$

On the other hand, where the supply of oxygen is restricted, the important cathodic reaction is the evolution of hydrogen gas as in Equation 6-19.

$$2H_2O_{(l)} + 2e^- \rightarrow H_{2(g)} + 2OH^-_{(aq)} \qquad 6\text{-}19$$

In these two equations, OH^- is the end product leading to an increase in the pH at the steel-electrolyte interface which resulted in decrease in corrosion rate. In CO_2 saturated solution, the product of cathodic reduction reaction is carbonic acid as shown in Equation 6-20.

$$CO_{2(g)} + H_2O_{(l)} + 2e^- \rightarrow H_2CO_{3(eq)} \rightarrow H_{2(g)} + CO_3^{2-} \qquad 6\text{-}20$$

The cations presence in seawater (Ca^{2+} and Mg^{2+}) combine with OH^- and CO_3^{2-} ions of Equations 6-18 to 6-20 to precipitate as $CaCO_3$ and $Mg(OH)_2$. These precipitates are seawater corrosion products called calcareous deposits and promote physical barrier against diffusion of oxygen from the bulk solution to the surface of the steels thereby reducing corrosion rate [168, 216, 238, 239]. Calcareous deposits can only precipitate at high pH value (> 9.8) [216, 239]. This is facilitated by the cathodic reduction reactions

of Equations 6-18 and 6-19 [168]. To maintain electrical neutrality, this high cathodic reaction is accompanied by a corresponding anodic dissolution of iron resulting to high initial corrosion rate with the attendant gradual formation of corrosion product ($CaCO_3$) in naturally aerated solution [216].

The corrosion performance of the proprietary micro-alloyed steels was appraised in naturally aerated and 0.5% CO_2 saturated simulated seawater at 25^0C and for 24 hours. The general evolution of corrosion rate with time presented in Figure 5-41 revealed that the corrosion rate for all the specimens in both naturally aerated and 0.5% CO_2 saturated seawater can be ranked as F65 < X65 < P110 < TN95. This trend corroborates the corrosion behaviour of the proprietary steels in the other media and environmental parameters used in this work. This was majorly attributed to difference in microstructure of the steels as discussed in Section 6-1. This study also revealed that the corrosion rate of all the specimens was higher in naturally aerated seawater than in 0.5% CO_2 saturated simulated seawater as illustrated in Figure 5-42. This difference in corrosion rate ranged from about 50% for Steel F65 to about 70% for Steel P110. This high corrosion rate in naturally aerated solutions can be ascribed to the presence of dissolved oxygen (DO) which is a precursor for cathodic reduction and for the formation of calcareous deposits. The dissolved oxygen (DO) initiated an early rapid corrosion attack as indicated in Figure 5-41(a) culminating in higher corrosion rate prior to the formation of corrosion products [216, 239]. Hartt, et al[239] reported a linear increase in current density with increase in dissolved oxygen (DO) in seawater. Elbeik, et al[216] investigated the formation of calcareous deposits ($CaCO_3$) as a result of oxygen reduction current density as a function of time and reported a sharp increase in current density during the first 60 hours but peaked at about 66 hours thus suggesting a complete coverage of the metal surface by corrosion products ($CaCO_3$). The lower corrosion rate exhibited bythe steels in 0.5 wt% CO_2 can be attributed to the low concentration of CO_2.

The post experimental surface analysis shown in Figure 5-46 indicated corrosion product free surface for all the specimens corroded in 0.5% CO_2 saturated seawater. This was validated by the XRD pattern which displayed only Fe peak as shown in figure 5-47(b). On the other hand, the surface morphology of all the specimens corroded in naturally aerated Lyman and Fleming solutions shown in Figure 5-45 revealed surfaces with non-uniform deposits of corrosion products. This is because part of the corrosion products had peeled off from the steel substrates. The composition of these corrosion products as

detected by XRD analysis are shown in Figure 5-47(a). The presence of $CaCO_3$ in the corrosion product of the specimens corroded in naturally aerated seawater can be linked to the direct reaction between calcium and carbonate ions. These carbonate ions are products of slow reaction of carbon dioxide from the atmosphere and water as expressed in Equations 6-21 to 6-23 [216, 239]

$$CO_{2(g)} + H_2O_{(l)} \rightarrow H_2CO_3 \qquad 6\text{-}21$$

$$H_2CO_3 \rightarrow H^+_{(aq)} + HCO^-_{3(aq)} \qquad 6\text{-}22$$

$$HCO^-_{3(aq)} \rightarrow H^{\mp}_{(aq)} + CO^{2-}_{3(aq)} \qquad 6\text{-}23$$

The presence of high dissolved oxygen in the naturally aerated solution provided OH^-ions (Equation 6-18) for the reactions in Equations 6-24 resulting in the formation of $CaCO_3$ as shown in Equation 6-25.

$$OH^-_{(aq)} + HCO^-_{3(aq)} \rightarrow H_2O_{(l)} + CO^{2-}_{3(aq)} \qquad 6\text{-}24$$

$$CaO^{2+}_{(aq)} + CO^{2-}_{3(aq)} \rightarrow CaCO_{3(s)} \qquad 6\text{-}25$$

This mechanism is not applicable for 0.5% CO_2 saturated simulated seawater because of the absence of dissolved oxygen and low concentration of CO_2 therefore justifying the absence of corrosion products in the XRD pattern presented in Figure5-47(b).

Magnesium (Mg) nor its compound was not detected on any of the corroded steel substrates regardless of high Mg content in Lyman and Fleming solution as shown in Table 4-7. This is in agreements with the reports of some authors [216, 239] that the preferential formation of $CaCO_3$ rather than $MgCO_3$ is due to higher solubility of $MgCO_3$ at pH < 9.5 [216]. On the other hand, $CaCO_3$ is thermodynamically stable in seawater being supersaturated in ambient pH [239]. The influence of magnesium in corrosion behaviour of steels is to promote the precipitation of $CaCO_3$ as aragonite which is a crystalline form of $CaCO_3$ that is very effective in covering the steel surface due to its orthorhombic crystal structure [238].

Many authors [168, 216, 238, 239] have reported that the function of $CaCO_3$ is to form physical barrier against the diffusion of dissolved oxygen from the bulk solution to the steel surface thus preventing and/or reducing corrosion rate. Although $CaCO_3$ was

detected in the XRD analysis of the specimens corroded in the naturally aerated solution yet the corrosion rate was high. This can be ascribed to the presence of high dissolved oxygen which initiated an early high corrosion attack on the specimens before the formation of enough corrosion products ($CaCO_3$) to cover the surface of the steels. It could be deduced from the SEM morphology that the corrosion products were porous, loose and non-adherence thus allowed the ingress of dissolve oxygen to continue further corrosion. Also the duration of this work (24 hours) was insufficient for the formation of enough corrosion product deposits to cover the steel substrate which according Elkeik et al [216] occurs after about 66 hours of immersion.

6.7 The corrosion behaviour of the micro-alloyed steels in 3.5 wt% NaCl using potentiostatic polarization and electrochemical impedance spectroscopy (EIS).

Potentiostatic, like galvanostatic and potentiodynamic, is a polarization technique that allows for the controlled polarization of metal surfaces in electrolytes, in order to observe cathodic and anodic behaviours. Recently researchers have used potentiostaic polarization to form corrosion products on the surface of metals either with different potentials and at constant time [208, 218, 240] or with constant potential and at different time [113, 208]. The stability of the corrosion products formed in each case was studies using EIS. Luo, et al [208] potentiostatically grew passive film on stainless steels at different potential values chosen within the passive and trans-passive regions in 1 wt% NaCl. The EIS results demonstrated that the corrosion behaviour of the steels was significantly affected by the potential used in forming the passive films. It showed that increasing the formation potential within the passive region, increased the corrosion resistance but showed opposite behaviour within the trans-passive section. Della, et al [218, 240] observed similar corrosion behaviour within the passive and trans-passive regions of shape memory stainless steels (SMSSs) in acidic environment and reported that the structure, thickness, composition, and semiconducting properties determine the protectiveness of passive films formed on stainless steels. Performing similar experiments with constant anodic potential but at different polarization time, Luo, et al [208] reported that the protective capability of the passive film formed on stainless steels increased with longer formation time.

Depending on the environmental conditions in the bulk solution, actively corroding steels in carbon dioxide saturated solution may form protective or non-protective corrosion products [113, 133]. $FeCO_3$ is the main corrosion product of carbon steel in CO_2 environment. The protectiveness of $FeCO_3$ depends on the materials characteristics and environmental parameters [23]. The effects of these parameters on the formation mechanism of $FeCO_3$ and its subsequent protective properties have been widely studied [132, 159, 162]. Alizadeh and Boardbar [162] investigated the protectiveness of corrosion scale formed on weld joints of steel grade API X70 after 90 days immersion in a mixture of three sodium salts at different concentrations and pH 9.7. The results showed that microstructures occasioned by heat treatment have significant effects on the electrochemical behaviour of the steel. Using potentiostatic polarization, Sun, et al [113] grew corrosion product scales on low alloyed steels at different time and employed EIS to investigate the electrochemical characteristics of the corrosion scale. The results showed that the protective property of the corrosion product, which is contrary to that formed on stainless steels, depend on the microstructure. Islam and Farhat [202] formed corrosion product layer on API X42 by immersion in CO_2 saturated 2 g/l NaCl solution at different time schedule and characterized the corrosion scale using SEM, XRD and XPS.

This section of this report is aimed at discussing the results presented in Section 5.1.7 on the electrochemical (protective) behaviour of anodically formed corrosion product on the micro alloy steels using two procedures namely

(iii) Applying different anodic potentials (100 $mV_{(Ag/AgCl)}$, 150 $mV_{(Ag/AgCl)}$ and 200 $mV_{(Ag/AgCl)}$) at constant time (24 hours).

(iv) Applying constant anodic potentials (150 $mV_{(Ag/AgCl)}$) for different time interval (0, 1, 2, 4, 8 12 and 24 hours).

The former was conducted by polarizing steels P110 and API 5L X65 at different formation potentials for 24 hours and using electrochemical impedance spectroscope (EIS) to study the protective ability of the corrosion products as presented in Section 5.1.7.1. In the latter case, anodic potential of 150 $mV_{(Ag/AgCl)}$ was applied on steels P110 and TN95 at different times to grow corrosion product and EIS was used to assess the properties of the corrosion product formed.

6.7.1 EIS investigation of the stability of the corrosion product formed on the steels by applying different anodic potentials at constant time.

The corrosion product layer was formed on steels P110 and X65 by applying three anodic potentials 100 $mV_{(Ag/AgCl)}$, 150 $mV_{(Ag/AgCl)}$ and 200 $mV_{(Ag/AgCl)}$ for 24 hours in 3.5 wt% NaCl solution saturated 0.5% CO_2 at 60^0C and pH6.5. The plots of the evolution of current density versus time for specimens P110 and API 5L X65 displayed in Figure 5-48 illustrated that the current density increased as the applied potential increased. This agrees with literature reports [4, 206, 217] which suggested that current density increased with potential within the active region due to activation control reaction. The microstructure and the grain size of the steels which depend on the chemical composition and thermo-mechanical treatment significantly determined the behaviour of the specimens demonstrating that the current density of API 5L X65 steel is lower than that of steel P110 within the range of applied potential. Steel P110 consists of more carbon content and finer grain size which provided greater pearlite/ferrite ratio with the attendant more micro galvanic cells [52] and more surface area for corrosion attack [54] than steel X65.

The Nyquist plots of steels P110 and X65 passivated with three different potentials (100 $mV_{(Ag/AgCl)}$, 150 $mV_{(Ag/AgCl)}$ and 200 $mV_{(Ag/AgCl)}$) for 24 hours in 3.5 wt% NaCl solution saturated with 0.5% CO_2 at 60^0C and pH 6.5 are shown in Figures 5-49. The Nyquist plot displayed similar features of one semi-capacitive arcs that did not meet at the low frequency axis. This can be ascribed to the non-homogeneity of the surface, frequency dispersion and mass transport resistant [54, 208]. The radius of the semi capacitive arcs decreased with increase in applied formation potentials demonstrating the characteristics of actively corroding steels that increase in potential increases the anodic current density [206]. This showed that the ability of the corrosion product to resist corrosion attack (film stability) decreased with increase in applied anodic potentials [209].

The radius of the impedance semi-arc represents the interface resistance of the charge transfer which corresponds to the corrosion resistance [54, 113]. This indicated that steel X65 which presented higher semi capacitive arc at the respective formation potentials showed better corrosion resistance than steel P110. This corroborated with the electrochemical behaviour of the steels earlier reported which was attributed majorly to the ferrite-pearlite microstructure of the steels and the mechanism schematically proposed

by Sun, et al [113]. Similar work conducted using active-passive metals (alloy 59 in 0.5 m H_2SO_4 [241], ultrahigh-strength stainless steel in 1 wt% NaCl [208], shape memory stainless steels (SMSSs) in 0.5 M H_2SO_4 [218] and stainless steel type 304 in 0.5 M H_2SO_4 [218]) with different formation potentials within the passive region revealed opposite results. These results indicated that for passive steels the capacitive arcs and the corresponding charge transfer resistance became larger as the applied potentials increased. This was attributed to the passive film which blocked the corrosive species from accessing the steel substrate. This means that the passive films formed at higher applied potentials are more protective and stable than that formed at lower applied potentials on active-passive steels. This is contrary to the behaviour observed with actively corroding micro-alloyed steels used in this work.

From the potentiostatic polarization and the impedance measurement results, it is observed that API 5L X65 steel demonstrated better resistance to general corrosion than steel P110X. This could be attributed to variation in microstructures and elemental specification of the steels [159]. Both steels consist of ferrite-pearlite microstructure as shown in Figure 5-2. During an electrochemical corrosion of micro-alloyed steels consisting of ferrite-pearlite microstructures, the ferrite phase is selectively dissolved first while the pearlite (Fe + Fe_3C) phase is left on the surface of the steel undissolved. With further dissolution of ferrite, more Fe_3C are exposed leading to galvanic effect and large cathodic site for hydrogen evolution reaction (HER) [11, 52]. The more the cathodic sites which could be due to high pearlite-ferrite ratio, the more the corrosion attack [47, 128]. With increase in applied potential, there was an increase in selective dissolution of ferrite leaving more protruding Fe_3C which in turn resulted in increased electrode/electrolyte interface area with the corresponding increase in corrosion rate [113]. It has been reported that increase in carbon content increases the pearlite phase [37, 166]. It is then expected that the specimens with higher carbon content should possess more pearlite phase which translates to greater cathode to anode ratio with the attendant higher corrosion rate. Fiji ImageJ analysis of the specimens (Table 5-1) showed that API 5L X65 steel has larger grain size than steel P110. Seikh, et al [54], observed higher corrosion rate for steels with small grain microstructures which implied greater surface area for corrosion thereby demonstrating higher susceptibility to corrosion attack. It can therefore be concluded that lower cathode-anode ratio and bigger grain size attributed to steel API 5L X65 presenting less general corrosion rate than steel P110.

The SEM micrographs of the evolution of surface morphology with applied potential revealed a progressive increase in thickness but increase in porosity resulting in the formation of less adhesive (flaky) double corrosion layer as illustrated in Figure 5-53 for steel P110. Similar double corrosion layer has been reported in literature [133, 202, 214] as primary (inner) and secondary (outer) layers respectively. The primary scale was formed directly on the surface of the steel and is usually thin, non-uniform and adherent to the steel surface. On the other hand, the secondary layer is thick, porous and less adherent to the primary layer.

The average maximum pit depth (average of the pit depths recorded at different potentials) identified using white light profilometer for steel P110 and X65 were 45 µm and 65 µm which corresponds to an average pit penetration rate (pit depth/time) of 16.41 mm/year and 23.75 mm/year respectively. This shows that steel P110 is more resistance to pitting corrosion than API 5L X65 steel which is in agreement with the SEM micrographs of the evolution of pits shown in Figure 5-56. Pits almost always initiate at some chemical or physical heterogeneity such as grain boundaries, chemical different phases (ferrite-pearlite), etc at the surface of metals [166, 242, 243]. The presence of aggressive anionic species of which chloride ions are the most common and is usually the cause of pitting corrosion can promote pit initiation. This is because chloride is an anion of a strong acid and its solution dissolve many metallic cations. Also chloride is a relatively small anion with a high diffusivity, it interferes with passivation, and it is pervasive as a contaminant [243]. Steel P110 with fine grain size and more pearlite content presumably has more pit initiation sites due to many grain boundaries than steel X65. It is well recognized that the grain boundaries are preferred corrosion sites in corrosion medium. Since the large density of crystal defects, and lattice distortion are within the grain boundary, atoms have high energies, and become more active, will take part in the reaction first. As a result, the larger the volume fraction of grain boundaries due to fine grains, the more the active atoms on the steel surface, which lead to increase in anodic current density [244]. It has also been established that the corrosion products formed on the steels by the applied anodic potential were porous allowing easy penetration of corrosion species (particularly chloride ions) to the surface of the substrate resulting in acidification and numerous micro-galvanic effects with the attendant shallow pits as revealed in Figure 5-56 for steel P110. On the other hand, steel X65 has few pit initiation sites due to larger grain size (few grain boundaries) leading to high

concentration of chloride ions resulting to high acidification due to chloride ion migration to these few grain boundaries with the attendant aggressive corrosion attack.

6.7.2 EIS investigation of the stability of the corrosion product formed on the steels by applying constant anodic potentials for different time interval.

Anodic polarization of 150 $mV_{(Ag/AgCl)}$ was used to form corrosion product layer on steels P110 and TN95 in naturally aerated 3.5 wt% NaCl solution at ambient temperature within different time interval of 1 to 24 hours. EIS was used to assess the stability of the corrosion film. The Nyquist and Bode plots of this investigations are presented in Figures 5-58 and 5-59. The impedance spectra of all the specimens exhibited similar features of incomplete semi-capacitive arcs that did not meet at the low frequency axis. The radius of these capacitive arcs decreased with increase in applied potential time depicting that the protective capabilities of the passive oxide films decreased with time.

In aerated NaCl solution, the dominant cathodic reaction is oxygen reduction shown in Equation 6-27 while the anodic reaction is the oxidation of iron as expressed in Equation 6-26. The addition of these two redox reactions results in the formation of ferrous hydroxide as in Equation 6-28. This ferrous hydroxide dehydrates via Schikorr reactions as expressed in Equations 6- 29.

$$Fe_{(s)} \rightarrow 2Fe^{2+}_{(aq)} + 4e^- \qquad 6\text{-}25$$

$$O_{2(g)} + H_2O_{(l)} + 4e^- \rightarrow 2OH^-_{(aq)} \qquad 6\text{-}27$$

$$2H_2O_{(l)} + O_{2(g)} + 2Fe^{2+} \rightarrow 2Fe(OH)_{2(s)} \qquad 6\text{-}28$$

$$3Fe(OH)_{2(s)} \leftrightarrow Fe_3O_{4(s)} + H_{2(g)} + 2H_2O_{(l)} \qquad 6\text{-}29$$

It has also been reported that the formation of Fe_3O_4 is thought to be favoured by the reactions in Equation 6-30 [245]

$$3Fe_{(s)} + 4H_2O_{(l)} \rightarrow Fe_3O_{4(s)} + 8H^+_{(aq)} + 8e^- \qquad 6\text{-}30$$

Magnetite which is the overall product of these reactions formed loosely, sludge-like and cracked surface morphology that grew in thickness and eventually detached from the surface of the steels after about 4 hours of polarization time as shown in Figures 5-62 and 5-63. The cracked surfaces facilitated the ingress of corrosive species resulting in increased corrosion rate. This is recorded in Figure 5-58 of

the Nyquist spectra as decrease in the radius of the capacitive arc. Magnetite is electrically conductive and nobler than carbon steel in the electrochemical series [246] therefore its deposition on the surface of steel may result in galvanic effect. In this case, the potential of the cathode (surface covered by Fe_3O_4) is more positive than that of the anode (bare steel surface). This can result in the enhancement of the dissolution of the anodic iron due to large cathodic site occasioned by more deposition of Fe_3O_4 thus accounting for the decrease in the radius of the semi capacitive arcs with polarization time.

According to basic electrochemical kinetics theory, a decrease in OCP (cathodic shift) with time indicates an increase in both anodic and cathodic reactions presumably due to absence of corrosion products with the resultant increase in corrosion rate [247]. This was observed in the plots of the evolution of OCP and corrosion resistance (Rp) of the steels where both OCP and corrosion resistance (Rp) demonstrated sharp decrease within the first few hours of polarization as revealed in Figures 5-60 and 61 respectively.

6.8 Further investigation in 3.5 wt% NaCl saturated with 99.98% CO_2

Further studies were carried out by repeating the experiments on temperature variation, simulated produced water and weight loss using 99.98% CO_2 saturated solutions. The results of these investigations presented in Section 5.1.8 are discussed in this Section and compared with the results obtained using 0.5% CO_2.

6.8.1 Effect of temperature variations on the corrosion behaviour of the specimens in 3.5 wt% NaCl saturated with 99.98% CO_2 environments

This section compares the results of the effect of temperature on the corrosion behaviour of steels P110, TN95 and X65 in 3.5 wt% NaCl solutions saturated with 0.5% CO_2 (Section 5.1.4) and 99.98% CO_2 (Section 5.1.8.1). The plots of the evolution of corrosion rate of these steels exhibited the same trend depicting an increase in corrosion rate with temperature. This signified similar corrosion mechanism and that corrosion product was not formed on the surface of the steels in both CO_2 conditions. In CO_2 environment, there are various ionic species in solution such as H^+, CO_3^{2+}, HCO_3^- and H_2CO_3 resulting in complexity of sweet (CO_2) corrosion of steel. Consequently various sweet (CO_2) corrosion mechanisms have been proposed and the most commonly used mechanism postulates three cathodic reactions involving these ionic species and one overall anodic reaction involving the oxidation of iron. Therefore, depending on temperature, pH and

carbon dioxide partial pressure, these ions, through series of chemical and electrochemical reactions form iron carbonate ($FeCO_3$) with the oxidised ferrous ion (Fe^{2+}) [23, 128]. $FeCO_3$ is the dominant corrosion product of sweet corrosion and its formation rate, stability and protectiveness determine the corrosion performance of carbon steel. The formation and growth of $FeCO_3$ is a slow temperature dependent process requiring high supersaturation of Fe^{2+} and CO_3^{2+} to form protective film [23, 70].

As it is obvious with most thermal activation process, temperature is one of the most influential environmental factors in CO_2 corrosion of carbon steel increasing the rate of corrosion at temperature below 60^0C since no protective layer is formed on the steel surface. On the other hand, at temperatures around or above 80^0C, compact, dense, and adherent corrosion product layer with the attendant protective properties are formed resulting in decrease in corrosion rate [157, 158, 204, 207]. The effect of temperature on the corrosion resistance of steels P110, TN95 and X65 was investigated in 3.5 wt% NaCl solutions saturated with 0.5% CO_2 and 99.98% CO_2 at temperatures less than 60^0C. In agreement with the reports in literature, the corrosion rate of the specimens increased with increase in temperature as shown in Figures 5-23 and 5-66. About 50% increase in corrosion rate for the steels was observed with increase in temperature from 25^0C to 45^0C but only about 25% increase was recorded as temperature increased from 45^0C to 60^0C in 99.98% CO_2 condition. This suggests that the rate of increase in corrosion attack reduced as the temperature increases towards and above 60^0C. This may be attributed to gradual formation of corrosion product at higher temperatures. With the gradual precipitation of corrosion product at higher temperature, the surface area available for corrosion is reduced thereby decreasing the general corrosion rate. This is evidenced in the evolution of the SEM surface morphology of the specimens corroded in 3.5 wt% NaCl solution saturated with 99.98% CO_2 as illustrated in Figures 5-72 to 5-74. These figures showed increase in the deposited corrosion products with increase in temperature. This is corroborated with the potentiodynamic polarization (Tafel) plots of the specimens shown in Figure 5-68 which demonstrated an increase in both anodic and cathodic current densities with increase in temperature. This increase in current densities with temperature was more pronounced with the cathodic curves signifying that the corrosion is mainly controlled by cathodic reaction. The cathodic curve also revealed a well-defined current plateau depicting the effect of mass-transport limitation of hydrogen reduction reaction [157, 204, 219, 220] which could have attributed to the formation of corrosion product.

The comparison of the results of the linear polarization resistance experiments (Figure 5-67) and the potentiodynamic polarization (Tafel) experiments (Figures 5-69 to 6-71) clearly indicated that all the specimens exhibited about 98% increase in corrosion rate in 99.98% CO_2 (22.72 mol/l) than in 0.5% CO_2 (0.114 mol/l). This corroborates with the difference in mol/l of CO_2 in both solutions which is about 99%.

The concentration of a gas in a system is proportional to its partial pressure. Therefore an attempt was made to discuss the effects of these two CO_2 concentrations based on their respective partial pressure. The total pressure in the 1 litre corrosion cell is 1 atm. Thus a corrosion cell containing 0.5% CO_2 and 99.98% CO_2 will have partial pressure of 0.005 atm and 0.998 atm respectively. CO_2 partial pressure plays an important role in CO_2 corrosion of carbon steels. Both experimental and field evidence have shown that an increase in CO_2 partial pressure increases the concentration of H_2CO_3 which decreases the pH value. This accelerates the cathodic reaction by increasing the rate of carbonic acid reduction and ultimately enhancing the corrosion rate [135, 189, 248]. Many researchers have postulated different relationships (models) for evaluating the effect of CO_2 partial pressure on the corrosion behaviour of carbon steel. The first model correlating the effects of carbon dioxide partial pressure and temperature on the corrosion behaviour of carbon steel was proposed by de Waard and Williams [129] and is expressed in Equation 6-31 .

$$\log CR = 5.8 - \frac{1710}{T} + 0.67 \log(P_{CO_2}) \qquad 6\text{-}31$$

This model predicts an increase in corrosion rate of carbon steel with increase in CO_2 partial pressure up to 1 MPa. Other models have generally predicted similar results particularly in scale free CO_2 corrosion and low partial pressure [11, 135]. However, none of these models have satisfactorily predicted the correlation between the corrosion rates of carbon steels on wide spectrum of CO_2 partial pressure. This points to the fact that the relationship is quite complicated arising from the different corrosion mechanism exhibited by surface morphology of carbon steels. It has been observed that CO_2 partial pressure play variance role for film-free surfaces and for film-forming surfaces. For film-free conditions, increase in CO_2 partial pressures increases the corrosion rate. This is ascribed to the increase in the concentration of H_2CO_3. This accelerates cathodic reactions which formed CO_3^{2-} in the solution resulting in decrease in pH and ultimately enhances

the corrosion rate. Alternatively, under film-forming conditions which is favoured by high supersaturation at the interface with the resultant precipitation of protective iron carbonate, high CO_2 partial pressures decreases the rate of corrosion rate due to reduction in cathodic sites [129, 135, 137]

In the potentiodynamic polarization experiments conducted in 3.5 wt% NaCl solution saturated with 0.5% CO_2 (ie 0.005 atm partial pressure) and 99.98% CO_2 (ie 0.9998 atm, this is almost equal to the total pressure for the corrosion environment), it was obvious from Figures 5-68 to 5-71 that the anodic reaction was under charge control and was not significantly affected by the different in both CO_2 conditions. On the other hand, the cathodic reaction is limiting current controlled depicting strong influence of CO_2 partial pressure (99.98% CO_2) on the limiting current density occasioned by cathodic reduction of carbonic acid. This resulted in the decrease in pH and subsequently increased the limiting current density. This corroborated the reports of Nesic, et al [189].

6.8.2 Corrosion behaviour of the micro-alloyed steels in simulated seawater saturated with 99.98% CO_2.

The results of the corrosion performance of steels P110, TN95 and X65 in simulated seawater saturated with 99.98% CO_2 using the test matrix in Table 4-8 and presented in Section 5.1.8.2 are discussed in this section. It is apparent from Figures 5-76 and 5-77 that the three micro-alloyed steels began to corrode at high corrosion rates generally associated with activation control reactions but decreased rapidly due to the dissolution of the air-formed oxide film. However, this rapid decrease in corrosion rate transits to gradual and almost stable corrosion rate within 4 to 8 hours of polarization. This trend of corrosion behaviour has been described by Melchers and Jeffrey [249] as initially highly non-linear and then almost linear. This is ascribed to concentration/diffusion control phenomenon attribute to the formation of porous and non-protective corrosion products called calcareous deposits [122]. The presence of Ca^{2+}, Mg^{2+} and HCO_3^- in seawater facilitated the formation of these calcareous deposits which restrain the diffusion of corrosive species thereby slowing down corrosion attack as discussed in Section 6.6.

The evolution of free corrosion potential with time for all the specimens as shown in Figure 5.76 revealed an initial decrease in potential (shift in the negative direction) within the first 1 to 4 hours. A closer look at this figure indicates that the curves of the evolution of corrosion rate and free potential with time for all the steels demonstrated opposite trend

(shape) suggesting an inverse proportionality characteristic between the corrosion rate and the free potential with time for carbon steel corrosion in CO_2 environment. Similar results were reported in literatures [203, 210]. It is also evidenced in Figure 5-77 and in agreement with other results presented earlier in this report that the corrosion resistance of the three micro-alloyed steels can be ranked as X65 > P110 > TN95.

The Nyquist diagrams (Figure 5-79a) consist of a capacitive semicircle in the high frequency range and another capacitive semicircle in the low frequency range. The low frequency semi-capacitive loops depict that the surface of the specimens are covered by corrosion products. The electrochemical impedance parameters were fitted using electrochemical equivalent circuit (EEC) shown in Figure 5-80. The fitted impedance parameters are listed in Table 5-16.

The high frequency loops are attributed to the charge-transfer resistance (R_1) of the corrosion reactions occurring at the solution/layer interface which is used to evaluate the corrosion resistance of the electrode. The high values of R_1 indicated that the steel resists metal dissolution process and possesses a better corrosion performance properties. On the other hand, the low frequency semi-capacitive loops suggest that the surface of the specimens are covered by corrosion products. This is attributed to the charge-transfer resistance (R_2) corresponding to corrosion reactions occurring at the layer/steel interface [132, 219, 244]. Higher values of R_2 indicated that the corrosion layer acted as an insulated resulting in the low corrosion rate exhibited by the steels.

A two-time constant behaviour can be observed from the Bode plot (Figure 5-79b) corroborating the characteristics of the Nyquist plot. Also the maximum magnitude of phase angle which is about 60^0 occurred at the medium frequency range and shift towards the low-frequency range revealing the corrosion susceptibility of the steels. This can be ascribed to the formation and deposition of the corrosion products on the surface of the substrate. The impedance modulus shown in Figure 5-79b spans between 4 to 32 $k\Omega.cm^2$ at the low frequency end agreeing that the corrosion resistance of X65 is better than the other two steel. It has been reported in literature that the impedance modulus at the low-frequency range is inversely proportional to the corrosion rate of the steel [132, 244]. Thus agreeing with the earlier results of this report.

The equivalent impedance Z, shown in Figure 5-80 can be written as in Equation 6-32:

$$Z_{CPE} = R_s + \frac{1}{\frac{1}{CPE_1} + \frac{1}{R_1 + \frac{1}{\frac{1}{CPE_2} + \frac{1}{R_2}}}} \qquad 6\text{-}32$$

The impedance Z, (R_2, CPE_2) can be denoted as Equation 6-33

$$Z_{CPE} = \frac{R_2}{1 + (j\omega)^n} \qquad 6.33$$

Where $\omega = 2\pi f$ is the angular frequency, f is the ordinary frequency (measured in Hertz), j is the imaginary number and n is the dispersion coefficient related to surface non-homogeneity. Depending on the value of n, CPE may be pure resistor (ie if n = 0 then Z_0 = R), pure capacitor (meaning that n = 1 when Z_0 = C) or inductor (ie when n = 0.5 and Z_0 = W) [54, 113, 209].

At the initial stage of polarization when the corrosion product is not yet formed, the corrosion process was totally controlled by the charge transfer resistance (R_2) and the total polarization resistance (Rp) is equal to R_2. With the formation of corrosion product, corrosion process is controlled by both activation and diffusion reactions and the total polarization resistance is the sum of, R_2 (the charge transfer resistance associated with the difficulty of the electrochemical reaction) and R_1 (the resistance of corrosion film) ie $R_p = R_1 + R_2$ [244].

Figure 5-82 shows the XRD pattern revealing Fe, (Ca, Mg)CO_3 and $CaCO_3$ as the constituents of the corrosion products. The mechanism of formation, deposition and functions of these corrosion products called calcareous deposits have been discussed in Section 6.6.

Figure 5-83 compares the corrosion performance of steels P110, TN95 and X65 in three different simulated seawater (SSW) conditions namely naturally aerated SSW, SSW saturated 0.5% CO_2 and SSW saturated with 99.98% CO_2. This figure shows that the specimens were least attacked in 0.5% CO_2 saturated while 99.98% CO_2 saturated SSW demonstrated the most aggressive medium. This is understandable considering the wide different in CO_2 concentrations between these two conditions as discussed in Section 6.8.1. The naturally aerated SSW exhibited corrosion attack in between these two extremes. The specimens exhibited higher corrosion rate in 99.98% CO_2 environment due

to decrease in pH as a result of hydrogen evolution reduction of cathodic reaction while in the naturally aerated condition the pH is high due to the formation of hydroxyl ions occasioned by O_2 reduction [216].

6.8.3 The corrosion behaviour of the steels by weight loss in 3.5 wt% NaCl solution saturated with 99.98% CO_2 at 25^0C and pH 6.5

The corrosion rate of the two worst corroded steels were also investigated by weight loss techniques in 99.98% CO_2 saturated 3.5 wt% NaCl at 25^0C, pH 6.5 and for 120 hours. Five of each of the specimens were used and each specimen was removed from the electrolyte after every 24 hours for corrosion rate calculation and surface analyses. The pH of the electrolyte was monitored during the five days of immersion. Figure 5-84 shows the transition of corrosion rate and pH for steels P110 and TN95 in 3.5 wt% NaCl saturated with 99.98% CO_2 at ambient temperature for 5 different days. It is obvious from this figure that the transition of corrosion rate and pH of the systems exhibited opposite trend suggesting a decrease in corrosion rate with increase in pH with time. The decrease in corrosion rate can be attributed to the formation of corrosion product scale as shown in the SEM micrographs of the corroded surfaces in Figures 5-85 and 5-86. These corrosion products prevent the corrosive media from easily accessing the steel substrate. On the other hand, the pH increase can be ascribed to increase in dissolution of iron into ferrous ions (Fe^{2+}) with time [202].

6.8.4 The tendency of the micro-alloyed steels to form protective $FeCO_3$ film in 3.5 wt% NaCl solution saturated with 99.98% CO_2 at 25^0C and pH 6.5

Carbon steel although very susceptible to sweet (CO_2) corrosion is still widely used in the oil and gas industry for structural equipment, production and transportation of crude oil and its products. These advantage of carbon steel is attributed to its ability to, among others, form protective iron carbonate ($FeCO_3$) crystal which presents a mass-transfer barrier that slows down the diffusion of cathodic species to the steel surface. $FeCO_3$ is known to directly cover the steel surface by blocking the anodic dissolution of iron thereby mitigating corrosion attack. Therefore, the intensity, severity and type (general corrosion or localized corrosion) of corrosion attack on carbon steel depend to a large extend on the protectiveness, rate of formation/precipitation, the stability and characteristic of the corrosion product film. Experimental results have equally shown that $FeCO_3$ precipitation is facilitated by increased pH, increased temperature, prolongation of time and by all other measures which can reduce the transport of reactants and

corrosion products to and from the steel surface [70, 154, 159, 220]. Dugstad [70] observed the formation of protective iron carbonate films on carbon steels in CO_2 environment at all temperatures provided that the pH and the dissolved iron carbonate concentration in the bulk solution is sufficiently high. However many researchers [210, 250, 251] suggested that the tendency to form protective $FeCO_3$ crystals in CO_2 corrosion of carbon steel is most likely to begin at 60^0C if other experimental conditions such as pH, and super-saturation are favourable. Thus to assess the corrosion performance of steels P110, TN95 and X65 on the basis of their propensity to form $FeCO_3$, linear polarization resistance test was conducted to investigate the rate of initiation and formation of protective $FeCO_3$ crystals at 60^0C, pH 6.5 and for 4 days. The results of this investigation are discussed in this section.

$FeCO_3$ is the most important corrosion product film that can form on carbon steels in sweet (CO_2) environments. $FeCO_3$ is very effective in mitigating corrosion attack by presenting physical barrier which retards the diffusion of corrosive species and prevent further metal dissolution of the steel surface. Reports have shown that protective $FeCO_3$ film precipitated on the carbon steel surface can decrease corrosion rate by one order of magnitude [252]. $FeCO_3$ formation is a complex, slow and temperature sensitive process. The complexity of the formation of corrosion products on carbon steel in CO_2 environment is occasioned by the effects of steel characteristics (microstructure, heat treatment history and alloying elements) and environmental variables (solution pH, temperature, solution composition, flow rate, super-saturation etc.) resulting in different surface morphology of the corrosion films with different composition and microstructures [23]. Super-saturation is a crucial factor in CO_2 corrosion and most environmental factors affect the formation and/or otherwise of CO_2 corrosion product via changing the supersaturation of $FeCO_3$ [207]. Therefore super-saturation is considered as the driving force for precipitation of $FeCO_3$ facilitating nucleation and particle growth [69]. Experimental results have shown that nucleation increases exponentially whereas the growth rate has an approximately linear relationship with relative supersaturation (RS) which can be defined as in Equation 6-34.

$$RS = \frac{Q - Q_{eq}}{Q_{eq}} = (S - 1) \qquad 6\text{-}34$$

Where Q is the concentration of the solute at any instant, Q_{eq} the equilibrium solubility and S is the supersaturation defined as Equation 6-35.

$$S = \frac{C_{Fe^{2+}} * C_{CO_3^{2-}}}{K_{sp}} \qquad 6\text{-}35$$

Where Ksp is the solubility product for $FeCO_3$, $C_{Fe^{2+}}$ and $C_{CO_3^{2-}}$ are the concentration of ferrous and carbonate ions in solution respectively [69, 155, 157]. The product of the reaction between these ions when their concentration exceed the solubility limit results in the formation of protective $FeCO_3$ as expressed in Equation 6-36 [141].

$$Fe^{2+}_{(aq)} + CO^{2-}_{3(aq)} \rightarrow FeCO_{3(s)} \qquad 6\text{-}36$$

At low relative supersaturation, particle growth is favoured while at high supersaturation the exponential dependency of nucleation rate may prevent particle growth resulting in coagulation of particle close to the steel surface or inside the film. At high temperature (> 60 ‘C) the precipitation rate is fast and the supersaturation is low resulting in relatively dense crystalline films with better protection. On the other hand at lower temperature (< 60^0C) a much lower precipitation rate was experienced, and the relative supersaturation is very high due to accumulation of dissolved iron carbonate leading to the formation of low crystalline film with porous, loosely adherent and much less protective [70].

The effect of microstructures on the corrosion behaviour of the specimens and its role in the formation and anchoring of the corrosion products to the substrate were discussed in Section 6.1. The ferrite-pearlite microstructures have continuous lamella within the pearlite which form lamellar Fe_3C plates that remained attached to the steel surface after the anodic dissolution of the ferrite. The dissolved ferrite increased the local concentration of ferrous ions thus favouring the formation of $FeCO_3$ in the presence of sufficiently high concentration of carbonic ions leading to decrease in corrosion attack. This is evidenced in the corrosion performance exhibited by steels P110 and X65 which have ferrite-pearlite microstructures. On the contrary, for bainite microstructure, the carbide particle distribution is not continuous but in discrete, rendering it less efficient in anchoring corrosion deposits on the surface of the metal. This means that microstructural characteristics can hinder or enhance good anchorage of protective film on the surface of the specimen. Therefore steel TN95 with bainite microstructure could not form Fe_3C

network but displayed the behaviour of a freshly braded surface with fewer $FeCO_3$ deposit. This necessitated the witnessed higher corrosion attack.

Precipitation of $FeCO_3$ is a slow, temperature-dependent process [23, 70, 250]. Time is required for the dissolution of ferrous and dissociation/reduction of carbonic acid (H_3CO_3) so as to yield sufficient concentration of Fe^{2+} and CO_3^{2-} ions that exceed the solubility limit and form enough skeleton of Fe_3C for anchoring and growth of $FeCO_3$. This is in agreement with the observation of Farelas et al [210] that there are three different stages involved in the formation of protective corrosion product scale in CO_2 corrosion of carbon steel. These stages include active corrosion, nucleation and growth of $FeCO_3$ and pseudo–passivation stage. In an experiment conducted using different types of steel in 0.1 wt% NaCl saturated with CO_2 at 60^0C and pH 6 Dugstad [70] observed that 2 to 3 days are required to precipitate sufficient $FeCO_3$ that could cover the entire surface of the steels and ultimately reduce corrosion attack.

The experiments for this section of the report were conducted at pH 6.5. From the plot of the ferrous ion concentration ($C_{Fe^{2+}}$) versus pH shown in Figure 3- 7 [161], it was evidenced that saturation with respect to $FeCO_3$ was established at the initial period of the experiments resulting in supersaturation at the surface of the steel. It was also obvious from Figure 5-88 that the electrochemical kinetics changed greatly during the 4 days of linear polarization resistance tests. This could be attributed to the formation of protective scale ($FeCO_3$) and the continued improvement in the protective ability of this scale evidenced by the increasing size of the scale ($FeCO_3$ crystals) as revealed in the SEM micrographs shown in Figures 5-89 to 5-91. $FeCO_3$ crystal size of 3, 2 and 5 µm for steels P110, TN95 and X65 respectively were observed within the first 24 hours of immersion. The decreasing corrosion rate (Figure 5-88) and the fact that $FeCO_3$ had precipitated on small portion of the surface (Figures 5-89(a), 5-90(a) and 5-91(a)), indicated that the precipitation process had started, but $FeCO_3$ has not grown to form continuous layer. The size of these $FeCO_3$ crystals progressively increased with time, expanding the coverage of the surface of the steels and becoming more compact. Similar results [252, 253] have shown that the size of $FeCO_3$ crystal (Cube or rohumbor) play an important role in offering protection with high crystalline and small crystal size providing better protection. In the presence of corrosion product scale mass transfer of corrosive species to and from metal surface dominate the corrosion process rather than cathodic hydrogen evolution. The SEM surface morphology of the corroded steels revealed that $FeCO_3$ crystal size

increased and became denser and more compact with time thus providing a mass transfer barrier. This corroborated the reports of [70, 210, 251]. XRD pattern shown in Figure 5-92 indicated $FeCO_3$ which is the inherent characteristics product of CO_2 corrosion of carbon steel. The number and the intensity of $FeCO_3$ peak increased with time.

6.9 Alloying of steels P110 and TN95 with Zr and Hf and investigation of the Corrosion behaviour of alloyed specimens in simulated produce water (SPW).

Carbon steel because of its tremendous and inherent properties [3, 4] has found extensive use as structural materials for exploration, production and transportation in the oil and gas industry. However, carbon steel is prone to the aggressive oilfield environments. Therefore efforts are being continuously made to improve carbon steel and/or develop new materials which are stronger, lighter, cheaper and more resistant to corrosion [254]. Micro-alloying is one the widely used techniques of providing materials with desirable combinations of excellent properties [51]. Therefore, this work improved the corrosion resistance of two steels by alloying them with Zr and Hf. The results of the characterization and the investigation of the corrosion performance of these alloys are presented in this Section.

6.9.1 Characterization of the alloyed steels

Most of the elements located at the left of iron in the periodic table are considered as strong carbide-formers [15]. These elements have found extensive application in micro-alloying of steels. Among these elements, Zr and Hf have not receive comparative application like the other neighbouring elements such as Ti, V, Nb, Cr etc [16]. Nevertheless, few researchers [50, 85, 87, 88, 222] have investigated the function of Zr as alloying elements in steels. Aliakbarzadeh, et al [85, 87] alloyed carbon steel with 0.005 wt% Zr and reported microstructural modification through grain refinement which ultimately resulted in improved mechanical properties such as increased hardness without any negative impact on toughness. Other authors [50, 88] have reported increase in hardness of steel with increase in Zr content. This was attribute to the formation of Zr-base intermetallic precipitates. Bairi, et al [88] reported that an optimum Zr content of 8 – 12 wt% resulted in the formation of best passive film stability and highest corrosion resistance. Kovalenko and Zats [50] also demonstrated that by alloying steel with 0.1 – 0.16 wt% Zr, the corrosion resistance of the steel in water increased. This was ascribed

to the decrease in the activity of the anodic process due to the thermodynamic stability of the anodic phase and its passivation.

The effects of different quantities (0.1, 0.2 and 0.4 wt%) of Zr and Hf on the mechanical, microstructural and corrosion properties of samples P110 and TH95 were studied using surface analysis and electrochemical techniques. The results of these investigations are presented in Section 5.2 of this report. Figures 5.93 and 5.94 show the SEM micrographs of steels P110 and TN95 alloyed with 0.1, 0.2 and 0.4 wt% Zr and Hf respectively. These figures revealed a decrease in grain size with increase in Zr and/or Hf additions. This was verified by Fiji ImageJ analysis coupled with the Jeffries Planimetric method of ASTM grain size number determination as specified in ASTM E-112 standard [194]. The results of this verification is presented in Figure 5-99. It is clear from this figure that while the ASTM grain size number increased, the average grain size decreased with increase in Zr and/or Hf content. This decrease in grain size with increase in Zr/Hf addition was due to the formation of Zr- and/or Hf-base intermetallic precipitates. These precipitates have the ability to pin down grain growth [87, 88, 222] thus contributing to the increased hardness and tensile strength observed with increase in Zr/Hf content as shown in Table 5.18. This increase in hardness can also be linked to the ability of Zr and Hf to increase extend solution period resulting in the delay and incomplete precipitation within the austenite phase [84]. It can be noted that the variation in grain size decrease was more pronounced with increase in Hf than with Zr content. This can be ascribed to more intermetallic precipitation occasioned by low solubility of Hf than Zr in Fe.

The XRD pattern of the alloyed steels P110 and TN95 are shown in Figure 5-100. Diffraction patterns were matched with reference patterns of pure substances from the powder diffraction database and the identified compounds with their matched 2θ values, diffraction planes and crystallographic structure are listed in Table 5-17. It is evident from this table that the XRD patterns of the unalloyed specimens consist of only α-Fe peaks while the alloyed steels, in addition to α-Fe peaks also contain intermetallic compounds such as $ZrFe_2/Zr_6Fe_{23}$ and ZrC for samples alloyed with Zr and $HfFe_2$ and HfC for samples alloyed with Hf. These intermetallic compounds are formed due to low solubility of Zr (4.5 at% (7 wt%) at 1357^0C) and Hf (0.15 at% (0.5 wt% at 1394^0C) in Fe [82, 88, 89]. All the alloyed specimens consist of similar intermetallic precipitate peaks but the number and intensity of the peaks increased with increase in the quantity of alloying elements. The peak intensities of the different alloys vary depending on the alloy

composition revealing that as the Zr and/or Hf concentration increased, the intensity of the intermetallic peaks increased while the α-Fe peaks decreased. This revealed an increase in the formation of the intermediate compounds with increase in the quantity of the alloying elements. Figure 5-100 also revealed that the width of the XRD peaks of the alloyed samples were broadened when compared with the unalloyed. This is attributed to the effect of grain refinement [228].

6.9.2 Corrosion behaviour of steels P110 and TN95 alloyed with Zr and Hf in simulated produce water (SPW)

The corrosion behaviour of steels P110 and TN95 alloyed with different quantities (0.1, 0.2 and 0.4 wt%) of Zr and Hf was studied using electrochemical techniques such as linear polarization resistance (LPR), Tafel polarization and electrochemical impedance spectroscopy (EIS). The surface morphology of the corroded alloyed steels was characterised by surface analysis techniques such as scanning electron microscope (SEM), energy dispersive x-ray spectroscopy (EDS) and X-ray diffraction (XRD). All the electrochemical experiments were conducted in simulated produced water (SPW) saturated with 99.98% CO_2 at 25^0C and pH 6.5. The results of these investigations as presented in Section 5.2.2 of this report are discussed in this Section.

6.9.1.1 Linear polarization resistance (LPR) of steels P110 and TN95 alloyed with Zr and Hf in simulated produce water (SPW)

Figure 5-101 presents the results of linear polarization resistance experiments performed on the unalloyed, alloyed samples (P110 and TN96) and reference specimen (X65) in simulated produced water (SPW) saturated with 99.98% CO_2 at 25^0C, pH 6.5 and for 24 hours. The figure shows that the samples alloyed with Zr and Hf exhibited better corrosion resistance than the unalloyed and the reference samples. This signified that Zr and Hf have suppressive effect on electrochemical reactions that could lead to passivation. Xu and Gao [119] performed similar experiments by corroding low-carbon steel alloyed with Cr and Cu and reported that alloying elements can enhance the corrosion resistance of steel either by improving the corrosion potential of steel through inhibiting anodic and cathodic reactions or by promoting the formation of protective rust layers which cover the steel substrate thereby slowing down the corrosion rate. Moore [255] defined passivity as resistance to further corrosion by forming protective barrier between metal and solution in an environment where the metal is thermodynamically unstable. Alloying

element can only reduce the corrosion rate of a base metal it passivates more readily. The alloying elements act as passivity promoters by combining low metal–metal bond strength with high metal–oxygen bond strength. The low metal–metal bond strength is beneficial for the rapid nucleation and growth of the oxide by facilitating the breaking of the surface metal–metal bonds in the early stages of passivation [220, 255]. Therefore, since Figure 5-101 shows that unalloyed samples corroded more than the alloyed specimens, it means that Zr and Hf passivate more readily than steel (Fe). It is believed that alloying elements (which are majorly transition metals) have this property because of the presence of unfilled d-orbitals. The filled orbitals of non-transition metals supply electrons to the d-band of transition metals and the alloy assumes transition metal properties. As long as the d-orbital are unfilled these properties remain. The transition alloying elements must be present to a certain minimum quantity to provide the resultant alloy with sufficient unfilled d-orbital in order to form passive film [255].

It can be observed from Figure 5-101 that the corrosion rate of the alloyed steels decreased with increase in the amount of alloying elements (Zr and Hf). This can be attributed to the microstructures of the alloyed specimens with the corresponding grain size, the corrosion medium (electrolyte) and corrosion products/films [228, 229, 256, 257]. The microstructure of the alloyed specimens shown in Figures 5-93 and 5-94 revealed solid solution matrix with finely dispersed intermetallic compounds of Zr and/or Hf such as Fe_2Zr, $Fe_{23}Zr_6$ and ZrC for samples containing Zr and Fe_2Hf and HfC for specimens alloyed with Hf. Figure 5-99 showed that grain size of the alloyed specimens decreased with increase in Zr and Hf content which is believed to have contributed significantly to the trend of corrosion resistance exhibited by the alloyed specimens. This suggests that the decrease in corrosion rate of alloyed steels P110 and TN95 can be ascribed to the formation of fine grains intermetallic compounds of Zr and Hf which resulted in high density of nucleation sites for passive films with the attendant high fraction of passive layers that hinder further corrosion attack. Similar reports have stipulated that grain refinement has a positive effect on the corrosion resistance of the metal [228, 229, 254, 256-258]. Some of these authors postulated that the initial corrosion product layer formed on the substrate of fine grain structured metals can inhibit the metal from further corrosion.

Wang and Li [254] demonstrated that the corrosion resistance of nanocrystalline surface of stainless steel 304 was markedly superior to that of original 304SS. This was attributed

to the formation of enhanced passive film with higher corrosion resistance, greater capability for re-passivation and higher chemistry stability. Using computation model of corrosion rate-grain size relationship of nanocrystalline zirconium, Zhang, et al [229], illustrated that the corrosion resistance of nanocrystalline zirconium was much superior to that of zirconium with coarse grain size demonstrating a decrease in corrosion rate with the decrease in grain size. Afshari and Dehghanian [228] studied the effect of grain size reduction on the electrochemical corrosion behaviour of Fe in alkaline solution and reported a considerable increased in corrosion resistance as the grain size decreased. This was attributed to the large number of grain boundary regions and the corresponding large specific interphase energy resulting in a high density of nucleation sites for passive films with the attendant high fraction of passive layers. These passive films increased the difficulty of active electrochemical species migrating to the surface to participate in further electrochemical reaction. In addition, the passive film formed on fine grain structures showed more protection than that formed on coarse grains because of the enhanced adhesive strength between the passive film and the substrate. This is due to the increase in the electron activity and possible pegging of the passive film at grain boundaries [258].

These contradict the classic corrosion theory that fine grains should accelerate corrosion by forming many micro-electrochemical (galvanic) cells between the huge amount of grain boundaries and the matrix as reported in literatures [47, 54, 259, 260]. In the quest to establish a fundamental mechanism and understanding of the relationship between grain refinement (grain size) and corrosion behaviour of alloys, Ralston and Birbilis [32] recently took a holistic review of literatures for a number of light metals (Mg, Al, and Ti) and transition metals (Fe/steel, Co, Ni, Cu, and Zn). The authors observed that conflicting results have been published claiming that decrease in grain size can variably increase and decrease corrosion resistance. This was attributed to the inability to decouple the effects of processing and processing route from grain size effect on corrosion resistance. Grain boundaries and triple junctions have been reported to have unique electrochemical properties that results in preferential dissolution in specific electrochemical circumstances, while being unaffected in other circumstances. It was then observed that grain refinement may act to aggravate the behaviour observed from courser grain structures in any specific environment. For example, if an electrolyte simulates active behaviour from a course-grained sample, then grain refinement will likely make the surface “more” active and tend to enhance corrosion. On the other hand, if a course-

grained microstructure is passive in a given electrolyte, then grain refinement will likely result in the formation of more stable passive film. This means that the electrolyte play significant role on the effects of grain refinement on the corrosion behaviour of alloys [32, 33]. This was verified in the work of Zeiger, et al [257] on the anodic dissolution of nanocrystalline FeA18 alloy in Na_2SO_4-solution with pH 1 and pH 6. In pH 1 solutions, polycrystalline samples were active and grain refinement led to increased rates of corrosion while in pH 6 solutions, polycrystalline samples demonstrated passive behaviour and grain refinement facilitated the formation of more robust passive film.

The corrosion behaviour of the alloyed specimens P110 and TN95 was investigated in near neutral environment (pH 6.5). The near neutral pH of the electrolytes must have facilitated the development of carbonate layers which were identified by XRD pattern in Figure 5-110 as $CaCO_3$. These passive layers enhanced the formation, growth and stability of passive film resulting in the witnessed decrease in corrosion rate with decrease in grain size of the alloyed specimens. The mechanism of formation and the effect of $CaCO_3$ on the corrosion of steels in simulated produced water was discussed in Section 6.6 of this report. This is in agreement with the report of Bairi, et al [88].

A closer look at Figure 5-101 (b,c,d) show that after about 20 hours of experiments, the reference sample exhibited better corrosion resistance than the specimens alloyed with 0.1 wt% Zr or Hf. On the other hand, the samples alloyed with 0.2 and 0.4 wt% Zr or Hf demonstrated superior corrosion resistance than the reference sample. It can then be stated that, at 0.1 wt% Zr/Hf, very few intermetallic precipitates and consequently few nucleation sites were formed resulting in the formation of less corrosion product that could not cover the entire steel substrate. This was not so with the specimens alloyed with 0.2 and 0.4 wt% Zr or Hf. It is postulated that these alloys have many intermetallic precipitates and huge nucleation sites leading to the formation of enough corrosion products. This is affirmed by the increasing number and intensity peaks of the intermetallic precipitates with the increase in alloying elements as revealed by XRD spectra of Figures 5-100 and 5-110. This intermetallic precipitates apart from facilitating grain refinements, enhanced the formation, growth and anchoring of the corrosion products to the steel substrate leading to decrease in corrosion rate.

The open circuit potential (OCP) is the potential of the working electrode relative to the reference electrode when no potential or current is being applied to the cell. It can be used

to monitor the nature of the reaction taking place at the surface of a specimen in an aqueous solution [182]. A negative shift in OCP signifies an increase in specimen dissolution, film destruction and the exposure of more of the bare metal to the aggressive solution. This corresponds to the initial high corrosion rate as recorded in Figure 5-101. On the other hand, a shift of potential towards a more positive value denotes film formation and thickening resulting in stable corrosion performance [33, 182, 206]. Figure 5-102 shows the OCP for the unalloyed and alloyed specimens monitored for 24 hours in simulated produced water saturated with 99.98% CO_2 at 25^0C and pH 6.5. This figure indicated that both the unalloyed and alloyed specimens demonstrated initial potential shift in the negative direction signifying a more active region resulting to metal dissolution. However, towards the end of the 24 hours duration (at about 14 hours of experiments), the OCP displayed a more noble values which can be attributed to the formation and growth of passive carbonate layer occasioned by the near neutral medium. This is in agreement with the report of Bairi, et al [88] where faster growth of passive film was observed in a medium at pH 8 leading to a nobler OCP than in the medium at pH 5. Figure 5-102 also revealed that the OCP for all the samples shifted to the positive direction with increase in Zr and Hf content. This means that the specimens exhibited better corrosion resistance as the quantity of Zr and Hf increase in agreements with the results of the evolution of corrosion rate with time shown in Figure 5-101.

6.9.1.2 Tafel polarization of steels P110 and TN95 alloyed with Zr and Hf in simulated produce water (SPW)

The Tafel polarisation curves for the unalloyed, alloyed steels (P110 and TN95) and reference specimens corroded in simulated produced water saturated with 99.98% CO_2 at 25^0C and pH 6.5 are shown in Figure 5-103 and the Tafel extrapolated parameters listed in Table 5-19. This table revealed a positive shift in corrosion potentials (E_{corr}) and a decrease in corrosion current density (i_{corr}) with increase in Zr and Hf content. This signified the formation of more stable passive oxide and an increase in corrosion resistance occasioned by the near neutral (pH 6.5) corrosion medium and decreasing grain size with increase in the quantity of Zr and Hf. This corroborate the mechanism and the results of the LPR experiments as discussed in Section 6.9.1.1.

A closer look at Table 5-19 and Figure 5-103 shows that all the alloyed samples displayed less corrosion current density (i_{corr}) than both the unalloyed and reference specimens. This confirmed the greater corrosion susceptibility of the unalloyed and reference specimens

when compared to the alloyed specimens and a good correlation to the results from linear polarization resistance measurements. This behaviour can be ascribed to different variables ranging from microstructure, grain size, electrolyte and corrosion products/films [228, 229, 256, 257] as explained in Section 6.9.1.1.

6.9.1.3 Electrochemical impedance spectroscopy (EIS) of steels P110 and TN95 alloyed with Zr and Hf in simulated produce water (SPW)

Electrochemical impedance spectroscopy (EIS) measurements were carried out in order to verify the results of LPR and Tafel polarization. It was also aimed at evaluating the stability of passive film formed on the surface of the alloyed specimens P110 and TN95 corroded in simulated produced water saturated with 99.98% CO_2 at 25^0C and pH 6.5 after 24 hours of LPR. The Nyquist plots for samples P110 and TN95 alloyed with different quantities of Zr and Hf are shown in Figure 5-104. This figure shows that the Nyquist plots of all the alloyed steels displayed similar features of two semi-capacitive-arcs at high and medium frequencies respectively. This can be ascribed to the non-homogeneity of the surface, frequency dispersion and mass transport resistant [54, 208]. Figure 5-104 also revealed that the radius of the capacitive arc increased with increase in the quantity of Zr and Hf addition. The radius of capacitive arc corresponds to the charge transfer resistance (R_2) and can be obtained from the intercept of the semicircle on the real axis at low frequency limits of the Nyquist spectra [58]. The interception of the semicircle with the abscissa at the low frequency end is the magnitude of the impedance which can represents the corrosion resistance and is inversely proportional to the corrosion rate [54, 113]. Increase in capacitive arc indicates an increase in the film stability (ie ability to resist corrosion) which can be attributed to initial rapid formation of corrosion films that hindered further corrosion attack. Alternatively decrease in capacitive arc signifies a decrease in the stability of the film [209] resulting in active dissolution of the steel substrates. Therefore it can be stated that addition of Zr and/or Hf improves the impedance response of the corrosion film formed on the surface of the alloys and that the impedance response increased with increase in the alloying elements. This agreed with the results of the LPR and Tafel polarization of this report.

The Bode plots of samples P110 and TN95 alloyed with different quantities of Zr and Hf and corroded in simulated produced water saturated with 99.98% CO_2 at 25^0C and pH 6.5 after 24 hours LPR are presented in Figure 5-105. This figure indicated that at the high frequency impedance magnitude (|Z|) which represents the solution resistance (Rs), the

Bode magnitude is constant. On the other hand, at the low frequency impedance magnitude (|Z|) which corresponds to the charge transfer resistance (R_2), the |Z| vs frequency plot is again constant. At the intermediate frequency, the Bode magnitude displayed a linear slope that is about -1. The phase angle at the high frequency end for all the alloyed specimens is 0^0 signifying that the impedance value is determined by the resistance of the electrolyte only. Within the intermediate frequencies, the Bode phase angle for all the specimens demonstrated a broad-phase angle which is the characteristic response of a capacitive behaviour. This revealed that the passive film formed on the surface of the electrodes are stable. Phase angles 5^0–10^0 can be observed at the low frequency axis of the Bode plots suggesting that the impedance values are high for all the samples. Similar results have been reported [109, 208, 209, 218]. It is evident from Bode plots that the impedance modulus at the low frequency increase with increased Zr and Hf addition. Similarly, the maximum phase angle at the intermediate frequency also increased with increase in the alloying element additions. This means that the results of the electrochemical impedance spectroscopy (EIS) are in agreement with the results of the LPR and Tafel polarization tests.

To simulate the electrochemical behaviour of the corrosion products formed on specimens P110 and TN95 alloyed with Zr and Hf after 24 hours of LPR in simulated produced water saturated with 99.98% CO_2 at 25^0C and pH 6.5, a two time constant with equivalent circuit (EC) shown in Figure 5-80 was proposed. This was because of the broad-phase angle of the Bode plots [206]. The variable of the electrical circuit elements are described in Section 5.1.8.2 of this report while the fitted parameters from the equivalent circuit are listed in Table 5-20. The seemingly perfect fits of the Nyquist curves (Figure 5-103) and the simulated data attested to the reliability of the proposed equivalent circuit presenting acceptable relative % errors for the corresponding fitted values as indicated in Table 5-20. It is evidenced from this table that while the charge transfer resistance (R_2) increased, the capacitance (CPE_2) decreased with increase in Zr and Hf content. Lower capacitance observed for the alloys with higher amount of Zr and Hf revealed higher stability of the corrosion film due to the formation of more protective corrosion film occasioned by the fine grain intermetallic compound of Zr and Hf [254]. This high film stability with the attendant high corrosion resistance can also be attributed to the near neutral pH (6.5) of the electrolytes which enhanced the formation of passive oxide [88].

6.9.1.4 Post experimental analysis of steels P110 and TN95 alloyed with Zr and Hf in simulated produce water (SPW)

The SEM micrographs of samples P110 and TN95 alloyed with different quantities (0.1, 0.2 and 0.4 wt%) of Zr and Hf and corroded for 24 hours in simulated produced water saturated with 99.98% CO_2 at 25^0C and pH 6.5 are shown in Figures 5-106 and 5-108. These figures displayed the evolution of microstructures indicating slight decrease in corrosion attack with increase in Zr and or Hf content. This decrease in corrosion attack can be attributed to the effects of alloying elements (Zr and or Hf) on the microstructure. According to Ralston, et al [32] alloying elements affect microstructure through grain refinement, development of new texture, creation of internal stresses, segregation of alloying additions to grain boundaries and formation of corrosion product ($CaCO_3$) [32]. For instance, addition of Zr in Fe produced microstructure with solid solution matrix and intermetallic precipitates which have significant influence on the corrosion behaviour of the alloy [229]. These intermetallic precipitates are easily formed because of the low solubility (7 wt% at 1357^0C) of Zr in Fe with the attendant grain refinements and other structural changes [87, 222]. The XRD spectra of Figure 5-110 showed that the corrosion product detected on the surface of the alloyed Steel P110 and TN95 was mainly $CaCO_3$. The intermetallic precipitates have been reported to possess the ability to pin down grain growth [87, 88, 222] resulting in decrease in grain size. This decrease in grain size with increase in Zr and Hf addition contributed to the slight decrease in corrosion attack revealed in SEM micrographs of Figures 5-106 and 5-108. Similar effects of grain size on corrosion behaviour have been reported [228, 229, 254, 256-258]. The formation of thes carbonate layers on the steel substrates were expedited by the near neutral pH (pH 6.5) of the electrolytes. The presence of iron carbide enhanced the formation, growth, anchoring and stability of passive film resulting in the witnessed decrease in corrosion rate with decrease in grain size of the alloyed specimens. The mechanism of formation and the effect of $CaCO_3$ on the corrosion of steels in simulated produced water was discussed in Section 6.6 of this report. This is in agreement with the report of Bairi, et al [88].

6.10 Summary

The main aim of this research is to improve the corrosion behaviour of three proprietary micro-alloyed steels by alloying them with non-conventional carbide forming elements. This report was based on comparative assessments of the corrosion behaviour of three

proprietary micro-alloy steels and their alloyed specimen (with Zr and Hf) in different corrosion media using different electrochemical techniquics as summarized in this section.

6.10.1 Preliminary investigation and assessments of the corrosion behaviours of three micro-alloyed steels in brine and simulated oilfield environments.

The three proprietary micro-alloy steels were designated as (i) ASTM A694-F65 forged steel bar (F65) (ii) improved collapsed grade P110 IC pipe (P110) and (iii) high collapsed sour service grade TN95 HS pipe (TN95). API 5L X65 steel grade was used as reference sample. The corrosion propensity of these steels were assessed in different media/electrolytes using different environmental parameters, electrochemical techniques (Linear polarization resistance (LPR), Tafel polarization (TP), Electrochemical impedance spectroscopy (EIS) and potentiostatic polarization (PP)) and weight loss measurements as outlined in Table 6-1. The media used include aerated and deaerated concentration (1, 3.5 and 10 wt%) of NaCl solution, 3.5 wt% NaCl solution saturated with 0.5% CO_2 at different pH (3.5, 5 and 6.5) and different temperature (25, 45 and 60^0C), simulated produced water saturated with 0.5% and 99.98% CO_2 respectively and 3.5 wt% NaCl solution saturated with 99.98% CO_2 at different temperature (25, 45 and 60^0C). Corrosion current densities (i_{Corr}) obtained using Tafel extrapolation methods in different environments were used to assess the corrosion propensities of the samples as presented in Figure 6-1.

The results of this preliminary investigations showed that steels F65 and X65 exhibited superior corrosion resistance in all the environments and with all the electrochemical techniques used than steels P110 and TN95 revealing a ranking order of corrosion rate of F65 < X65 < P110 < TN95. These behaviours were ascribed to microstructure and chemical composition [128, 205, 227] of the respective samples. In like manner, the least corrosion rate of the samples were observed in deaerated solutions due to the absent of dissolved oxygen [177, 202] while the highest corrosion rate was observed in 3.5 wt% NaCl saturated with 99.98% CO_2 which was attributed to the thermal activation of the electrochemical species [157, 158]. The high concentration of CO_2 resulted in high dissociation of carbonic acid (ie lower pH value) in the solutions saturated with 99,98% CO_2 demonstrating a more aggressive attack on the specimens than the solutions saturated with 0.5% CO_2. The corrosion performance of all the specimens in the various

environments and the aggressiveness of the different media used are presented in Figure 6-1

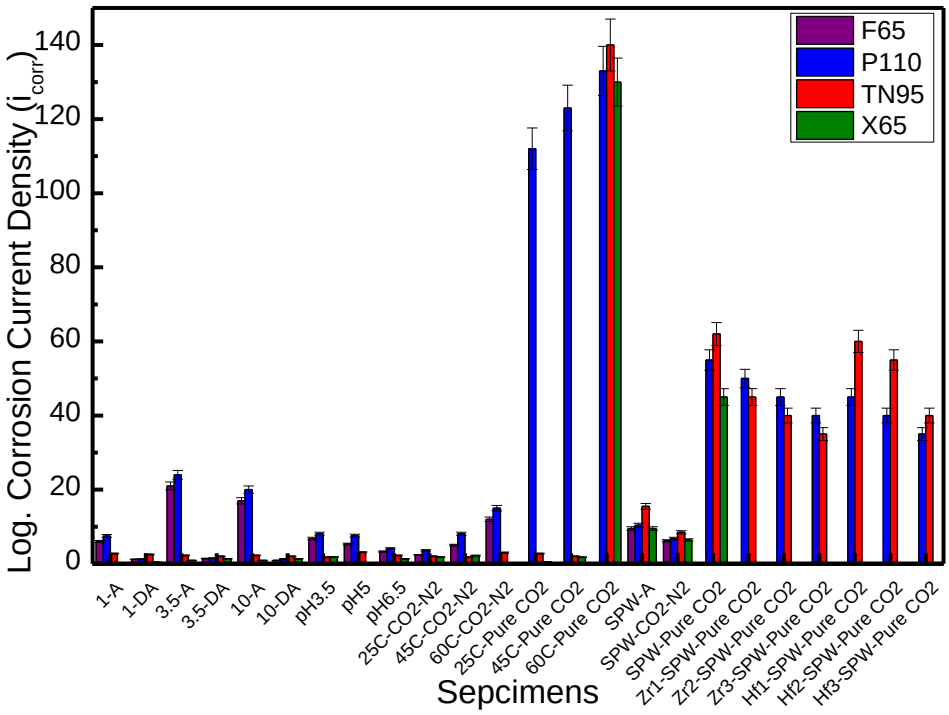

Figure 6-1: Corrosion Current Densities (μA/cm^2) of Samples extracted using Tafel extrapolation method in different media and environmental parameters

6.10.2 Alloying the micro-alloyed steels with non-conventional carbide forming elements.

The results of the preliminary investigations in the different electrolytes revealed that the corrosion rate of the three micro-alloy steel and the reference sample (API 5L X65) can be ranked as ASTM F65 < API 5L X65 < P110 IC < TN95 SH. This means that steels P110 IC and TN95 SH exhibited the worst corrosion rate and therefore were alloyed with different quantities (0.1, 0.2 and 0.4 wt%) of Zr and Hf respectively. This was aimed at improving the corrosion resistance of steels P110 and TN95 SH. The analysis of the alloyed specimens showed microstructural modification through grain refinement with increase in alloying elements (Zr and Hf). This was attributed to the formation of Zr- and/or Hf-base intermetallic precipitates. These precipitates have the ability to pin down austenite grain growth resulting in improved mechanical properties such as increased hardness and tensile strength without any negative impact on the toughness of the alloyed samples [87, 88, 222].

6.10.3 Corrosion behaviour of the alloyed specimens in simulated produced water saturate with 99.98% CO_2

The corrosion propensity of steels (P110 IC and TH95 HS) alloyed with different weight percent Zr and Hf respectively were investigated in simulated produced water (SPW) using the same parameters and electrochemical techniques applied for the preliminary investigation. The corrosion current densities (i_{Corr}) of both the alloyed and the unalloyed steels are also listed in Table 6-1. The percentage improvements of corroded alloyed steels P110 and TN95 in CO_2 saturated simulated produced water (SPW) at 25^0C and pH 6.5 are shown in Figure 6-2. The % improvement was calculated using Equation 6.37.

$$\% \text{ Improvement} = \frac{i_{Corr_{(\text{Unalloyed sample})}} - i_{Corr_{(\text{alloyed sample})}}}{i_{Corr_{(\text{Unalloyed sample})}}} * 100 \qquad 6.37$$

From Figure 6-2, it can be deduced that the corrosion resistance of steels P110 and TN95 alloyed with different quantity of Zr and Hf improved from about 3% to 37% for the specimen alloyed with Hf. On the other hand, about 7% to 44% was exhibited by specimens alloyed with Zr. This shows thatZr demonstrated more improvement than Hf. This can be attributed to lower solubility of Hf (0.5 wt% at 1394^0C) than Zr (7 wt% at 1357^0C).

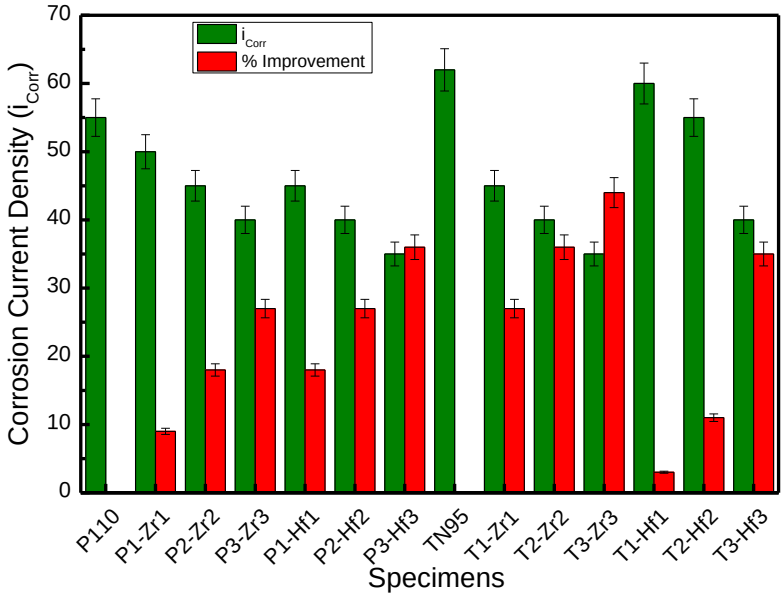

Figure 6- 2: % improvements in corrosion current density occasioned by alloying steel P110 and TN95 with various quantities of Zr and Hf respectively

Table 6- 1: The different electrolytes, electrochemical techniques, environmental parameters used for assessments and corrosion current densities obtained using Tafel extrapolation methods

Environments	Parameters			Specimens	Electrochemical Techniques	Corrosion Current Density (i_{Corr})			
	Temperature (^{0}C)	pH	Duration (Hours)			F65	P110	TN95	X65
Aerated 1 wt% NaCl (1-A)	Ambient	Unbuffered	6	F65, P110, TN95 and X65	LPR and TP	6	7.5	11	6.5
Aerated 3.5 wt% NaCl (3.5-A)	Ambient	Unbuffered	6	F65, P110, TN95 and X65	LPR and TP	21	24	28	21.5
Aerated 10 wt% NaCl (3.5-A)	Ambient	Unbuffered	6	F65, P110, TN95 and X65	LPR and TP	17	20	23	18
Deaerated 1 wt% NaCl (1-DA	Ambient	Unbuffered	6	F65, P110, TN95 and X65	LPR and TP	1.19	1.25	1.37	1.22
Deaerated 3.5 wt% NaCl (3.5-DA)	Ambient	Unbuffered	6	F65, P110, TN95 and X65	LPR and TP	1.4	1.5	1.6	1.4
Deaerated 10 wt% NaCl (3.5-DA)	Ambient	Unbuffered	6	F65, P110, TN95 and X65	LPR and TP	0.9	1.3	1.4	1.16
Aerated 3.5 wt% NaCl (3.5-A)	Ambient	Unbuffered	24, 48, 72	F65, P110, TN95 and X65	WL				
3.5 wt% NaCl-CO_2-N_2		3.5	24	F65, P110, TN95 and X65	LPR, TP and EIS	6.8	8.1	8.3	7.3
3.5 wt% NaCl-CO_2-N_2		5	24	F65, P110, TN95 and X65	LPR, TP and EIS	5.3	7.6	7.9	6.6
3.5 wt% NaCl-CO_2-N_2		6.5	24	F65, P110, TN95 and X65	LPR, TP and EIS	3.3	4.1	7	3.9
3.5 wt% NaCl-CO_2-N_2	25	Unbuffered	24	F65, P110, TN95 and X65	LPR, TP and EIS	2.4	3.6	4.1	2.6

Table 6- 2: The different electrolytes, electrochemical techniques, environmental parameters used for assessments and corrosion current densities obtained using Tafel extrapolation methods

Environments	Parameters			Specimens	Electrochemical Techniques	Corrosion Current Density (i_{Corr})			
	Temperature (^{0}C)	pH	Duration (Hours)			F65	P110	TN95	X65
3.5 wt% NaCl-CO_2-N_2	45	Unbuffered	24	F65, P110, TN95 and X65	LPR, TP and EIS	5	8.1	9	7
3.5 wt% NaCl-CO_2-N_2	60	Unbuffered	24	F65, P110, TN95 and X65	LPR, TP and EIS	12	15	17	14
3.5 wt%-PureCO_2	25	Unbuffered	24	F65, P110, TN95 and X65	LPR, TP and EIS		112	114	110
3.5 wt%-PureCO_2	45	Unbuffered	24	F65, P110, TN95 and X65	LPR, TP and EIS		123	125	122
3.5 wt%-PureCO_2	60	Unbuffered	24	F65, P110, TN95 and X65	LPR, TP and EIS		133	140	130
SPW-A	25	6.5	24	F65, P110, TN95 and X65	LPR and TP	9.5	10.4	15.5	9.5
SPW-N_2-CO_2	25	6.5	24	F65, P110, TN95 and X65	LPR and TP	6.2	6.8	8.5	6.4
SPW-Pure CO_2	25	6.5	24	P110, TN95 and X65	LPR, TP and EIS		55	62	1.5
3.5 wt% NaCl-CO_2-N_2	60	6.5	24 (100, 150 and 200 mV)	P110 and X65	Potentiostatic and EIS				
3.5 wt% NaCl-CO_2-N_2	60	6.5	1, 2, 4, 8, 12 and 24 (150 mV)	P110 and TN95	Potentiostatic and EIS				
SPW-Pure CO_2	25	6.5	24	P110 and TN96	WL				

Table 6- 3: The different electrolytes, electrochemical techniques, environmental parameters used for assessments and corrosion current densities obtained using Tafel extrapolation methods

Environments	Parameters			Specimens	Electrochemical Techniques	Corrosion Current Density (i_{Corr})			
	Temperature (^{0}C)	pH	Duration (Hours)			F65	P110	TN95	X65
SPW-Pure CO_2	60	6.5	96 (24 and 48)	P110, TN95 and X65	LPR				
Zr_1-SPW-Pure CO_2	25	6.5	24	P_1-Zr_1 and T_1-Zr_1	LPR, TP and EIS		50	45	
Zr_2-SPW-Pur CO_2	25	6.5	24	P_2-Zr_2 and T_2-Zr_2	LPR, TP and EIS		45	40	
Zr_3-SPW-Pure CO_2	25	6.5	24	P_3-Zr_3 and T_3-Zr_3	LPR, TP and EIS		40	35	
Hf_1-SPW-Pure CO_2	25	6.5	24	P_1-Hf_1 and T_1-Hf_1	LPR, TP and EIS		45	60	
Hf_2-SPW-Pure CO_2	25	6.5	24	P_2-Hf_2 and T_2-Hf_2	LPR, TP and EIS		40	55	
Hf_3-SPW-Pure CO_2	25	6.5	24	P_3-Hf_3 and T_3-Hf_3	LPR, TP and EIS		35	40	

Chapter 7 Conclusions, Industrial Relevance and Future Study

This chapter presents the core findings and the conclusions drawn from the various experiments conducted during the course of this research pointing out some of the benefits of these results to the industry. This chapter ended by attempting to outline relevant future works emanating from this study that will enhance the struggle of mitigating corrosion problems in the oil and gas industry.

7.1 Conclusions

A comprehensive investigation and assessment of the corrosion behaviour of three proprietary micro-alloy steels (designated as F65, P110 and TN95) and API 5L X65 as reference sample was carried out in various simulated oilfield environments using different electrochemical (Linear polarization resistance (LPR), Tafel polarization (TP), Electrochemical impedance spectroscopy (EIS) and potentiostatic polarization (PP)), weight loss and surface analysis techniques. This was followed by alloying the two worst corrosion rate steels (P110 and TN95) with Zr and Hf and the improvement on the corrosion resistance of these samples was investigated. The main findings of this study are summarized in this section.

7.1.1 Preliminary investigation and assessments of the corrosion behaviours of the proprietary micro-alloyed steels in brine and simulated oilfield environments.

- All the electrochemical investigations conducted revealed that the corrosion performance of the micro-alloy steels used in this study can be ranked as follow: F65 > X65 > P110 > TN95. This means that out of the three proprietary steels, F65 exhibited better corrosion resistance than the reference sample (X65). Therefore P110 and TN95 were considered as the worst corrosive steels.
- The assessments of the corrosion performance indicated that microstructures, chemical composition and grain size of the micro-alloy steels play significant role. The micro-alloy steels with higher carbon content have lower ferrite-pearlite ratio. This is because of the effect of carbon content and thermo-mechanical processes (heat treatment routes) on the precipitation, volumetric fraction, uniformity and distribution of pearlite in micro-alloyed steels. Pearlites on the other hand act as cathodic sites and being more than ferrites in ferrite-pearlite specimens resulted in lower corrosion resistance for steel P110.

- The high carbon content (0.26 wt%) in steel TN95 is assumed to have suppressed the formation of protective Cr_2O_3 leading to increased corrosion rate.
- The presence of alloying elements such as Nb, Ti and V in the as-received samples triggered grain refinements resulting to large surface area for corrosion and so the corrosion attack increase with decrease in grain size of the specimens in acidic environments. Opposite results was obtained in near neutral and alkaline medium in the presence of Zr and Hf which impacted finer grain size on the samples.
- The severity of corrosion attack was about 90% more in aerated solutions than in the de-aerated solutions. This was ascribed to the effect of dissolved oxygen as electron acceptor (in the oxidation and reduction reactions) and depolarizer thus accelerating the dissolution of metals in chloride environment.
- The threshold of corrosion rate of the steels in NaCl concentration experiments was observed at 3.5 wt% demonstrating an increase in corrosion rate with NaCl concentration less than 3.5 wt%. This was attributed to the increase in the solubility of DO with increase in NaCl concentration. On the other hand, increase in NaCl concentration above 3.5 wt% demonstrated increase in corrosion resistance which could be linked to the decrease in the solubility of DO with further increase in concentration (above 3.5 wt%) of NaCl solution and the adsorption of chloride on the surface of the steel due to salting out effect.
- The corrosion resistance of all the specimens increased with increase in temperature in both 0.5% and 99.98% CO_2 concentrations because the inherent protective CO_2 corrosion product ($FeCO_3$) could not form within the experimental conditions. Therefore the increase in corrosion rate can be ascribed to thermal activation of the reacting species and porous and un-protective corrosion product that formed on the surface of the steels.
- The corrosion rate of the specimens in 3.5 wt% NaCl solution was about 98% higher in 99.98% CO_2 (22.72 mol) than in 0.5% CO_2 (0.114 mol). This corroborates with the difference in mol/l of CO_2 in both solutions which is about 99% signifying that the concentration of CO_2 plays vital role in determining the corrosion rate of the specimen. The specimens exhibited higher corrosion rate in 99.98% CO_2 environment due to the decrease in pH as a result of hydrogen evolution reduction of cathodic reaction. On the other hand, the speciemns showed superior corrosion resistance in naturally aerated electrolytes than in 0.5% CO2 which can be ascribed to the presence of dissolved oxygen as a precursor for cathodic reduction thus facilitating the formation corrosion product.

- The pH of the solution plays important role in determining the kinetics and mechanism of CO_2 corrosion of micro-alloyed steels. pH was observed to affects corrosion rate of the steels through acidification of the medium whereby the corrosion rate increased with decrease in pH. At lower pH (pH, 4) the cathodic reduction of H^+ ions with the corresponding anodic preferential dissolution of ferrite and the formation of cementite network through the process of hydrogen evolution facilitate corrosion rate. At higher pH, the dominant cathodic reactions are the reduction of carbonic acid within $4 < pH < 6$ and reduction of bicarbonate ions at $pH > 6.5$ resulting in pseudo-passivation of the corroding interface.
- Specimens with coarse grain size exhibited better general corrosion resistance but poor pitting corrosion resistance. Alternatively, samples with fine grain size demonstrated poor general corrosion but hindered pitting corrosion. This is because of the chemical or physical heterogeneity such as grain boundaries and different chemical phases at the surface of metals and the presence of aggressive anionic species such as chloride ions. Fine grain specimen has many pit initiation sites which results to numerous micro-galvanic effects with the attendant shallow pits. On the other hand, specimen with larger grain size (few grain boundaries) has few pit initiation sites leading to high concentration and migration of chloride ions to few grain boundaries with the attendant aggressive (pitting) corrosion attack.
- It was observed that the anodic current density within the active region of an actively corroding steel increased with increase in applied potential. Increase in anodic current density means increased dissolution of iron which corresponds to increase in corrosion rate. This is attributed to activation control reactions which is the characteristics of actively corroding steels. Therefore it is pertinent to conclude that the stability of the corrosion products formed by potentioststic polarization increased with decrease in the applied potential.

7.1.2 Characterization and corrosion performance of the alloyed steels.

- Alloying of specimens P110 and TN95 with Zr and Hf decreased the grain size and consequently increased the hardness and tensile strength of the alloys. This was attributed to the formation of Zr- and Hf- rich intermetallic compounds which possessed the ability to pin down grain growth and form barrier to dislocation movements.

- The experimental results showed that the grain size of the alloyed specimens decreased with increase in Zr and Hf content.
- From Figure 6-2, it can be deduced that the corrosion resistance of steels P110 and TN95 alloyed with different quantity of Zr and Hf improved from about 3% to 37% for the specimen alloyed with Hf. On the other hand, about 7% to 44% was exhibited by specimens alloyed with Zr. This shows thatZr demonstrated more improvement than Hf. This can be attributed to lower solubility of Hf (0.5 wt% at 1394^0C) than Zr (7 wt% at 1357^0C).
- These alloying elements (Zr and Hf) enhanced the corrosion potential of the alloys by inhibiting anode and cathode reactions and by facilitating the formation of protective corrosion product layers which cover the steel substrate thereby slowing down the corrosion rate.
- The corrosion resistance of the alloyed steels increased with increase in the amount of alloying elements (Zr and Hf).
- The microstructures coupled with the corresponding grain size, the corrosion medium (electrolyte) and the corrosion products/films significantly affect the corrosion behaviour of the alloyed specimen. The effect of fine grain intermetallic compound is attributed to the large number of grain boundary and triple junction which provided nucleation sites for initial rapid formation of passive oxide that hinders the substrate from further corrosion attack
- The passive film formed on fine grain structures showed more protection than that formed on coarse grains because of the enhanced adhesive strength between the passive film and the substrate. This is due to the increase in the electron activity at grain boundaries and possible pegging of the passive film to the grain boundaries
- The near neutral pH (6.5) of the electrolytes facilitated the formation of oxide layers ($CaCO_3$) which enhanced the formation, growth and stability of passive film resulting in the decrease in corrosion rate with decrease in grain size of the alloyed specimens
- The stability of the passive film formed on the alloyed specimens increased with increase in Zr and Hf addition which is ascribed to the effect of decreasing grain size in near neutral pH solution.

7.2 Relevance of the study to the industry

- ✓ The effect of CO_2 corrosion on oilfield facilities is enormous. An improvement of about 3% to 44% in the corrosion resistance of the proprietary micro-alloy steels used in the work was achieved. This will obviously go a long way in alleviating the cost of CO_2 in oil and gas industry.
- ✓ The micro-alloy steels used in this research are new generation steels whose corrosion behaviour has not been adequately understood. Within the experimental conditions of this work, these micro-alloy steels demonstrated acceptable corrosion resistance for effective used in oil and gas industry.
- ✓ The corrosion behaviour of these steels was assed in different simulated oilfield environments using different electrochemical techniquics. Thus wide range of experimental data were generated. These data could serve as precousor for future research to develop models/relationships for:
    - o Optimum quantity for effective use of Zr and Hf as alloying elements in industry
    - o Relationship between electrolytes-grain size-corrosion rate of micro-alloyed steels.

7.3 Recommended future research

- The corrosion propensity of the alloyed steels was investigated in simulated produced water and for 24 hours. It will be worthwhile to subject these alloys to other environmental variables and for longer duration.
- The research reported an increase in corrosion resistance with decrease in grain size of the alloyed samples. This is contrary to the result obtained with the unalloyed samples in similar environment. A study is recommended to investigate if the reversal is caused by the alloying elements or the grain size. Also if it is attributed to the grain size, there is a need to determine the optimum grain size when the corrosion rate will decrease with decrease in grain size.
- The individual effects of Zr and Hf were respectively investigated, therefore further study on the synergistic effect of Zr and Hf on the corrosion behaviour of these steels is recommended.
- The pH of the electrolyte and the grain size of the alloys were reported as the main reasons for decrease in corrosion rate with increase in amount of alloying

elements, therefore studies on the variations of pH and grain size to determine the best combination of these variables is recommended.

- The micro-alloy steels used in this study consist of many alloying elements and so it was difficult to isolate with certainty the respective effects of Zr and Hf on the mechanical and corrosion properties of the new alloys. Therefore, it is recommended that this study be repeated using low carbon steel containing only basic alloying elements (Fe, C, Mn).

Reference

1. Javaherdashti, R., C. Nwaoha, and H. Tan, *Corrosion and materials in the oil and gas industries*. 2016: CRC Press.
2. Perez, T.E., *Corrosion in the Oil and Gas Industry: An Increasing Challenge for Materials.* JOM, 2013. **65**(8): p. 1033-1042.
3. Suárez Bermejo, J.C. and M.A. Herreros Sierra, *New Fiber-Metal Hybrid Laminated Material, MALECON.* 2008.
4. Ilman, M., *Analysis of internal corrosion in subsea oil pipeline.* Case Studies in Engineering Failure Analysis, 2014. **2**(1): p. 1-8.
5. Place, T., *Managing Corrosion of Pipelines that Transport Crude Oils.* Materials Performance, 2013.
6. Kermani, M. and D. Harr. *The impact of corrosion on oil and gas industry*. in *Giornata di studio IGF S. Donato Milanese 1996*. 2008.
7. El-Lateef, H.A., et al., *Corrosion protection of steel pipelines against CO 2 corrosion—a review.* Chem. J, 2012. **2**(2): p. 52-63.
8. Perry, J., et al., *Assessment of the corrosion rates and mechanisms of a WC–Co–Cr HVOF coating in static and liquid–solid impingement saline environments.* Surface and Coatings technology, 2001. **137**(1): p. 43-51.
9. Ren, Y. and C. Zeng, *Corrosion protection of 304 stainless steel bipolar plates using TiC films produced by high-energy micro-arc alloying process.* Journal of Power Sources, 2007. **171**(2): p. 778-782.
10. Varela, F., M. Tan, and M. Forsyth, *An electrochemical method for measuring localized corrosion under cathodic protection.* ECS Electrochemistry Letters, 2015. **4**(1): p. C1-C4.
11. Lopez, D., T. Perez, and S. Simison, *The influence of microstructure and chemical composition of carbon and low alloy steels in CO 2 corrosion. A state-of-the-art appraisal.* Materials & Design, 2003. **24**(8): p. 561-575.
12. Lopez, D.A., S. Simison, and S. De Sanchez, *The influence of steel microstructure on CO 2 corrosion. EIS studies on the inhibition efficiency of benzimidazole.* Electrochimica Acta, 2003. **48**(7): p. 845-854.
13. Kermani, B., et al. *Development of low carbon Cr-Mo steels with exceptional corrosion resistance for oilfield applications*. in *CORROSION 2001*. 2001. NACE International.
14. Morrison, W. *Overview of microalloying in steel*. in *The Proceedings of the Vanitec Symposium, Guilin, China*. 2000.
15. Maalekian, M., *The effects of alloying elements on steels (I).* TU Graz, 2007. **IWS-Materials**.
16. Wang, H., W. Wang, and J. Gao, *Precipitates in two Zr-bearing HSLA steel plates.* Materials Letters, 2010. **64**(2): p. 219-222.
17. Lieser, M. and C. Stek, *Composites and the Future of Society: Preventing a legacy of costly corrosion with modern materials.* Owens Corning, 2010.

18. Schmitt, G., *Global needs for knowledge dissemination, research, and development in materials deterioration and corrosion control.* World Corrosion Organization, 2009: p. 3-8.

19. Koch, G.H., et al., *Corrosion cost and preventive strategies in the United States*. 2002.

20. Shaw, B.A. and R.G. Kelly, *What is corrosion?* Interface-Electrochemical Society, 2006. **15**(1): p. 24-27.

21. Davis, J.R., *Corrosion: understanding the basics*. 2000, Materials Park, OH: ASM International.

22. Craig, B.D. and D.S. Anderson, *Handbook of corrosion data*. 1994: ASM international.

23. Kermani, M. and A. Morshed, *Carbon dioxide corrosion in oil and gas production-A compendium.* Corrosion, 2003. **59**(8): p. 659-683.

24. Fruehan, R., *Overview of steelmaking processes and their development.* The Making, Shaping and Treating of Steel: Steelmaking and Refining volume, 1998: p. 2-3.

25. Adamczyk, J., *Development of the microalloyed constructional steels.* Journal of Achievements in Materials and Manufacturing Engineering, 2006. **14**(1-2): p. 9-20.

26. Davis, J.R., *Alloying: understanding the basics*. 44073.0002 2001, Materials Park, OH ASM international.

27. DeArdo, A., et al., *On strength of microalloyed steels: an interpretive review.* Materials Science and Technology, 2009. **25**(9): p. 1074-1082.

28. Baker, T., *Microalloyed steels, Ironmaking & Steelmaking.* ISSN: 0301-9233 (Print) 1743-2812 (Online) Journal homepage, 2016. **43**(4): p. 264 - 307.

29. Fernández, J., S. Illescas, and J. Guilemany, *Effect of microalloying elements on the austenitic grain growth in a low carbon HSLA steel.* Materials Letters, 2007. **61**(11): p. 2389-2392.

30. Illescas, S., J. Fernández, and J. Guilemany, *Kinetic analysis of the austenitic grain growth in HSLA steel with a low carbon content.* Materials Letters, 2008. **62**(20): p. 3478-3480.

31. Matlock, D. and J. Speer, *Microalloying concepts and application in long products.* Materials Science and Technology, 2009. **25**(9): p. 1118-1125.

32. Ralston, K., N. Birbilis, and C. Davies, *Revealing the relationship between grain size and corrosion rate of metals.* Scripta Materialia, 2010. **63**(12): p. 1201-1204.

33. op't Hoog, C., N. Birbilis, and Y. Estrin, *Corrosion of pure Mg as a function of grain size and processing route.* Advanced Engineering Materials, 2008. **10**(6): p. 579-582.

34. Beavers, J.A. and N.G. Thompson, *External corrosion of oil and natural gas pipelines.* ASM handbook, 2006. **13**: p. 1015-1025.

35. Deeley, P.D., K.J. Kundig, and H.R. Spendelow, *Ferroalloys & alloying additives handbook*. 1981: Shieldalloy Corp.

36. Billingham, J., et al., *Review of the performance of high strength steels used offshore.* Health Saf. Exec, 2003. **111**.

37. Edmonds, D.V. and R.C. Cochrane, *The effect of alloying on the resistance of carbon steel for oilfield applications to CO2 corrosion.* Materials Research, 2005. **8**(4): p. 377-385.

38. Zhao, J., Y. Lu, and H. Liu, *Corrosion and control of P110 oil tube steel in CO2-saturated solution.* Corrosion Engineering, Science and Technology, 2008. **43**(4): p. 313-319.

39. Baker, T., *Role of zirconium in microalloyed steels: a review.* Materials Science and Technology, 2015. **31**(3): p. 265-294.

40. Holmes, D., *Corrosion of hafnium and hafnium alloys.* ASM Handbook, 2005. **13**: p. 354-359.

41. Fairchild, H.B., *The Properties of Zirconium and Its Possibilities for Thermal Reactors*. 1949, Oak Ridge National Lab., Tenn.

42. Miller, G.L., *Metallurgy of Rarer Metals - 2; Zirconium, Butterworths Scientific Publications, London.* 1957. **Second Edition**: p. 1 - 19, 305 - 326.

43. Golden, L.B., *The Corrosion Resistance of Zirconium and its alloys.* Symposium of American Society of Metals: Metallurgy of Rarer Metals 2: Zirconium, 1953: p. 305 - 326.

44. Geanta, V., I. Voiculescu, and E. Stanciu. *Hafnium influence on the microstructure of FeCrAl alloys*. in *Book of Abstracts*.

45. ATI, *HafniumAlloy Addition (UNS R02001).* Technical Data Sheet, 21/2/2014. **Version 1**: p. 1 to 5.

46. Nielsen, R.H., *Hafnium and hafnium compounds.* Kirk-Othmer Encyclopedia of Chemical Technology, 2000.

47. Sarkar, P., et al., *Microstructural influence on the electrochemical corrosion behaviour of dual-phase steels in 3.5% NaCl solution.* Materials Letters, 2005. **59**(19): p. 2488-2491.

48. Townsend, H., *Effects of alloying elements on the corrosion of steel in industrial atmospheres.* Corrosion, 2001. **57**(6): p. 497-501.

49. Chase Jr, M., et al., *JANAF thermochemical tables, 1978 supplement.* Journal of Physical and Chemical Reference Data, 1978. **7**(3): p. 793-940.

50. Kovalenko, V. and E. Zats, *Effect of zirconium on the corrosion resistance of steel.* Metal Science and Heat Treatment, 1964. **6**(4): p. 223-224.

51. HSLA, S., *High-Strength Low-Alloy Steels*, in *ASM International: Alloying: Understanding the Basics*. 2001.

52. Al-Hassan, S., et al., *Effect of microstructure on corrosion of steels in aqueous solutions containing carbon dioxide.* Corrosion, 1998. **54**(6): p. 480-491.

53. Zhao, Y., et al., *The mechanical properties and corrosion behaviors of ultra-low carbon microalloying steel.* Materials Science and Engineering: A, 2007. **454**: p. 695-700.

54. Seikh, A.H., *Influence of Heat Treatment on the Corrosion of Microalloyed Steel in Sodium Chloride Solution.* Journal of Chemistry, 2013. **2013**(Article ID 587514,): p. 7 pages.

55. Sherif, E.-S.M. and A.H. Seikh, *Effects of grain refinement on the corrosion behaviour of microalloyed steel in sulphuric acid solutions.* Int. J. Electrochem. Sci, 2012. **7**: p. 7567-7578.

56. Nabhani, F., A. Jasim, and S. Graham. *Electrochemical Behaviour of Low Carbon Steel in Aqueous Solutions*. in *Proceedings of the World Congress on Engineering*. 2007.

57. Wang, S., et al., *Preparation and electrochemical corrosion behavior of bulk nanocrystalline ingot iron in HCl acid solution.* The Journal of Physical Chemistry B, 2005. **109**(7): p. 2499-2503.

58. Wang, S., et al., *The electrochemical corrosion of bulk nanocrystalline ingot Iron in acidic sulfate solution.* The Journal of Physical Chemistry B, 2006. **110**(1): p. 377-382.

59. Matlock, D., G. Krauss, and J. Speer, *Microstructures and properties of direct-cooled microalloy forging steels.* Journal of materials processing technology, 2001. **117**(3): p. 324-328.

60. Mazurovsky, V., et al. *Carbide formation during crystallization upon welding*. in *Third International Conference on Mathematical Modeling and Computer Modeling and Computer Simulation of Materials Technologies MMT*. 2004.

61. Bian, C., et al., *Electrochemical response of mild steel in ferrous ion enriched and CO 2 saturated solutions.* Corrosion Science, 2015. **96**: p. 42-51.

62. Tanupabrungsun, T., B. Brown, and S. Nesic. *Effect of pH on CO2 Corrosion of Mild Steel at Elevated Temperatures*. in *CORROSION/2013 NACE INTERNATIONAL Conference & Expo. Ohio University*. 2013.

63. Steels, L.-A., *High-Strength Low-Alloy Steels, Alloying: Understanding the Basics*. Vol. #06117G. 2001: ASM International.

64. Morrison, W., *Microalloy steels–the beginning.* Materials Science and Technology, 2009. **25**(9): p. 1066-1073.

65. Kerman, B., et al. *Development of superior corrosion resistance 3% Cr steels for downhole applications*. in *CORROSION 2003*. 2003. NACE International.

66. Bentiss, F., M. Traisnel, and M. Lagrenee, *The substituted 1, 3, 4-oxadiazoles: a new class of corrosion inhibitors of mild steel in acidic media.* Corrosion science, 2000. **42**(1): p. 127-146.

67. Sherif, E.-S.M., *A comparative study on the electrochemical corrosion behavior of iron and X-65 steel in 4.0 wt% sodium chloride solution after different exposure intervals.* Molecules, 2014. **19**(7): p. 9962-9974.

68. Edelugo, S., *The Timed Response of Different Types of GRP Laminates on Exposure to Various Strengths of Alkaline and Acidic Environments.* J. adv. mats., 2009. **41**(2): p. 79-87.

69. Dugstad, A. *Fundamental aspects of CO2 metal loss corrosion-part 1: mechanism*. in *CORROSION 2006*. 2006. NACE International.

70. Dugstad, A., *Mechanism of Protective Film Formation During CO2 Corrosion of Carbon Steel.* Proceedings: NACE Intenational Conference, 1998. **1998**(Paper No 31): p. 31/1 - 31/11.

71. Park, S., J. Kim, and J. Yoon, *Effect of W, Mo, and Ti on the corrosion behavior of low-alloy steel in sulfuric acid.* Corrosion, 2013. **70**(2): p. 196-205.

72. Gorni, A. and J.D. da Silveira, *Accelerated cooling of steel plates: the time has come*, in *Quenching and Cooling, Residual Stress and Distortion Control*. 2010, ASTM International.

73. Ouchi, C., *Development of steel plates by intensive use of TMCP and direct quenching processes.* ISIJ international, 2001. **41**(6): p. 542-553.

74. Porter, D.A., K.E. Easterling, and M. Sherif, *Phase Transformations in Metals and Alloys, (Revised Reprint)*. 2009: CRC press.

75. Gladman, T., *The physical metallurgy of microalloyed steels*. Vol. 615. 1997: Maney Pub.

76. Demiroren, H. and M. Aksoy, *Electrochemical synthesis of ferritic stainless steels alloyed with 1 wt-% Ti, V and Nb in sulphuric acid solution.* Corrosion Engineering, Science and Technology, 2009. **44**(5): p. 347-351.

77. Howard, S.M., *Ellingham Diagrams.* SD School of Mines and Technology, 2006.

78. Acid, H., *Corrosion Resistance of Zircadyne Alloys In Specific Media.* 2011. **07**.

79. Abraham, D.P., J.W. Richardson Jr, and S.M. McDeavitt, *Formation of the Fe23Zr6 phase in an Fe-Zr alloy.* Scripta materialia, 1997. **37**(2): p. 239-244.

80. Servant, C., C. Gueneau, and I. Ansara, *Experimental and thermodynamic assessment of the Fe・Zr system.* Journal of Alloys and Compounds, 1995. **220**(1-2): p. 19-26.

81. Liu, Y., S.M. Allen, and J.D. Livingson, *An investigation of Fe3Zr phase.* Scripta metallurgica et materialia, 1995. **32**(8): p. 1129-1132.

82. Wei, C.-C., et al., *Understanding the phase equilibrium and irradiation effects in Fe–Zr diffusion couples.* Journal of Nuclear Materials, 2013. **432**(1-3): p. 205-211.

83. Satyendra, *Zirconium in Steels.* ISPAT DIGEST, 3rd Dec 2014.

84. Akbarzadeh, H., et al., *Mechanical properties and microstructures of Zr-microalloyed cast steel.* ISIJ international, 2005. **45**(8): p. 1201-1204.

85. Aliakbarzadeh, H., et al., *Investigation of Hardness and Impact Toughness of Zr-Microalloyed Cast Steel.* 2005.

86. Chase, M., *NIST—JANAF thermochemical tables (journal of physical and chemical reference data monograph no. 9).* American Institute of Physics, 1998.

87. Aliakbarzadeh, H., S. Mirdamadi, and M. Tamizifar, *Effect of low Zr addition on microalloyed cast steel.* Materials Science and Technology, 2010. **26**(11): p. 1373-1376.

88. Bairi, L.R., et al., *Microstructural analysis and corrosion behaviour of D9 stainless steel–Zirconium metal waste form alloys.* Corrosion Science, 2010. **52**(7): p. 2291-2302.

89. Idbenali, M., et al., *Thermodynamic assessment of the Fe–Hf binary system.* Journal of Alloys and Compounds, 2008. **456**(1-2): p. 151-158.

90. Levy, O., G.L. Hart, and S. Curtarolo, *Hafnium binary alloys from experiments and first principles.* Acta Materialia, 2010. **58**(8): p. 2887-2897.

91. Okamoto, H., *Phase diagrams for binary alloys.* ASM International, 2000. **268**.

92. Cahn, R.W., *Binary Alloy Phase Diagrams–Second edition. TB Massalski, Editor-in-Chief; H. Okamoto, PR Subramanian, L. Kacprzak, Editors. ASM International, Materials Park, Ohio, USA. December 1990. xxii, 3589 pp., 3 vol., hard-back. $995.00 the set.* Advanced Materials, 1991. **3**(12): p. 628-629.

93. Genesca, J., et al., *Conventional DC electrochemical techniques in corrosion testing.* Manuscript submitted for publication, Metallurgical Engineering, UNAM City University, Mexico City, Mexico, 2002.

94. Tait, W.S., *An introduction to electrochemical corrosion testing for practicing engineers and scientists*. 1994: Clair, Racine, Wis.

95. G102-89, A., *Standard Practice for Calculation of Corrosion Rates and Related Information from Electrochemical Measurements*. 1999, ASTM International West Conshohocken, Pa.

96. Hinds, G., *The electrochemistry of Corrosion.* Corrosion Doctor publications, 1996: p. 4-5.

97. Ahmad, Z., *Principles of corrosion engineering and corrosion control*. 2006: Butterworth-Heinemann.

98. Wessel, J.K., *The handbook of advanced materials: enabling new designs*. 2004: John Wiley & Sons.

99. Uhlig, H.H., *Corrosion and corrosion control; and introdiction to corrosion sciende and engineering*. 1964: Wiley.

100. Samples, M., *Corrosion Coupons & Weight Loss Analysis*. Metal Samples Company: Houston.

101. Walter, G., *Problems arising in the determination of accurate corrosion rates from polarization resistance measurements.* Corrosion Science, 1977. **17**(12): p. 983-993.

102. Scully, J.R., *Electrochemical Methods for Laboratory Corrosion Testing*, in *Corrosion Testing and Evaluation: Silver Anniversary Volume*. 1990, ASTM International.

103. Denny, A.J., *Principles and prevention of corrosion.* Prentice-Hall Inc., Upper Saddle River, NJ, 1996: p. 76-90.

104. Perez, N., *Electrochemistry and corrosion science*. 2004: Springer Science & Business Media.

105. Oelssner, W., F. Berthold, and U. Guth, *The iR drop–well-known but often underestimated in electrochemical polarization measurements and corrosion testing.* Materials and Corrosion, 2006. **57**(6): p. 455-466.

106. Barnartt, S., *Magnitude of IR-Drop Corrections in Electrode Polarization Measurements Made with a Luggin-Haber Capillary.* Journal of The Electrochemical Society, 1961. **108**(1): p. 102-104.

107. Simpson, T.C., et al., *Electrochemical Impedance Measurements for Evaluating and Predicting the Performance of Organic Coatings for Atmospheric Exposure*, in *Corrosion Testing and Evaluation: Silver Anniversary Volume*. 1990, ASTM International.

108. Silverman, D.C., *Simple Models/Practical Answers Using the Electrochemical Impedance Technique*, in *Corrosion Testing and Evaluation: Silver Anniversary Volume*. 1990, ASTM International.

109. Loveday, D., P. Peterson, and B. Rodgers, *Evaluation of organic coatings with electrochemical impedance spectroscopy.* JCT coatings tech, 2004. **8**: p. 46-52.

110. Ijsseling, F., *Application of electrochemical methods of corrosion rate determination to systems involving corrosion product layers: Part 1: Linear polarization resistance measurement as an example of a simple method that can be performed with commercially available instruments.* British Corrosion Journal, 1986. **21**(2): p. 95-101.

111. Andrade, C. and C. Alonso, *Corrosion rate monitoring in the laboratory and on-site.* Construction and Building Materials, 1996. **10**(5): p. 315-328.

112. Instruments, G., *Gamry instruments software tutorials and primers.* Gamry Instrumrnt INC, 2005.

113. Sun, J., et al., *The formation mechanism of corrosion scale and electrochemical characteristic of low alloy steel in carbon dioxide-saturated solution.* Corrosion Science, 2012. **57**: p. 131-138.

114. Wang, R., et al., *Electrochemical corrosion performance of Cr and Al alloy steels using a J55 carbon steel as base alloy.* Corrosion Science, 2014. **85**: p. 270-279.

115. Wang, Z., et al., *Study of the corrosion behavior of weathering steels in atmospheric environments.* Corrosion Science, 2013. **67**: p. 1-10.

116. Choi, Y.-S., J.-J. Shim, and J.-G. Kim, *Effects of Cr, Cu, Ni and Ca on the corrosion behavior of low carbon steel in synthetic tap water.* Journal of alloys and compounds, 2005. **391**(1): p. 162-169.

117. Shifler, D.A., *Understanding material interactions in marine environments to promote extended structural life.* Corrosion Science, 2005. **47**(10): p. 2335-2352.

118. Nishimura, T., *Rust formation and corrosion performance of Si-and Al-bearing ultrafine grained weathering steel.* Corrosion Science, 2008. **50**(5): p. 1306-1312.

119. Xu, Q., et al., *Effects of alloyed Cr and Cu on the corrosion behavior of low-alloy steel in a simulated groundwater solution.* Corrosion Science, 2016. **102**: p. 114-124.

120. Melchers, R.E., *Effect of small compositional changes on marine immersion corrosion of low alloy steels.* Corrosion science, 2004. **46**(7): p. 1669-1691.

121. Park, S.A., W.S. Ji, and J.G. Kim, *Effect of chromium on the corrosion behaviour of low-alloy steels containing copper in FGD environment.* Int. J. Electrochem. Sci, 2013. **8**: p. 7498-7509.

122. Vera, R., F. Vinciguerra, and M. Bagnara, *Comparative Study of the Behavior of API 5L-X65 Grade Steel and ASTM A53-B Grade Steel against Corrosion in Seawater.* Int. J. Electrochem. Sci, 2015. **10**: p. 6187-6198.

123. Farelas, F., Y. Choi, and S. Nešic, *Corrosion behavior of API 5L X65 carbon steel under supercritical and liquid carbon dioxide phases in the presence of water and sulfur dioxide.* Corrosion, 2012. **69**(3): p. 243-250.

124. Sherif, E.-S.M., et al., *Electrochemical studies on the corrosion behavior of API X65 pipeline steel in chloride solutions.* International journal of electrochemical science, 2013. **8**: p. 9360-9370.

125. Pankratz, L., *Thermodynamic properties of carbides, nitrides, and other selected substances.* 1995.

126. Yau, T.-L. and R. Webster, *The effects of iron on the corrosion resistance of zirconium.* Corrosion, 1983. **39**(6): p. 218-226.

127. Li, Y., et al., *The effects of vanadium, niobium, titanium and zirconium on the microstructure and mechanical properties of thin slab cast steels.* ISIJ international, 2004. **44**(6): p. 1093-1102.

128. Popoola, L.T., et al., *Corrosion problems during oil and gas production and its mitigation.* International Journal of Industrial Chemistry, 2013. **4**(1): p. 1-15.

129. Zhang, Y., et al., *Discussion of the CO 2 corrosion mechanism between low partial pressure and supercritical condition.* Corrosion Science, 2012. **59**: p. 186-197.

130. Zhang, G. and Y. Cheng, *On the fundamentals of electrochemical corrosion of X65 steel in CO 2-containing formation water in the presence of acetic acid in petroleum production.* Corrosion Science, 2009. **51**(1): p. 87-94.

131. Cui, Z., et al., *Corrosion behavior of oil tube steels under conditions of multiphase flow saturated with super-critical carbon dioxide.* Materials letters, 2004. **58**(6): p. 1035-1040.

132. Zhao, G.-X., et al., *Formation characteristic of CO 2 corrosion product layer of P110 steel investigated by SEM and electrochemical techniques.* Journal of Iron and Steel Research, International, 2009. **16**(4): p. 89-94.

133. Palacios, C. and J. Shadley, *Characteristics of corrosion scales on steels in a CO2-saturated NaCl brine.* Corrosion, 1991. **47**(2): p. 122-127.

134. De Waard, C. and D. Milliams, *Carbonic acid corrosion of steel.* Corrosion, 1975. **31**(5): p. 177-181.

135. Schmitt, G. and M. Horstemeier. *Fundamental aspects of CO2 metal loss corrosion-Part II: Influence of different parameters on CO2 corrosion mechanisms*. in *CORROSION 2006*. 2006. NACE International.

136. Nesic, S., et al. *Electrochemical properties of iron dissolution in the presence of CO2-basics revisited*. in *CORROSION 96*. 1996. NACE International.

137. Nešić, S., *Key issues related to modelling of internal corrosion of oil and gas pipelines–A review.* Corrosion Science, 2007. **49**(12): p. 4308-4338.

138. Fang, H., B. Brown, and S. Nešic, *Sodium Chloride Concentration Effects on General CO2 Corrosion Mechanisms.* Corrosion, 2013. **69**(3): p. 297-302.

139. Mishra, B., et al., *Development of a predictive model for activation-controlled corrosion of steel in solutions containing carbon dioxide.* Corrosion, 1997. **53**(11): p. 852-859.

140. Nesic, S., J. Postlethwaite, and S. Olsen, *An electrochemical model for prediction of corrosion of mild steel in aqueous carbon dioxide solutions.* Corrosion, 1996. **52**(4): p. 280-294.

141. Nordsveen, M., et al., *A mechanistic model for carbon dioxide corrosion of mild steel in the presence of protective iron carbonate films-Part 1: Theory and verification.* Corrosion, 2003. **59**(5): p. 443-456.

142. Ogundele, G. and W. White, *Some observations on corrosion of carbon steel in aqueous environments containing carbon dioxide.* Corrosion, 1986. **42**(2): p. 71-78.

143. Mora-Mendoza, J. and S. Turgoose, *Fe 3 C influence on the corrosion rate of mild steel in aqueous CO 2 systems under turbulent flow conditions.* Corrosion Science, 2002. **44**(6): p. 1223-1246.

144. Fang, H., et al. *General CO2 corrosion in high salinity brines*. in *CORROSION 2006*. 2006. NACE International.

145. Bockris, J.M., D. Drazic, and A. Despic, *The electrode kinetics of the deposition and dissolution of iron.* Electrochimica Acta, 1961. **4**(2): p. 325-361.

146. Crolet, J.L., N. Thevenot, and A. Dugstad. *Role of free acetic acid on the CO2 corrosion of steels*. in *CORROSION 99*. 1999. NACE International.

147. Nazari, M.H., S. Allahkaram, and M. Kermani, *The effects of temperature and pH on the characteristics of corrosion product in CO 2 corrosion of grade X70 steel.* Materials & Design, 2010. **31**(7): p. 3559-3563.

148. Moiseeva, L. and N. Rashevskaya, *Effect of pH value on corrosion behavior of steel in CO 2-containing aqueous media.* Russian journal of applied chemistry, 2002. **75**(10): p. 1625-1633.

149. Tran, T., B. Brown, and S. Nesic, *Corrosion of mild steel in an aqueous CO2 environment—basic electrochemical mechanisms revisited.* CORROSION/2015, 2015.

150. Wu, S., et al., *Characterization of the surface film formed from carbon dioxide corrosion on N80 steel.* Materials Letters, 2004. **58**(6): p. 1076-1081.

151. Kvarekval, J. and A. Dugstad. *Corrosion Mitigation with pH Stabilization in Slightly Sour Gas/Condensate Pipelines*. in *CORROSION 2006*. 2006. NACE International.

152. Söhnel, O. and J.W. Mullin, *Interpretation of crystallization induction periods.* Journal of colloid and interface science, 1988. **123**(1): p. 43-50.

153. Gao, K., et al., *Mechanical properties of CO 2 corrosion product scales and their relationship to corrosion rates.* Corrosion Science, 2008. **50**(10): p. 2796-2803.

154. Li, W., et al., *Investigation of pseudo-passivation of mild steel in CO2 corrosion.* Corrosion, 2013. **70**(3): p. 294-302.

155. Nešic, S., et al., *A mechanistic model for carbon dioxide corrosion of mild steel in the presence of protective iron carbonate films-Part 2: A numerical experiment.* Corrosion, 2003. **59**(6): p. 489-497.

156. Yap, K.-M. and S. Srinivasan. *Key factors in development of a CO2/H2S corrosion prediction model for multiphase oil/gas production systems*. in *CORROSION 2010*. 2010. NACE International.

157. Yin, Z., et al., *Effect of temperature on CO2 corrosion of carbon steel.* Surface and interface analysis, 2009. **41**(6): p. 517-523.

158. Lin, G., et al., *Effect of temperature and pressure on the morphology of carbon dioxide corrosion scales.* Corrosion, 2006. **62**(6): p. 501-507.

159. Dugstad, A., H. Hemmer, and M. Seiersten, *Effect of steel microstructure on corrosion rate and protective iron carbonate film formation.* Corrosion, 2001. **57**(4): p. 369-378.

160. Vuppu, A. and W. Jepson. *The effect of temperature in sweet corrosion of horizontal multiphase carbon steel pipelines*. in *SPE Asia Pacific Oil and Gas Conference*. 1994. Society of Petroleum Engineers.

161. Wei, L., et al., *Formation mechanism and protective property of corrosion product scale on X70 steel under supercritical CO 2 environment.* Corrosion Science, 2015. **100**: p. 404-420.

162. Alizadeh, M. and S. Bordbar, *The influence of microstructure on the protective properties of the corrosion product layer generated on the welded API X70 steel in chloride solution.* Corrosion Science, 2013. **70**: p. 170-179.

163. Ma, Y., Y. Li, and F. Wang, *Corrosion of low carbon steel in atmospheric environments of different chloride content.* Corrosion Science, 2009. **51**(5): p. 997-1006.

164. Chen, Y., et al., *Corrosion resistance and mechanical properties of low-alloy steels under atmospheric conditions.* Corrosion Science, 2005. **47**(4): p. 1001-1021.

165. Castaño, J., et al., *Atmospheric corrosion of carbon steel in Colombia.* Corrosion Science, 2010. **52**(1): p. 216-223.

166. Guo, J., et al., *Influence of carbon content and microstructure on corrosion behaviour of low alloy steels in a Cl− containing environment.* Corrosion Science, 2009. **51**(2): p. 242-251.

167. Liu, Y., et al., *Electrochemical polarization study on crude oil pipeline corrosion by the produced water with high salinity.* Engineering Failure Analysis, 2016. **60**: p. 307-315.

168. Moller, H., E. Boshoff, and H. Froneman, *The corrosion behaviour of a low carbon steel in natural and synthetic seawaters.* JOURNAL-SOUTH AFRICAN INSTITUTE OF MINING AND METALLURGY, 2006. **106**(8): p. 585.

169. Smith, P., et al., *A model for the corrosion of steel subjected to synthetic produced water containing sulfate, chloride and hydrogen sulfide.* Chemical engineering science, 2011. **66**(23): p. 5775-5790.

170. Boucherit, M. and D. Tebib, *A study of carbon steels in basic pitting environments.* Anti-Corrosion Methods and Materials, 2005. **52**(6): p. 365-370.

171. Eliyan, F.F., F. Mohammadi, and A. Alfantazi, *An electrochemical investigation on the effect of the chloride content on CO 2 corrosion of API-X100 steel.* Corrosion Science, 2012. **64**: p. 37-43.

172. Zeng, Z., R. Lillard, and H. Cong, *Effect of Salt Concentration on the Corrosion Behavior of Carbon Steel in CO2 Environment.* Corrosion, 2016. **72**(6): p. 805-823.

173. Han, J., J.W. Carey, and J. Zhang, *Effect of sodium chloride on corrosion of mild steel in CO2-saturated brines.* Journal of Applied Electrochemistry, 2011. **41**(6): p. 741-749.

174. yari, M., *An Intro to Pipeline Corrosion in Seawater.* CorrosionPedia, 01/12/2015.

175. Cáceres, L., T. Vargas, and L. Herrera, *Influence of pitting and iron oxide formation during corrosion of carbon steel in unbuffered NaCl solutions.* Corrosion Science, 2009. **51**(5): p. 971-978.

176. Ismail, A. and N. Adan, *Effect of oxygen concentration on corrosion rate of carbon steel in seawater.* Am. J. Eng. Res, 2014. **3**: p. 64-67.

177. Jung, H., et al., *Effect of dissolved oxygen (DO) on internal corrosion of water pipes.* Environmental Engineering Research, 2009. **14**(3): p. 195-199.

178. Martin, R.L. *Corrosion consequences of oxygen entry into oilfield brines*. in *CORROSION 2002*. 2002. NACE International.

179. Asaduzzaman, M., C.M. Mohammad, and I. Mayeedul, *Effects of concentration of sodium chloride solution on the pitting corrosion behavior of AISI 304L austenitic stainless steel.* Chemical Industry and Chemical Engineering Quarterly, 2011. **17**(4): p. 477-483.

180. Tawancy, H., L.M. Al-Hadhrami, and F. Al-Yousef, *Analysis of corroded elbow section of carbon steel piping system of an oil–gas separator vessel.* Case Studies in Engineering Failure Analysis, 2013. **1**(1): p. 6-14.

181. Oh, S.J., D. Cook, and H. Townsend, *Characterization of iron oxides commonly formed as corrosion products on steel.* Hyperfine interactions, 1998. **112**(1-4): p. 59-66.

182. El Desouky, H. and H.A. Aboeldahab, *Effect of Chloride Concentration on the Corrosion Rate of Maraging Steel.* Open Journal of Physical Chemistry, 2014. **4**(04): p. 147.

183. Nešic, S. and K.-L. Lee, *A mechanistic model for carbon dioxide corrosion of mild steel in the presence of protective iron carbonate films-Part 3: Film growth model.* Corrosion, 2003. **59**(7): p. 616-628.

184. Dugstad, A., H. Hemmer, and M. Seiersten. *Effect of steel microstructure upon corrosion rate and protective iron carbonate film formation*. in *CORROSION 2000*. 2000. NACE International.

185. Ochoa, N., et al., *CO 2 corrosion resistance of carbon steel in relation with microstructure changes.* Materials Chemistry and Physics, 2015. **156**: p. 198-205.

186. Nyborg, R. *Overview of CO2 corrosion models for wells and pipelines*. in *CORROSION 2002*. 2002. NACE International.

187. Nyborg, R. *CO2 corrosion models for oil and gas production systems*. in *CORROSION 2010*. 2010. NACE International.

188. Choi, Y.-S. and S. Nešić, *Corrosion behavior of carbon steel in supercritical CO2-water environments.* CORROSION 2009, 2009.

189. SNesic, S., K. George, and S. Wang, *High pressure CO2 corrosion electrochemistry and the effect of acetic acid.* CORROSION 2004, 2004.

190. Watanabe, Y., et al., *Integrated model for microstructural evolution and properties of steel plates manufactured in production line.* ISIJ international, 1992. **32**(3): p. 405-413.

191. Grossmann, M.A. and E.C. Bain, *Principles of heat treatment*. 1964: American Society for Metals.

192. *Tenaris_Pipe Body Performance Properties Catalogue.*, in *Brochures and catalogs*.

193. ASTM, E., *Standard Guide for Preparation of Metallographic Specimens*. 2001, American Society for Testing Materials.

194. E-112, A., *Standard test methods for determining average grain size*. 2010, ASTM International USA.

195. Schmit, J., *An introduction to non-contact surface metrology*, in *Bruker Nano Surface Division*. 2013, Bruker

196. Standard, A., *G31-72.* Standard Practice for Laboratory Immersion Corrosion Testing of Metals. Annual Book of ASTM standards. Philadelphia, PA: American Society for Testing and Materials, 2004.

197. 90, A.G., *Standard Practice for Preparing, Cleaning, and Evaluating Corrosion Test Specimens*, in *Standard*. 1999: ASTM, 100 Barr Harbor Drive, West Conshohocken, PA 19428-2959, United States.

198. 94, A.G., *Standard Guide for Examination and Evaluation of Pitting Corrosion*, in *Designation: G 46 – 94 (Reapproved 2005)*. 2005, ASTM International,: 100 Barr Harbor Drive, PO Box C700, West Conshohocken, PA 19428-2959, United States.

199. 98, A.D., *Standard Practice for the Preparation of Substitute Ocean Water*, in *Standard*. 2003, An American National Standard.

200. Wu, Q., et al., *Corrosion behavior of low-alloy steel containing 1% chromium in CO 2 environments.* Corrosion Science, 2013. **75**: p. 400-408.

201. Weast, R.C., M.J. Astle, and W.H. Beyer, *CRC handbook of chemistry and physics*. Vol. 69. 1988: CRC press Boca Raton, FL.

202. Islam, M.A. and Z.N. Farhat, *Characterization of the Corrosion Layer on Pipeline Steel in Sweet Environment.* Journal of Materials Engineering and Performance, 2015. **24**(8): p. 3142-3158.

203. Mameng, S.H., A. Bergquist, and E. Johansson. *Corrosion of Stainless Steel in Sodium Chloride Brine Solutions*. in *CORROSION 2014*. 2014. NACE International.

204. Henriquez, M., et al., *Electrochemical investigation of the corrosion behavior of API 5L-X65 carbon steel in carbon dioxide medium.* Corrosion, 2013. **69**(12): p. 1171-1179.

205. Yin, Z., et al., *Electrochemical behavior and mechanism of CO2 corrosion on P110 steel in simulated oilfield solution.* Anti-Corrosion Methods and Materials, 2011. **58**(5): p. 227-233.

206. Yu, C., X. Gao, and P. Wang, *Electrochemical Corrosion Performance of Low Alloy Steel in Acid Sodium Chloride Solution.* Electrochemistry, 2015. **83**(6): p. 406-412.

207. Gao, M., X. Pang, and K. Gao, *The growth mechanism of CO 2 corrosion product films.* Corrosion Science, 2011. **53**(2): p. 557-568.

208. Luo, H., et al., *Passive Film Properties and Electrochemical Behavior of Co-Cr-Mo Stainless Steel in Chloride Solution.* Journal of Materials Engineering and Performance, 2017. **26**(5): p. 2237-2243.

209. Luo, H., et al., *The electrochemical behaviour of 2205 duplex stainless steel in alkaline solutions with different pH in the presence of chloride.* Electrochimica Acta, 2012. **64**: p. 211-220.

210. Farelas, F., B. Brown, and S. Nesic, *Iron carbide and its influence on the formation of protective iron carbonate in CO2 corrosion of mild steel.* CORROSION/2013, paper, 2013(02291).

211. Ma, Y., Y. Li, and F. Wang, *The atmospheric corrosion kinetics of low carbon steel in a tropical marine environment.* Corrosion Science, 2010. **52**(5): p. 1796-1800.

212. Jiang, X., et al., *Electrochemical Investigation of the Role of Cl-on Localized Carbon Dioxide Corrosion Behavior of Mild Steel.* Corrosion, 2012. **69**(1): p. 15-24.

213. Gao, X., B. Brown, and S. Nesic, *Effect of chloride on localized corrosion initiation of carbon steel in a CO2 aqueous environment.* CORROSION/2014, San Antonio, TX, USA, 2014.

214. de Moraes, F., et al. *Characterization of CO2 corrosion product scales related to environmental conditions*. in *CORROSION 2000*. 2000. NACE International.

215. Choi, Y.-S., J.-J. Shim, and J.-G. Kim, *Corrosion behavior of low alloy steels containing Cr, Co and W in synthetic potable water.* Materials Science and Engineering: A, 2004. **385**(1): p. 148-156.

216. Elbeik, S., A. Tseung, and A. Mackay, *The formation of calcareous deposits during the corrosion of mild steel in sea water.* Corrosion science, 1986. **26**(9): p. 669-680.

217. Mohammed, S., et al., *Investigating pitting in X65 carbon steel using potentiostatic polarisation.* Applied Surface Science, 2017. **423**: p. 25-32.

218. Della Rovere, C., et al., *Characterization of passive films on shape memory stainless steels.* Corrosion Science, 2012. **57**: p. 154-161.

219. Zhang, Y., et al., *Corrosion behavior of X65 carbon steel in simulated oilfield produced water.* Materials and Corrosion, 2015. **66**(4): p. 366-374.

220. Liu, Z., et al., *Corrosion behavior of low-alloy steel with martensite/ferrite microstructure at vapor-saturated CO2 and CO2-saturated brine conditions.* Applied Surface Science, 2015. **351**: p. 610-623.

221. Zhu, S., et al., *Corrosion of N80 carbon steel in oil field formation water containing CO 2 in the absence and presence of acetic acid.* Corrosion Science, 2011. **53**(10): p. 3156-3165.

222. He, K.-j. and T. Baker, *Effect of Zirconium additions on Austenite grain coarsening of C–Mn and microalloy steels.* Materials Science and Engineering: A, 1998. **256**(1-2): p. 111-119.

223. Durand-Charre, M., *Microstructure of steels and cast irons*. 2013: Springer Science & Business Media.

224. Korchynsky, M. *A New Role for Microalloyed Steels − Adding Economic Value*. in *The Use of Vanadium in Steel - Proceedings of the Vanitec Symposium* 2001. Beijing, China.

225. Smith, L. and B. Craig. *Corrosion mechanisms and material performance in environments containing hydrogen sulfide and elemental sulfur*. in *SACNUC Workshop 22nd and 23rd October*. 2008.

226. Singer, M., et al., *Combined effect of CO2, H2S and acetic acid on bottom of the line corrosion.* CORROSION 2007, 2007.

227. Chilingar, G.V., R. Mourhatch, and G.D. Al-Qahtani, *The Fundamentals of Corrosion and Scaling for Petroleum & Environmental Engineers; A Handbook for Petroleum and Environmental Engineers*. 2013: Gulf Punlishing Company.

228. Afshari, V. and C. Dehghanian, *Effects of grain size on the electrochemical corrosion behaviour of electrodeposited nanocrystalline Fe coatings in alkaline solution.* Corrosion Science, 2009. **51**(8): p. 1844-1849.

229. Zhang, X., et al., *The influence of grain size on the corrosion resistance of nanocrystalline zirconium metal.* Materials Science and Engineering: A, 2007. **448**(1-2): p. 259-263.

230. Ueda, M., H. Takabe, and P.I. Nice. *The development and implementation of a new alloyed steel for oil and gas production wells*. in *CORROSION 2000*. 2000. NACE International.

231. David, E., C. Robert, and G. Rosa, *Effect of Microalloying, Principally With Vanadium, Processing Conditions and Microstructure on Resistance to CO2 Corrosion.* Journal of Iron and Steel Research (International), 2011. **1**.

232. Zhang, D., et al., *Corrosion Behavior of Low-C Medium-Mn Steel in Simulated Marine Immersion and Splash Zone Environment.* Journal of Materials Engineering and Performance, 2017: p. 1-9.

233. Kear, G. and F.C. Walsh, *The characteristics of a true Tafel slope.* Corrosion and materials, 2005. **30**(6): p. 51-55.

234. McCafferty, E., *Validation of corrosion rates measured by the Tafel extrapolation method.* Corrosion Science, 2005. **47**(12): p. 3202-3215.

235. Instruments, G., *Getting Started with Electrochemical Corrosion Measurement*. 2011.

236. Prawoto, Y., K. Ibrahim, and W. Wan Nik, *Effect of pH and chloride concentration on the corrosion of duplex stainless steel.* Arabian Journal for Science and Engineering, 2009. **34**(2): p. 115.

237. Sverdrup, H.U., M.W. Johnson, and R.H. Fleming, *The Oceans: Their physics, chemistry, and general biology*. Vol. 7. 1942: Prentice-Hall New York.

238. Möller, H., *The influence of Mg 2+ on the formation of calcareous deposits on a freely corroding low carbon steel in seawater.* Corrosion science, 2007. **49**(4): p. 1992-2001.

239. Hartt, W.H., C.H. Culberson, and S.W. Smith, *Calcareous deposits on metal surfaces in seawater—a critical review.* Corrosion, 1984. **40**(11): p. 609-618.

240. Della Rovere, C., et al., *Corrosion behavior of shape memory stainless steel in acid media.* Journal of Alloys and Compounds, 2011. **509**(17): p. 5376-5380.

241. Luo, H., et al., *Characterization of electrochemical and passive behaviour of Alloy 59 in acid solution.* Electrochimica Acta, 2014. **135**: p. 412-419.

242. Clover, D., et al., *The influence of microstructure on the corrosion rate of various carbon steels.* Journal of applied electrochemistry, 2005. **35**(2): p. 139-149.

243. Frankel, G., *Pitting corrosion of metals a review of the critical factors.* Journal of the Electrochemical Society, 1998. **145**(6): p. 2186-2198.

244. Zhang, S., et al., *Effect of Tempering Temperature on the Corrosion Behavior of R5 Steel in Artificial Seawater.* INTERNATIONAL JOURNAL OF ELECTROCHEMICAL SCIENCE, 2017. **12**(3): p. 2453-2465.

245. Han, J., et al., *Chemistry and structure of the passive film on mild steel in CO2 corrosion environments.* Industrial & Engineering Chemistry Research, 2009. **48**(13): p. 6296-6302.

246. Chan, E.W.L., *Magnetite and its galvanic effect on the corrosion of carbon steel under carbon dioxide environments*. 2011, Curtin University.

247. Han, J., et al., *Roles of passivation and galvanic effects in localized CO2 corrosion of mild steel.* CORROSION/2008, paper, 2008(08332).

248. Mahlobo, M., K. Premlall, and P. Olubambi. *Effect of CO2 partial pressure and different CO2 phases on carbon steel corrosion*. in *IOP Conference Series: Materials Science and Engineering*. 2017. IOP Publishing.

249. Melchers, R.E. and R. Jeffrey, *Early corrosion of mild steel in seawater.* Corrosion Science, 2005. **47**(7): p. 1678-1693.

250. Hernandez, J., A. Muñoz, and J. Genesca, *Formation of iron-carbonate scale-layer and corrosion mechanism of API X70 pipeline steel in carbon dioxide-saturated 3% sodium chloride.* Afinidad, 2012. **69**(560).

251. Forero, A., M. Núñez, and I. Bott, *Analysis of the corrosion scales formed on API 5L X70 and X80 steel pipe in the presence of CO2.* Materials Research, 2014. **17**(2): p. 461-471.

252. Berntsen, T., M. Seiersten, and T. Hemmingsen, *Effect of FeCO3 supersaturation and carbide exposure on the CO2 corrosion rate of carbon steel.* Corrosion, 2013. **69**(6): p. 601-613.

253. Kinsella, B., Y. Tan, and S. Bailey, *Electrochemical impedance spectroscopy and surface characterization techniques to study carbon dioxide corrosion product scales.* Corrosion, 1998. **54**(10): p. 835-842.

254. Wang, X. and D. Li, *Mechanical and electrochemical behavior of nanocrystalline surface of 304 stainless steel.* Electrochimica Acta, 2002. **47**(24): p. 3939-3947.

255. Moore, J.J., *Chemical metallurgy*. 2nd ed. 2013: Elsevier.

256. Ralston, K. and N. Birbilis, *Effect of grain size on corrosion: a review.* Corrosion, 2010. **66**(7): p. 075005-075005-13.

257. Zeiger, W., et al., *Corrosion behaviour of a nanocrystalline FeA18 alloy.* Nanostructured Materials, 1995. **6**(5-8): p. 1013-1016.

258. Wang, L., et al., *Electrochemical corrosion behavior of nanocrystalline Co coatings explained by higher grain boundary density.* Electrochimica Acta, 2007. **52**(13): p. 4342-4350.

259. Pisarek, M., et al., *Effect of hydrostatic extrusion on passivity breakdown on 303 austenitic stainless steel in chloride solution.* Journal of Solid State Electrochemistry, 2009. **13**(2): p. 283-291.

260. Li, Y., F. Wang, and G. Liu, *Grain size effect on the electrochemical corrosion behavior of surface nanocrystallized low-carbon steel.* Corrosion, 2004. **60**(10): p. 891-896.

Appendices

Appendix A: Average grain size of $FeCO_3$ crystals formed on the surface of the steels

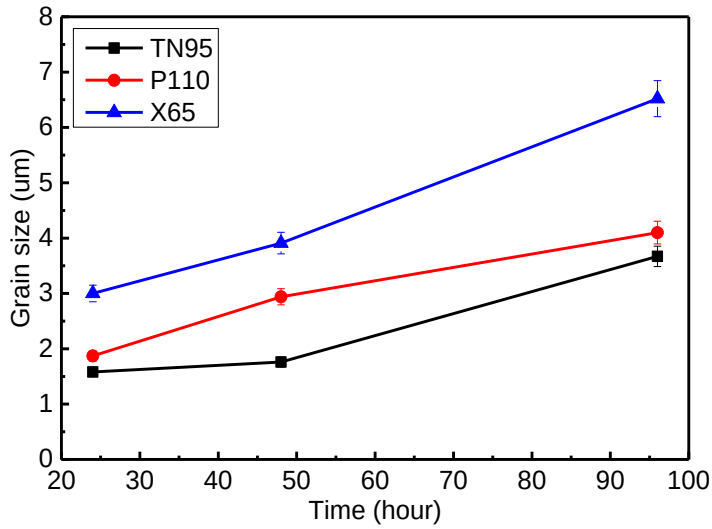

Figure A- 1: Average grain size of $FeCO_3$ crystals formed on the surface of the specimens corroded in 3.5 wt% NaCl solution saturated with 99.98% CO_2 at 60^0C, pH 6.5 for 96 hours.

Appendix B1: EDS spectra of alloyed steels P110 and TN95

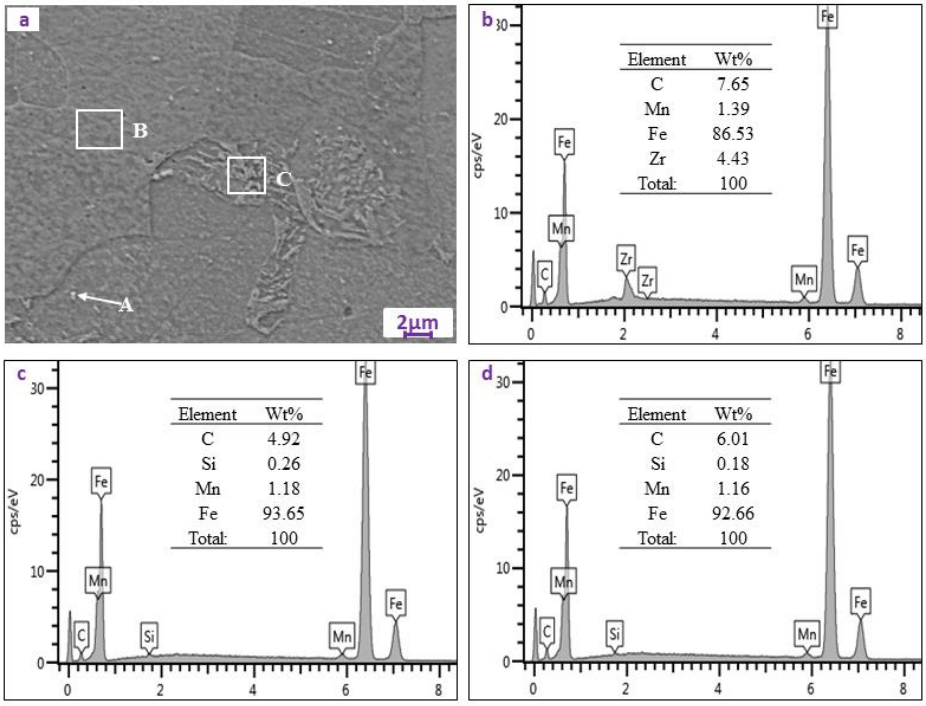

Figure B1- 1: EDS analyses of P_1-Zr_1 (a) microstructure of as cast P_1-Zr_1, (b) EDS of point A in (a), (c) EDS at point B in (a) and (d) EDS of small particle at point C in (a)

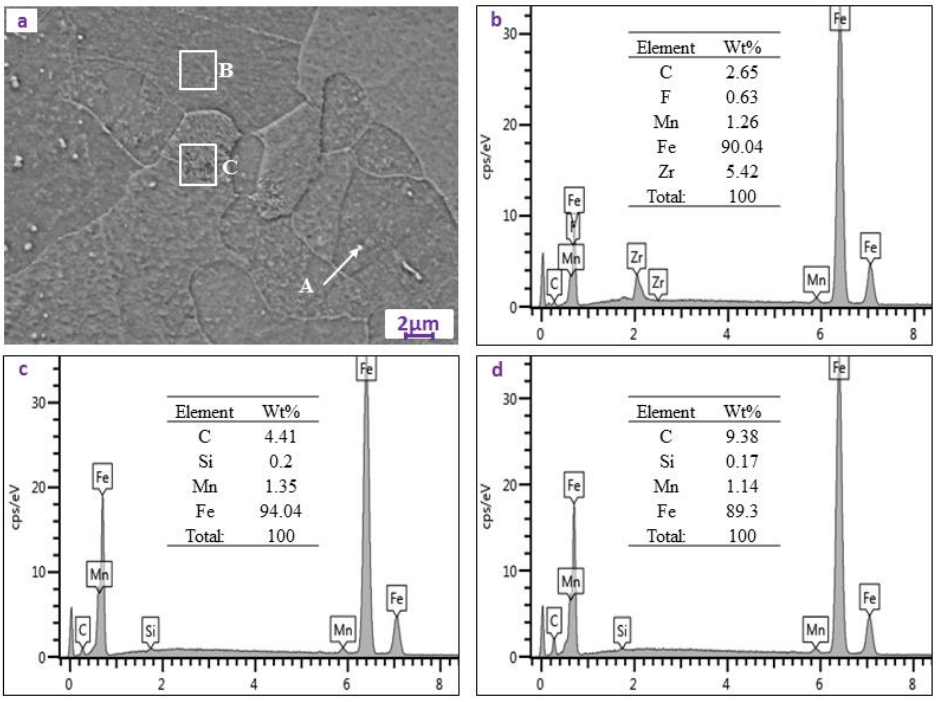

Figure B1- 2: EDS analyses of P_2-Zr_2 (a) microstructure of as cast P_2-Zr_2, (b) EDS of point A in (a), (c) EDS at point B in (a) and (d) EDS of small particle at point C in (a)

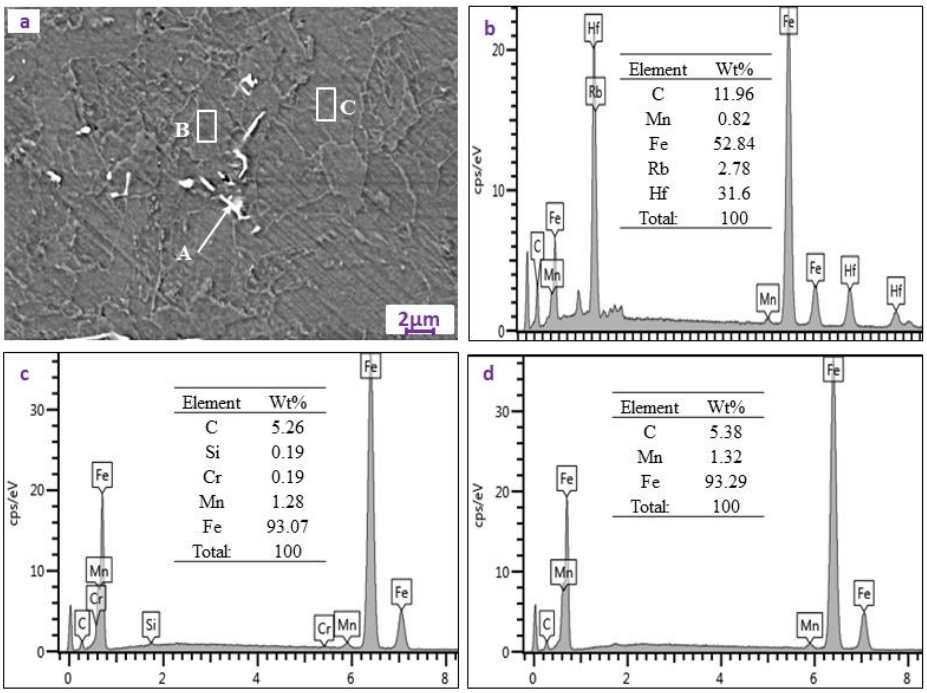

Figure B1- 3: EDS analyses of P_3-Zr_3 (a) microstructure of as cast P_3-Zr_3, (b) EDS of point A in (a), (c) EDS at point B in (a) and (d) EDS of small particle at point C in (a)

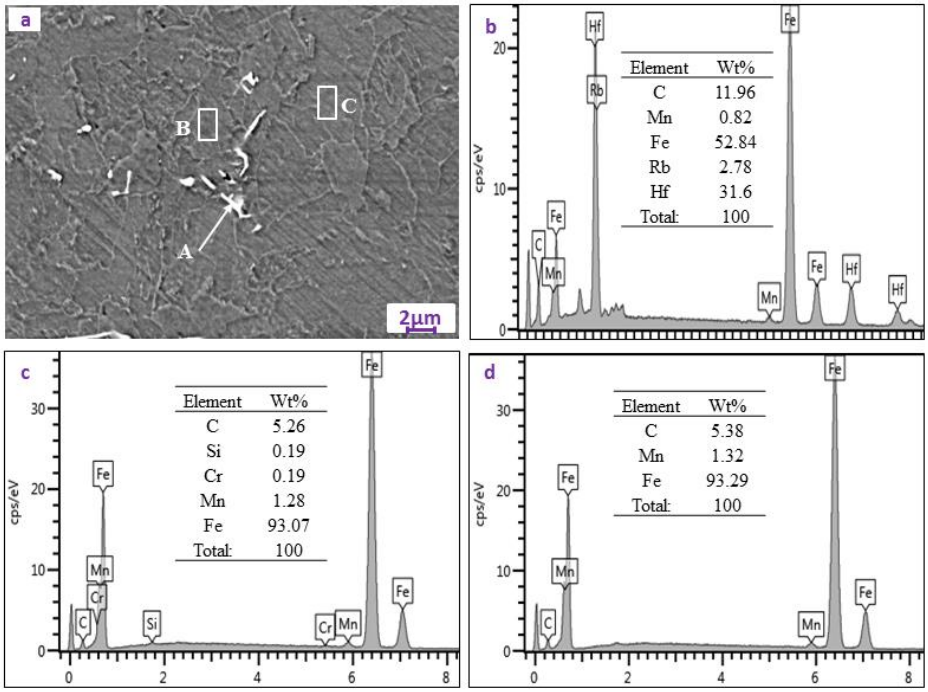

Figure B1- 4: EDS analyses of P_1-Hf_1 (a) microstructure of as cast P_1-Hf_1, (b) EDS of point A in (a), (c) EDS at point B in (a) and (d) EDS of small particle at point C in (a)

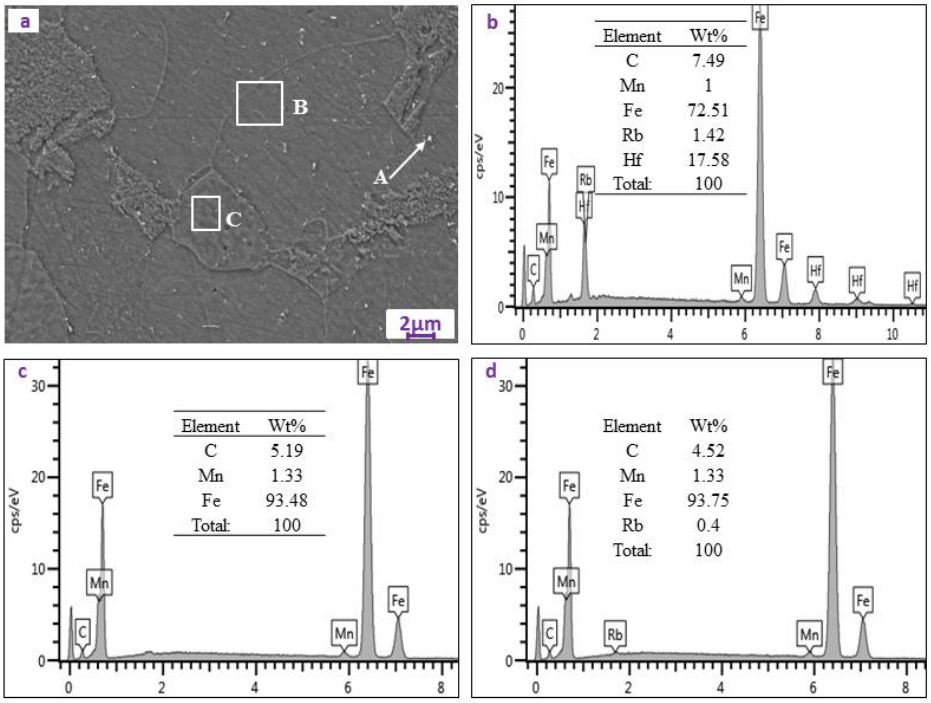

Figure B1- 5: EDS analyses of P_2-Hf_2 (a) microstructure of as cast P_2-Hf_2, (b) EDS of point A in (a), (c) EDS at point B in (a) and (d) EDS of small particle at point C in (a)

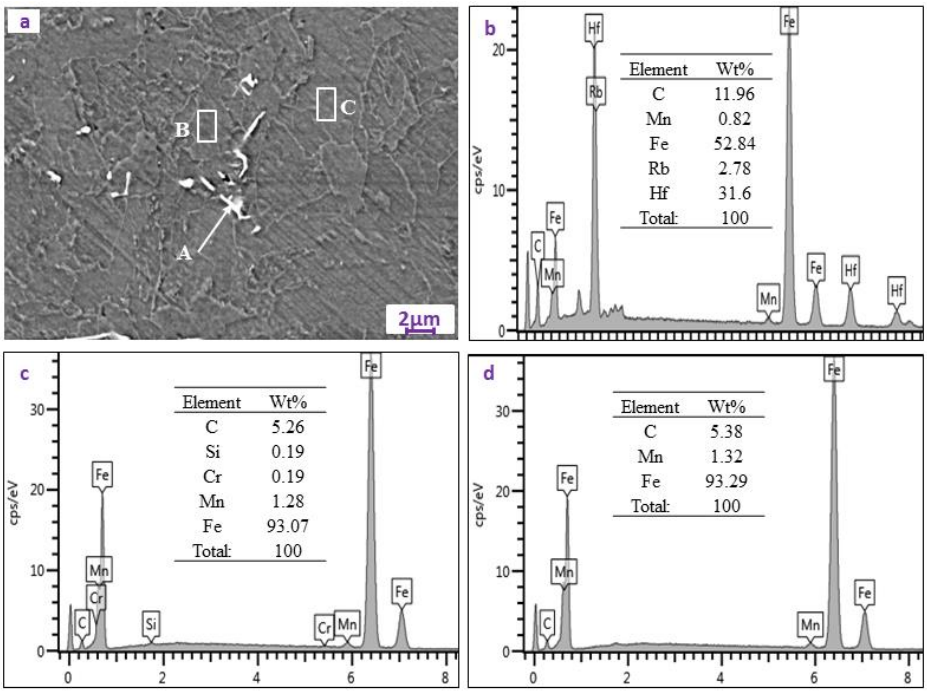

Figure B1- 6: EDS analyses of P_3-Hf_3 (a) microstructure of as cast P_3-Hf_3, (b) EDS of point A in (a), (c) EDS at point B in (a) and (d) EDS of small particle at point C in (a)

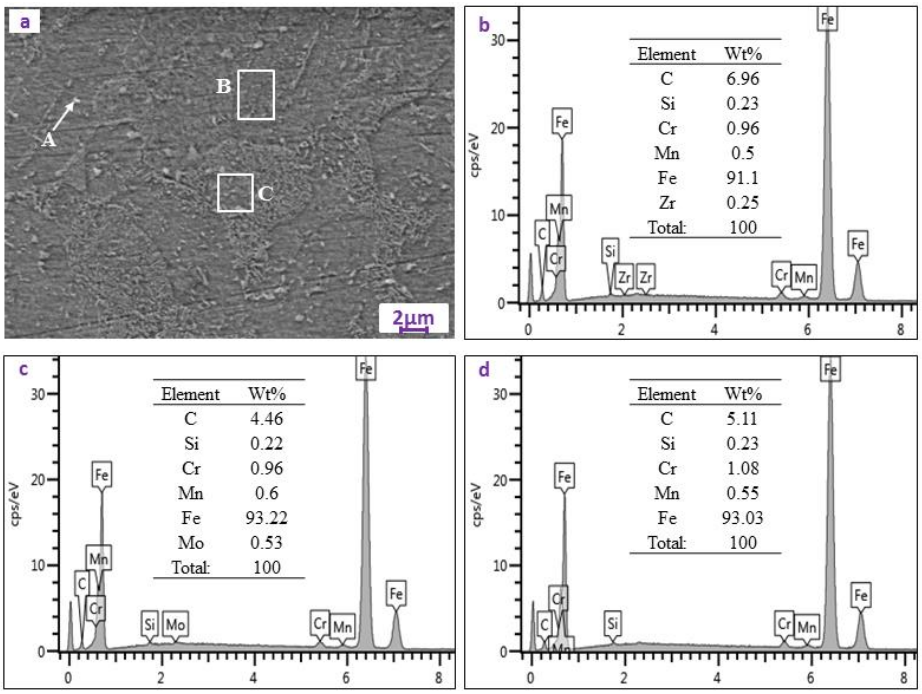

Figure B1- 7: EDS analyses of T_1-Zr_1 (a) microstructure of as cast T_1-Zr_1, (b) EDS of point A in (a), (c) EDS at point B in (a) and (d) EDS of small particle at point C in (a)

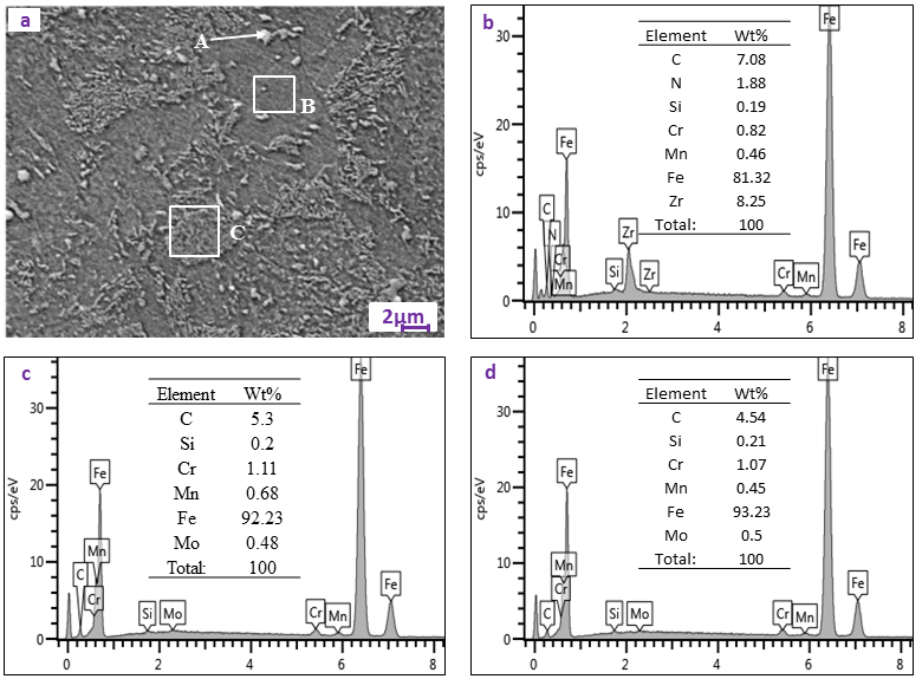

Figure B1- 8: EDS analyses of T_2-Zr_2 (a) microstructure of as cast T_2-Zr_2, (b) EDS of point A in (a), (c) EDS at point B in (a) and (d) EDS of small particle at point C in (a)

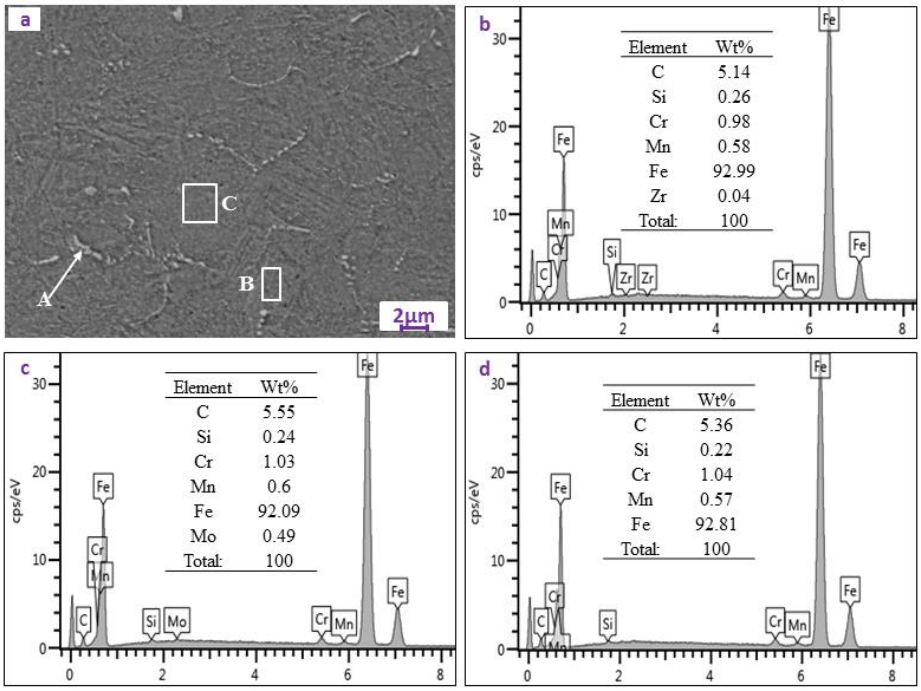

Figure B1- 9: EDS analyses of T_3-Zr_3 (a) microstructure of as cast T_3-Zr_3, (b) EDS of point A in (a), (c) EDS at point B in (a) and (d) EDS of small particle at point C in (a)

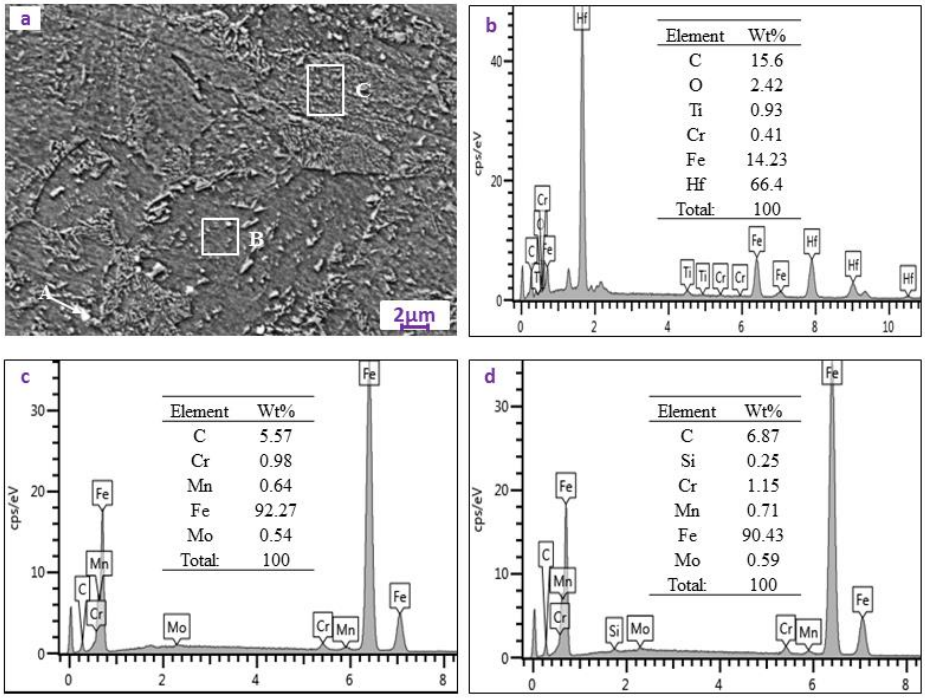

Figure B1- 10: EDS analyses of T_1-Hf_1 (a) microstructure of as cast T_1-Hf_1, (b) EDS of point A in (a), (c) EDS at point B in (a) and (d) EDS of small particle at point C in (a)

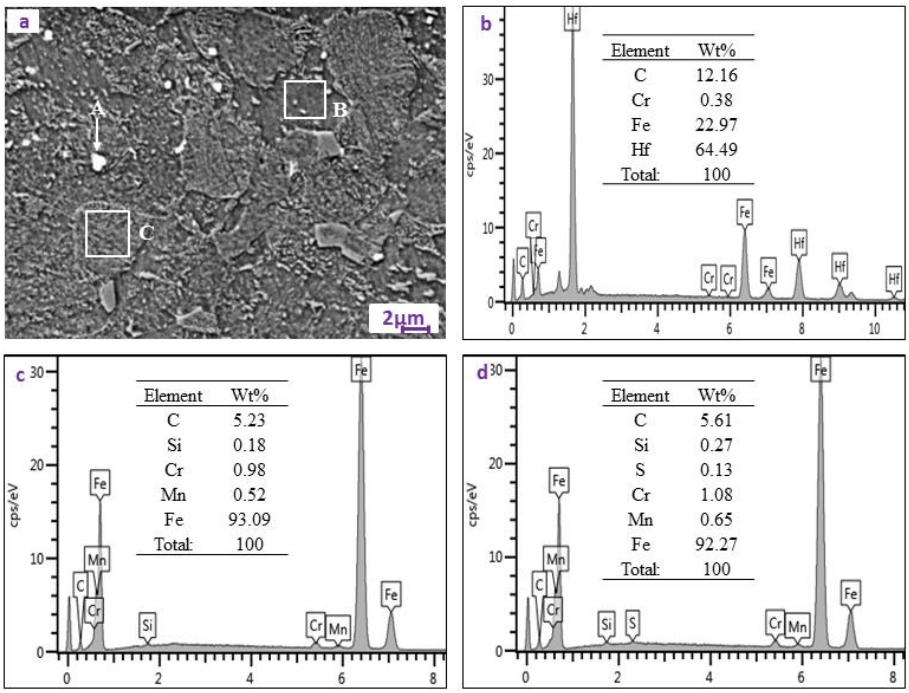

Figure B1- 11: EDS analyses of T_2-Hf_2 (a) microstructure of as cast T_2-Hf_2, (b) EDS of point A in (a), (c) EDS at point B in (a) and (d) EDS of small particle at point C in (a)

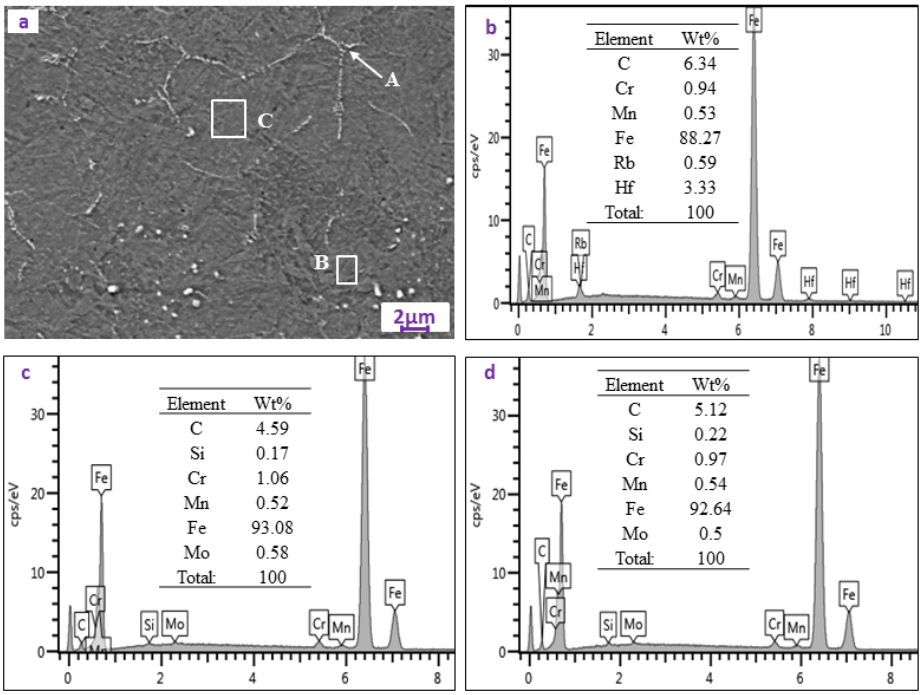

Figure B1- 12: EDS analyses of T_3-Hf_3 (a) microstructure of as cast T_3-Hf_3, (b) EDS of point A in (a), (c) EDS at point B in (a) and (d) EDS of small particle at point C in (a)

Appendix B2: EDS mapping of alloyed steels P110 and TN95

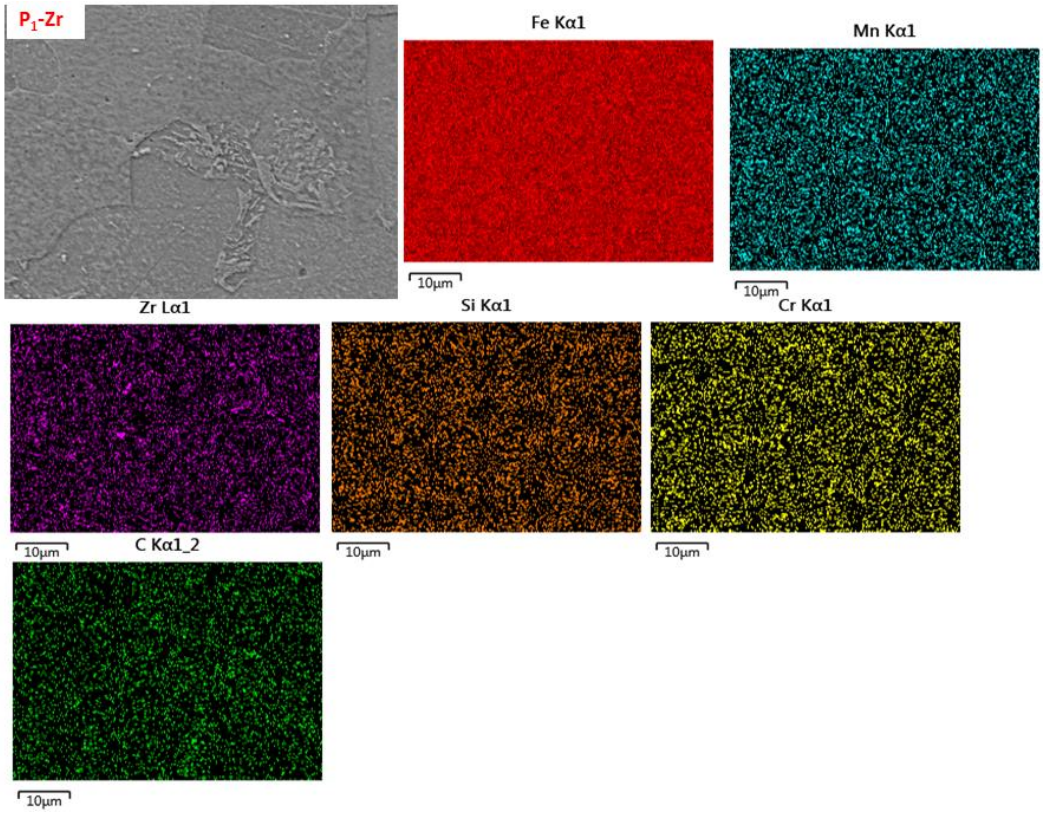

Figure B2- 1: EDS elemental mapping of P_1-Zr_1

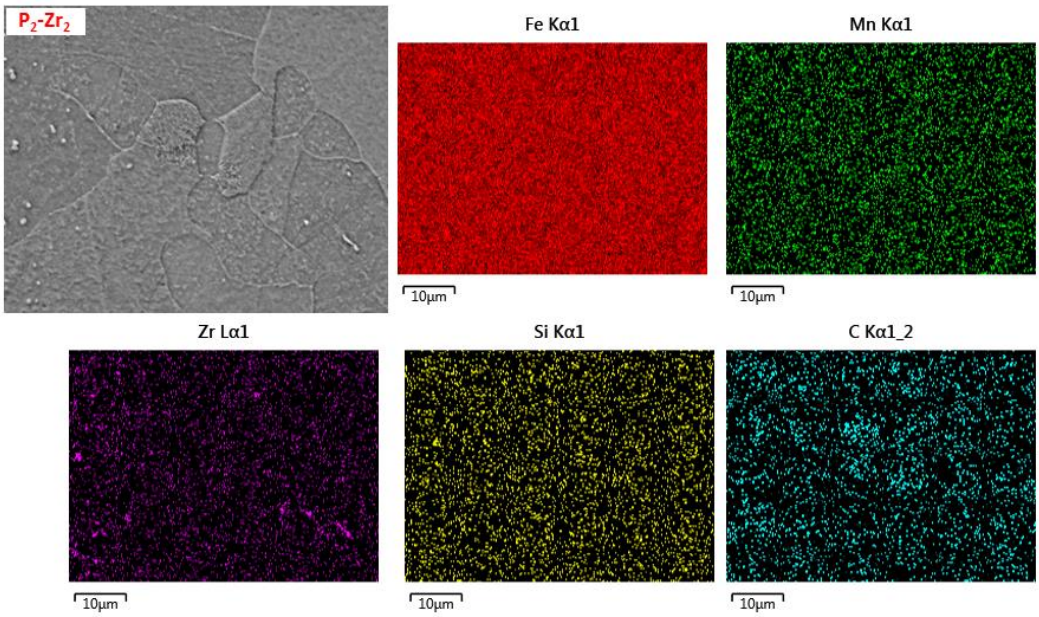

Figure B2- 2: EDS elemental mapping of P_2-Zr_2

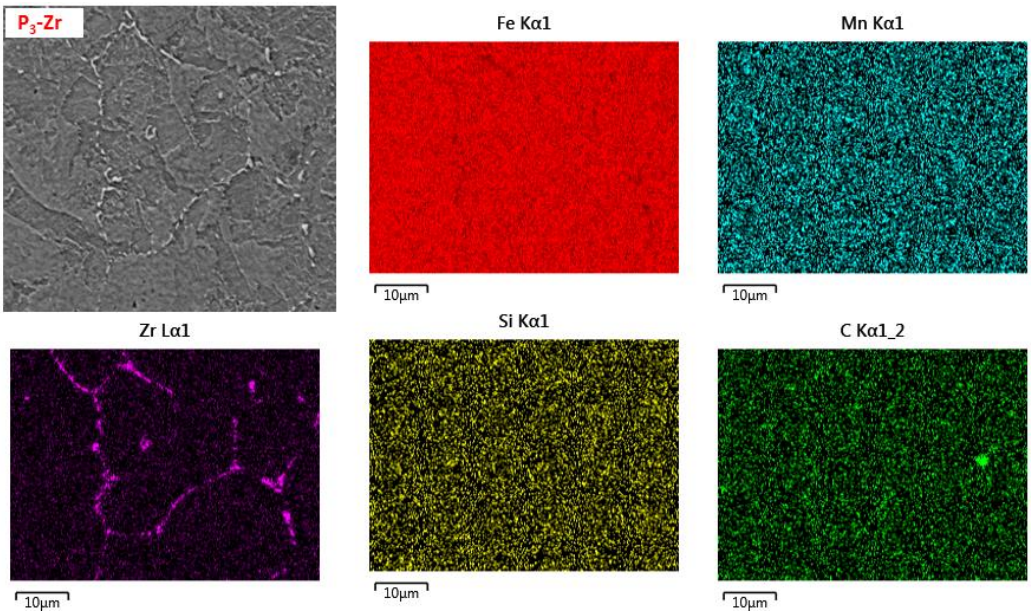

Figure B2- 3: EDS elemental mapping of P_3-Zr_3

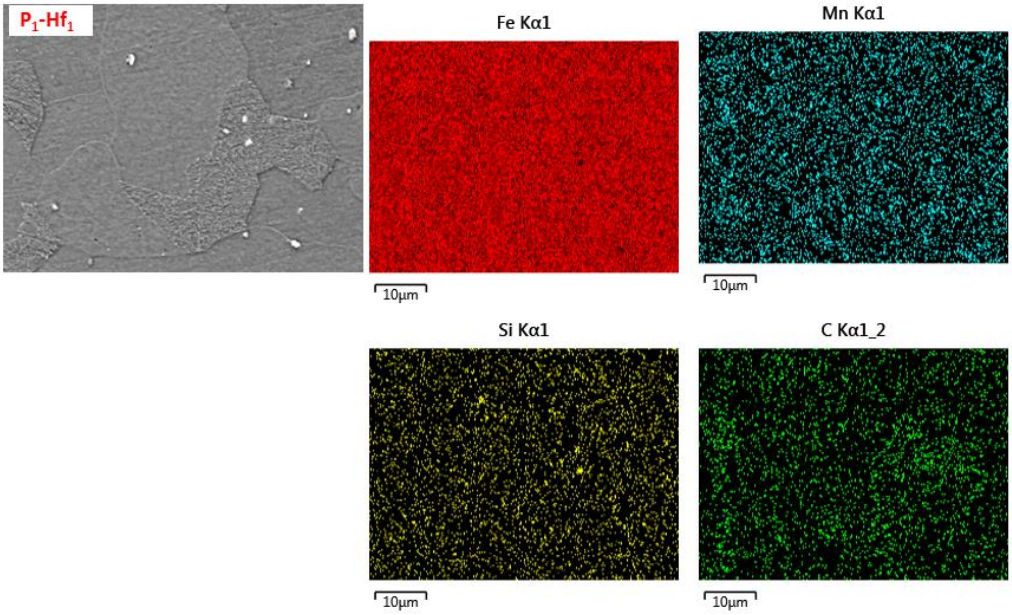

Figure B2- 4: EDS elemental mapping of P_1-Hf_1

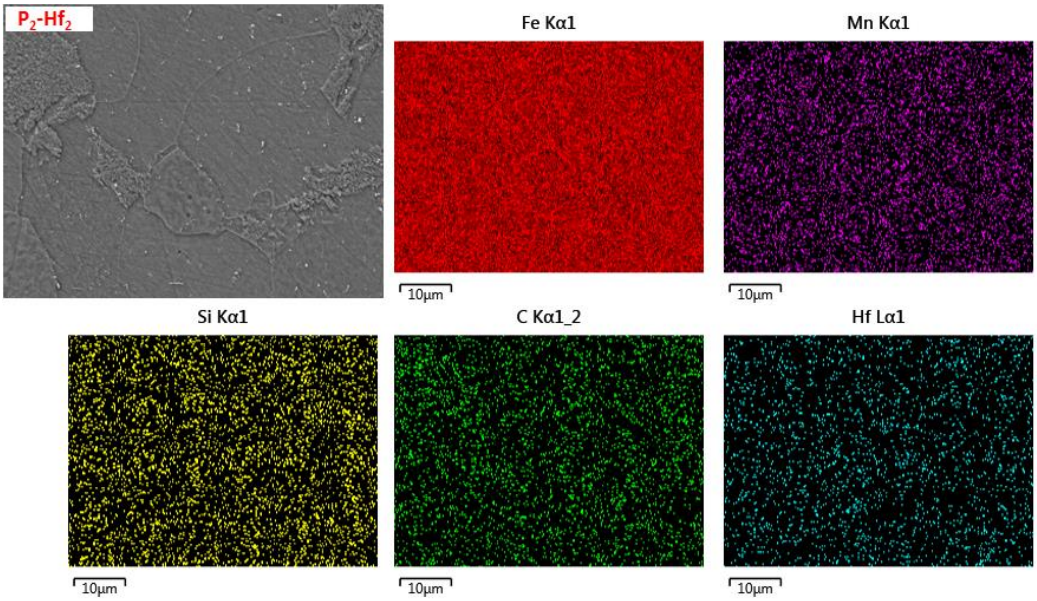

Figure B2- 5: EDS elemental mapping of P_2-Hf_2

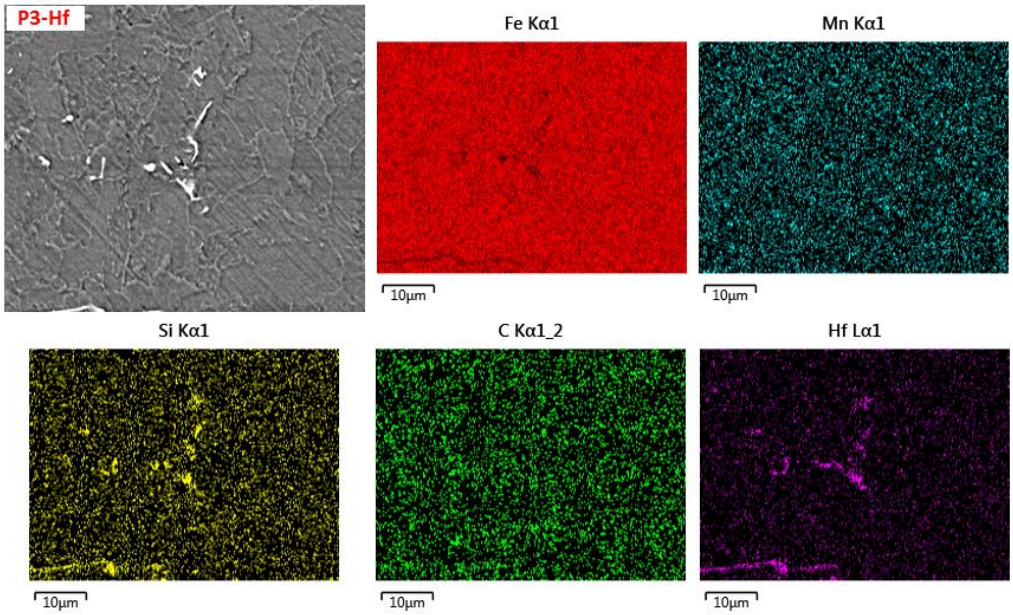

Figure B2- 6: EDS elemental mapping of P_3-Hf_3

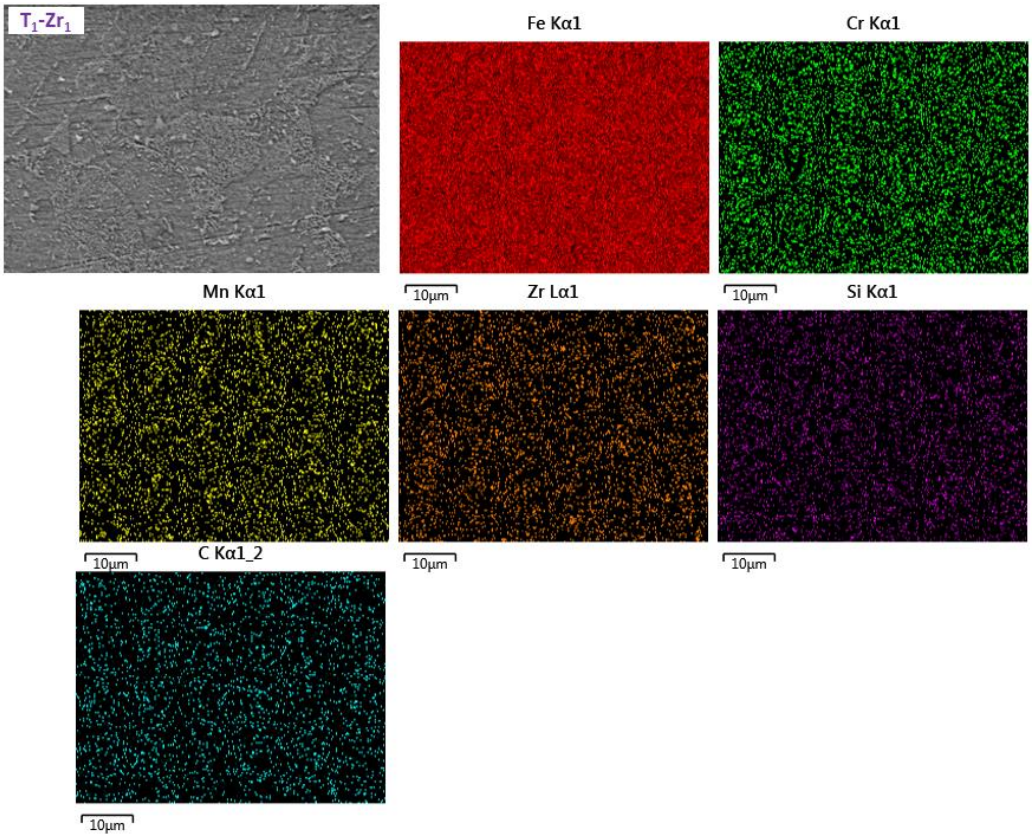

Figure B2- 7: EDS Elemental mapping of T_1-Zr_1

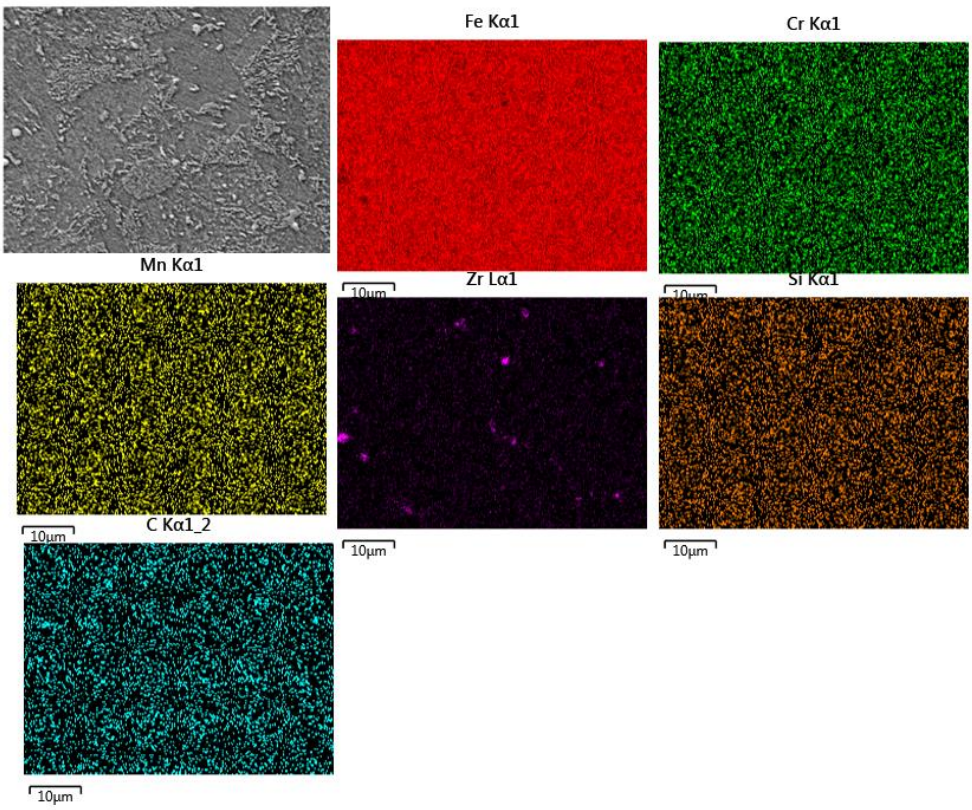

Figure B2- 8: EDS Elemental mapping of T_2-Zr_2

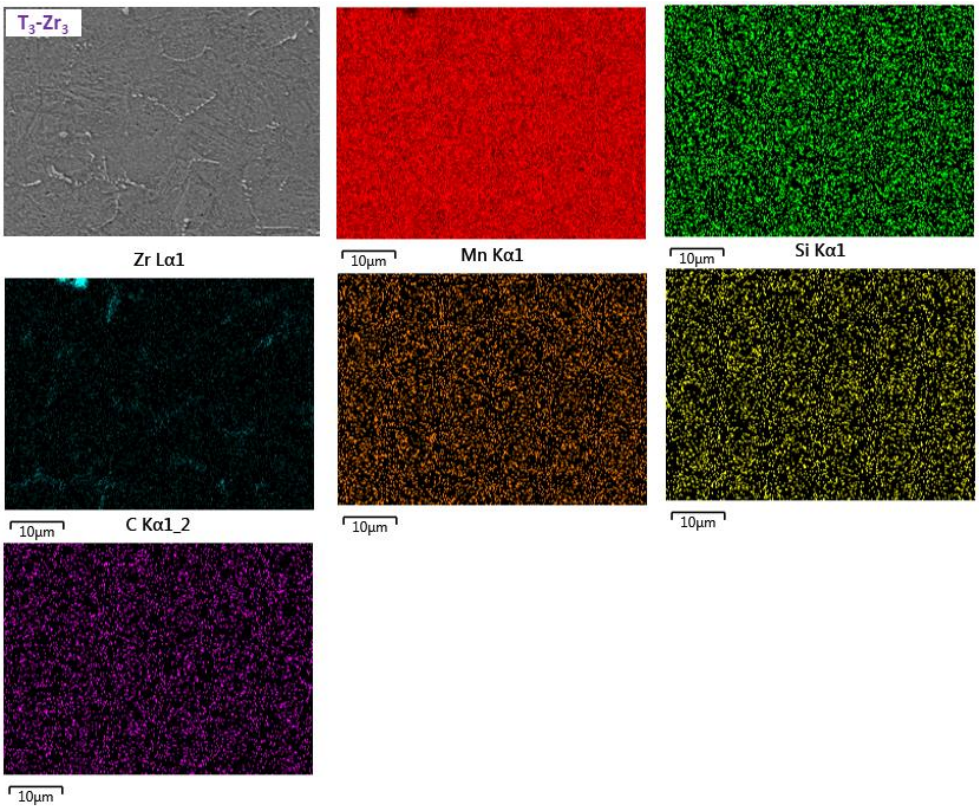

Figure B2- 9: EDS Elemental mapping of T_3-Zr_3

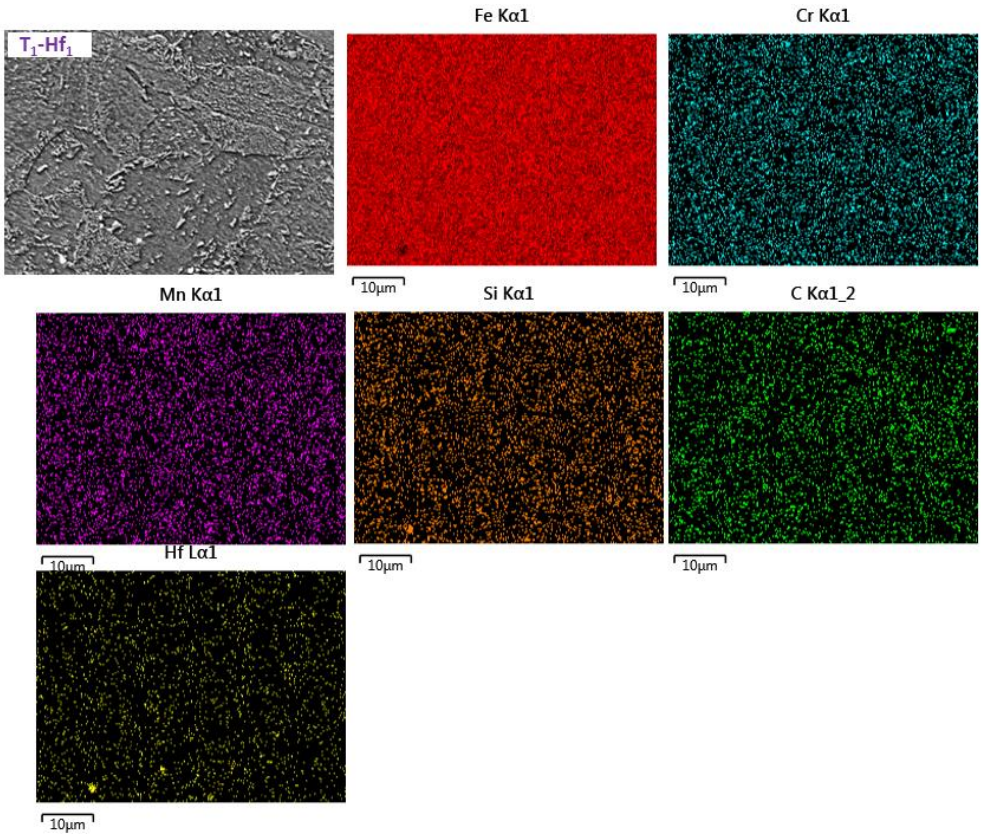

Figure B2- 10: EDS Elemental mapping of T_1-Hf_1

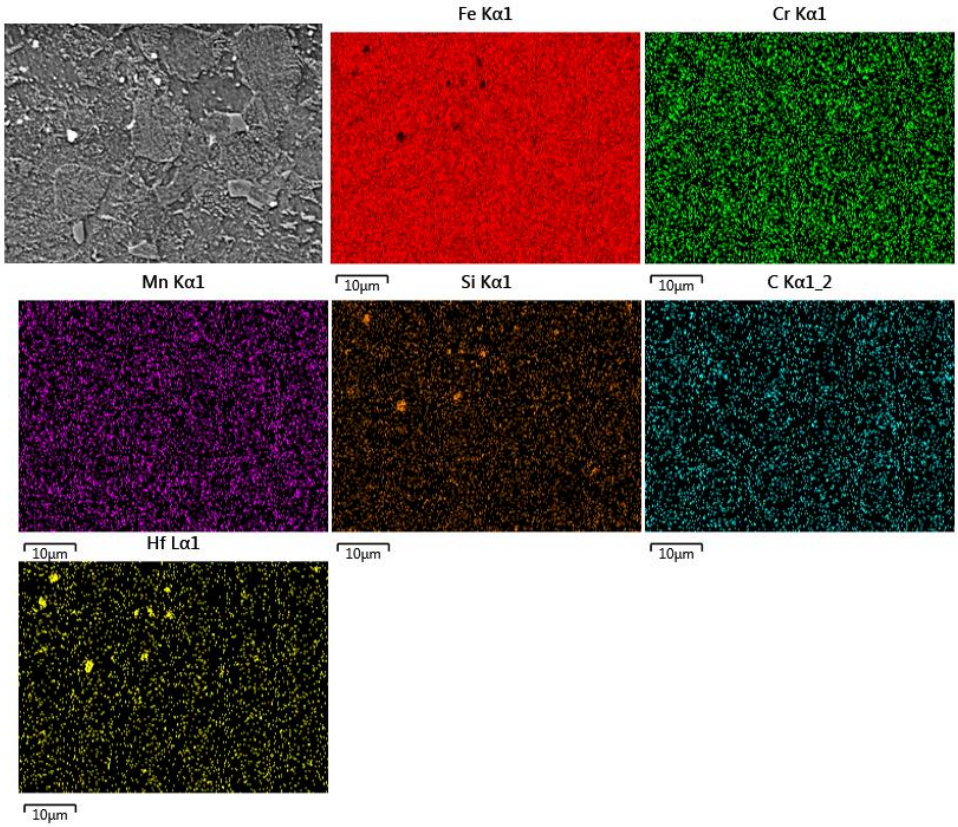

Figure B2- 11: EDS Elemental mapping of T_2-Hf_2

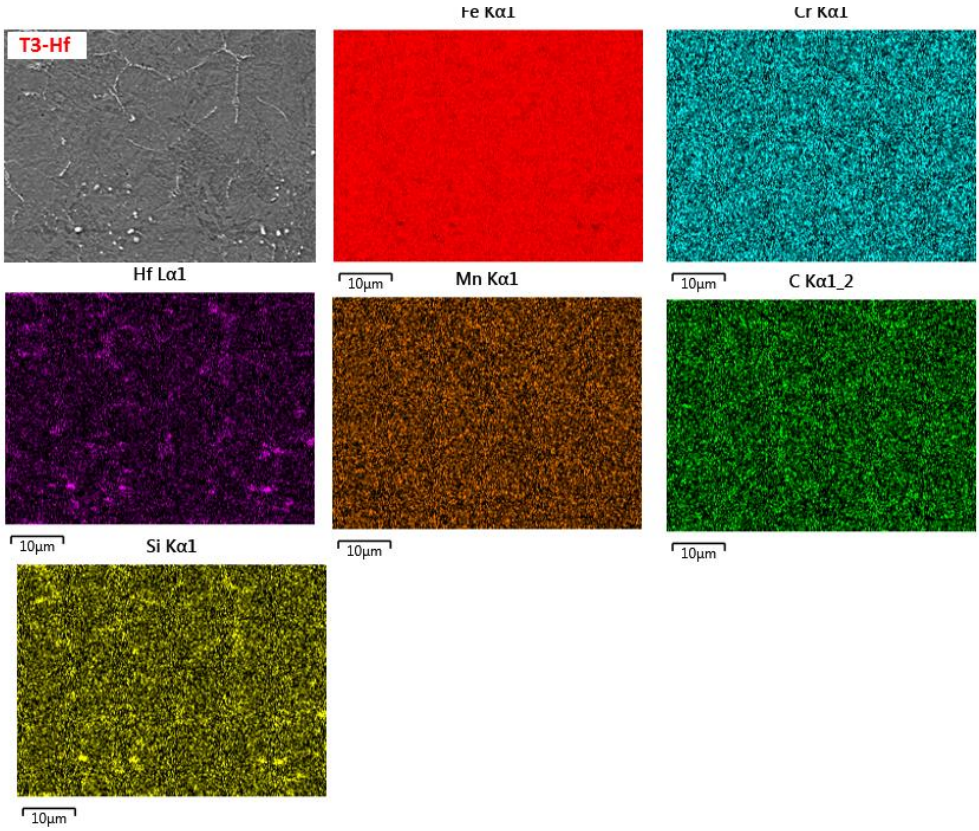

Figure B2- 12: EDS Elemental mapping of T_3-Hf_3

Appendix C1: EDS spectra of corroded alloyed P110 and TN95

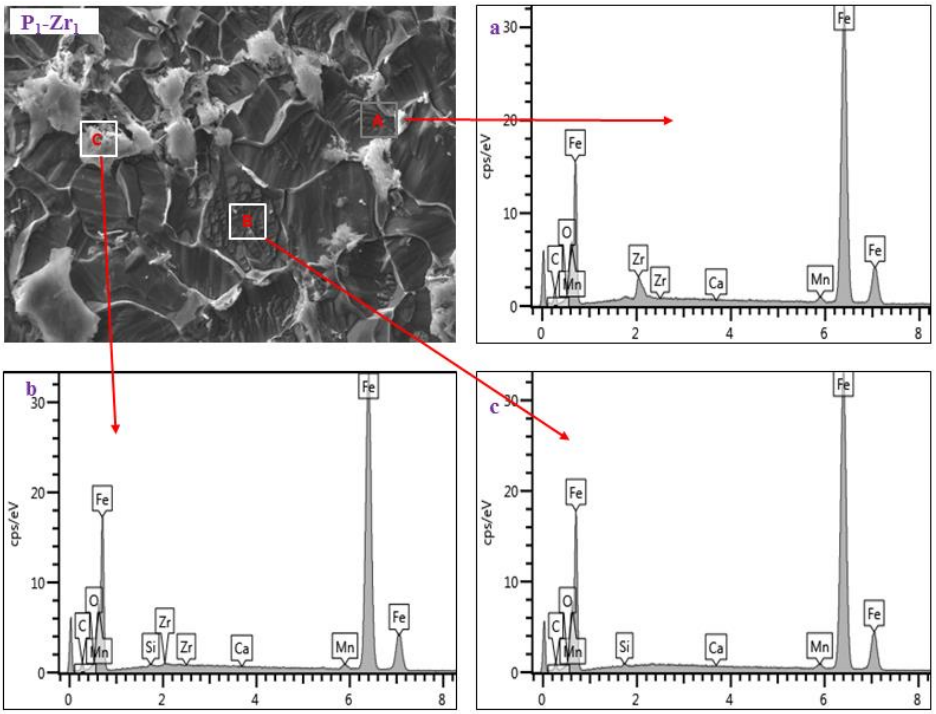

Figure C1- 1: EDS elemental analysis of alloyed specimen P_1-Zr_1 corroded in simulated sea water at 25^0C, pH6.5 and for 24 hours

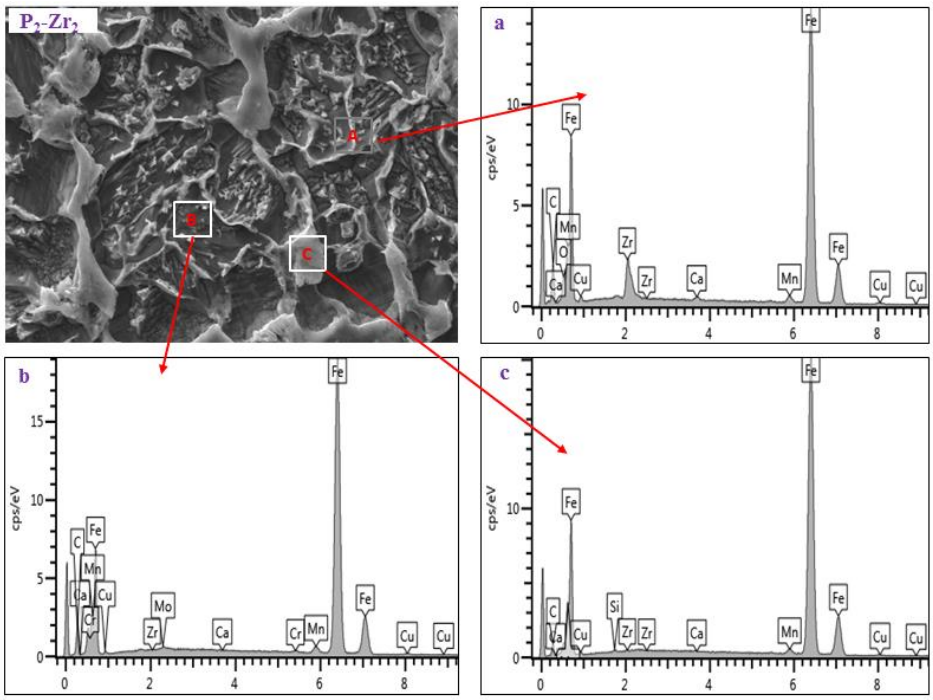

Figure C1- 2: EDS elemental analysis of alloyed specimen P_2-Zr_2 corroded in simulated sea water at 25^0C, pH6.5 and for 24 hours

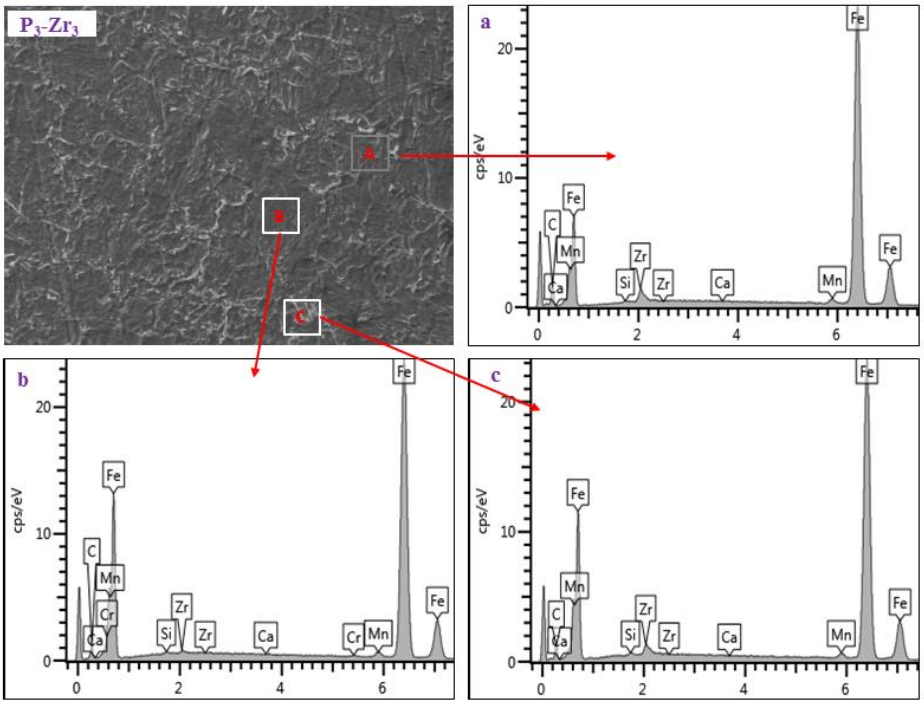

Figure C1- 3: EDS elemental analysis of alloyed specimen P_3-Zr_3 corroded in simulated sea water at 25^0C, pH6.5 and for 24 hours

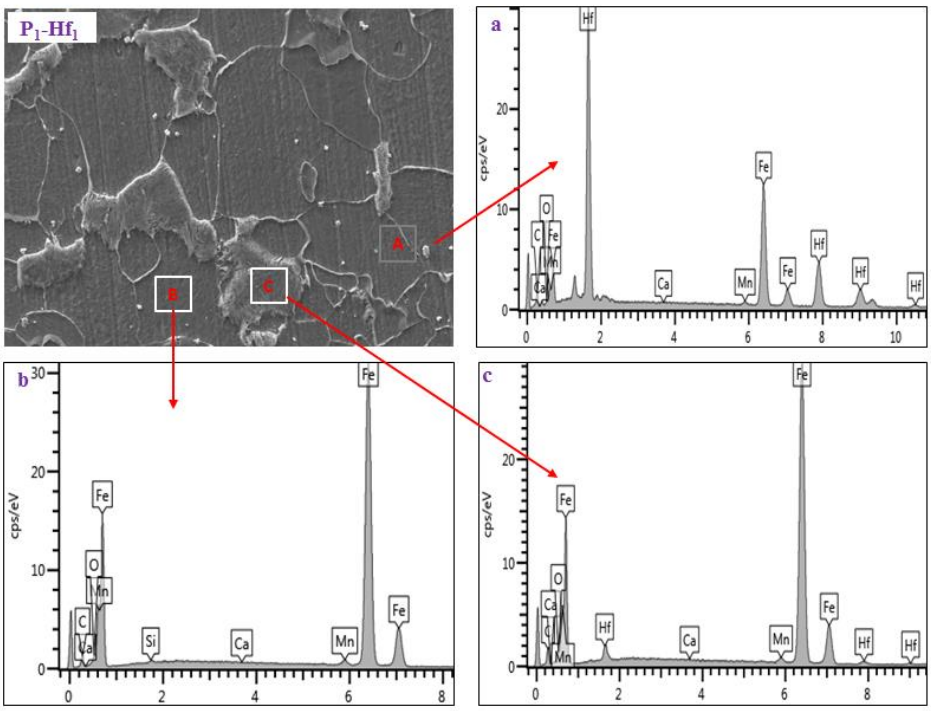

Figure C1- 4: EDS elemental analysis of alloyed specimen P_1-Hf_1 corroded in simulated sea water at 25^0C, pH6.5 and for 24 hours

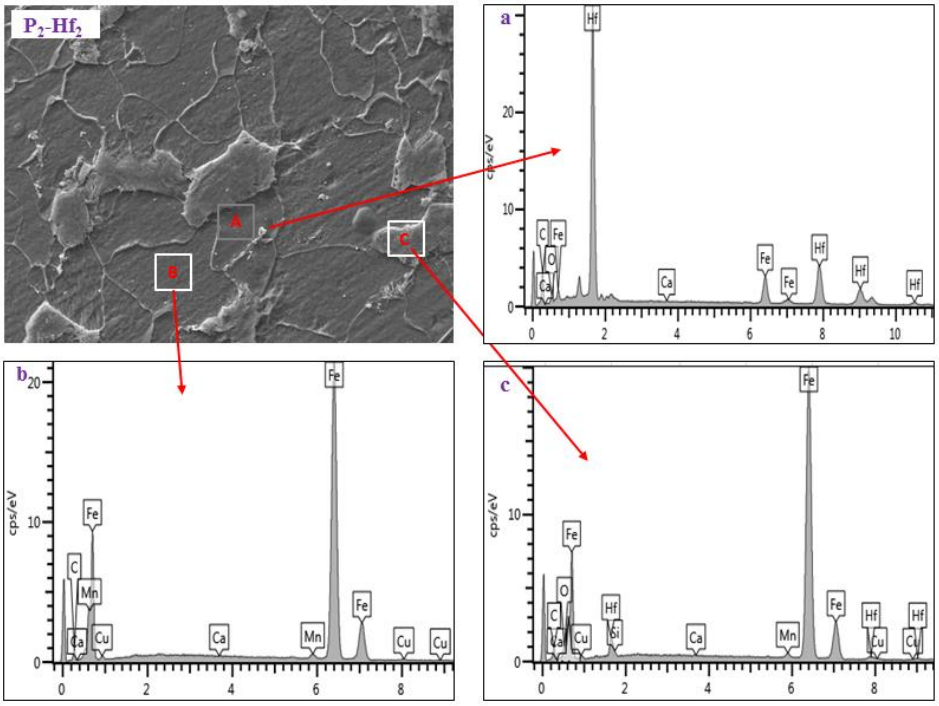

Figure C1- 5: EDS elemental analysis of alloyed specimen P_2-Hf_2 corroded in simulated sea water at 25^0C, pH6.5 and for 24 hours

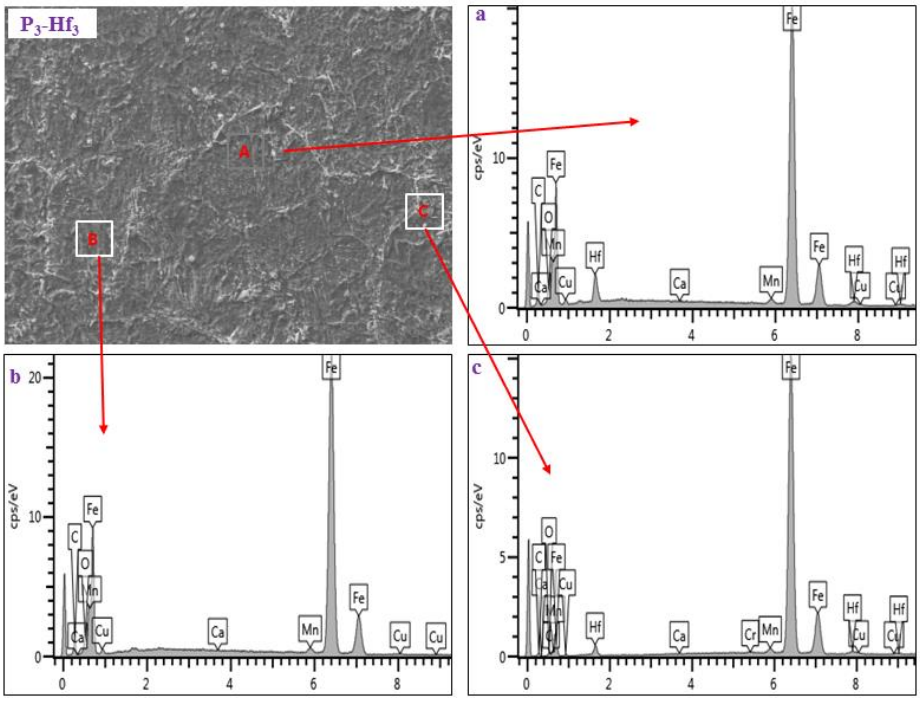

Figure C1- 6: EDS elemental analysis of alloyed specimen P_3-Hf_3 corroded in simulated sea water at 25^0C, pH6.5 and for 24 hours

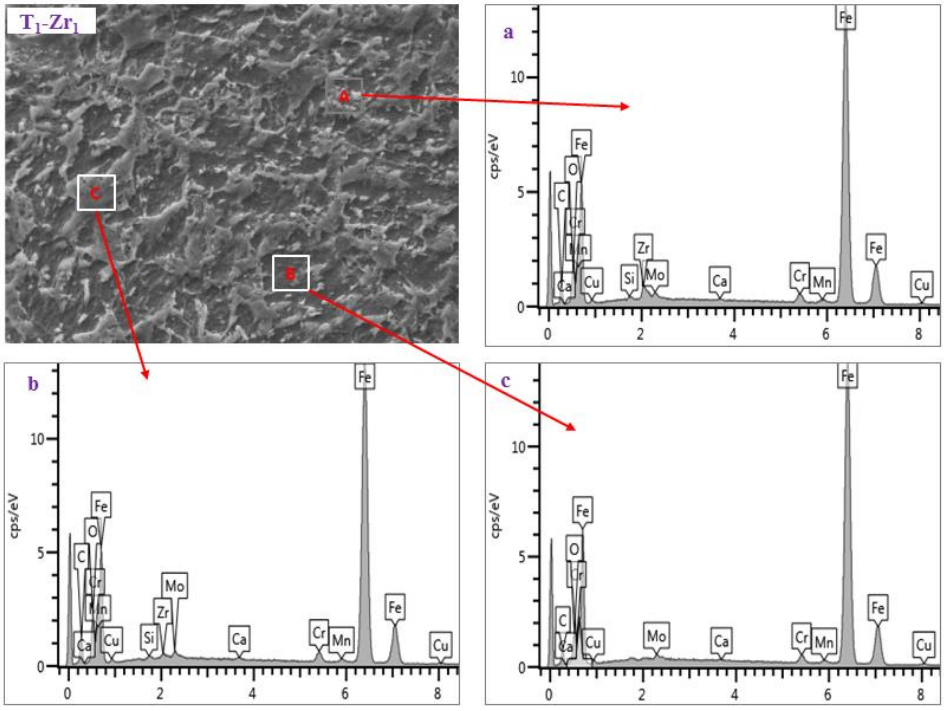

Figure C1- 7: EDS elemental analysis of alloyed specimen T_1-Zr_1 corroded in simulated sea water at 25^0C, pH6.5 and for 24 hours

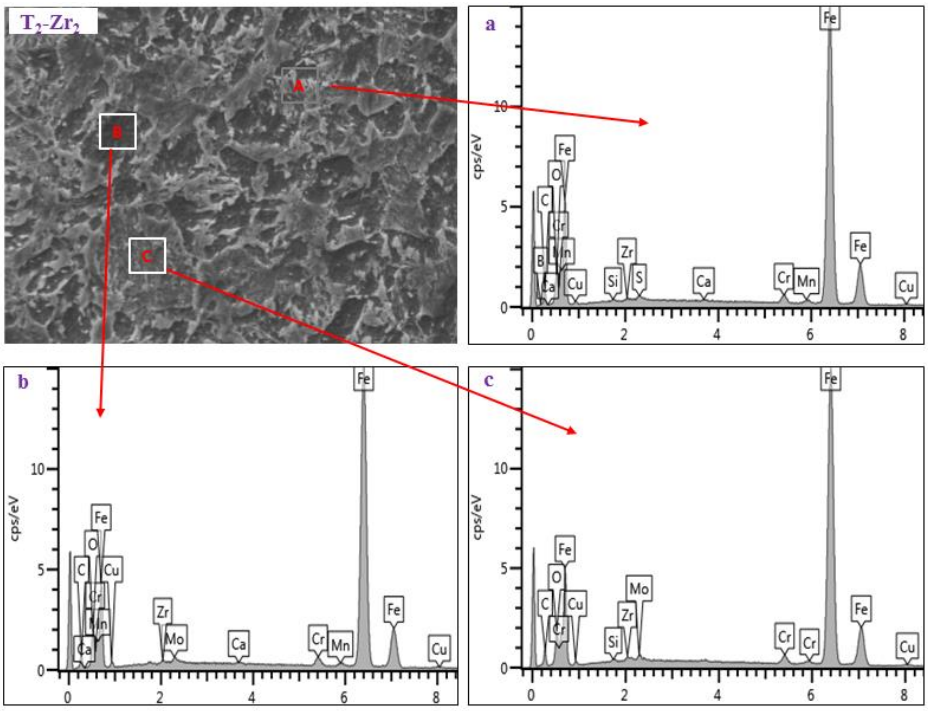

Figure C1- 8: EDS elemental analysis of alloyed specimen T_2-Zr_2 corroded in simulated sea water at 25^0C, pH6.5 and for 24 hours

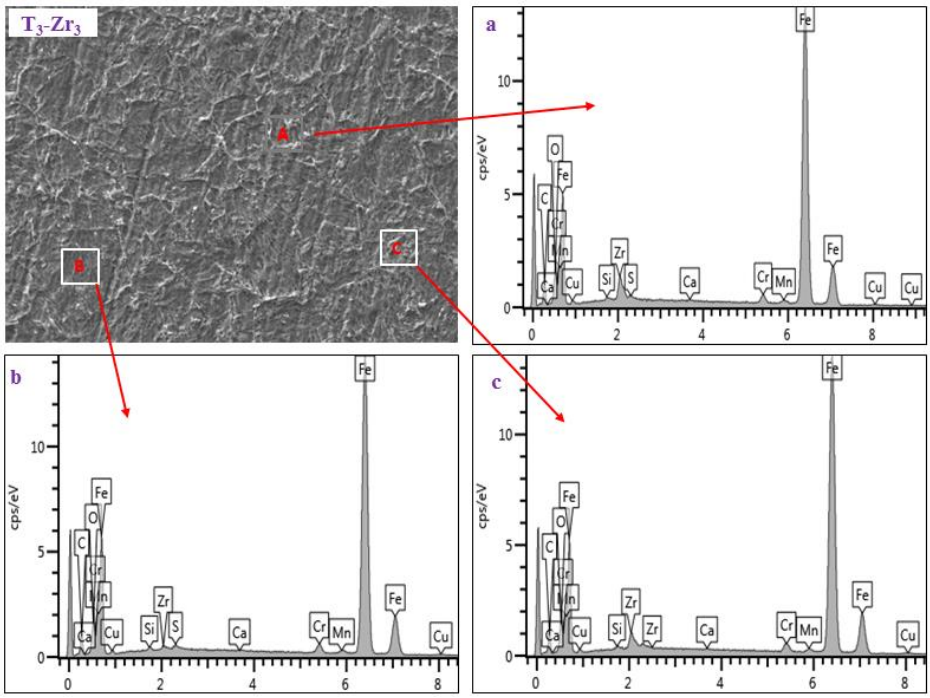

Figure C1- 9: EDS elemental analysis of alloyed specimen T_3-Zr_3 corroded in simulated sea water at 25^0C, pH6.5 and for 24 hours

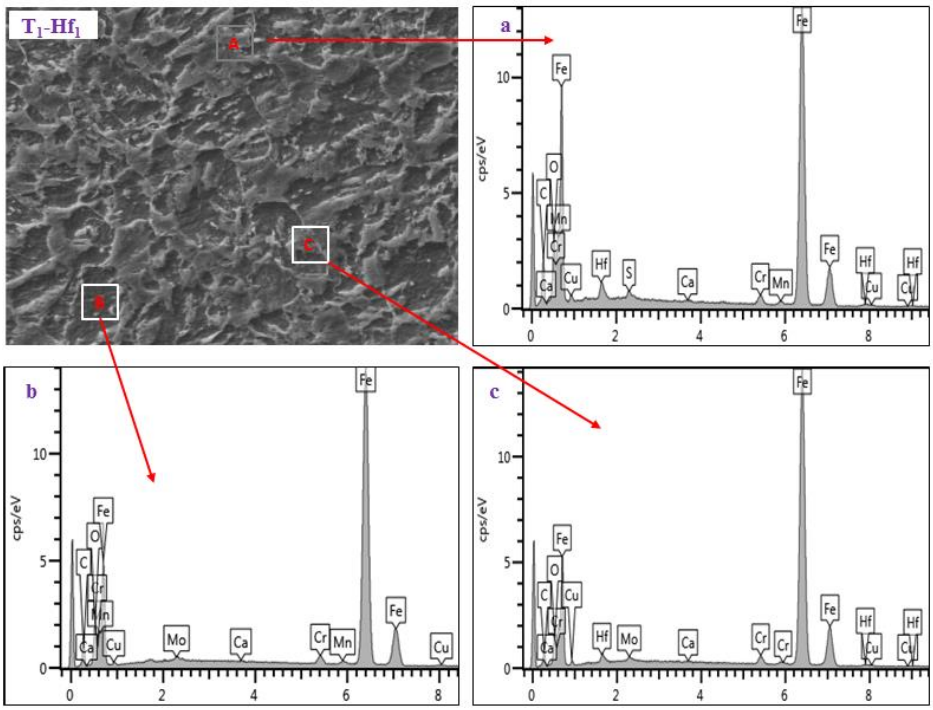

Figure C1- 10: EDS elemental analysis of alloyed specimen T_1-Hf_1 corroded in simulated sea water at 25^0C, pH6.5 and for 24 hours

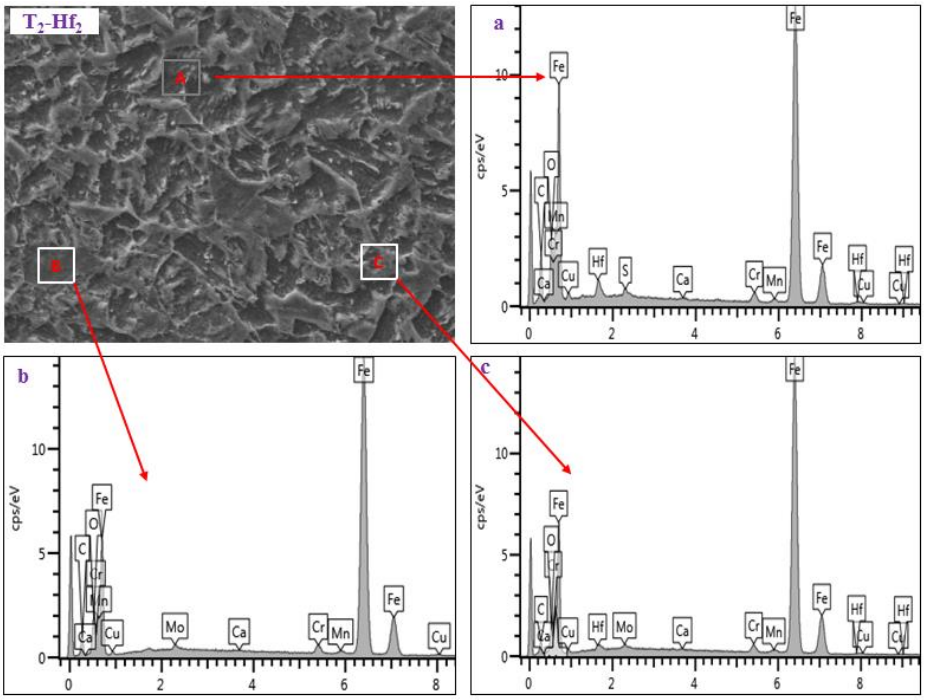

Figure C1- 11: EDS elemental analysis of alloyed specimen T_2-Hf_2 corroded in simulated sea water at 25^0C, pH6.5 and for 24 hours

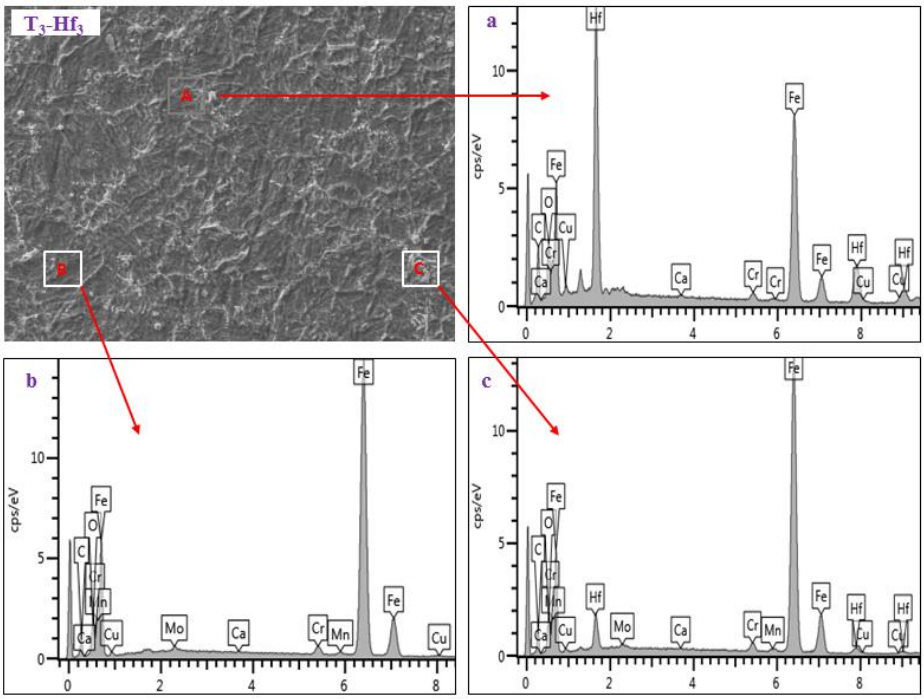

Figure C1- 12: EDS elemental analysis of alloyed specimen T_3-Hf_3 corroded in simulated sea water at 25^0C, pH6.5 and for 24 hours

Appendix D: ASTM grain size No and grain size

Table D- 1: ASTM grain size number and grain size of the specimens alloyed with different amount of Zr and Hf

Specimens	Unalloyed		Alloyed with 0.1 wt%		Alloyed with 0.2 wt%		Alloyed with 0.4 wt%	
	ASTM Grain Size No	Av. Grain Size (µm)	ASTM Grain Size No	Av. Grain Size (µm)	ASTM Grain Size No	Av. Grain Size (µm)	ASTM Grain Size No	Av. Grain Size (µm)
P-Zr	5.57	53.4	7.35	26.7	8.33	22.5	8.41	18.9
P-Hf	5.57	53.4	8.72	15.9	9.34	13.3	9.97	11.2
T-Zr	5.77	44.9	9.2	13.3	9.78	11.2	10.4	7.9
T-Hf	5.77	44.9	9.62	11.3	10.23	9.2	10.72	6.4